



HAL
open science

Study of the structure-function relationship of triarylamine, based supramolecular polymers

Melodie Galerne

► **To cite this version:**

Melodie Galerne. Study of the structure-function relationship of triarylamine, based supramolecular polymers. Organic chemistry. Université de Strasbourg, 2020. English. NNT : 2020STRAF002 . tel-04961321

HAL Id: tel-04961321

<https://theses.hal.science/tel-04961321v1>

Submitted on 21 Feb 2025

HAL is a multi-disciplinary open access archive for the deposit and dissemination of scientific research documents, whether they are published or not. The documents may come from teaching and research institutions in France or abroad, or from public or private research centers.

L'archive ouverte pluridisciplinaire **HAL**, est destinée au dépôt et à la diffusion de documents scientifiques de niveau recherche, publiés ou non, émanant des établissements d'enseignement et de recherche français ou étrangers, des laboratoires publics ou privés.

ÉCOLE DOCTORALE 222

UPR 22 - CNRS

THÈSE présentée par :
Melodie GALERNE

soutenue le : **30 janvier 2020**

pour obtenir le grade de : **Docteur de l'université de Strasbourg**

Discipline/ Spécialité : **CHIMIE SUPRAMOLECULAIRE**

**Study of the Structure – Function
Relationship of Triarylamine-Based
Supramolecular Polymers**

THÈSE dirigée par :

M GIUSEPPONE Nicolas

Professeur, Université de Strasbourg, France

Mme MOULIN Emilie

Docteur, Université de Strasbourg, France


RAPPORTEURS :

M WALTHER Andreas


Professeur, Albert-Ludwigs University of Freiburg, Germany

M AVARVARI Narcis

Docteur, Université de Angers, France



Acknowledgements



First, I would like to express my gratitude to **Professor Nicolas Giuseppone** for giving me the opportunity and honor to be part of his laboratory. For entrusting me with inspiring and exciting research projects, for his guidance and support through these years. On the same occasion I would like to give my thanks to **Doctor Emilie Moulin**, who, together with Nicolas Giuseppone co-directed my thesis.

I'd like to thank the International Research and Training Group for Soft Matter Science (**IRTG SoMaS**), especially **Professor Gunter Reiter** and **Professor Jörg Baschnagel**, for financial support, and for providing me with the extra-ordinary opportunity to be part of this research group. It has helped me develop many indispensable skills (communication, writing, presenting), let me grow in a scientifically divers setting and nourished my curiosity towards other research domains.

My thanks also go towards the jury members, **Professor Andreas Walther** and **Doctor Narcis Avarvari**, who accepted to evaluate my manuscript and PhD defense.

Of course, I am very thankful to **Doctor Andreas Vargas Jentsch**, who has been a tremendous help during these years. For the, sometimes long, discussions we had on various scientific topics, all the explanations and revelations he provided, with sarcasm and humor throughout. I would also like to thank him for reading and re-reading my manuscript, to help me progress and grow as a scientist and as a person.

I would like to express my gratefulness for **Professor Mounir Maaloum**, who works miracles with the AFM, is always ready to hear some of my new ideas, and has taught me how to use the AFM. Thanks to **Doctor Gad Fuks** and **Doctor Marc Schmutz**, for their help with the SEM and TEM, and providing me with the knowledge on how to use them. Thanks to **Doctor Bertand Vilen**, for his help with the EPR. **Nathalie Kyritsakas-Gruber**, for her help elucidating the crystallographic structures. **Doctor Patrick Kekicheff**, for his work at SOLEIL. **Guillaume Fleith**, for the X-ray scattering experiments. **Doctor Thomas Pfohl** and **Christophe Mélar**, for their help with the wave-guiding experiments.

I'd like to thank **Professor Thomas Heiser** and **Doctor Patrick Lévêque** from ICube, for our collaboration and for their help and expertise on the conductivity experiments.

A great thank you to all the technicians of the institute, and especially **Odile Gav**, **Julie Lemoine** and **Marie-Céline Samy-Arlay**, who ensure the labs are working in tip-top order. I would equally like to thank the **atelier mécanique** and **Patrick Allgayer**, who made all my ideas for experimental set-ups

realities. I'd certainly also like to acknowledge the **administrative staff**, both from the ICS and IRTG. Finally, I would like to thank **all the other members of Institute Charles Sadron** for their help. I have spent three wonderful years here thanks to the good atmosphere, and the occasional activities and get-togethers which allowed us all to enjoy ourselves and celebrate together. On that note, I would also like to acknowledge the **BJC**.

My time here would not be the same without all the amazing people I have met and friends made. To my **IRTG fellows**, thank you for the fun we had during the workshops and summer schools, as well as all your help. To **everyone from the lab, both former and current members**, thank you for all the laughs we shared; the very non-scientific discussions; the crazy ideas, games and the occasional nights out. Thank you **Artem**, for all the syntheses performed; protocols written and for helping me getting started. Thank you **Flavio, Joakim** and **Vasily**, my awesome office mates, for your help, advices and jokes. To **Damien, Flavio** and **Yali**, with who I started this adventure: I would like to thank you for these three years in which we surmounted all challenges together. Thank you **Jean-Rémy** and (again) **Joakim**, for helping me with the French language especially. Thank you **Simon, Chris, Jean-Rémy, Chloé, Ting** and **Qing** former members of our group; **Claire**, almost member of our group; **Alexis, Raphael, Lara, Christian, Nicolas, Xuang, Xiaoqin, Chuan** and **Wenzhi**.

I would also like to thank all my friends, either from home: **Brigitte, Daphne, Fabian** and **Gino**, or from Strasbourg: **Jeni** and **Clément, Pauline** and **Hugo, Florian, Lili** and **Antoine, Loïc** and **Cecile, Fifi, Ben** and **Antonin**. Thank you **Adrienne** and **Eloi**, as well as everyone here that has made me feel warm and welcomed me into their family.

A special thanks to **Marvin**, for keeping me *motay*-vated, cooking delicious meals and for always making me laugh. I can't wait for the adventures to come with you by my side.

Finally, I would like to thank my **family**. Dank je **mam** en **pap**, voor jullie constante ondersteuning en aanmoedigingen, zoals alle uren dat jullie aan de telefoon hebben gehangen om me moed in te spreken. Dat jullie me hebben opgevoed met zoveel liefde en nieuwsgierigheid voor de wereld om me heen. Zonder jullie had ik hier nu niet gestaan. Merlin, **broer**, mijn beste vriend, dank je voor alles. Je bent altijd een rots geweest op wie ik kan steunen en alles mee kan delen, zelfs al zitten er wat kilometers tussen ons. **Stéphanie, Emma** en **Rémy**, dank jullie alle drie voor de goede tijden en dat jullie onze familie compleet hebben gemaakt. **Opa, oma** en **mamie** ook zonder jullie was ik nooit zo ver gekomen.

TABLE OF CONTENTS

ABSTRACT	i
RÉSUMÉ EN FRANÇAIS	iii
ABBREVIATIONS AND SYMBOLS	xxviii
GENERAL INTRODUCTION AND OBJECTIVES	xxxii
CHAPTER I. BIBLIOGRAPHY	1
I.1 Physical Properties of Triarylaminines	1
A. Molecular structure of triarylaminines	1
B. Electrochemical properties of triarylaminines	4
i. Electronic structure and redox potentials of triarylaminines	4
ii. Electron and charge transfer in triarylaminines	9
C. Conductivity properties of triarylaminines	13
D. Optical properties of triarylaminines	15
i. Absorption and fluorescence	15
ii. Aggregation Induced Emission with triarylaminines.....	27
I.2 Applications of Triarylaminines.....	30
A. Solar cells	30
i. Triarylaminines in organic solar cells.....	32
ii. Triarylaminines in dye sensitized solar cells	34
iii. Triarylamine in perovskite solar cells.....	36
iv. Triarylamine derivatives as hole transporting layer.....	37
B. Organic light emitting diodes	39
i. Triarylamine derivatives as HTMs in OLEDs.....	41
ii. Triarylamine derivatives as singlet emitters in OLEDs.....	42
iii. Triarylamine derivatives as triplet emitters in OLEDs.....	45
C. Organic field effect transistors.....	46

i. Triarylamine derivatives in OFETS.....	48
ii. Triarylamine polymers.....	48
iii. Small triarylamine molecules	50
D. Water splitting applications.....	53
i. Triarylamines in water splitting applications.....	54
ii. Photocatalytic water splitting	55
iii. Photoelectrochemical water splitting.....	57
E. Xerox processes	59
F. Chemical sensors.....	62
i. Photo-induced electron transfer mechanism.....	62
ii. Electronic energy transfer mechanism.....	64
iii. (Excited state) charge transfer	65
iv. Other mechanisms.....	65
I.3 Supramolecular Chemistry and Supramolecular Polymers.....	66
A. Supramolecular chemistry and self-assembly	66
B. Supramolecular polymers	68
i. Supramolecular polymerization mechanisms	69
ii. Hydrogen bonding	73
iii. Ionic and metal coordination	75
iv. π - π Interactions	76
v. Charge transfer interactions	78
vi. Hydrophobic interactions.....	79
vii. Host-guest interactions	81
C. Supramolecular electronics.....	83
I.4 Physical Properties and Applications of Self-Assembled Triarylamine Structures	85
A. Triarylamines in MOF and COF	85
B. Self-assembled triarylamine monolayers.....	86
C. Supramolecular triarylamine polymers.....	87

i. Mechanism of oxidation induced supramolecular polymerization	88
ii. Diversity in monomeric structures and self-assemblies thereof	93
D. Physical properties of triarylamine self-assemblies	98
i. Electron and charge transfer	98
ii. Conductivity properties	99
iii. Optical properties	101
E. Applications of triarylamine self-assemblies	108
i. Solar cells.....	108
ii. Organic light emitting diodes	109
iii. Organic field effect transistors.....	111
iv. Water splitting applications	112
v. Chemical sensors	113
CHAPTER II SUPRAMOLECULAR ELECTROPOLYMERIZATION	117
II.1 Introduction.....	117
II.2 Bibliography	118
A. Electropolymerization	118
B. Electric-field induced alignment.....	119
i. Electric-field induced alignment of preformed supramolecular systems in organic solvents...	121
ii. Electric-field induced alignment of preformed supramolecular structures in aqueous media.	123
iii. Electric-field induced alignment of in situ self-assembled structures	125
II.3 Results and Discussion	131
A. Synthesis.....	131
B. Supramolecular electropolymerization in presence of electrolytes	131
C. Supramolecular electropolymerization in absence of electrolytes	134
D. Spatially addressed supramolecular electropolymerization and alignment in an electric-field...	135
E. Charge transport in <i>in situ</i> electropolymerized and aligned TAA-C8 supramolecular polymers	141
II.4 Conclusions and Perspectives	144

CHAPTER III. TOWARDS SUPRAMOLECULAR TRIARYLAMINE-BASED PLASMONIC STRUCTURES.....	147
III.1 Introduction	147
III.2 Bibliography	148
A. Plasmonics and the plasmonic effect.....	148
B. Plasmonic coupling.....	149
C. Plasmonic wave-guiding.....	150
D. Characterization techniques	151
E. Organic nanoparticles	156
III.3 Results and Discussion	158
A. Synthesis.....	158
B. Self-assembly and crystallization	158
i. Small TATA-Ac crystals	158
ii. Large TATA-Ac crystals	160
iii. TATA-Ac nanoparticles	167
iv. TATA-C4 nanoparticles	169
C. Redox properties.....	173
D. Plasmonic properties	178
i. Waveguiding.....	178
ii. Plasmonic nanoparticles	181
III.4 Perspectives	183
Towards TATA-Ac plasmonic nanoparticles.....	183
Towards TATA-C4 plasmonic particles	183
III.5 Conclusions	185

CHAPTER IV. ELECTRONIC TRANSPORT IN VARIOUS TRIARYLAMINE SUPRAMOLECULAR POLYMERS	187
IV.1 Introduction	187
IV.2 Bibliography	188
A. Conductivity and charge transport.....	188
B. Charge carrier mobility.....	190
C. Charge transport in various organic supramolecular materials	194
i. Aromatic molecules	196
ii. Sulfur-based heterocycles.....	199
IV.3 Results and Discussion.....	202
A. Synthesis.....	202
B. Triarylamine mono- and trisamide supramolecular polymers.....	202
i. TAA and TATA supramolecular polymers in solution	203
ii. TAA and TATA supramolecular polymers as physical gels	205
iii. Thin films	207
C. Triarylamine trisacetamide crystals.....	208
i. Conductivity of small neutral crystals deposited on OFET substrates.....	208
ii. Conductivity of small and large neutral crystal using conductive-AFM.....	211
C. Triarylamine norbornene supramolecular physical and chemical gels.....	216
i. Conductance of gels.....	216
ii. Local conductivity and charge transport properties.....	219
IV.4 Perspectives	221
A. Application in photovoltaic devices	221
B. Further comparisons between different TAA and TATA supramolecular polymers	221
IV.5 Conclusions	223
GENERAL CONCLUSIONS AND PERSPECTIVES	225
OUTLOOK AND PERSPECTIVES	229
Triarylaminas as potential thermoelectric materials.....	229

100% quantum efficiency OLEDs: chiral triarylamine as spin filter	230
ANNEXES	I
Chapter II.....	I
Chapter III	V
Chapter IV	XIV
MATERIALS AND METHODS	XVII
General procedures	XVII
Chapter II.....	XXII
Chapter III	XXIV
Chapter IV	XXV
Synthesis.....	XXIX
REFERENCES	XLV

ABSTRACT

Triarylamine (TAA) derivatives have been studied in a wide range of scientific and industrial fields, from organic synthesis, characterization of molecular processes and physical properties, to organic electronics. Due to their outstanding properties, they have been incorporated in numerous applications. For example, in Xerography[®], because of their morphological stabilities and photosensitivity; in photovoltaics, OLEDs and OFETs, because of their hole transporting abilities, low ionization potential and adjustable optical and electronic properties; in water splitting, for their reversible redox potential, and in chemical sensing. Ten years ago, our research group discovered a new function for this omnipresent motif: when the TAA core motif is appended with at least one amide function, it is able to self-assemble into supramolecular structures, such as polymers and crystals. The molecules in these self-assemblies are at close enough distances to strongly couple electronically and, per consequence, enhanced electronic and optical properties have been observed.

In this thesis, we continued our research on the electronic and optical properties of triarylamine derivatives to deepen our knowledge on the relationship between TAA molecular structure, their self-assembled architectures and the emerging physical properties, to pave the way towards their integration into organic electronic devices. First, we have demonstrated their bottom-up integration in microelectronic circuitries, using supramolecular electropolymerization. The electric field, used to initiate polymerization, is also responsible for the anisotropic alignment of the fibers between the electrodes.

Then, we investigated the formation and characterization of TAA-based plasmonic structures. We demonstrated that light is able to propagate along TAA crystals up to $\sim 500 \mu\text{m}$. Whereas neutral crystals showed a passive wave-guiding mechanism, oxidized (doped) crystals exhibited an active plasmonic wave-guiding mechanism. The same molecules can also form nanoparticles of different size and shapes, such as spheres and cubes for instance. Preliminary results show that they exhibit plasmonic properties.

Finally, we compared charge transport in various TAA-based supramolecular polymers. The measured conductivities are, for solutions and gels, surprisingly comparable, independent of alkyl chain lengths and number of amide groups. TATAs demonstrate a better stability of their conductive properties than TAAs after oxidation. Furthermore, in thin films, the presence of long side chains reduces the electronic contact of the fibers with each other and with the electrodes. We further discovered that “formally” neutral TATA crystals are able to conduct charges, whereas doping is normally necessary to obtain conductive TAA self-assemblies. Finally, we demonstrated that mechanically enhanced TATA gels, by ROMP, retain their local optical and charge transport properties.

RÉSUMÉ EN FRANÇAIS

Ce manuscrit de thèse de doctorat contient les recherches effectuées pendant trois ans sur le thème de la relation structure - fonction des polymères supramoléculaires à base de triarylamine. L'objectif général était d'approfondir notre compréhension de la relation entre la structure moléculaire des TAA, leurs architectures auto-assemblées et leurs propriétés physiques émergentes, afin d'ouvrir la voie à leur intégration dans des dispositifs électroniques organiques. Le travail est divisé en quatre principaux projets de recherche multidisciplinaires qui comprennent la recherche bibliographique, la synthèse, l'analyse chimique et la caractérisation physico-chimique.

Le premier chapitre du manuscrit constitue d'une recherche bibliographique profond, sur les 1) les propriétés physiques des triarylamine simples; 2) les applications dans lesquelles les triarylamine sont fréquemment utilisées ; 3) la chimie supramoléculaire en général et polymères auto-assemble en spécifique ; 4) les propriétés physiques des triarylamine auto-assembles, ainsi que leur applications.

Le premier projet de recherche avait pour objectif principal de développer le premier véritable processus d'électropolymérisation supramoléculaire. Cela a nécessité une étude détaillée des propriétés électrochimiques du monoamide de triarylamine utilisé et de ses fibres auto-assemblées, dans de multiples conditions, comme la présence d'électrolytes et de solvants de différentes constantes diélectriques. Le processus de polymérisation induite électrochimiquement a été exploité vers l'intégration des polymères résultants aligné entre des microélectrodes.

Dans le second projet, nous avons voulu poursuivre nos travaux antérieurs sur les propriétés plasmoniques des polymères supramoléculaires de triarylamine. Auparavant, nous avons démontré leur caractère plasmonique en *i*) les construisant entre des nanoparticules d'or, où elles fonctionnaient comme des interconnexions plasmoniques ; *ii*) en réalisant des cristaux qui se sont avérés être des guides d'ondes plasmoniques actifs lorsqu'ils étaient à l'état oxydé. Nous avons poursuivi avec ce deuxième système et avons exploré jusqu'à quelle échelle de longueur les plasmons de surface pouvaient se propager le long des cristaux. Ensuite, nous avons voulu examiner si des plasmons de surface localisés pouvaient également être générés. À cet égard, nous avons envisagé la génération et la caractérisation de nanoparticules de triarylamine.

Le projet final visait à caractériser le transport électronique dans divers polymères de triarylamine supramoléculaires en vue de leur éventuelle intégration dans des dispositifs photovoltaïques. Le fait que l'empilement étroit entre les centres d'azote centraux dans les polymères supramoléculaires de triarylamine entraîne un fort couplage électronique avec l'amélioration concomitante des propriétés électroniques et de transport de charge, a été démontré précédemment par la conductivité

exceptionnelle ($5 \times 10^3 \text{ Sm}^{-1}$) des électrons de type métallique dans les fibres de triarylamine construites entre les nano-électrodes. Nous allons ici étudier l'effet que différents substituants à la périphérie de la triphénylamine, qui donnent naissance à des structures auto-assemblées sensiblement différentes, ont sur son transport électronique.

Chapitre I. Bibliographie

Propriétés structurelles des dérivés triarylamine

Merz et Weith ont été les premiers à synthétiser le motif central de la triarylamine (TAA) en 1873.¹ A partir de cette date, différentes voies de synthèse ont été développées et une grande famille de dérivés de TAA, composée de petites molécules discrètes, de (oligo-) polymères et de structures auto-assemblées, a été créée. Le motif central du TAA, presque planar, a un axe de symétrie en C_3 , est hybridé sp^2 et adopte une forme dit *propeller* en raison de la rotation hors plan des cycles phényle (Figure 1A).² Bien que la structure du noyau du TAA soit dictée par un nombre limité de paramètres, la combinaison de ceux-ci affecte la géométrie, la chiralité, les propriétés optiques et de transfert de charge, la conductivité, ainsi que les mécanismes d'émission induite par auto-assemblage ou agrégation.

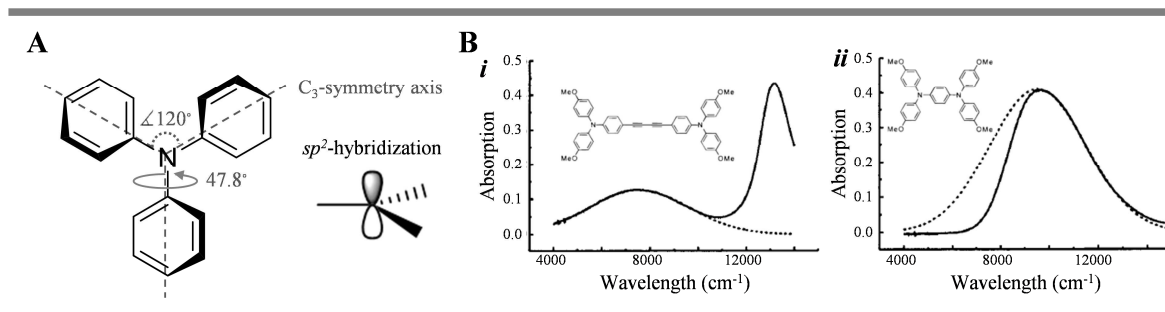


Figure 1. A) Structure moléculaire du motif central de triarylamine ; B) spectres d'absorption Vis-NIR de deux dérivés triarylamine, pris en CH_2Cl_2 + TBAH (lignes pleines) présentant des bandes IV-CT et des ajustements de bandes gaussiennes (lignes pointillées).³

Propriétés électrochimiques des dérivés triarylamine

Les triarylamine oxydés dans leur état de cation radical ($\text{TAA}^{\bullet+}$) subissent généralement une dimérisation vers les composés de tétraphénylbenzidine. Cependant, lorsque il y a des substituants au position *para* sur le periphérie, lorsqu'ils sont volumineux, ou lorsqu'il s'agit d'oligomères de TAA, une oxydation réversible d'un électron en un état cationique (méta-) stable ($\text{TAA} \leftrightarrow \text{TAA}^{\bullet+}$) peut être réalisée. Certains dérivés sont également capables d'une oxydation à deux électrons ($\text{TAA} \leftrightarrow \text{TAA}^{2+}$), mais il s'agit généralement d'un processus irréversible. Il a été démontré que les groupes accepteurs

d'électrons augmentent le potentiel d'oxydation des dérivés du TAA, alors que les groupes donneurs d'électrons le diminuent.^{4,5} De plus, lors de l'oxydation, le motif central du TAA devient plus planar, en raison d'une réduction de l'angle de torsion des cycles phényle, pour mieux stabiliser la charge positive. Cela signifie qu'une oxydation plus facile peut être obtenue en⁴⁻⁶ *i*) stabilisant le cation radical formé par les groupes donneurs d'électrons fonctionnalisés en position *para* ; *ii*) en diminuant l'énergie de réorganisation, qui augmente à la fois pour les groupes accepteurs et donneurs d'électrons ; *iii*) en employant des dérivés présentant de faibles variations d'énergie libre (ΔG°).

L'oxydation peut être réalisée par des moyens chimiques, comme le Cu^{2+} dans l'acétonitrile, mais aussi par des méthodes non invasives, comme la radiation et la photo-oxydation. La photo-oxydation dans les solvants chlorés est notamment avantageuse car l'énergie nécessaire pour provoquer la photo-oxydation est nettement inférieure à leur potentiel d'oxydation.⁷ Ceci est attribué à la réaction simultanée de dissociation de l'attachement des électrons, générant un anion chlorure et un radical dichlorométhyle dans le chloroforme.

Propriétés de transfert d'électrons et de charges des dérivés triarylamine

Les dérivés de triarylamine sont susceptibles d'avoir d'excellentes propriétés de transfert d'électrons et de charges en raison⁸ *i*) de la présence d'un centre redox de l'azote dans le motif central du TAA ; *ii*) des états séparés de charge peuvent être facilement obtenus en raison de leur faible potentiel d'ionisation ; *iii*) ils présentent de grands coefficients d'extinction ; *iv*) les états séparés de charge ont une longue durée de vie en raison de la stabilité des états radicaux ; *v*) ils ont de faibles énergies de réorganisation, car seuls de petits changements géométriques des centres redox se produisent pendant le transfert d'électrons et le transfert des charges. Les processus de transfert d'électrons et de charges ont été largement étudiés à l'aide de dérivés du triarylamine, car leur caractérisation est relativement facile. Le TAA et le TAA^{+} ont tous les deux des bandes d'absorption caractéristiques qui sont bien séparées. Cependant, bien que les dimères TAA soient d'excellents candidats, c'est la nature de l'unité de liaison qui affecte principalement le comportement de transfert d'électrons (Figure 1B).

Propriétés de conductivité des dérivés triarylamine

L'atome d'azote du motif central du TAA est de nature à donner des électrons. De plus, en raison de leurs faibles potentiels d'ionisation et de leurs états radicaux stables avec de grands coefficients d'extinction, les triarylamine donnent naissance à des matériaux transporteurs de trous avec d'excellentes conductivités. La conductivité des dérivés triarylamine peut être améliorée par des adaptations de sa structure moléculaire et par un dopage de type *p*.

Propriétés optiques des dérivés triarylamine

Les triarylamines neutres possèdent une bande d'absorption intense proche de 300 nm, correspondant à une transition $\pi-\pi^*$ d'un électron localisé sur les anneaux phényles (Figure 2Bi).⁴ Les triarylamines oxydés présentent trois bandes d'absorption (Figure 2Bii).^{4,9} La première, qui est également la plus intense, se situe autour de 670-730 nm. La deuxième est située autour de 570-630 nm. La troisième bande d'absorption se situe autour de 350 nm. Lorsqu'ils sont oxydés d'avantage jusqu'à leur état di-cationique, la bande d'absorption autour de 670-730 nm disparaît tandis qu'une nouvelle bande d'absorption autour de 520 nm augmente en intensité. Grâce à la photo spectroscopie, il a été démontré que toutes les solutions radicales sont stables pendant plusieurs semaines et qu'elles sont 100% récupérables.

En solution, les triarylamine neutres sont fluorescents (émission de 382 à 532 nm). Cependant, leur émission diminue de façon linéaire avec la concentration des cations radicaux présents.¹⁰ À l'état agrégé, les triarylamines neutres conservent leur fluorescence. L'émission peut même augmenter en intensité car la forme *propeller* du motif central empêche les interactions $\pi-\pi$ d'empilement et limite le mouvement intramoléculaire. C'est un phénomène connu sous le nom d'émission induite par agrégation. Les TAA oxydés, en revanche, restent non fluorescents à l'état agrégé.

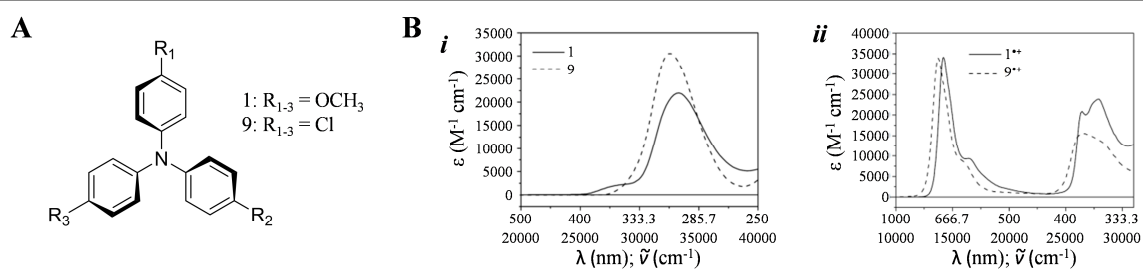


Figure 2. Structure moléculaire du motif central de triarylamine plus les groupements R_{1-3} sur la périphérie ; B) spectres d'absorption des molécules 1 et 9 à l'état neutre (i) et du cation radical (ii) pris dans CH_2Cl_2 .⁴

Applications des dérivés triarylamine

En raison de leurs propriétés exceptionnelles, les triarylamines ont été incorporées dans de nombreuses applications. Dans l'industrie, ils sont utilisés dans les procédés Xerographic[®], comme ceinture de photorécepteurs photosensibles, en raison de leur grande stabilité morphologique et de leur photosensibilité.

Ils sont également largement utilisés dans le secteur photovoltaïque, les diodes électroluminescentes organiques (OLED) et les transistors organiques à effet de champ (OFET), en raison de leurs capacités de transport de trous, de leur faible potentiel d'ionisation et de leurs propriétés optiques et électroniques réglables.

Autres applications des triarylamines peuvent être trouvées dans la séparation de l'eau, en raison de leur potentiel d'oxydoréduction réversible, et la détection chimique, en raison de leurs propriétés optiques et de transport d'électrons et de charges.

Polymères supramoléculaires de triarylamine

Il existe différentes structures auto-assemblées de dérivés de la triarylamine. Les polyèdres organo (métalliques)¹¹ et les cadres métallo-organiques (MOF)¹² représentent la première classe d'auto-assemblages ayant incorporé des dérivés triarylamine dans leur structure. La deuxième classe de structures auto-assemblées qui sont construites avec des dérivés triarylamine sont les monocouches auto-assemblées (SAM).¹³ La troisième et dernière classe de structures de triarylamines auto-assemblées a été découverte il y a une décennie dans notre groupe de recherche. Lorsqu'au moins une fonction amide est présente sur la périphérie de la triarylamine, les triarylamines sont capables de s'auto-assembler en polymères supramoléculaires (**Figure 3AB**).¹⁴ La polymérisation supramoléculaire des triarylamines ouvre la possibilité de combiner ses propriétés physiques, telles que la photosensibilité, l'électrochimie, la photoconductivité et le transport des charges, avec des architectures supramoléculaires contrôlées, pour obtenir des matériaux réactifs et fonctionnels qui pourraient éventuellement améliorer les performances des applications.

Le processus d'auto-assemblage des monoamides de triarylamine (TAA) se déroule en 4 étapes (**Figure 3C**).¹⁵ Tout d'abord, une quantité catalytique de molécules est oxydée dans son état cationique radical (**Figure 3Ci**), afin de déclencher une polymérisation supramoléculaire. Ceci est généralement obtenu par photo-oxydation dans des solvants chlorés, tels que le chloroforme ou le tétrachloroéthane. Cependant, l'oxydation peut également être réalisée par des oxydants chimiques (par exemple par TBQ ou des vapeurs d'I₂) ou par ensemencement. Un noyau à transfert de charge est alors formé entre les dimères TAA^{•+} – Cl⁻, dans un arrangement en double colonne impliquant des liaisons hydrogène (**Figure 3Cii-vi**). À ce noyau, des monomères triarylamines neutres peuvent s'ajouter (**Figure 3Cvii**). Enfin, de grands faisceaux de polymères supramoléculaires sont formés par des agrégations secondaires qui ont lieu sous l'effet des forces de van der Waals.

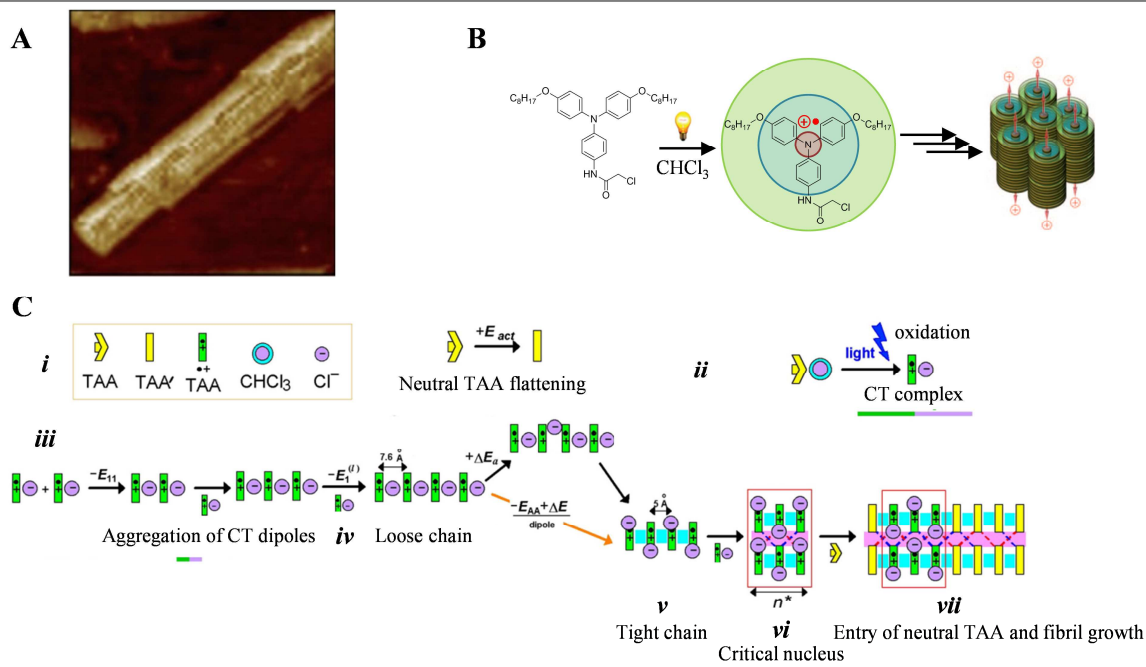


Figure 3. A) Image AFM haute résolution d'un polymère supramoléculaire de triarylamine monoamide; B) représentation schématique simplifiée du processus d'auto-assemblage qui a lieu après la photo-oxydation de monomères neutres de triarylamine ; C) représentation schématique détaillée du processus d'auto-assemblage de triarylamine monoamide.^{14,15}

Le processus d'auto-assemblage des triarylamine trisamides (TATAs) diffère de la polymérisation supramoléculaire des triarylamine monoamides de plusieurs façons (**Figure 4**).¹⁶ Tout d'abord, en raison des fortes liaisons triples d'hydrogène, les TATAs s'auto-assemblent plus facilement et rapidement. Les polymères supramoléculaires oxydés peuvent être obtenus par photo-oxydation dans des solvants chlorés, et les polymères supramoléculaires neutres dans des solvants organiques apolaires appropriés (par exemple, l'acétonitrile et le toluène). Une deuxième conséquence de la triple liaison hydrogène est que le noyau s'assemble maintenant dans un arrangement mono colonnaire. Troisièmement, des structures hélicoïdales sont formées.

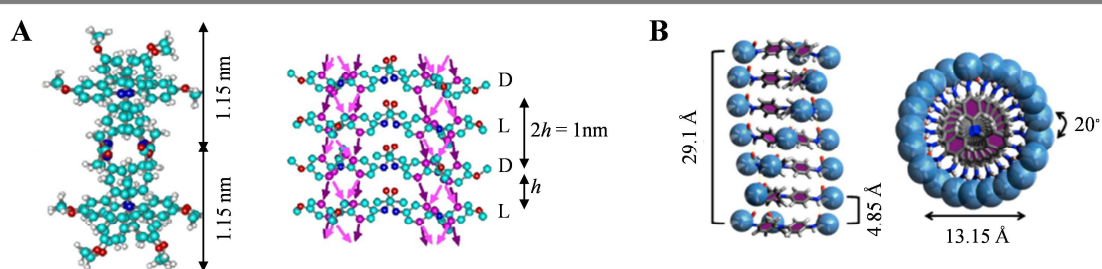


Figure 4. A) Vue de dessus (gauche) et de côté (droite) de l'auto-assemblage supramoléculaire proposé pour les polymères supramoléculaires triarylamine monoamide dans une disposition en double colonne B) vue de côté (gauche) et de dessus (droite) de l'auto-assemblage supramoléculaire proposé pour les polymères supramoléculaires triarylamine trisamide dans une disposition hélicoïdale en mono colonne, telle qu'elle résulte des calculs de DFT.^{15,16}

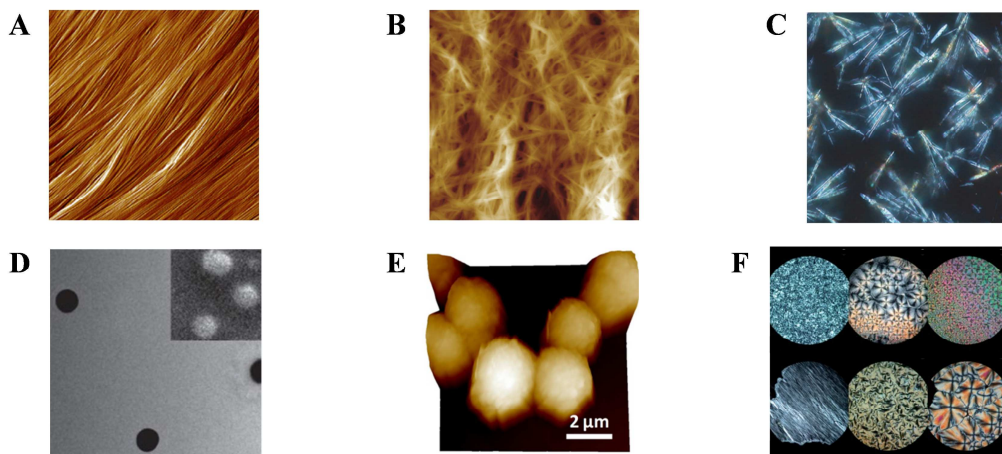


Figure 5. Différentes structures supramoléculaires qui peuvent être obtenues pour les triarylamines mono- et tris-amides. A) polymères supramoléculaires de triarylamine trisamides en solution¹⁶ ; B) polymères supramoléculaires de triarylamine trisamides formant un gel physique¹⁶ ; C) cristaux de triarylamine triacétamide¹⁷ ; D) complexes de coordination homoleptiques TAA-terpyridine zinc formant des nanoparticules¹⁸ ; E) auto-assemblages TAA-fullerène formant des bâtonnets courts qui s'agrègent en sphères¹⁹ ; F) film mince de dérivés de TAA-gallate présentant des propriétés de cristaux liquides.²⁰

Les mono et trisamides de triarylamine sont capables de former une gamme variée de structures supramoléculaires (Figure 5). En général, ils forment des polymères supramoléculaires, soit en solution, soit sous forme de gel.¹⁶ En fonction de la longueur des chaînes alkyles, placées à la périphérie de la triarylamine, on obtient des polymères mous ou des structures plus rigides, mais on peut aussi former des cristaux dans le cas des groupes terminaux acétamides.¹⁷ En outre, des nanoparticules ont été réalisées en utilisant des interactions de coordination supplémentaires du zinc,¹⁸ et selon l'intensité lumineuse, des fibres ou des bâtonnets sont formés pour les triarylamines fonctionnalisées par le fullerène.¹⁹ Elles peuvent également former des cristaux liquides.²⁰ Le dénominateur commun entre ces structures est que les centres d'azote sont étroitement empilés et que les monomères peuvent se coupler électroniquement. Lors de l'oxydation, les cations radicaux sont ainsi délocalisés sur toute la structure supramoléculaire, ce qui conduit à des propriétés physiques nouvelles et améliorées (Figure 6).

Par exemple, la conductivité des polymères supramoléculaires de triarylamine, mesurée entre deux électrodes en or espacées de 80 nm, a un caractère métallique et ne peut être égalée que par des nanotubes de carbone.²¹ En outre, il a été démontré que les polymères supramoléculaires TAA agissent comme des interconnexions plasmoniques lorsqu'ils sont cultivés entre des nanoparticules d'or.²² Leur caractère plasmonique a également été mis en évidence par les cristaux de trisacétamide, qui agissent comme des guides d'ondes plasmoniques.¹⁷ Enfin, les triarylamines peuvent également être construites comme des canaux de membranes artificielles.²³

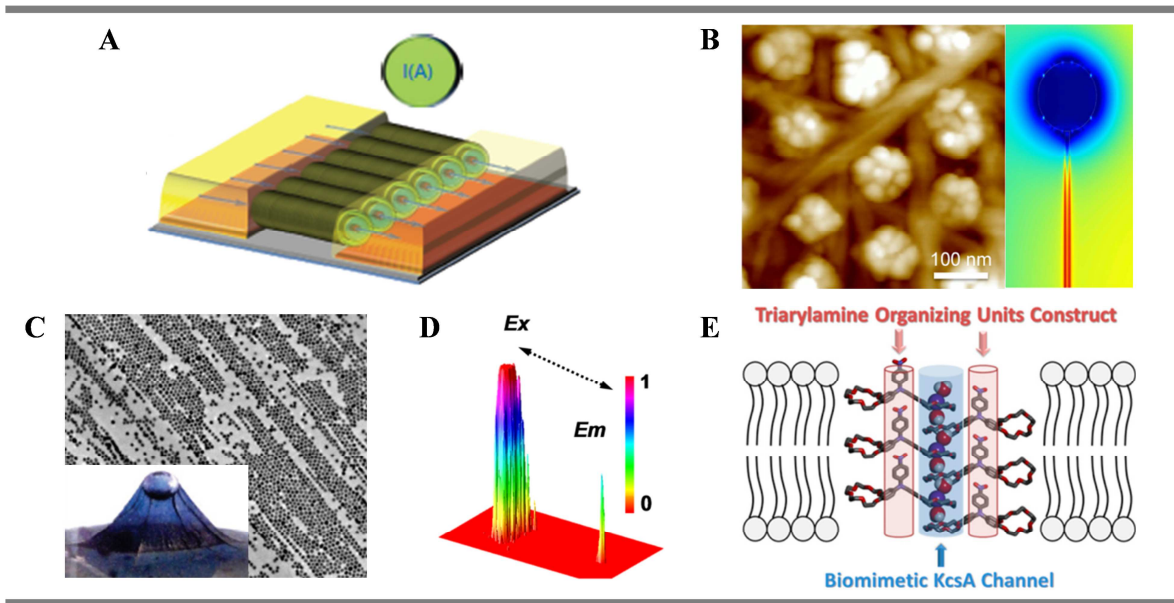


Figure 6. A) Représentation schématique de la construction de polymères supramoléculaires TAA entre des électrodes métalliques par *drop casting* d'un solution dans l'obscurité et exposition ultérieure à un rayonnement lumineux tout en appliquant un Ef^{21} ; B) images d'un réseau hybride de polymères supramoléculaires TATA-C12 et des nanoparticules d'or comme interconnexions plasmonique²² ; C) film hybride (Au NP : TATA-C12) formé à une interface liquide-liquide de l'eau chloroformé après auto-assemblage de TATA-C12 induit par la lumière et après centrifugation à 1000 G²⁴ ; D) représentation 3D, obtenue à partir des images de microscopie, de l'intensité lumineuse pendant le guidage des ondes le long du cristal TATA-Ac¹⁷ ; E) représentation schématique des canaux artificiels de potassium, construite par TAAs, dans un membrane phospholipidiques.²³

Chapitre II. Electropolymerisation supramoléculaire

Dans ce premier chapitre de recherche nous avons étudié la polymérisation *in situ* d'un monoamide de triarylamine, fonctionnalisé avec des chaînes alkyles à huit atomes de carbone (TAA-C8, **Figure 7A**), entre des électrodes. Afin d'obtenir une nucléation adressée dans l'espace et une orientation optimale à longue distance des polymères supramoléculaires, nous avons développé un nouveau procédé d'électropolymérisation supramoléculaire. L'alignement macroscopique des polymères supramoléculaires a été démontré en utilisant des microélectrodes de différentes géométries. Ce projet de recherche, publié dans *Angew. Chem. Int. Ed.* **2018**, *57*, 3796-3805, est le résultat d'une collaboration entre Dr T. Ellis (ancien chercheur post-doctoral dans le groupe SAMS), Dr J. J. Armao IV (ancien doctorant dans le groupe SAMS), Dr A. Osypenko (ancien doctorant dans le groupe SAMS) et Dr D. Martel (CR à l'ICS).

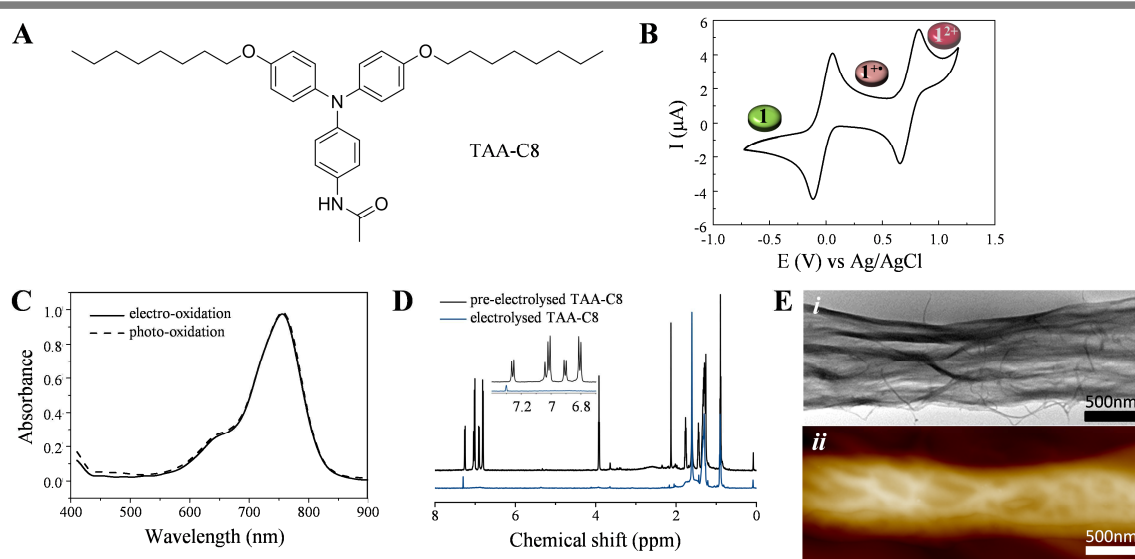


Figure 7. A) Structure moléculaire du TAA-C8 ; B) voltamogramme cyclique d'une solution TAA-C8 de 0,1 mM en TCE en présence de 100 mM de TBAPF6 enregistrés à une vitesse de balayage de 100 mVs⁻¹ ; C) spectres d'absorption normalisés des solutions 0.1 mM TAA-C8 dans du TCE en présence de 100 mM TBAHPF électro- et photo-oxydés; D) des spectres RMN ¹H pris avant et après l'électrolyse pour une solution de TAA-C8 dans du TCE-d2 maintenue à 25 V pendant 30 minutes, en l'absence d'électrolytes ; E) des images TEM (i) et AFM (ii) de polymères supramoléculaires formés par un processus de polymérisation supramoléculaire déclenché électrochimiquement.

Nous avons d'abord cherché à savoir si le TAA-C8 pouvait s'auto-assembler en polymères supramoléculaires par un déclencheur électrochimique. En présence des contre ions et dans des solvants chlorés (chloroforme et tétrachloroéthane), une électro-oxydation réversible est possible, comme a été démontré par CV (**Figure 7B**). La photo spectroscopie et la spectroscopie RMN ¹H, réalisées sur des solutions électro-oxydées, ont donné des spectres qui se sont révélés identiques à ceux obtenus après la photo-oxydation, ce qui indique que la polymérisation supramoléculaire a lieu

après l'électro-oxydation (Figure 7C-D). Cela a été prouvé par la visualisation des polymères supramoléculaires par microscopie TEM et AFM (Figure 7E).

Le processus d'électropolymérisation a ensuite été étudié en l'absence des contre ions, et en utilisant un solvant à faible constante diélectrique (l'heptane), afin de pouvoir aligner les polymères supramoléculaires sur de plus longues distances. Dans ces conditions, en utilisant une cellule électrochimique ITO et à un champ électrique de $1 \times 10^7 \text{ V}\cdot\text{m}^{-1}$, nous avons montré que *i*) la formation de polymères supramoléculaires n'est pas déclenchée par une transition sol-gel et *ii*) un contact électrique direct est nécessaire pour une polymérisation supramoléculaire complète. Cela indique que, même sans électrolyte, le contact direct entre le TAA-C8 et l'électrode, dans des champs électriques élevés, crée une surface d'ensemencement oxydée à partir de laquelle des polymères supramoléculaires TAA neutres peuvent se développer. Ainsi, nous avons atteint le premier objectif du projet : la nucléation adressée spatialement.

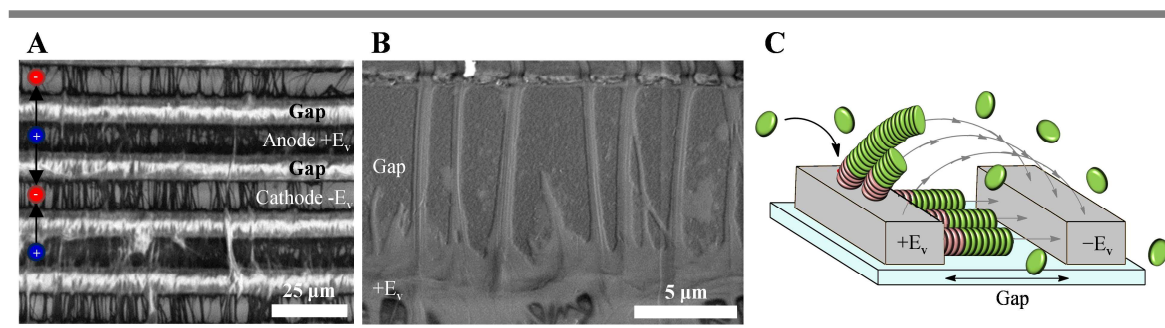


Figure 8. A) Image MEB d'une electrode interdigitées après *drop casting* d'une solution de 5 mg/mL de TAA-C8 en présence d'un champ électrique de $1,25 \times 10^7 \text{ V}\cdot\text{m}^{-1}$; B) Image MEB d'une electrode interdigitées après *drop casting* d'une solution de 2 mg/mL de TAA-C8 en présence d'un champ électrique de $1,25 \times 10^7 \text{ V}\cdot\text{m}^{-1}$; C) Représentation schématique en 3D du processus d'électropolymérisation supramoléculaire se produisant entre les electrodes interdigitées. Les ovales vert et rouge représentent respectivement le TAA-C8 et le TAA-C8**

Ensuite, nous avons étudié le deuxième objectif de ce projet de recherche : l'orientation à longue distance de polymères supramoléculaires entre des électrodes interdigitées de géométries différentes. Des échantillons ont été préparés par *drop casting* d'une solution de 5 mg/mL de TAA-C8 (chauffée à 60 °C et refroidie à 30 °C) sur les électrodes interdigitées tout en appliquant un champ électrique continu. Le champ électrique a été coupé après l'évaporation du solvant. Des expériences de contrôle ont démontré que: 1) la gélification n'a pas lieu pendant la durée de l'évaporation du solvant ; 2) les solutions ne doivent pas être refroidies en dessous de la température de gélification, car même après réchauffement, les fibres restent en suspension ; 3) la réorientation des fibres par un champ électrique, après enchevêtrement, n'est pas possible. Ainsi, selon le protocole décrit, la polymérisation supramoléculaire ne se produit pas par d'autres effets que l'électropolymérisation. Le champ électrique minimal requis pour induire l'électropolymérisation est de $1 \times 10^6 \text{ V}\cdot\text{m}^{-1}$. L'alignement des polymères

supramoléculaires a commencé à se produire à $5 \times 10^6 \text{ V}\cdot\text{m}^{-1}$ et s'est avéré optimal à un champ électrique de $1,25 \times 10^7 \text{ V}\cdot\text{m}^{-1}$ (Figure 8A).

À des concentrations plus faibles (2 mg/mL), on obtient des polymères supramoléculaires isolées qui couvrent la distance entre les électrodes (Figure 8B). A partir de ces échantillons, on a pu observer que la nucléation commence toujours à l'anode, les fibres se développant vers la cathode, en suivant les lignes des champs électriques. De plus, un dépôt de matériaux amorphe est visible sur la cathode, ce qui prouve qu'aucune oxydation ni polymérisation n'a lieu à cet endroit.

À partir de ces expériences et de la visualisation *in situ* du processus de nucléation/croissance, nous proposons le mécanisme suivant (Figure 8C) : *i*) les TAA en solution subissent une électro-oxydation et se transforme dans leur forme de cation radical (TAA^+) lorsqu'ils sont en contact direct avec l'anode ; *ii*) des complexes de transfert des charges forment des noyaux sur l'anode, formant une surface d'ensemencement ; *iii*) des TAA neutres s'empilent sur les noyaux ; *iv*) les polymères supramoléculaires croissent dans la direction du champ électrique vers la cathode.

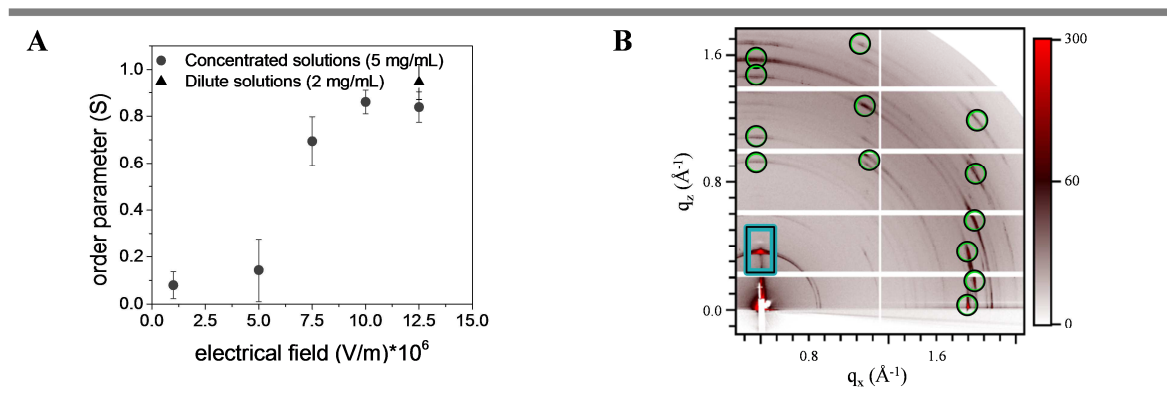


Figure 9. A) tracé du paramètre d'ordre S en fonction de l'intensité du champ électrique appliqué (points : [TAA-C8] = 5 mg/mL ; triangle : [TAA-C8] = 2 mg/mL). B) Carte GIWAXS d'une goutte de film TAA-C8 de 2 mg/mL coulée sur un IDE 10 μm sous un champ électrique continu de $1,25 \times 10^7 \text{ V}\cdot\text{m}^{-1}$ appliqué. Le faisceau de rayons X est focalisé perpendiculairement aux polymères supramoléculaires à $9,913^\circ$. Les cercles verts indiquent les pics de diffraction caractéristiques de la structure auto-assemblée des polymères supramoléculaires. Le carré bleu indique l'alignement des polymères le long du champ électrique.

La qualité de l'alignement a été évaluée par 1) calcul du paramètre d'ordre ; 2) la diffusion des rayons X à grand angle à incidence rasante (GIWAXS). Des paramètres d'ordre moyens de $0,94 \pm 0,08$ et $0,87 \pm 0,09$ ont été calculés, pour les polymères supramoléculaires simples qui couvrent la distance entre les électrodes (2 mg/mL) et les fibres simples qui couvrent la cathode (5 mg/mL) respectivement, ce qui indique une très haute qualité de l'alignement qui n'est pas affectée par la densité des polymères supramoléculaires présentes (Figure 9A). Les expériences GIWAXS confirment la présence des polymères supramoléculaires d'une architecture supramoléculaire hautement

ordonnée, et indiquent également que les polymères sont alignés le long des lignes de champs électriques avec un ordre élevé (Figure 9B).

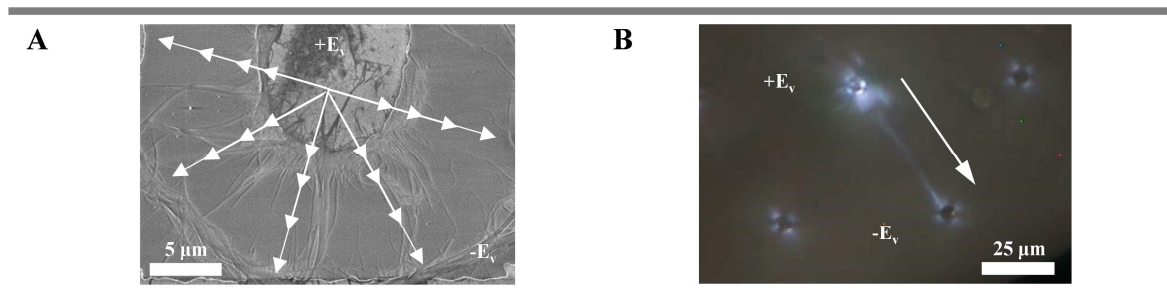


Figure 10. A) Image MEB d'un virage en U dans l'électrode interdigitées circulaire concentrique, obtenue à partir d'une *drop cast* d'une solution TAA-C8 de 2 mg/mL en présence d'un champ appliqué de $1,25 \times 10^7 \text{ V}\cdot\text{m}^{-1}$, conduisant à une orientation radiale des fibres dans le dispositif ; B) Image POM d'une électrode à micro-réseau montrant une seule fibre cultivée de l'anode à la cathode, parallèle au champ électrique (flèche blanche) et sur une distance de 50 μm.

Enfin, il a été démontré que de tels systèmes hautement ordonnés pouvaient être obtenus même en utilisant des IDE à géométrie plus complexe, comme des électrodes circulaires concentriques interdigitées, ou sur des distances sans précédent, comme le montre le pontage de deux électrodes ponctuelles espacées de 50 μm (Figure 10).

Ce système pourrait encore être amélioré. Par exemple, la conductance des polymères supramoléculaires pourrait être améliorée en dopant (chimiquement) les fibres par la suite ou en remplaçant le TAA-C8 par un tris-amide (TATA). Une autre perspective concerne la réversibilité du système. En effet, il pourrait être intéressant de développer un système dans lequel les polymères supramoléculaires sont assemblées et désassemblées par un cycle redox pour obtenir des dispositifs avec une capacité d'interrupteur marche/arrêt.

En général, les résultats obtenus dans ce travail pourraient être utilisés pour contrôler spatialement les processus d'auto-assemblage pour la construction de dispositifs optoélectroniques, allant des capteurs aux cellules solaires. Ils pourraient également être utilisés pour le développement d'outils d'électrochimie sans déchets pour contrôler les polymérisations supramoléculaires (vivantes). Ou encore le développement d'un câblage électrique 3D dans des organogels. Enfin, on peut imaginer qu'elle pourrait être utilisée pour concevoir des environnements d'oxydoréduction hors équilibre pour des systèmes auto-organisés

Chapitre III. Vers des structures plasmonique supramoléculaire a base des triarylamines

La miniaturisation et l'amélioration des performances du traitement de l'information par les circuits électroniques deviennent de plus en plus difficiles. Une nouvelle réduction des dimensions entraînerait une augmentation importante de la résistance et une dissipation de puissance plus importante, ce qui à son tour diminue les performances des dispositifs. À cet égard, la lumière a été proposée comme support d'information au lieu des électrons. Elle peut voyager à des vitesses plus élevées, transportant ainsi plus d'informations par seconde, et n'interagit que faiblement avec son environnement, ce qui minimise les pertes d'énergie. La localisation, le guidage et la manipulation de la lumière en dessous de la limite de diffraction est le domaine de la plasmonique. Dans ce troisième chapitre, nous poursuivons l'étude des propriétés plasmoniques des polymères supramoléculaires de triarylamine, commencée précédemment dans notre groupe de recherche. Il a été démontré que les cristaux TATA-Ac oxydés agissent comme des guides d'ondes plasmoniques organiques sur de petites distances ($\sim 40 \mu\text{m}$)¹⁷ et le premier objectif de ce projet de recherche était d'explorer jusqu'à quelle longueur les plasmons de surface à l'échelle de l'échelle peuvent se propager le long des cristaux TATA-Ac. Nous avons donc envisagé la formation de cristaux TATA-Ac simples d'une longueur de quelques millimètres à quelques centimètres. Ensuite, nous nous sommes demandé si les structures cristallines TATA-Ac pouvaient supporter des plasmons de surface localisés, ce qui n'a pas encore été démontré pour les matériaux organiques. Comme seules les structures environ dix fois plus petites que la longueur d'onde de la lumière incidente présentent des réponses plasmoniques, nous avons conçu la génération et la caractérisation de nanoparticules de triarylamine.

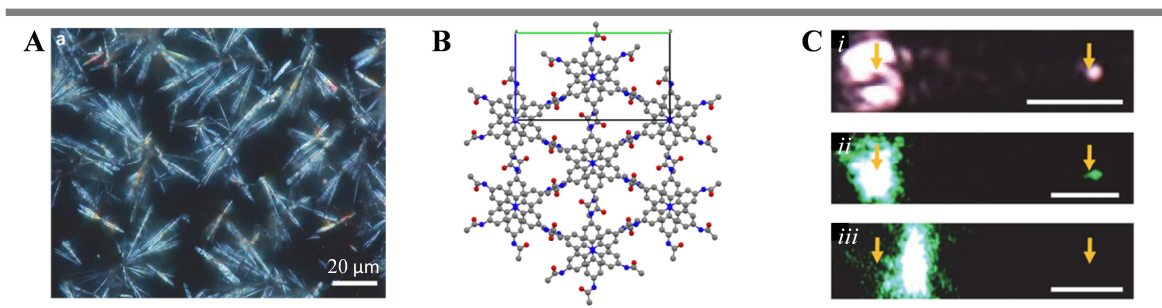


Figure 11. A) Photographie de petits cristaux simples de TATA-Ac par microscopie optique sous polariseurs croisés ; B) vue de dessus de la structure cristalline (2 molécules d'épaisseur) montrant les cavités intercolonnaires et les dimensions des cellules unitaires monocliniques ; C) guidage optique des ondes dans les petits cristaux simples de TATA-Ac par irradiation avec un laser de 785 nm (*i*) ou 532 nm (*ii-iii*). Dans les cas (*i*) et (*ii*), le laser est focalisé sur l'extrémité distale gauche et une sortie guidée par onde est observée à l'autre extrémité distale. Dans (*iii*) le laser est focalisé loin de l'extrémité, ici aucun guidage d'onde n'est observé. Les barres d'échelle représentent 4 μm.¹⁷

De petits cristaux de TATA-Ac transparents en forme d'aiguille (Figure 11A) ont été obtenus par évaporation lente dans un mélange de solvants de 12,8 mM de méthanol-toluène (75:25), comme décrit précédemment dans *Nano Lett.* **2016**, *16*, 2800-2805. Les cristaux sont formés dans un système monoclinique, dans une disposition monocolumnaire, avec les centres d'azote empilés le long de l'axe principal et un angle dièdre de 60° entre les monomères consécutifs (Figure 11B). Dans cette configuration, tous les groupes amide sont impliqués dans la liaison hydrogène intercolumnaire. Les cristaux oxydés ont été obtenus par photo-oxydation des cristaux dans leur suspension de chloroforme, ou par des vapeurs d'iode. Les cristaux neutres et oxydés ont fait preuve de guidage d'ondes lorsqu'on a pointé un laser, focalisé à travers un objectif de microscope, sur une extrémité du cristal et observé le résultat à l'autre extrémité (Figure 11C). Pour les cristaux oxydés, un mécanisme plasmonique actif de guidage des ondes était à l'origine de la propagation de la lumière car *i*) les cristaux n'absorbent pas la longueur d'onde des lasers utilisés ; *ii*) aucune fluorescence n'a été observée ; *iii*) aucun guidage des ondes n'est observé lorsque le laser est pointé n'importe où mais à l'extrémité distale ; *iv*) une distance de photo lixiviation accrue est observée lorsque les cristaux sont recouverts d'un colorant photosensible en raison de la création d'un champ proche évanescent par l'énergie se propageant à l'intérieur du cristal.

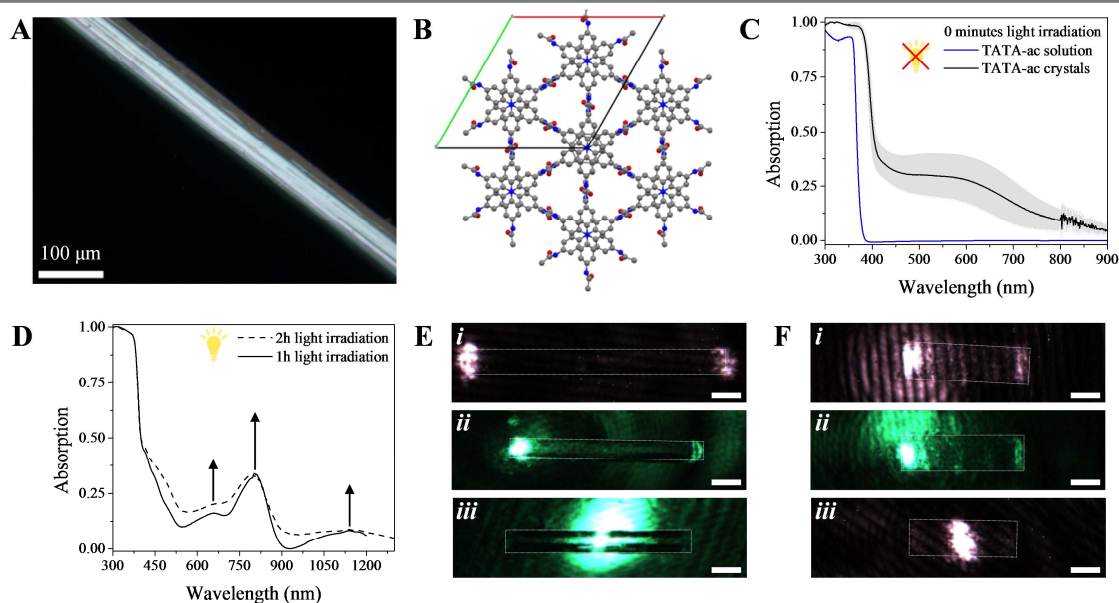


Figure 12. A) Photographie en microscopie optique d'un monocristal obtenu à partir d'une solution lentement refroidie de 70 °C à température ambiante pendant 54 heures ; B) vue de dessus de la structure cristalline (2 molécules d'épaisseur) montrant les cavités intercolumnaires et les dimensions des cellules unitaires hexagonal ; C) spectres d'absorption de cristaux neutres de TATA-Ac enregistrés à l'état solide. La ligne bleue présente les monomères TATA-Ac neutres en solution, la ligne noire les cristaux TATA-Ac neutres à l'état solide. La zone grise représente l'écart-type ; D) les spectres d'absorption des cristaux de TATA-Ac photo-oxydés dans une suspension de chloroforme, enregistrés à l'état solide, après élimination du solvant ; E-F) photographes en microscopie optique des cristaux TATA-Ac neutres (E) et photo-oxydés (F) démontrant le guidage des ondes optiques

après illumination de l'extrémité distale gauche des cristaux avec un laser à 785 nm (*i*) et à 532 nm (*ii*). Aucun guidage d'onde n'est observé lorsque le laser est focalisé au milieu du cristal (*iii*). Les rectangles blancs en pointillés tracent les contours des cristaux. La barre d'échelle représente 50 μm .

De gros cristaux ont été obtenus après un lent refroidissement, de 70 °C à 20 °C, d'un mélange de solvants à base d'acétate d'éthyle et de méthanol (5:95) de 1,6 mM (Figure 12A). La diffusion des rayons X et les expériences cristallographiques montrent que ces grands cristaux s'auto-assemblent dans un système de symétrie hexagonale. Les monomères sont empilés dans des arrangements monocolumnaires avec leurs centres d'azote positionnés le long de l'axe principal, tout comme dans les petits cristaux. On observe également la même rotation de 60° d'angle dièdre entre deux molécules consécutives. La différence réside dans l'augmentation de la distance entre deux centres d'azote empilés, et la diminution de la distance entre les centres d'azote des piles adjacentes (Figure 12B). Les cristaux neutres présentent une large bande d'absorption entre 450 et 700 nm qui résultent de la structure auto-assemblée en l'absence de cations radicaux (Figure 12C). Les spectres d'absorption après photo-oxydation montrent les bandes caractéristiques à 600, 800 (radicaux délocalisés sur les noyaux phényle) et 1100 nm (à travers les radicaux délocalisés dans l'espace) (Figure 12D). Les mesures EPR montrent que, même après une heure de photo-oxydation, seule une petite quantité de radicaux est présente (< 1 %). Dans l'ensemble, on peut conclure que l'oxydation des grands cristaux de TATA-Ac est plus difficile à réaliser et à mesurer que celle des petits cristaux. Nous avons postulé que cela pourrait être le résultat de *i*) l'instabilité des cations radicaux après élimination du solvant et/ou exposition à l'air ; *ii*) la taille accrue, qui conduit à des sites d'oxydation moins facilement accessibles ; *iii*) une oxydation moins efficace en raison de la structure cristalline différente. Pour les expériences de guidage d'ondes, les cristaux ont été décomposés en plus petits morceaux afin de s'adapter au champ de l'objectif. Les cristaux neutres et oxydés retiennent leur capacités de guider la lumière, sur des distances jusqu'au 485 nm, ce qui représente la longueur maximale pouvant être mesurée avec ce dispositif (Figure 12E).

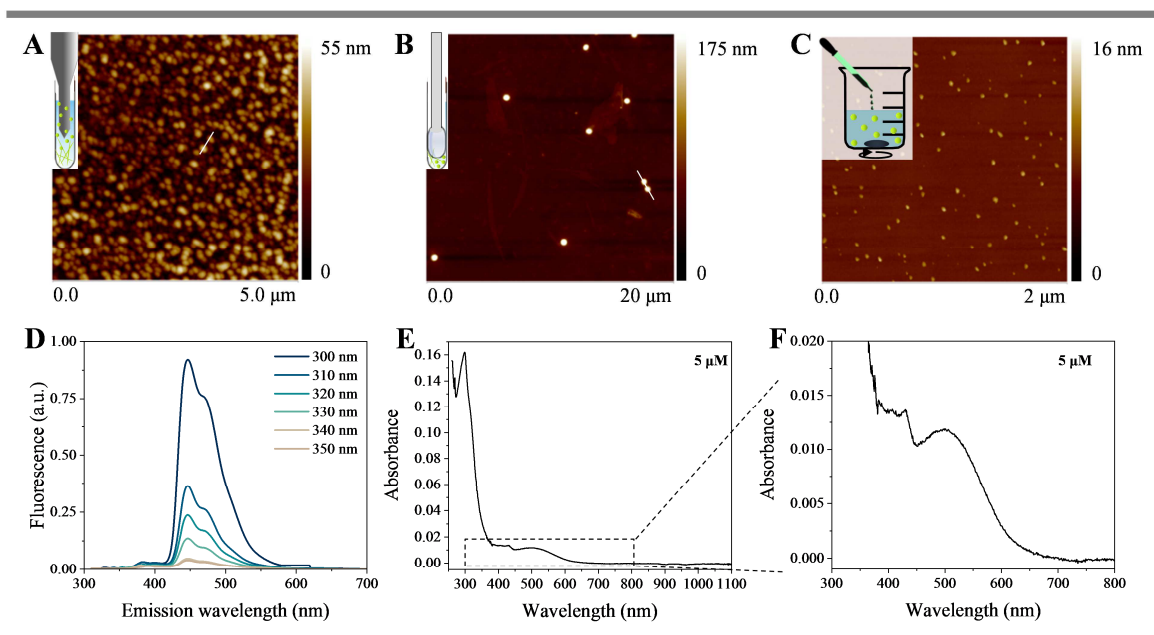


Figure 13. Images AFM de nanoparticules TATA-Ac obtenues par A) sonication en pointe de gros cristaux dans de l'acétate d'éthyle ; B) broyage de gros cristaux dans du cyclohexane avec un mortier de verre ; C) reprecipitation d'une solution 0.5 mM de TATA-Ac (méthanol chloroforme 25:75) dans 10 ml d'acétate d'éthyle ; D) spectres de fluorescence d'une suspension de nanoparticules à 5 μ M TATA-Ac obtenue par reprecipitation ; E) spectre d'absorption enregistré pour une suspension de nanoparticules à 5 μ M TATA-Ac obtenue par reprecipitation ; F) zoom du spectre présenté en (E).

Les nanoparticules TATA-Ac peuvent être formées par plusieurs méthodes. Par sonication en pointe de gros cristaux en suspension dans l'acétate d'éthyle, on obtient des nanoparticules d'environ \sim 20 nm (Figure 13A). Cependant, l'agrégation se fait rapidement par la suite. Une autre méthode est le broyage de gros cristaux dans 1 mL de du cyclohexane, à l'aide d'un mortier de verre (Figure 13B). On obtient alors des nanoparticules isolées. Malheureusement, leur taille est beaucoup plus grande (\sim 150 nm). De plus, les deux méthodes se sont avérées difficiles à reproduire. La troisième méthode, la reprecipitation, est la plus prometteuse. Les nanoparticules de taille accordable peuvent être obtenues par l'addition de volumes variables (10 ou 100 μ L) d'une solution de TATA-Ac de 0,5 mM (méthanol chloroforme 25:75) à 10 ml d'acétate d'éthyle (Figure 13C). Des nanoparticules de respectivement \sim 6,5 nm et \sim 21,5 nm ont été obtenues. Les particules oxydées et neutres peuvent être réalisées par irradiation de la solution TATA-Ac. La spectroscopie de fluorescence indique que les particules sont de nature cristalline car le pic émissif contient un épaulement qui peut être attribué à un état vibratoire (Figure 13D). Le spectre d'absorption d'une suspension de 5 μ M TATA-Ac NP montre une bande d'absorption à 500 nm (Figure 13E). Cette bande ne peut pas être attribuée aux transitions électroniques qui se produisent normalement dans les auto-assemblages TATA, ce qui donne lieu à la forte supposition qu'il s'agit d'une bande plasmonique.

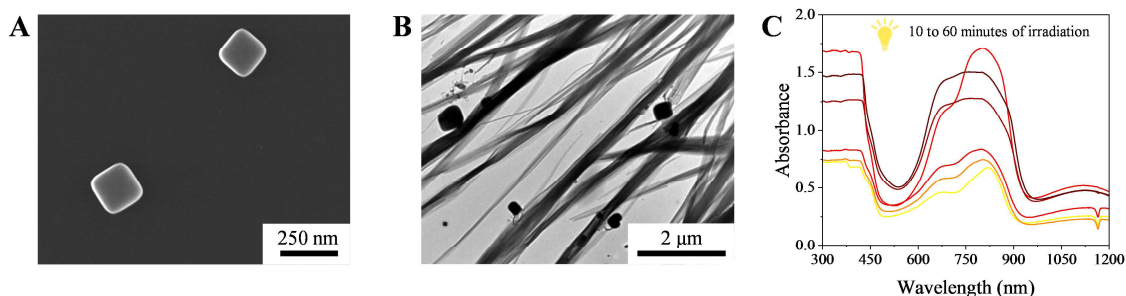


Figure 14. A) image MEB d'une solution de TATA-C4 de 15 mM dans du méthanol TCE (5:95), irradiée pendant une heure et *drop casted* sur une grille MET ; B) image MET de structures fibreuses que l'on trouve habituellement dans les échantillons de TATA-C4 ; C) spectres d'absorption d'une solution de TATA-C4 de 15 mM dans du méthanol TCE (5:95) enregistrés entre 10 et 60 minutes d'irradiation.

La formation de nanoparticules TATA-C4 a également été étudiée, car cette molécule est plus soluble et une approche ascendante pourrait être plus réalisable. Des nanoparticules cubiques ont été obtenues en chauffant et en sonisant une solution de TATA-C4 de 15 mM dans un mélange de solvants à base de méthanol et de tétrachloroéthane (5:95), puis en refroidissant la solution à la température ambiante (Figure 14A). Les nanoparticules oxydées et neutres peuvent être réalisées par l'ajout d'une étape d'irradiation lumineuse pendant le refroidissement de la solution. Bien que des nanoparticules cubiques soient toujours présentes, il arrive souvent que d'autres structures auto-assemblées, telles que des fibres, soient également présentes (Figure 14B). Afin de favoriser la formation de cube plutôt que la formation de fibres, le pourcentage de méthanol, le temps d'irradiation de la lumière, la vitesse de refroidissement et la concentration de TATA-C4 ont été systématiquement modifiés. Malheureusement, cela n'a pas permis de contrôler la formation de l'une ou l'autre des espèces auto-assemblées. Nous avons également étudié, mais sans succès, la possibilité de séparer les fibres des nanocubes après auto-assemblage par dilution, centrifugation et filtration. Les spectres d'absorption des solutions TATA-C4 sont conformes aux spectres généralement obtenus pour la famille TATA. Ce n'est qu'à des durées d'irradiation supérieures à 15 minutes que la bande à 60 et 800 nm s'élargit et se chevauche, ce qui peut s'expliquer par la précipitation du matériau ou par la présence de différentes espèces (nanocubes et fibres) (Figure 14C). Les propriétés plasmoniques des nanoparticules n'ont pas encore été caractérisées, car des échantillons de particules isolées n'ont pas encore été obtenus.

Chapitre IV. Le transport électronique dans divers polymères triarylamine supramoléculaires

Les triarylamines se caractérisent généralement par leurs propriétés électroniques et optiques. Ces propriétés sont renforcées dans les polymères supramoléculaires de triarylamine en raison de l'empilement étroit entre les centres d'azote centraux, qui se traduit par un fort couplage électronique. Cela a déjà été démontré par l'alignement de polymères de triarylamine supramoléculaires entre des électrodes avec des canaux d'espacement de 80 nm, sous l'influence d'un champ électrique. Les fibres, formées par photo-oxydation, présentent des conductivités exceptionnelles ($> 5 \times 10^3 \text{ S}\cdot\text{m}^{-1}$) et une faible résistance de contact ($< 2 \times 10^{-4} \Omega\cdot\text{m}$) en raison de la présence d'électrons de type métallique dans leur structure.²¹

Cependant, on sait que de grandes différences de mobilité de charge peuvent être trouvées en fonction de la morphologie, de la taille, de la structure chimique et supramoléculaire. En fonction du nombre de groupes amide sur le motif central du TAA, les triarylamines s'auto-assemblent dans des arrangements doubles ou monocolumnaires. En outre, en fonction de la longueur des chaînes alkyles, on obtient soit des fibres souples en solution, soit des gels, soit des structures cristallines. Afin de pouvoir choisir le meilleur dérivé à incorporer dans les dispositifs électroniques organiques, nous avons mené une étude comparative pour établir si, et dans quelle mesure, les différences de structure moléculaire, de processus de nucléation et d'architecture supramoléculaire affectent les propriétés de conductivité électronique des auto-assemblages résultants.

Dans la première partie de cette étude, nous avons comparé la conductance de plusieurs polymères supramoléculaires de triarylamine mono- et trisamide (TAA-C1, TAA-C8, TATA-C4, TATA-C9 et TATA-C12) en fonction de leur état physique (polymères en solution, gels physiques et films minces).

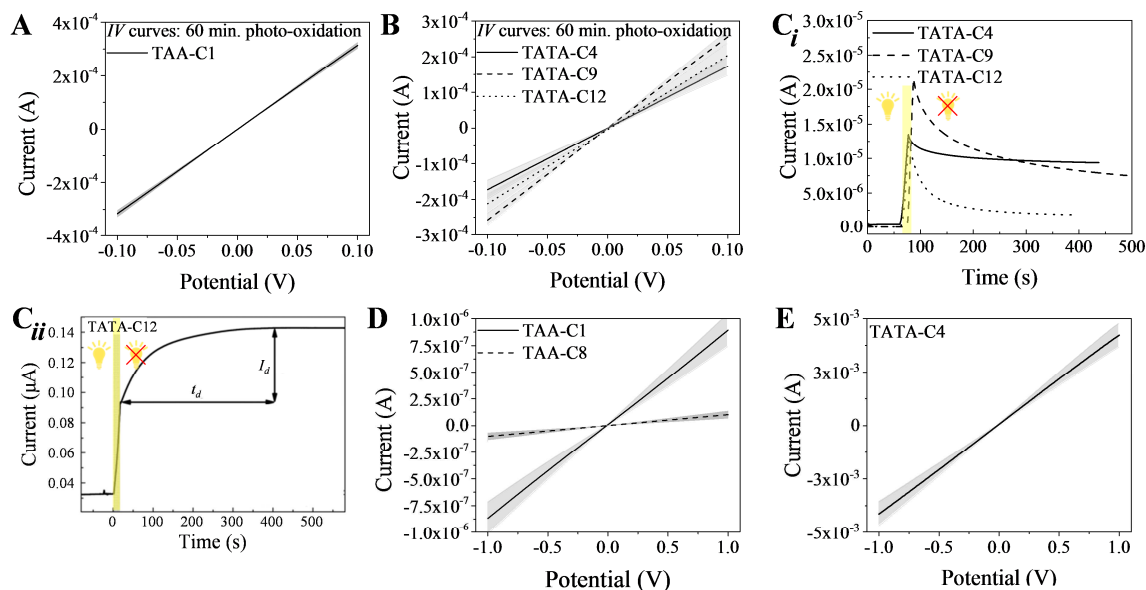


Figure 15. A-B) courbes I/V de solutions de 15 mM de TAA-C1, TATA-C4, TATA-C9 et TATA-C12 préparées dans du TCE, insérées dans des cellules ITO et enregistrées après 60 minutes de photo-oxydation à l'intérieur des cellules ITO ; C) tracé du courant en fonction du temps enregistré sous un biais de 0,1 V pour des solutions TATA de 15 mM (i) et les gels physiques de 17 mM (ii)¹⁶ tous les deux formés dans du TCE. La zone jaune clair correspond au temps d'irradiation ; E-F) courbes I/V enregistrées pour des films minces de TAA et TATA-C4 obtenus par *drop casting* d'une solution irradiée de 15 mM sur des IDE, sous un biais de 0,5 V. Les films ont été séchés sous vide avant les mesures afin d'éliminer tout solvant. Les zones grises correspondent à l'écart-type pris sur deux à trois expériences.

Les conductances des fibres en solution sont mesurées à l'aide de cellules électrochimiques ITO. Avant la photo-oxydation, on ne mesure que peu ou pas de conduction. Après irradiation par la lumière, la photo-oxydation et la polymérisation supramoléculaire ont lieu (Figure 15AB). En conséquence, les échantillons passent à un état conducteur présentant un comportement ohmique. Cela s'accompagne d'une augmentation de la conductivité de trois ordres de grandeur ($\sim 485 \Omega$). Malgré les différences dans l'assemblage supramoléculaire, les efficacités d'oxydation, les stabilités radicalaires et la densité possible des porteurs de charge, aucune différence significative n'est observée entre les courants mesurés pour les fibres supramoléculaires TAA et TATA. On peut donc conclure que les conductivités des polymères supramoléculaires TAA et TATA sont similaires, ce qui indique fortement que l'auto-assemblage des noyaux d'azote empilés, qui sont responsables du transport de charge, est suffisamment similaire pour assurer une bonne conductivité, quels que soient les substitués placés à la périphérie.

Ensuite, nous avons comparé la conductance des fibres dans les solutions avec celles qui forment un gel physique (également réalisé dans les cellules électrochimiques ITO). Avant la photo-oxydation, une plus grande conduction est possible à travers les gels physiques car un nombre nettement plus important de fibres sont présentes. Après 60 secondes d'irradiation lumineuse, la résistance chute de 3

à 4 ordres de grandeur et les conductances des solutions et des gels sont comparables. Lorsque l'irradiation est effectuée pendant une durée plus longue (60 minutes), la conductance des gels est supérieure d'environ 2 ordres de grandeur à celle des solutions, en accord avec le nombre plus élevé de polymères supramoléculaires présents. Après photo-oxydation, les fibres en solution et en gel sont toutes deux à l'état conducteur et présentent un comportement ohmique (respectivement $\sim 485 \Omega$ et $\sim 315 \Omega$). Une différence marquée est observée après de courtes durées d'irradiation (15 secondes), où le courant mesuré se stabilise pour les solutions, mais augmente de 30 à 50 % sur une période de ~ 400 s avant de se stabiliser pour les gels physiques (Figure 15C). Comme les fibres des gels sont formées avant la photo-oxydation, elles subissent une optimisation de leur structure supramoléculaire par la diffusion de polarons dans le champ électrique.

Enfin, nous avons examiné des films minces photo-oxydés, préparés sur des électrodes interdigitées (Figure 15DE). Les couches minces de TAA-C1 et TAA-C8 présentent toutes deux une conductance, bien que des courants plus faibles soient mesurés par rapport à leurs polymères supramoléculaires en solution. En particulier, le TAA-C8 présente une conductance réduite. Aucun courant n'a pu être mesuré pour les films minces de TATA-C9 et TATA-C12, tandis que les films de TATA-C4 présentent une excellente conductance. Par conséquent, nous postulons que des chaînes alkyle plus nombreuses ou plus longues entraînent des conductances réduites, car elles entravent la communication électronique entre les polymères supramoléculaires eux-mêmes et entre les polymères supramoléculaires et les électrodes. En outre, la conductance élevée des films TATA-C4 peut également s'expliquer par leur morphologie plus cristalline. Actuellement, ces films minces sont étudiés en tant que couches de transport de trous dans les cellules solaires à pérovskite et à colorant en collaboration avec l'école polytechnique fédérale de Lausanne.

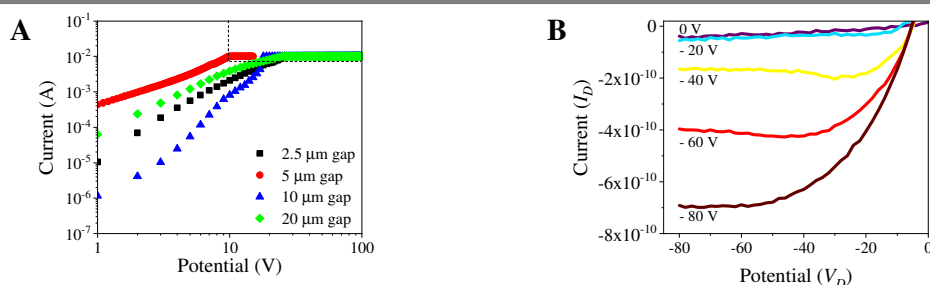


Figure 16. A) Courbes log-log IV enregistrées pour les petits cristaux neutres TATA-Ac à haute couverture de surface. Les points à l'intérieur du rectangle en pointillés sont situés au-dessus de la conformité de l'unité de mesure au courant ; B) courbes de sortie des OFET traités par HMDS avec un canal de $20 \mu\text{m}$ large, couvert par de petits cristaux TATA-Ac neutres. La tension de grille appliquée (V_G) varie de 0 à -80 V.

Dans la deuxième partie de ce projet de recherche, nous avons étudié le transport de charge dans les cristaux TATA-Ac. Nous avons émis l'hypothèse qu'en raison de l'empilement plus étroit des centres d'azote, ainsi que de sa nature cristalline, la communication électronique est améliorée et des conductances élevées sont prévues. Nous avons commencé avec de petits cristaux neutres déposés sur des structures OFET et nous nous attendions à ce qu'ils aient une mauvaise conductance, comme on l'observe normalement pour les auto-assemblages de triarylamines neutres. Cependant, lorsque la structure OFET a été entièrement recouverte par des cristaux neutres, nous avons atteint la conformité de l'unité de mesure à 10V (10^{-2} A) (Figure 16A). Ainsi, les cristaux neutres de trisacetamide sont en fait conducteurs. Lorsque les expériences ont été répétées, on a observé que les cristaux présentaient également un effet OFET (Figure 16B). Les courbes de sortie et de transfert ont été utilisées pour calculer la mobilité des trous à l'intérieur des cristaux, qui s'est avérée être de $\sim 30 \times 10^{-8} \text{ cm}^2 \cdot \text{V}^{-1} \cdot \text{s}^{-1}$. Cette mobilité des trous plutôt faible s'explique par le mauvais contact entre les cristaux et les électrodes et le diélectrique, ainsi que par la couverture de surface des cristaux sur la structure OFET et leur orientation respective.

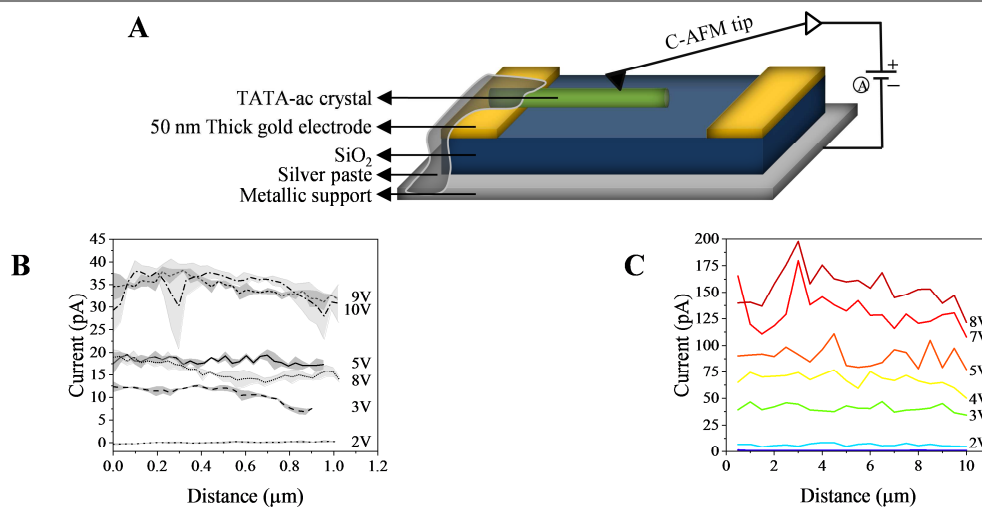


Figure 17. A) Représentation schématique de la configuration de l'AFM conducteur pour les mesures sur des cristaux TATA-Ac isolées. La pâte d'argent a été ajoutée uniquement pour les gros cristaux ; B) courant enregistré sur les 1000 premiers nm d'un petit cristal TATA-Ac neutre ; C) courant enregistré sur les 10 premiers μm d'un gros cristal TATA-Ac neutre.

Afin de contourner ces inconvénients, nous avons tenté de mesurer la conductance de petits cristaux neutres par AFM conducteur (Figure 17A). La plupart des petits cristaux ne présentaient aucune conductivité, en raison d'un mauvais contact des cristaux avec l'électrode. Un cristal, qui présentait un comportement conducteur, a révélé un potentiel de seuil de 2 V et des mobilités de trous de 4 à 6 ordres de grandeur supérieurs à ceux calculés précédemment à l'aide du set-up OFET (Figure 17B). De plus, bien que de gros défauts soient présents, le cristal est capable de conduire sur de grandes distances (~ 10 micromètres). Les mêmes expériences ont été menées sur de grands cristaux

TATA-Ac neutres (Figure 17C). De grandes différences de conductivité ont été constatées en fonction de la qualité du cristal et de la direction précise de l'empilement des monomères. La mobilité des trous, calculée pour le cristal présentant les courants les plus élevés, est inférieure d'environ 2 ordres de grandeur à celle des petits cristaux neutres, ce qui peut s'expliquer par la plus grande distance parcourue par l'ensemble du cristal et l'augmentation de la distance entre les centres d'azote. Ces cristaux démontrent que la conductivité à longue distance est possible sur des distances allant jusqu'à au moins 70 μm de l'électrode.

Ce projet de recherche est toujours en cours car, pour déduire le mécanisme de transport de charge et les véritables propriétés intrinsèques de conductivité, il faudrait effectuer davantage de mesures. Notamment plus loin des électrodes, et avec plus de points de données. Les propriétés de conductivité des cristaux oxydés devraient également être examinées.

Dans la troisième et dernière partie de ce chapitre, nous avons étudié le transport de charges dans des gels physiques et chimiques de TATA-norbornène (TANBE). Les gels chimiques sont obtenus par la réticulation chimique de gels physiques par polymérisation par métathèse par ouverture de cycle (ROMP) à l'aide du catalyseur Grubs III. Ce travail fait partie du projet de doctorat du Dr Ting Liang et a été publié dans *Chem. -A Eur. J.* **2019**, 25, 14341-14348.

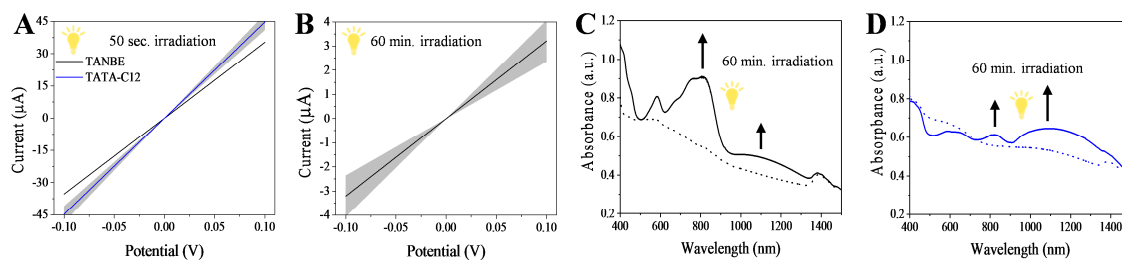


Figure 18. A) Courbes I/V enregistrées pour des polymères supramoléculaires TANBE (ligne noire) et TATA-C12 (ligne bleue) en solution (TCE) de 17 mM, après 50 secondes d'irradiation lumineuse. Les zones grises correspondent à l'écart-type pris sur trois expériences ; B) courbes I/V enregistrées pour des gels physiques TANBE 15 mM (toluène tétrachloroéthane 90:10), irradiés pendant 60 minutes. Les zones grises correspondent à l'écart-type pris sur trois expériences ; C-D) spectres vis-NIR de gels chimiques obtenus par ROMP de gels physiques neutres (C) et de gels physiques irradiés pendant 60 minutes (D). Les lignes pointillées correspondent aux gels chimiques ainsi obtenus, les lignes pleines aux gels chimiques ré-irradiés pendant 60 minutes supplémentaires.

Les polymères supramoléculaires TANBE présentent les mêmes propriétés conductrices que les fibres TATA simples (Figure 18AB). Ainsi, les groupes terminaux du norbornène n'affectent pas le transport de charge et nous pouvons confirmer à nouveau l'observation faite que la conductivité à travers les motifs du noyau d'azote empilé reste non perturbée par les substituants à la périphérie. Des gels physiques ont été préparés dans des mélanges de solvants à base de toluène et de tétrachloroéthane (90:10). Même avec ce faible pourcentage de solvant chloré, les gels deviennent

conducteurs après seulement 15 minutes d'irradiation lumineuse. Les courants maximaux ont été mesurés lorsque les solutions sont irradiées directement dans des cellules ITO (jusqu'à $\sim 2500 \Omega$). La réticulation chimique conserve la structure supramoléculaire ; cependant, aucun courant n'a pu être mesuré. Nous supposons que deux facteurs sont à l'origine de cette observation. Premièrement, le caractère dynamique du gel physique est perdu lors de la réticulation chimique. En conséquence, les polymères supramoléculaires ne peuvent plus se recombinaer et réarranger leur structure pour améliorer leur contact avec les électrodes. Il en résulte un empêchement de l'injection et de l'extraction de la charge. Deuxièmement, par la réticulation chimique, la couche isolante entourant les centres conducteurs d'azote augmente. Cela réduit la probabilité de transfert de charge à la fois entre les fibres et à l'interface fibre-électrode, réduisant ainsi la conductivité globale. Néanmoins, des mesures de photospectroscopie ont montré que les propriétés optiques et conductrices locales sont conservées (**Figure 18CD**). De plus, elles peuvent être réglées en choisissant les bonnes conditions de préparation.

En conclusion, nous avons montré dans la première partie que, indépendamment du mécanisme d'auto-assemblage ou de la longueur de la chaîne alkyle, les polymères supramoléculaires passent à l'état conducteur après la photo-oxydation. En outre, les gels physiques montrent une augmentation continue de la conductivité dans l'obscurité grâce à une optimisation de leur structure supramoléculaire. La conductivité des films minces dépend de la longueur des chaînes d'alkyle et de la morphologie du film mince.

Dans la deuxième partie, nous avons démontré que les cristaux neutres de TATA-Ac sont conducteurs sur de longues distances. Cependant, d'autres expériences doivent être réalisées afin d'obtenir des résultats concluants sur le mécanisme de transport de charge et les mobilités des porteurs de charge.

Dans la troisième partie, la conductivité des gels chimiques a été sondée. Tout d'abord, nous avons vérifié que les grands substituants n'affectaient pas le transport de charge le long des polymères supramoléculaires en solution et en gel physique. En revanche, aucune conductivité n'a pu être mesurée pour leur équivalent chimique. Néanmoins, les propriétés optiques et de transport de charge locales ont été conservées.

ABBREVIATIONS AND SYMBOLS

°C	degree Celsius	DSC	differential scanning calorimetry
1PA	one photon absorption	$E_{1/2}$	redox potential
2PA	two photon absorption	EA	electron acceptor
A	acceptor	EBHT	electron blocking hole transporting
A	area	EELS	electron energy loss spectroscopy
Å	angstrom	EET	electronic energy transfer
Ac	acetyl	E_f	electric field
AC	alternate current	EPR	electron paramagnetic resonance
ACQ	aggregation caused quenching	<i>eq.</i>	equivalent
AFM	atomic force microscopy	ESCT	excited state charge transfer
AIE	aggregation induced emission	ET	electron transfer
CBT	carbonyl-bridged triarylamine	<i>etc.</i>	et cetera
CD	circular dichroism	EtOAc	ethyl acetate
COF	covalent organic framework	EtOH	ethanol
CT	charge transfer	FET	field effect transistor
CV	cyclic voltammetry	<i>FF</i>	fill factor
<i>D</i>	diffusion coefficient	<i>G</i>	Gibbs free energy
DC	direct current	<i>G</i>	conductance
DCM	dichloromethane	<i>H</i>	enthalpy
DFT	density functional theory	h	hour
DLS	dynamic light scattering	HBC	hexabenzocoronene
DNA	deoxyribonucleic acid	HBET	hole blocking electron transporting
DOS	density of state	HOMO	highest occupied molecular orbital
DRC	dendron rodcoils	HOPG	highly oriented pyrolytic graphite

Abbreviations and Symbols

HPLC	high performance liquid chromatography	mM	millimolar
HTM	hole transporting material	mmol	millimolar
ICT	inter molecular charge transfer	MOF	molecular organic framework
IDE	interdigitated electrode	MPA	multi-photon absorption
I_{ds}	drain-source current	NIR	near infra-red
I_p	ionization potential	nm	nanometer
IR	infra-red	NMR	nuclear magnetic resonance
I_{sc}	short circuit current	NP	nanoparticle
ITO	indium tin oxide	OFET	organic field effect transistor
IV-CT	intervalence charge transfer	OLED	organic light emitting diode
J	coupling constant	OM	optical microscopy
K	kelvin	OSC	organic solar cell
k	kilo	PCE	photo conversion efficiency
L	liter	PD	poly dispersity
l	length	PET	photo -induced electron transfer
LC	liquid crystal	POM	polarized optical microscopy
LED	light emitting diode	ppm	parts per million
LUMO	lowest unoccupied molecular orbital	PSC	perovskite solar cell
M	molar	PTAA	polymer triarylamine
m	meter	R	resistance
HTM	hole transporting material	<i>ref.</i>	reference
MeOH	methanol	S	Siemens
min	minute	S	entropy
mL	milliliter	S	order parameter
mm	millimeter	s	second
SAMs	self-assembled monolayers	V_{oc}	open-circuit potential
SAXS	small angle X-ray scattering	V_{th}	threshold potential

Abbreviations and Symbols

SC	solar cell	WAXS	wide angle X-ray scattering
SEM	scanning electron microscopy	δ	chemical shift
SOMO	single occupied molecular orbital	λ	wavelength
T	temperature	λ	reorganization energy
TAA	triarylamine	μ	charge carrier mobility
TATA	triarylamine trisamide	μL	microliter
TBQ	tetrabromoquinone	μm	micrometer
TCE	tetrachloroethane	μM	micromolar
TEA	triethylamine	μmol	micromole
TEM	transmission electron microscopy	ρ	resistivity
TICT	twisted intermolecular charge transfer	σ	electric conductivity
TLC	thin layer chromatography	σ	photo absorption cross-section
TPA	triphenylamine		
TTF	tetrathiafulvalene		
UPLC	ultra-performance liquid chromatography		
UV	ultra-violet		
V_{ds}	drain-source voltage		
V_{gs}	gate-source voltage		
vis	visible		

GENERAL INTRODUCTION AND OBJECTIVES

Triarylamine derivatives form a very large family of molecules, consisting of small discrete molecules, (oligo-) polymers and self-assembled structures that have been studied extensively for over 60 years, both in academia and industry. They have received great attention because their characteristics span a broad range of scientific and industrial interests, from organic synthesis, to fundamental physical properties and molecular processes, to their incorporation in numerous electronic devices. In 2010, our research group demonstrated that, when at least one amide function is present on the periphery of the triphenylamine core motif, the molecules stack in columnar arrangements. This discovery has led to numerous studies²⁵ involving the elucidation of its unique supramolecular polymerization mechanisms¹⁴ (Figure 19A), their excellent functional properties^{16,17,20,22} and their possible implementation in devices^{23,26} (Figure 19B).

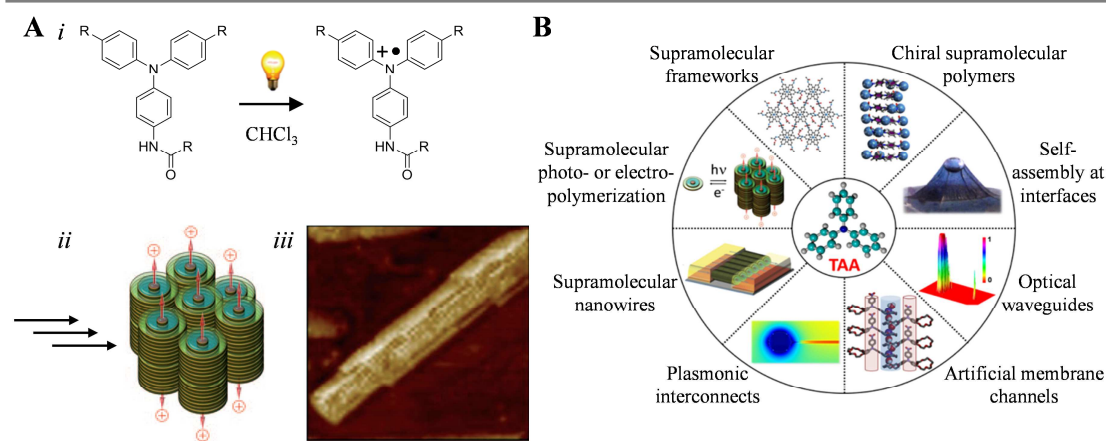


Figure 19. A) i) Photo-oxidation induced self-assembly of triarylamine molecules into supramolecular polymers; ii) schematic presentation and iii) high resolution AFM image of triarylamine monoamide supramolecular polymer; B) overview of the possibilities in supramolecular self-assembly of triarylamine mono- and trisamides and applications thereof. This Figure is adapted from reference 1

The general goal of this PhD is to deepen our understanding of the electric transport and plasmonic properties of different triarylamine self-assemblies in relation with their chemical and supramolecular structures towards their integration into organic electronic devices. The work is divided in three main multidisciplinary research projects which include synthesis, chemical analysis and physical chemistry characterizations.

A major difficulty when first approaching these topics is the enormous amount of existing literature. More than 2500 papers have been published that use the triarylamine core motif. Moreover, in the year 2018 alone, over 550 articles and over 200 patent applications were based on triarylamine derivatives. A review connecting all these subjects has yet to be written, making it truly challenging to become well informed about their wide-ranging potential. Therefore, an elaborative bibliographic chapter has been realized that introduces different fields in which triarylamines are applied. The purpose of this bibliographic chapter is to draw a general picture of the broad interests of triarylamine derivatives; the references supplied are not comprehensive.

The first project had as primary objective to develop the first genuine supramolecular electropolymerization process. This necessitated a detailed study of the electrochemical properties of the triarylamine monoamide used and their self-assembled fibers, under multiple conditions, such as the presence of electrolytes and solvents of different dielectric constants. The electrochemically induced polymerization process was exploited towards the integration of the resulting polymers onto microelectrodes.

In the second project we aimed to continue our previous work on the plasmonic properties of triarylamine supramolecular polymers. Previously, we have demonstrated the possibility of plasmonic coupling and transport between gold nanoparticles and triarylamine fibers (Figure 20A-C).^{22,24} The plasmonic propagation was equally evidenced in oxidized triarylamine crystals that act as active plasmonic wave-guides (Figure 20D).¹⁷ A first goal was to explore up to which length scale such surface plasmons could propagate. Secondly, we were interested to examine if localized surface plasmons could also be generated. In this regard, we envisioned the generation and characterization of triarylamine nanoparticles.

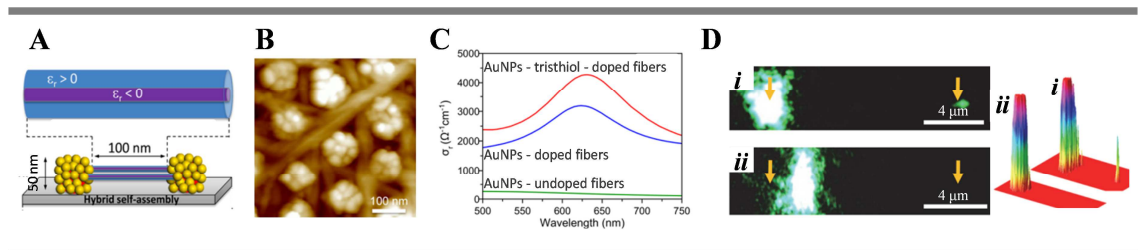


Figure 20. A) Schematic view and B) AFM image of triarylamine fibers interconnecting gold nanoparticles; C) optical conductivities measured depending on surface treatment of the AuNPs and the doping (oxidation) of the fibers; D) triarylamine single crystals displaying optical wave-guiding exclusively when the laser source is pointed on the distal end, showing an output at the other distal end. This Figure is adapted from references 5 and 6.

The final project aims at characterizing the electronic transport of various supramolecular triarylamine polymers and their possible integration into photovoltaic devices. Triarylamine molecules are typically characterized by their electronic and optical properties. The close stacking

between the central nitrogen centers in triarylamine supramolecular polymers results in strong electronic coupling with the concomitant improvement of the electronic and charge transport properties. This was already shown by the exceptional conductivity ($5 \times 10^3 \text{ Sm}^{-1}$) of metal-like electrons in triarylamine fibers as metal-interconnects (Figure 21).²⁶ Here, we will investigate the effect that different substituents on the triphenylamine periphery, which give rise to significantly different self-assembled structures, have on its electronic transport.

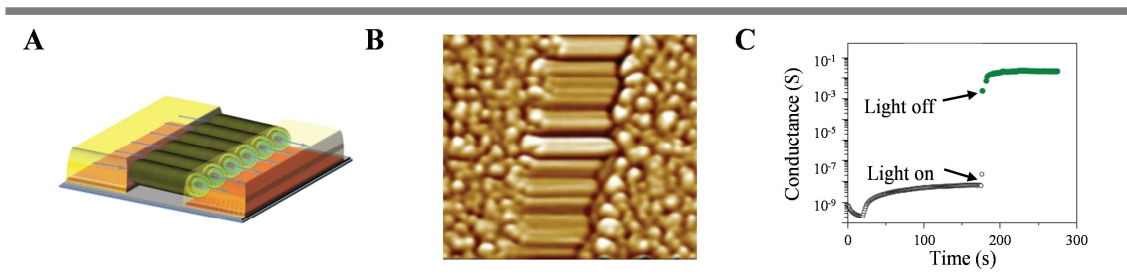


Figure 21. A) Schematic view and B) AFM image of triarylamine supramolecular polymers as interconnects between gold electrodes spaced 80 nm apart formed after photo-induced supramolecular polymerization. Aligned in the electrode gap is achieved simultaneously by an electric field; C) conductance measured as a function of time in the dark (prior to alignment) and subsequent submission to light irradiation (attraction and alignment of polymers in the gap between the electrodes). This Figure is adapted from reference 10.

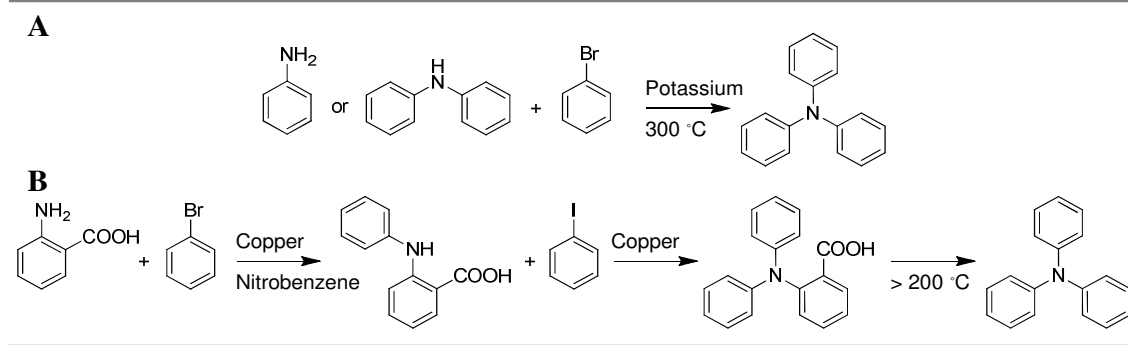
CHAPTER I. BIBLIOGRAPHY

Triarylamine (TAA) derivatives have been investigated over 60 years, in a wide range of scientific and industrial fields (e.g. organic synthesis; physical characteristics and associated molecular processes; incorporation in organic electronic devices). Here, we will summarize the large amount of existing literature to create an overview introducing all different research fields accompanied by key-examples from literature. The first part of this chapter will be dedicated to a discussion on the physical traits of triarylamine derivatives, such as molecular structure, electrochemical, conductive and optical properties, followed by the applications that these characteristics have led to. The second part of the chapter will focus on supramolecular chemistry and the emergent properties and applications of self-assembled supramolecular triarylamine polymers.

I.1 Physical Properties of Triarylamines

A. Molecular structure of triarylamines

It was Merz and Weith who, in 1873, were the first to synthesize the triarylamine (TAA) core motif, by reacting aniline or diphenylamine with bromobenzene as detailed in **Scheme 1A**.¹ In 1907, Goldberg and Nimerovsky proposed a second synthetic protocol comprising an Ullmann-coupling reaction between anthranilic acid and bromobenzene, followed by reaction with iodobenzene and a decarboxylation reaction (**Scheme 1B**).^{27,28} Nowadays, three principal reaction pathways exist. The first alternative includes many variations of the protocol proposed by Goldberg and Nimerovsky, now allowing TAA synthesis under mild conditions.²⁹⁻³¹ The second possibility involves a palladium-catalyzed Buchwald-Hartwig coupling reaction.^{32,33} Finally, the TAA core motif can also be obtained by aromatic nucleophilic substitution reactions.³⁴



Scheme 1. A) First synthetic protocol of the TAA core motif as derived by Merz and Weith; B) three-step synthesis of TAA core motif as proposed by Goldberg and Nimerovsky.

Triarylamine derivatives have been studied intensively and it is the TAA core motif itself that lies at the origin of many physical characteristics. Although the structure of the TAA core is dictated by a limited number of parameters, the combination thereof affect geometry, chirality, optical and charge transfer properties, conductivity, as well as self-assembly and aggregation induced emission mechanisms. The structural aspects of triphenylamine (TPA) core motif discussed below can be extended to the large family of TAAs as a whole.

From the TAA core motif one can see the C_3 -symmetry that is also observed for, for example, trimethylamine (Figure 22A). In contrast to such analogues, that adopt sp^3 -hybridizations, the TAA core is nearly planar, corresponding to a sp^2 -hybridization (Figure 22B). C-N-C angles of $119.6 - 119.9^\circ$ are found by single crystal X-ray diffraction.³⁵⁻³⁷ This value is confirmed by additional techniques, such as electron diffraction in the gas phase², vibrational spectroscopy in an argon matrix³⁸ and multiple computational methods.^{38,6} Although the core is planar, the phenyl groups rotate out of plane to adopt a propeller-like shape, with dihedral angles of 47.8° between the phenyl rings in respect to the C_3 -axis (Figure 22C).⁶ In doing so, the steric hindrance between the phenyl rings is relieved. This equally means that two enantiomeric forms exist with either Δ or Λ conformations (Figure 23A). The energy required to transform from one enantiomer to the other was calculated by the group of Fausto (Figure 23B-C).³⁸ Upon ionization only minor geometrical changes occur.⁶ The TAA core motif remains planar, but the dihedral angles of the phenyl groups decrease to $\sim 40^\circ$ to optimize conjugation and stabilize the charge. Moreover, the C-N bonds are slight shortened.

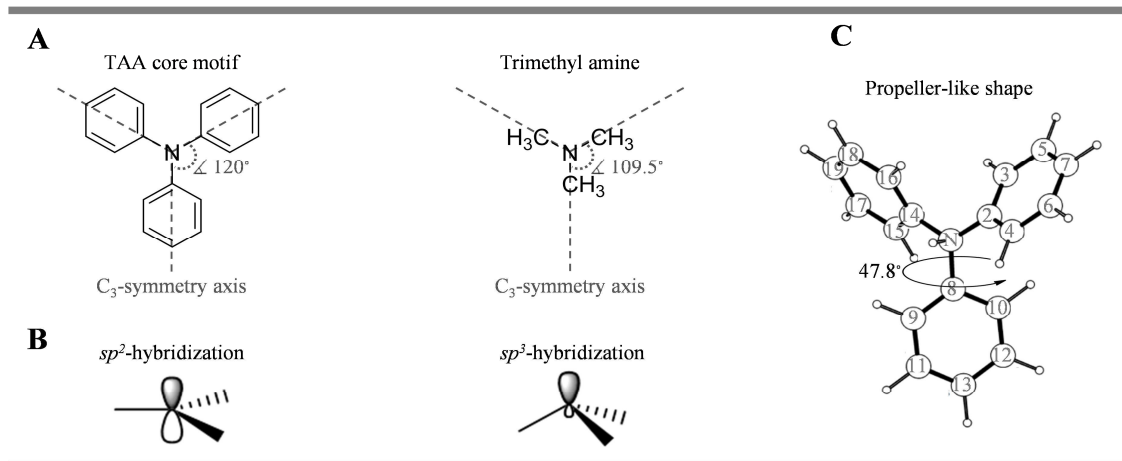


Figure 22. A) Molecular structure of the planar TAA core motif (left) and pyramidal trimethyl amine (right) exhibiting C_3 -symmetry; B) sp^2 hybridization of TAA-core motif; C) TAA-core's propeller-like shape.² This Figure is adapted from references 6, 35-37

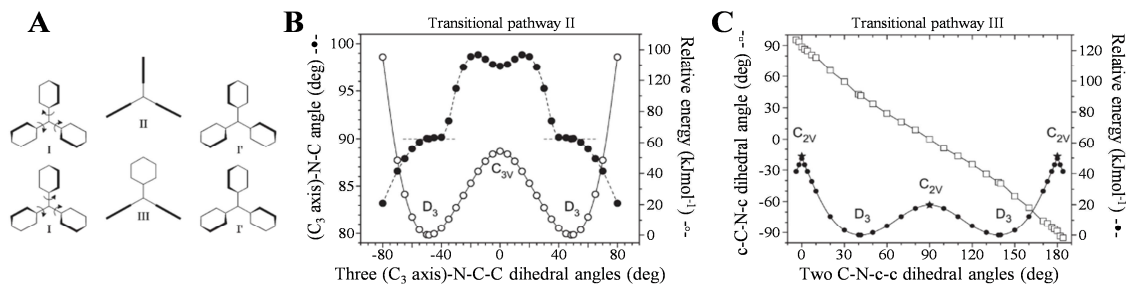


Figure 23. A) Schematic representation of the two enantiomeric forms of the TAA core motif and the two possible transformational pathways between them; B-C) relative energies of the TAA core motif for the I-II-I' and I-III-I' transformation depending on the dihedral C-N-C-C angles. This Figure is adapted from reference 38

From this TAA core motif a large family of compounds has evolved, comprising discrete TAA derivatives, star-burst TAAs, bridged TAAs, TAA oligomers and TAA polymers. The structures of some of such derivatives are given in **Figure 24** as examples.

As will become evident in the following sections, the molecular structure has a direct and profound effect on its physical properties. For example, TAA dimers are ideal candidates to realize donor-acceptor (push-pull) or mixed-valence compounds that give rise to electron and charge transfer, as well as one and multi-photon absorption.

Small molecules can enhance the crystallinity of materials, whereas bulky substitutions increase its amorphous nature. Moreover, star-burst TAAs not only increase the amorphous nature, but also allow for extended π -conjugation. Dipole moments can be enhanced by additional electron withdrawing or donating groups. Also chirality can be added, for example by unsymmetrical substituted TAA cores or by introducing chiral chains on the periphery.

Furthermore, carefully designing the structure and functionalities of substituents will affect the solubility of TAA derivatives in various solvents. For example linear oligomeric TAAs exhibit low solubility in common solvents because good packing of such chains is possible, whereas star-shaped TAAs are generally highly soluble.

Polymeric TAAs improve the intrinsic stability of TAA derivatives. Here also a wide variety of compounds with adjustable physical properties can be obtained. The TAA moiety can be incorporated either in the main chain or as side chain, the latter exhibiting less interaction between TAA groups. However, in both cases both conjugated and non-conjugated polymers can be realized; even large dendrimeric polymers have been synthesized. Another advantage of TAA polymers is that they are more facile to process. All previously mentioned structural possibilities together dictate the resulting morphology and persistence lengths of aggregates and polymers. Finally, bridged TAAs are known to self-assemble by π - π stacking because of the imposed planarity of the phenyl rings.

In Chapter I 1.4 *Physical Properties and Applications of Self-Assembled Triarylamine Structures* the relation between molecular structures of non-bridged TAA derivatives and subsequent self-assembly will be discussed in detail.

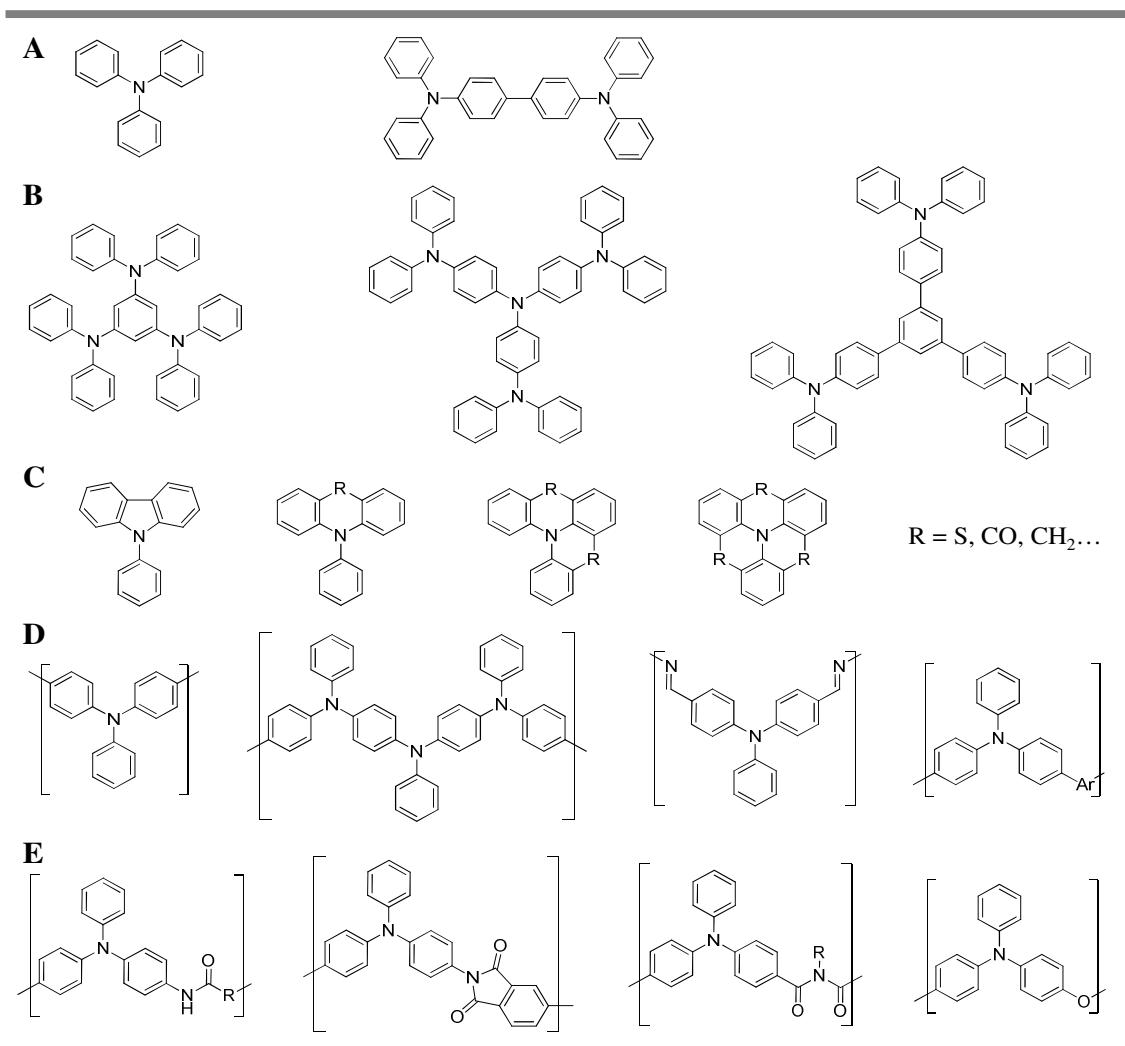


Figure 24. Examples of basic molecular structures of TAA derivatives: A) TAA monomer and dimer; B) star-burst TAAs; C) bridged TAAs; D) conjugated TAA polymers; E) non-conjugated TAA polymers.

B. Electrochemical properties of triarylamines

i. Electronic structure and redox potentials of triarylamines

The most prominent properties of TAA derivatives are their optical characteristics and electrochemical properties, such as intra- and intermolecular charge and electron transport and conductivity. These characteristics have led to TAA application into organic electronic devices. Studies investigating them data back to the 1960s.³⁹⁻⁴¹

TAA-derivatives that undergo oxidation into their radical cation state (TAA^{•+}) are known to undergo dimerization towards tetraphenylbenzidine compounds (also called triphenyldiamine TPD). After dimerization, the resulting dimer has lost two protons in comparison with its monomeric structures. Therefore, it is more easily oxidized and by two subsequent one-electron oxidation steps a dicationic state can be obtained (TAA → TAA^{•+} → TPD → TPD^{•+} → TPD²⁺). On the other hand, when all *para* positions bear substituents, or when TAA derivatives are bulky, or when it concerns TAA-oligomers, reversible one electron oxidation into a (meta-) stable cationic state (TAA ↔ TAA⁺) is achieved. Some derivatives are also able to undergo two electron oxidation (TAA ↔ TAA²⁺), which is generally irreversible. Furthermore, by choosing the nature of the substituents, the oxidation potentials can be tuned.^{42,43} The group of Lambert studied the oxidation potential of simple symmetric and asymmetric substituted TAAs in function of electron donor and acceptor ability.⁴ The results are summarized in **Figure 25A**. As anticipated, electron accepting groups (Cl) were shown to increase the oxidation potential with regards to alkyl substituents (691 mV and 332 mV respectively), while electron donating groups (OMe) decrease it (109 mV). The relationship between the shift in oxidation potential and number of electron accepting and donating groups proved to be linear (oxidation potential of TAA derivatives vs. ferrocene (Fc/Fc⁺)):

$$E_{1/2}(\text{I}) \approx 332 + 110 \cdot n[\text{Cl}] - 75 \times n[\text{OMe}] \quad (1)$$

The group of Audebert equally studied the substituent effect on the oxidation potential (**Figure 25B**).⁵ Just as Lambert, they found that electron donating substituents (Me; OMe; *p*-MeOPh) lower the oxidation potential and electron accepting groups (halides, aldehyde, nitrile) increase it. All together this means that easier oxidation can be obtained by functionalizing electron donating groups on the *para*-positions, as they will have a stabilizing effect on the radical. The inclusion of *p*-MeOPh in their study permitted the investigation of the effect of extended conjugation. The authors observed that by an extension of the conjugated link, which increases the distance between the electron donating group and the nitrogen core, the oxidation potential increases a little. The oxidation potential does not seem to be affected when bromine is replaced by iodine. In another article they studied the redox properties of TAA-tetrazine bichromophores for the development of a redox-fluorescent switch.¹⁰ By oxidizing the TAA moiety into its cationic state the photo-induced electron transfer to the tetrazine unit is disrupted and fluorescence is switched off. Both moieties act as independent redox centers and only the oxidation potentials of the TAA unit are listed in **Figure 25C**. Molecules 3 and 6 that are not substituted in the *para* position undergo polymerization upon oxidation and the oxidation potentials listed are estimates. Although electron transfer is possible between TAA and tetrazine, TAA is unaffected by the substituents on the tetrazine unit; only the *para* position substituents alter the oxidation potential.

A			B			C					
	R ₁	R ₂	E _{1/2}		R ₁	R ₂	E°		R	X	E° _{TPA}
1		OCH ₃	0.109	11	CHO	Br	0.79	17	CH ₃	Cl	0.48
2		CH ₃	0.332	12	CHO	I	0.78	18	Br	Cl	0.72
3	CH ₃	OCH ₃	0.180	13	CN	Br	0.85	19	H	Cl	0.67
4	CH ₃	Cl	0.576	14		OCH ₃	0.17	20	CH ₃	TAA-R	0.48
5	OCH ₃	Me	0.250	15	OCH ₃	CH ₃	0.22	21	Br	TAA-R	0.75
6	OCH ₃	Cl	0.463	16		<i>p</i> -CH ₃ OPh	0.25	22	H	TAA-R	0.55
7	Cl	CH ₃	0.460					23	CH ₃	OCH ₃	0.51
8	Cl	OCH ₃	0.290					24	Br	OCH ₃	0.7
9		Cl	0.691								
10		Cl (R ₁), CH ₃ (R ₂), OCH ₃ (R ₃)	0.359								

Figure 25. A-B) First oxidation potential (V) and standard potential (V) of symmetrically and non-symmetrically substituted TAAs vs. ferrocene (Fe/Fe⁺) in CH₂Cl₂ + TBAPF₆;^{4,5} C) standard potential (V) of the TAA moiety in TAA-tetrazine bichromophores vs. ferrocene (Fe/Fe⁺) in CH₂Cl₂ + TBAPF₆.¹⁰ This Figure is adapted from references 5 and 10.

Cias *et al.* performed *ab initio* computations and DFT calculations to determine the electronic structure of symmetric TAA derivatives in function of a large range of electron donating and accepting *para* substituents.⁶ First, they demonstrated that electron donating groups render the molecular structure more flexible upon ionization, in contrast to electron accepting groups that make it more rigid. Then they calculated (and collected additional values from other research groups) the energy levels, reorganization energies (λ), ionization potentials (I_p) and oxidation potentials ($E_{1/2}$) (Figure 26). The energy levels refer to the HOMO and LUMO levels. The reorganization energy λ_+ is defined as the stabilization energy of the radical cation by geometry relaxation. It is the sum of λ_1 , energy of the vertical ionization process minus the energy of the adiabatic process, and λ_2 , energy of the vertical electron affinity minus the electron affinity of the adiabatic ionization process. These concepts are schematically depicted in Figure 26A. The ionization potential is the energy needed to remove an (valence) electron, whereas the oxidation potential is defined as an electrical potential that indicates the spontaneity of oxidation/reduction compared to a standard hydrogen electrode. From the data gathered, the authors drew the following conclusions:

- First, the authors conclude that the reorganization energy increases for both electron accepting and donating groups compared to non-substituted TAA, although more strongly

- for the latter (Figure 26B). This is in direct relationship with the structural changes that occur.
- The second observation made is that donating groups increases the HOMO and LUMO levels and, as a result, the ionization energy decreases (Figure 26C-E). The inverse is true for the accepting groups. This can easily be understood by the increase and decrease of electron density in the TAA core motif due to the nature of the substituents. Moreover, accepting groups affect LUMO levels more than HOMO levels, whereas donor groups have a larger effect on the HOMO levels than the LUMO. With regards to non-substituted TAA, the energy gap between the two levels always decreases and this effect is larger for the strongest donor and acceptor groups.
 - Finally, a pronounced linear relation is found between the ionization and oxidation potentials (Figure 26D).

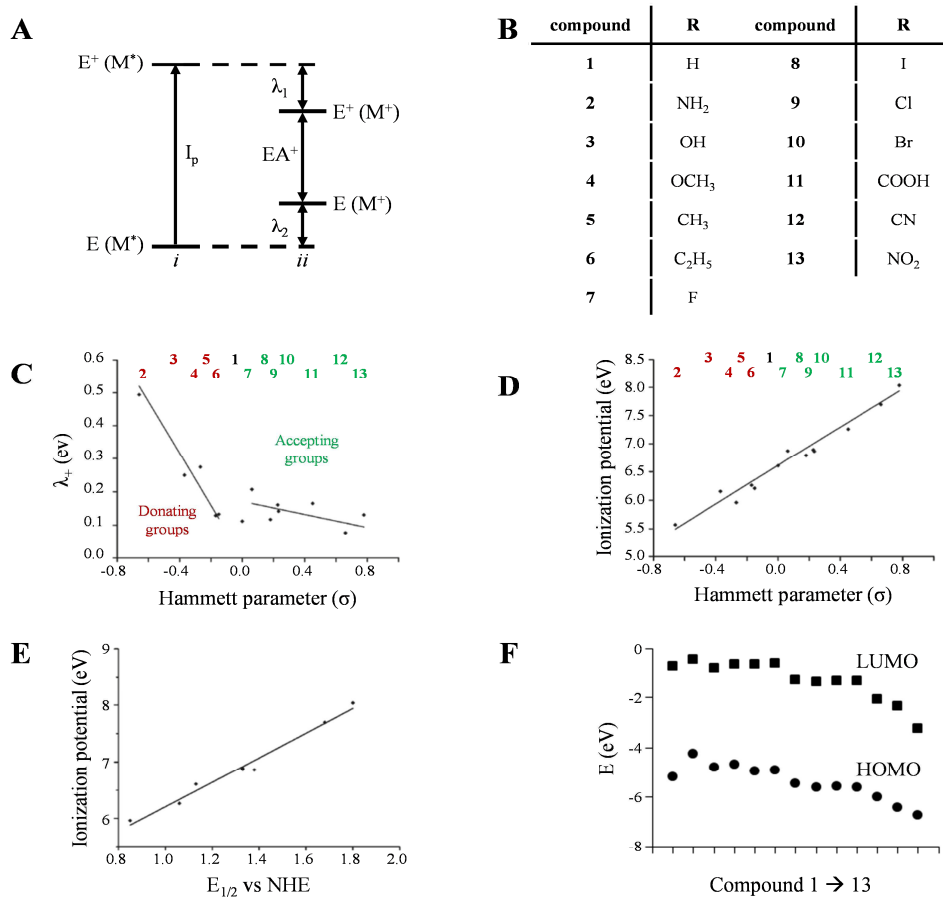


Figure 26. A) Detailed schematic depiction of reorganization energy upon oxidation where I_p is the vertical ionization energy, EA^+ the vertical electron affinity, λ_1 the reorganization energy of the cationic state and λ_2 the reorganization energy of the neutral state; B) Compounds studied; C) calculated reorganization energies; D) ionization potentials in function of the Hammett parameter; E) relation between the ionization potential and oxidation potentials; F) calculated HOMO-LUMO energy levels. This Figure is adapted from reference 6

The mechanistic and kinetic aspects of TAA radical cation formation was reported upon by the group of Flowers II.⁹ A series of TAA derivatives was synthesized and transformed into their radical state and subsequently into their tetraphenylbenzidine (TPB) equivalents by copper(II) perchlorate in acetonitrile (ACN) (Figure 27AB). They followed this process by monitoring the intensity of the radical absorption band using stopped-flow spectroscopy. As expected, radical formation is faster for derivatives with the smallest free energy change (ΔG°) and slower for molecules with larger ΔG° . Rate constants (k_{et}) calculated from the slope of the plots presented in Figure 27CD, varied between $1.02 \times 10^2 - 2.15 \times 10^5 \text{ M}^{-1}\cdot\text{s}^{-1}$ for a change in free energy between +3.67 and $-8.56 \text{ kcal}\cdot\text{M}^{-1}$. The same group equally studied the formation of the dication of tris(4-anisyl)amine.⁴⁴ The first oxidation process is thermodynamically attainable by Cu^{2+} in ACN ($\Delta G^\circ = -10.61 \text{ kcal}\cdot\text{mol}^{-1}$) and hence instantaneous. On the other hand, the formation of a dicationic state by two electron oxidation is an endergonic process ($\Delta G^\circ = +4.38 \text{ kcal}\cdot\text{mol}^{-1}$) and the complete reaction was only observed after 10 to 30 minutes of mixing.

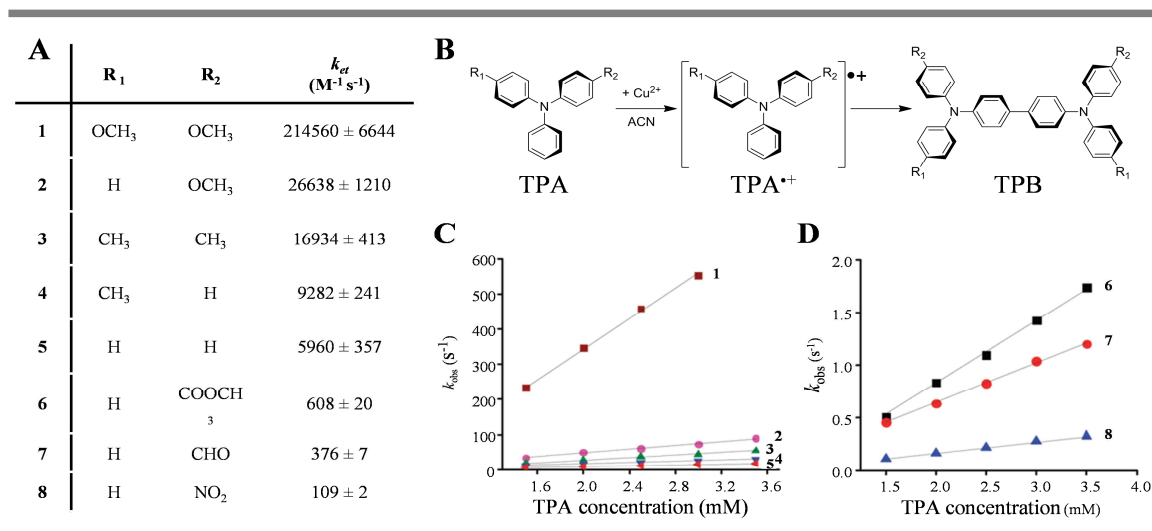
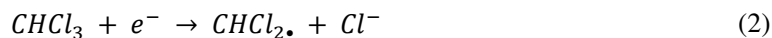


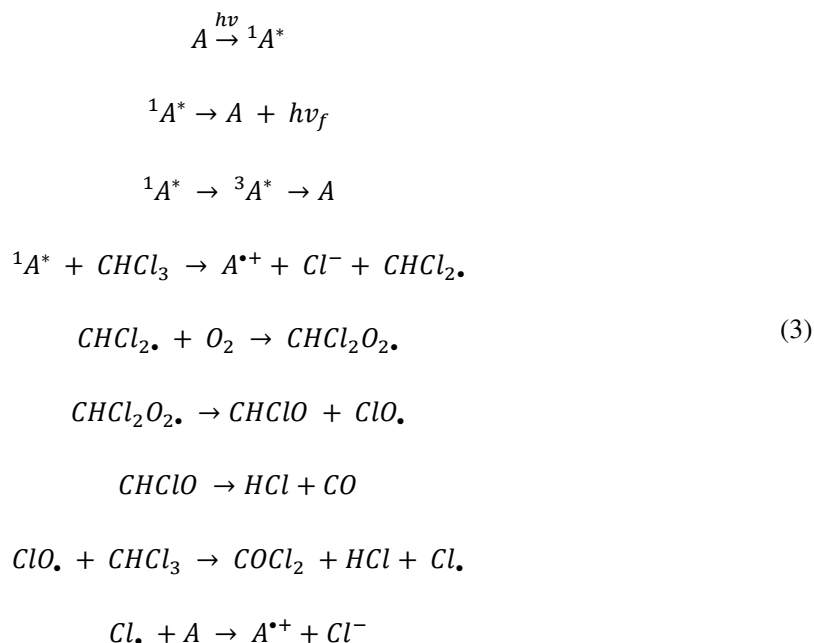
Figure 27. A) Table summarizing the TPA derivatives studied and the corresponding rate constants; B) reaction scheme for the formation of TPA^{•+}; C-D) pseudo first order reaction rate constants in function of the TPA concentration. This Figure is adapted from reference 9.

In all the previous examples, chemical oxidation by Cu^{2+} in acetonitrile is used to transform TAA into its radical state. Nevertheless also non-invasive oxidation methods exist in literature, such as radiation- and photo-oxidation. In our group mainly photo-oxidation in chlorinated solvents is used to oxidize and self-assemble TAA into *p*-doped supramolecular polymers, as will be detailed in *Chapter I 1.4 Physical Properties and Applications of Self-Assembled Triarylamine Structures*. It was the group of Richtol that, in 1971, investigated the photochemical oxidation of substituted aromatic amines, such as TAAs, in chloroform.⁷ The first observation they made was that the energy needed to cause photo-oxidation ($\sim 80.7 \text{ kcal}\cdot\text{mol}^{-1}$ or $\sim 3.4 \text{ eV}$) is notably lower than their oxidation potentials ($\sim 140 - 680$

kcal·mol⁻¹ or 6 – 7 eV). This is ascribed to the simultaneous dissociative electron attachment reaction, generating a chloride anion and a dichloromethyl radical in chloroform:



The heat generated during this reaction (exothermic by ~16 kcal·mol⁻¹ for chloroform), combined with the solvation energy of the ionic products, is enough to make the oxidation of the aromatic amines possible. They proposed the following mechanism for photo-oxidation in chloroform, where *A* is the aromatic amine; ¹*A*^{*} its excited singlet state; *A*^{•+} its radical cation state and *hν_f* a quantum of fluorescent light:



As it can be seen from this mechanism, oxygen plays an important role in the photo-induced oxidation process. Experiments show that air-saturated solutions have a twice as large oxidation efficiency compared to degassed samples.

ii. Electron and charge transfer in triarylamines

Following the description of Heckmann and Lambert, electron transfer (ET) is defined as the transfer of an electron through a molecular system, giving rise to either a second electronic ground state or to an electronically excited state. Charge transfer (CT) is defined as only involving a partial electron transfer between donor and acceptor parts of one or more molecules. It is characterized by the appearance of a “charge-transfer absorption band” of lower energy.⁸ Both processes can take place in mixed-valence and donor-acceptor compounds. The two classes of materials contain at least two

redox centers: one as electron acceptor, the other as electron donor, between which ET and CT can take place. The difference between the two classes however, lies in their electronic ground state. Mixed-valence compounds are open-shell systems (cationic or anionic), whereas donor-acceptor compounds are closed-shell systems (neutral or charged).⁸ Examples of ET in mixed-valence and donor-acceptor compounds are given in Figure 28A.

In the simplest terms, electron transfer can be explained by Marcus theory where the two states, before and after ET, are regarded as two isolated diabatic systems. The ET process can be induced by thermal energy (following the energy minima along the reaction coordinate x) or by optical energy (following Frank-Condon principle), as is depicted in Figure 28B. Just as electron transfer, also charge transfer can be induced by either thermal or optical energy (Figure 28C). Here, charge is transmitted from one redox center to the other accompanied by solvent dipole reorientation and leading a total geometric and electronic mirror of the previous state. In thermally induced CT, the geometries and electronic states of the two centers change simultaneously while keeping the total free energy of the system constant. This is in contrast to optically induced CT where the electronic state changes first after which solvent and geometries changes take place to adapt to this new state.

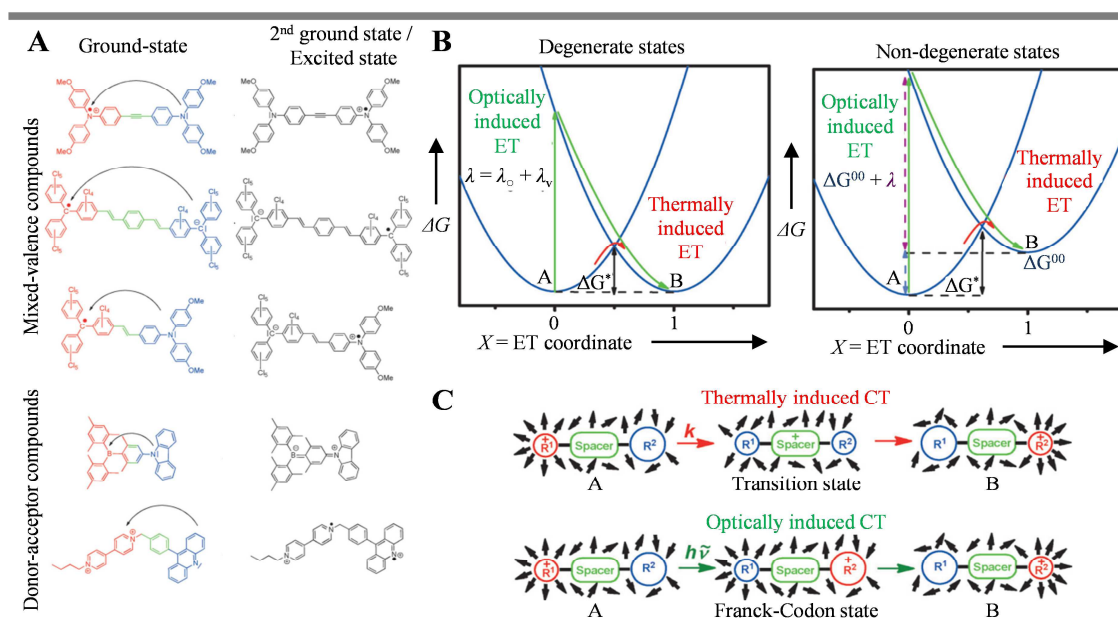


Figure 28. A) Examples of ET in mixed valence and donor-acceptor molecules. Electron donor moieties are colored blue, acceptor moieties in red and bridges in green; B) Schematic depiction of free energy surfaces during ET in molecules where the two states, either degenerate or non-degenerate, are regarded as isolated adiabatic states; C) Schematic depiction of CT pathways in molecules containing two identical redox centers. The dipole moments of solvent molecules are presented by the black arrows. This Figure is adapted from reference 8.

The previous description, however, cannot be applied for systems in which the electronic communication between the redox centers is large. For these systems, the Marcus-Hush theory that includes calculations of the electronic coupling V is more appropriate (Figure 29A-C).⁸ In this description, the energetic minima are stabilized by resonance delocalization. Such systems, that is systems having two chemically equivalent centers exhibiting different oxidation states, display an intramolecular intervalence charge-transfer (IV-CT) absorption band, usually located in the near-infrared region as it is the lowest energy transition (Figure 29D). Strong electronic coupling results in an asymmetric IV-CT band, whereas small coupling ($0 < V < \lambda/2$) in a symmetric band.

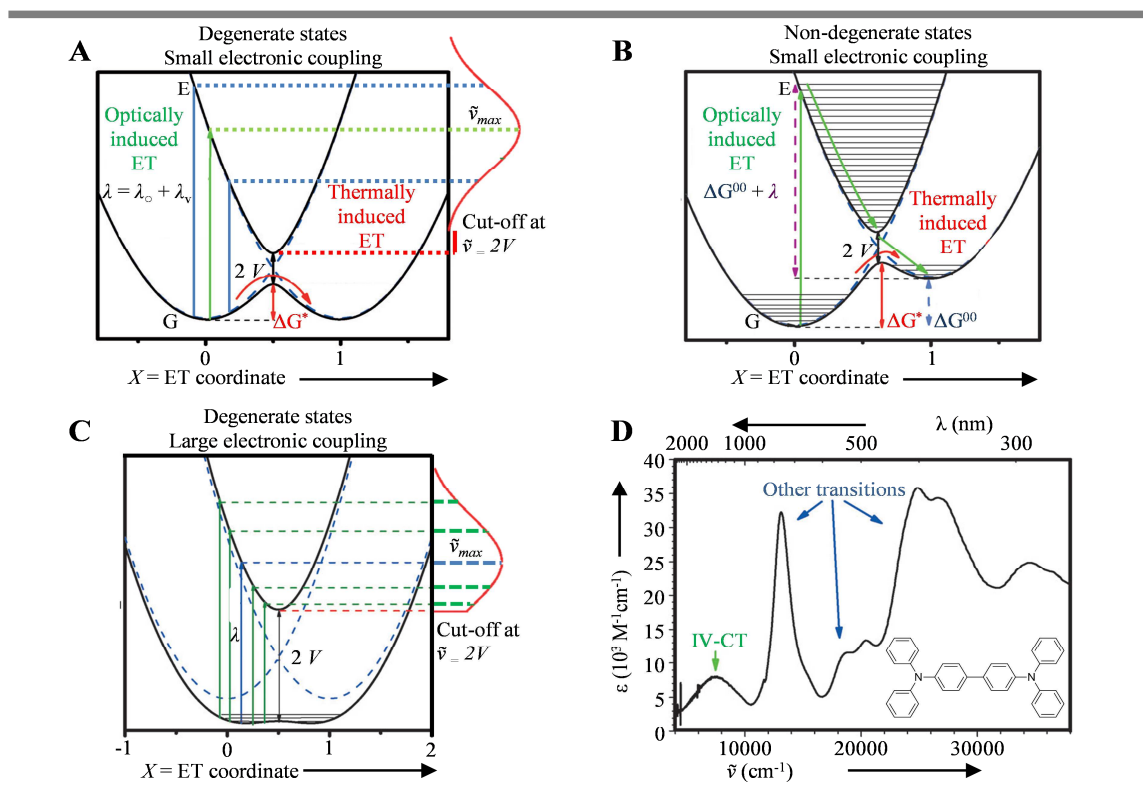


Figure 29. Schematic depiction of free energy surfaces during ET in molecules where either A-B) small or C) large electronic coupling takes place between ground (G) and excited (E) states; D) absorption spectrum of TAA dimer displaying a IV-CT band as lowest energy transition. This Figure is adapted from reference 8.

TAA derivatives are prone to have excellent ET and CT properties because:

- Presence of a nitrogen redox-center in the TAA core motif.
- Low ionization potential (read facile formation of charge separated states)
- Large extinction coefficient
- Stable radical states (read long lifetime of charge separated states)
- Facile optical characterization (both TAA and TAA^{•+} have characteristic and well separated absorption bands)

- Low reorganization energy (λ_v) (only small geometrical changes of the redox centers occur during ET and CT)

Hence an important number of articles describing the ET and CT involving TAA derivatives exist, which is thoroughly summarized in multiple articles and reviews.^{8,45-48} Here, we will only summarize the most important observations made. We will further limit ourselves to TAA derivatives that only use TAA core motifs as redox centers.

Although TAA dimers are excellent candidates, it is the nature of the linker unit that predominantly affects the ET behavior. In the group of Heckmann and Lambert, the effect of linker length on ET was investigated.^{3,49,50} Derivatives with short linker units exhibit strong electronic coupling, as shown by more asymmetric IV-CT bands (**Figure 30A**). Moreover, their electronic nature proves not only dependent on their chemical nature but also on solvent polarity.⁵¹ This effectively means that their electronic character will switch from localized to delocalized in function of solvent polarity. The observation of a broad IV-CT band and a radical absorption band at the same time indicates that ET takes place and electronic coupling occurs, but the charges are mostly localized on one center than the other (**Figure 30Bi**). This is also shown by the shift of the band depending on the solvent used. A narrower IV-CT band of higher intensity that displays little sensitivity to the solvent used, on the other hand, indicates a fully delocalized character of the radical (**Figure 30Bii**).⁵⁰ Interestingly, calculations tend to suggest that even in TAA dimers linked by (very) long spacers the electronic coupling is important. In spite of this, the group of Barlow only found extremely small electronic coupling for very long linkers.^{52,53} Paracyclophane is an interesting linker unit because electron and hole motion could occur by a through bond ET (σ -bonds), a through space ET (π faces) or by direct π - π stacking. Observations made, however, show that it primarily acts as a through space mechanism.⁵⁴ For linkers of equal lengths but different size (decreasing HOMO-LUMO band gaps for more extended π conjugation), delocalization is highly dependent on solvent polarity, although increasing HOMO levels increases electronic coupling and at the same time facilitate ET by incoherent hopping.⁵⁵ The inverse effect is observed for linkers that have increased steric interactions with the TAA redox centers due to a larger angle between all moieties.⁵⁶

A family of linkers that have received particular interest because of their common application in organic electronic devices involves biphenyl bridged moieties. It has been demonstrated that the functionalities substituted to the linker have a great effect on the electronic coupling for the same reasons discussed before (solvent polarity and steric hindrance). Furthermore, electron donating substituents will lower the oxidation potential, whereas compounds with a twisted conformation exhibit higher oxidation potentials.⁵⁷ The effect of non-degenerate states was studied by Nöll, who incorporated different functionalities to the phenyl rings on the TAA core.⁵⁸ Electron accepting groups increase the redox potential splitting and the IV-CT shifts to higher energies. Because the substituents

have only a small impact on the adiabatic dipole moments, the electronic coupling remains constant for constant ET distances.

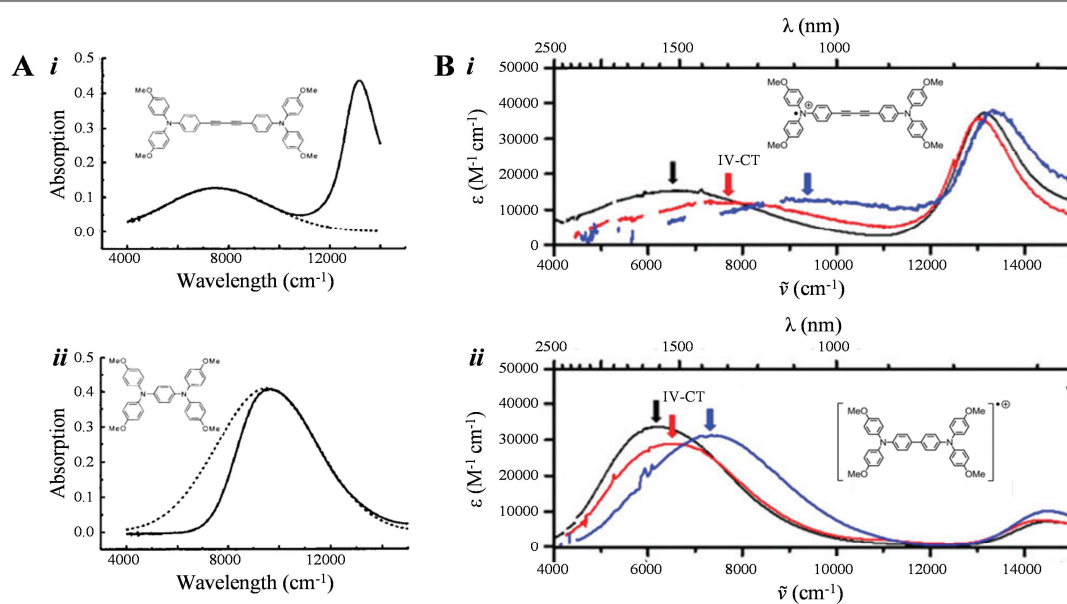


Figure 30. A) Vis-NIR absorption spectra taken in $\text{CH}_2\text{Cl}_2 + \text{TBAH}$ (solid lines) displaying IV-CT bands and Gaussian band fits (dotted lines)³; B) vis-NIR absorption spectra taken in DCM (black lines), PhNO_2 (red lines) or MeCN (blue lines) displaying IV-CT band indicated by the arrows.⁵⁰ This Figure is adapted from references 51 and 50.

C. Conductivity properties of triarylamines

Traditionally electronic devices are made of inorganic semiconductors (e.g. silicon) and conductors (e.g. metals). However the development of such devices becomes impeded because the materials used are expensive and/or rare, can be toxic and lack flexibility. All of which requires strict fabrication steps, which increases the cost of fabrication. Therefore, organic semi-conductors have received increasing interest. They are made of earthly abundant materials of low (to none) toxicity, enable facile synthesis, display high stability and possible flexibility leading to easy processability. TAA derivatives, as detailed in the previous sections, exhibit low ionization potentials and stable radical states with large extinction coefficients, leading to excellent photo- and charge carrier conduction. From this point of view, TAA derivatives are considered ideal candidates for (opto-) electric devices and their conductivity properties have been extensively studied. The nitrogen atom in the TAA core motif has an electron donating nature, therefore they give rise to hole transporting materials.

Conductivity can take place following different mechanisms. Electron and hole transport can occur in a coherent or incoherent manner. In coherent motion, energy transfer takes place because of electronic coupling between the different energy states of the molecule. This promotes the

delocalization of electronic excitations, and one can compare it to a delocalized band-like transport mechanism. In incoherent motion, energy transfer takes place by localized electron or hole diffusive hopping (incoherent tunneling between functionalities of the same molecule or between molecules).

One of the earliest studies on TAA conductivity dates from 1989 by the group of Noma, who studied the formation of amorphous glassy organic materials using the starburst compounds TDATA and MTDATA (Figure 31A).⁵⁹ The authors made amorphous glassy films and measured conductivities of $\sim 10^{-10} \text{ S}\cdot\text{cm}^{-1}$ at room temperature with an activation energy of 0.38 eV. Its relatively high conductivity and low resistivity were attributed to the partial and spontaneous oxidation of the material by air. Hole transport in TAA glassy films (TTB and TPD, see Figure 31B) was investigated in 1995 by Heun and Borsenberger.⁶⁰ The authors concluded that hole transport takes place by an incoherent hopping mechanism, which implies that *i*) transition from non-dispersive to dispersive hole transport will take place at a critical temperature; *ii*) hole mobility is field dependent ($\log(\mu) \propto E^{1/2}$); *iii*) hole mobility is temperature dependent ($\log(\mu) \propto T^{-2}$). The hole mobilities, measured by time-of-flight techniques, are $\mu_0 = 3.0 \times 10^{-2} \text{ cm}^2\cdot\text{V}^{-1}\cdot\text{s}^{-1}$ and $3.2 \times 10^{-2} \text{ cm}^2\cdot\text{V}^{-1}\cdot\text{s}^{-1}$ for TTB and TPD respectively at an electrical field of $1.0 \times 10^5 \text{ V}\cdot\text{cm}^{-1}$.

Dendrimeric structures have the advantage that multiple active units can be brought in close proximity. However, branching generally disrupts conjugation and most structures are thus regarded as ensembles of linear chromophores with little inter-chromophore charge transfer. Normally, resonance interactions between chromophores leads to coherent energy transfer between them. For dendrimers, however, this effect is cancelled out due to the interactions with its environment, as well as molecular motion. Instead localized states are created and as a consequence incoherent energy transfer will take place. The group of Goodson III investigated the coherent effects in inter-chromophore energy transfer for branched dendritic molecules by time-resolved fluorescence anisotropy spectroscopy.⁶¹ They found that in the triarylamine trimer (Figure 31C), in contrast to tetrahedral dendrimers with a carbon or adamantane core, coherent energy transport seems to take place.

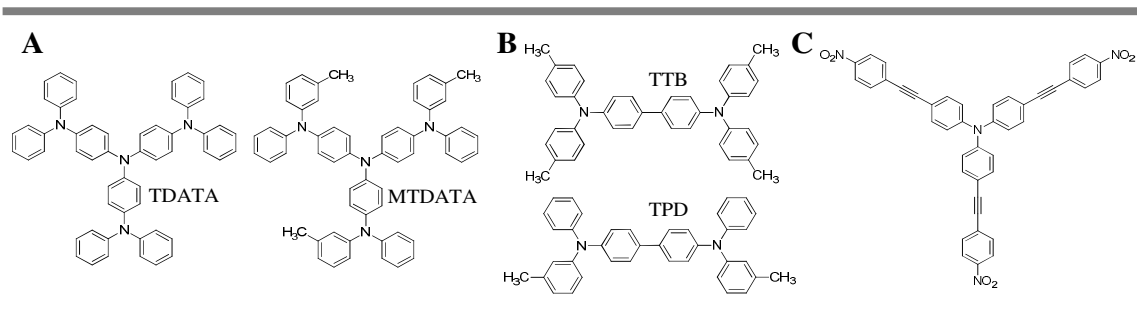


Figure 31. Molecular structures studied by the group of A) Noma; B) Heun and Borsenberger; C) Goodson III.

The conductivity of TAA derivatives can be improved by adaptations in its molecular structure and by p-type doping. Typically, research groups take advantage of the commonly utilized photo-doping properties of TAA derivatives, however chemical doping is also very promising.^{62,63} Using lithium salts or Copper (III), conductivities of at least 10^{-5} S·cm⁻¹, but going up to 10^{-2} S·cm⁻¹ can be obtained. The relation between molecular structure, material morphology and conductivity of TAA derivatives are mostly studied in parallel to the development of OLEDs and OFETs. This will be discussed in detail in *Chapter I 1.2 Applications of Triarylamines*.

D. Optical properties of triarylamines

i. Absorption and fluorescence

Classical photon absorption, or one photon absorption (1PA), is a linear absorption process whereby one photon is absorbed by an atom or molecule which is consequently excited from a lower energy state (E_{initial}) (usually the ground-state) to an excited state (E_{final}). For a photon to be absorbed, its energy has to be equal to or greater than the energy difference ($E_{\text{excitation}}$) between two energy states. In cascaded photon absorption, multiple photons are absorbed in multi-step one photon absorption processes. In contrast, in multi-photon absorption, which is a non-linear absorption process, multiple photons are absorbed simultaneously. Here, the $E_{\text{excitation}}$ is equal to, or higher than, the sum of the energies of the photons absorbed. $E_{\text{excitation}} = hv_1 + hv_2 + hv_n$. These processes are schematically depicted in **Figure 32**.

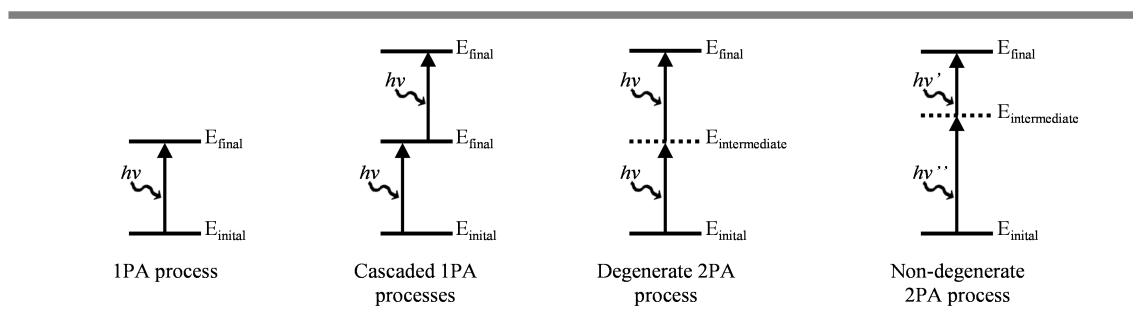


Figure 32. Schematic depiction of 1 photon absorption cascaded one photon absorption and multi-photon absorption.

It was Maria Goppert–Mayer who, during her PhD thesis in 1931, first described the concept of multi-photon absorption (MPA).^{64,65} Using the newly introduced concepts of quantum theory of radiation and eigenstates she hypothesized the existence of intermediary energy states ($E_{\text{intermediate}}$). Using these intermediary states, she postulated that two photon absorption (2PA) should lead to the excitation of an atom or molecule from a lower energy state (E_{initial}) to an excited state (E_{final}). However, the probability of 2PA is small and cannot be measured using an incoherent light source. Therefore, it was only after the invention of the laser in 1961 that 2PA was observed for the first

time.⁶⁶ Nowadays also three or four photon absorptions have been observed. Several reviews exist that deal with the various aspects of MPA, from the basic introduction to MPA to applications, including structural design strategies and structure-property relationships.⁶⁷⁻⁷⁰ Each of these aspects will be summarized briefly below.

MPA active materials have received much attention in both fundamental studies and in applied science. This is because MPA lies at the origin of several phenomena.^{67,68} First of all, it leads to the non-linear transition from a lower to a higher energy state. But it can also enhance changes in refractive-indexes, lead to molecular dissociation or ionization and induce surface electron emission, conductivity and polymerization. Furthermore, because the energy absorbed is proportional to the squared intensity of the incident light, enhanced spatial selectivity and resolution can be obtained. 2PA is possible at half the frequency of the actual energy gap, thus lasers with longer wavelengths and deeper tissue penetration can be used. Moreover, as longer wavelengths are used, less scattering effects and less photochemical decomposition takes place. As a result, 2PA active materials are especially well suited for 3D fluorescence imaging, biological imaging, 3D optical data storage, 3D lithographic microfabrication, photodynamic cancer therapy and optical limiting.

Whether a molecule is 2PA active will depend on its cross-section (σ_2 or σ'_2), which is a measure of 2PA sensitivity. The cross section is a structure-property relationship that describes the electronic eigenstates as well as the transition behavior of a molecule. From this, two intrinsic properties needed for 2PA have been defined⁷¹: *i*) a permanent ground-state dipole moment; *ii*) a transition dipole moment connected to either the ground state or the excited state. Moreover, when comparing the electronic eigenstates with the photo physical processes of a molecule, a strong relation between intramolecular charge-transfer and 2PA can be found. However, experimental factors that influence the 2PA cross-section should also be considered. For example, the local environment (solvents, matrices) that perturbs to a certain degree the structural state of a molecule. The occurrence of other non-linear absorptions and/or photochemical events may cause structural changes as well.

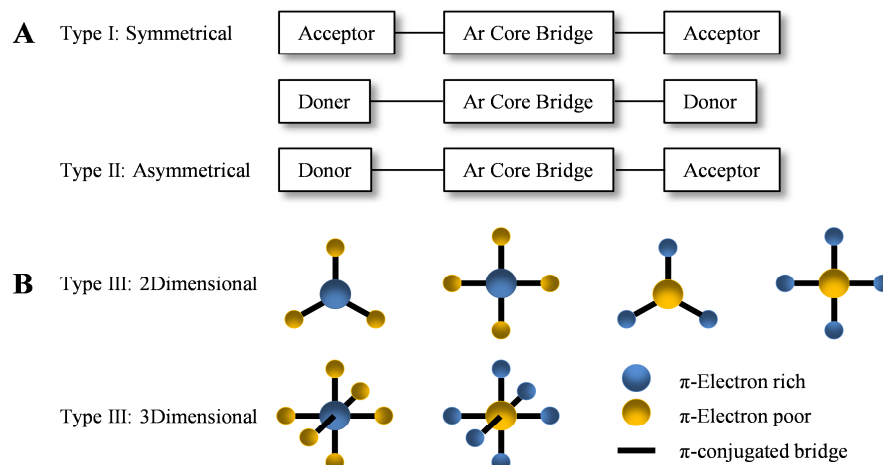


Figure 33. Molecular structural motifs giving rise to A) one B) two and three dimensional two photon absorption (Ar = aromatic building block). This Figure is adapted from reference 67.

2PA active molecules requisite several structural motives (Figure 33).^{67,68} First of all, the presence of strong π -donor and/or strong π -acceptor moieties in the molecular structure is of importance. The stronger the donor-acceptor character, the greater the charge transfer potential and the larger the transition dipole moment is. Hence, strong π -donor-acceptors result in large 2PA cross-sections. Secondly, the π -conjugation length (polarizable π -bridge) plays a pivotal role, as it allows for extended charge separation. To further enhance the efficiency of intermolecular charge transfer (ICT), co-planarity is critical. However, meta-linkages are disadvantageous. Moreover, the ground-state dipole moment of non-symmetric molecules or the multipolar transition-dipole moment in centrosymmetric molecules has been shown to greatly influence the 2PA in organic systems. In other words, increasing the π -conjugation length and/or linking multiple linear paths into a 2D or 3D configuration significantly increases the probability of 2PA. The existence of higher dimensionality conjugated systems (multibranching and dendrimeric structures) improves the 2PA cross-section due to the branching effect, also called cooperative enhancement. In cooperative enhancement the measured cross-section value is greater than the sum of cross-sections of the discrete units the molecular system is made up of. Triazines, 2,4,6-alkylpyridinium, 1,3,5-tricyanobenzene, 1,3,5-benzene, truxene and 3,5-dicyano-2,4,6-tristyrylpyridine are known to give rise to cooperative enhancement. Finally, solvent polarity, which influences H-bonding and aggregation of the material, are also important factors to take into account. Especially because the 2PA cross section seems to be more sensitive to the polarity of the local environment than the intrinsic 2PA properties.

As donor-groups, generally (di-) substituted amino groups (e.g. (di)alkylamino or (di)phenylamino) are used because they are readily available, exhibit good air stability, the good electron-donating capability of the amine, and the stability of its oxidative state. N-Substituted

carbazoles and pyrroles are also acceptable terminal donor moieties. Triaryl amines as donor groups exhibit most of the same advantages:

- TAA is a strong electron donor.
- TAAs display good co-planarity between the central nitrogen atom and the three surrounding carbon atoms. Ergo, they can maintain uninterrupted conjugation between the electron lone pair of the central nitrogen atom and the three phenyl rings.
- TAA core motif can be used to induce/enhance the branching effect.
- TAAs enhance nonlinear responses.
- The amino groups on the periphery of the TAA core can be substituted to modulate the solubility of the molecule and provide more electron density to the structure.

One, two and multi-photon absorption in TAA derivatives

As previously discussed in *Chapter I B. Electrochemical properties of triaryl amines*, the group of Lambert performed a systematic study on the oxidation potentials of various simple symmetrically and asymmetrically *p*-substituted TAAs.⁴ In the same work also the linear optical properties were investigated. This second part is summarized in **Figure 34** and described in the following paragraphs.

Typically, in IPA processes, neutral TAAs have one intense absorption band near 300 nm as the result of a π - π^* transition of an electron localized on the phenyl rings. Upon absorption C_3 symmetrical TAAs transform into a single degenerate state (E_{S1}) by a HOMO (S_0) \rightarrow LUMO (S_1) excitation. Asymmetrical TAAs on the other hand transition into two degenerate states (E_{S1} and E_{S2}) by HOMO (S_0) \rightarrow LUMO (S_1) and HOMO (S_0) \rightarrow LUMO+1 (S_2) excitations. Electron acceptor groups (e.g. OCH_3) will cause bathochromic shifts in the absorption maximum, electron donating groups (e.g. Cl) cause hypsochromic shifts. In a more polar solvent (CH_3CN as compared to CH_2Cl_2) the spectra are blue-shifted, suggesting a slight charge-transfer character.

The IPA spectra of radical cation TAA^{*+} display three absorption bands. The first and most intense one is located around 670-730 nm. The second is located around 570-630 nm. The third absorption band is found around 350 nm. Just as neutral TAAs, C_3 symmetrical TAA^{*+} transform into a single degenerate state (E_{D1}) by a HOMO (D_0) \rightarrow SOMO (D_1) excitation whereas asymmetrical TAA^{*+} transition into two degenerate states (E_{D1} and E_{D2}) by HOMO (D_0) \rightarrow SOMO (D_1) and HOMO-1 (D_0) \rightarrow SOMO (D_2) excitations. When substituted by either methoxy- or chloro-groups, absorption maxima are shifted to lower energies because of the extension of the π -conjugated system. However, C_3 symmetrical TAAs and TAA^{*+} can also display two absorption bands, evidence of two different states S_1/D_1 and S_2/D_2 . This could be the result of C_3 -symmetry breaking by solvent

interactions and/or planarization of the radical cation TAA (reduced out of plane rotation of the phenyl rings).

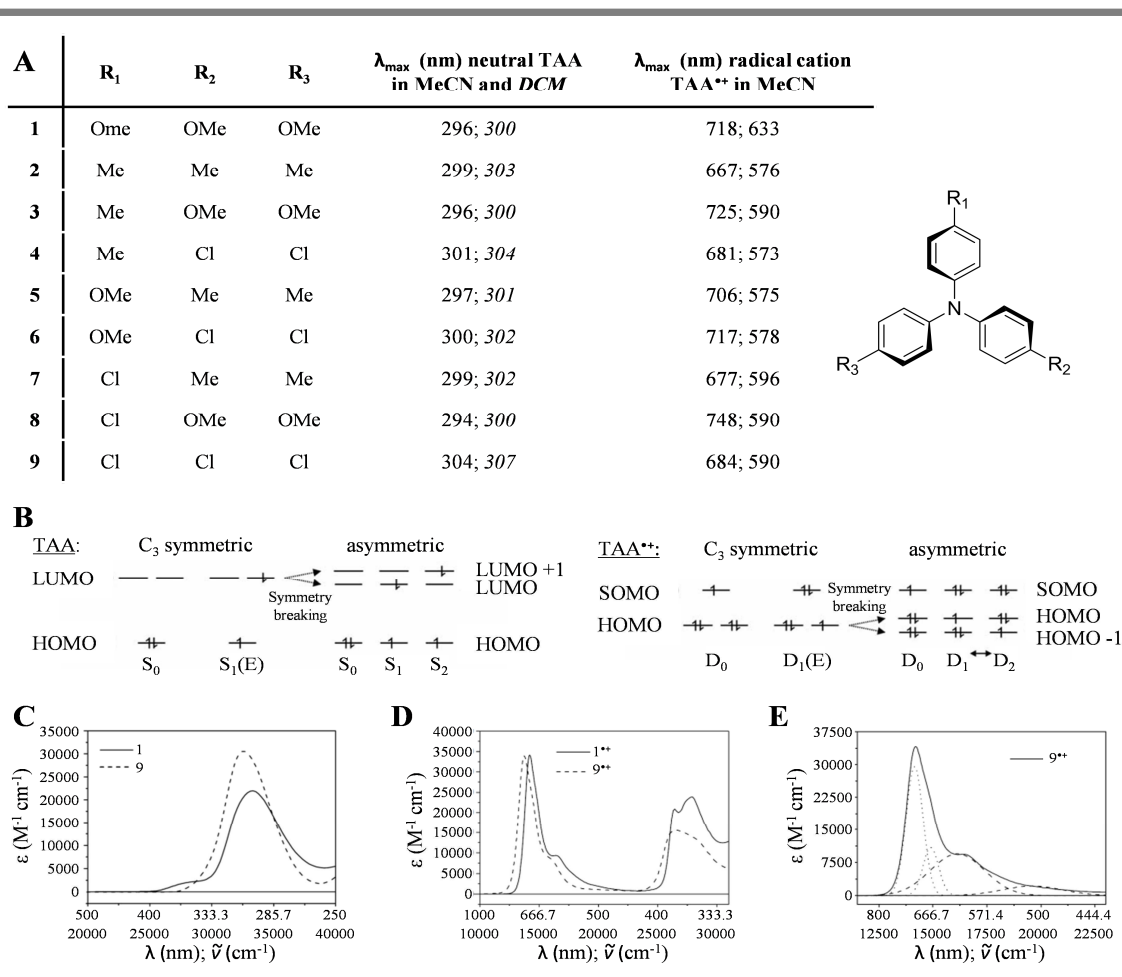


Figure 34. A) Molecular structure and substituents of the *p*-substituted TAAs studied by the group of Lambert. In the same table the maximum absorption peaks of the neutral molecule and its corresponding radical cation are listed; B) Schematic depiction of the ground (S_0 , D_0) and excited states (S_1 , S_2 , D_1 , D_2) of symmetrically and non-symmetrically substituted TAAs in its neutral (left) and radical cation (right) state; Absorption spectra of molecule 1 and 9 in its neutral (C) and radical cation (D) state taken in CH_2Cl_2 ; Deconvolution of the absorption spectrum of molecule 9^+ to visualize the $D_0 \rightarrow D_1$ (dotted lines) and $D_0 \rightarrow D_2$ (dashed lines) transitions. This Figure is adapted from ref 4.

The absorption properties of several TAA derivatives, in function of oxidation, were also studied in group of Flowers II (Figure 35).⁹ The formation of radical TAAs^{•+}, formed upon reaction with copper (II) perchlorate in acetonitrile, results in a strong absorption band in the 650 – 730 nm region (Figure 35B, D), which is thus in accordance with the intense absorption peak observed by Lambert. The same method can be employed for the generation of the di-cation of tris(4-anisyl)amine.⁴⁴ In Figure 35D, the evolution of the absorption bands in function of Cu^{2+} is plotted. Upon addition of one equivalent Cu^{2+} , TAA transforms almost instantly in its radical form and absorption around 717 nm is

maximal. Addition towards two equivalents of Cu^{2+} results in a decrease in absorption intensity at 717 nm and an increase at 520 nm. When 2 equivalents are added, the 717 absorption band has disappeared and the 520 nm absorption band is maximal. Thus the absorption band around 717 nm can be attributed to radical TAA and the band at 520 nm is characteristic for the presence of TAA di-cations. This was also verified by ^1H and ^{13}C NMR spectroscopy, as well as infra-red spectroscopy. One should note that the di-cation formation is relatively slow compared to the cation formation. Furthermore, the radical solutions obtained turned out to be stable for multiple weeks and 100% recoverable. Upon addition of neutral TAA to the di-cation solution, TAA^{*+} is formed. Neutral TAA can be obtained from TAA^{*+} by simply adding some triethylamine (TEA).



Finally, they measured an extinction coefficient (ϵ) of $32800 \text{ M}^{-1}\cdot\text{cm}^{-1}$ for TAA^{*+} and $22200 \text{ M}^{-1}\cdot\text{cm}^{-1}$ for TAA^{2+} , which agrees with the $\epsilon \approx 33000 \text{ M}^{-1}\cdot\text{cm}^{-1}$ and $20000 \text{ M}^{-1}\cdot\text{cm}^{-1}$ measured by Lambert.

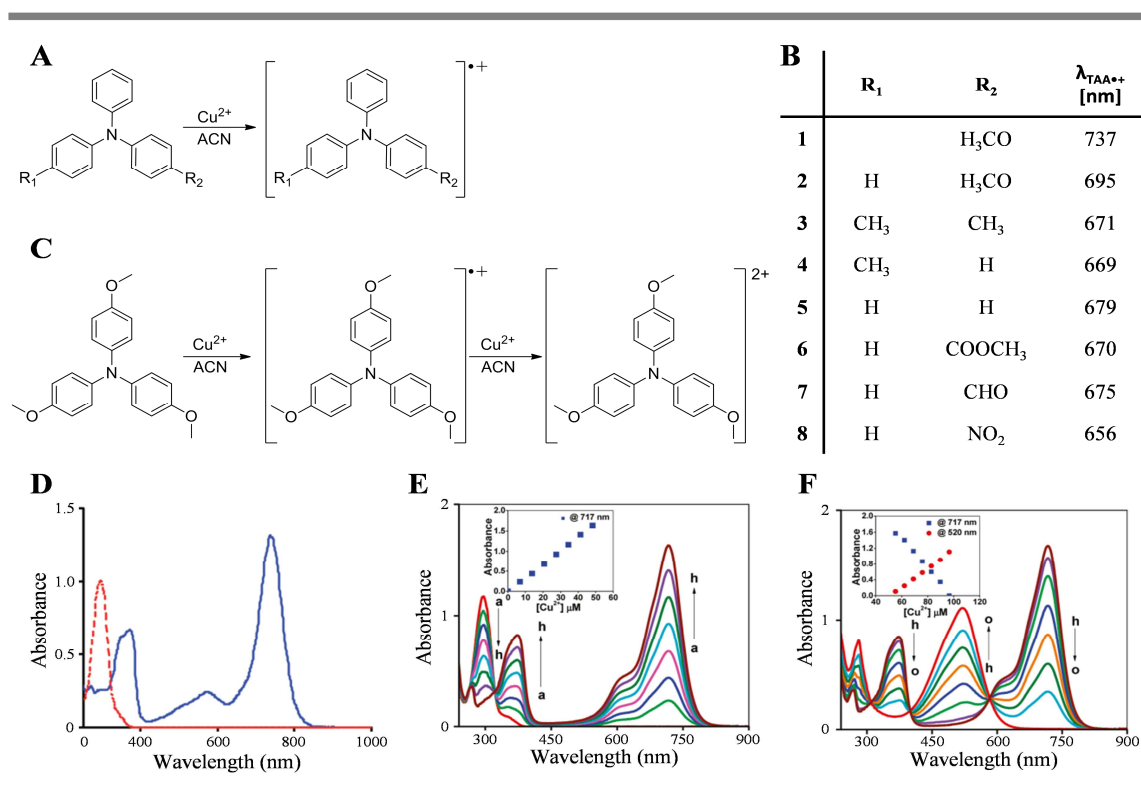


Figure 35. Molecular structures of the A) neutral, cationic and C) di-cationic TAAs studied by the group of Flowers II. In the table (B) the substituents, as well as their maximum absorption peaks, are listed. D) Absorption spectrum of molecule 1 in neutral (red line) and cationic (blue line) state taking

in acetonitrile; E-F) Absorption spectra of the molecule depicted in (C) upon the addition of E) 0 to 1 equivalents of oxidant and F) 1 to 2 equivalents of oxidant. The spectra are taken in acetonitrile. This Figure is adapted from references 9 and 44.

In the group of Audebert, the absorption *and* emission properties of a TAA bi-chromophore in function of oxidation were studied.¹⁰ They coupled an electron-rich TAA fluorophore to an electron-poor tetrazine fluorophore by an oxygen atom spacer (**Figure 36A**). The same Cu^{2+} / ACN oxidation process was used as described in the previous paragraph. The absorption of the bi-chromophores proved approximately the sum of the individual parts. In neutral form the TAA moiety shows typical absorption spectra, as reported earlier by Lambert. In general three absorption bands can be observed: *i*) ~ 300 nm, $\pi\text{-}\pi^*$ transition on TAA and tetrazine, *ii*) ~ 460 nm for homo disubstituted tetrazines, *iii*) ~ 530 nm, forbidden $n\text{-}\pi^*$ transition on tetrazine unit. As expected, intense bands around 360 and 706 nm appear upon titration with Cu^{2+} , which corresponds to the radical cation. At the same time, and also in correspondence with previously reported data, the $\pi\text{-}\pi^*$ band around 300 nm decreases (**Figure 36B**). Both moieties are fluorescent, however when bound, fluorescence quenching occurs through a photo-induced electron transfer (PET) process from TAA to tetrazine. When TAA is oxidized the PET process is disrupted and the fluorescence of tetrazine is restored. Maximum fluorescence intensity was reached for 1.5 equivalents of Cu^{2+} .

In a second article they reported the redox-controlled fluorescence of another series of TAA molecules (**Figure 36C**).⁵ In the neutral state, the absorption spectra concur with previous research, with the $\pi\text{-}\pi^*$ transition absorption band between 283 – 357 nm depending on the substituent. Overall, the fluorescence emission spectra, with one intense band between 382 and 532 nm, are good mirror images of the absorption spectra (**Figure 36D**). Fluorescence quantum yields vary around 0.05; fluorescence lifetime depends on the substituent and ranges from 0.9 to 3.6 ns. Although the absorption and emission wavelengths do not change between bromine and iodine, both quantum yield and lifetime decreases for the latter due to a stronger heavy atom quenching effect. Upon titration with Cu^{2+} / ACN the two bands characteristic for $\text{TAA}^{+\cdot}$ appear (**Figure 36E**). TAA substituted with electron donating groups display the highest chromatic contrast in these series. The fluorescence decreases almost linearly with the concentration of $\text{TAA}^{+\cdot}$ formed. $\text{TAA}^{+\cdot}$ is thus non-fluorescent (**Figure 36F**). Nonetheless, the fluorescence lifetimes do not change during the oxidation process.

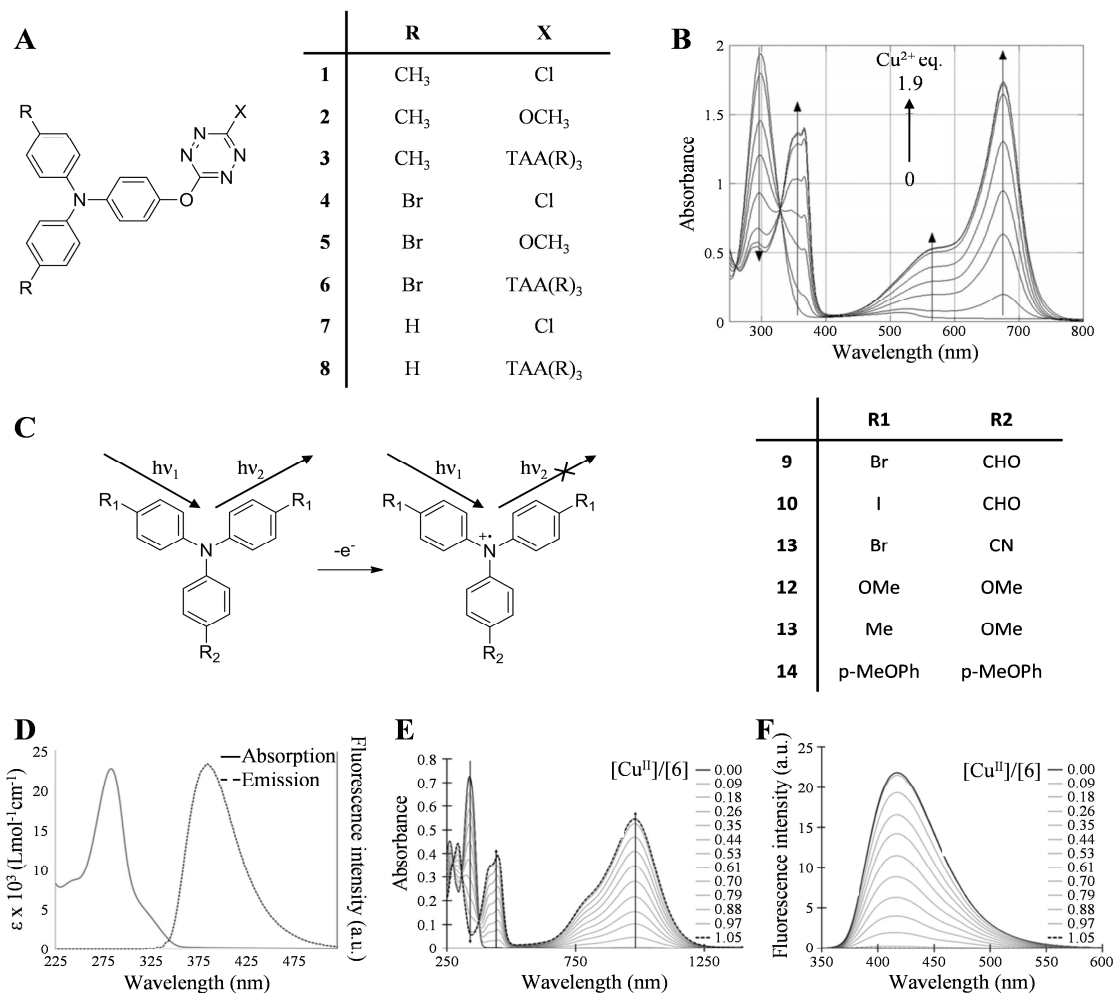


Figure 36. A) Molecular structure of TAAs studied by the group of Audebert in reference 23; B) absorption spectra of molecule 1 upon addition of 0 to 1.9 equivalents of oxidant. The spectra are taken in CH₃CN; C) molecular structure of the two redox states of TAAs studied by the group of Audebert in reference 22; D) absorption (solid line) and fluorescence (dashed line) spectra ($\lambda_{\text{excitation}} = 309$ nm) of molecule 4 in neutral state; E) absorption and fluorescence spectra ($\lambda_{\text{excitation}} = 307$ nm) spectra of molecule 6 upon addition of 0 to 1.05 equivalents of oxidant. This Figure is adapted from references 10 and 5

Hundreds of articles can be found in which molecular structures containing a TAA moiety are studied for their use as multi photon absorption (MPA) active materials. Only the most pertinent ones will be discussed in the following paragraphs.

To the best of our knowledge, the first articles describing MPA in TAA derivatives were published by the group of Rebane between 2001 and 2005.^{72–76} The authors studied the enhancement of the 2PA cross-section by designing different three-dimensional dendrimers, comprising multiple repeating 2PA active units. First they demonstrated that, using BDPAS Generation 0, 1, 2 (Figure 37AB) after an initial jump in cross-section, the 2PA cross section increases almost linearly with the

number of repeating units (Figure 37D).⁷⁵ Moreover, they obtained the largest cross-section measured at that time for the third generation molecule ($\sigma = 1.1 \times 10^{46} \text{ cm}^4 \cdot \text{s} \cdot \text{photon}^{-1}$). Then they studied the 2PA enhancement in function of the extend of π -electron delocalization using BDPAS 3- and 4-arm dendrimers in which all N-C bonds lie in a common plane (Figure 37C).⁷⁴ The 2PA spectrum of these molecules is shifted towards lower wavelengths, which is a sign that cooperative enhancement takes place (Figure 37E). Furthermore, the cross-sections were found to be proportional to the number of TAA groups (Figure 37F). This means that the TAA moieties act as the principal chromophoric units. Most importantly the cross-section increases almost in a $\sigma_2 \propto N^2$ manner (N being the number of TAA units), making it the first irrefutable proof of cooperative enhancement of 2PA in organic systems. Larger dendrimers ($N > 6$) display structural deformation and reduced π -conjugation, and σ_2 increases in a linear fashion. By increasing the π -bridge length, for example by replacing stilbene by distyrylbenzene, low generation dendrimers could almost reach the same 2PA cross-section as the 4-arm generation 2 molecule.⁷⁶ The authors also studied the 3PA processes of these molecules.⁷³ Within a conjugated domain the 3PA cross-section scales as N^3 , but regarding the whole molecule σ_3 scales as $N^{1.7}$. This means that the nitrogen center is most important for MPA, as it allows for π -conjugation, while stilbene groups break the π -conjugation even at lower generations ($N^x < N^3$). One of the largest 3PA cross-sections for any organic molecule was demonstrated for the G2 molecule. In accordance with its largest 3PA cross-section, G2 also showed the greatest coherence size (length of electronic delocalization).

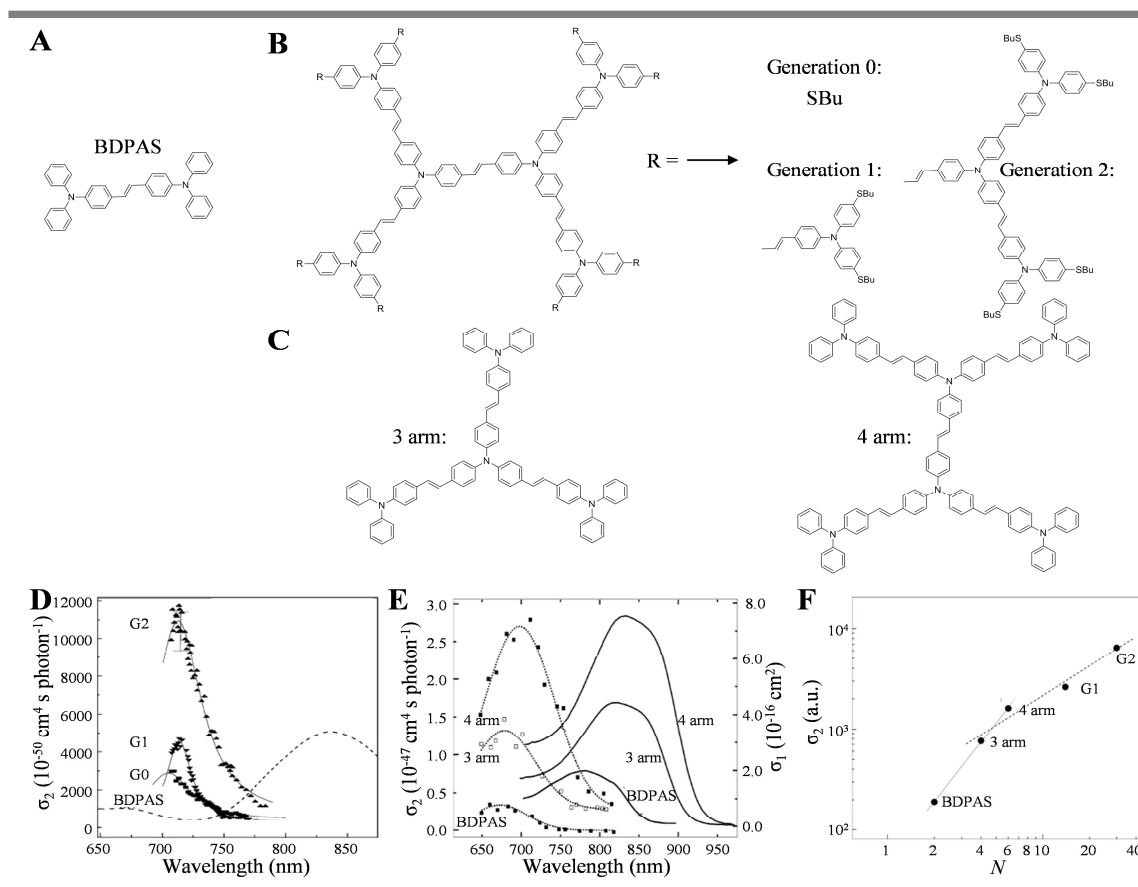


Figure 37. Molecular structures of A) the BDPAS parent molecule; B) zeroth (G0), first (G1) and second (G2) generation dendrimers; C) three and four arm BDPAS dendrimers; D) two photon absorption cross-section in function of wavelength of BDPAS, G0, G1 and G2 molecules; E) two photon absorption cross-section (left axis, dashed lines) and one photon absorption cross-section (right axis, solid lines) in function of wavelength of BDPAS, three and four arm dendrimers; F) Relation between the maximum two photon absorption cross-section and the number of TAA moieties. This Figure is adapted from references 75 and 74

Finally, using two new series of TPA containing molecules (N-Fl₃ and N-PA₃, **Figure 38**), they examined *i*) the effects of linear and dendrimeric structures; *ii*) dendrimer core topology; *iii*) branch structure on the size of coherent domains and, per consequence, on the cooperative enhancement of MPA.⁷⁷ They demonstrated that in both series the 3PA cross section scales faster than linearly, with a record large intrinsic 3PA cross section for molecule N-PA₃ OM87C2 ($\sigma_3 = 2.2 \times 10^{-79} \text{ cm}^6 \cdot \text{s}^2 \cdot \text{photon}^{-1}$). Upon comparison of the N-PA₃ series with the former BDPAS series it could be concluded that π -conjugation persists over longer distances in larger generations 3 arm dendrimers with phenyl-acetylene branches than in 4 arm dendrimers with stilbene branches. Studying the N-Fl₃ series the authors demonstrated that the 3PA cross-section could be significantly increased by replacing the phenyl rings in the π -conjugated system with larger and flat aromatic fluorenyl rings; as well as by enlargement of the peripheral aromatic groups. Additionally, in contrast to the stilbene π -bridge,

augmentation of the fluorenyl π -bridge length up to three repeating units does not break the π -conjugation.

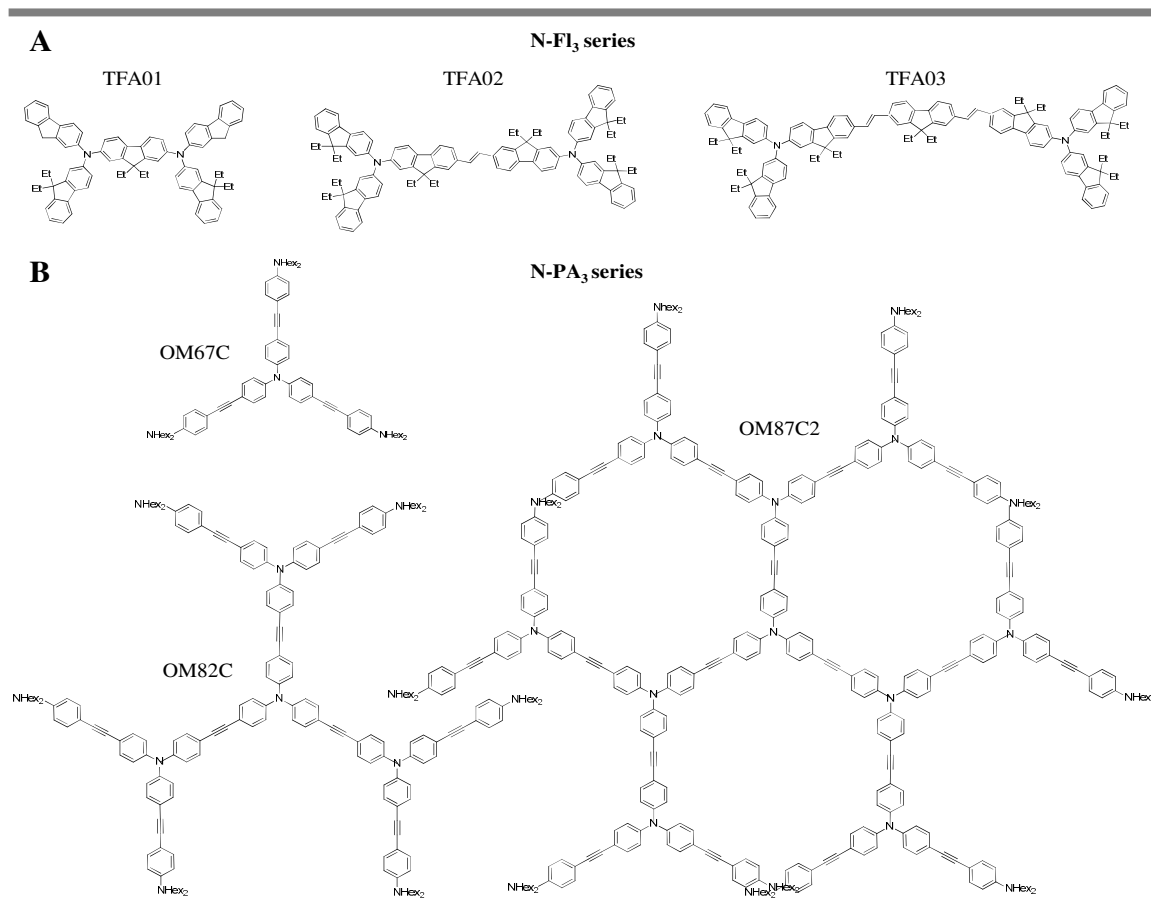


Figure 38. Molecular structures of N-Fl₃ and N-PA₃ series of molecules studied by the group of Rebane. This Figure is adapted from reference 77

Lu and co-workers were, to the best of my knowledge, one of the first (2007) to show not only 3 but also 4PA in a TPA containing chromophore.⁷⁸ The absorption spectrum shows two maxima: the first at 1250 nm, is attributed to 3PA; the second, at 1475 nm, is the result of vibrational resonance enhanced 4PA. Interestingly, the 4PA process has almost the same absorption probability as the 3PA process.

These types of molecules have been investigated intensely and elaborative studies on linear dipolar, bent dipolar, quadrupolar and octupolar geometries have been carried out to study MPA in TAA molecules. Often, the obtained cross-sections would be among the best reported.^{79,80,81,82}

After excitation the molecules return to their ground state by. Interestingly, one and two photon emission spectra resemble each other in both shape and wavelength, which suggests that relaxation from an excited state, obtained by either linear or non-linear processes, occur via similar emission

relaxation pathways.⁷⁹ Furthermore, as shown for hyper branched phenylene vinylenes with a donor- π -donor or donor- π -acceptor (D = TPA; A = nitrobenzene) structure, blue shifts can be observed due to twisted molecular conformations. Red-shifts are also observed and might originate from inter chain interaction species.⁷²

To overcome fluorescence quenching at higher concentrations, multi-branched TPA derivatives, with large σ_2 , exhibiting aggregation induced emission (AIE) were designed.^{83,84} For example, folic acid functionalized 2PA active nanoparticles, used for MCF-7 cancer cell imaging, exhibit a 2PA cross section of $500 \times 10^{-50} \text{ cm}^4 \cdot \text{s} \cdot \text{photon}^{-1}$, which is unusually high for water soluble 2PA materials.⁸⁴

As exemplified in the previous paragraph, optical properties can change dramatically from solution to solid state. One manner of resolving this issue is by designing push-pull molecular systems. In this type of systems the solid-state emission can be tuned by the ICT strength, while their absorption band and principle structural backbone remain unchanged. One way of achieving this is by taking advantage of the strong electronic coupling between the three branches in starburst TAA, as shown by the group of Léaustic (Figure 39).⁸⁵ Although the chromophores exhibit small 2PA cross-sections in amorphous state, the nanoparticles are able to reach exceptional 2PA cross-sections ($\sigma_2 > 10^{-43} \text{ cm}^4 \cdot \text{s} \cdot \text{photon}^{-1}$). The authors explain this phenomenon by exciton coupling.

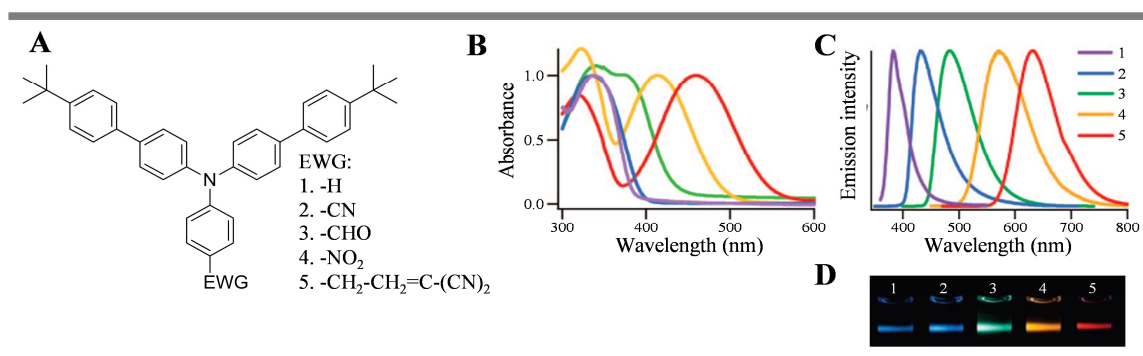


Figure 39. A) Molecular structure of unsymmetrically substituted push-pull TAA chromophores studied by the group of Léaustic; B) absorption and C) emission spectra of 100 nm thick films of compounds 1-5; D) fluorescence of nanoparticles of compounds 1-5 dispersed in water. This Figure is adapted from reference 85.

So far, aggregation induced emission chromophores and push-pull chromophores, have been demonstrated to be able to overcome the hydrophobicity problem of MPA active materials, which is of importance for biological applications. Another simple method is to bring hydrophobic MPA chromophores in aqueous solution by encapsulating them in micellar structures.⁸⁶ In micelles, the 2PA cross-section and quantum yield do not only strongly dependent on the molecular structure of the chromophores, but also on the diameter of the micelles, as well as its concentration. Previously, 2PA cross-sections of chromophores in water were always below $100 \times 10^{-50} \text{ cm}^4 \cdot \text{s} \cdot \text{photon}^{-1}$. Using this method cross-sections up to $\sigma_2 = 2790 \times 10^{-50} \text{ cm}^4 \cdot \text{s} \cdot \text{photon}^{-1}$ were found in water.⁸⁶

The group of Teulade-Fichou published a series of articles on MPA in TAA derivatives for their incorporation into biological applications. They studied TAA derivatives capable of 2PA and ds-DNA staining.^{87,88,89} Although their 2PA induced fluorescence is weak in water, it increases upon binding with ds-DNA because rotational de-excitation modes are inhibited due to its immobilization in the DNA matrix. Increased 2PA cross sections up to $1080 \times 10^{-50} \text{ cm}^4 \cdot \text{s} \cdot \text{photon}^{-1}$ were obtained.⁸⁹ The authors were able to establish the origin of the increase in cross-section: the molecule undergoes geometrical rearrangements in its ground state due to the tight fit inside the minor groove of AT-rich DNA (Figure 40A). By combining these optical properties with its biological properties (high photo stability, live-cell permeant, no RNase treatment necessary, works at sub micromolar concentrations) it outperforms the best DNA stainers (Figure 40B).

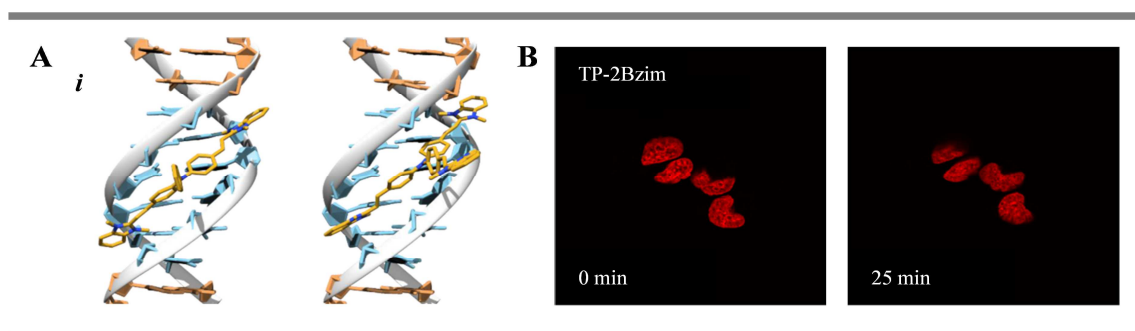


Figure 40. A) Molecular structure of TP-Py and TP-Bzim dyes; B) molecular models of interaction between *i*) TP-2Bzim, *ii*) TP-3Bzim and ds-DNA. AT base pairs are denoted in pale blue; C) confocal microscopy images of MRC-5 cells stained with TP-2Bzim. The fluorescence signal remains stable over a period of 30 minutes. This Figure is adapted from reference 89.

ii. Aggregation Induced Emission with triarylamines

Luminescent materials have found many applications such as OLEDs, sensing and imaging. However, most organic lumiphores possess planar aromatic functions; hence they aggregate at high concentrations due to π - π stacking and lose their luminescent properties (Figure 41A). This phenomenon, known as aggregation caused quenching (ACQ), greatly limits their application in devices. Although already in 1853 compounds exhibiting strong emissive properties in solid state were discovered by Stokes,⁹⁰ it was only in 2001 that their full potential was realized. It was the group of Tang that discovered a new group of luminescent organic molecules that exhibit this inverse effect.⁹¹ These molecules are not, or only weakly, emissive when dissolved, but become highly emissive in aggregated state. This is now known as aggregation induced emission (AIE) (Figure 41A).^{92,93,94} In contrast to conventional lumiphores, most AIEgens have twisted propeller-like molecular structures. In solution, dynamic intramolecular rotation is thus possible, which quenches emission due to high non-radiative decay rates. Upon aggregation, this intramolecular motion becomes restricted while π - π stacking is still impossible because of the propeller shape. The non-radiative decay rate is then suppressed, giving rise to radiative decay (Figure 41B). As explained in

previous sections, the TAA core motif has exactly such a propeller-like structure, thus making it an excellent candidate for AIEgens.

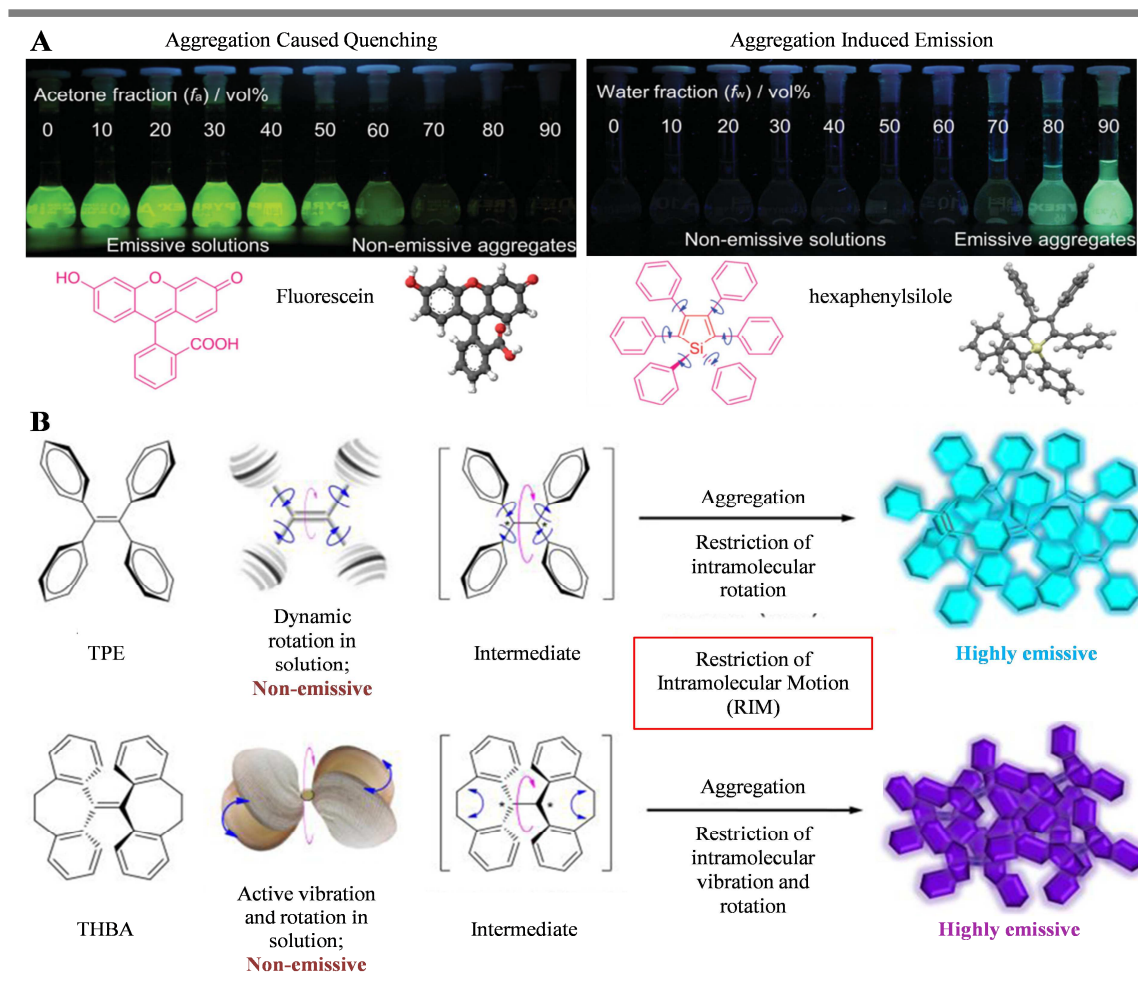


Figure 41. A) Photographs of fluorescent materials exhibiting aggregation caused quenching (fluorescein in solutions containing increasing levels of acetone, left series) and aggregation induced emission (hexaphenylsilole in solutions containing increasing levels of water, right series); B) tetraphenylethene is non-fluorescent when dissolved because of dynamic intermolecular rotation. THBA is non-emissive under these circumstances because of both dynamic intermolecular rotation and vibration. Upon aggregation these intermolecular motions are restricted, while, due to the molecules propeller shape, π - π stacking remains impossible. Subsequently the compounds become highly emissive. This Figure is adapted from reference 93.

The first AIE molecules incorporating TPA in their structure date from 2007-2009.⁹⁵⁻⁹⁷ Hu *et al.* investigated the luminescent properties of TAA-BODIPY compounds that show twisted intramolecular charge transfer (TICT) in function of solvent polarity, and AIE in function of temperature and poor solvent content (Figure 42).⁹⁷ Red shifts occur because of TICT in polar solvents, which can be significantly increased by aggregation (Figure 42C). Many TAA derivatives are capable of AIE and emission wavelengths can be fine-tuned by carefully designing the lumiphore.⁹⁸⁻¹⁰¹ Most of them are developed for their direct incorporation into electro organic devices as will become

evident in *Chapter I 4E. Applications of triarylamine self-assemblies*. Nonetheless, some groups have studied more fundamental aspects. For example the group of He Tian, who, among others^{102–104}, investigated TAA derivatives (in their case large cyano and triazine substituted TPA) exhibiting both AIE and two photon absorption, leading to aggregation induced two-photon excited fluorescence.^{105,106}

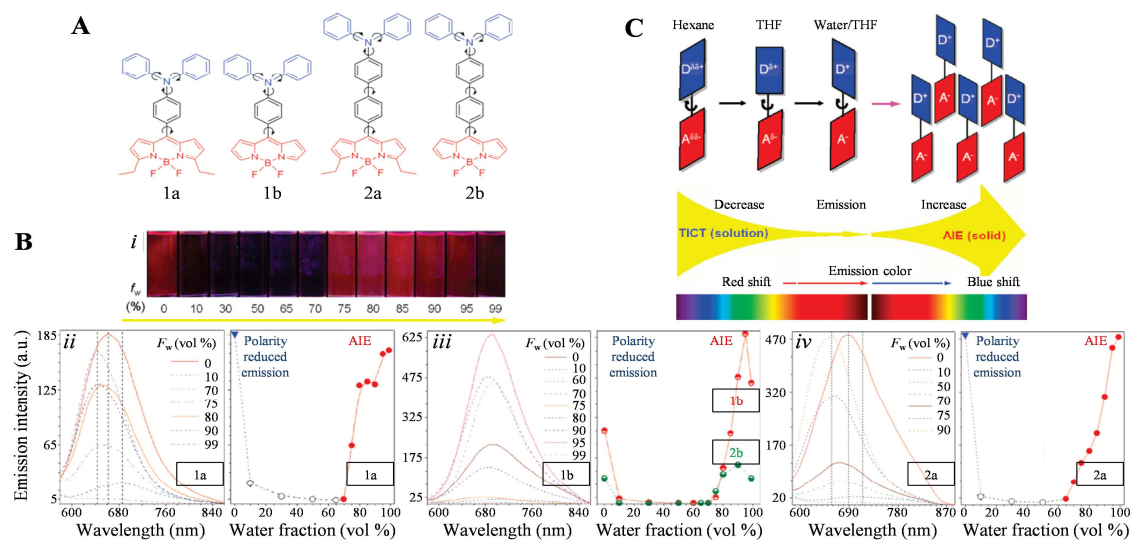


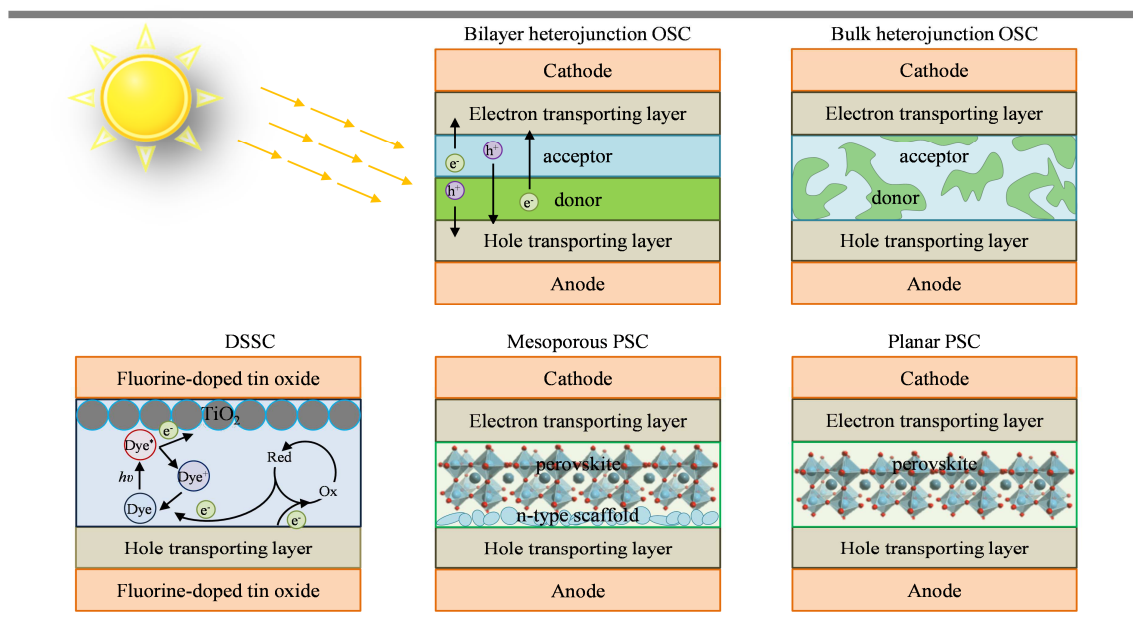
Figure 42. A) Molecular structures of TAA-BODIPY compounds studied by Hu *et al.*; B) photographs taken under UV irradiation of 1a in THF with increasing water content (left to right); emission spectra and plots of maximum emission intensity of ii) 1a iii) 1b, 2b and iv) 2a; C) Proposed mechanism of AIE and TICT in TAA-BODIPY compounds. This Figure is adapted from reference 97.

1.2 Applications of Triarylamines

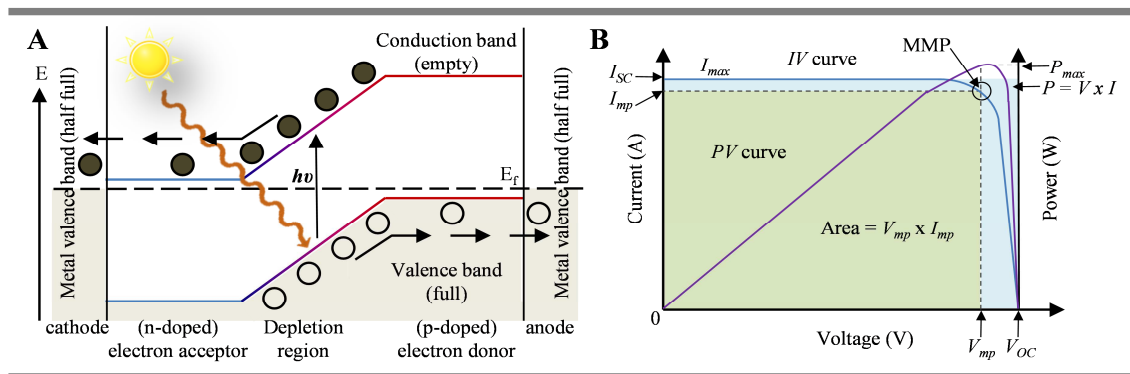
TAA derivatives are incorporated in many applications because of the electronic, charge and electron transfer and optical properties that have been described in *Chapter I 1.1 Physical Properties of Triarylamines*. Most of the applications can be found in organic electronics, where they are used as hole transporting materials. Here, we will briefly describe all different applications, but highlight only the most important examples with regards to innovation and performance.

A. Solar cells

In photovoltaics, a voltage or electric current is generated within a material upon exposure to light. Solar cells utilize and optimize this photovoltaic effect in order to harvest energy from sun light, as renewable energy source. The three main types of solar cells are (in)organic solar cells (OSCs), dye-sensitized solar cells (DSSCs) and perovskite solar cells (PSCs) (*Scheme 2*). They all function on the principle of charge generation in an active layer inside the device upon light exposure, and subsequent charge separation and harvesting at the electrodes.



Scheme 2. Schematic representation (from left to right and top to bottom) of a bilayer and bulk heterojunction organic solar cell (OSC), a dye-sensitized solar cell (DSSC) and a mesoporous and a planar perovskite solar cell (PSC). These illustrations are inspired from reference 109



Scheme 3. A) Schematic illustration of the photovoltaic process in a single-junction solar cell; B) Scheme of a typical IV plot (blue curve) and corresponding power plot (purple curve) of a photovoltaic device. These plots are adapted from the 'Alternative energy tutorials' internet site.¹⁰⁷

The efficiency of a photovoltaic device can be expressed by different parameters. First, there is the open circuit voltage (V_{OC}), which is the maximum voltage that can be obtained from the photovoltaic device. Then, there is the short-circuit current (I_{SC}) that corresponds to the current obtained when the photovoltaic device operates in the short-circuited regime. The power output is the product of the maximal current (I_{mp}) and the corresponding voltage (V_{mp}). Both I_{mp} and V_{mp} are in reality smaller than I_{SC} and V_{OC} . From these parameters the photoconversion efficiency, PCE (η), is calculated as the ratio between the maximal power output of the device (P_{max}) and the power of the incident light source (P_{in}) times the fill factor (FF). The fill factor is the ratio between P_{max} and the product of V_{OC} and I_{SC} .

$$\eta = \frac{V_{OC} I_{SC} FF}{P_{in}} \quad (5)$$

TAA derivatives form a versatile group of molecules that are commonly used as hole transporting material in an interfacial layer at the anode, or as donor material in the active layer. The reason for this can be found in some of their physical characteristics:

- Non-planar configuration, which gives rise to amorphous materials and allows for different aggregation states.
- Good thin film properties, such as low roughness, stable morphology and homogeneous features.
- Low ionization potentials and thus a strong electron donating, hole accepting character.
- Adjustable optical and electronic properties
- Relatively facile chemical modification

In OSCs and DSSCs, TAA derivatives can be used as electron donor materials in the active layer, or as hole transporting materials in a selective layer between the active layer and the anode. In PSCs it is

exclusively used as hole transporting layer. Several comprehensive review articles exist that discuss the use of TAA derivatives in solar cell applications.^{108–111} In the following sections, we will briefly summarize the most important features of TAAs for SC devices that were brought forward in the reviews.

i. Triarylaminines in organic solar cells

Organic solar cells generally exist of 5 layers: *i*) anode; *ii*) cathode; *iii*) semi-conducting active layer; *iv*) hole blocking and electron transport layer (HBET); *v*) electron blocking and hole transport layer (EBHT). The active layer consists of a donor and acceptor material. Upon exposure to light an exciton is formed in the donor material. The exciton then diffuses to the donor-acceptor interface where charge separation takes place. The positively charged holes remain in the donor material, whereas the electrons are transferred into the acceptor material. The charges then migrate to the respective electrodes (holes to the cathode and electrons to the anode) under the influence of thermodynamic driving force. Electron and hole transporting layers are often incorporated before the cathode and anode respectively to aid the charge transport and collection.

PCE improvement by TAA incorporation

Three groups of TAA derivatives can be used as donor material: *i*) star-burst TAA; *ii*) small TAA molecules; *iii*) polymer-TAA. Their efficiency in OSCs depend on their electron donating ability and molecular structure, as these characteristics have a direct effect on their optical and electronic properties, as well as their morphology. With this in mind, some common strategies have been investigated to improve the PCE in OSCs.

The first strategy is the broadening of, and/or red-shift in, absorption spectra. This is desirable in order to cover more of the solar spectrum and thereby improve light harvesting. Furthermore, a red-shift in absorption spectra promotes photocurrents at longer wavelengths and, as a consequence, the short circuit current density (J_{SC}) can be improved. Using TAA, the absorption wavelengths can be tuned by the conjugation length and extend of ICT processes. The conjugation length directly affects the charge transport. It depends on the linkage between the TAA core and the arms, as well as the nature and number of repeating units (usually thiophene) in the arms. In starburst TAA, longer thiophene arms have a negatively effect¹¹², while for linear small TAA derivatives longer conjugation lengths can be beneficial.¹¹³ ICT processes can be enhanced by the combination of good electron donating (TAA) and accepting groups (e.g. fluorine, dicyanovinyl, cyanoacetate, DPP, BT).

The second objective is to design photovoltaic materials with low HOMO levels and small optical bandgaps. Decreasing HOMO levels is a manner in which the V_{OC} (the positive correlation between donor HOMO level and acceptor LUMO level) can be enhanced. Moreover, it also leads to improved

ICT. Just as before, both enhanced V_{OC} and ICT can be obtained by incorporating good electron donating and accepting groups.

Thirdly, good charge carrier mobility is desired, as it leads to high FFs and enhanced J_{SC} . This can be achieved by optimizing the structural properties of the TAA derivatives. Planarity and low torsion angles of the TAA core, which depends on the linkage between the TAA core and the conjugated arm(s), lead to broader absorption spectra, efficient conjugation, improved π - π stacking, and hence improved charge carrier mobility. In general, long alkyl chains on the arms and end groups should be avoided, because they could decrease the PCE as a result of increased steric hindrance and torsion that reduce the ICT, exciton separation and charge carrier life time. Crystallinity can be advantageous, as it allows high charge carrier mobility, but can also be disadvantageous because it equally leads to larger domains and phase separations in the active layer. As a result exciton separation and diffusion is low.

Star-burst TAA in OSCs

Star-burst TAA molecules usually exhibit low crystallinity, and have the advantage of extended π -conjugation and ICT. The first example of OSCs incorporating star-burst TAA, comes from the group of Roncali.¹¹⁴⁻¹¹⁶ The authors synthesized a series of molecules of TAA core (D), thiophene arms (D) and dicyano or thienylenevinyl end groups (A). They demonstrated that such structures give rise to both efficient ICT and increased oxidation potentials. In comparison with derivatives unable of ICT, the PCE values increased significantly to 1.20%. One of the highest PCE was obtained by the group of Ko, using planar starburst molecules of a D-D-A-D motif (Figure 43A).¹¹⁷ Due to aggregation in the film, which is optimized towards small domain sizes using a solvent additive, charge transport efficiency is improved. Furthermore, it equally causes a red-shift in the absorption spectrum. Moreover, when the TAA core is fused, a more planar configuration is obtained that further red-shifts its absorption spectrum and enhances its conjugation and the ICT processes. Solar cells constructed with these derivatives have reached PCEs of 3.88% and 5.81% for normal and fused TAA core derivatives.

Small linear TAA in OSCs

Small linear TAA molecules can be advantageous because they are able to aggregate, or even to crystallize, which improves charges transport. It is also this type of molecules that have given rise to the best PCEs in OSCs. The group of Wong and Darling succeeded in constructing OSCs with PCEs (6.8%) higher than other OSC incorporating TAAs, and are among the best organic vacuum deposited single cells in general.^{118,119} They achieved this by replacing the electron donor bridge by an electron acceptor, thus from a D-D-A to a D-A-A structure (Figure 43B). This effectively lowers the optical

band-gap and HOMO levels, thereby increasing J_{SC} and V_{OC} . Moreover, due to the large dipole moments, the molecules stack into dimers in an antiparallel manner. This facilitates electron delocalization.

Polymer TAA in OSCs

Solution processability and good film formation are the advantages of polymer-TAA in OSCs. Additionally, the alternation of donating and accepting groups in the polymer allows for ICT and improved absorption spectra. Polymeric TAAs are separated in two groups: with TAA in the backbone of the polymer, or as side-chain. It was Jen and co-workers who demonstrated high PCEs using a TAA in the backbone.¹²⁰ They synthesized two fluorene TAA copolymers with thienylenevinylene side chains and two different electron accepting end-groups (Figure 43C). As a result of the incorporation of electron accepting groups, the absorption was enhanced. The authors measured PCEs of 4.19 - 4.47%, with maximum values up to 4.74%. The group of Tan, on the other hand, synthesized a copolymer with BDT and thiophene in the backbone and TPA in the side-chain (Figure 43D).¹²¹ The derivatives with longer conjugated lengths in the side chain showed red-shifted absorption and stronger ICT. In accordance, the derivative with the longest conjugation showed the highest PCE (5.16%).

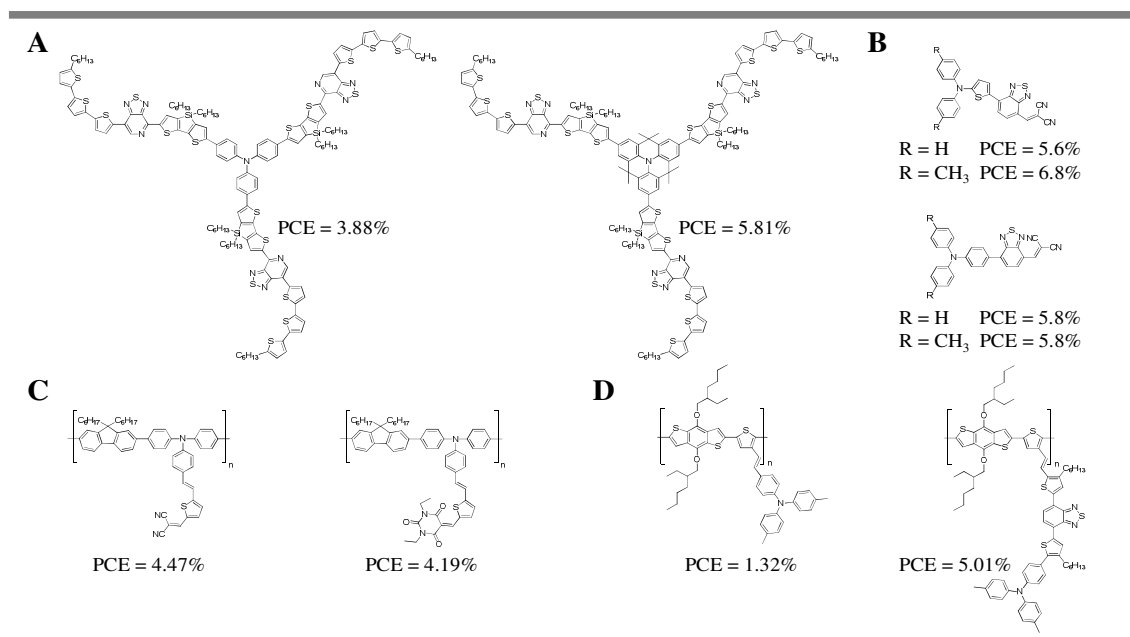


Figure 43. Molecular structures of star-burst¹¹⁷ (A); linear small^{118,119} (B); and polymer^{120,121} (C-D) TAA derivatives that have resulted in high PCE values in OSCs.

ii. Triarylaminines in dye sensitized solar cells

In dye sensitized solar cells (DSSCs) the active layer generally consists of a semi-conductor thin film, customarily nano crystalline TiO₂, a sensitizer organic dye, and an electrolyte or hole

transporting material. Upon light irradiation exciton formation occurs in the organic dye. The dye is anchored to the semiconductor and, through photo-induced electron injection, charge separation takes place at their interface. The electrolyte or hole transporting material regenerates the dye and is on its turn restored to its oxidative state at the counter electrode. DSSCs have the advantage that they usually exhibit high performance. This is a result of the fact that light absorption and charge transport can be optimized independently as they are separate steps in the working mechanism. Furthermore, DSSCs are more facile to construct.

As dye sensitizer TAA has to fulfill several requirements:¹⁰⁹

- First of all, its absorption spectrum should cover a large part of the solar spectrum in order to optimize light harvesting. As seen in *Chapter I 1D. Optical properties of triarylamines*, the absorption spectrum can be tuned by functionalizing substituents on the para-positions of the aryl rings.
- Secondly, its LUMO should be higher than the conduction band of the semi-conductor, while its HOMO should be below that of the hole transporting material or electrolyte. This is to ensure a thermodynamic driving force and dye regeneration.
- Thirdly, good charge transport abilities are beneficial to charge migration to the respective electrodes. TAA derivatives with a strong electron donor character could ensure this.
- Fourthly, the dye should not aggregate. Aggregation often leads to quenching, limited charge transport and non-optimal charge injection into the semi-conductor. The propeller-like structure of the TAA core motif is known to prevent such aggregation.
- Finally, the dye should display good light, thermal and electrochemical stability, to warrant a long lifetime. As dye sensitizers simple TAA, alkoxy-, alkyl-, aryl- and porphyrin-substituted TAA have been investigated among others.

The first DSSC incorporating TAA was constructed by Yanagida.¹²² The dye structure consists of a TAA bridged by a double bond to the electron accepting cyanacrylic acid. Increasing the conjugation length by inserting a second double bond caused a red-shift in absorption spectra and enhanced ICT. On consequence, the PCE increased from 3.3% to 5.3%. However, increasing the conjugation length could equally reduce its effectiveness because exciton lifetimes are reduced and recombination increases. The best dyes were synthesized by the groups of Marks and Demadrille (*Figure 44A*).^{123,124} The first used planar-thiophene tetrathienoacene conjugated bridges and reached PCEs up to 10.1%.¹²⁴ The highest value was obtained by the dye that formed the densest layer and had small angles with the semi-conductor. The group of Demadrille inserted an electron accepting group in the conjugated bridge to enhance ICT and obtained a PCE of 10.2%.¹²³

Similar maximum PCE values can be obtained using alkyl-, alkoxy-, and aryl substituted TAA derivatives (*Figure 44B-C*).¹²⁵⁻¹²⁷ The advantage of such groups is that their presence lowers the

probability of charge recombination between the semi-conducting and the hole-transporting layer or electrolyte. Also, such electron donating groups can enhance ICT. Furthermore, aggregation is much less plausible for aryl-substituted TAA, because of their bulky size. Some additional advantages can be obtained by combining TAA with porphyrins, such as higher extinction coefficients, facile chemical modification to fine tune optical and electrical properties, as well as good photo and thermal stability. The first TAA-porphyrin organic dye was reported by the group of Grätzel.¹²⁸ By using two dyes simultaneously, light harvesting was enhanced and a PCE of 12.3% was measured (Figure 44D). An even higher PCE value was obtained (12.75%) three years later.¹²⁹ The authors incorporated an electron accepting benzothiadiazole (BTD) group before the phenyl group of the conjugated bridge (Figure 44E). The addition of the BTD group improves the absorption spectrum across the visible region and up to 800 nm. Now, no co-sensitizer is needed anymore. The phenyl ring on the other hand, prevents charge recombination. The PCE was further augmented to 13% by the replacement of the hexyl groups by bulky substituents (Figure 44F).¹³⁰

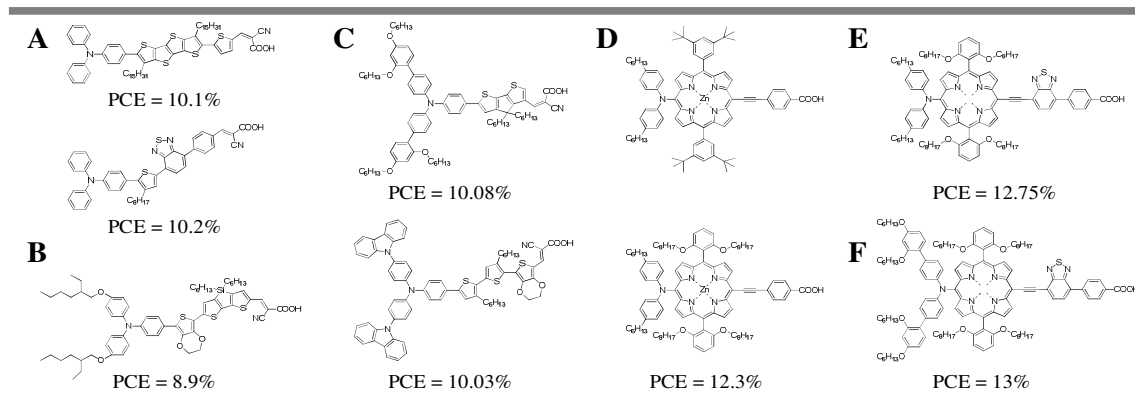


Figure 44. Molecular structures of simple^{123,124} (A); alkyl-¹²⁷ (B); aryl-¹²⁶ (C); and porphyrin-^{128,129,130} (D-F) substituted TAAs that have given rise to high PCE value DSSCs.

iii. Triarylamine in perovskite solar cells

Mesoporous perovskite solar cells (PSCs) resemble DSSCs in structure. The perovskites are present in a porous network of semi-conductor (TiO_2), and form a layer on top of it. This top layer is coated by a hole transporting material. In planar PSCs the necessity of a porous semi-conductor is omitted. Here a layer of perovskites is placed between electron and hole transporting layers. Charge transport is significantly more efficient in perovskites ($> 1 \mu\text{m}$) and thus a thick layer can be incorporated to ensure efficient light harvesting. Charge separation is ensured as perovskites are ambipolar non-excitonic materials. This means that free charges are created upon light absorption instead of an exciton, and that the perovskite is capable of transporting both the electrons and holes separately. TAA derivatives are only used as hole transporting materials in PSCs.

iv. Triarylamine derivatives as hole transporting layer

Hole transporting layers are incorporated into SC devices for three reasons: 1) improved hole extraction; 2) improved hole transport; 3) blocking of electrons to prevent charge recombination. In order to fulfill these functions hole transporting materials (HTM) should *i*) have an absorption spectrum that does not overlap with the absorption region of the light harvesting material; *ii*) have a HOMO level above the HOMO level of the active layer and below the valence band of the electrode in order to generate a thermodynamic driving force and high V_{OC} ; *iii*) display high hole mobilities to prevent charge recombination; *iv*) display high thermal, light, air stability etc. in order to ensure long device life-times. TAA derivatives meet these requisites as they generally demonstrate:

- Thermal and morphological stability
- Amorphous state due to propeller-like conformation
- Excellent hole carrier transport
- Facile oxidation of the N-center, due to appropriate ionization potentials.
- Adjustable energy levels by chemical modification of the substituents on the periphery

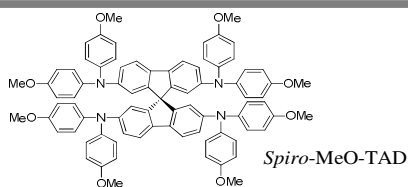


Figure 45. Molecular structure of *spiro*-MeO-TAD

The most-widely used hole transporting material is *spiro*-MeOTAD (Figure 45). Due to the *spiro* structure, it has a high glass transition temperature ($T_g \sim 120^\circ\text{C}$) and can be classified as an amorphous molecular glass. This is important as it prevents the formation of crystalline structures and grain boundaries. Normally, device efficiency decreases when such domains are formed, because charges can be trapped at the boundaries and charge recombination increases. Another advantage of using amorphous molecular glasses as HTM is that they ensure the optical properties of the device. In contrast to polycrystalline materials that are more prone to scatter light. Furthermore, the amorphous state equally improves the contact surface with the other layers.

Another advantage of the *spiro*-MeO-TAD compound is its high hole mobility transport character, which is the result of the bis(*p*-methoxy-phenyl)-amine moieties that ensure high HOMO energy levels. When substituted to the *ortho* position higher performances were attained (16.7 % vs 15.2 % for *spiro*-MeO-TAD) due to its better electron blocking properties as a result of higher lying LUMO energy level.¹³¹ Changing the bis(*p*-methoxy-phenyl)-amine moieties on the *para* position by other substituents, can result in higher efficiencies by tuning its electronic properties to the other

layers of the solar cell.¹³² Despite the high efficiencies solar cells have been reached using *spiro*-MeO-TAD (PCE > 20%), it is a poor hole transporter and is therefore usually doped with additives. Additionally, its synthesis and purification are difficult to achieve. Therefore, current research focusses on replacing it for more cost-effective, large scale producible, dopant free HTMs.

Small molecular TAA as HTMs

TAA-based HTMs can be divided in 2 classes: small molecular TAA and polymer TAA. Small molecular TAA, of different architectures such as *spiro*-type structures, four-armed, star-shaped, and linear TAA, have been investigated as HTMs. Out of all these structures, the *spiro*-type generally outperforms the others and is most extensively used. Yet, the use of other small molecules can still be advantageous.

A four-armed TPA structure, out-performing *spiro*-MeO-TAD was reported by Li and co-workers.¹³³ The TAA derivative consisted of a thiophene or bithiophene core, substituted with four TPA groups (Figure 46A). Because of its extended π -conjugation its absorption spectrum was red-shifted by 27 and 58 nm respectively compared to *spiro*-MeO-TAD, its HOMO energy level, on the other hand, laid lower.

Star-shaped TAA as HTMs have several advantages. It has a high thermal and morphological stability due to their bulky and nonplanar structure, and generally forms molecular glasses. Its stability can further be enhanced with increasing molecular weight.¹³⁴⁻¹³⁶ Star-shaped molecules that have more rigid and planar structures exhibit larger conjugation and, as a result, the time of life of charge separated states could be enhanced as greater delocalization of the radical takes place.^{137,138} It also results in a red-shift in their absorption spectra. Although the efficiencies reached using these compounds do not exceed those obtained by *spiro*-MeO-TAD under the same circumstances, the PCEs are actually quite similar. An example comes from Chen and co-workers, who reported on a star-burst compound, constructed of truxene core and three TPA groups (Figure 46B).¹³⁹ Its hole mobility is two orders of magnitude higher than that of *spiro*-MeO-TAD, due to its crystalline nature. Although it does not form an amorphous glass, it still proved to be beneficial to device stability because it does not need doping.

The final class of small molecular HTMs comprises linear TAAs. Their T_g can be augmented significantly by increasing the number of TAAs moieties (dimer $T_g = 60$ °C; pentamer $T_g = 145$ °C).¹⁴⁰ At the same this will improve its hole mobility properties.¹⁴¹ Several linear TAA HTMs have been reported with PCEs exceeding that of *spiro*-MeO-TAD. For example, Zhu *et al.* reported on three linear HTMs with a diphenyl core, TPA end groups, and with a varying number of ethylene linker groups (Figure 46Ci).¹⁴¹ Derivatives with one to three ethylene groups demonstrate high efficiencies. However, the addition of more ethylene linkers decreases the PCE due to solubility

problems. The high efficiencies are the result of high HOMO energy levels, which were shown to increase with increasing number of ethylene groups (-5.00 to -4.9 eV). Another example was presented by Jin and co-workers. The HTM was composed of a TPA core substituted with phenylcarbazole and dioctylfluorene moieties, and terminated by spirobifluorene end groups (Figure 46c).¹⁴² The phenylcarbazole and dioctylfluorene moieties were incorporated to increase the hole mobility and solubility. Due to their electron withdrawing character, they equally caused a bathochromic shift in the absorption spectra. Although both the HOMO energy level and hole mobility were comparable to those of *spiro*-MeO-TAD, it lead to higher PCE because of its *i*) hydrophobic nature and resultant larger water contact angle and its *ii*) increased stability.

Polymer TAA as HTMs

Using polymers can be advantageous because of their low cost and easy processability. Polymer HTMs are usually made of polythiophene and TAA derivatives. The best performing polymer TAA is polytriarylamine (Figure 46D).^{143–145}

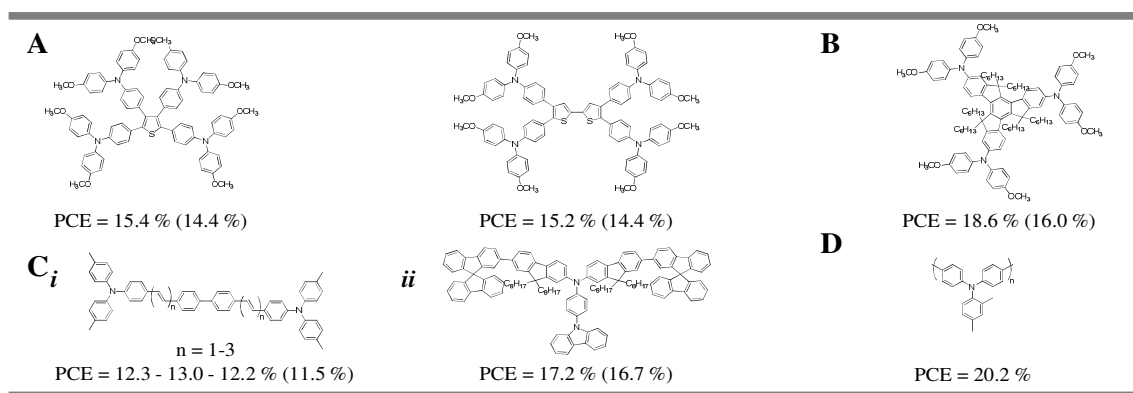
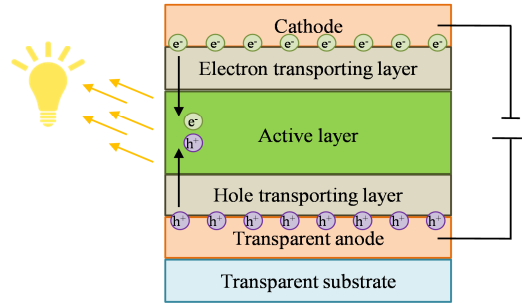


Figure 46. Molecular structures of four-armed (A); star-burst (B); linear (C) and; polymer (D) TAA HTMs. The PCE in between parenthesis indicates the PCE obtained with *spiro*-MeO-TAD under the same conditions.

B. Organic light emitting diodes

Light emitting diodes (LEDs) use electroluminescent materials to emit light when a potential is applied to the device. In Scheme 4, the general set-up of LED devices is schematically represented. Holes and electrons are injected at the (ITO) anode and (metal) cathode respectively and are transported through the active layer. Here, charge recombination takes place, which induces the excitation of the molecule by exciton formation. The excited state molecule then returns to the ground state releasing energy in the form of light.



Scheme 4. Schematic depiction of LED device.

The efficiency of the device depends on *i*) balanced electron and hole transport; *ii*) high charge transport at low operating potential; *iii*) efficient charge recombination and; *iv*) efficient light emission from excited states. Charge injection, transport and recombination can be aided by EBHT and HBET layers. Furthermore, the device should be protected from oxygen to prevent oxidation reactions. Optimal charge transport can only take place for homogeneous active layers, with little defects. For efficient light emission quenching should be prevented. Quenching takes primarily place at the cathode, as hole injection and transport generally occurs more easily and, as a result, charges recombine near the cathode. In order to eliminate quenching, HBET layers can be used. Normally, only 25% of excitons are in singlet state and will generate light. However, using triplet emitters 100% of the excitons formed would generate light. The efficiency of the device can be calculated by the electroluminescence efficiency:

$$\eta_{ext} = \gamma \times \eta_{ex} \times \phi \times \eta_{ph} \quad (6)$$

Here, η_{ext} is the external quantum yield, η_{ex} the fraction of excitons that result in radiative decay (0.25 for fluorescent materials and 1 for phosphorescent materials) and η_{ph} the light out-coupling efficiency. γ is the electron-hole ratio and ϕ the intrinsic quantum efficiency for radiative decay.

Organic light emitting diodes (OLEDs) often have amorphous active layers and charge transport takes place on the molecular level. This is in contrast to LEDs who have single crystalline active layers and charge transport throughout the lattice. The charge carrier mobilities in OLED devices are generally lower than in LED devices ($10^{-3} - 10^{-5} \text{ cm}^2 \cdot \text{V}^{-1} \cdot \text{s}^{-1}$ and $1 - 1500 \text{ cm}^2 \cdot \text{V}^{-1} \cdot \text{s}^{-1}$ respectively). Furthermore, the stability of the active layer is often problematic in OLEDs. Due to thermal stress amorphous material is converted into more stable crystalline states. This causes the formation of grain boundaries between polycrystalline domains, which leads to charge trapping and decreased device efficiency. On the other hand, LEDs demonstrate good stabilities. Yet, OLEDs do have multiple advantages over LEDs. For example, they can be processed at lower temperatures using either sublimation or spin casting, and are scalable to large areas. Furthermore, they can be prepared on any substrate. Also, organic devices are usually thin, light weight and exhibit flexibility, while LEDs are

rigid structures. They can operate at low power, are transparent when turned off and its emitting color can be tuned by chemistry. Finally, OLEDs are less costly to produce than their inorganic counterparts.

TAA derivatives are employed in OLED devices because:

- Non-planar configuration, which gives rise to amorphous materials and allows for different aggregation states
- Good thin film properties, such as low roughness, stable morphology, homogeneous features and the ability to form amorphous glasses
- High thermal stability
- Low ionization potentials and thus a strong electron donating, hole accepting character.
- Adjustable HOMO level, to match the anode work function
- Adjustable optical properties, which allows for color tuning of emitted light
- Good charge transport
- Relatively facile chemical modification
- High quantum yield of photoluminescence

They are used as HTMs in multilayered devices and as bifunctional materials in the active layer. Both categories will be discussed below.

i. Triarylamine derivatives as HTMs in OLEDs

One of the main roles of TAA derivatives is that of HTM. In OLED devices HT layers are incorporated to *i*) improve hole transport; *ii*) blocking of electrons to prevent quenching near the cathode; *iii*) stability of the amorphous phase.

In order to obtain highly stable amorphous materials research was focused on the development of new materials with high glass transition temperatures (T_g). One of the first attempts was reported by Okada, who used linear oligomeric structures containing 1 to 5 TAA cores.¹⁴⁰ Transparent smooth films were obtained by vacuum deposition with T_g of 130 – 140 °C. The films did not suffer degradation and, even at 100 °C for 100 h, showed great thermal stability.

Around the same time Shirota worked on star-burst TAA derivatives as HTM. TDATA and MTDATA form glassy states with T_g of 89 °C and 75 °C respectively, which was ascribed to their non-planar shape that prevents spatial reorientation and crystallization.¹³⁵ The authors found that a methyl group at *meta* position (m-MTDATA) further increased this effect, and a T_g of 151 °C was measured.¹⁴⁶ Tri(N-phenothiazinyl)TPA has a T_g of 141 °C and, when doped by iodine vapors, demonstrates a conductivity of $10^{-5} - 10^{-2} \text{ S}\cdot\text{cm}^{-1}$.¹³⁶ Films made of these derivatives showed

homogeneous smooth morphologies. Also, they were transparent, ensuring high light collecting efficiency. Furthermore, they demonstrate low I_p and their first oxidation is reversible.^{135,136,146} Different groups continued on this line. For example, Lee demonstrated that the incorporation of such HTMs could significantly enhance device performance due to an improved hole electron balance.¹⁴⁷ The continuous development of new star-burst TAA derivatives has led to HTM with increasingly high T_g (400 °C).^{148,149} For the interested readers, many other star-burst TAA derivatives designed for their incorporation into OLED devices are described in the review of Thelakkat.¹⁵⁰

Also other TAA derivatives were developed as HTM. For example, TAAs with a benzene center (TDAB derivatives).^{151,152} In contrast to the molecules reported by Shirota, which could be crystallized from a benzene-hexane solvent mixture, these derivatives could not be crystallized under any circumstance,¹⁵¹ and thermal decomposition only occurs at temperatures higher than 273 – 320 C (air atmosphere, at a heating rate of 10 °C·min⁻¹), even up to 505 °C. In the latter case, hole mobilities of $2.09 \times 10^{-3} \text{ cm}^2 \cdot \text{V}^{-1} \cdot \text{s}^{-1}$ were measured, which is almost one order of magnitude higher than their NPB analogue. This resulted in better hole electron balance and enhanced recombination.¹⁵²

Another group of HTMs consists of di-TPA substituted with two biphenyl units. However, T_g are normally less elevated.¹⁵³ Replacing the biphenyl with a fluorene, on the other hand, increases the thermal stability by ~ 20 °C.^{154,155} Additionally, it lowers the I_p by ~ 0.11 – 0.14 V. The hole mobilities of both groups of HTMs were comparable.

Other structures contain truxene cores and *spiro*-compounds, which have already been discussed in relation to photovoltaic devices.

ii. Triarylamine derivatives as singlet emitters in OLEDs

Triarylamine derivatives have been widely applied in OLED devices. Researchers have been particularly interested in them because they can act, not only as emitter, but also as hole transporting layer (HTM). In other words, using TAA, bifunctional materials can be realized. Bifunctional materials are advantageous for several reasons:

- It omits the use of additional HTEB layers, which:
 - simplifies device fabrication and reduces the cost
 - enhances device performance due to reduced interfacial diffusion and augmented uniformity
 - avoids, or significantly reduces, exciplex formation at interfaces
- It balances electron and hole transport, which leads to more efficient charge recombination.
- It stabilizes exciton formation due to the D-A structure of most bifunctional compounds

Research is mostly directed at solving some of the issues that arise from bifunctional materials, such as *i*) bathochromic effects; *ii*) decreased electroluminescence efficiency due to large ICT in D-A type molecules; *iii*) bipolar quenching; *iv*) crystallization due large dipole moment. Furthermore, the materials should have high thermal and morphological stability and an HOMO energy level that matches that of ITO for efficient charge injection. TAA derivatives can be designed to have high T_g and morphological stability, as explained in the sections on HTMs. Furthermore, as was equally discussed before (*Chapter I 3Ai. Triarylaminines in organic solar cells*), its charge transport properties and HOMO and LUMO levels can be adjusted by its conjugation length, number of repeating units and nature of donor and acceptor moieties. Although TAA may lack in sufficient emissive character, this can be overcome by incorporation of lumniphore groups. Thus, most TAA derivatives in OLED devices have a D-A type architecture, where TPA (D) is used to enhance charge injection, charge transport, and film forming abilities, and an acceptor group is used to ensure good electroluminescence and electron transport.

One of the best known bifunctional materials is TPD (*Figure 47A*) It shows good electroluminescent (EL) properties, but has a rather low thermal stability. Its thermal stability is augmented in α -NPD (*Figure 47B*), from a T_g of 62 °C to 95 °C, which is commercially used in mono-color displays.

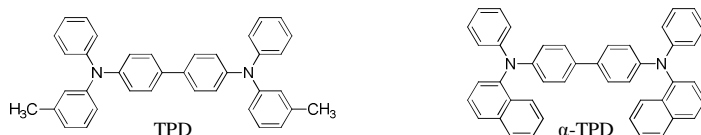


Figure 47. Molecular structure of TPA and α -TPD

An example of a commonly introduced lumniphore is thiophene. Although its PL quantum efficiency is reduced in polycrystalline films, it is maintained in amorphous state. Furthermore, its emission wavelength can be tuned by varying the conjugation length. Shirota was one of the first to synthesize a TPA bifunctional material.¹⁵⁶ He incorporated one to five thiophene units between two TPA moieties. By doing so, thermal and morphological stable amorphous glasses were obtained, whose emission wavelength was red-shifted (456 – 532 nm) with increasing conjugation length. The conjugation length did not have an effect on the relatively low ionization potential. As bifunctional material inside a double layer OLED device with a Alq₃ ETHB layer, quantum efficiencies were significantly improved due to more balanced electron and hole transport. The authors thus described a promising new class of bifunctional materials. Over the years, thiophene based materials with increasing stabilities ($T_g > 170$ °C¹⁵⁷) were reported, that are able of either hole or electron transport¹⁵⁸ or both.^{159,160}

An ambipolar, trifunctional compound was reported by Leung, who combined thiophene as emitter, with TPA and oxadiazole.¹⁶¹ In these architectures, TPA was incorporated as hole transporter, but was also shown to affect the emission color. Oxadiazole, an electron withdrawing group, rendered the compound electron transporting. However, it increased the ionization potential and HOMO energy level of TPA. This could be resolved by adding substituents (e.g. tetraphenylbenzidine) that reduce the electron withdrawing effects on the TPA moiety. The compound performed exceptionally well as HTM, exceeding common HTs as TPD and α -NPD. Yet, they are not suited in real devices because of rapid degradation at high electric fields. The authors postulate that this is caused by the reactivity of the thiophene units.

In the design of bifunctional materials, also fluorene units are frequently employed, because of their high thermal stability and high photoluminescence quantum yield. Zhang reported, for example, a bleu emitting OLED from fluorene substituted with 4 TPA units.¹⁶² The thermal stability of these compounds can be increased by increasing the molecular weight, as shown by Takagi.¹⁶³ The authors synthesized a new bifunctional compound with a truxene core, surrounded by 9 fluorene groups, which are appended by TPA. The OLED device made from this compound showed similar EL to OLEDs incorporating the commonly used TPD, but with much higher stabilities.

Compounds incorporating anthracene usually display good PL and EL characteristics, as well as excellent electrochemical properties. Additionally, different groups can easily be attached to this core unit, in order to get the desired properties. One of the best reports for bleu emitters (at the time the article came out) used a TPA(D)-anthracene(E)-benzimidazole(A) molecule.¹⁶⁴ The emission wavelength could be tuned by attaching bulky group to the C9 and C10 positions of anthracene, as well as by the linker length between anthracene and its functional groups. Furthermore, the presence of bulky and non-planar groups equally prevent π - π stacking and crystallization.¹⁶⁵ Thus, highly stable materials could be obtained. Furthermore, substitution of di- and tri-phenyl benzene by di- and tri-phenyl amine on the anthracene core, increased the luminescence and power efficiency two-fold.¹⁶⁵

Carbazole-cores are frequently used to raise the thermal stability of the material. Of particular interest though, is that, when combined with TPA, they can be used to create bleu emission OLEDs. However, the large optical bandgap can be problematic in light harvesting: electron injection from the Alq₃ ETL to the active layer was proven difficult due to the high LUMO energy barrier.

Excellent ET compounds can be obtained by the incorporation of organoboron compounds, as they have an unoccupied π - π orbital on the boron center and highly polarized electronic transitions are possible from substituent groups to the boron center.¹⁶⁶ Highly stable amorphous films can be obtained by boron-TPA compounds in which both centers have two different substituents, giving rise to star-shaped structural isomers. Regrettably, these structures proved to be poor emitters as a result of

the diminished π -conjugation between boron and TPA. Finally, also quinoline and quinoxaline groups should be mention, as they are often incorporated as electron transport moiety in bifunctional materials.¹⁶⁷

In all previous examples the internal EL quantum efficiencies cannot exceed 25%, as they are all singlet emitters. In order to exceed the 25 % limit several approaches can be taken. The first solution is using phosphorescent emitters in which radiative decay is possible from both singlet and triplet excited states. Another is by reducing the amount of triplet states created, which can be achieved by triplet- triplet annihilation (TTA), or thermally-activated reverse intersystem crossing (RISC). The latter can be thermally activated and results in delayed fluorescence. In order to realize the theoretically forbidden spin flip involved, one needs the presence of excitons with weak binding energies. Weakly bound excitons can be created in compounds with CT states, as they have a large separation between the donor and acceptor orbitals. This makes the probability of singlet states more probable, and thus emitting groups with CT states are beneficial. However, low fluorescence efficiencies are usually the result. Localized excited (LE) states, on the other hand, are more efficient in radiative decay. Therefore, the combination of CT and LE states should result in good EL quantum efficiencies that exceed the 25% limit. This was investigated by the group of Yuguang Ma.¹⁶⁸ They designed a TPA-thiadiazol D-A molecule with a twisted molecular structure. By the incorporation of TPA, a CT state is created and the emission is red-shifted. Furthermore, the emission wavelength shifts in function of solvent polarity because of the large dipole moment present. This equally indicates a low-lying excited state. Thiadiazole has a LE state. The authors showed that in polar solvents the CT state predominated, but the inverse is true in non-polar solvents. Thus, in solvents of moderate polarity, a hybridized CT-LE state might exist. The presence of this hybridized state was proved by the presence of a single fluorescence life-time. The extend of hybridization could further be controlled by controlling the twist between the two groups, where a reduced twisted structure resulted in increased coupling. As a result the internal quantum efficiency reached 93%, the final external efficiency of their device was 2.8%.

iii. Triarylamine derivatives as triplet emitters in OLEDs

As stated before, phosphorescent OLED devices are of interest as all excitons formed can lead to radiative decay from the excited state molecule by intersystem crossing. Most of them are not pure organic compounds but metalorganic complexes. In the design of phosphorescent bifunctional materials it is advantageous to use TPA over, for example carbazole, because it has higher triplet state energies and higher HOMO levels (thus more efficient charge injection).¹⁶⁹

Liao reported on a blue phosphorescent OLED with external quantum efficiencies exceeding 25% by designing a phosphorescent TPA bifunctional material.¹⁷⁰ They synthesized a *spiro*-TAA

derivative that acts a bipolar host material, which means that it conducts both holes and electrons. The *spiro*-core prevents intermolecular interactions, resulting in enhanced solubility and hindered crystallization. Because the two halves of the molecule are orthogonal to one another, good hole transport from the TPA moiety is ensured while the bipolar character can be enhanced on the other half by appending electron withdrawing groups on the fluorene moiety. This also signifies that no additional TPA groups are necessary, which is beneficial for the triplet state energy level. In this example, phosphine oxide groups are functionalized on the fluorene as emitting material.

Two other strategies were reported by Ma.^{169,171} The first uses benzimidazole-TPA as bipolar material and phosphor as host emitter for the fabrication of green and red phosphorescent devices.¹⁷¹ The combination of benzimidazole and TPA, while connected by a rigid π -linker, enhances the intramolecular charge transport. As a result, the emission wavelength will be little affected and the energy levels of triplet states will not greatly be lowered. Another approach is to combine TPA with oxadiazole, which led to green and yellow OLED devices of 23% external quantum efficiencies.¹⁶⁹

C. Organic field effect transistors

Field effect transistors (FETs) are used as on-off devices in electronic circuits. In FETs the output current depends on the electric field it operates in.^{172,173} It consists of three main components: i) an (organic) semiconductor layer; ii) a dielectric layer; iii) three conducting electrodes. It works as a three-terminal capacitor, which means that the charge carriers, either electrons or holes, flow in the active (organic) semi-conductive channel between two Ohmic contacts, the source and drain electrodes. An electrical field is applied to the (organic) semi-conductive channel by a third electrode, known as the gate electrode, thereby controlling the density of charge carriers that can pass through (Figure 48A). The device is turned off when no gate-source voltage (V_{GS}) is applied, as in this case no charges accumulate in the channel. The device is turned on when a V_{GS} polarizes the dielectric and charges accumulate in the semi-conductor. To inject charges, first the injection barrier (defined by the work function) needs to be overcome. Then the voltage applied should be greater than the threshold voltage (V_{TH}). In organic FETs V_{TH} coincides with the minimal V_{GS} at which traps in the channel fill up, otherwise said, the minimal V_{GS} to induce the channel. The application of a drain-source voltage (V_{DS}) then forces the accumulated charges to migrate from the source to the drain, resulting in a drain current (I_D). The charge transport mechanism and mobility ($\text{cm}^2 \cdot \text{V}^{-1} \cdot \text{s}^{-1}$) depend on the (semi-) conducting material used and include hopping (organics), polaron (conjugated organics), and band-like models (metals and inorganics). But possibly also tunneling (Poole-Frenkel mechanisms) or a multiple trapping and release model can take place. The efficiency of a device is often defined by the charge transport mobility (response of a charge carrier to the electric field), the threshold voltage (related to number of traps) and the on-off ratio (maximal I_{DS} / minimal I_{DS}). These characteristics can

be derived from the output (I_{DS} vs V_{DS} for a fixed V_{GS} , Figure 48B) and transfer (I_{DS} vs V_{GS} for a fixed V_{DS} , Figure 48C) curves.

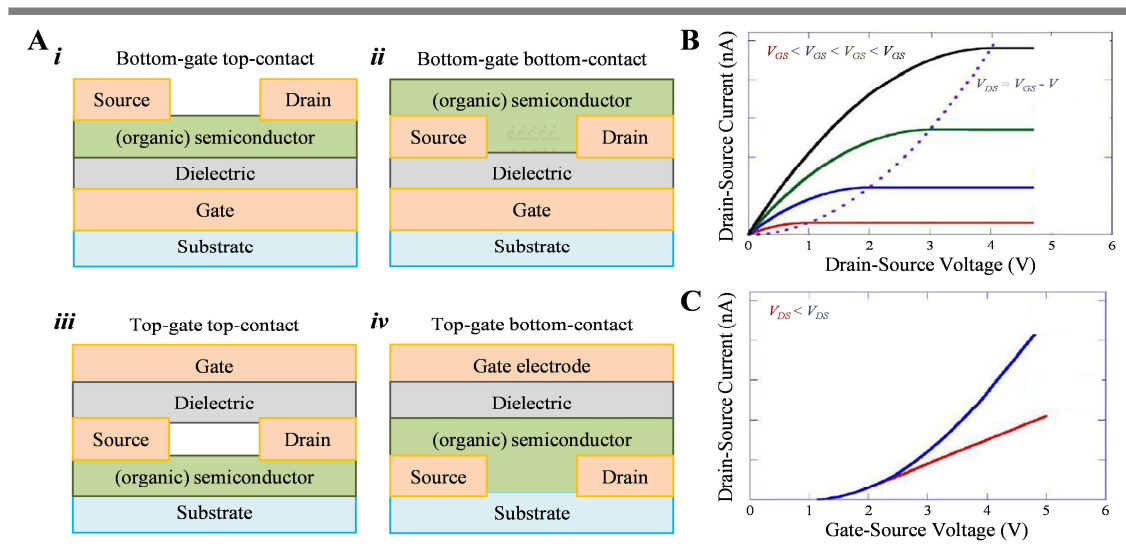


Figure 48. A) Schematic depiction of FET device structures; B) typical output curves for fixed gate-source potentials; C) typical transfer curves for fixed drain-source potentials.

OFETs are commonly classified following either their architecture (Figure 48A), the form in which the organic semi-conductor is present (organic thin film FETs, single crystal FETs), or the type of material used (small organic molecules, organic polymers, blends). Current research focusses both on the chemical and physical aspects of organic semi-conductors. The chemical structure of the organic semi-conductor has a large impact on the charge transport. But the charge transport efficiency can also be greatly affected by the use of blends, as this has a direct impact on the percentage of amorphous or crystalline domains, as well as the number of grain boundaries. Further important physical characteristics are the topology of the material and the order present. Finally, one should consider the interactions of the organic semi-conductor with the dielectric interface, as charge transport along a surface differs from bulk charge transport. Other parameters of interest include the doping percentage, deposition methods, insulator functionalization and solvent effects.

TAA derivatives have attracted much attention in OFET research because:

- It is a p-type material
- It has a reversible redox potential
- Its low ionization potential (IP)
- It displays good air stability and is operational in ambient conditions
- Its easy processability and low cost
- Divers topologies are possible (polymer-TAA adds flexibility, small molecules can be used for crystallinity, self-assemblies for enhanced electronic coupling)

i. Triarylamine derivatives in OFETS

To the best of our knowledge the first article in which triarylamine chemistry was used to develop OFET devices dates from 2003. Veres and co-workers designed a range of highly stable polymer triarylaminers (PTAA) semiconductors with charge transport up to $6 \times 10^{-3} \text{ cm}^2 \cdot \text{V}^{-1} \cdot \text{s}^{-1}$, which is close to the bulk mobility ($10^{-2} \text{ cm}^2 \cdot \text{V}^{-1} \cdot \text{s}^{-1}$).¹⁷⁴ They choose to work with PTAA because they can be handled in air, the devices work under ambient condition and the mobilities measured exceed $10^{-3} \text{ cm}^2 \cdot \text{V}^{-1} \cdot \text{s}^{-1}$. Moreover, most PTAA are in amorphous state, which allows for easy characterization, as morphology effects can be neglected. In 2005, the group of Grell compared OFET devices incorporating either pentacene or PTAA as semi-conductor. In a first article, they described the improvements made in OFETs using Titanium anodized gate insulators capped by PAMS or OTS, in order to prevent gate leakage.¹⁷⁵ In contrast to pentacene, a considerable performance variance is observed for PTAA in function of differently treated insulator surfaces. A second article from this research group, published the same year, describes the decrease in injection barrier using electrodeposition of PEDOT/PSS on the source electrode. When PTAA is used as semi-conducting material, the difference between injection from gold and from PEDOT/PSS modified gold is more pronounced, than when pentacene is used, improving the drain saturation current from $1.6 \times 10^{-3} - 6 \times 10^{-3} \text{ cm}^2 \cdot \text{V}^{-1} \cdot \text{s}^{-1}$ to $9.5 \times 10^{-3} - 6 \times 10^{-3} \text{ cm}^2 \cdot \text{V}^{-1} \cdot \text{s}^{-1}$.¹⁷⁶ At the same time, the group of Strohrriegl reported novel star-shaped compounds with a triphenylamine core and carbazole or fluorene sidearms capable of forming molecular glasses. Mobilities of $3 \times 10^{-4} \text{ cm}^2 \cdot \text{V}^{-1} \cdot \text{s}^{-1}$, high on/off ratios of up to 10^5 and low threshold voltages were obtained. Furthermore, they show very small hysteresis and a high stability under ambient conditions.¹⁷⁷

Since then, TAA derivatives have been widely used in OFETs. We have classified these devices by the nature of the TAA used. The largest class comprises polymer TAAs, either in pure form or in a blend. But also OFETs with small molecule TAA, starburst TAA and self-assembled TAA have been reported. Here, we will only discuss articles in which TAA is the focus of the study. For comparisons sake, at the end of this section a table summarizing OFET performances in different devices can be found.

ii. Triarylamine polymers

Triarylamine polymers

As introduced in the previous section, the first triarylaminers to be incorporated into OFETs were polymer TAAs.^{175,176} In the years thereafter, no great advances were made in charge mobility or OFET enhancement. However, important work was done to better understand the structure-function relationships and the nature of the PTAA used. This is well illustrated by the work presented by the

group of Tsutsui. They studied the influence of molecular weight, pendant groups, π -conjugated main chains or side chains and side chains of different lengths on the hole mobility in amorphous PTAA (10^{-6} to 10^{-3} $\text{cm}^2 \text{V}^{-1} \text{s}^{-1}$).¹⁷⁸ In doing so, the authors provided a basis for new molecular design of TAA in OFETs. A year later, Hüttner *et al.* showed that the electrical properties do not depend on the molecular weight due to their amorphous character.¹⁷⁹

Anglin *et al.* studied both neutral and chemically oxidized PTAA thin films on Si dielectric interfaces.¹⁸⁰ Hole mobilities could be significantly improved (6.8×10^{-5} $\text{cm}^2 \cdot \text{V}^{-1} \cdot \text{s}^{-1}$) by functionalizing the dielectric by HMDS-d18. They hypothesize that this stems from electronic polaron absorbance, which is analogue to what is observed in chemically doped bulk PTAA films. Particularly interesting is that one of their devices displayed ambipolar behavior. This was also observed by Reitzenstein *et al.* and Chaing *et al.*¹⁸¹⁻¹⁸² They first realized this by synthesizing a PTAA consisting of alternating TPA and perchlorotriphenylmethyl radical moieties, which exhibited electron and hole mobilities of $\sim 3 \times 10^{-5}$ $\text{cm}^2 \cdot \text{V}^{-1} \cdot \text{s}^{-1}$. The second by synthesizing novel conjugated polymers of acceptor-donor type, with hole and electron mobilities of 7×10^{-3} and 4×10^{-3} $\text{cm}^2 \cdot \text{V}^{-1} \cdot \text{s}^{-1}$.

The group of Turner realized a library of TAA copolymers and provided essential information for further OFET development. PTAA copolymers, containing 2,7-fluorene 3,7-dibenzothiophene and 2,7-carbazole units in the backbone, show charge transport properties that can be tuned by altering the nature of the fused ring structure and substitution of the pendant benzene of the arylamine.¹⁸³ Fluorene containing polymers displayed the highest mobilities (4.7×10^{-3} $\text{cm}^2 \cdot \text{V}^{-1} \cdot \text{s}^{-1}$). Controllable p-type doping could be achieved by immersing complete top-contact OFETs in a solution of 2,3,5,6-tetrafluoro-7,7,8,8-tetracyanoquinodimethane in acetone.¹⁸⁴ This proved a reliable method for controllable doping, resulting in threshold voltages up to + 12 V and mobilities up to 2.2×10^{-3} $\text{cm}^2 \cdot \text{V}^{-1} \cdot \text{s}^{-1}$ (versus 0.8×10^{-3} $\text{cm}^2 \cdot \text{V}^{-1} \cdot \text{s}^{-1}$ for non-doped materials). However, PTAA devices are less sensitive to this oxidation method than P3HT devices. Even higher mobilities were obtained for polymers derived from indenofluorene (5.0×10^{-2} $\text{cm}^2 \cdot \text{V}^{-1} \cdot \text{s}^{-1}$).¹⁸⁵ The authors attribute this to higher reorganization energies.

PTAA is cannot only be used as semi-conductor, but also as electrets.¹⁸⁶ TAA polymer electrets are used as an additional layer between the dielectric and semi-conductor and aid (ambipolar) trapping behavior. Therefore it could be used to enhance electrical memory performance.

Triarylamine polymers - polymer blends

Only one article could be found in which a PTAA – polymer blend is used. Madec *et al.* described an amorphous PTAA - amorphous and semi crystalline insulating polymer blend, in which thin film morphology and electronic properties are strongly dependent on the deposition method.¹⁸⁷ In amorphous blends hole mobilities are found to decrease with semi-conductor content down to a

critical percolation threshold. For crystalline blends on the other hand, hole mobility increases when the PTAA content exceeds 50 wt%. Additionally, more polar blends equally show a monotonic decrease in hole mobility.

Triarylamine polymers - small molecule blends

Polymer – small molecule blend OFETs have the advantage over pure crystalline small molecule OFETs because they are easier to process and have improved flexibility, while retaining high field effect mobilities.

It was the group of Anthopoulos that first to used such a blend (PTAA : 2,8-difluoro-5,11-bis(triethylsilylethynyl) anthradithiophene), thereby significantly increasing the charge carrier mobilities ($>2 \text{ cm}^2 \cdot \text{V}^{-1} \cdot \text{s}^{-1}$). Independent of film morphology, which consisted of either spherulitic grains or large grain micro structures, charge trapping at grain boundaries occurred to be the predominant transport mechanism.¹⁸⁸ However, this effect is less pronounced for large grains. Film morphology could be optimized by using electrostatic spraying deposition (ESD), which led to extensive crystallization and microstructural organization implying distinct phase separation.¹⁸⁹ Electrode treatment, to lower to the charge injection barrier, resulted in maximum mobilities up to $2.47 \text{ cm}^2 \cdot \text{V}^{-1} \cdot \text{s}^{-1}$.¹⁸⁸ Blend ratio affected the film crystallinity, and maximum hole mobilities were measured for acene-rich highly crystalline regions ($\geq 39 \text{ wt}\%$).¹⁹⁰ The importance of blend film morphology was also demonstrated by the group of Kippelen.¹⁹¹ They investigated solvent and polymer matrix effects on the phase segregation behavior of the blend (PTAA: 6,13-bis(triisopropylsilylethynyl) pentacene (TIPS-pentacene)). The microstructures obtained depended strongly on the solvent used, as the boiling points aid in achieving distinct phase segregation/crystallization of TIPS-pentacene in blends. Remarkable mobilities up to $2.82 \text{ cm}^2 \cdot \text{V}^{-1} \cdot \text{s}^{-1}$ were obtained for such systems.

Finally, the group of Yong-Young Noh reported exceptionally high hole mobilities of $\sim 4.6 \text{ cm}^2 \cdot \text{V}^{-1} \cdot \text{s}^{-1}$ using PTAA: diF-TESADT blends forming polycrystalline films.¹⁹² These results were achieved under highly blended conditions. While the diF-TESADT would form large crystals, high flexibility was still realizable due to the PTAA (bending radius of 7.5 mm).

iii. Small triarylamine molecules

As should be clear from the previous section, the crystallinity of the deposited thin films plays a pivotal role in charge transport at the organic semiconductor - dielectric interface. This illustrates the importance and inevitable emergence of small organic molecules for OFET devices and towards further comprehension of structure–property relationships.¹⁹³

Star-burst triarylamines

As already discussed in the first section, one of the first TAA used in OFET devices were star-burst TAA.¹⁷⁷ Generally, in amorphous state it is important that the chromophores are as large as possible to allow for maximal intermolecular interaction. Wren *et al.* studied the effect of dendronisation, by synthesizing TAA chromophores with 1-2 thiophene units per arm, and first generation biphenyl dendrons with 2-ethylhexyloxy surface groups.¹⁹⁴ They proved more easily processable than their non-dendronised counterparts, and hole mobilities of 1.7×10^{-6} and $1.1 \times 10^{-5} \text{ cm}^2 \cdot \text{V}^{-1} \cdot \text{s}^{-1}$ were measured for dendrimers with one and two thiophene units respectively. Threshold voltages were found to be around 10 V and on-off ratios in the range 10^2 to 10^3 V. The efficiency of symmetrical planar, fused and tilted TPA- [DTS(BTTh₃)]₃ molecules in OFETs and organic solar cells, was investigated by Peak and co-workers.¹⁹⁵ The planar architectures showed more efficient performances with a hole mobility of $7.6 \times 10^{-3} \text{ cm}^2 \cdot \text{V}^{-1} \cdot \text{s}^{-1}$ and an on-off ratio of 5×10^6 V. In contrast, a third article discussing star-shaped TAA (and already discussed in the section on self-assembled TAA), used unsymmetrical functionalized TAA. This highlights how the addition of different functionalization's (donor and acceptor moieties) affects molecular packing and electronic energy levels and OFET performances.

Other small molecule triarylamines

Using small molecule blends, charge transfer complexes can be formed. For example, Swensen *et al.* used a MTDATA-TPA – F3TCNQ-Adl blend forming charge transfer complexes between donor and acceptor in p-doped films.¹⁹⁶ Hole mobilities first increase in function of F3TCNQ-Adl content, then slightly decreases (4.5×10^{-7} at 0%; 7.1×10^{-7} at 20%; $5.7 \times 10^{-7} \text{ cm}^2 \cdot \text{V}^{-1} \cdot \text{s}^{-1}$ at 30 mol %).

m-MTDATA is often used in OFETs, either as semi-conductor (blend) or as hole injection layer. Yu and co-workers demonstrated that the hole mobility could be significantly enhanced by employing m-MTDATA as hole injection layer between the pentacene semi-conductor and gold electrodes.¹⁹⁷ A four time increase in hole mobility (to $1.61 \text{ cm}^2 \cdot \text{V}^{-1} \cdot \text{s}^{-1}$) was attributed to an intermediate energy level formed between semi-conductor and electrodes, leading to a remarkable reduction of contact resistance at the metal-organic interface. Using the same system (Au – m-MTDATA – pentacene), Li *et al.* improved the saturation current, field-effect mobility, on-off current ratio and threshold voltage.¹⁹⁸ The authors hypothesized that m-MTDATA is proven to be one of the best hole injection layers because it adsorbs metal atoms well, which effectively protects the OSC layer. Furthermore, it has a suitable HOMO energy level of -5.1 eV, which provided the best energy match between pentacene and the gold electrodes. After film thickness optimization hole mobility's of $0.67 \text{ cm}^2 \cdot \text{V}^{-1} \cdot \text{s}^{-1}$ were recorded.

In the group of Krishnamoorthy they choose to work with donor-acceptor-donor type small molecules, constituted of *i*-indigo and TPA to increase the intermolecular contacts.¹⁹⁹ The propeller shaped TPA increases the solubility of the small molecule as well as the isotropic charge transport. Intermolecular spacing was low and did not change upon thermal annealing at 150 °C. Thermal annealing did change, however, the thin film morphology and hole transport mobility's (0.3×10^{-3} and $0.5 \text{ cm}^2 \cdot \text{V}^{-1} \cdot \text{s}^{-1}$ before and after thermal annealing).

In small molecule OFETs, naphthalene bisimides have emerged as one of the most promising class of organic semiconductors. Rybakiewicz *et al.* investigated the influence of different substituents at the imide nitrogen atom (alkylaryl, thienylene and triarylamine) and at the naphthalene core (triarylamine).²⁰⁰ When functionalized with two TAA moieties the ionization potential and electron affinity are lowered. Bisimides core- or N-substituted with TAA undergo a quasi-reversible oxidation associated with the transformation of the substituent into a radical cation and yield IP of 4.13 eV and -4.04 eV EA, IP of 5.49; 5.5 eV and 5.71; 5.56; 5.6 eV respectively.

Table 1. Summary of TAA OFET characteristics.

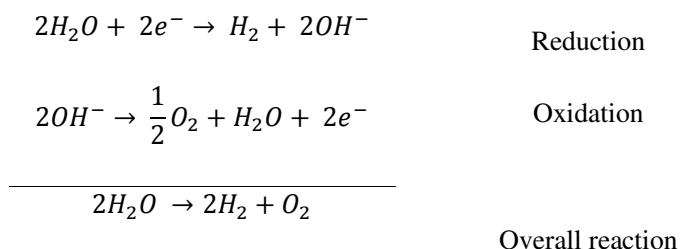
Reference	Type	$\mu \text{ (cm}^2 \cdot \text{V}^{-1} \cdot \text{s}^{-1}\text{)}$	$V_{th} \text{ (V)}$	on-off ratio
174	PTAA	6×10^{-3}		
175	PTAA	$1.6 \times 10^{-3} - 6 \times 10^{-3}$	- 16	2.3 - 2.5
176	PTAA	9.5×10^{-3}		
	PTAA	$1.6 \times 10^{-4} - 8.3 \times 10^{-4}$	- 36	$2.2 \times 10^3 - 6.7 \times 10^3$
178	PTAA	$5.6 \times 10^{-5} - 4.6 \times 10^{-4}$	- 45 -- 15	$3.2 \times 10^2 - 4.4 \times 10^3$
	PTAA	$6.4 \times 10^{-6} - 6.4 \times 10^{-4}$	- 60 -- +3	$3 \times 10^1 - 7.5 \times 10^3$
179	PTAA	$10^{-7} - 10^{-4}$	- 45 -- -4	$4 \times 10^1 - 1.6 \times 10^3$
180	PTAA	$0.8 \times 10^{-5} - 6.8 \times 10^{-5}$	- 26 - 0	
181	PTAA	3×10^{-5}		
182	PTAA (p-type)	7×10^{-3}	- 13 -- 15	10^5
	PTAA (n-type)	4×10^{-3}	+11 -- +13	10^6
201	PTAA	$1.1 \times 10^{-5} - 2.7 \times 10^{-5}$		10^3
183	PTAA	$5.4 \times 10^{-5} - 3.4 \times 10^{-3}$		$8 \times 10^2 - 4 \times 10^4$
184	PTAA	$0.8 \times 10^{-3} - 2.2 \times 10^{-3}$	- 12 -- -1	$10^3 - 10^4$
185	PTAA	$1.8 \times 10^{-3} - 5.1 \times 10^{-2}$		$2 \times 10^3 - 2 \times 10^5$
186	PTAA	$1 \times 10^{-1} - 2.7 \times 10^{-1}$		
187	PTAA : amorphous polymer	$10^6 - 10^4$		>200
	PTAA : crystalline polymer	$10^4 - 10^3$		>200
188	PTAA : small molecule	$7 \times 10^{-2} - 2.47$	- 6.8 -- -3.8	
190	PTAA : small molecule	1.8		
189	PTAA : small molecule	1.7	- 7.9	3.28
202	PTAA : small molecule	$2.8 \times 10^2 - 2.82$	- 11.9 -- -3	
192	PTAA : small molecule	$1 \times 10^2 - 4.6$	- 5.4 -- -2	
177	Starburst	$1 \times 10^{-3} - 3 \times 10^{-3}$	- 2	$10^5 - 10^3$
194	Starburst	$1.7 \times 10^{-6} - 1.1 \times 10^{-5}$	+10	$10^2 - 10^3$
195	Starburst	7.6×10^{-3}		5×10^6
203	small molecule			
196	small molecule	$4.5 \times 10^{-7} - 7.1 \times 10^{-7}$		
200	small molecule			
199	small molecule	$3 \times 10^{-4} - 0.5$		10^5
204	small molecule	8.85×10^{-5}	- 5	2×10^2
197	small molecule	1.61	- 13	

198	small molecule	0.67	- 4.2	36×10^4
205	self-assembly*	$2.0 \times 10^{-3} - 2.3 \times 10^{-3}$	- 35 - - 14.5	$1 \times 10^5 - 2 \times 10^5$
193	self-assembly*	1.5×10^1	- 16	10^7

* will be discussed in Chapter I 4. E. Applications of triarylamine self-assemblies

D. Water splitting applications

Because of their photo and redox properties, a third application of TAA derivatives can be found in water splitting. Water splitting is the two electron reduction of water into hydrogen and oxygen and occurs in four steps:²⁰⁶



1. electron-hole pair formation by excitation
2. charge separation and migration to the surface
3. electrons at the surface participate in the reduction reaction of water towards H_2
4. holes at the surface participate in the oxidation reaction of water towards O_2

Hydrogen production is nowadays of great importance, not only for chemical industries (e.g. ammonia synthesis), but foremost as clean energy source for fuel cells. It can be realized by several methods: *i*) electrolysis; *ii*) radiolysis; *iii*) thermal decomposition; *iv*) photocatalytic; *v*) photoelectrochemical; *vi*) photosynthesis. The use of organic chromophores has both advantages and disadvantages.²⁰⁷ For example, their synthesis can be realized by established methods and their absorption spectrum can be adjusted to extend the whole solar spectrum. On the other hand, the instability of their oxidized forms and subsequent decomposition of the material can be major disadvantages. As well as the possible inability of oxidized forms to activate water oxidation catalysts, and an insufficient reducing excited state for electron injection into appropriate semiconductors. However, the use of TAA-derivatives may circumvent many of these disadvantages.

- They have excellent photosensitive properties
- They have a strong electron donating ability
- They can be used as reversible electron donors.
- Many TAA derivatives have already been developed for dye-sensitized solar cells (DSSCs) and the same molecules could be used for water splitting systems.

- Its non-planar molecular structure, imposed by the three benzene rings, can suppress intermolecular aggregation and π - π stacking

TAA derivatives incorporated into water splitting systems are used as *i*) sensitizers and as *ii*) redox center to pass the radicals to the catalytic surface sites. In the sections below the systems are ordered by the mechanisms behind water splitting.

i. Triarylamines in water splitting applications

To the best of our knowledge the first two articles discussing hydrogen generation using TPA derivatives were published in 1979 and 1980 by Okura and Kim-Thuan.^{208,209} They showed that after radicalization of TPA under NIR irradiation their system undergoes photo sensitized electron transfer from TPA via the catalyst methyl viologen (MV), thereby generating hydrogen (Figure 49AB). With this system they demonstrated for the first time the possibility to omit the use low oxidation-state transition metal ions. However, it was only in 1994 that a real water splitting system incorporating TPA was presented.²¹⁰ Among other parameters, Katakis and Mitsopoulou studied the effect of reversible electron donors: triphenylamine and diphenylamine. To achieve this they used a single photocatalyst-catalyst (PC-C) and a reversible electron acceptor (EA = MV) (Figure 49C). Interestingly, TPA improved the efficiency of energy storage by 20%, while DPA had no effect. They postulated that TPA is able to coordinate with PC-C, water and MV to form a nine-coordinated complex, which is the actual photosensitizer. They also hypothesize that water splitting is further facilitated due to the fact that the electron density can be transferred through the mediating tungsten metal center to MV. However, direct interaction between MV and TPA cannot be excluded.

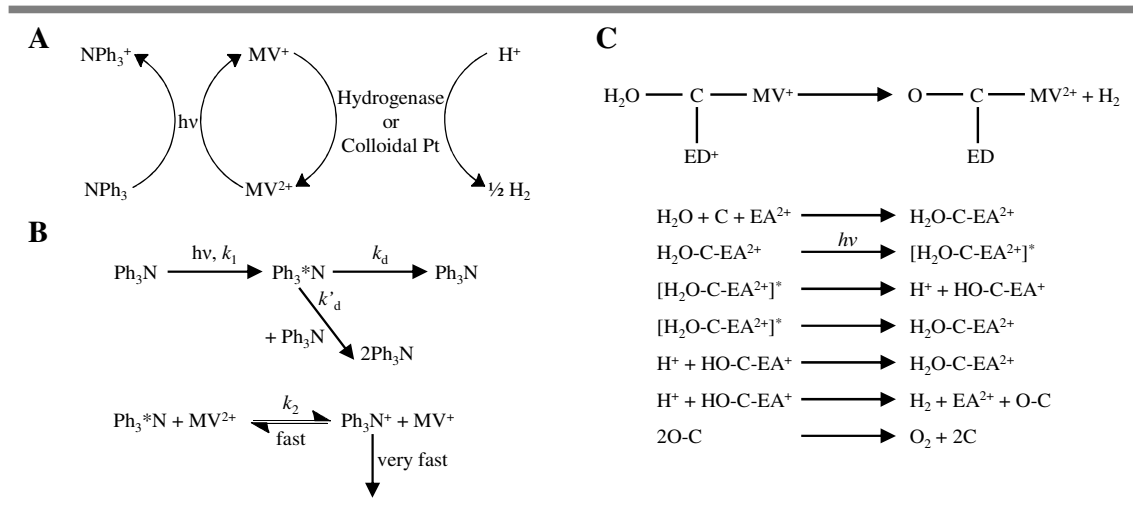


Figure 49. A) Proposed photosensitized electron transfer process from TPA (NPh₃) to the catalyst capable of hydrogen production via methyl viologen (MV)²⁰⁸; B) proposed scheme for the reduction of methyl viologen (MV)²⁰⁹; C) Proposed reaction for water splitting using methyl viologen. The

catalyst is denoted as C. Below the general mechanism for water splitting is given, wherein MV is replaced by EA (electron acceptor).²¹⁰

ii. Photocatalytic water splitting

Most photocatalytic water splitting systems incorporating TAA derivatives are built on the foundations laid by research on dye-sensitized solar cells (DSCs). Both involve the sensitization of a wide band-gap semiconductor with light harvesting dye molecules. Dye regeneration can be obtained by either using reversible redox couples or materials that both catalyze water oxidation (photoanode) and hydrogen production (photocathode).²¹¹ The advantages of donor-bridge-acceptor designs for photosensitizers was demonstrated by the group of Wang.²¹² It enables highly efficient energy and electron transfer. Hydrogen production was significantly higher when the TPA electron donor is linked through an ethylene (π) bridge to the multibranching porphyrin electron acceptor than when connected by an ester.

Significant increase in photocatalytic efficiencies were made by Huo and Zeng. In a first article they constructed nanocomposites from TPA functionalized bithiazole-metal complexes and C_{60} .²¹³ The nanocomposites perform the role of both photosensitizer and photocatalyst and, after optimization of component ratios, photocatalytic efficiencies were multiplied 4 to 6 times to analogous systems. This led to a photocatalytic activity of $7.39 \text{ mmol}\cdot\text{h}^{-1}\cdot\text{g}^{-1}$. The advantages of this system, however, lie in the low production costs and rather good reusability. In a second article they proposed a system containing TPA functionalized onto cobalt-2TPABTz.²¹⁴ This photosensitizer was sensitized by silver nanoparticles (catalyst). Under visible light, photocatalytic hydrogen generation proved highly efficient with a photocatalytic activity of $20.65 \text{ mmol}\cdot\text{h}^{-1}\cdot\text{g}^{-1}$. The authors attributed this high efficiency to the unique porous structure of Co-2TPABTz and the strong surface plasmon resonance effect of Ag NPs. Moreover, it shows outstanding long-term stability after eight-cycle tests (32 h).

Jing *et al.* reported an entirely new approach by constructing a supramolecular system that encapsulates an organic TPA dye molecule into the pocket of a redox-active metal-organic polyhedron (Co_4L_4) (Figure 50).²¹⁵ In this system, TPA acts as photosensitizer and the cobalt as catalytic redox site. Because of their close proximity, pseudo-intramolecular PET is possible from the excited state of TPA to the cobalt, thereby generating turnover values (TON = moles of hydrogen per mole of catalyst) comparable to the highest values reported for related systems (11000 TON).

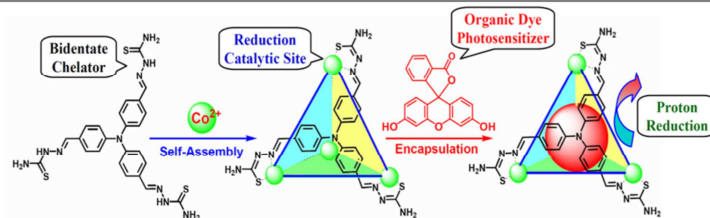


Figure 50. Scheme of the encapsulation process of a TPA dye in the metal-organic polyhedron for the construction of an artificial supramolecular system for water splitting. This figure is adapted from reference 215

All examples given up to now use metal-organic dye photosensitizer. This is because metal-free photosensitizers (PS) often suffer from chromophore instability and poor photocatalytic activity. The group of Park showed that environmental pollutants could be avoided using ruthenium free donor- π -acceptor organic dyes of TPA core, both in absence or presence of triethanolamine (TEOA) and ethylenediaminetetra-acetic acid (EDTA)) as electron donor groups (Figure 51A).²¹⁶ Their results suggest that the optimal dye structure varies depending on the purpose and application. The group of Huang presented a metal free water splitting system with a notable turn over number of 10200 in 48h (Figure 51B).²¹⁷ The stability of the metal-free photosensitizer lies in the starburst structure of TPA that is hydrophobic and has electron-rich moieties. The authors hypothesize that these moieties function like a shield, preventing the photosensitizer becoming reduced. Secondly, the starburst design could also help the regeneration of the dye because of the large surface area it occupies.

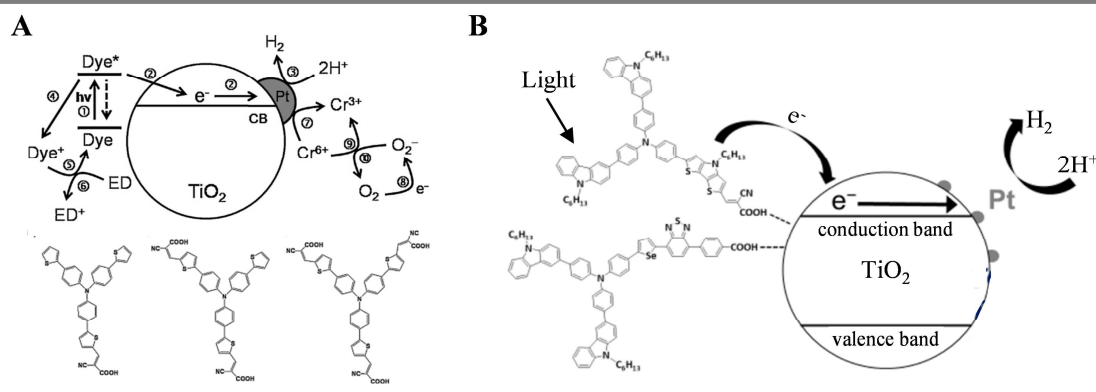


Figure 51. Two examples of TPA dye photosensitizers used in light induced water splitting. The image on the left shows the different processes that occur: 1) photoexcitation TPA-dye, 2) e^- injection in TiO_2 (or Pt/TiO_2), 3) H_2 production, 4) oxidation of dye, 5) dye regeneration, 6) electron donor oxidation, 7,9) reduction of Cr(VI) , 8) reduction of O_2 to a superoxide anion, 10) oxidation of superoxide anion. Below the structures of the dye photosensitizers investigated²¹⁶ B) water splitting scheme using star-burst TPA dye photosensitizers as developed by Huang. This Figure is adapted from references 216 and 217.

Another group that made great improvements on existing water splitting systems, with regards to photocurrent, oxygen production and incident photon to current efficiencies, was the group of Meyer.²⁰⁷ They presented three new metal-free TPA donor-acceptor organic dyes that work within the visible light spectrum (Figure 52A). First they showed that the instability and decomposition of the dye depends on the time it spends in its oxidized state. Several structural properties affected this instability: i) thiophene moieties increase instability under aqueous conditions; ii) TPA functionalized with ether will lead to irreversible oxidation under aqueous conditions; iii) substituents on the para-position of TPA generally have important effects under oxidative conditions. Overall, the device performance could be enhanced by simplifying the dye structure. Furthermore, they demonstrated that by tuning the thickness of the Al_2O_3 layer, electron transfer from the oxidative state can be facilitated (Figure 52B). This greatly improved both device performance and longevity.

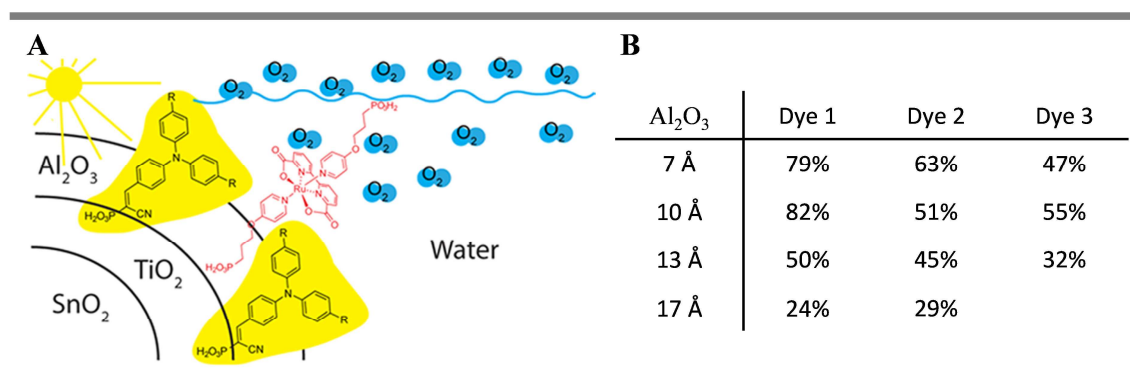


Figure 52. A) scheme representing a TAA dye sensitized visible light induced water splitting system; B) Faradaic efficiencies of the system presented in A, with varying amounts of Al_2O_3 . This Figure is adapted from reference 207

iii. Photoelectrochemical water splitting

Photoelectrochemical water splitting is also known as artificial photosynthesis. Therefore, the two are brought under in the same section. To achieve (artificial) photosynthesis (Figure 53A) multiple cycles of photo-induced charge separation need to occur at the catalytic sites in order to acquire enough redox equivalents. No sacrificial electron donors or acceptors are present in these systems. This is called “accumulative charge separation” or “accumulative electron transfer”.²¹⁸

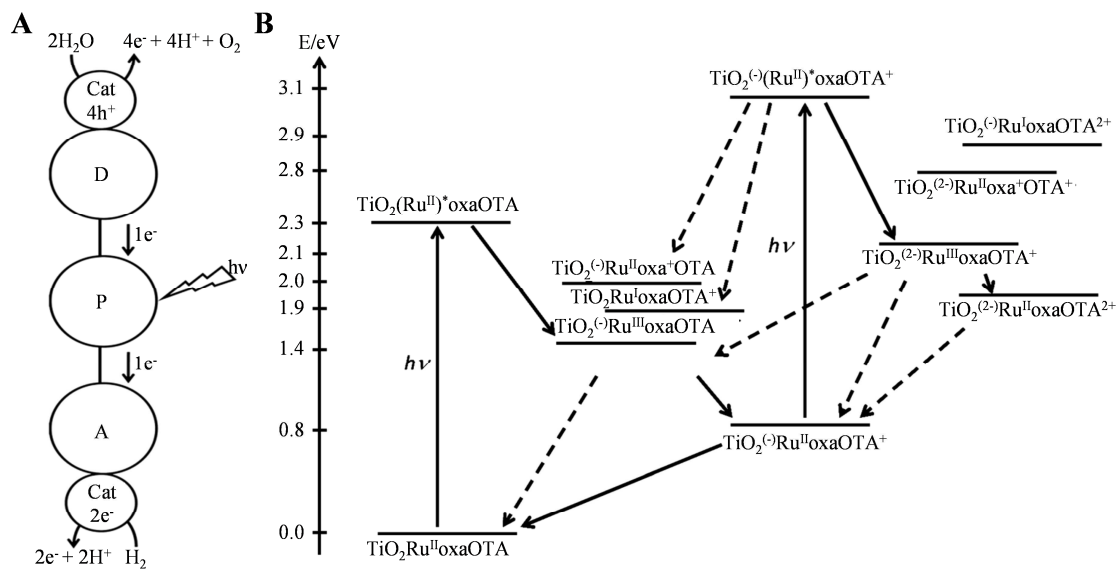


Figure 53. A) Scheme of artificial photosynthesis. Here charge separation in the donor-photosensitizer-acceptor molecule is directly coupled to catalytic water splitting and fuel production; B) Energy diagram for the 1st and 2nd charge separation in the TiO₂ (Ru^{II})-oxazole-oligoTAA system. This Figure is adapted from reference 218.

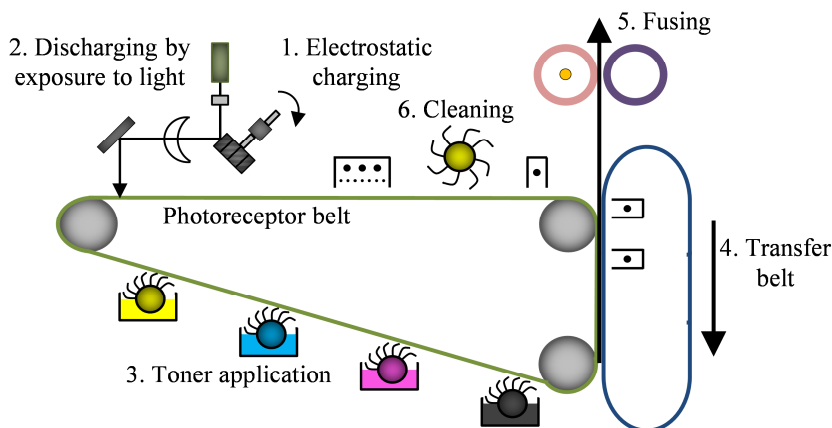
This process is well described by the group of Hammerstrom, whom studied five artificial photosynthesis system based on RuII-polypyridine as photosensitizer linked to TAA or oligo-TAA and nanoporous TiO₂.²¹⁸ The efficient accumulative electron transfer and overall high yields are attributed to the formation of a two-electron charge-separated state, which is formed upon successive excitation by two photons (Figure 53B). The authors have thus successfully realized an accumulative two-electron charge separation system. This is quite remarkable because most artificial photosynthesis systems fail in this aspect due to competing reactions.

One of the best known examples comes from the group of Sun.²¹⁹ Water splitting was achieved using an organic dye-sensitized tandem photo electrochemical cell. By simply connecting the organic photosensitized dye coated TiO₂ anode (oxidation site) with the TPA photosensitized cobalt coated NiO cathode (reduction site) hydrogen was produced under visible light, neutral pH and without applying a bias. Shit and co-workers constructed a robust photoelectrocatalyst that consists only of earth-abundant elements: cobalt sulfide nanoparticles grafted onto a TPA-porous organic polymer (CoS_x@POP).²²⁰ Due to the high porosity of the resulting catalyst, electrolyte diffusion is facilitated and efficient electron transfer is made possible. Additionally, the catalyst possesses a tunable bandgap, which could contribute to its high photoelectrochemical activity (~10 and 1.94 fold increase compared to pristine POP and CoS_x). Finally, they showed it has an improved chemical stability and longevity.

However, TPA is not always the best choice as photosensitive dye in photoelectrochemical cells. For example, the group of Kubo showed that their BODIPY dye sensitized photoelectrochemical cell exhibit efficiencies 5.4 times larger than their TPA dye sensitized photoelectrochemical cell.²²¹

E. Xerox processes

TAA derivatives are widely used in xerography (Xerox[®] process) due to their photoconductive and charge transfer properties. Xerography, also known as electrophotography, is a dry copying and laser printing technique, invented by Chester F. Carlson in 1938. The Xerox[®] process (Scheme 5) can be divided in six steps.^{222,223} First a photoreceptor material, positioned on a drum or belt, is electrostatically charged. Then a pattern replicating an original image is created on this electrostatically charged photoconductive material by discharging areas by light exposure. The pattern is developed into an image by a dry ink (toner). The toner is a charged powder consisting of pigmented thermoplastic particles that are attracted to the electrostatic charges. The resulting toner image is transferred to a substrate, such as paper. The toner is fixed by softening and fusing of the particles with the substrate. Finally, the photoreceptor material is cleaned before beginning another cycle.



Scheme 5. Schematic depiction of a cyclic color xerographic process. This Figure is adapted from reference 222

The photoconductive material, which is usually a multi-layered organic composite material, has to satisfy several requisites.²²² It has to be able to operate under tough conditions, such as heat, corona charging, contact with toner, substrates and cleaning systems, efficient release of the toner, and repeated flexion and tension by the rotation of the belt. Furthermore, the charges generated by electrostatic charge generation must transfer several layers in order to discharge upon exposure to light. Thus, the material experiences mechanical deteriorations, such as abrasion and scratching, and

electrostatic deteriorations usually caused by oxidation processes, such as decrease in maximum charge quantity, increase in decay of charges in the dark and decreased photosensitivity.

Initially, photoreceptor materials were fabricated from inorganic substances, such as sulphur or zinc oxide, but also from organic materials, such as anthracene and anthraquinone. It was in the sixties that triarylamine derivatives were used for the first time as photoconductive coatings.²²⁴ Both substituted and non-substituted TAA proved suitable. However, particularly sensitive coatings were achieved for amino and alkylamino para-substituted TAA compounds. As a general rule, any substituent that *i*) is inert to the operating conditions; *ii*) do not augment the electrical conductivity above the desired level and that *iii*) do not have an active hydrogen atom, can be used. The 13 TAA compounds displaying the best xerographic properties from this patent are shown in Figure 54. They show light sensitivity in the visible region of the spectrum and display better photo-conductivities than their organic predecessors. An advantage is that they can be charged both positively and negatively. This means that direct and reversal images can be obtained from the same master used to pattern the photoreceptor material, simply by changing the polarity of the corona. Furthermore, as most compounds are transparent, images can also be made in reflex mode, provided that the support is equally transparent.

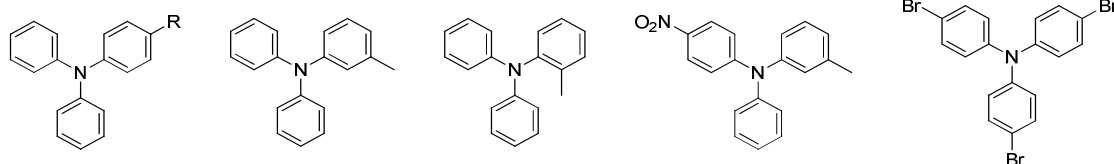


Figure 54. Molecular structures of TAA derivatives that have excellent xerographic properties. Substituents on the first structure are: H, NH₂, NHCOCH₃, N(CH₃)₂, OCH₃, OC₂H₅, CH₃, Cl, NO₂. This Figure is adapted from patent US 3180730.

In a patent submitted by Brantly, Contais and Fox, new photoreceptor materials consisting of TAA derivatives in which at least on aryl radical is substituted with an active hydrogen containing group are presented.²²⁵ These compounds show significant improvements with regards to process speed. Although none of them are sensitive to light, when a sensitizing compound is present electrical speeds exceeding those of TAA compounds without active hydrogen group are obtained. Furthermore, compounds with phenyl radicals also display improved photo-conducting properties with respect to alkyl substituted compounds.

Tamura *et al.* patented an invention in which the multi-layer photoreceptor *i*) increases abrasion resistance, *ii*) preserves its charge transfer properties in long-term use, *iii*) is capable of generating images without defects caused by high temperature or humidity operating conditions and *iv*) exhibits increased sensitivity and time of life.²²⁶ The photoreceptor consists of an electro conductive substrate, and a photosensitive layer. The latter is composed of a charge generation material, a charge transport

material and filler. The charge transport material is composed of a polymer with a soft backbone and TAA as side group. Both substituted and non-substituted aryl rings are used, including halogen atoms, linear and branched alkyl groups, alkoxy, aryloxy, mercapto, amino and acyl groups. In general however, functionalities of less than 4 carbon atoms are preferred.

Along the same lines, Suzuki and co-workers invented an electrophotographic photoconductor that has a high abrasion resistance and a long time of life.²²⁷ They achieved this by incorporating a highly cross-linked top layer. Additionally, this top-layer has a particularly smooth surface, minimizing toner leakage and preventing striped images. Charge transport materials made of non-functionalized low molecular weight derivatives, crystallize and form clouding in the cross-linked surface, reducing its mechanical properties. Furthermore, they show reduced sensitivity and increased residual potential. Bi- or more- functionalized derivatives, which are placed in the cross-linked structure by multiple interactions, hinder the formation of stable cationic radical intermediate states during charge transport, resulting in decreased sensitivity and charge trapping. However, when fused with polycyclic quinone and diphenoquinone structures, or electron accepting aromatic rings containing cyano or nitro groups, good results are obtained. Particularly effective charge transport and good electrical properties were obtained for the triarylamine structures TAA 1 and TAA 2, presented in Figure 55A. The different structures of photoconductive material are presented in Figure 55B-C.

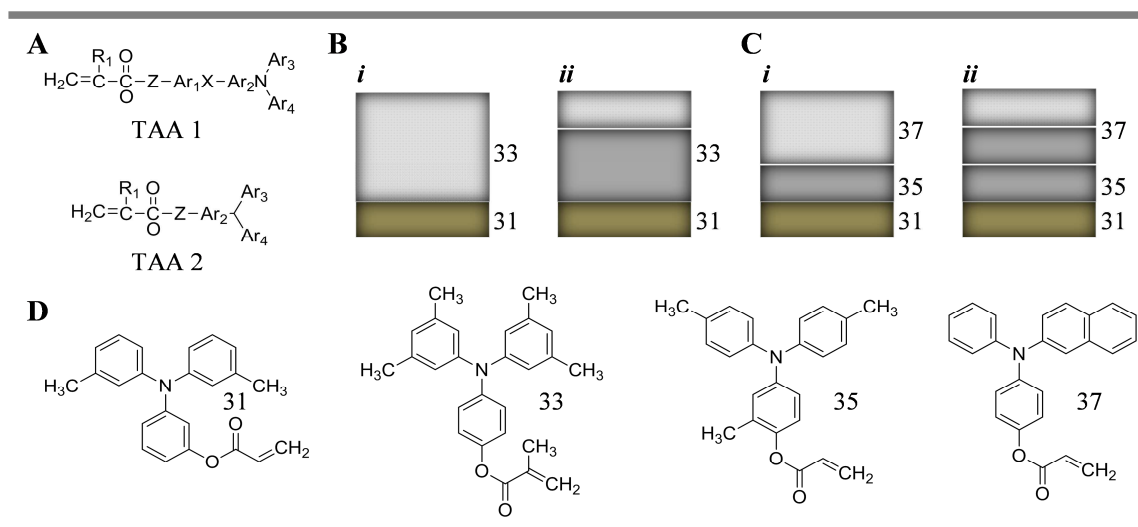


Figure 55. A) General molecular structure of TAA 1 and TAA 2 that show good xerographic properties; Cross-sections of electrophotographic photoconductor materials comprising B) a single layered photoconductive layer (33) exhibiting both charge generation and charge transport properties positioned on a conductive substrate (31). In *i*) the whole photoconductive layer is cross-linked, whereas in *ii*) only the surface part of the photoconductive layer is cross-linked; C) a laminated structure comprising a charge generation layer (35) and a charge transport layer (37) positioned on a conductive substrate (31). In *i*) the whole charge transport layer is cross-linked, whereas in *ii*) only the surface part of the charge transport layer is cross-linked; D) Molecular structures of TAA derivatives used in the examples presented in B and C. This Figure is adapted from patent US 20080020305A1.

F. Chemical sensors

A last application for TAA derivatives is their incorporation into chemical sensors. Chemosensors are able to recognize and monitor chemical, environmental and biological events. Some examples of common analytes are explosives, pesticides, thiols, anions, aliphatic amines, acids and metal ions. It is thus clear that such sensors are of great importance for detection and cleaning purposes as well as homeland security. The molecular configuration of a typical optical chemosensor consists of i) a receptor site for analyte recognition; and ii) a lumophore, which translates the recognition event into a light emitted signal (Figure 56). The advantage of molecular chemosensors is that they exhibit high sensitivity (down to a single molecule), fast response times (to the sub millisecond resolution), easy readings and portability. Furthermore, they have “*on-off*” switch alternatives. In turn-on chemosensors, the initial emission intensity of the lumophore is enhanced upon binding with a specific analyte, whereas it is quenched for turn-off sensors.

Multiple mechanisms exist by which signals from receptor sites towards lumophores are transmitted (e.g. $n\pi^*$ or $\pi\pi^*$ excited states, metal-centered excited states, charge transfer excited states, all organic triplet excited states, photo-induced electron transfer, monomer-excimer systems, electronic energy transfer and aggregation induced emission). Nowadays many of the structural features of small organic molecules and polymers by which the fluorescence can be controlled have been described. Polymers have multiple advantages: *i*) signal amplification is more easily realizable, as multiple recognition sites can be present; *ii*) high binding efficiency and recognition selectivity can be accomplished; *iii*) they can provide more detailed information based on the combination of different outputs; *iv*) they allow for easy processability and incorporation into devices. Triarylamines, which are known for their bright fluorescence, are functionalized onto recognition sites as lumophores for signal processing.

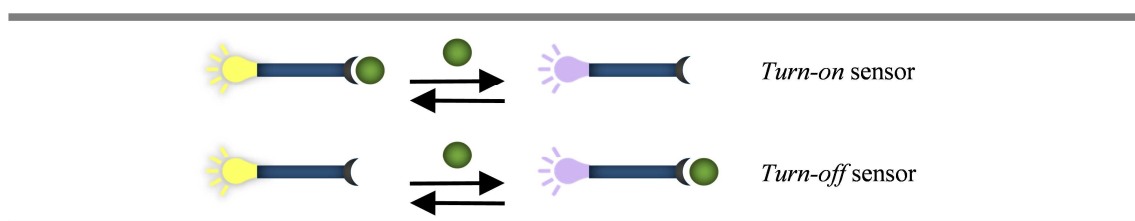


Figure 56. Schematic depiction of a *turn-on* and a *turn-off* chemosensor that is made up of a lumophore, a bridge that ‘translates’ the incoming signal and a receptor binding site (from left to right).

i. Photo-induced electron transfer mechanism

To the best of our knowledge the first article incorporating TAA into chemosensors was published by Gosh and Masanta.²²⁸ They described the size-selective binding of dicarboxylic acids through hydrogen bonding with neutrally charged pyridyl amide receptor sites (Figure 57A1-2). Photo-induced

electron transfer (PET) was shown to be the mechanism behind TPA fluorescence quenching (Figure 57B1-2). Titration studies showed that upon analyte binding, changes in absorption spectra were minor and, besides fluorescence quenching, no other changes occurred in the emission spectra. This is typical for PET behavior. In this example, TPA is connected to the recognition site by rigid amide spacers, and therefore the sole interaction possible is through electron transfer. When the binding complex has formed, the structure becomes more rigid and electron transfer from the binding complex towards the TPA unit induces fluorescence quenching. The same group published a second article with 2 new sensors for the recognition of dicarboxylic acids using pyridyl amide receptor sites with concomitant quenching of fluorescence of the TPA unit (Figure 57AB3-4).²²⁹ In a third article they reported a TPA-based chemosensor for the detection of fluoride, acetate and dihydrogenphosphate ions in different solvents, which makes use of the same PET mechanism for fluorescence quenching.²³⁰ Other groups took advantage of the same strategy of rigidification induced PET quenching as well (e.g. the groups of Guan²³¹ and of Ponnuval²³²).

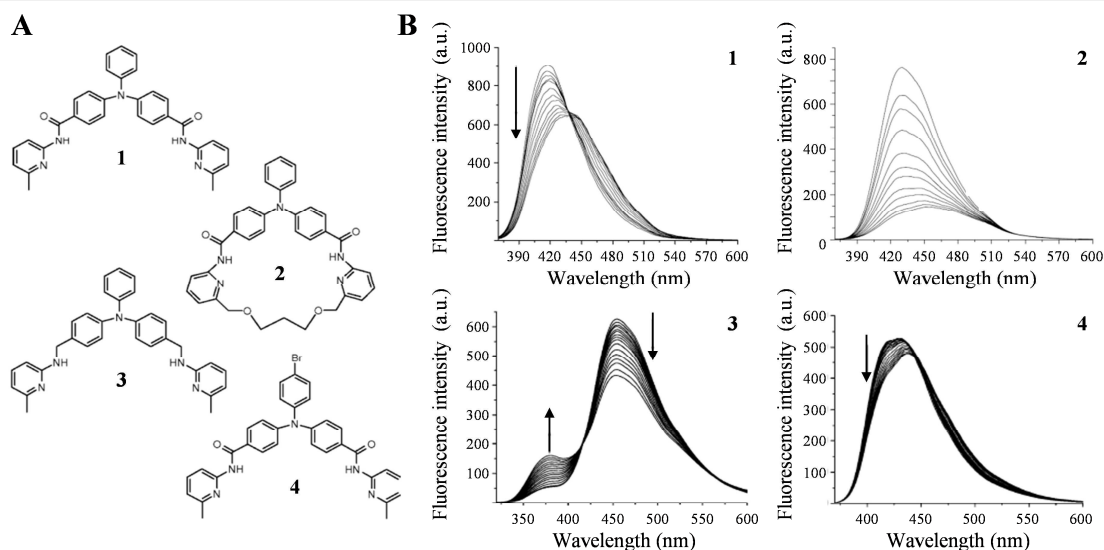


Figure 57. A) Molecular structures of chemosensors 1 and 2, used in reference 154, and 3 and 4, used in reference 155; B) fluorescence spectra of chemosensors 1, 3 and 4 in chloroform upon titration with glutaric acid and of chemosensor 2 in chloroform upon titration with 2,2-dimethylmalonic acid. This Figure is adapted from reference 228-229.

Another approach is dynamic quenching, in which the PET process is disturbed by a collision between the lumophore and analyte. Yang *et al.* first proposed this mechanism when describing their TPA-polyfluorene – di(2-picoly)amine chemosensor for the detection of Fe^{3+} ions.²³³ Similarly, Juang and co-workers presented a Cu^{2+} ion sensitive TPA-polyfluorene – terpyridine chemosensor, where fluorescence is quenched by the collision between Cu^{2+} and TPA.²³⁴

PET induced fluorescence quenching can also be caused by intraligand charge transfer, as presented in an article of Pan *et al.*, who reported 2 Schiff base derivatives, containing either TPA or indole as lumophore groups.²³⁵ The strong point of their research is that it works in a wide range of pH and it is selective for Fe^{3+} over other counter ions. Furthermore, it is able to function in aqueous environments and shows good cell permeability. The sensors can thus be applied in biological environments. Geng *et al.* equally used inter ligand charge transfer for PET induced fluorescence quenching.²³⁶ Here PET is possible between the electron-rich sensor (TPA-pyridine) and the electron-poor nitroaromatic analyte (picric acid). A final example can be given using the article of the group of Zhou, who presented a two photon absorption “on-off-on” system (Figure 58).²³⁷ Upon coordination with Cu^{2+} fluorescence is quenched by PET. Then the sequential detection of homocysteine returns the sensor to its “on” state. This chemosensor can thus be used for both monitoring water pollution by Cu^{2+} ions and homocysteine tracking in living cells (Figure 58D).

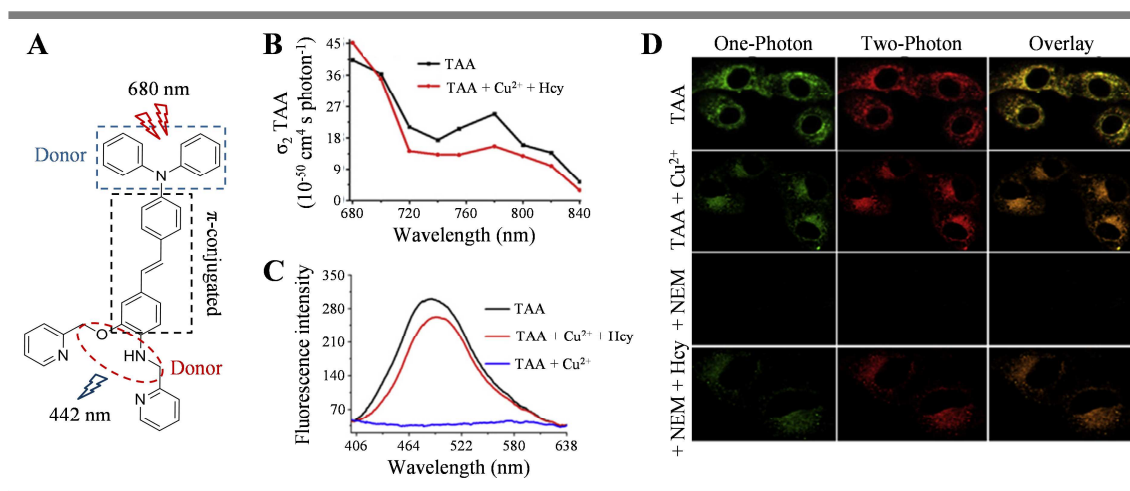


Figure 58. A) Donor- π -donor molecular structure of TAA chemosensor that favors intramolecular charge transfer; B) two photon absorption cross section of TAA chemosensor (black) and chemosensor + Cu^{2+} + homocysteine (hCy) (red) in DMSO solutions; C) fluorescence intensity (a.u.) demonstrating the on-off-on switch ability of the TAA chemosensor; D) Confocal fluorescent images of HeLa cells incubated with TAA chemosensor; TAA - Cu^{2+} ; TAA - Cu^{2+} and pretreated with N-ethylmaleimide; TAA - Cu^{2+} - hCy and pretreated with N-ethylmaleimide. This Figure is adapted from reference 237.

ii. Electronic energy transfer mechanism

Electronic energy transfer (EET) is another manner in which fluorescence quenching can be obtained. Feng *et al.* reported linear and hyper branched TPA and divinyl bipyridyl conjugated copolymers (LTP and HTP) for the recognition of transition metal ions.²³⁸ They postulate that the observed fluorescence quenching could be attributed to energy or electron transfer between the metal complexes and the polymer backbone. HTP proved to be more sensitive towards fluorescence quenching than LTP, and its efficiency depends on the coordination ability of the metal ions with the 2,20- bipyridyl moieties.

iii. (Excited state) charge transfer

The group of Cheng was the first to report a TPA chemosensor (a poly heterocyclic pyridine-imide film containing TPA) making use of intramolecular charge transfer.²³⁹ Gu *et al.* studied a similar chemosensor using N,N'-di[3-(diphenylamine)benzyl]-piperazine (TPA-pip).²⁴⁰ The authors demonstrate, through both experimental and theoretical studies, why rather an excited state charge transfer mechanism occurs instead of PET. This is because upon protonation mainly TPA, and not pip, affects the luminescence properties. They hypothesize that the HOMO energy level of the TPA moiety is higher than that of pip in the TPA-Pip molecule and therefore no PET process can occur.

The group of Goswami published an article on highly selective TPA-based indolylmethane derivatives as Cu²⁺ chemosensors making use of internal charge transfer (ICT).²⁴¹ Upon binding of Cu²⁺ the TPA moiety is deprotonated, leading to an electronic change between the indolyl-TPA. The electron donating ability of TPA increases and consequently leads to an enhanced ICT process and a large decrease in fluorescence intensity.

Cheng *et al.* presented fluorescent and colorimetric ICT chemosensors for mercury detection, by functionalizing various electron-donating thiophene groups to a TPA backbone with an aldehyde group as the electron acceptor.²⁴² Remarkable sensitivity down to 10 nM of Hg²⁺ could be obtained due by further enhancement of the ICT by extending the length of π conjugation. The group of Yang also successfully increased the sensitivity and ratiometric change of their chemosensor.²⁴³ Here they achieved this by making use of 2 photon absorption instead of 1 photon absorption. A final example of exceptional analyte detection is a cyanide sensor which detection limit lays two orders of magnitude below the concentration guideline of cyanide in drinking water.²⁴⁴

Many more examples can be found in literature.^{245–251}

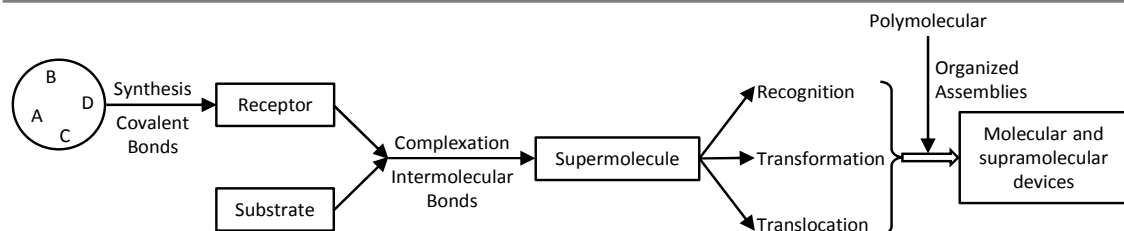
iv. Other mechanisms

As mentioned in the introduction, many other working mechanisms exist. This is well illustrated by the groups of D'Souza, who used piezoelectric microgravimetry,²⁵² and of Zhang and Bao, who reported on reversible piezofluorochromism.²⁵³ Also solvatochromism is used in TPA-based chemosensors.²⁵⁴

I.3 Supramolecular Chemistry and Supramolecular Polymers

A. Supramolecular chemistry and self-assembly

The field of supramolecular chemistry studies processes or assemblies of molecules that are governed by non-covalent interactions. This field of chemistry was defined by J.-M. Lehn, D. Cram and C. Pedersen who received the Nobel Prize for “their development and use of molecules with structure-specific interactions of high selectivity” in 1987.²⁵⁵



Scheme 6. From Lehn’s *Angewandte Chemie* 1988 ‘from molecular to supramolecular chemistry: molecules, supermolecules, molecular and supramolecular devices’

Supramolecular chemistry can be used to achieve control over the bottom-up generation of complex self-organized architectures, whose structural motifs can be controlled over a wide range of length scales. An object can be called to be self-assembled if it is formed spontaneously and exhibits reasonable thermodynamic or kinetic stability. This field can be of great interest as the structuring of (nano) materials at higher scales can result in emerging properties that did not exist in the sub-components. In other words, materials with potentially advanced functions could be realized by the self-assembly of different nano-structures.

The fact that these processes are governed by non-covalent interactions gives rise to some important features. First of all, non-covalent bonds are weaker than covalent bonds, 2 to 300 kJ·mol⁻¹ and 150 to 450 kJ·mol⁻¹ respectively. However, by combining multiple non-covalent interactions, stable supramolecular structures can be formed. Secondly, they are kinetically labile. This means that the self-assembly process is dynamic and reversible. This equally offers the potential to fabricate stimuli-responsive materials (e.g. temperature, polarity, pH, redox, light, concentration, stress), with self-healing properties. Furthermore, non-covalent interactions can impose directionality. They partly govern structure selectivity and enable programmability of supramolecular systems.

The most important types of non-covalent interactions used in supramolecular chemistry are summarized in **Table 2**. The strongest interactions typically are, (metal) ion-ligand coordination and electrostatic interactions. Moderate interactions are for example hydrogen bonding, π - π stacking, host-

guest and hydrophobic interactions. Van der Waals forces are the weakest interactions one might have.

Table 2. Summary of main non-covalent interactions in order of descending bond strength

Type of interaction	Bond strength (kJ/mol)	Examples
Ion - ion	200 – 300	(n-Bu) ₄ N ⁺ Cl ⁻
Ion - dipole	50 – 200	Na ⁺ [15]crown-5
Dipole - dipole	5 – 50	Acetone
Hydrogen bonding	4 – 120	C-G and A-T nucleotide pairs in DNA
Cation - π	5 – 80	K ⁺ in benzene
$\pi - \pi$	0 – 50	Graphite
Van der Waals	<5 (depends on surface area)	Liquid crystals; molecular crystals
Hydrophobic	Depends on solvents interactions	Micelles; films; inclusion complexes

The primary concepts studied in supramolecular chemistry are: *i*) molecular recognition; *ii*) molecular self-assembly; *iii*) dynamic (covalent) supramolecular chemistry.²⁵⁶

Molecular recognition is the specific association of two or more molecules through a ‘recognition’ process. Here, recognition refers to both binding, through a specific non-covalent bond, and selection, to reach a predestined purpose.²⁵⁵ In nature, molecular recognition plays a key role in enzyme-substrate interactions.²⁵⁷ An example of molecular recognition is the formation of inclusion networks, classically the binding of alkali metal ions to crown ethers.²⁵⁸

Molecular self-assembly is defined by the non-covalent organization of (macro) molecules into supramolecular structures leading to either discrete (e.g. micelles, cages, capsules) or infinite (e.g. fibers, membranes, networks) objects. The driving forces behind it are molecular recognition and programming, leading to predictable structures. In contrast to molecular organization, it does not need a continuous energy source. Hierarchical molecular self-assembly has the distinction that it takes place over multiple length scales.²⁵⁹

As mentioned before, supramolecular self-assemblies are dynamic in their make-up due to the lability of non-covalent interactions. Dynamic supramolecular chemistry deals with this reversibility of connections made between molecules. Such features can also be introduced into molecular chemistry, through the introduction of labile covalent bonds (e.g. imine bond and disulphide bonds).

This would then give rise to constitutional dynamic chemistry, covering both molecular and supramolecular levels.²⁵⁶ Dynamic covalent structures and their supramolecular assemblies are capable of modifying their constitution in response to external stimuli. This type of chemistry is a powerful tool for screening large numbers of compounds for the discovery and design of new drugs and materials. Moreover, lately, it has received a lot of attention because it leads to adaptive and evolutive chemistry.

Supramolecular chemistry plays an important role in many scientific fields. In biology, for example, it is related to systems chemistry and chemical evolution. In material science, it has helped develop materials with novel functionalities, such as responsiveness, tunability and self-healing properties. In organic electronics, supramolecular chemistry gave rise to supramolecular electronics. In this thesis supramolecular polymers are studied for their possible application in this field of supramolecular electronics. Therefore, first, the concept of supramolecular polymers will be discussed. Then, we will examine how and which supramolecular polymers can be used in supramolecular electronics.

B. Supramolecular polymers

Conventionally, polymers consist of long molecular chains build from repeating covalently linked monomeric units. The covalent polymerization process occurs under kinetic control because the activation barrier of the forward polymerization process is much smaller than the activation barrier of the reverse depolymerization. As a consequence, the degree of polymerization does not change upon dilution or heating.

In contrast, supramolecular polymers are made up of non-covalently, reversibly linked monomers bearing complementary binding groups. These directional secondary interactions are the five standard interactions implemented in supramolecular chemistry: *i*) hydrogen bonding; *ii*) ionic or electrostatic interactions; *iii*) π - π interactions; *iv*) charge transfer interactions; *v*) hydrophobic interactions. Due to the reversibility of the interactions supramolecular polymers display multiple distinctive properties. First of all, they are usually formed under thermodynamic control, although kinetic parameters can still play a role. Hence, the chain length can be correlated directly to the bond strengths, monomer concentration and temperature. Secondly, it gives them extraordinary dynamic and responsive properties. They also exhibit self-healing/recycling properties. Finally, they allow for easier processing. Combining these properties with the attractive features of conventional polymers (such as excellent mechanical properties) will lead to a new class of polymers that can be used for many innovative applications.

The first publications in this field were published by Lehn and co-workers in the early nineties.^{260,261} Since then the field has been growing immensely, continuing to today.^{256,262-265}

In the following sections we will discuss supramolecular polymerization mechanisms and the role of several types of non-covalent interactions in the self-assembly process. Usually, however, interplay between multiple attractive and repulsive forces are combined to induce self-assembly in a cooperative or anti-cooperative manner, to stabilize the resulting nano objects.

i. Supramolecular polymerization mechanisms

As mentioned in the previous section, supramolecular polymerization is a dynamic process under thermodynamic, but also kinetic, control in which monomers, oligomers and supramolecular polymers co-exist in equilibrium. There are three manners in which supramolecular polymerizations can be described: *i*) physical origin of the secondary interactions; *ii*) structure and number of monomer(s) used; *iii*) thermodynamic processes during polymerization. The first two classifications omit many mechanistic details. Therefore, the thermodynamic approach, that takes into account the change in Gibbs free energy in function of the conversion of monomers into a supramolecular polymer, is the one most used in literature and the one discussed in the following paragraphs.

Three different mechanisms were identified and described by the group of Meijer²⁶⁶: *i*) isodesmic; *ii*) (anti-) cooperative; *iii*) ring-chain. Which mechanism is followed during polymerization depends on the nature of the monomer (which comprises both the physical nature of the reversible secondary interactions, as well as the structure of the monomer), the concentration of monomers and the temperature. Most importantly, it considers the association constant (K) of each monomer addition (Figure 59).

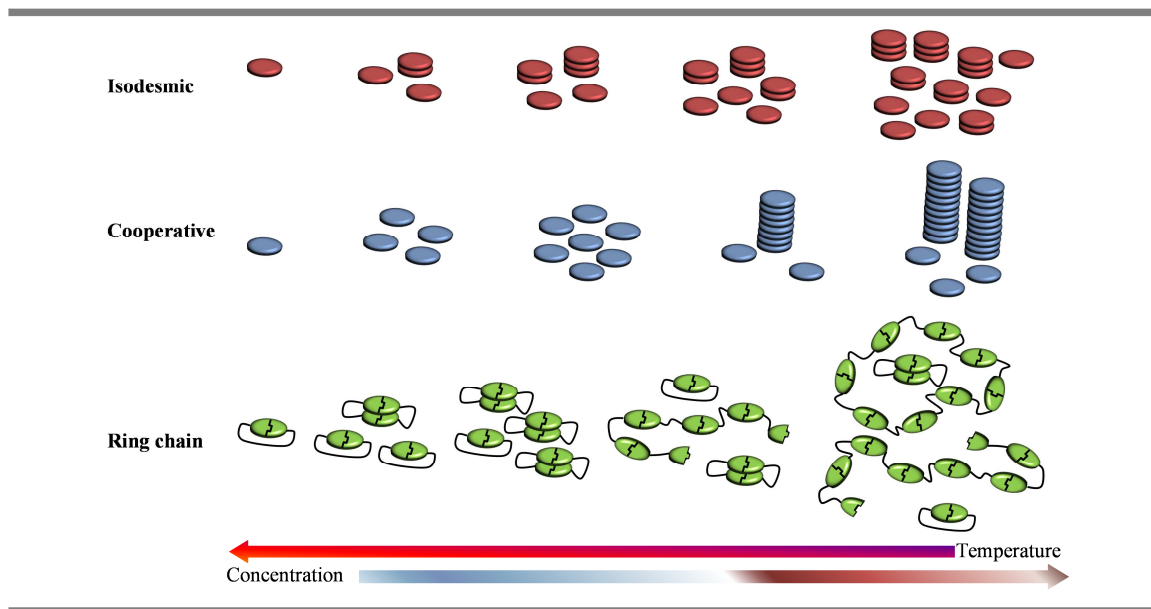


Figure 59. Graphical representation of isodesmic, (anti-) cooperative and ring-chain supramolecular polymerization mechanisms

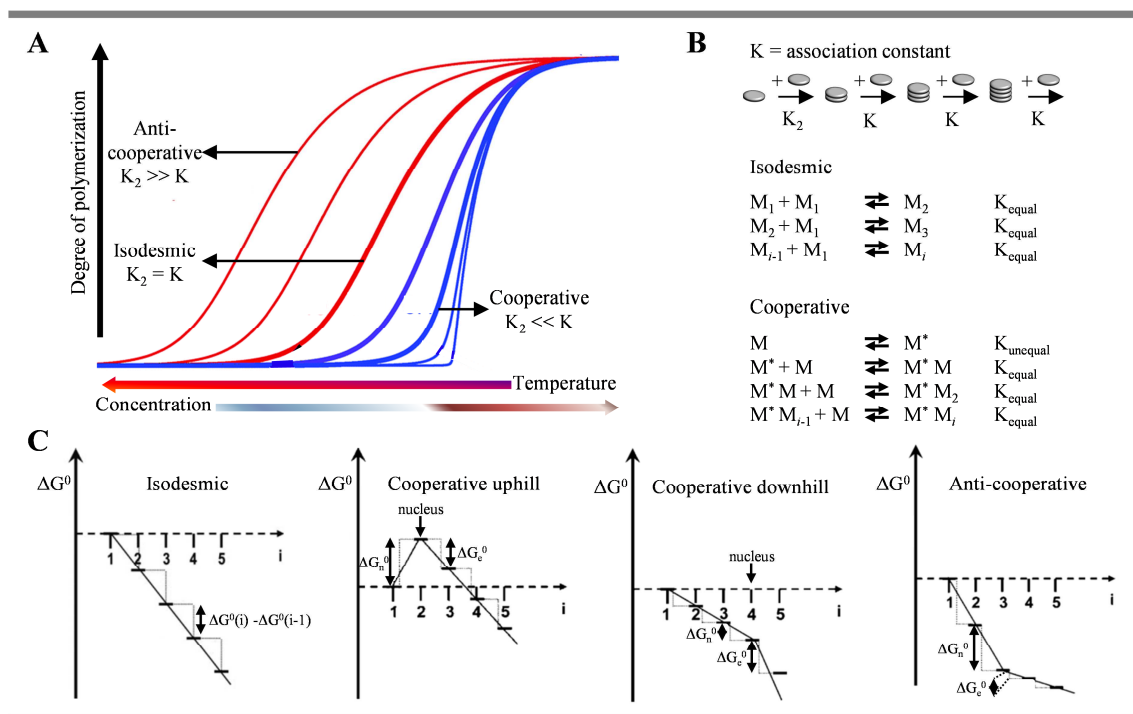


Figure 60. A) Graphical representation of the degree of polymerization in function of temperature and concentration for anti-cooperative, isodesmic and cooperative supramolecular polymerization. B) Chemical equilibria present during isodesmic and cooperative supramolecular polymerization. C) Schematic free energy diagrams for isodesmic, cooperative uphill (nucleus size was chosen to be a dimer), cooperative downhill (nucleus size was chosen to be a tetramer) and anti-cooperative supramolecular polymerizations. The Y-axis shows the Gibbs free energy in arbitrary units, the X-axis the size of the aggregates. This Figure is adapted from reference 266

The supramolecular polymerization mechanisms will be described for *single* ditopic monomers. However, one should keep in mind that the same pathways are followed when two different monomers are present. The difference being that in the latter case the change in Gibbs free energy also depends on the stoichiometry between the two monomers. The most important features are summarized in **Figure 60**.

The first mechanism is called *isodesmic*, however in literature it can also be found under the name multistage open association model²⁶⁷ or free association model.²⁶⁸ It can be compared to reversible step-growth polymerizations that follows Flory's *principle of equal reactivity*, such as polycondensation reactions.²⁶⁹ The isodesmic model can be characterized by two main phenomena. First of all, all steps during polymerization are kinetically and thermodynamically identical. There is a single association constant (K_{equal}) for each monomer addition and as a consequence the decrease in Gibbs free energy is also constant. In other words, the reactivity of the secondary interactions is identical for monomers and supramolecular polymer end-groups. This means that the likelihood of monomer addition is independent of the polymer length. The second characteristic is that no cyclic intermediates will be present during supramolecular polymerization. The process described hereunder is an idealized case. In reality the free energy landscape may include some kinetic barriers.

Another result of the equivalency of polymerization steps is that isodesmic self-assembly processes do not have a critical concentration nor critical temperature.^{267,268,270–276} Nevertheless, the polymerization is still dependent on both of them, as will be further illustrated here. Monomers will always be the most abundant species present and co-exist in solution with polymers of varying lengths. When the total concentration is increased, both the concentration of monomers and polymers increases.²⁷⁶ From this stems the disadvantage that only at high concentrations of monomers, polymers with a large degree of polymerization are formed. Thus the polydispersity in such systems is always much greater than 1 ($PD \gg 1$), growing steadily to a value of 2. The temperature dependency is more complicated. Although no critical temperature will exist, there is an optimal polymerization temperature. This was first explained by Dainton and Ivin^{277,278} who revealed the relation between the enthalpy of propagation (ΔH_{pr}), the entropy of propagation (ΔS_{pr}) and the initial monomer mole fraction to the temperature. When ΔH_{pr} and ΔS_{pr} are positive, polymerization only occurs above a minimum temperature. This ‘floor’ temperature is elevated enough for the entropy term to exceed the enthalpy term. When ΔH_{pr} and ΔS_{pr} are negative, polymerization is driven by enthalpy and only takes place below a maximum, ‘ceiling’, temperature. However, for this model to be exact a sharp transition for monomer-rich and polymer-rich phases should exist.²⁶⁸ Although this is the case for cooperative supramolecular polymerizations, as will be explained in the following section, it is not for isodesmic supramolecular polymerizations.²⁶⁸

The second mechanism is the (*anti*-)cooperative supramolecular polymerization, which occurs in two steps. The first stage in cooperative polymerization is known as the nucleation phase and follows an isodesmic polymerization process in which the addition of each monomer occurs with the same association constant K_n . When a nucleus of size s is formed a second linear isodesmic polymerization process will follow, known as the elongation phase, with an association constant K_e that is greater than K_n . A further distinction can be made between cooperative *up-hill* and *down-hill* polymerizations. In an up-hill process, as defined by Ferrone,²⁷⁹ the Gibbs free energy increases in the nucleation stage and is maximal for the nucleus of size s . The nucleus is thus the least stable species and is therefore lowest in number. Then, because of several possible cooperative effects, polymerization becomes energetically more favorable. In a down-hill process the Gibbs free energy does not increase during nucleation, but decreases at a slower rate than during elongation.²⁷⁹ This means that not the nucleus but the monomer is the least stable species. Whether an up-hill or down-hill process occurs depends on the concentration. With increasing monomer concentration an initially up-hill process can turn into a down-hill process.^{280,281} In an anti-cooperative process supramolecular polymerization occurs at a higher association constant in the first phase than in the second phase. The advantage of this mechanism is that discrete objects of low polydispersity can be obtained. Experimentally (*anti*-)cooperative polymerization can be distinguished from an isodesmic polymerization in three manners²⁸²: *i*) the observation of a lag-time in the polymerization process; *ii*) the lag-time can be

annulled by seeding (the addition of nuclei); *iii*) the observation of a critical concentration or temperature at which the monomer is in equilibrium with the supramolecular polymer. Parameters that can lead to (anti-) cooperativity during polymerization are, for example, structural and electronic properties. The degree of cooperativity (σ) is defined as the ratio between the association constant in the nucleation phase (K_n) and the association constant in the elongation phase (K_e):

$$\sigma = \frac{K_n}{K_e} \quad (7)$$

If σ is one, the polymerization follows an isodesmic mechanism. When σ is much smaller than one, polymerization is highly cooperative. For anti-cooperative systems σ will be greater than one.

As mentioned before, in contrast to isodesmic polymerizations, (anti-)cooperative polymerizations are subject to a critical concentration and temperature. This fact is well illustrated by Zhao and Moore who developed a model with a dimer as nucleus.²⁷⁶ Below the critical concentration supramolecular polymerization will be almost non-existent. However, when raised above this critical point, but still in a rather narrow concentration range, chain growth will occur and practically all monomers will be transformed into high (cooperative) or low (anti-cooperative) molecular weight polymers. Thus, in contrast to isodesmic polymerization, by increasing the total concentration, the monomer concentration will remain constant and only the polymer concentration increases. Additional control over the polydispersity can be obtained by modulating the association constant of the elongation phase and the degree of cooperativity. Above the critical temperature, a regime called nucleation temperature, almost no polymeric species will be present in the system, whereas below this temperature, also called the elongation temperature, a sharp increase in polymer species can be observed.

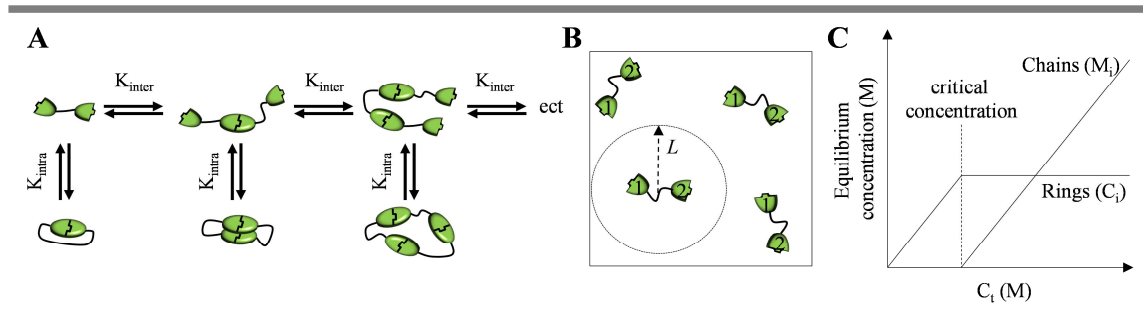


Figure 61. A) Schematic representation of ring-chain supramolecular polymerization. K_{inter} is the intermolecular association constant, K_{intra} is the intra molecular association constant. B) Schematic representation of the effective concentration (C_{eff}). End-group 1 cannot exit the area defined by radius L (L = stretched length of the chain). As a result end-group 2 experiences an effective concentration for end-group 1 that is higher than the actual concentration of end-groups in solution. Thus intramolecular cyclization between end-group 1 and 2 is favored. C) Schematic diagram showing the effect of the effective molarity on the formation of rings and chains. This Figure is adapted from reference 266

The third mechanism is called *ring-chain*. Here, because of the rapid association and dissociation of reversible bonds, the formation of linear supramolecular polymers is in thermodynamic equilibrium with the formation of their cyclic counterparts (Figure 61A). In most examples, the two end-groups on a monomer responsible for reversible binding are connected by a flexible hydrocarbon chain (the linker). The predisposition for intramolecular cyclization highly relies on the conformational properties of the linker group that separates the two end-groups. Kuhn quantified the probability of intra- versus intermolecular binding by introducing the effective concentration (C_{eff}), which is defined as the local concentration of one chain end in the proximity of another chain end of the same polymer (Figure 61B). He determined the relation between the mean squared end-to-end polymer chain length and the probability for cyclization and predicted that it would decrease for $N^{-3/2}$, N being the number of bonds in a chain.²⁸³ The effective concentration can be replaced by the effective molarity (EM), which is the ratio between the intra- and intermolecular equilibrium constants. At a concentration above EM linear polymers are formed, below EM cyclization is favored.

$$EM_i = \frac{K_{(intra)i}}{K_{inter}} \quad (8)$$

ii. Hydrogen bonding

One of the most commonly used non-covalent bonds are hydrogen bonds. Hydrogen bonds are formed between a δ^+ hydrogen atom typically linked to an electronegative atom (e.g. nitrogen or oxygen) to a δ^- electronegative atom (Figure 62A). The strength of the hydrogen bond depends on the electronegativity of the atoms that are participating. Although classified as weak to moderate interactions (4-120 $\text{kJ}\cdot\text{mol}^{-1}$), by designing multiple hydrogen bonding moieties in a molecular framework, both the increased strength as well as the imposed directionality could be used towards supramolecular polymerization. The bonding strength is also influenced by secondary attractive and repulsive electrostatic interactions (Figure 62BC). Ultimately, the hydrogen bonding character and directionality can be increased over several orders of magnitude by designing motifs containing multiple moieties capable of hydrogen bonding (Figure 62C).²⁸⁴ In doing so, a vast range of motifs can be designed that show directionality and specificity, to form an almost endless variety of supramolecular structures.

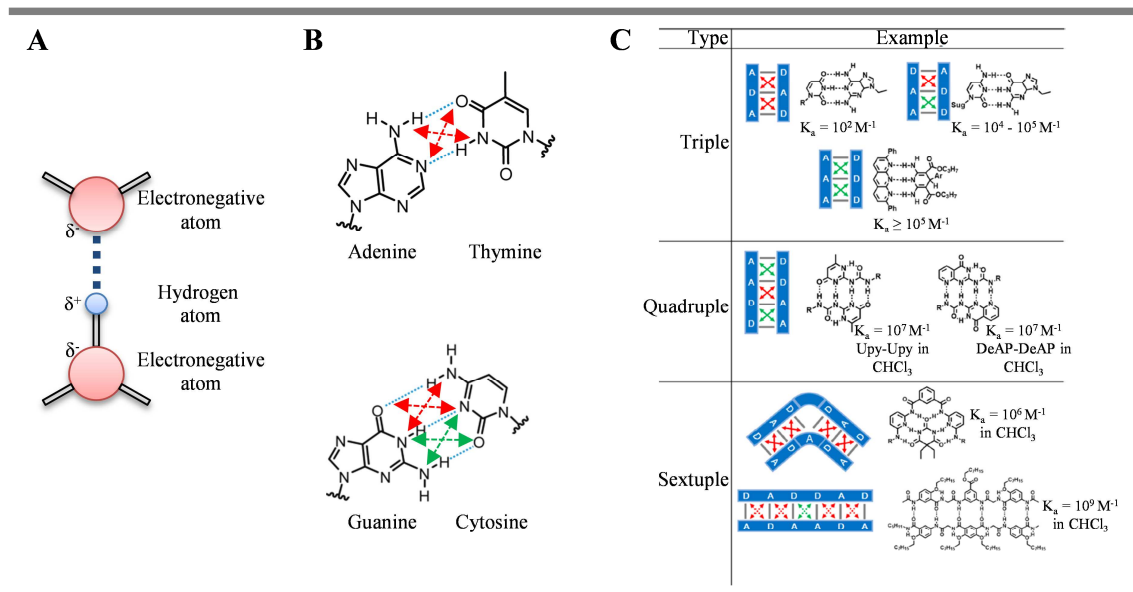


Figure 62. A) Schematic depiction of hydrogen bonding between a δ^+ hydrogen atom to a δ^- electronegative atom; B) hydrogen bonding (blue dotted lines) and attractive (green arrows) and repulsive (red arrows) interactions present between DNA base-pairs²⁸⁵; C) Examples of triple, quadruple and sextuple motifs of hydrogen bonding interactions, as well as the secondary attractive and repulsive interactions that are present, with the resulting bond strengths.²⁸⁴

Hydrogen bonding plays an extremely important role in many biological systems. Well known examples thereof are the nucleic acid base-pairing in DNA as proposed by Watson and Crick²⁸⁵ (Figure 62B), protein folding (Pauling and Corey²⁸⁵) and enzymatic catalysis. The very first artificial supramolecular polymer was also based on hydrogen bonding (Figure 63).^{260,261} 2,6-diacetylpyridine (P) and uracil (U) precursors, obtained from *D*- and *L*-tartaric acid, were mixed to form a triple hydrogen bonding supramolecular DAD-ADA structured polymer (D stands for donor and A for acceptor) (Figure 63AB). Scanning electron microscopy showed the formation of helical super structures where the handedness is imposed by the uracil moiety (Figure 63C-F).

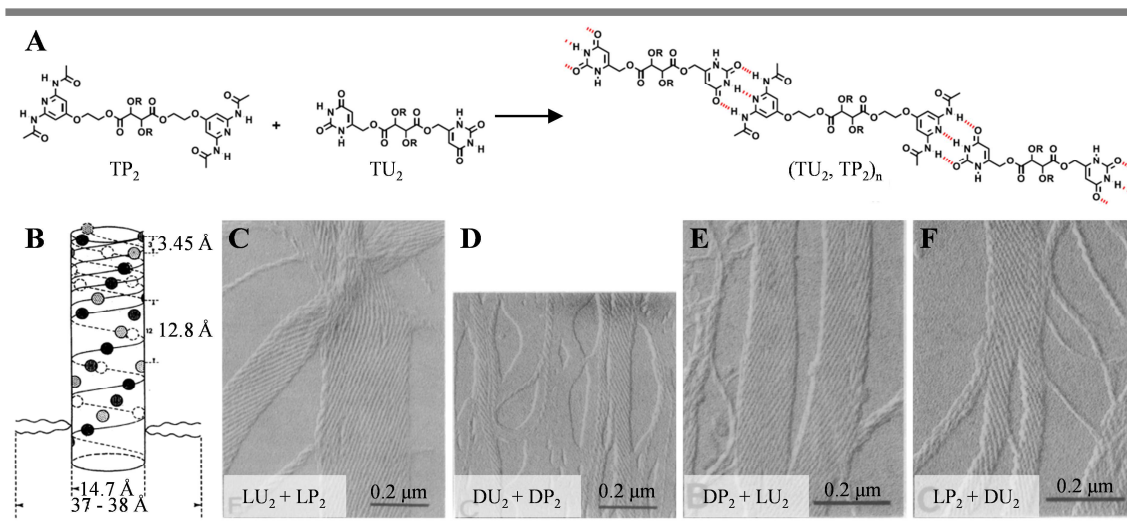


Figure 63. A) molecular structure of TP_2 and TU_2 monomers (T stands for *L*-, *D*- or *meso*-tartaric acid) and the resulting supramolecular polymer formed by hydrogen bonding; B) schematic depiction of the columnar superstructure formed; C-F) TEM images of $LU_2 + LP_2$ (C), $DU_2 + DP_2$ (D), $DP_2 + LU_2$ (E) and $LP_2 + DU_2$ super helical structures formed in $CHCl_3$ at a concentration of $500 \mu\text{g} / \text{mL}$. This Figure is adapted from reference 260.

iii. Ionic and metal coordination

Ion-ion, dipole-ion and dipole-dipole interactions are formed due to attractive Coulombic forces between opposite charges. The strength of the interaction depends highly on the charges of the participating compounds (full charges for ions and partial charges for dipoles) and the distance between them (proportional to the square root). Where ion-ion interactions are non-directional, dipole-ion and dipole-dipole interactions are (Figure 64).

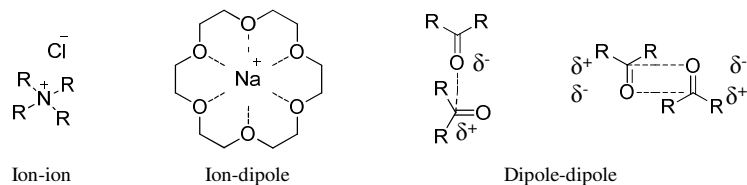


Figure 64. Examples of ion-ion, ion-dipole and dipole-dipole interactions. The dotted lines indicate the directionality of the interactions.

Supramolecular polymers containing reversible metal-ligand interactions are called metallosupramolecular polymers (MSP). The binding strength, specificity, directionality, reversibility and even the solubility of MSPs can all be altered by making use of the wide variety of metals ions and ligands.²⁸⁴ Some generalities, however, can be observed: typically, complexes of multi-dentate ligands and multi-valent metal ions exhibit higher binding constants. They are therefore preferentially used when a high degree of polymerization is desired. Also geometry is a key factor. In order to favor MSP formation, linear coordination configurations and flexible linkers should be employed. When

non-linear coordination configurations and rigid ligands are present self-assembly leads rather to cyclic structures (e.g. metal-organic frameworks, coordination cages).

It was the group of Reahn, in 1996, that first reported on a soluble and well-defined MSP (Figure 65).²⁸⁶ They found that in order to obtain stable, constitutionally homogeneous, high molecular mass MSPs, the exclusion of competitive ligands, including solvent molecules, is primordial.

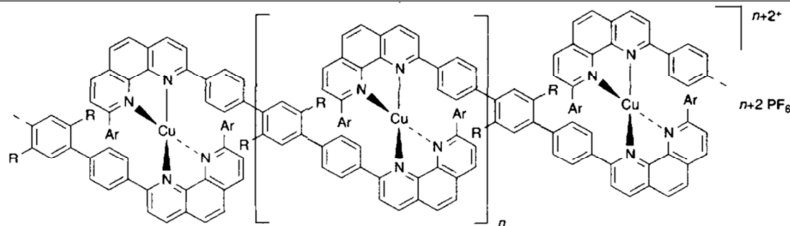


Figure 65. First soluble and well-defined MSP as reported by the group of Reahn.²⁸⁶

iv. π - π Interactions

Supramolecular polymerization could be difficult to achieve when the sole interaction present is aromatic π - π stacking, as this interaction²⁸⁷ is often weak and less directional.²⁸⁴ This disadvantage can however, be overcome by introducing additional directional groups on the periphery of the aromatic ring. Besides driving supramolecular polymerization, π - π interactions have additional values, such as their effect on the electric and optical properties. The monomers can either stack in a columnar or in a linear manner. A well-known example from nature is DNA, which is essentially a natural supramolecular polymer. It uses, among other non-covalent interactions, columnar π - π stacking in its structure. The group of Häner, inspired by DNA, investigated artificial systems mimicking DNA for the construction of adaptive polymeric platforms.²⁸⁸ They attached an oligopyrene unit, responsible for the π - π stacking, to an oligodeoxynucleotide (DNA part) and were able to form one dimensional helical ribbons in aqueous media (Figure 66).

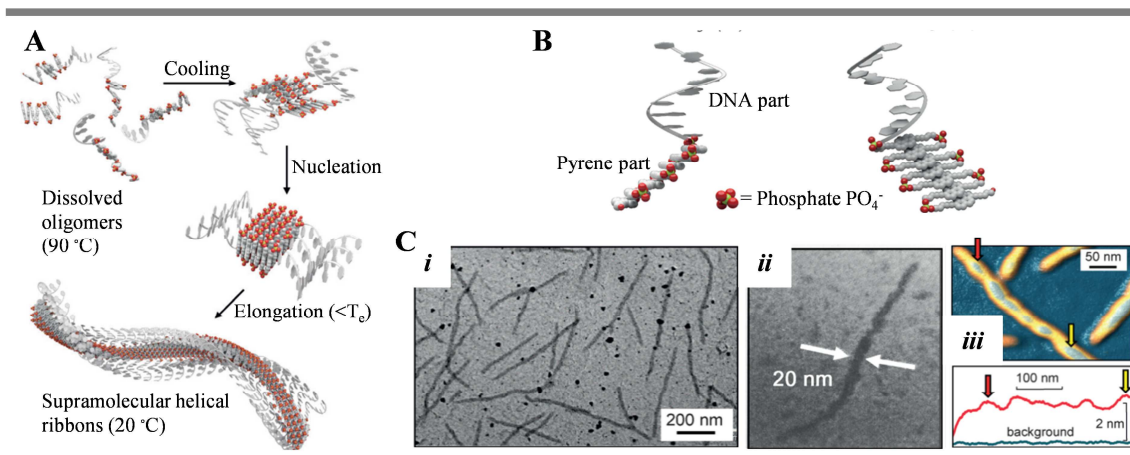


Figure 66. A) Schematic depiction of the self-assembly process into DNA grafted supramolecular polymers from chimeric DNA-pyrene oligomers; B) schematic depiction of the pyrene-DNA chimeric oligomers used. The pyrene units stack in a stair-like manner, with the negatively charged phosphodiester groups located on the edge of the column. The DNA part is linked to the phosphodiester groups; C) TEM (*i-ii*) and AFM (*iii*) images of the resulting supramolecular polymers. This Figure is adapted from reference 288.

When the monomers assemble in a linear manner, often a molecular tweezer motif is used. This was demonstrated by Wang *et al.*²⁸⁹ They synthesized a heteroditopic (AB-type) tweezer-guest monomer, wherein two bis[alkynyl]platinum(II)terpyridine moieties functioned as tweezer and pyrene as guest (Figure 67). Following a ring-chain polymerization mechanism, flexible supramolecular polymers are formed. Interestingly, the addition of anthracene and cyano-functionalized dienophile derivatives provokes reversible disassembly and assembly respectively by Diels-Alder chemistry. The authors thus achieved the creation of a novel supramolecular stimuli-responsive polymer, whose (dis-) assembly can be regulated in a controlled and easy way.

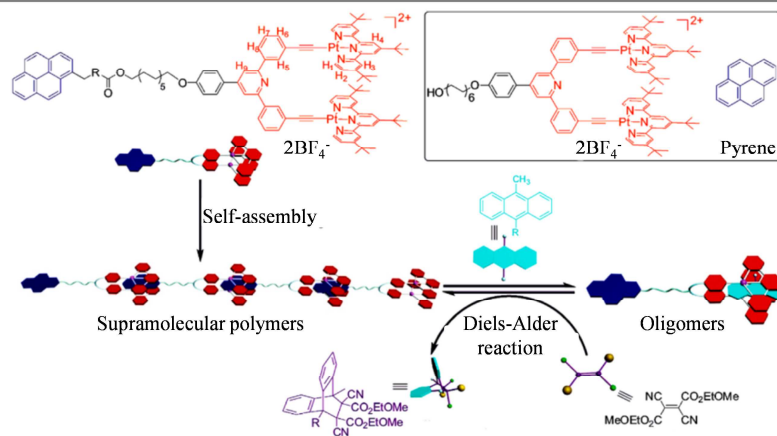


Figure 67. Schematic depiction of the linear ring-chain polymerization of $2BF_4^-$ -pyrene monomers, via tweezer-guest π - π interactions, to obtain Diels-Alder reaction responsive supramolecular polymers. This Figure is adapted from reference 289.

Besides columnar and linear stacking, numerous other structures have been reported. For example, the group of Würthner, working with wedge-shaped perylene bisimides and dumbbell-shaped hexabenzocoronene, reported spherical micelles for the former and nanorods for the latter. By combining the two, hollow vesicles can be obtained (Figure 68).²⁹⁰ These self-assembled structures were studied as nanocarriers and in supramolecular organic electronics.

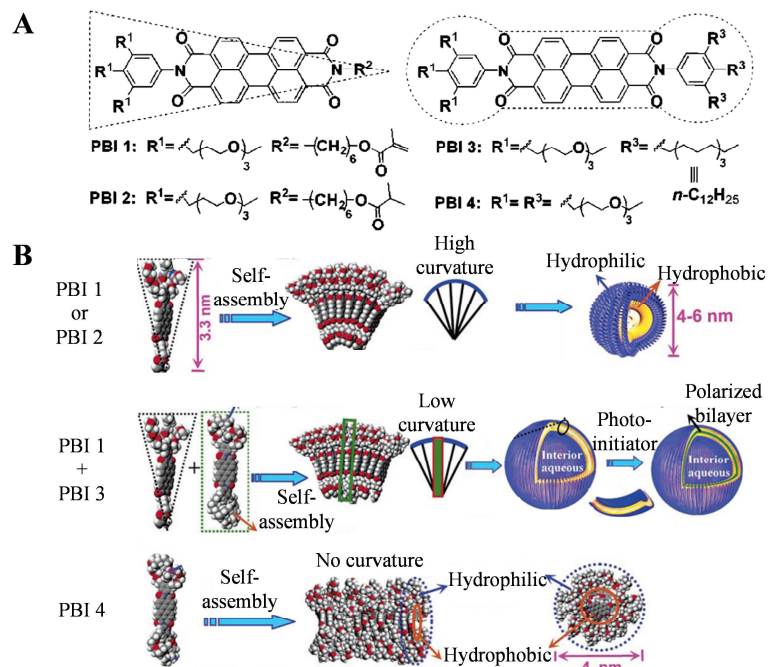


Figure 68. A) Molecular structures of wedge-shaped perylene bisimides and dumbbell-shaped hexabenzocoronene molecules studied; B) illustration of their self-assembly into micelles (top), bilayer vesicles (middle) and rods (bottom). This Figure is adapted from reference 290.

v. Charge transfer interactions

Charge transfer (CT) interactions can be viewed as a special kind of π - π interactions. Here an aromatic ring functions as an electron donor group and self-assembles with an electron acceptor. They are usually employed as additional interactions for cooperative supramolecular polymerization, as their interaction strength and directionality are relatively weaker than π - π interactions. One example, reported by Ghosh and Das, highlights how the subtle interplay between the nature and dynamics of non-covalent interactions could affect the supramolecular structures formed.²⁹¹ A naphthalene diimide monomer self-assembles by hydrogen bonding and π - π stacking into a reverse vesicle when below the critical solution temperature. Above this temperature the system collapses. Interestingly, above an upper critical solution temperature the system reassembles into a reverse micelle (Figure 69A). Moreover, upon the addition of the electron rich pyridine-functionalized pyrene, the electron deficient naphthalene diimide will establish charge-transfer interactions. As a result they assemble alternately into stacks and ultimately form reverse micelles with mixed-stack core (Figure 69B).

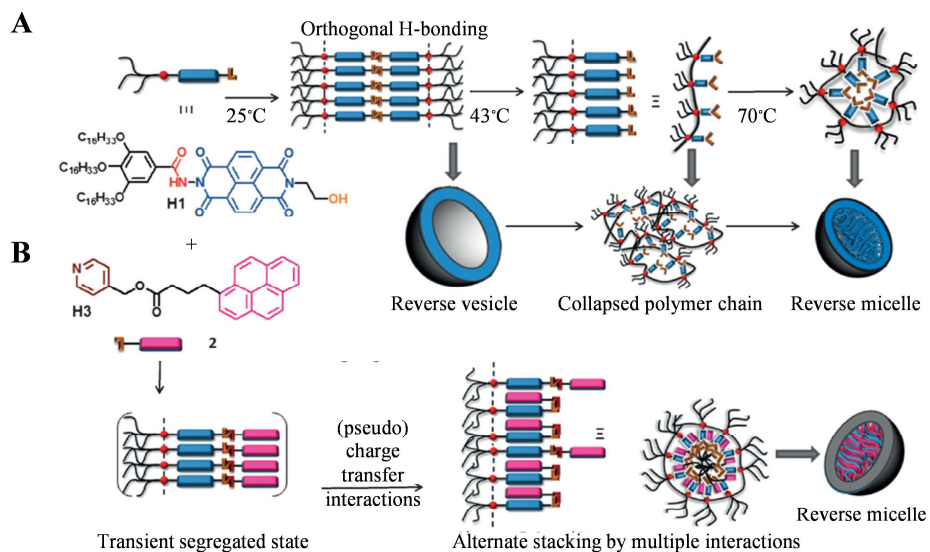


Figure 69. Schematic depiction of the self-assembly of naphthalene diimide by hydrogen bonding and π - π stacking into reverse vesicles ($T < 43^\circ\text{C}$) and reverse micelles ($T > 43^\circ\text{C}$) (A), as well as the self-assembly into reverse micelles by charge transfer interactions upon the addition of pyridine-functionalized pyrene (B). This Figure is adapted from reference 291.

vi. Hydrophobic interactions

Due to the low solubility of hydrophobic moieties in water they experience unusually strong attractive forces towards one another in aqueous media and self-assemble into various structures. The hydrophobic force is such that it can even take part in long-range interactions over 200 \AA .²⁹² It plays a pivotal role in many (biological) thermodynamic processes such as micelle formation, protein folding and self-sustainability of cellular membranes. Artificial self-assembled micelles and vesicles can be realized with varying (core) sizes and functionalities to adapt to the requirements needed in a wide range of applications. One example comes from the group of Yan who reported the self-assembly and disassembly of non-covalent supramolecular janus particles into unilamellar bilayer vesicles (Figure 70).²⁹³ The janus particles, or amphiphiles, form through host-guest interaction and self-assemble further into vesicles of narrow size distribution by the hydrophobic effect. Disassembly is achieved by irradiation with UV light.

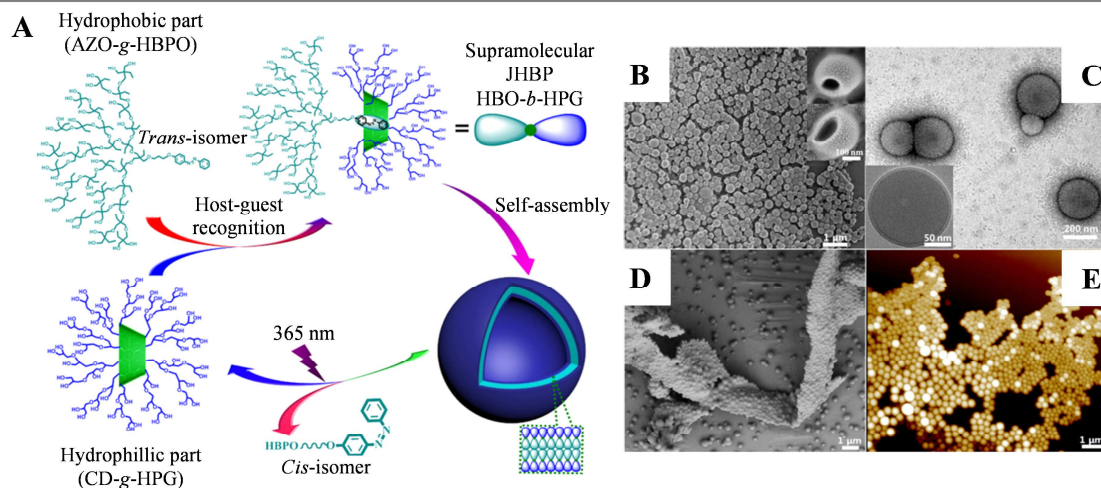


Figure 70. A) Schematic depiction of the self-assembly of supramolecular janus particles by host-guest interactions and the subsequent self-assembly into vesicles by the hydrophobic effect; B-E) SEM (B, D), freeze-dried TEM (C) and AFM (E) images of the self-assembled vesicles. This Figure is adapted from reference 293.

The groups of Meijer and van Esch have taken advantage of the hydrophobic effect to construct supramolecular polymers with controlled growth, chirality and shape. Meijer and co-workers studied the self-assembly process of the discotic molecule, bipyridine-extended 1,3,5-benzenetricarboxamide (**Figure 71A**).²⁹⁴ Depending on the solubility of the side-chains in the solvent used, it is able to form one-dimensional polymers. Self-assembly takes place by the hydrophobic effect and aromatic interactions. Although hydrogen bonding groups are present in the molecule, they do not have a cooperative effect on the mechanism, because they all form intramolecular hydrogen bonds. Multiple aggregated states (co-)exist, which is the result of different self-assembly processes taking place in function of concentration and temperature (**Figure 71B**). As the orientation of the molecule inside a self-assembly is critical for the functional properties, it is key to understand and control the (competing) self-assembly processes. In this article, the authors present a general method to elucidate if multiple mechanisms concur and which one dominates under the circumstances used.

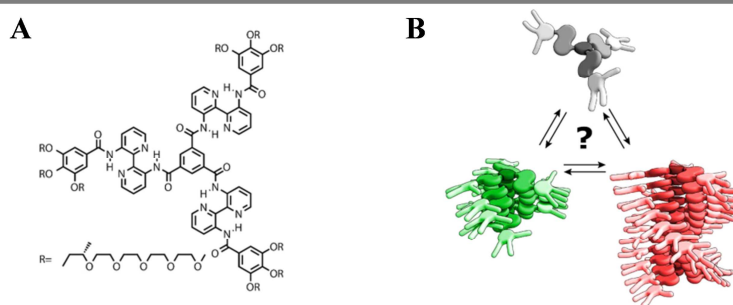


Figure 71. A) Molecular structure of bipyridine-extended 1,3,5-benzenetricarboxamide; B) schematic representation of the monomer and the two aggregated states possible. This Figure is adapted from reference 294.

Van Esch constructed a multi-segment amphiphile from a gelator and a micelle forming surfactant.²⁹⁵ Individually, they form columnar stacks and micelles by orthogonal self-assembly (Figure 72A). The multi-segment amphiphile (hydrophobic and hydrophilic parts are colored dark and light blue respectively) self-assembles into fibrils at low concentrations and into fibers and tapes at increased concentrations (Figure 72BD). The aggregation process is governed by the cooperative effect between three-fold hydrogen bonding of the amide groups, π - π interactions between phenyl rings and hydrophobic interactions between alkyl chains.

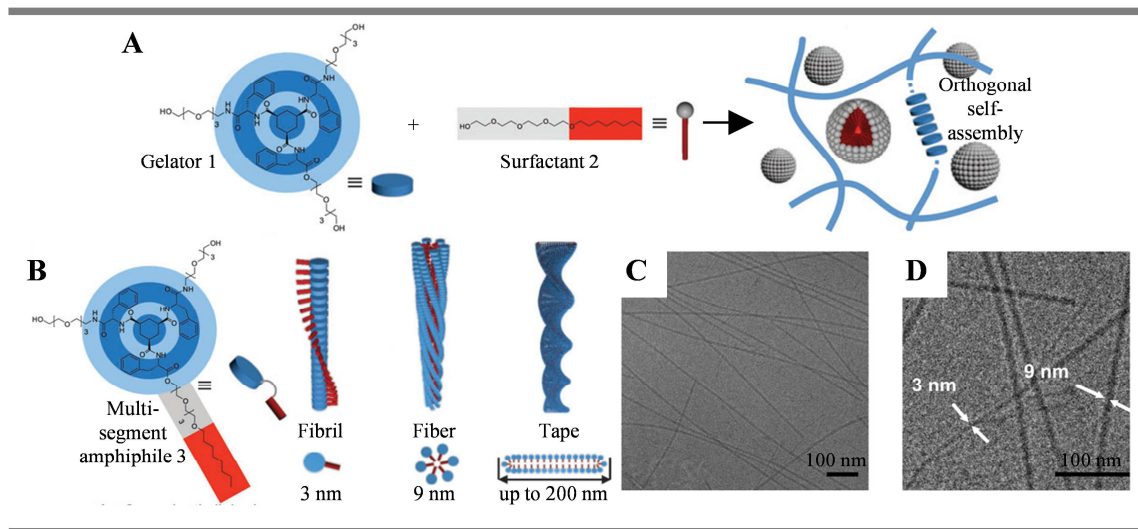


Figure 72. A) schematic depiction of the orthogonal self-assembly of the individual monomers into columnar stacks and micelles; B) schematic depiction of the self-assembly of the multi-segment amphiphile into fibrils, fibers and tapes depending on the concentration; C-D) cryo-TEM images of a fibrous networks at 0.25 mM. This Figure is adapted from reference 295.

vii. Host-guest interactions

The interactions present in supramolecular host-guest polymers are a combination of all before mentioned forces (hydrogen bonding, coordination and electrostatic interactions, van der Waals forces and hydrophobic interactions) working together in a cooperative manner. Some common host molecules (denoted as A) are cyclodextrines, crown ethers, cucurbit[8]urils and pillar[n]arenes. Guest molecules (denoted as B) are general organic molecules of the right size and shape to fit inside the cavity of the host (Figure 73A). The types of monomers they can form, together with the corresponding supramolecular polymer are schematically depicted in Figure 73B.

A			B		
Host	Molecular structure	Guest	Type	Monomer	Supramolecular polymer
β -cyclodextrin		Adamantane Coumarin	AB		
Cucurbit[8]uril		Methyl viologen Charged naphthalene Anthracene Alkane	AA/BB		
Calixarene		Charged alkane Viologen	Host/BB		
Crown ether		Viologen Charged amine	Host/AB		
Pillararene		Charged imidazole Charged DABCO	BA		

Figure 73. A) Table summarizing common host guest molecules; B) Table summarizing different types of host-guest monomers and their resulting supramolecular polymer structures. This Figure is adapted from reference 296.

Cucurbinitrils rarely form supramolecular polymers, but rather dimers and oligomers, due to their low solubility in aqueous media. Calixarenes, on the other hand, are easier to functionalize and solubility can thus be improved. One of the first examples of Calixarene-based supramolecular polymers was reported by Guo *et al.* in 2012.²⁹⁶ Most commonly, however, is the use of crown ethers and pillararenes for the construction of supramolecular polymers. Early work in this field was done by Stoddart *et al.*, who created a supramolecular polymer from a crown ether host and dibenzylammonium salt guest (Figure 74).²⁹⁷

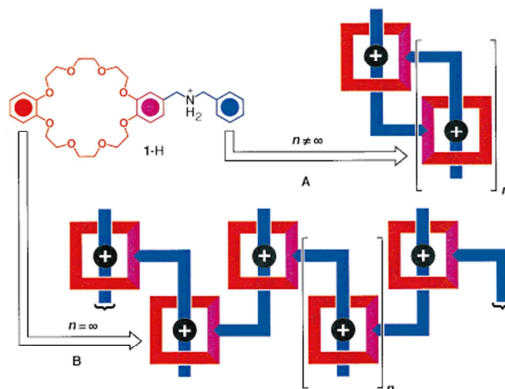


Figure 74. Schematic representation of (A) oligomeric daisy-chain-like self-assembly into macrocycles and (B) the supramolecular polymerization in a linear array that is comparable to a macromolecular daisy chain, from a crown ether host. This Figure is adapted from reference 297.

C. Supramolecular electronics

Supramolecular electronics is an interdisciplinary field, which has emerged from the marriage of supramolecular chemistry and organic electronics.^{298,299} It uses organic supramolecular semi-conductors instead of more conventional metal conductors or inorganic and organic semi-conductors.

The use of organic materials is advantageous because they are often less toxic and more abundant, thus cheaper. In organic electronics they are used as polymers and small molecules. However, although polymers are facile to synthesize, add flexibility and have easy processability, the precise ordering of their crystalline layers in the bulk is limited, which negatively affects the charge carrier mobility.³⁰⁰ Low-molecular-weight π -conjugated organic molecules, on the other hand, lead to significantly enhanced crystalline orientations but can be difficult to process (especially single crystals)³⁰¹ and achieving good electrode contact can be problematic. Furthermore, down-scaling into sub-micrometric devices is difficult.

The fact that supramolecular organic semi-conductors are formed by self-assembly processes under thermodynamic control leads to more advantages. First, it is an intermediary-scale approach and the active components can be integrated into miniaturized electronic devices.^{302,299} This is possible by taking advantage of bottom-up self-assembly strategies, to create moldable organic electronic components, with “pseudo-crystalline” electroactive domains. The length scales of the components are in the range of 5 – 100 nm, comprised between plastic electronics (μm) and molecular electronics (\AA) (Figure 75). Secondly, supramolecular self-assembly processes show high reproducibility due to the intrinsic reversibility non-covalent bond, leading to intrinsic error-correction. Furthermore, these strategies are convenient because, to self-assemble, the components just have to be mixed in suitable solutions, at the right concentrations and temperature. Besides, they retain the advantage of normal

organic semi-conductors, such as cost, toxicity and flexibility. For these reasons, the field of supramolecular electronics is a fast growing and competitive field of research and development.

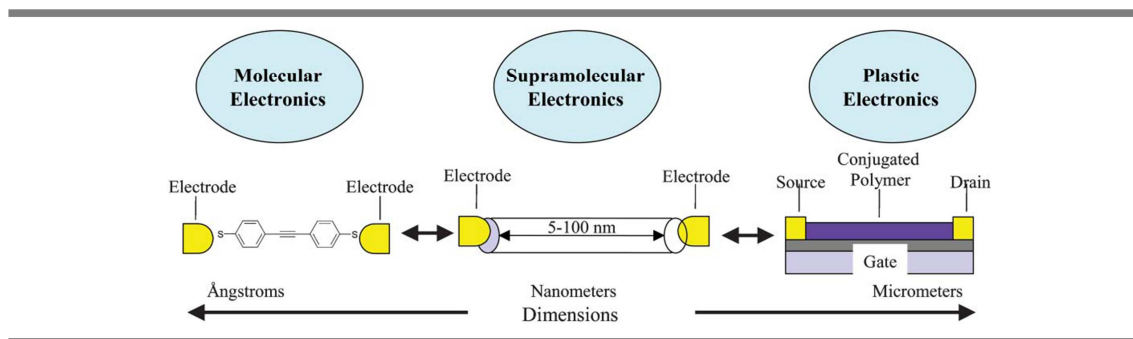


Figure 75. Illustration of the length scales between molecular, supramolecular and plastic electronics. In supramolecular electronics the construction of supramolecular optoelectronic nano architectures, connected to electrodes, is studied. This Figure is adapted from reference 298

As mentioned in the previous section supramolecular polymers comprising π - π interactions are advantageous because they are capable of efficient charge transport. Moreover, because these interactions are stronger than the hydrophobic forces present, the self-assembly is highly anisotropic. Furthermore, by functionalizing the phenyl rings with different functionalities the softness, solubility and processability of the assembly can be improved. This type of supramolecular polymers can be classified into three categories: *i*) aromatic molecules; *ii*) sulfur based heterocycles; *iii*) light triggered self-assemblies of triarylamine.³⁰³ The electronic conductivity properties of the first two categories will be discussed in *Chapter IV 2C. Charge transport in various organic supramolecular materials*. The conductivity properties of supramolecular triarylamine polymers will be discussed in more detail in *Chapter I 4*

D. Physical properties of triarylamine self-assemblies.

I.4 Physical Properties and Applications of Self-Assembled Triarylamine Structures

After having elaborated on the chemistry of triarylamine derivatives, we will now discuss its supramolecular chemistry. The literature is divided in 3 sub-sections. First, different types of self-assemblies incorporating TAA derivatives into their structure will be discussed. A large emphasis will be placed on the oxidation-triggered self-assembly of supramolecular polymers, which was first demonstrated in our research group. Here, the mechanisms behind supramolecular polymerization will be detailed. Then, the diversity of self-assembled structures, that use this specific type of supramolecular recognition, is outlined. In the second section, the emergent physical properties of such supramolecular polymers are investigated. We will conclude this chapter with a discussion on the applications in which self-assembled TAA derivatives can be found.

A. Triarylaminines in MOF and COF

Organo (metallic) polyhedrons and metal-organic-frameworks (MOF) represent the first class of self-assemblies to have incorporated TAA derivatives into their structure. Metal-organic-frameworks (MOF) are defined as crystalline coordination complexes made of multi-dentate organic linker molecules that come together at metal cation nodes. They form cage-like structures that repeat themselves into a crystal lattice. They are open frameworks of high porosity and find applications in gas storage, purification, separation, catalysis and sensing. It was Field *et al.* who, in 2002, first reported on a purely organic tetrahedral structure made of a TAA derivative through hydrogen bonding (**Figure 76A**).¹¹ In the following years more tetrahedral structures incorporating both TAA and metal cations were reported.^{304,305} The first TAA-based MOF dates from 2012 and was reported by the group of Lu.¹² The MOF is constructed from TAA with carboxylic acid end groups that form coordination complexes with either zinc or copper (**Figure 76B**). The authors demonstrated its catalytic nature in Fiedel-Crafts alkylation reactions and postulate it is equally promising for CO₂ storage and as luminescent material. Since then numerous examples of TAA-based MOFs can be found. Studies include MOF construction and optimization of its porosity and interpenetration.^{306,307} Others focus on the functional properties such as (photo)catalytic synthesis,^{308–310} sensing,^{311–313} redox activity,^{314–316} luminescence³⁰⁶ and sorption.^{317–320} The examples given only represent a selection of articles that can be found on these topics.

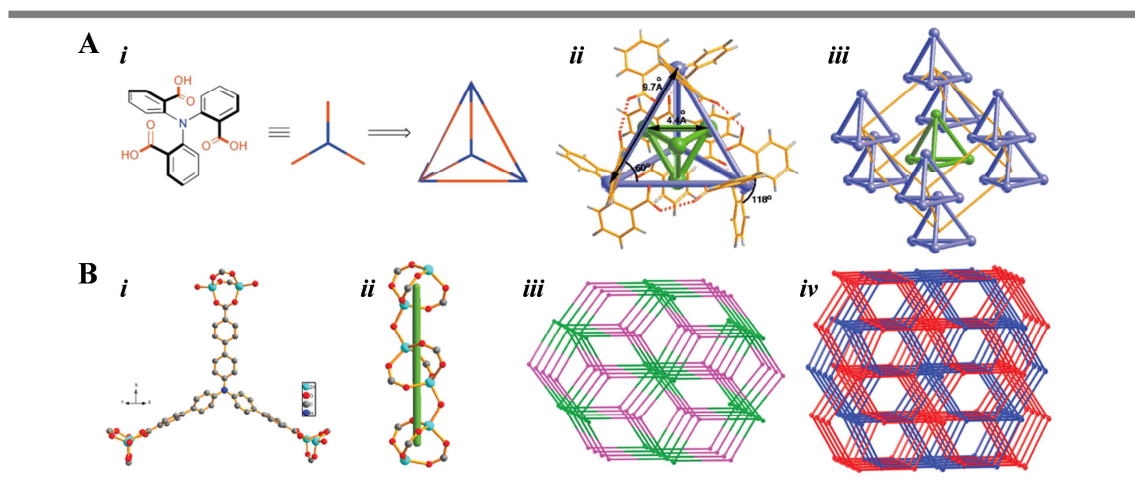


Figure 76. A) The molecular structure and its schematic representation as a tetrahedral synthon (*i*); the supramolecular structure of one synthon (*ii*) and its bcc-like self-assembly (*iii*) into the first fully organic TAA-based polyhedron (a tetrahedral structure in this case). The self-assembled structure is realized via hydrogen bonding¹¹; B) the molecular structure and presentation of coordination modes of zinc and TAA-ligand (*i*); the chain structure formed by non-covalent interactions between hydroxy groups and zinc (*ii*); the resulting three dimensional network (*iii*); the two-fold interpenetrating three dimensional network (*iv*).¹² This Figure is adapted from references 11 and 12

B. Self-assembled triarylamine monolayers

Self-assembled monolayers (SAMs) are organic monolayers that form spontaneously on surfaces by non-covalent interactions such as metal-organic coordination, adsorption, hydrogen bonding *etc.*. They are able to form organized assemblies that often bear functional groups to enhance reactivity or promote charge transfer from the surface towards additional layers. Moreover, they can enhance the performance of organic electronic devices by coupling to the electrodes and overcoming discontinuity of material surfaces. They represent the second class of self-assembled structures to have TAA-derivatives incorporated into their structure. SAMs incorporating TAA derivatives have been reported in studies on SAMs stability and surface interaction^{321,322}, electron transport^{323,324}, intermolecular charge transfer³²⁵, molecular triads³²⁶, as well as for the enhancement of OLED^{13,327–332} and solar cell devices.^{333,334}

One of the first examples dates from 2002 from the research group of Marks.¹³ They addressed the problem of decohesion that arises between indium tin oxide (ITO) surfaces and TAA after moderate heating. The authors introduced the TAA derivative TDP as a self-assembled monolayer by spin-coating or through covalent bonds (Figure 77). X-ray diffraction and modeling indicates that the molecular planes in the self-assembly are predominantly tilted by 30° with respect to the substrate. Not only did they thereby increase the adhesion force, they equally significantly enhanced the hole-injection capacities, luminescence properties, quantum efficiencies and reduced turn-on voltages of OLED devices.

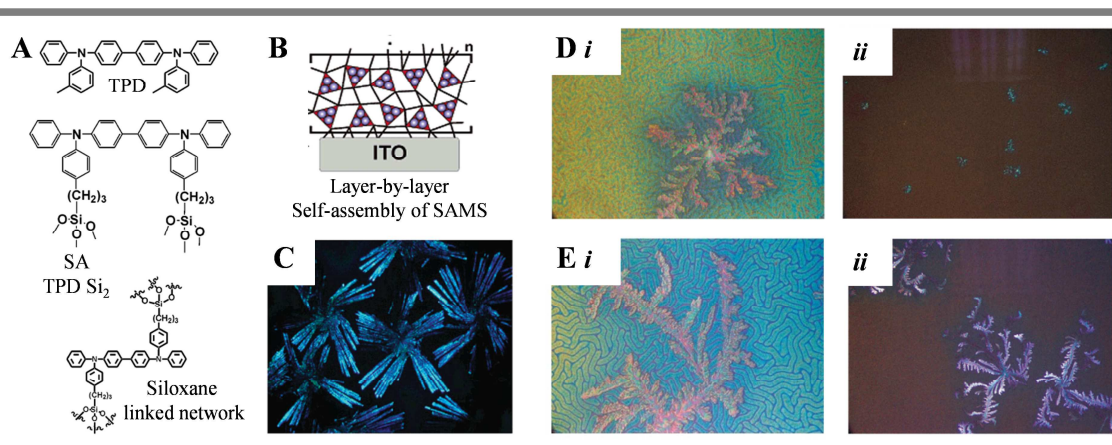


Figure 77. A) Molecular structure of the TPD molecule, its self-assembled structure on silica and covalently linked in a siloxane network; B) schematic representation of the SAM on an ITO surface by layer-by-layer self-assembly and siloxane condensation; C) image of a 500 Å TPD SAM between a 100 Å ITO/CuPc surface and a 500 Å hole transporting layer, obtained by polarized optical microscopy after annealing at 80 °C; D) image of a 1000 Å TPD SAM between a 100 Å ITO/CuPc surface and a 500 Å Alq layer, obtained by polarized optical microscopy (1500 and 50x magnification for (i) and (ii)) after 30 minutes of annealing at 90 °C and E) at 110 °C. This Figure is adapted from reference 13

C. Supramolecular triarylamine polymers

It was in 2010 that our research group discovered that triarylamines with at least one amide function could form supramolecular polymers (Figure 78).¹⁴ The presence of an amide function on the TAA periphery later turned out a general criterion for triarylamine self-assembly. The supramolecular polymerization of triarylamines opens up the opportunity to combine its physical properties, such as photosensitivity, electrochemistry, photoconductivity and charge transport, with controlled supramolecular architectures to obtain responsive and functional materials that could be used to enhance its performance in applications. First, however, the mechanism behind its supramolecular polymerization, the range of self-assembled structures and physical characteristics were investigated.

The first observation made was that polymerization is triggered by photo-oxidation. When a TAA solution was irradiated for some minutes by visible light in chlorinated solvents (which functions as electron acceptor), it would turn green, which is an optical indication of TAA oxidation. A combination of magnetic resonance and photo-spectroscopic techniques showed the first indications of supramolecular self-assembly.¹⁴ In the ¹H NMR spectrum the signals corresponding to the aromatic protons, the aliphatic center and the acetamide protons disappeared (Figure 78B). This indicates both the presence of TAA⁺ and the formation of supramolecular structures. The absorption spectrum revealed: i) decrease in intensity of the 300-350 nm band, characteristic for neutral TAA; ii) the rise of new absorption bands around 400 nm, 650 nm and 800 nm, which are characteristic for TAA⁺ radicals in self-assemblies (Figure 78C). EPR measurements exhibited a three line pattern, typical for radicals residing on a nitrogen atom, and the formation of 11% of TAA⁺ compared to the total

number of molecules (Figure 78D). Additional DLS measurements displayed changes in the autocorrelation curve during light irradiation, indicating the formation of aggregates. Interestingly, these observations remained present for long periods of time when kept in the dark (at least one week). Only the EPR signal decreased over the course of 16 hours to 6 radicals per 1000 molecules. These results indicate a radical-stabilization mechanism. Furthermore, the total disappearance of ^1H NMR signal is the result of self-assembly rather than the presence of a few $\text{TAA}^{+\bullet}$. Finally, the final proof of self-assembly into supramolecular polymers was obtained by AFM imaging, which unveiled the presence of fibrillary structures with well-defined ordering (Figure 78E).

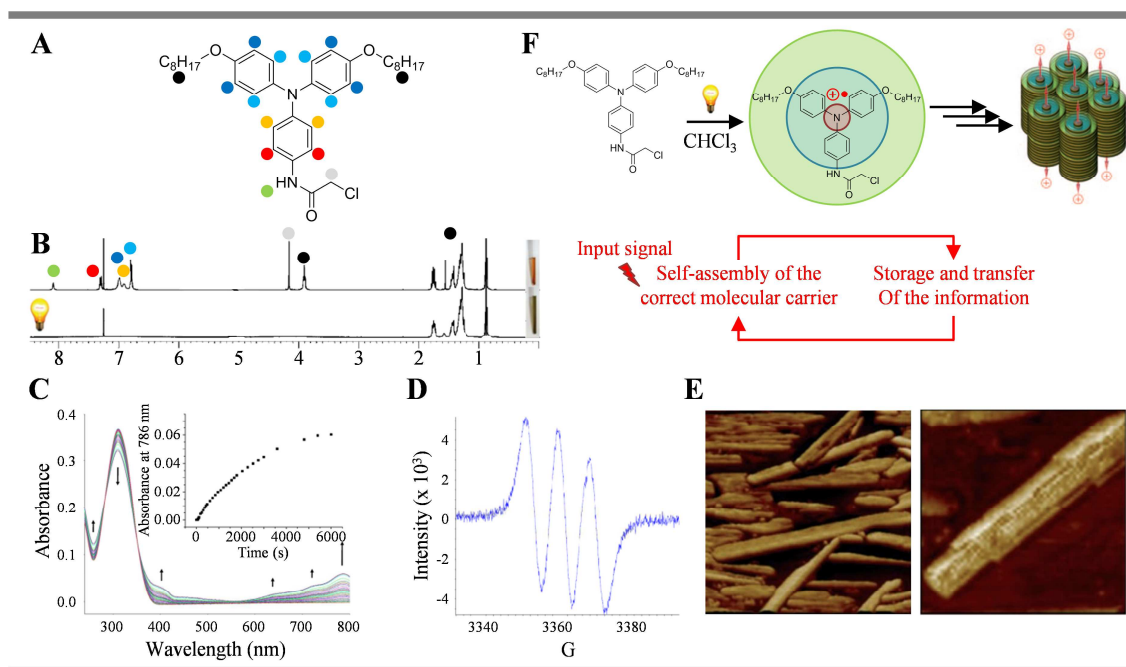


Figure 78. A) Molecular structure of the TAA derivative, substituted with one amide function, that was studied in the first article describing TAA supramolecular polymerization; B) ^1H NMR spectra before (upper spectrum) and after (lower spectrum) 10 minutes of light irradiation of a 10 mM solution in CHCl_3 ; C) absorption spectra measured during light-irradiation of a 0.1 mM solution in CHCl_3 ; D) EPR spectrum of a 10 mM solution in CHCl_3 after 10 minutes of light irradiation; E) AFM images of TAA supramolecular polymers obtained in CHCl_3 after light irradiation and evaporation of the solvent. On the left is the phase image of an ensemble of polymers. On the right, a high resolution height image of a single self-assembled polymer; F) schematic representation of the hierarchical self-assembly process that takes place after photo-oxidation of neutral TAA monomers. This Figure is adapted from reference 14

i. Mechanism of oxidation induced supramolecular polymerization

Triarylamine monoamides

After this first example of supramolecular polymerization of triarylamine monoamides (TAA), extensive experimental and theoretical studies on the mechanism were conducted.¹⁵ The first finding made was that the polymerization is autocatalytic, as derived from the sigmoidal shape of the self-

assembly curve (Figure 79). Furthermore, the self-assembly can be triggered, not only by photo-oxidation, but by chemical oxidants (TBQ) or seeding (fibrilized TAA) as well.

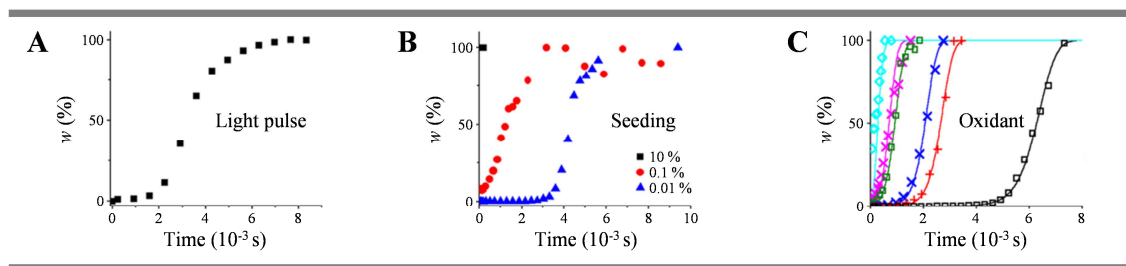


Figure 79. Fraction of supramolecular self-assembled TAA polymers after A) irradiation of a 10 mM TAA solution by a 1s light pulse; B) seeding of 1 mM non-irradiated solution with irradiated molecules; C) chemical oxidation of a 10 mM TAA solution by 1, 0.5, 0.1, 0.01% TBQ. Data points are obtained by time-resolved NMR. This Figure is adapted from reference 15

Kinetic EPR, NMR and UV-vis-NIR photospectroscopy, as well as all atomic calculations were employed to gain insight in the mechanism of aggregation (Figure 80A-B). First a geometrical change in the molecular structure of TAA occurs. Neutral TAAs show a pyramidal conformation due to the out-of-plane rotation of the aromatic rings. Upon oxidation charge delocalization in the rings forces the structure to flatten (“propeller-like” shape) (Figure 80Ai). This facilitates stacking of the monomers. Thus, assembly of TAA is directly correlated to the formation of TAA^{*+} . TAA^{*+} , together with the Cl^- or TBQ^- counter-ions present, form stable charge-transfer (CT) complexes (Figure 80Aii). Because the attraction energy for dimer stabilization is high, other dimers will stack to it right away (if $[\text{TAA}^{*+}] > 10^{-7}$) (Figure 80iii). This causes the formation of ‘loose’ chains, which are strings of dipoles made of alternating TAA^{*+} and counter-ions (Figure 80Aiv). Chains exceeding the length of a trimer are able to rearrange from the ‘loose’ chain into the energetically more favorable ‘tight’ chain that benefits from optimal van der Waals forces and correct π - π stacking (Figure 80Av). The tight chains then aggregate into double columnar “snow-flake” arrangements, involving intercolumnar hydrogen bonding and side-to-side van der Waals forces, as the energy level of such structures lies $\sim 15 k_{\text{B}}T$ lower. A minimum of three dimers is required however, in order to form stable double columnar arrangements (Figure 80Avi). At this point neutral TAA can stack unto the ends of these nuclei for further end-growth of fibers by aromatic stacking and hydrogen bonding (Figure 80Avii). Hereby, the neutral TAA will equally adopt a “propeller-like” shape. The final fiber is expected to contain one TAA^{*+} for every 160 neutral TAA molecules. Thus, in theory, in a supramolecular defect-free polymer the radical is delocalized over ~ 80 nm.

During elongation fibers grow from both ends. However above a certain length scission will take place. This also means that as fibers break, new ends are created and more TAA can be assembled. Hence the sigmoidal shape of the self-assembly curve. Moreover, both scission rate and end-growth rate are independent of irradiation time, oxidant concentration or number of seeds.

Molecular dynamic simulations were used to clarify the structure of the supramolecular polymers and they confirm the snow-flake double columnar packing. These findings were experimentally verified by AFM and powder X-ray diffraction (Figure 80C-D).

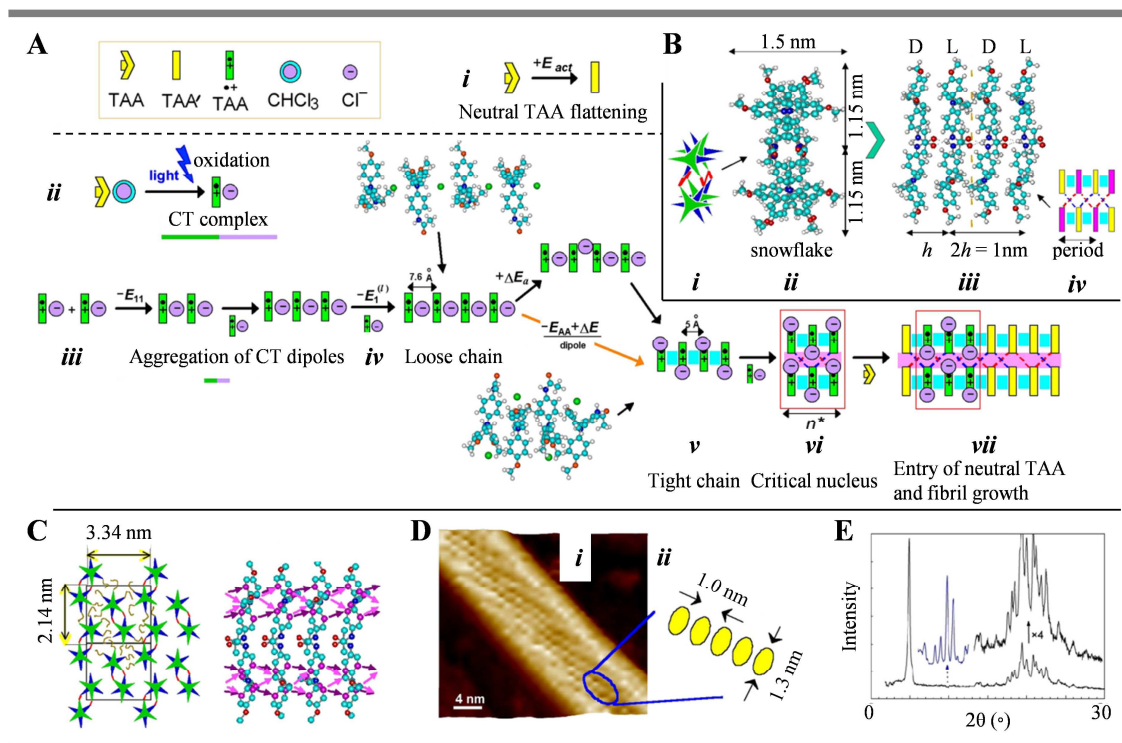


Figure 80. A) Schematic presentation of the mechanism of light-induced supramolecular polymerization of triarylamine monoamides (TAA). (i) The spontaneous flattening of TAA is very unlikely to occur. (ii) After photo-oxidation TAAs are transformed into flattened TAA⁺⁺ that are complexed with counter ions. (iii) Two TAA⁺⁺-Cl⁻ charge transfer complexes dimerize in a head-to-tail fashion and, subsequently, a growing stack of TAA⁺⁺s is formed in a (iv) loose chain configuration. (v) This chain rearranges in a tight chain whereby the Cl⁻ ions are moved sideways and non-covalent interactions are optimized. (vi) further stabilization takes place by the formation of a double columnar arrangement via hydrogen bonding. (vii) the supramolecular polymer grows by the stacking of TAA onto its ends. B) Schematic presentation of the double columnar snow-flake self-assembly showing (i) the alternating orientation of TAA molecules in the columns. Top (ii) and side (iii) view of the self-assembly. (iv) illustration of a double TAA chain that shows the hydrogen bonds that connects the columns. C) Supramolecular self-assembled structure obtained by X-ray diffraction (left) and all-atomic simulations (right). D) AFM height image (i) of a supramolecular polymer obtained in a 1 mM CHCl₃ TAA solution after 60 minutes of light irradiation. Next to it the dimensions of the maize-like structures formed (ii) are given. E) X-ray diffraction pattern from a 10 mM TAA sample (bottom) and a magnification in the WAXS region (upper spectrum). This Figure is adapted from reference 15

Triarylamine trisamides

After having elucidated the workings behind TAA self-assembly and finding that the presence of an amide function is crucial, the next logical step was to probe the possibility of triarylamine trisamide (TATA) self-assembly (Figure 81A).¹⁶

Similar to TAA, TATAs readily self-assemble in chlorinated solutions under photo-oxidation. ¹H NMR spectra of monomeric solutions could be obtained in a mixture of methanol and toluene (Figure 81B). Upon addition of 5 vol% of chloroform and light irradiation the signals of the aromatic protons, as well as the signals of the neighbouring methylene protons on the alkyl chains, disappeared. This indicates successful supramolecular self-assembly. However, and in sharp contrast to TAA, they equally aggregate in multiple organic solvents (e.g. acetonitrile, toluene) without the need of any oxidation process (seen by ¹H NMR). Above a critical concentration, which decreases with longer alkyl chains, they are even able to form organo gels. This can be explained by strong three-fold hydrogen bonding (confirmed by IR).

Using AFM, freeze fracture TEM, SAXS, WAXS and DFT calculations the structure of the fibers could be determined (Figure 81C).¹⁶ TATA form soft, well-defined fibers with high persistence lengths and overall lengths that surpass 10 μm . Contrary to TAA, the monomers arrange in a single column of smectic packing. This helical arrangement is called ‘mercedes-benz’. The periodicity of the helical pitch is 30 \AA and corresponds to 7 molecules. The distance between adjacent nitrogen centers is 4.85 \AA and the distance between aromatic rings involved in π - π stacking is 3.1 - 3.2 \AA . Single fibers have a diameter of 16 \AA (measured for TATA-C12).

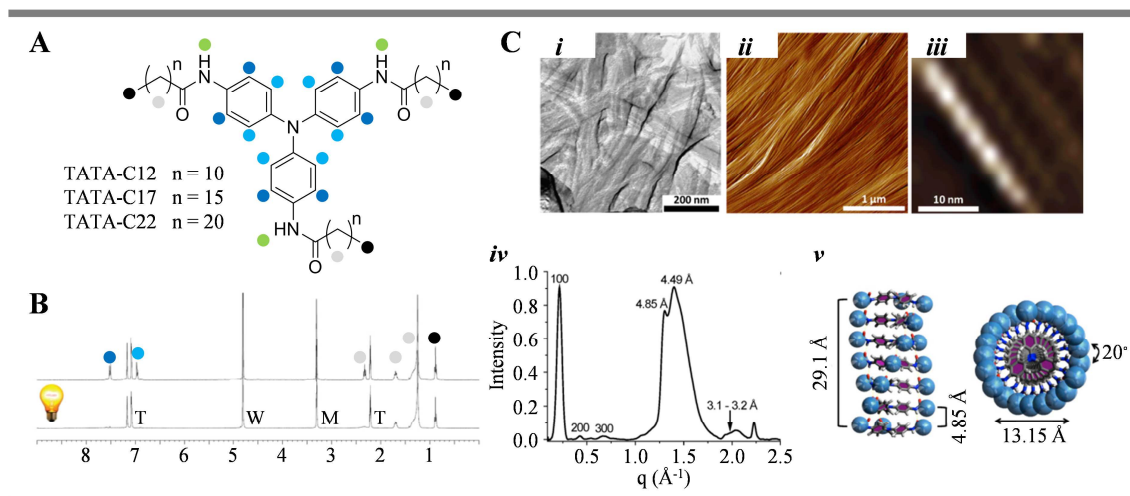


Figure 81. A) Molecular structure of TATAs studied¹⁶; B) ¹H NMR spectra before (upper spectrum) and after (lower spectrum) light irradiation of a TATA-C12 methanol-*d*₄:toluene-*d*₈ solution containing 5 vol% of CHCl₃ (T = toluene, W = water, M = methanol); C) Freeze-fracture TEM (i) and AFM (ii-iii) images of TATA-C12 fibers, obtained from drop casted CHCl₃ solutions. (iv) X-ray diffraction spectrum of TATA-C12 fibers drop casted from a CHCl₃ solution on mica. (v) Side (left)

and top (right) view of the proposed supramolecular self-assembly in a helical mono columnar arrangement, as derived from DFT calculations. This Figure is adapted from reference 16

These fibers displayed some novel characteristics not yet observed in other TAA self-assemblies.¹⁶ First of all, photo-oxidation of supramolecular polymers leads to a novel absorption band at 1100 nm at short irradiation times (Figure 82A). This is ascribed to intermolecular through-space charge-transfer between TATA cores. In early stages of irradiation primarily this new absorption increases in intensity due to the formation of delocalized TATA radical cations, which is also attested by the increasing asymmetry of the band. Then, as the number of radicals increases, delocalization decreases and the absorption band at 800 nm, characteristic for localized TATA radical cations, rises in intensity. EPR shows similar results (Figure 82B). At short irradiation times a five line hyperfine splitting pattern suggests partially delocalized radical cations between two TATA monomers. This transforms into a one line pattern, corresponding to fully delocalized radical cations. Finally, a three line pattern emerges, corresponding to localized radical cations. Moreover, the radicals proved extremely stable over time (> six months), probably because the three alkyl chains act as insulating shell that protect the $TATA^{++}$ core. A combination of additional experiments evidence the presence of a half-filled polaronic conduction band positioned above the valence band. Interestingly, the same could be observed for solutions irradiated for only 3 minutes and then kept in the dark. This indicates an intrinsic structural evolution in time. AFM imaging and SAXS measurements of thin films and gels confirmed this hypothesis (Figure 82C-D), revealing a significant decrease in structural defects and a narrowing of the coherence length for irradiated samples. Thereby demonstrating the self-healing capacity of TATA fibers upon photo-oxidation.

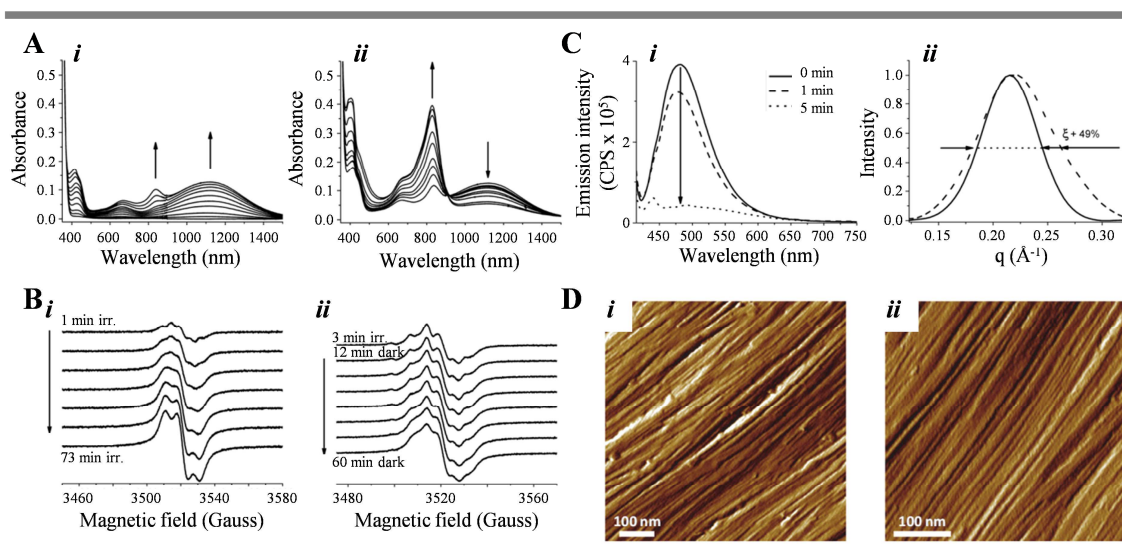


Figure 82. A) Absorption spectra taken in function of light-irradiation ((i) first six minutes; (ii) 7-73 minutes) of 0.1 mM TATA-C12 solution in $CHCl_3$; B) EPR spectra taken in function of light irradiation (i) and put subsequently in the dark (ii) of a 1 mM TATA-C12 solution in $CHCl_3$; C) fluorescence spectra of TATA-C12 (I) taken in function of light-irradiation showing the quenching of emission due to the formation of polarons. SAXS spectra (ii) of non-irradiated (dotted line) and irradiated (solid

line) TATA-C12 thin films, demonstration the increase of coherence length; D) AFM images of TATA-C12 thin films obtained by drop casting a CHCl_3 solution before (i) and after (ii) 15 minutes of light irradiation, demonstrating the decrease in structural defects. This Figure is adapted from reference 16

ii. Diversity in monomeric structures and self-assemblies thereof

The last 2 sections highlighted the assembly of ‘simple’ TAAs and TATAs into soft fibers and gels. However, a large variety of mono- and trisamides were synthesized, both in our group and other research groups, to investigate their physical properties, possible applications and the range of different self-assemblies possible.

The diversity in self-assembled structures that can be obtained depend both the enantiomeric form of the TAA core motif and on the functionalization of its periphery. As detailed in *Chapter I 1A. Molecular structure of triarylamines*, the core exists as two conformational enantiomers that can be seen as chiral propellers. During the supramolecular polymerization process this leads to chiral fibers. In TAA supramolecular polymers, the cores alternate handedness in a snowflake arrangement.²⁹¹ In TATA supramolecular polymers cores of the same handedness stack in a Mercedes-Benz arrangement with M or P helicity.²⁹² Another structural parameter affecting the supramolecular self-assembly behavior is the number of amide substituents, which dictates whether hydrogen bonding takes place primarily between columns (TAA fibers in snowflake arrangement) or along a single column (TATA fibers in Mercedes-Benz arrangement). Finally, other functional groups placed on the periphery can also affect the structures formed.

For example, a series of TAA conjugates with multiple large and/or bulky functionalities were synthesized, demonstrating that TAA is able to retain its self-assembly properties even when more steric hindrance is present (Figure 83).^{18,19} In addition, not only supramolecular polymers can be obtained. TAA-terpyridine conjugates complexed with Zn^{2+} ions assemble into spheres of monodisperse size (160 nm) in chloroform after light irradiation (Figure 83A-B).¹⁸ TAA-fullerene conjugates exhibit even more remarkable self-assembly behavior (Figure 83C-D).¹⁹ The intensity of light in the UV range has a direct effect on the structures formed. Long fibers are formed at low intensities and short rods that aggregate into spheres of micrometric diameter at higher intensities. This is in agreement with the formerly proposed nucleation-growth mechanism.¹⁴ Higher intensities of UV light generate more nuclei and as a consequence shorter structures in larger amounts will form.

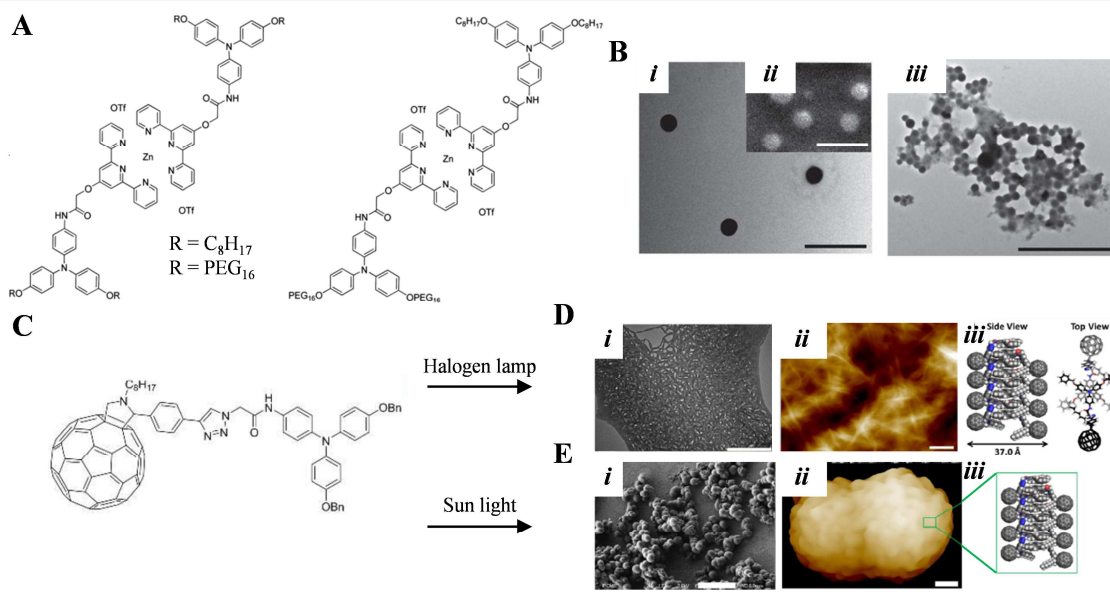


Figure 83. A) Molecular structures of homoleptic (left) and heteroleptic (right) TAA-terpyridine zinc coordination complexes; B) TEM (i and iii) and SEM (ii) images of homoleptic TAA-terpyridine ($R = C_8H_{17}$) zinc coordination complexes self-assembled in a 0.1 mM $CHCl_3$ solution upon light irradiation. Scale bars are 600 nm, 500 nm and 2 μm for image (i), (ii) and (iii) respectively; C) molecular structure of TAA-fullerene donor-acceptor conjugate; D) TEM (i) and AFM (ii) images of TAA-fullerene self-assemblies drop casted from a 0.1 mM TAA solution in $CHCl_3$ irradiated with low intensity light. The scale bars correspond to 1 μm (i) and 2 μm (ii). The corresponding supramolecular self-assembly, into long-fibers, obtained by molecular modeling (iii); E) SEM (i) and AFM (ii) images of TAA-fullerene self-assemblies drop casted from a 0.1 mM solution in $CHCl_3$ irradiated with high intensity light. The scale bars correspond to 10 μm (i) and 10 μm (ii). The corresponding supramolecular self-assembly, into short rods that aggregate into spheres, obtained by molecular modeling (iii). This Figure is adapted from references 18 and 19

TAAAs have equally been synthesized into daisy-chains.^{335–337} This provides the combination of self-assembly into supramolecular fibers with molecular switches using various stimuli, which enlarges the scope of molecular machines.

Another point of interest is the chirality, or the amplification thereof, of supramolecular polymers. Indeed, TAA and TATA fibers have a helicity due to their particular propeller like-shape, which can be used for this purpose.^{338,339} This was demonstrated, for instance, by the group of Kim.³³⁸ They synthesized TATA molecules functionalized with diactelylene moieties. The CD spectra showed that their supramolecular polymers preferentially form with a single handedness when irradiated with circularly polarized light. They could then lock the supramolecular chirality by photo-polymerization of the diactelylene unites, without losing its electrical conductivity properties. Another example comes from the group of Aida and Miyajima, who successfully amplified the chirality of supramolecular polymers made of gallate functionalized TAAAs.³³⁹ Making use of a sergeant and soldier system they could fully control the handedness of the fibers. As the ratio is 1:500, this represents a remarkable amplification of chirality.

In our own research group TAA-gallate was synthesized to study the mesomorphic properties of the assemblies in solution and as thin films (**Figure 84**).²⁰ All derivatives were capable of self-assembly upon photo-oxidation in chlorinated solutions and their aggregates demonstrated aggregation-induced emission. Nanosheets were obtained when gallate was functionalized to the amide, whereas bundles of fibers were observed when functionalized to phenolic moieties. Once again, it becomes evident that the molecular design of TAAs greatly affects the packing and, by consequence, the self-assembled structure. These derivatives also demonstrated phase transition behavior between (plastic and liquid) crystalline (meso-) phases (**Figure 84B**).

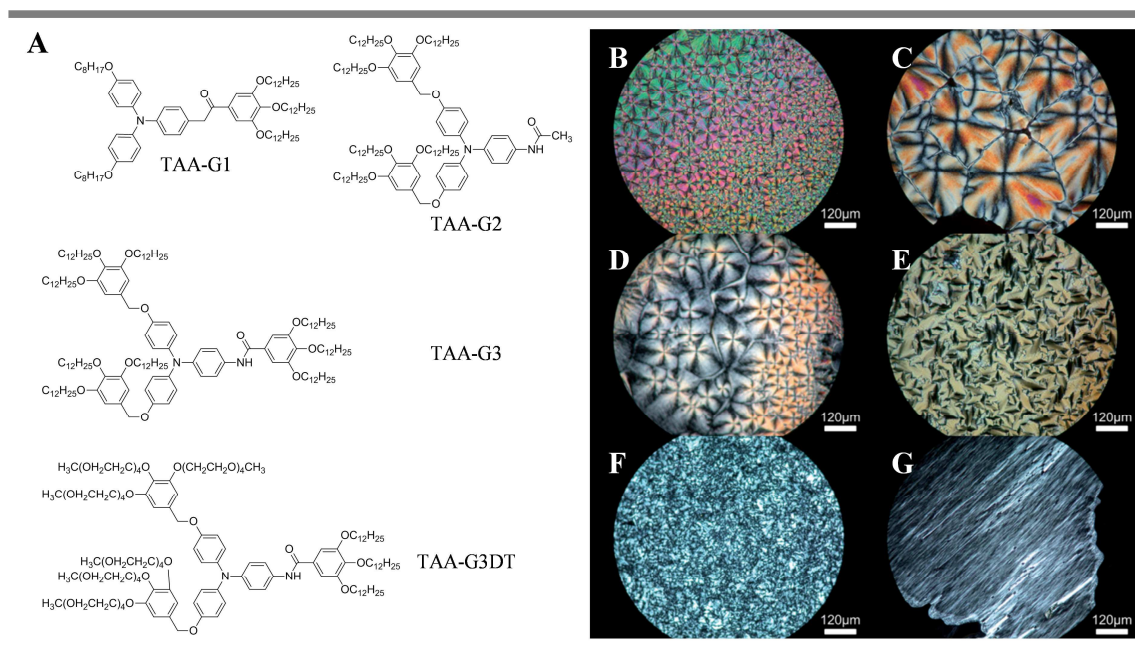


Figure 84. A) Molecular structures of TAA-gallate derivative studied; B-G) cross-polarized microscopy images of thin films drop casted from light-irradiated solutions of TAA-G1 at room temperature after annealing (B); of TAA-G2 at 65 °C (C); of TAA-G3 at room temperature before (D) and after (E) annealing; of TAA-G3DT at room temperature after annealing (F) and subsequent shearing (G). This Figure is adapted from reference 20

The group of Meijer demonstrated how to control the helicity of supramolecular fibers in function of temperature, using not TAA derivatives, but carboxamides.³⁴⁰ The authors incorporated a chiral center in the side chains in order to bias to helicity of the fibers that form in apolar solvents via cooperative hydrogen bonding. They could control the helicity by working either at elevated temperatures or below room temperature. At elevated temperatures, a nucleation-growth mechanism is followed. When the solution containing the supramolecular polymers is brought below room temperature, the molecular cores switch to their 2nd configuration without depolymerization taking place (**Figure 85A**). In another article, using mono-columnar flat carbonyl bridged TATAs, they revealed that entioselective pathways (isodesmic and nucleation-growth), leading to fibers of opposite helicity, could be accessed by working under different temperature profiles (**Figure 85B**).³⁴¹ Following

these lines of work, Dr Artem Osypenko, PhD student in our group at the time, studied thermally activated supramolecular polymerization of TATAs bearing chiral and achiral side chains.³⁴² During gelation both self-assembly processes followed nucleation-growth mechanisms. However, upon fast cooling and at relatively high concentrations, the fibers tend to aggregate faster. This results in fibers of one helicity displaying limited entanglement. When the self-assembly is carried out under slow cooling, super helical fibers of opposite helicity will form (Figure 85C). We propose that a combination of primary and secondary nucleation steps, resulting from the activation energy needed to flatten the propeller-like structure, lie at the origin of the difference in supramolecular helicity.

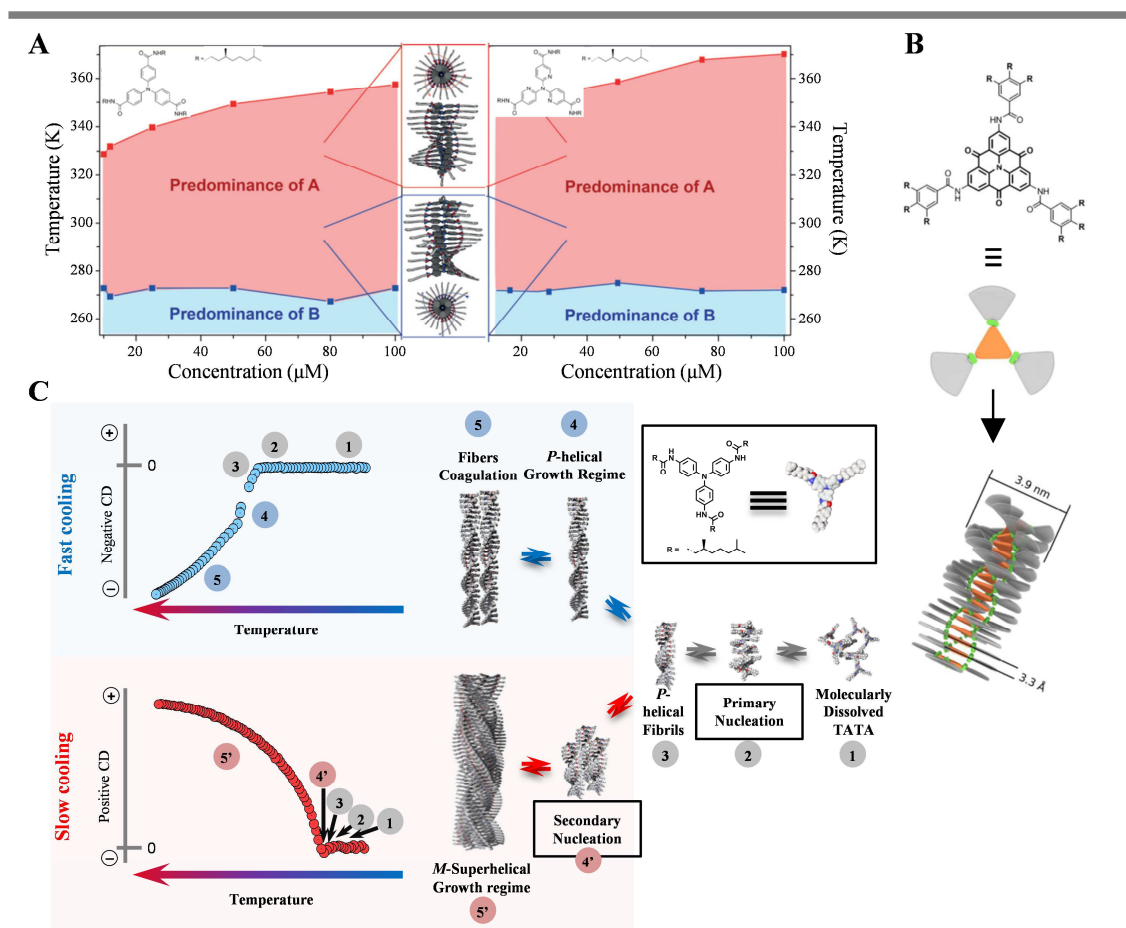


Figure 85. A) Temperature – concentration state diagrams. The red areas indicate the elongation temperature, the blue areas the inversion temperature. The diagram on the left is recorded in MCH, the diagram on the right in decalin³⁴⁰; B) molecular structure (top) and schematic representation (middle) of carbonyl-bridged TAA that self-assembles into supramolecular nanofibers (bottom) of different helicity depending on the temperature profile³⁴¹; C) schematic representation of self-assembly pathways of chiral-TATAs, leading to structures of opposite helicity depending on the temperature profile.³⁴² This Figure is adapted from references 340, 341 and 342

In other work of the group of Meijer it was demonstrated that TATA derivatives could be employed to form block copolymers under thermodynamic conditions.^{343,344} They could be obtained by either mixing preassembled homo-polymers or by slowly cooling a mixture containing both monomers (co-polymerization).

Besides soft fibers more rigid structures could be formed by increasing the number of non-covalent interactions and decreasing the lengths of the functional side-arms. This was shown by the crystallization of triarylamine trisacetamide (TATA-Ac) (Figure 86A).¹⁷ Crystals, in the form of small transparent needles, (~30 μm of length) could be formed by a slow and differential evaporation process of a methanol:toluene (75:25) solvent mixture (Figure 86B). The monomers stack in a monocolumnar “snow-flake” arrangement, in which TATA-Ac monomers alternate handedness. Neighbouring columns are all held at identical distances, giving rise to a crystalline structure, due to the fact all amide functions participate in intercolumnar hydrogen bonding (Figure 86C).

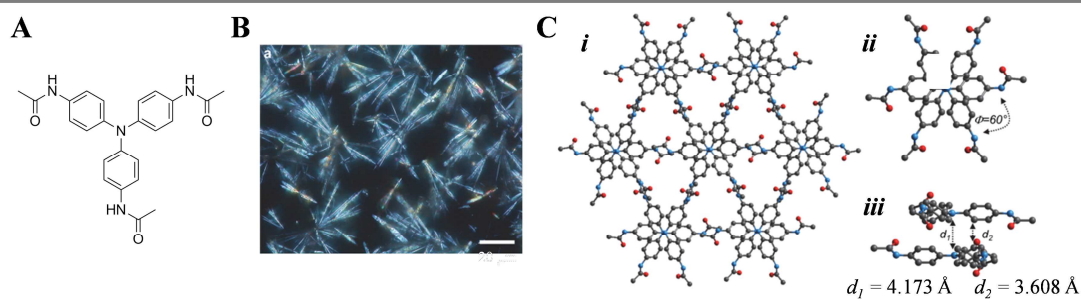


Figure 86. A) Molecular structure of TATA-Ac; B) crystals formed after a slow evaporation process in methanol : toluene (75:25); C) top view (i) of the TATA-Ac crystal structure obtained by X-ray diffraction. Top (ii) and side (iii) view of two TATA-Ac molecules stacked in a snow-flake monocolumnar arrangement. This Figure is adapted from reference 17

An example that beautifully highlights the complexity of self-assemblies, obtained by taking advantage of the molecular structure and intrinsic self-organization of TAAs, shows the formation of artificial potassium channels in phospholipid membranes.²³ To this end TAA were functionalized with crown ethers. In crystalline form, X-ray analysis confirmed that the monomers stack, just as TATA-ac, in a mono-columnar “snow-flake” arrangement. Surprisingly, it also revealed that the molecular structure had formed a succinimide by intramolecular cyclization. However, the exact packing in the membrane cannot directly be derived from this. Most importantly, these artificial channels, just as biological KcsA potassium channels, are able to selectively transport wires made of K^+ cations and water molecules.

D. Physical properties of triarylamine self-assemblies

When self-assembled in supramolecular polymers, the TAA core motifs are stacked at close enough distances to strongly couple electronically. Therefore, many of its original physical properties, such as charge transfer, optical sensitivity and photoconductivity may be enhanced. Furthermore, this close packing can also give rise to entirely novel properties, such as a plasmonic response. An equally important attribute of the self-assemblies is that electron delocalization takes place primarily along the main axis of the supramolecular fibers, imposing anisotropy in its characteristics. Examples of TAA and TATA self-assemblies exhibiting such remarkable physical properties, and applications incorporating such assemblies will be discussed in the last two sub-chapters of this bibliographic chapter.

i. Electron and charge transfer

Improved energy transfer, by coherent long-range energy transport, in supramolecular polymers has been demonstrated by the group of Schmidt and Hildner.³⁴⁵ Although the authors used a carbonyl-bridged TAA (CBT), the resultant fibers closely resemble supramolecular TAA polymers. Just as TAA, CBTs stack co-facially in a one-dimensional manner via π - π interactions between the aromatic rings and intermolecular hydrogen bonding between amide functions (Figure 87A). The periphery is decorated by photoluminescent 4-(5-hexyl-2,9-bithiophene)-naphthalimide (NIBT). By microscopy techniques, both single fibers (6 nm diameter; ~2-6 μ m in length) and small bundles were observed (Figure 87B). When one distal end of a fiber is excited by a laser, a photo-luminescent signal is observed that persists over the whole length of the supramolecular structure (Figure 87C-E). This photo-luminescent signal is attributed to efficient excitation energy transport, in which the distance that can be traveled by the exciton only depends on the length of the fiber. A wave-guiding mechanism is ruled out because of the small diameter of the fibers. Moreover, direct excitation was ruled out, by additional control experiments, for distances exceeding 500 nm. Furthermore, the authors show that energy transport only takes place in uniaxial direction along closely stacked CBT cores due to the strong electronic coupling that exists between them. Energy loss during transport is primarily caused by energy transfer to the NIBT periphery at defects in the alignment of CBT cores. This can be seen by peaks in photo-luminescence intensity (Figure 87C-E). Nonetheless, this effect is small compared to the total energy transfer. The transportation mechanism proposed is a combination between incoherent diffusive hopping and by coherent motion, with a larger contribution of the latter. The transportation distances are estimated to be ~ 100 nm and 8 μ m for incoherent and coherent motion respectively. The electronic coupling of the system is estimated to be ~44 meV, which is among the highest values measured for intermolecular coupling.

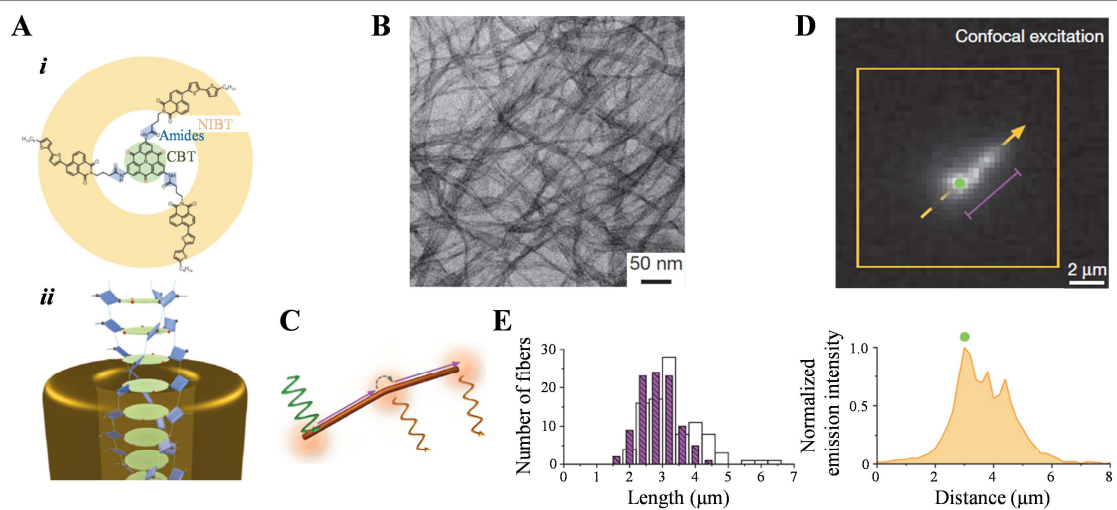


Figure 87. A) Molecular structure of the CBT derivative studied in the group of Schmidt and Hildner (i) and an illustration of its self-assembly into supramolecular polymers (ii); B) TEM image of the supramolecular polymers; C) schematic representation of the energy transport mechanism upon light excitation (green arrow) of one polymer end. The violet arrow indicates coherent energy transport along CBT cores. Photo-luminescence (orange arrows) occurs at defects (here illustrated by a kink), where incoherent energy transfer takes place to the NIBT periphery, and at the distal end of the fiber. Incoherent energy transfer can also occur between two ordered domains, as represented by the grey dotted arrow; D) photo-luminescent image of a CBT supramolecular polymer upon confocal excitation of its bottom left end; E) on the left: bar diagram of the distribution of fibers' lengths (open bars) and the energy transport distances (violet bars) measured on the same set of 97 fibers. On the right: photo-luminescent intensity signal measured along the fiber imaged in (D). This Figure is adapted from reference 345

ii. Conductivity properties

The enhanced electronic coupling present between stacked cores results in efficient electron transfer (as discussed here above), and could, thereby, equally lead to improved conductivity properties. A compelling indication is that, in TAA supramolecular polymers, the cationic radical can be delocalized along the stacking direction of the cores. This was already evidenced by the rise of an intermolecular through-space charge-transfer absorption band at 1100 nm upon light irradiation, as well as EPR measurements.¹⁶

The conductivity of TAA supramolecular polymers was demonstrated in our research group by the construction of self-assembled supramolecular TAA polymers between two metallic electrodes (Figure 88).²¹ A nano trench of 80 nm was immersed in a tetrachloroethane solution containing TAA monomers, while a bias of 0.3 – 0.8 V was applied. The first stage of the experiment is conducted in the dark and practically no conductance could be measured. Then, the sample was irradiated to trigger the photo-oxidation induced self-assembly process (Chapter I 4B. *Self-assembled triarylamine monolayers*). The nuclei thus formed migrate to the electrodes because of the electrical field applied and the elongation process takes place along the lines of the electrical field. This is accompanied by

an increase of six orders of magnitude in the conductance measured. After switching off the light the conductance remains stable suggesting the successful construction of low resistance interconnects between the electrodes (Figure 88A-D). The formation of uniformly aligned nanofibers was verified by AFM imaging (Figure 88C). *IV* measurements performed on rinsed and dried electrodes show ohmic behavior, characteristic for conductive materials (Figure 88E-F). The conductivities obtained ($5 \times 10^3 \text{ S}\cdot\text{m}^{-1}$) decrease with decreasing temperatures from which we can deduce a metallic character. Overall, only single-walled metallic carbon nanotubes can rival the results obtained. Multiple factors probably contribute to this exceptional high conductivity: *i*) large density of hole carriers; *ii*) charge delocalization along the nanowire; *iii*) TAAs share their electronic wave functions with the metallic electrodes. The group of Sanvito estimates, employing theoretical calculations, that the electron mobility in these nanowires at room temperature are in the order of $10 \text{ cm}^2\cdot\text{V}^{-1}\cdot\text{s}^{-1}$.³⁴⁶ Finally, in a collaboration with the group of Barboiu, the wires were self-assembled into biocompatible hybrid electrodes made of oriented mesoporous silica.³⁴⁷

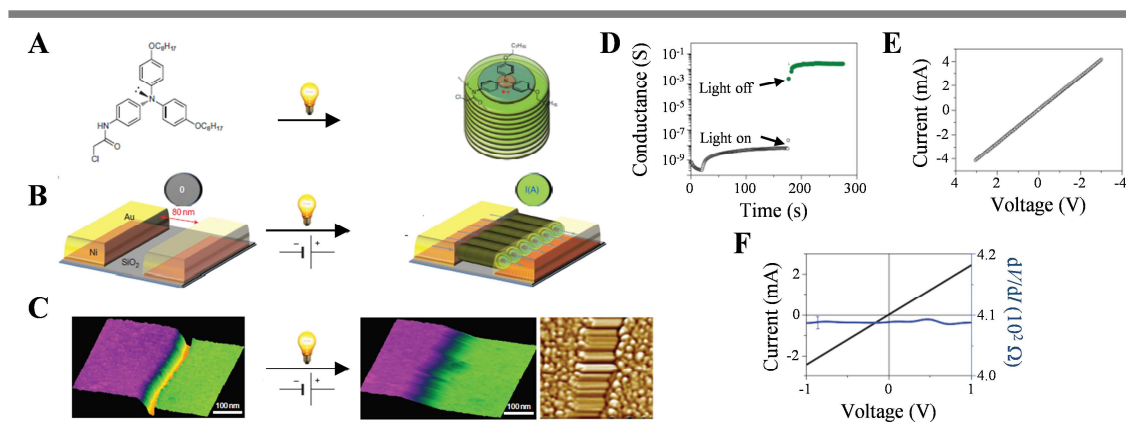


Figure 88. A) Molecular structure and light irradiation triggered self-assembly of the TAA derivative studied in reference 294; B) schematic representation of the construction of TAA supramolecular polymers between metallic electrodes by drop casting a 1 mg/mL $\text{C}_2\text{H}_2\text{Cl}_4$ solution in the dark and subsequently exposure to light irradiation while applying an Ef; C) AFM images on the nanotrench before light irradiation (left) and after light irradiation (right). On the outer most right image one can clearly observe the supramolecular polymers that span the gap in the direction of the Ef lines; D) Conductance measurement before, during (10 s) and after light irradiation of a nanotrench immersed in a TAA solution; E) *IV* curve measured on the nanotrench after construction of the supramolecular polymers; F) *IV* curve measured at 4K and at atmospheric pressure, on the nanotrench after construction of the supramolecular polymers and subsequent rinsing and drying. This Figure is adapted from reference 21

The conductivities of self-assembled supramolecular TATA polymers were equally investigated (Figure 89).¹⁶ Tetrachloroethane solutions containing TATA monomers (C12, C17, C22 or non-assembling), at a concentration above the critical gelation concentration, were inserted in ITO cells (4 μm electrode gap). Prior to photo-oxidation induced self-assembly some conduction is possible through preformed fibers (0.1 V bias). During irradiation radical species are introduced into the fibers and, as a consequence, the resistance decreases multiple orders of magnitude. The final conductivities

of the assembling TATA fibers are equal to one another, six orders of magnitude larger than the non assembling control and stable in the dark (Figure 89C). IV measurements reveal the transition from a semi-conductor to conductor state after photo- and electro-oxidation (Figure 89D-E). Furthermore, these fibers exhibit self-healing properties upon light irradiation. This effect could also be observed by irradiation of the ITO cell with a short light pulse. This initiates the formation of some radical centers and subsequent diffusion of polarons through the fibers, which leads to reorganization and optimization of their supramolecular structure. As a result, the conductivity continues to increase after the light has been switched off, until it reaches a maximum value (Figure 89F).

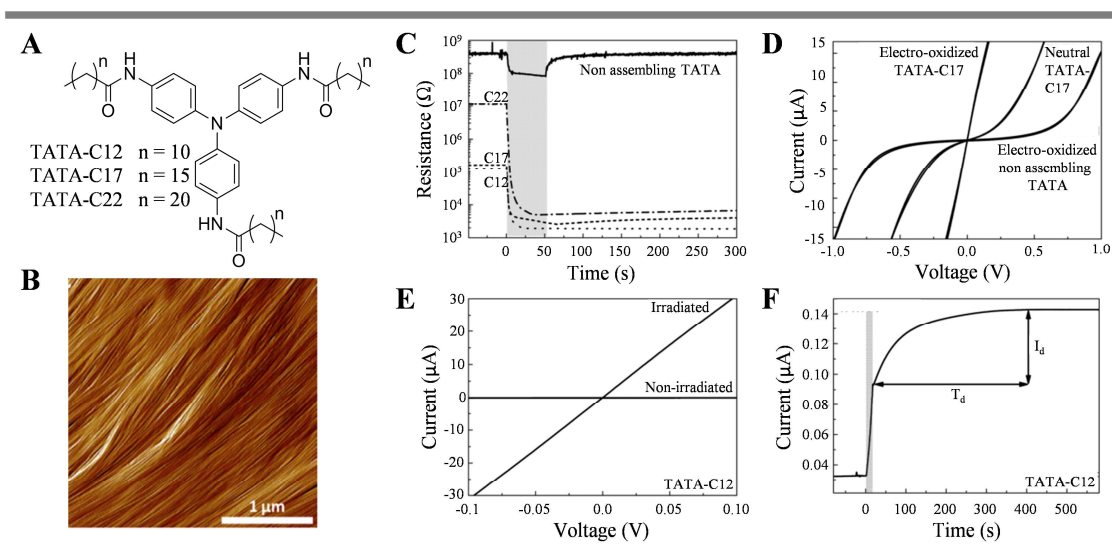


Figure 89. A) Molecular structure of TATAs investigated; B) AFM image of TATA-C12 fibers drop casted from an irradiated CHCl_3 solution; C) plot of the resistance versus the time of non-self-assembling TATA and assembling TATA-C12, C17 and C22 in pure tetrachloroethane, before, during (60 s, and indicated by the grey area) and after light irradiation; D) IV curves of non-self-assembling, neutral and electro-oxidized TATA-C17 in pure tetrachloroethane; E) IV curves for neutral and irradiated TATA-C12 in a solution containing 5 vol % of tetrachloroethane; F) plot of the current versus time of a TATA-C12 solution, before, during (15 s, and indicated by the grey area) and after light irradiation. T_d stands for the dark conductivity increase time. This Figure is adapted from reference 16

iii. Optical properties

Absorption and fluorescence

For the absorption and fluorescence of supramolecular triarylamine polymers the reader is referred to *Chapter I C. Supramolecular triarylamine polymers*.

Wave-guiding properties

Recently, due to the rapid rise of computer technologies, major advancements have been made in the development of electronic circuits for information processing, communication systems, sensors

and logic circuits for example. In order to circumvent some of the fundamental limitations³⁴⁸ with regards to device miniaturization and performance improvement, light instead of electrons has been studied as information carriers. The use of photons has several advantages³⁴⁸: *i*) they can travel at greater speed in dielectrics, thus carrying a larger amount of information per second; *ii*) the bandwidth of dielectrics (used in photonics) is greater than the bandwidths of metals (used in electronic devices); *iii*) less energy losses occur as photons do not interact as strongly with their environment as electrons do. Photons can be carried by optical wave-guides. These are structures that are able to confine and guide light. In 2009 the Nobel Prize in Physics was awarded on this topic to Charles K. Kao “*for ground-breaking achievements concerning the transmission of light in fibers for optical communications*”.³⁴⁹ Optical wave-guides can be classified according to the materials used: *i*) organic waveguides; *ii*) photonic crystal waveguides; *iii*) polymer dielectric waveguides; *iv*) inorganic-semiconductor wave-guides; *v*) metallic-plasmonic waveguides. Classes *i*, *ii*, and *v* will be briefly discussed, as they are the most important in relation to TAA derivatives.

Organic waveguides are known as classical or traditional waveguides. Passive organic waveguides are constructed of an inner, high permittivity and often transparent, dielectric surrounded by an outer low permittivity dielectric. This ensures total internal reflection of the photons inside the material, which propagate inside the waveguide. To minimize losses the interface between the dielectrics should be smooth with regards to the wavelength of light. Furthermore sharp angles in the wave-guide can lead to energetic losses to the surroundings: when the angle of the incident light is too large for total internal reflection it will escape. Additionally, the materials used should not absorb the wavelength of the light being guided, as this would also lead to large optical losses. Finally, miniaturization of such waveguides is limited. Active organic waveguides use photo-luminescence to transmit light. First the incident light excites an organic chromophore to the excited state. Then, because of the close stacking of chromophores, exciton-polarons are created which can diffuse along the wire due to resonance energy.

The principles behind photonic crystal wave-guides were first discussed by Yablonovitch³⁵⁰ and John³⁵¹ and its workings can be compared to that of semi-conductor crystals.³⁴⁸ Where the latter possesses an electronic bandgap, a crystal wave-guide possesses a photonic one, which is defined as a range of frequencies in which light cannot propagate. Defects and errors in the periodicity of photonic crystals create localized photonic states in the band gap that are otherwise forbidden. As a result, point defects lead to micro cavities, planar defects to mirrors and line defects to wave-guides.³⁴⁸

Metallic-plasmonic wave-guides are able to couple the incident light of a focused laser beam or an evanescent field, to the free conducting electrons of the (metallic) structure giving rise to plasmonic electromagnetic modes.^{352,353} The resulting surface plasmons possess greater momenta than

light of the same frequency.³⁵³ For this reason the associated electromagnetic fields cannot propagate away from the surface. Hence, surface plasmons are confined to the surface and propagate along it. At the other end of the wave-guide the plasmons are reconverted back to light.³⁵⁴ Just as for traditional wave-guides, passive and active plasmonic wave-guides have been defined. Passive plasmonic wave-guides are linear nanostructures, whereas active plasmonic wave-guides are defined as branched nanowire systems. In the latter the oscillation amplitude and phase at the branch point controls the plasmon propagation.³⁵⁴ In *Chapter IV. Towards supramolecular triarylamine based plasmonic structures* the plasmonic wave-guiding mechanism, as well as the experimental techniques involved, will be discussed in more detail.

Triarylamine-based waveguides

To the best of my knowledge almost all wave-guiding TPA derivatives are used in traveling-wave lasing, also called amplified spontaneous emission (ASE). The first example dates from 2001 from the group of Penzkofer.³⁵⁵ They synthesized TPA-based copolymers that emit in the red and green (conjugated copolymers) or bleu (non-conjugated copolymers) spectrum. The polymer thin films were shown to act as organic passive wave-guides. Furthermore, upon picosecond pulse excitation strong lasing was demonstrated. Whereas Penzkofer investigated lasing in function on conjugation, the group of Horhold investigated lasing of similar TPA polymers in function of molar mass.³⁵⁶ In both studies it is the film forming properties that affects the lasing properties. The group of Sun reported an active organic TPA-based wave-guide. The needle-like crystals exhibit two photon absorption, where after the upconverted light (fluorescence) is confined to and guided along the axis of the crystal. The crystal equally displays two photon induced ASE, with a low threshold value comparable to one photon pumped systems.³⁵⁷ One problem encountered with bleu lasing materials is their photo stability and durability. This obstacle was tackled by Adachi who developed HBP-*spiro*-bifluorene and TPA- *spiro*-bifluorene polymer wave-guide bleu lasers.³⁵⁸

TAA-based organic plasmonic wave-guides were first presented by our research group in 2016.¹⁷ Triarylamine trisacetamide (TATA-ac) (**Figure 90A**) assembles into small crystals of approximately 40 μm in length following a “snow-flake” arrangement consisting of two TATA-ac molecules (**Figure 90B**). The wave-guiding ability of doped and undoped crystals was demonstrated by pointing a laser on one end of the crystal and observing the output at the other end (**Figure 90C-D**). A photo luminescent mechanism was ruled out because *i*) the crystals do not absorb the wavelength of the lasers used; *ii*) no fluorescence was observed (**Figure 90E**) and *iii*) no wave-guiding is observed when the laser is pointed anywhere but at the distal end (**Figure 90Ciii**). When coated in indocyanine dye, oxidized crystals still displayed their wave-guiding ability, in contrast to neutral crystals (**Figure 90Dii-iii**). Subsequent fluorescence bleaching experiments **Figure 90F-G**) showed that undoped crystals exhibit a passive wave-guiding mechanism, whereas doped crystals display a plasmonic wave-guiding

mechanism. Light scattering along the surface of dye covered crystals is the cause for photo bleaching of undoped crystals. In doped crystals, the photo bleaching distance significantly increases due to the evanescent near-field of the energy propagating inside the crystal. Thus the metallic electrons present in the half-filled polaronic band, generated by photo-oxidation, are able to couple to the incident light and transfer the energy through the crystal by plasmon resonance.

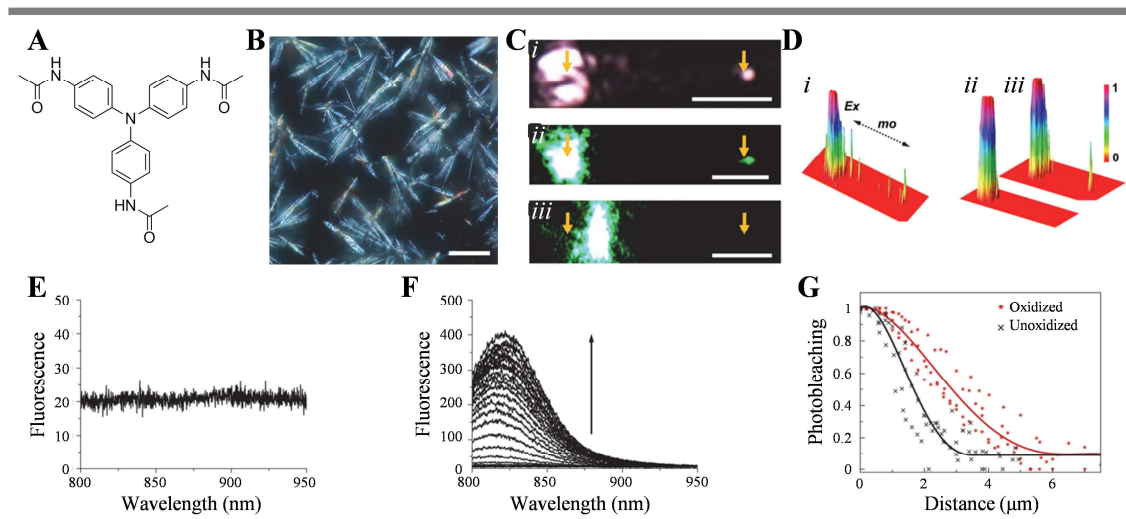


Figure 90. A) Molecular structure of TATA-ac; B) optical microscopy image of TATA-ac crystals; C) optical wave guiding in TATA-ac crystals upon irradiation with a 785 nm (i) or 532 nm (ii-iii) laser. In (i) and (ii) the laser is focused on the left distal end and a wave-guided light out-put is observed at the other distal end. In (iii) the laser is focused away from the end, here no wave-guiding is observed. The scale bars represent 4 μm ; D) 3D representation, obtained from the microscopy images, of the light intensity during wave-guiding along the crystal. In (i) multiple outputs are visible because of defects in the crystal. In (ii) and (iii) the propagation of light along neutral (ii) and oxidized (iii) crystals coated with indocyanine dye is presented; E) fluorescence spectrum of an oxidized crystal excited by a 785 nm laser; F) fluorescence spectra of an oxidized crystal coated with indocyanine dye after performing the wave-guiding experiment. The arrow indicates the increasing distance from the irradiated distal end; G) photo-bleaching results in function of the distance from the irradiated distal end of oxidized and unoxidized crystals coated with indocyanine dye after performing the wave-guiding experiment. This Figure is adapted from reference 17

More recently, the plasmonic wave-guiding property of soft TATA-C12 fibers was also demonstrated. Supramolecular TATA-C12 fibers were formed, by photo-irradiation induced self-assembly, into a nematic layer at the chloroform-water liquid-liquid interface.²⁴ Negatively charged Au nanoparticle (NPs), present in the water phase, adsorb to the positively charged (oxidized) TATA-C12 fibers, resulting in an anisotropic interfacial layer of conductive fibers and plasmonic AuNPs (Figure 91A-B). The ordering of the AuNPs is templated by the fibers and can be improved by centrifugation (Figure 91C). As a result of the high anisotropy and co-alignment of TATA-C12 fibers and AuNPs, the latter act as plasmonic wave-guides, as demonstrated by electron energy loss spectroscopy (Figure 91D-E).

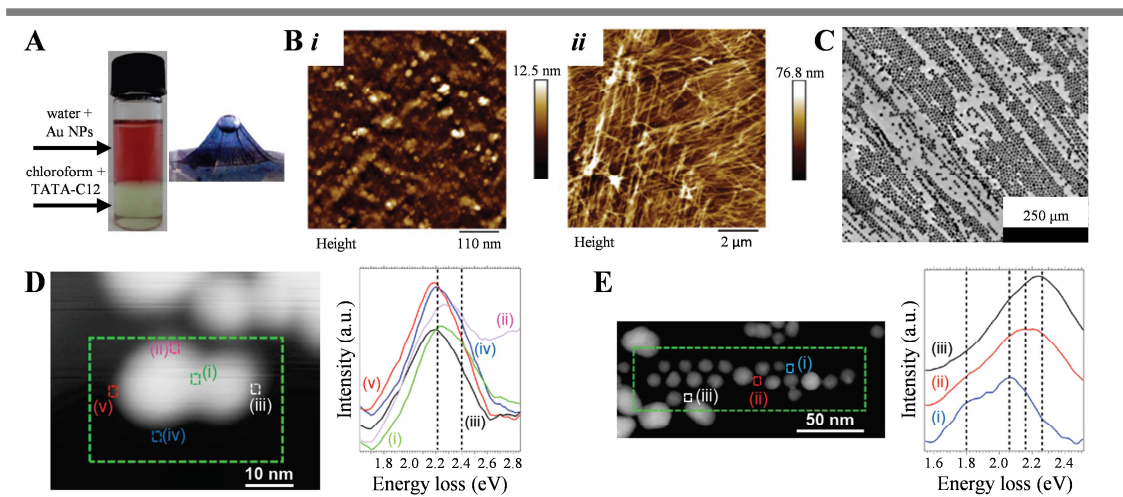
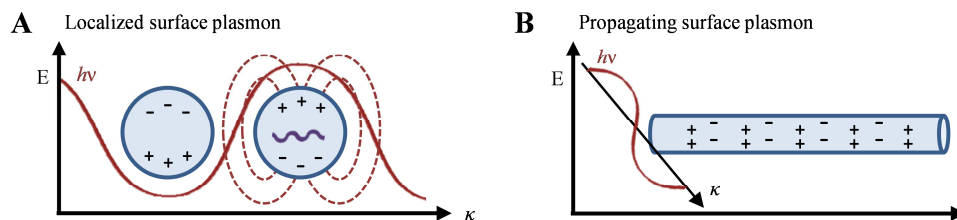


Figure 91. A) On the left can be seen a photograph of the 2 layer system consisting of water containing AuNPs and chloroform containing TATA-C12. On the right a photograph of a hybrid film (Au NP : TATA-C12) formed at the liquid-liquid interface after light induced self-assembly of TATA-C12; B) AFM images of the interfacial film imaged from the top side (i) and bottom side (ii); C) TEM image of the interfacial film after 1000 G centrifugation for a duration of 1 hour; D) STEM image of two adjacent AuNPs and electron energy loss spectroscopy (EELS) spectra obtained from the areas marked in the STEM image; E) STEM image from a string of Au NPs and the EELS spectra obtained from the areas marked in the STEM image. This Figure is adapted from reference 24

Plasmonic properties

The study of plasmonics encompasses the localization, guiding and manipulation of light, converted into localized electromagnetic fields, far below the diffraction limit.³⁵⁹ It studies the fundamental scientific aspects, as well as possible technological applications, emerging from the novel optical responses resulting from a materials plasmonic response.

Plasmons can be defined as the collective oscillations of free electrons of a plasmonic material in response to an external electromagnetic field. They exist either as bulk plasmons, when the free electrons in the bulk oscillate in resonance with the incident electromagnetic wave, or as surface plasmons. Surface plasmons can further be divided in localized and propagating plasmons (Scheme 7).^{359–361} In localized surface plasmons, the free electrons on the surface oscillate at the resonance frequency in three dimensions. This is the case for spherical particles of a diameter significantly smaller than the wavelength of the incident electromagnetic wave. When the free electrons only oscillate in one or two dimensions of the electromagnetic wave, propagating surface plasmons are formed. This is the case, for example, for nano rods and wires. In *Chapter III 2A. Plasmonics and the plasmonic effect*, more detail will be given on plasmon generation, the plasmonic effect and plasmonic coupling.



Scheme 7. Schematic illustration of spherical nanoparticles that give rise to localized surface plasmons in response to a uniform electromagnetic field (A), and of a nanorod that give rise to propagating surface plasmons, because it experiences a non-uniform electromagnetic field (B).

Plasmonic responses in triarylamine derivatives

Only few articles can be found in which plasmonic responses of TAA derivatives are described or investigated. It was Terrell and co-workers who first published on this topic in 2006.³⁶² They investigated the photo luminescent (PL) properties of three conjugated blue emitting polymers: two polyfluorenes-cyanophenylene (PF-CNP, 1:1 and 3:1) and polyfluorenes-triphenylamine-quinoline (PF-TPA-Q). The polymers were spun onto a quartz substrate that has half of its surface coated with a 50 nm Ag layer. Then, they investigated the photo luminescent properties of the polymers deposited on quartz and on silver. Interestingly, the polymers deposited on Ag showed PL enhancements of 3, 3.2, and 4.4 times respectively (Figure 92A-B). Furthermore, maximum enhancement ratios were observed for shorter wavelengths (Figure 92C). This observation suggests a contribution of surface plasmons to the PL enhancement, because these shorter wavelengths match with the silver plasmon resonance frequency. The authors proposed that the excited polymers are able to couple to the electron vibration energy of the Ag layer. As a result, during molecular relaxation, a surface plasmon is generated instead of a photon, which increases the spontaneous recombination rate (Figure 92F).

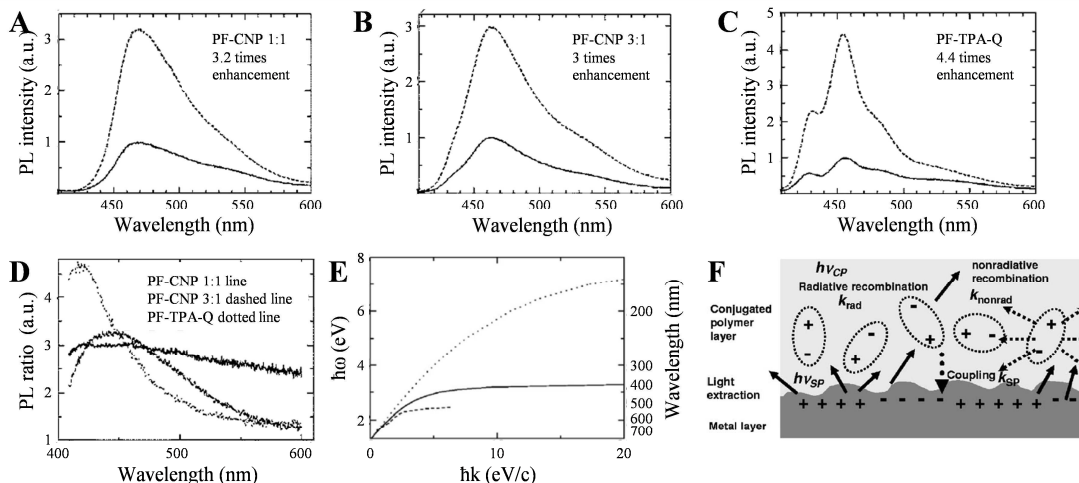


Figure 92. Photoluminescence of PF-CNP 1:1 (A), PF-CNP 3:1 (B) and PF-TPA-Q (C) polymers on quartz (solid lines) and on Ag (dashed line); D) photoluminescent enhancement ratio's versus the wavelength; E) diagram on the surface plasmon dispersion for polymers placed on Au (dashed line), F) schematic of the surface plasmon dispersion mechanism.

Ag (solid line) and Al (dotted line); F) illustration of the physical mechanism underlying the photoluminescence enhancement by plasmonic coupling. This Figure is adapted from reference 362

Only years later, in 2017, a second article was published on TPA plasmonic properties. This time by the group of Zhang.³⁶³ They reported on a fast-responsive and highly sensitive assembly (Figure 93A-B) that is constructed from a metal-insulator-metal (MIM) nanohole array and the electrochromic polymer TPA poly-amide (TPA-PA). The TPA-PA polymer is able to shift its plasmonic response in response to external fields. In the proposed assembly, the plasmonic response is altered, neither by the morphology of the metal nanostructure nor by the angle of incident light, but by the electrical stimulus-responsive dielectric properties of TPA-PA. This electroplasmonic shift can be actively controlled. Moreover, the authors measured the largest shift recorded in literature, which is up to 72 nm (Figure 93C).

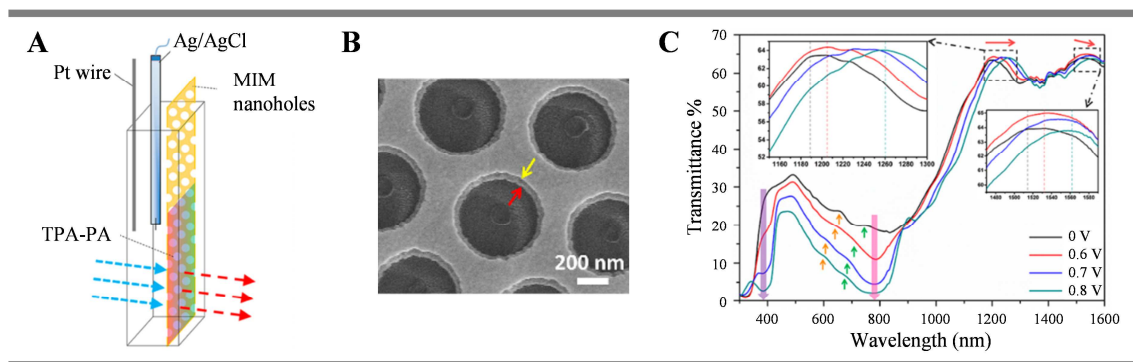


Figure 93. A) Illustration of the Fano resonance device that is made up of a three electrode MIM nanohole array wrapped with TPA-PA (working electrode); B) SEM image of the MIM nanohole array. The red arrow indicated the lower part, the yellow arrow the upper part; C) transmittance spectra for different biases applied. The thick arrows indicate the absorption wavelengths, the thin ones the SPR resonances. This Figure is adapted from reference 363

One of the challenges in plasmonics is how to align and couple plasmonic structures that are smaller than the optical wavelength. In this regard, our group has investigated the plasmonic coupling and wave-guiding properties of TATA supramolecular polymers and crystals. Wave-guiding TATA structures have been discussed in the previous section. The plasmonic coupling of TATA-C12 supramolecular polymers and gold nanoparticles (Au NPs) was actually demonstrated before that, in early 2016, with the construction of optical nanocircuits.²²

Photo oxidation of TATA supramolecular polymers leads to the generation of metallic electrons in a through space half-filled polaronic conduction band.¹⁶ Such fibers exhibit a negative dielectric constant for the photo-oxidized core which is surrounded by lateral alkyl chains of positive dielectric constant. Following the theory, these kinds of structures are appropriate for the exploitation towards plasmonic waveguides.^{364,365} The plasma frequency of oxidized TATA-C12 fibers, as determined by reflectance measurements and fitted by the Drude model, is 1.16 eV.¹⁶ In order to construct nanocircuits, TATA-C12 supramolecular polymers need to be grown between arrays of Au NPs

(Figure 94Bi). To accomplish this, first a monolayer of TATA molecules decorated with thiols was deposited parallel to the Au surface. Then, through a supramolecular recognition process by hydrogen bonding, TATA-C12 monomers strongly connect to the tris-thiol monolayer. Doped (oxidized) fibers are formed in a time span of 24 hours under light irradiation in chloroform; undoped (neutral) fibers are grown in absence of photo-irradiation (Figure 94Bii-iii). A large red-shift in plasmonic response is observed for Au NPs connected by doped nanowires, as well as an increase in dielectric values. This indicates a primarily non-radiative Landau damping of the plasmonic resonances in the Au NPs by the generation of hot electron-hole pairs. As is depicted in the energy diagram (Figure 94E) the excited metallic electrons can be transferred into the oxidized fibers' half-filled polaronic band and propagate towards the opposing NP, creating plasmonic interconnects. Because of this plasmonic coupling the optical conductivity (σ), derived from the imaginary part of the dielectric constant, increases tremendously from 259 to 4271 $\Omega^{-1}\cdot\text{cm}^{-1}$ (Figure 94D).

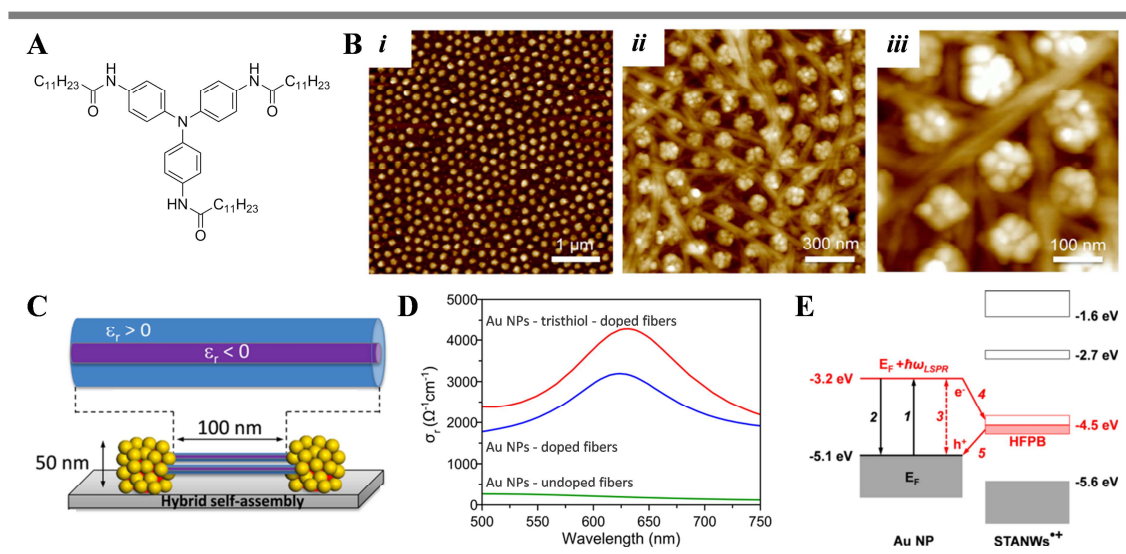


Figure 94. A) Molecular structure of TATA-C12; B) AFM images of the naked Au NPs array (*i*) and the hybrid array of Au NPs and TATA-C12 supramolecular polymers as metallic interconnects (*ii-iii*); C) schematic illustration of the optical nanocircuit. The metallic core of TATA-C12 supramolecular polymers is depicted in purple, the insulating sheath formed by the alkyl chains in blue; D) Overlay of the optical conductivities obtained from ellipsometry measurements; E) energy band gap diagram of Au NPs and TATA-C12 supramolecular polymers displaying the pathways for plasmonic excitation (1), radiative damping (2) and non-radiative damping (3) with the formation of hot electron-hole pairs that can be accepted in the half-filled polaronic band (HFPB) (4). This Figure is adapted from reference 22

E. Applications of triaryamine self-assemblies

i. Solar cells

Dr Osypenko incorporated TAA supramolecular polymers in perovskite solar cells as HTM, during his PhD in our group.³⁶⁶ He hypothesized that such assemblies were capable of improving the

charge transport between the active perovskite layer and the electrode. The molecular structures were designed to have energy levels matching that of the perovskite and good solubility in organic solvents, because of the octyloxy moieties, and self-assembling properties due to the amide groups. The scheme and characteristics of the PSCs are presented in **Figure 95**. Chemically-doped polymers showed poor PCEs, but photo-oxidized polymers, used without additives, demonstrated PCEs as high as 7.5 %. Although high PCEs have been reached, it does not yet measure up to the *spiro*-gold standard. This can be attributed to low fill factors, which indicates low conductivity in the HTM. Furthermore, because PSCs with non-self-assembling TAA analogues were not fabricated, it is unclear whether the performance of the PSCs had been ameliorated.

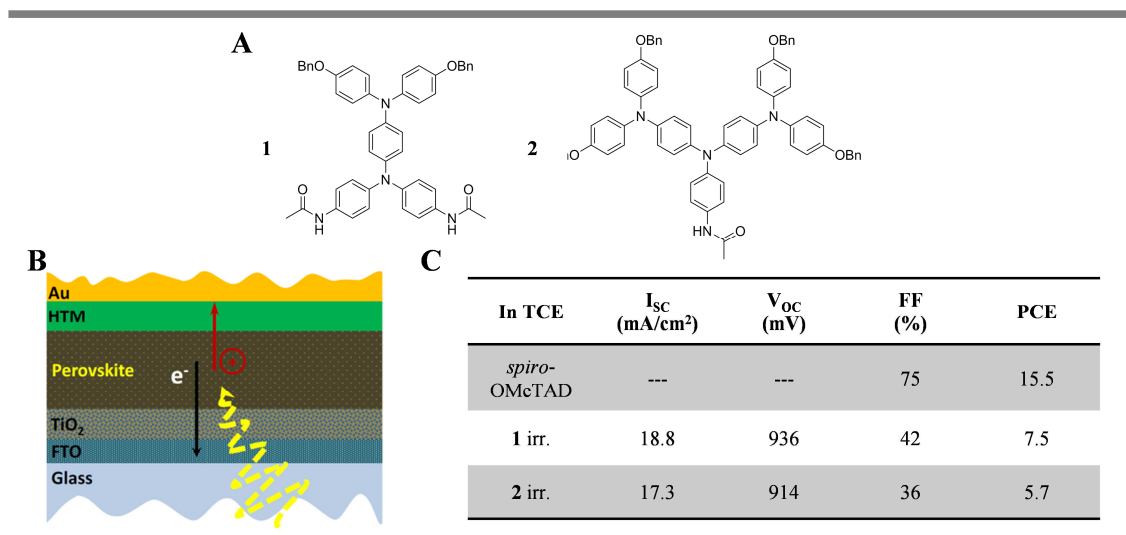


Figure 95. A) Molecular structures of compounds 1 and 2 studied as supramolecular polymer HTM; B) schematic representation of PSC; C) table summarizing the performance of the PSCs. This Figure is adapted from reference 366

ii. Organic light emitting diodes

As discussed in **Chapter I. 1D. Optical properties of triarylamines**, TAA derivatives could be used to design aggregation induced emission molecules. TAAs displaying this property can be used in OLED devices.

Especially in the early years of AIE research, most AIE compounds (with Alq₃ or siloles) showed moderated to good electron transporting properties. However, hole transporting AIE compounds were rarer. By incorporation of TPA, electroluminescent materials exhibiting both solid state emission and good hole transport could be envisioned. This would obviate the use of additional layers and would simplify OLED fabrication and costs.

One of the first groups to demonstrate the potential of AIE TPA derivatives in OLED devices was Tang, using TPA-TPE and TPA-TPE-TPA.³⁶⁷ TPE (tetraphenylethylene) is a classic AIE

chromophore because the out of plane rotation of the four phenyl rings that prevent π - π stacking in aggregated state. Both TPA-TPE and TPA-TPE-TPA are weak emitters in dissolved state, but their photoluminescence increases 103- and 192-fold respectively upon aggregation. At high water vol%, which is a non-solvent, the blue shift in emission wavelength suggests the transition from amorphous to crystalline state. While TPE alone has a photoluminescence efficiency of 49.2%, it reaches 100% for the TPA appended molecules. Further important characteristics for their application in OLEDs are their thermal stability and electron and hole transporting properties. Thin films exhibited high morphological stability ($T_g = 119\text{ }^\circ\text{C}$ for TPA-TPE-TPA) and TPA ensured good hole transport. These results demonstrate the potential of such derivatives in OLED devices, both as emitting and hole transport layer. This was also evidenced by the construction of an OLED device of 4.4 % photoluminescence efficiency.

In a second article, the authors synthesized a D-A molecule of TPA or dimer-TPA functionalized with electron withdrawing cyano groups (TPAN) (Figure 96A).³⁶⁸ These compounds show ICT, as was deduced from the 390 nm absorption band. In contrast to many AIE compounds, the ground state electronic structures are independent of solvent polarity and only minor dipole moments are associated with the ICT transitions. On the other hand, fluorescence emission spectra are red-shifted for polar solvents as larger dipole moments were associated with the excited states. Although TPA is an ACQ chromophore, TPAN had already been shown to exhibit crystallization induced emission (CIA), rendering the molecules fluorescence upon aggregation (Figure 96B). Thin films show good thermal stabilities with T_g 's of 127 $^\circ\text{C}$ and 141 $^\circ\text{C}$ for TPA3TPAN and DTPA4TPAN respectively. The overall external quantum efficiency was highest for a device including a ETHB layer, but without HTEB layer (PCE = 2.78%), which demonstrates that the hole transport ability of the material is enough to omit a HTEB layer.

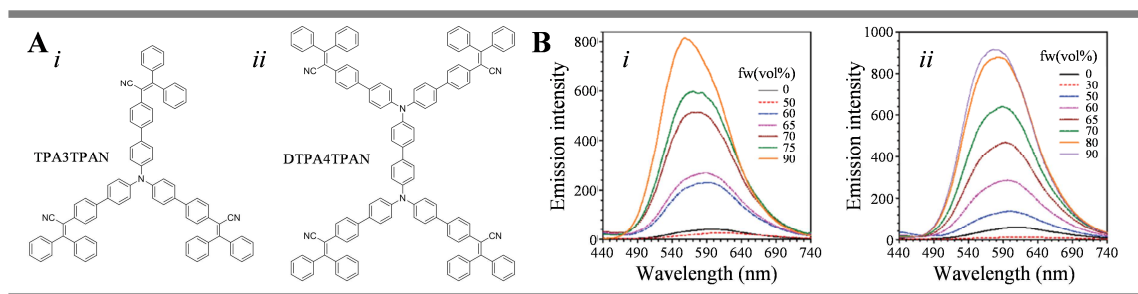


Figure 96. A) Molecular structures of TPA3TPAN (i) and DTPA4TPAN (ii); B) fluorescence spectra of TPA3TPAN (i) and DTPA4TPAN (ii) caused by AIE upon increasing water content. This Figure is adapted from reference 368

The D-A approach used in the previous example is advantageous because it could lead to balanced electron and hole transport and efficient charge recombination in the emissive layer. However, D-A interactions should be tuned carefully, as strong interactions cause ICT and decrease photoluminescence efficiencies in aggregated state molecules. Furthermore, the material was a poor electron transporter, and an additional ETHB layer was necessary to prevent cathode quenching. In another article, they remedied these problems. The authors functionalized TPE with benzimidazole, an electron transporting moiety, and TPA.³⁶⁹ Absorption spectra of compounds with and without TPA moiety indicate only weak ICT processes. Thin films of these compounds exhibit high photoluminescent efficiencies 99.3 and 98.9 % and good thermal and morphological stabilities ($T_g = 141\text{ }^\circ\text{C}$ and $157\text{ }^\circ\text{C}$). OLED devices made of compounds having a TPA moiety demonstrated lower turn-on voltages, because its HOMO energy level matches that of the HTM better than compounds without TPA. Furthermore, due to efficient charge injection and balanced hole and electron transport, light emission was three times brighter.

iii. Organic field effect transistors

Preliminary work towards the design of OFETs incorporating self-assembled triarylamine derivatives, was done by the group of Friend, who in 2004 reported the self-organization of TFB and BCB to produce semiconductor-dielectric bilayers (Figure 97).³⁷⁰ During spin-casting the two molecules go through a phase-separated binary fluid state before it forms a solvent free self-assembled thin film of structural integrity. The final morphology is dependent on the trajectory speed during spin casting. Such bilayers improve device performance by ensuring trap-free and robust gate-dielectrics. Because of this, the mobilities measured were limited only by the semiconductor and not by the quality of the interface. This proved to be a general method for other composites and compatible with different deposition techniques.

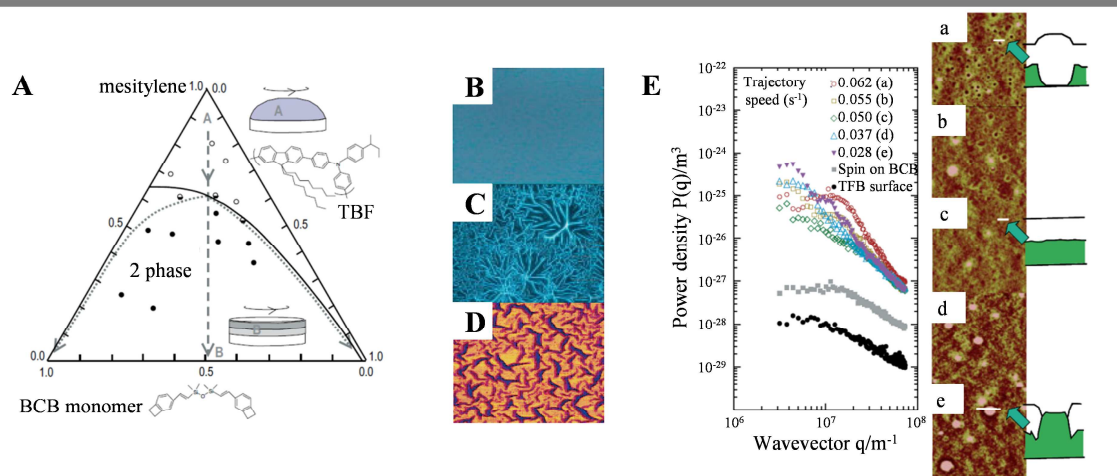


Figure 97. A) Thermodynamic phase diagram of the self-organization of TFB and BCB; B) fluorescent microscopy image of the bilayer formed upon rapid thermal cross-linking; C) fluorescent microscopy

image of the cross-linked BCB layer after dipping in xylene to visualize eventual defects; D) AFM image of the surface folds to further confirm the absence of defects. The images are 150 x 120 μm (B and C) and 50 x 40 μm (D) in size; E) plots of the isotropic power density in function of wavevector for different interface surfaces and their corresponding AFM images (10 x 10 μm), as well as the schematic presentation thereof. This Figure is adapted from reference 370

Song and co-workers synthesized three new macrocycles: *compound 1*) two TPA linked by ethylene; *compound 2*) compound 1 bearing two additional n-butyl chains; *compound 3*) four TPA linked by ethylenes bearing four n-butyl chains.²⁰⁵ Compound 1 and 2 formed single crystals packed into columns with a ‘layer-by layer’ pattern and loosely packed 1D slipped-stacks respectively (**Figure 98A**). Compound 3 formed 1D fiber-like supramolecular nano structures (**Figure 98B**). Such self-assemblies were expected to promote π - π stacking and thereby increasing intermolecular electronic coupling. Hence, the authors tested them in OFET devices. Compound 2 and 3 displayed mobilities of 2.3×10^{-3} and $2.0 \times 10^{-3} \text{ cm}^2 \cdot \text{V}^{-1} \cdot \text{s}^{-1}$ respectively. The additional value of self-assembled structures to promote charge mobilities was also shown by the group of Nagarajan.¹⁹³ In order to retain the original molecular structure, a series of unsymmetrically functionalized TAA were synthesized. Only one compound was able to self-assemble. Confirm to the expectation, the self-assembled TAA derivative displayed best hole mobilities ($15 \times 10^{-2} \text{ cm}^2 \cdot \text{V}^{-1} \cdot \text{s}^{-1}$) and on-off ratio is the series.

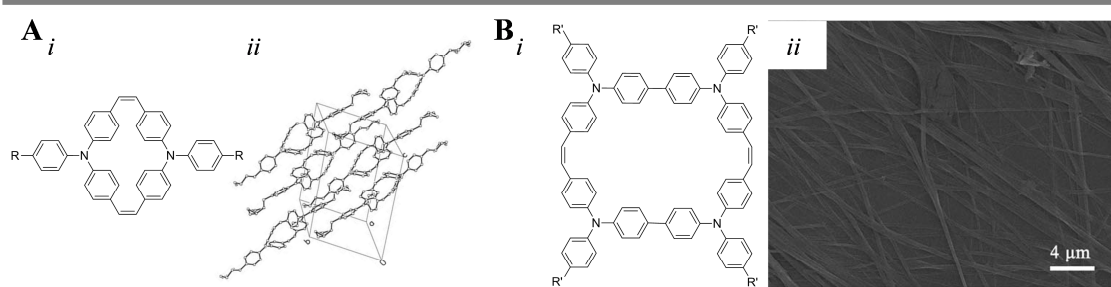


Figure 98. A) Molecular (i) and crystal (ii) structure of compounds 1 and 2; B) Molecular structure (i) and self-assembled fibers (ii) of compound 3. This Figure is adapted from reference 205

iv. Water splitting applications

Meijer and Naaman used self-assembled helical Zn-porphyrins - TAA structures to overcome two limitations frequently encountered in water splitting systems³⁷¹: decrease in efficiency due to overpotential, and decrease in efficiency due to the competing process of hydrogen-peroxide production which negatively affects the oxidative stability. The helical structures (**Figure 99A**) are formed from chiral organic semi-conductors (**Figure 99B**) and function as sensitizers. By coating the anode with the chiral structures, strong spin selection takes place (**Figure 99C**). As a result the formation of hydrogen peroxide decreases significantly and subsequently, overall photocurrent and water splitting efficiency are increased (**Figure 99D**).

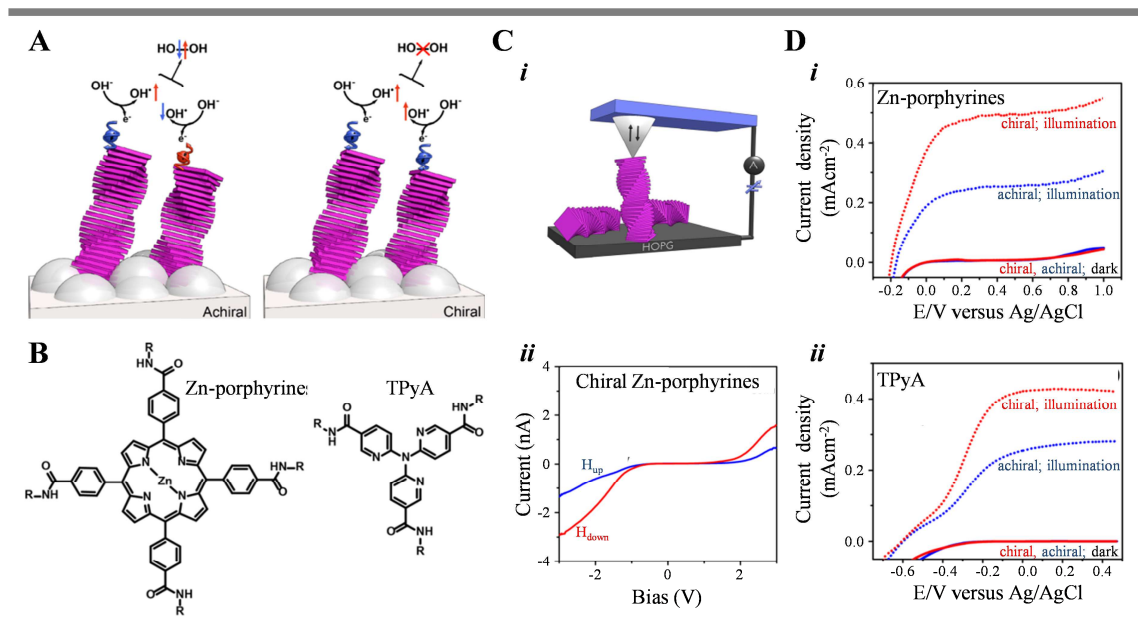


Figure 99. A) Schematic depiction of the anode surface coated with either achiral or chiral helical photosensitizer structures and their corresponding reactions; B) molecular structures of photosensitizers investigated; C) schematic depiction of the set-up of the magnetic conducting AFM used to measure the spin selective conductance in the photosensitizer helical assemblies (i); *IV* characteristics of chiral Zn-porphyrin structures (ii) obtained by the experimental set-up shown in (i); D) current density as a function of potential measured in a photoelectrochemical cell. This Figure is adapted from reference 371.

v. Chemical sensors

Self-assembly, or aggregation, of TAA derivatives is a widely employed technique to construct chemical and biological sensors. Just as in OLED devices incorporating self-assembled triaryl amines, the working mechanism behind self-assembled chemical sensor is aggregation induced emission.

The first group to incorporate TAA with AIE properties into a chemosensor was the group of Tang.³⁷² They realized a starburst lumophore with a TPA core which is highly emissive upon aggregation in poor solvents. Its emission could be quenched exponentially by the addition of picric acid. In the same line, the group of Ziqiang synthesized two self-assembled AIE carbonyl-based TPA derivatives for picric acid detection (Figure 100).³⁷³ The particularity of this work is that the fluorescence will be quenched in both liquid and gas phase as the morphology of the aggregates changes from large flaky feathers to smaller loose feathers and short rods upon hydrogen-bond mediated complexation (Figure 100C). Other examples on AIE fluorescence quenching by analyte binding come from the groups of Siva and Cao.³⁷⁴⁻³⁷⁵

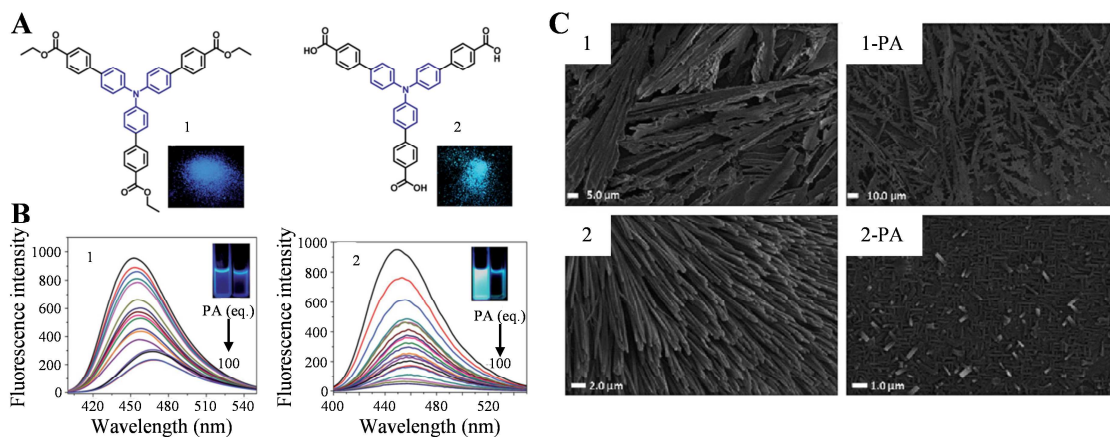


Figure 100. A) Molecular structure of the two carbonyl-based TPA derivatives and photographs of AIE of the powders under 365 nm UV irradiation; B) fluorescence spectra of derivatives 1 and 2 upon addition of picric acid in THF; C) SEM images of the self-assembled structures of derivative 1 and 2 before and after addition of picric acid. This Figure is adapted from reference 373

In contrast to AIE *turn-off* chemosensors, also examples of *turn-on* devices can be found.^{83,376,377}
³⁷⁸ To the best of our knowledge, it was the group of Zhou that reported on this for the first time.³⁷⁹
 They made use of the AIE properties of TPA-triazines and the selective binding abilities of thymines. Upon coordination with Hg^{2+} aggregation occurs and the chemosensor becomes strong red-fluorescent.

Hua developed a red *turn-on* chemosensor for the detection of Al^{3+} , a known neurotoxin.³⁸⁰
 Especially striking is that the authors achieved real-time monitoring of Al^{3+} in living HeLa cells. This is possible because of the good water solubility and biocompatibility of the chemosensor. Two articles in particular caught my interest as they displayed some novel and unexpected characteristics. The first comes from Yang *et al.*³⁸¹ This work distinguishes itself from other chemosensors reported because, although it does not display remarkable selectivity and high sensitivity, it exhibits low cytotoxicity, good membrane permeability and is operational in almost pure aqueous solutions. The second example comes from Wei and co-workers.³⁸² The authors achieved constructing a Zn^{2+} *turn-on* AIE chemosensor that would self-assembled in metal-organic vesicles (Figure 101). The design of such a supramolecular metal-organic coordination vesicle incorporating AIE molecules is the first in its kind.

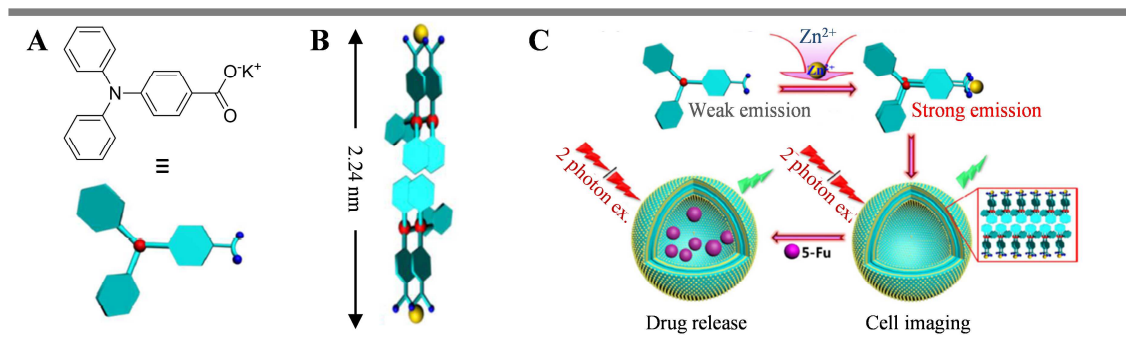


Figure 101. A) Molecular structure and its schematic representation of TAA derivative used; B) schematic representation of AIE TAA-Zn²⁺ bilayer; C) schematic representation of the self-assembled TAA-Zn²⁺ vesicle exhibiting 2 photon emission and capable of drug loading. This Figure is adapted from reference 382

Other types of supramolecular self-assembled chemosensors include fibers^{377,378,383}, nanospheres³⁸⁴ and MOFs³⁸⁵. The group of Yang reported Cd²⁺ and Cu²⁺ chemosensors exhibiting AIE, morphology dependent luminescence and red-shifted (two photon) absorption and fluorescence (with increased quantum yields) upon analyte binding.³⁸⁶ Interesting is the range of morphologies that can be obtained (Figure 102). Although the crystal structure of single crystals was elucidated, the self-assembled structure of the fibers, spheres and cubes was not.

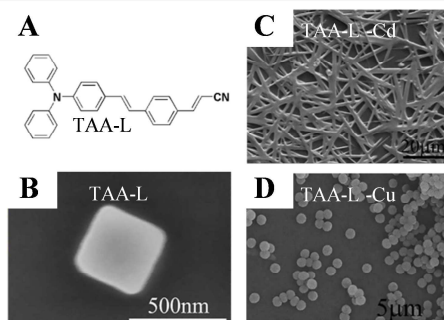


Figure 102. A) Molecular structure of TAA-L; SEM images of TAA-L (B); TAA-L-Cd (C); TAA-L-Cu (D). This Figure is adapted from reference 386

Aggregation induced fluorescence quenching should also be mentioned, wherein soluble fluorescent chemosensors aggregate upon analyte binding and subsequently exhibit a decrease in fluorescent properties.³⁸⁷

CHAPTER II SUPRAMOLECULAR ELECTROPOLYMERIZATION

II.1 Introduction

Gaining control over the precise placement of supramolecular polymers is a subject of high fundamental interest as it is expected to significantly improve the design and efficiency of organic (supramolecular) electronic devices. A current challenge in organic electronics is the bottom-up integration of electroactive wires into nano- and microscale circuitries. For the integration of organic conducting polymers, the use of supramolecular polymers, which are able to switch from a disassembled to an assembled state due to their dynamic character, is of particular interest. For example, their functional properties are modified simultaneously to their self-assembled state.³⁸⁸ In extension, this could result in efficient *on-off* ratios in devices. In this regard, the use of fast and non-invasive stimuli, such as light³⁸⁹ or redox stimuli,³⁹⁰ are advantageous compared to chemical stimuli³⁹¹ that systematically generate wastes in the system.

To achieve this integration, multiple fundamental issues must be addressed. For instance, one has to control the placement and orientation of supramolecular polymers between electrodes, which necessitates *i*) the directed self-assembly of supramolecular polymers at the metallic surface and *ii*) their alignment in the gap separating the electrodes. Using triarylamine supramolecular polymers, we developed a methodology that fulfils these requisites.

The first goal in this project was to address the initiation process of supramolecular polymerization. Up to now, the oxidation of triarylmines into their radical cation form was usually achieved by photo- or chemical-oxidation.^{14,15,26} In this work, we explored the possibility to induce nanowire formation by electro-oxidation. Electricity, which is both the most powerful oxidant and reducing agent known, was chosen because it can be easily controlled by regulating multiple parameters (e.g. type, field strength, current density, *etc.*). Subsequently, also fragile objects can be handled. Additionally, we hypothesized that it could guide the self-assembly process as well.

The second goal of the project was to gain control over the localization and orientation of the supramolecular polymers,^{298,299,392,393} for their bottom-up integration in electronic circuits of various geometries. First, we studied spatially-addressed nucleation at the electrodes to obtain directed self-

assembly. Secondly, we investigated the possibility to use the electric-field to impose field directed growth and alignment of the supramolecular polymers.

This chapter is the result of a collaborative work³⁹⁴ with Dr T. Ellis (former post-doctoral researcher in the SAMS group), Dr J.J. Armao IV (former PhD student in the SAMS group), Dr A. Osypenko (former PhD student in the SAMS group) and Dr D. Martel (CR at ICS). It is published in *Angew. Chem. Int. Ed.* **2018**, *57*, 3796-3805. My work mainly contributed to the second goal of the project and the resulting conductivity properties.

II.2 Bibliography

A. Electropolymerization

Electrochemistry can be used for the electropolymerization of conducting covalent organic polymers, such as polyanilines³⁹⁵, polythiophenes³⁹⁶, polypyrenes³⁹⁷ and polypyrroles.³⁹⁸ One of the advantages of using electropolymerization for the preparation of organic polymer thin films, is that the films exhibit good adhesion and contact to the electrode surface.³⁹⁹ Furthermore, the thickness of such polymer films can be controlled by the electric-field applied. From a practical point of view, these films are favorable, because they can be switched rapidly from a conducting state to an insulator state by redox cycling. Examples can be found of organic films and porous membranes, formed by electropolymerization, displaying supramolecular features.⁴⁰⁰⁻⁴⁰² However, the films are created by covalent electropolymerization of self-assembled structures. Thus, electropolymerization was not the driving force behind the self-assembly process itself. For instance, the group of Hai-Bo Yang, reported the formation of neutral supramolecular films, using a dicarboxylated TPA monomer and a di-Pt(II) functionalized TPA monomer (**Figure 103**).⁴⁰² These two monomers form a self-assembled structure through non-covalent metal-coordination interactions. Then, through electro-oxidation, the TPA moieties dimerize, leading to the formation of neutral polymeric films on the cathode. To the best of our knowledge, no electropolymerization process has been reported that leads to the supramolecular self-assembly of molecular monomers.

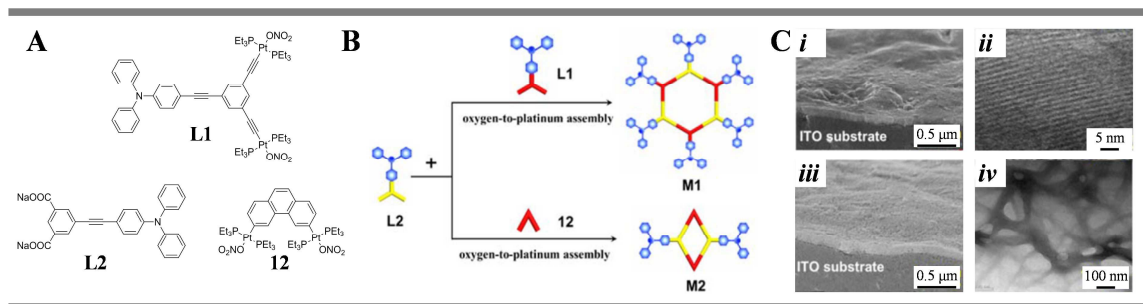


Figure 103 A) Molecular structures of monomers used in the electropolymerization of self-assembled structures towards polymer thin films; B) schematic presentation of coordination-driven self-assembly process; C) SEM (*i* and *iii*) and TEM (*ii* and *iv*) images of M1 (*i-ii*) and M2 (*iii-iv*) polymer thin films. This Figure is adapted from reference 402

B. Electric-field induced alignment

As mentioned in the introduction, in the field of supramolecular electronics it is of particular interest to attain control over the precise localization and orientation of conducting (nano) wires. It is expected that high degrees of order, at the nano- and microscale, will result in materials with enhanced mechanical, optical and electronic properties with regards to their disordered counterparts.^{299,403} Therefore, the alignment of different kinds of nanoobjects, such as polymers, small molecules and inorganic structures, has been investigated and several approaches have been proposed:⁴⁰³ 1) self-assembly of small molecules; 2) template modeling; 3) electric-field induction; 4) magnetic field induction; 5) geometry-restricted evaporation induction; 6) liquid crystal assisted orientation; 7) nanoimprint lithography; 8) direct drawing strategy and 9) micropillar guiding approach (Table 3). Traditionally, unidirectional external forces (e.g. electrical and magnetic fields) have been the main focus for the alignment of one dimensional nanostructures. This strategy is of particular interest for the fabrication of electronic (nano) devices as it allows for the orientation of nanostructures, directly in between electrodes.

In electric-field induced alignment, an object, placed in an electric-field, gets polarized due to field inhomogeneity. As a result, the nanostructures become charged and start to oscillate. They are thus forced towards the region with the highest field gradient; due to shear forces fibers are aligned along the direction of the electric-field. This technique is used primarily to align pre-existing nanostructures. Excluding liquid crystals, only few examples can be found that report on electric-field induced alignment of supramolecular nanostructures, and even fewer on supramolecular structures formed *in situ*. In the following sections the advances in electric-field induced alignment of supramolecular systems will be presented. They are divided in three parts:

- i*) Electric-field induced alignment of preformed supramolecular systems in organic solvents
- ii*) Electric-field induced alignment of preformed supramolecular systems in aqueous media
- iii*) Electric-field induced alignment of *in situ* self-assembled structures

Table 3. Summary of existing alignment methods for various compounds. This Table is adapted from reference 403

Alignment Method	Chemical structures of molecules	Substrates
<p>Electric field induction</p>	<p> $(\text{CH}_2-\text{CH}(\text{CN}))_n$ (PAN) $(\text{CH}_2-\text{CH}(\text{OH}))_n$ (PVA) </p>	<p>SiO₂ substrate Aluminium foil</p>
<p>Magnetic field induction</p>	<p> $(\text{CH}_2-\text{CH}(\text{OH}))_n + \text{Fe}_3\text{O}_4$ </p>	<p>Aluminium foil Glass slides</p>
<p>Geometry-restricted evaporation induction</p>	<p> </p>	<p>Glass plates Silicon plates Mica surfaces</p>
<p>Liquid crystal assisted orientation</p>	<p> $\text{C}_{12}\text{H}_{25}$ </p>	<p>Rubbed polyimide films</p>
<p>Nanoprint lithography</p>	<p> C_6H_4, C_6H_4, $\text{C}_{12}\text{H}_{25}$, $\text{C}_{12}\text{H}_{25}$ </p>	<p>Silicon substrate</p>
<p>Direct drawing strategy</p>	<p> </p>	<p>Silicon plates Glass substrates PS plates</p>
<p>Micropillar guiding approach</p>	<p> $(\text{CH}_2-\text{CH}(\text{O}-\text{CH}_2-\text{O}))_n$ (PVF) </p>	<p>Hydrophobic PDMS surfaces Superhydrophobic pillar-structured substrates</p>

i. Electric-field induced alignment of preformed supramolecular systems in organic solvents

The first reports on electric-field induced alignment of supramolecular structures in organic solvents originate from the group of Stupp.^{404–406} This group studied dendron rodcoils (DRC) (**Figure 104A**), which were shown to self-assemble in various solvents, such as toluene and CHCl_3 , at concentrations as low as 0.2 wt%.⁴⁰⁵ DRCs, that have at least 4 hydroxyl groups, form head-to-head dimers by hydrogen bonding. The dimers consequently assemble into long nanoribbons due to π - π stacking of the aromatic rings in the rod parts (**Figure 104BC**). The coils ensure that the nanostructures can be solubilized and hinder further crystallization. First, the nanoribbons were oriented in electric-fields by incorporating ZnO nanocrystals into the fibers (**Figure 104D**).⁴⁰⁴ Later, they demonstrated the alignment of fibers alone.⁴⁰⁶ These ordered films could be obtained by drop casting a toluene solution of preformed fibers, in an alternating current (AC) electric-field (**Figure 104EF**). Interestingly, the authors found that these films exhibit conductivities three orders of magnitude larger than films of amorphous morphology. The authors explain this observation by a better π -orbital overlap between molecules within the nanostructures.

A second group reporting on electric-field induced alignment of supramolecular structures is the group of Singer and Duzhko.^{407,408} The authors worked with discotic molecules of a metal-free alkoxy-substituted phthalocyanine derivative, that self-assembles in dodecane due to π - π interactions between phthalocyanine cores (**Figure 105A**). The self-assembled structures show tilted molecular arrangements at low temperatures and co-facial arrangements upon heating.⁴⁰⁷ Furthermore, larger stacks can form as a result of van der Waals interactions. Fibers, drop casted in a spatially inhomogeneous DC electric-field, show clear alignment along the fields' lines (**Figure 105B-D**).⁴⁰⁸ These experimental observations are in accordance with calculations made from electric-field intensity maps (**Figure 105E-F**). It was further demonstrated that, when experiments were performed under illumination, larger numbers of fibers, and better ordered fibers, were found in the gap region. The authors postulated that upon photoexcitation, charges are generated in the nanofibers, which are efficiently spatially separated when placed in an electric-field. Thus, greater dipole moments are generated and fibers will have a stronger interaction with the applied field. Finally, they presented the deposition of a single nanofiber between gold electrodes spaced 7 μm apart, thereby demonstrating that this approach allows for easy nanofiber manipulation.

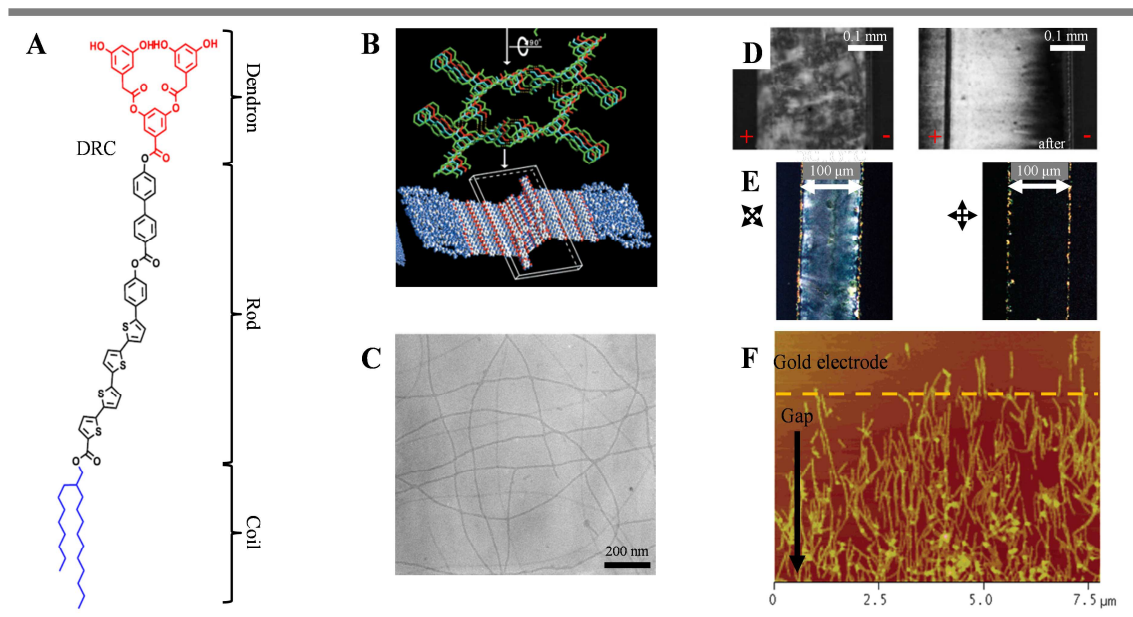


Figure 104. A) Molecular structure of a tetrathiophene member of the DRC family; B) side view of the ribbon-like structure derived from the crystal structure and schematic representation of a DRC fiber; C) TEM image of drop cast DRC fibers; D) POM images of a 2 wt% DRC-ZnO₂ solution before and after exposure to a 1500 V·cm⁻¹ electric-field; E) POM images of a 4T-DRC film aligned parallel and perpendicular to the applied AC field, indicating the uniaxial orientation of the optic axis of the film. F) AFM image of aligned nanofibers of 4T-DRC on Au/Cr patterned mica substrate. This figure is adapted from reference 404-406

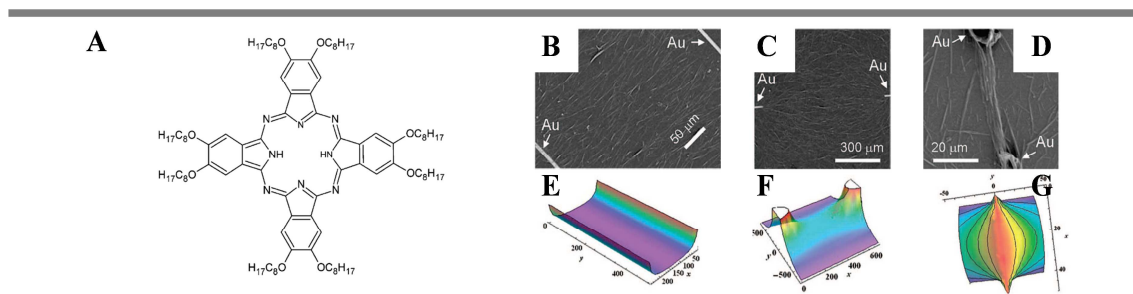


Figure 105. A) Molecular structure of the phthalocyanine derivative studied; B-D) SEM images of nanofibers, self-assembled in dodecane, drop-casted in an inhomogeneous DC electric-field between nano-patterned gold electrodes; E-F) calculated electric-field geometry of nano-patterned gold electrodes used in (B-D); G) calculated electric-field strength for the same geometry as in (F), but normalized to the central line connecting the electrodes. The strength of the electric-fields calculated is given in arbitrary units. This figure is adapted from reference 408

At the same time, Castillo *et al.* showed the alignment of self-assembled amyloid peptide nanotubes in between gold micro electrodes spaced 1 μm apart.⁴⁰⁹ Both bundles and single nanotubes were successfully aligned by tuning the frequency and amplitude of the field applied (Figure 106A). This set-up allows for the study of electric properties of bionano-assemblies and it opens the door to efficient integration of such materials in biosensing and bioelectronic devices.

Cristadoro *et al.* demonstrated the self-assembly of ultrathin nanographene (HBC-PhC₁₂) in presence of an electric-field ($4 - 5 \times 10^5 \text{ V}\cdot\text{m}^{-1}$).⁴¹⁰ HBC-PhC₁₂ assembles in a tilted edge-on columnar arrangement on highly oriented pyrolytic graphite (HOPG) surfaces, with their long axes perpendicular to the fields' direction. Interestingly, the alignment of the columns, which orientated themselves perpendicular to the fields' direction, was proven to be independent from the HOPG lattice orientation underneath. Thus, the electric-field induced alignment was favored above the strong intermolecular interactions between HOPG and HBC (Figure 106B). In absence of an electric-field, HBC-PhC₁₂ disks show epitaxial growth from the surface, by stacking of the extended aromatic ring system (Figure 106C).

Kuwahara *et al.* demonstrated the unidirectional alignment of lipophilic paddlewheel biruthenium complexes that self-assemble into halogen-bridged coordination polymers in n-decane.⁴¹¹ When placed in an AC electric-field, chloro-bridged polymers accumulate upon consecutive application of the AC field, whereas iodo-bridged polymers show fast and reversible alignment (Figure 106D). The latter nicely exhibits the potential of electric-field responsive and reversible aligned of nanomaterials in an electric-field.

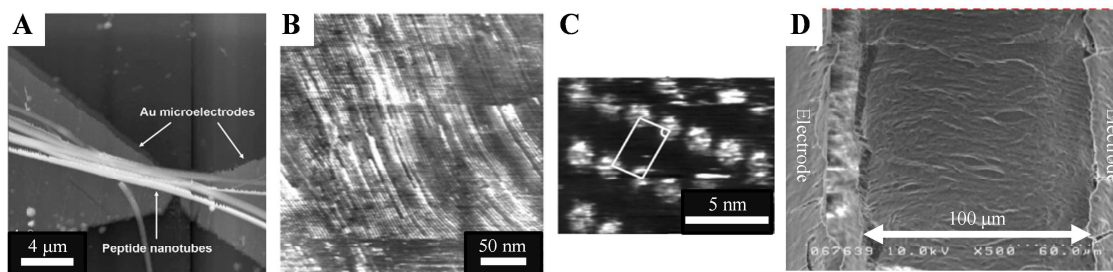


Figure 106. A) AFM image of self-assembled amyloid peptide nanotubes immobilized and aligned on Au electrodes;⁴⁰⁹ B) STM current image of the surface of a dry electric-field-oriented HBC-PhC₁₂ film in air;⁴¹⁰ C) STM current image of a dry film HBC-PhC₁₂ adsorbed film without electric-field;⁴¹⁰ D) SEM image of chloro-bridged biruthenium polymers immobilized between opposing electrodes. The specimen was prepared by freeze-drying a cyclohexanesolution of 100 mM under the applied AC electric-field.⁴¹¹

ii. Electric-field induced alignment of preformed supramolecular structures in aqueous media

Electric-field induced alignment in aqueous media is quite challenging in comparison with alignment in organic solvents. For the alignment to be effective, the dielectric constant of the nanostructures should be higher than the dielectric constant of the medium, which is often not the case in aqueous media. Due to the resulting low susceptibility of the nanostructures to the electric-field, higher fields are required. This leads to parasitic phenomena, such as Joule heating, polymerization, convective flows and electrochemical degradation of materials due to Faradaic reactions on the electrodes. However, several approaches have been developed to avoid these problems.

In a first approach, the electric-field capillary set-up established by Dozov *et al.*,⁴¹² initially used to study the electric-field induced alignment of athermal lyotropic mineral liquid crystal (LMLC) beidellite particles in water, was further developed by Asdonk *et al.*⁴¹³ With this technique, instead of directly manipulating nanomaterials by an electric-field, the electric-field direction is imposed through an intermediate LMLC template. The template is positioned in an isolated glass capillary and has a high electro-responsiveness. This circumvents the problems previously discussed: *i*) electrochemical degradation of the solution is prevented because there is no direct contact between electrodes and solution; *ii*) electrokinetic effects (convection and flow alignment) are prevented at high frequencies; *iii*) experimental flexibility is possible, because electrodes are not physically attached to the capillary wall. Furthermore, the absence of interactions between the dispersed material and the template renders the technique generally applicable.

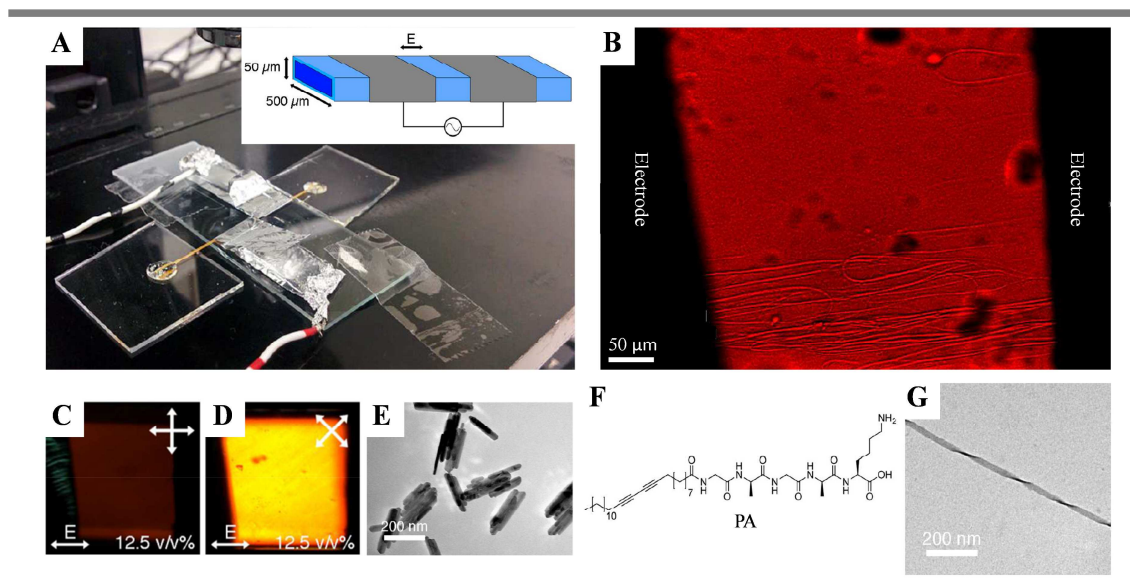


Figure 107. A) Photo and schematic representation of the electric-field capillary setup. Aluminum foil strips are wrapped around a rectangular capillary and attached to a power supply and function generator. The AC electric-field is applied along the long axis of the capillary; B) Electric-field alignment (153 V, 1 MHz AC electric-field) of PA bundles ($0.15 \text{ mg}\cdot\text{mL}^{-1}$) on a goethite template (6.5% vol/vol). Noteworthy is the observation of how bundles are positioned near the maximum electric-field strength (top part $0.39 \text{ V}\cdot\mu\text{m}^{-1}$; lower part $0.43 \text{ V}\cdot\mu\text{m}^{-1}$); C-D) Nematic goethite (12.5 v/v%) at $0.38 \text{ V}\cdot\mu\text{m}^{-1}$, 1 MHz under crossed polarizers parallel (C) and at 45° (D) with respect to electric-field direction; E) TEM image of goethite (prepared from 0.026% vol/vol in water, 3000 \times diluted); F) Molecular structure of amphiphile PA; (G) TEM image of PA ($0.20 \text{ mg}\cdot\text{mL}^{-1}$ in water, 30 \times diluted). This Figure is adapted from reference 413.

Using this technique, the authors studied the alignment of peptide amphiphiles in aqueous media (Figure 107). The peptide amphiphiles (Figure 107F) self-assembled into twisted beta-sheet-like nanofibers (Figure 107G) through the hydrophobic collapse of the alkyl tails and internal hydrogen bonding. Goethites, which were used as LMLC template, are board-shaped iron oxide nanoparticles that form liquid crystalline phases at 6.5% vol/vol in response to an AC electric-field of 1 MHz

(Figure 107C-E). When peptide self-assemblies are introduced to this system, anisotropic alignment of the fibers, parallel to the electric-field, is observed. Moreover, fibers migrate to regions where the electric-field is highest (Figure 107B).

In a second approach, the group of Mertig demonstrated the possibility to orient tubular self-assembled DNA origami structures conjugated with gold nanoparticles in an AC electric-field.⁴¹⁴ DNA origami structures (Figure 108A) are normally trapped on an electrode surface, as the dielectric constant of the structures is about 8-fold smaller than the dielectric constant of water. They migrate to the electrode surface in electric-fields of $5 \times 10^5 \text{ V}\cdot\text{m}^{-1}$ and higher (Figure 108B). However, this trapping behavior is significantly affected when DNA origami structures are conjugated to nanometer-sized gold particles every 42 nm. Trapping at the electrode surface occurs already at $1 \times 10^5 \text{ V}\cdot\text{m}^{-1}$ and, at $1 \times 10^6 \text{ V}\cdot\text{m}^{-1}$ the structures form linear chains that align in between electrodes (Figure 108C). The authors explain these observations by the increased dielectric constant of conjugated structures (higher polarizability) and claim that the gold nanoparticles act as electric-field concentrators (floating electrodes). Once the electric-field is turned off, the linear chains disassemble.

Although more complicated, these examples demonstrate that it is indeed possible to align supramolecular self-assembled organic and organometallic nano objects in aqueous media by an electric-field.

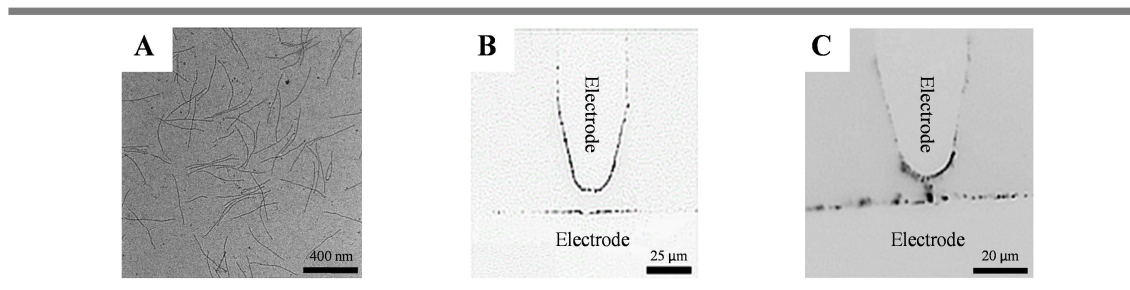


Figure 108. A) TEM image of tubular DNA origami structures (six-helix bundles); B) inverted fluorescence microscopy image of dielectrophoretic manipulation of six-helix bundle trapping by positive DEP at an electric-field strength of $1 \times 10^6 \text{ V}\cdot\text{m}^{-1}$ and 16 MHz; C) inverted fluorescence microscopy image of dielectrophoretic manipulation of gold nanoparticle-conjugated six-helix bundles at $1 \times 10^6 \text{ V}\cdot\text{m}^{-1}$, 16 MHz and after 16 min. This Figure is adapted from reference 414.

iii. Electric-field induced alignment of *in situ* self-assembled structures

In the previous two sections, we have illustrated the alignment of preformed organic and organometallic nanostructures in an electric-field, both in organic and aqueous media. Now, we will deal with electric-field assisted self-assembly systems wherein nanostructures are self-assembled and aligned *in situ*. This approach is singularly useful for the bottom-up construction of conducting nano circuits, as we will show shortly. However, to the best of our knowledge, only few electric-field assisted self-assembled systems are reported in literature.

The first report in this domain is the electric-field assisted self-assembly and alignment of single organic supramolecular fibers at a surface, from the group of Esch and Samori in 2006.^{415,416} They used a gel-forming 1,3,5-triamide cis,cis-cyclohexane derivative (CTG), that self-assembles into supramolecular fibers due to the three amide groups that form intermolecular hydrogen bonds, perpendicular to the cyclohexane rings (Figure 109A). These kinds of fibers have been shown to assemble in both aqueous and organic media. Organic solvents, however, are more straightforward for their use in electronic devices. Therefore, the authors used 1-octanol in this example. Furthermore, owing to large dipole moments of the fibers, they are ideal candidates for electric-field assisted self-assembly and alignment. A solution is drop casted onto two gold electrodes arranged in source–drain geometry with a 5 μm separation, while a 2 V DC bias was applied (Figure 109D-E). After cooling the system below its sol-gel transition temperature, fibers were predominantly observed on the cathode (Figure 109B-F). SEM images were used for statistical analysis, which proved the directional growth along the lines of the local electric-field (Figure 109G-H).

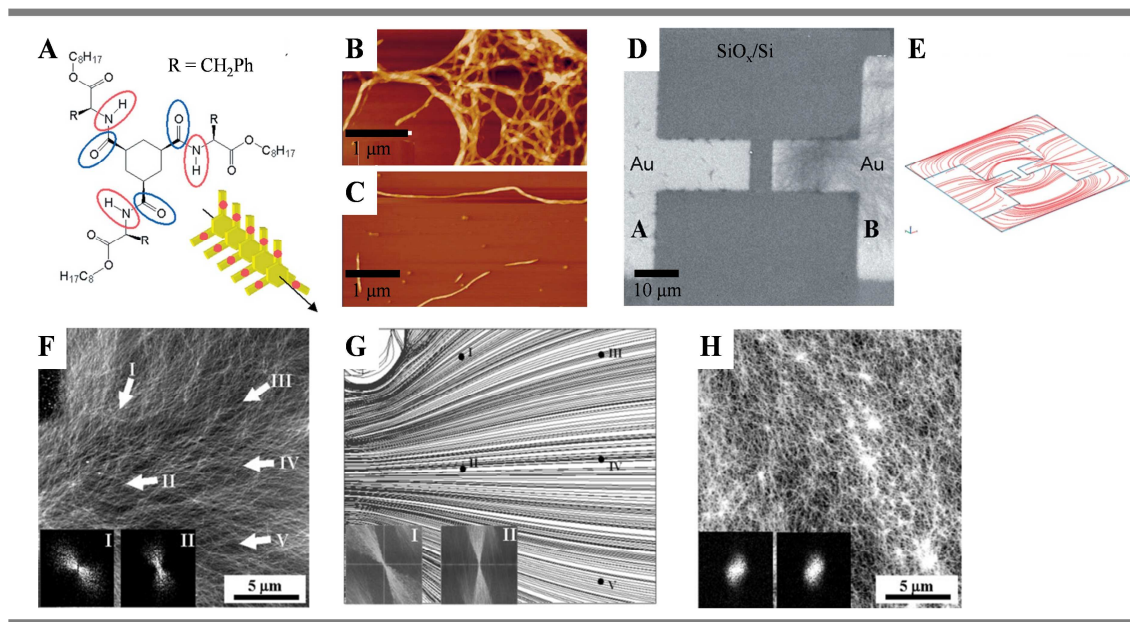


Figure 109. A) Molecular structure of cyclohexane trisamide gelator, CTG, and the schematic representation of a self-assembled fiber. In red and blue are highlighted the hydrogen bond donor (red) and hydrogen bond accepting (blue) groups. The arrow indicates the direction of the dipole moment; B-C) AFM images of the fibers; D) SEM image of the electrode set-up, showing the selective adsorption of aligned fibers on the cathode (electrode B), while applying 2 V bias for the duration of 1 h (80 °C to 20°C); E) calculated electric-field lines; F) SFM image of the cathode, showing the orientation of the fibers. The insets display the 2D FFTs. The white arrows show the main fiber's orientation; G) electric-field lines calculated over the same area of (f); H) SEM image of fibers deposited on an unbiased electrode showing isotropic orientation. This Figure is adapted from reference 415-416

In this first example it was assumed that the large dipole moment of the fibers formed would aid in the electric-field induced alignment and this was proved three years later by Yoshio *et al.*⁴¹⁷ They synthesized a set of self-assembling rod-shaped mesogens in dodecylbenzene, with and without lateral fluorination, that form thermoreversible organogels through intermolecular hydrogen bonding between amide moieties. The fibers which are laterally fluorinated dispose of larger dipole moments (Figure 110A, molecules **1a** and **2a**). A third molecule was synthesized with a diacetylene moiety in the spacer to improve the mechanical stability of the resulting fibers through photopolymerization (Figure 110A, molecule **3**). Solutions above the gelation temperature were drop casted onto gold comb-shaped electrodes, and were subsequently let to cool down below their gelation temperature in the presence of an electric-field (Figure 110B-E). In absence of an electric-field, disordered fibers (of molecules **1a**, **1b**, **2a**, **2b**) were observed. In the presence of an electric-field, fibers of **1a** and **3** aligned between the electrodes. In contrast, fibers of **2a** and **2b** remain randomly entangled, probably due to their lower dipole moments. Regarding these results it has been shown that the dipole moments indeed contribute to the formation of aligned fibrous aggregates under an AC electric-field. Additionally, the magnitude and frequency of the electric-field was studied. Alignment only occurred for fields above $0.5 \text{ V} \cdot \mu\text{m}^{-1}$ at a frequency of 1 kHz; and for fields of $1 \text{ V} \cdot \mu\text{m}^{-1}$ at frequencies ranging from 10 to 100 kHz. Interestingly, no alignment occurred (molecule 1a), when a direct current electric-field was applied.

The importance of large dipole moments in electric-field induced alignment processes, was also demonstrated by Shoji *et al.*⁴¹⁸ The authors synthesized phenylbithiophene fibers, that are able to self-assemble through π - π stacking, with and without the presence of laterally fluorinated phenylene groups (Figure 111A). Although both derivatives assembled, only the fluorinated fibers aligned themselves in the applied field (Figure 111C-D). The authors then compared the photoconductive behavior of aligned and entangled fibers. The photoconductive behavior is the result of the close π - π stacking inside the fibers, and currents up to 300 nA were measured when the fibers, that were placed in a DC electric-field, were irradiated by UV light. However, very little difference in photoconductive behavior was found between aligned and entangled fibers.

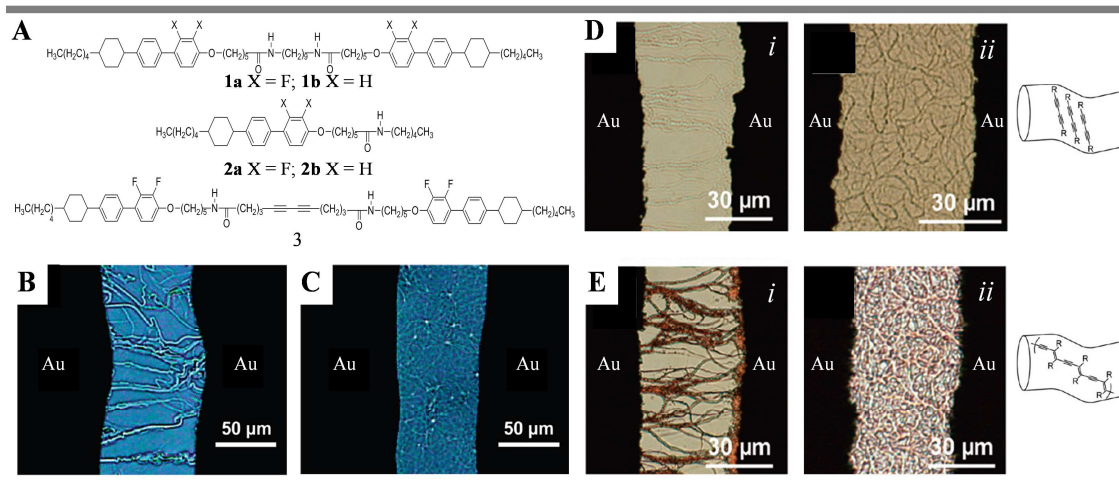


Figure 110. A) Molecular structure of the different molecules used; B) Optical microscopy image of fibers of 1a formed between gold electrodes under an AC electric-field ($1.0 \text{ V} \cdot \mu\text{m}^{-1}$, 1 kHz); C) Optical microscopy image of randomly entangled fibers of 2b formed between gold electrodes under an AC electric-field ($1.0 \text{ V}/\mu\text{m}$, 1 kHz); D) Optical microscopy images and illustration of fibers of 3 before (d) and after (E) UV irradiation, in the presence (i) and absence (ii) of an AC electric-field. This Figure is adapted from reference 417

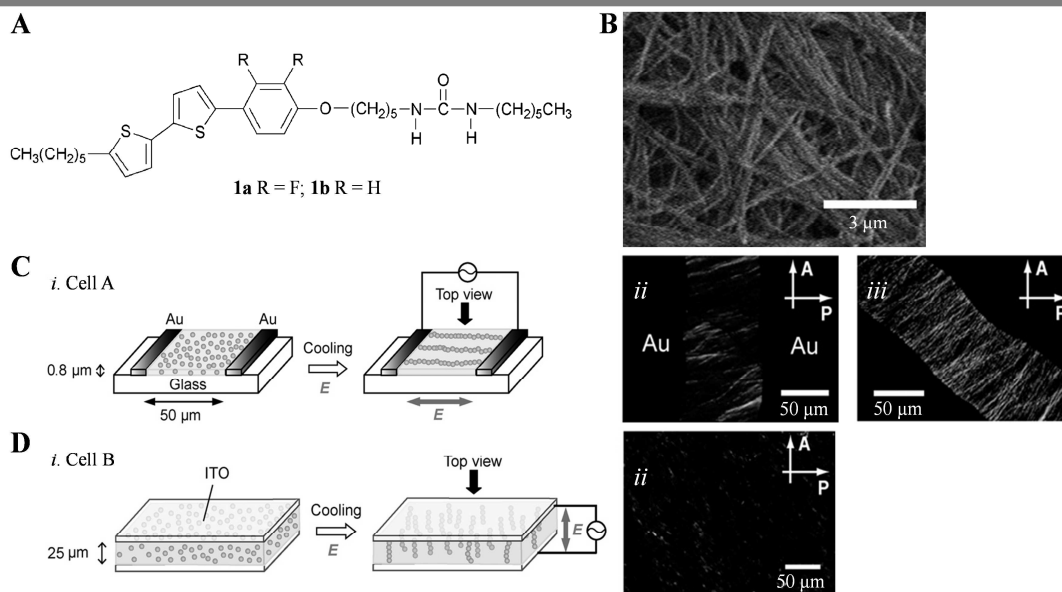


Figure 111. A) Molecular structure of self-assembling phenylbithiophene derivatives; B) SEM image of 1a fibers; C) schematic representation of the set-up of cell A (i) and POM images (ii, iii) of the resulting aligned 1a fibers, which have been formed between two gold electrodes by applying an AC Ef of $0.5 \text{ V} \cdot \mu\text{m}^{-1}$ at 1 kHz while cooling down to room temperature. In image (iii), the sample was rotated 45° from the position in image (i); D) schematic representation of the set-up of cell B (i) and POM images (ii) of the resulting aligned 1a fibers, which have been formed between ITO electrodes by applying an AC Ef of $0.5 \text{ V} \cdot \mu\text{m}^{-1}$ at 1 kHz while cooling down to room temperature. This Figure is adapted from reference 418

In all the examples discussed until now, the *in situ* self-assembly processes are sol-gel transitions. However, the electric-field can be used, not only for alignment, but also to control nucleation and growth processes, as well as electromigration phenomena. This was partially shown by Musumeci *et al.*⁴¹⁹ The authors demonstrated that the morphology of conductive PEDOT can be tuned, directly in between electrodes, by electropolymerization. Nanostructures, such as fibers (strong electric-fields in low viscosity media) and thin films (weak electric-fields), with variable electric properties, can be constructed *in situ* between electrodes (Figure 112). To the best of our knowledge, no such systems have been reported in literature for supramolecular self-assembled structures.

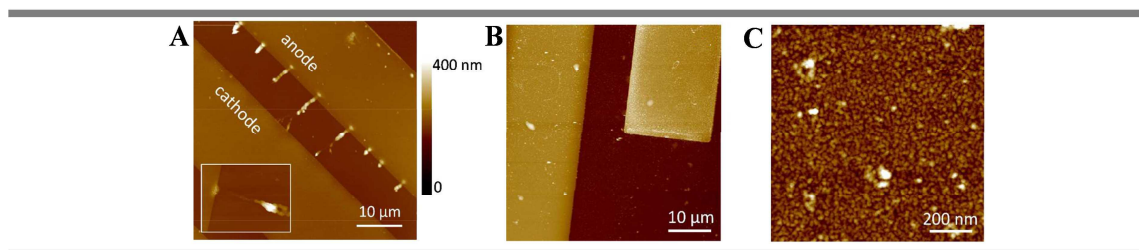


Figure 112. A) AFM image of aligned PEDOT fibers crossing a 10 μm wide gap, obtained after 5 seconds of electropolymerization of a 0.1 M PEDOT solution; B) AFM image of a thin film positioned in a 10 μm wide gap, obtained after 5 seconds of electropolymerization of a 0.1 M PEDOT solution; C) magnification of image (B) of the region in between the electrodes. This Figure is adapted from reference 419.

The last example on the electric-field induced alignment of *in situ* self-assembled structures, comes from our research group (*Chapter I 4D. Physical properties of triarylamine self-assemblies*). In this article the photo-oxidation induced self-assembly of triarylamine supramolecular polymers in chloroform, between nano-sized electrodes, was demonstrated, in the presence of a DC electric-field (Figure 113).²⁶ The resultant fibers show exceptionally high conductivities. However, this system, similar to other systems reported up to date, does have some limitations. Firstly, the nucleation is not spatially addressed. This makes it poorly adaptable to various geometries. It also signifies that nuclei are formed everywhere in the solution; only after rinsing a clean nano circuit is obtained. The second limitation is related to its size: the alignment of TAA supramolecular polymers was shown to be restricted to path lengths below 100 nm. The standing hypothesis states that this partly stems from the necessity of chlorinated solvents to trigger the self-assembly process. At further distances from the electrode, the *i*) high amounts of TAA^{*+} present everywhere in solution; *ii*) their respective chloride counter ions and; *iii*) the solvent, effectively shield the polymers from the electric-field applied. The strong electric-field necessary to overcome this problem and align the wires would have destructive side reactions as explained in the beginning of this section.

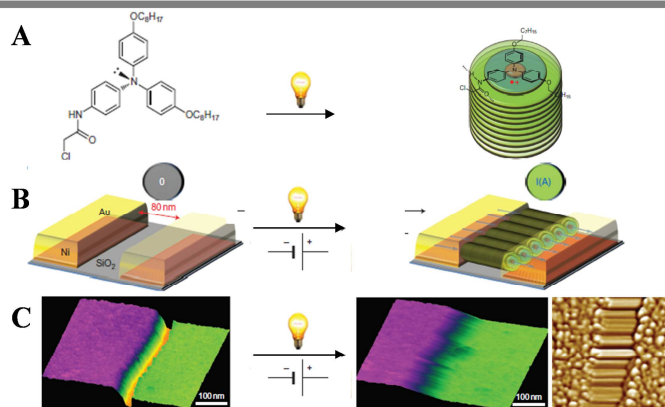


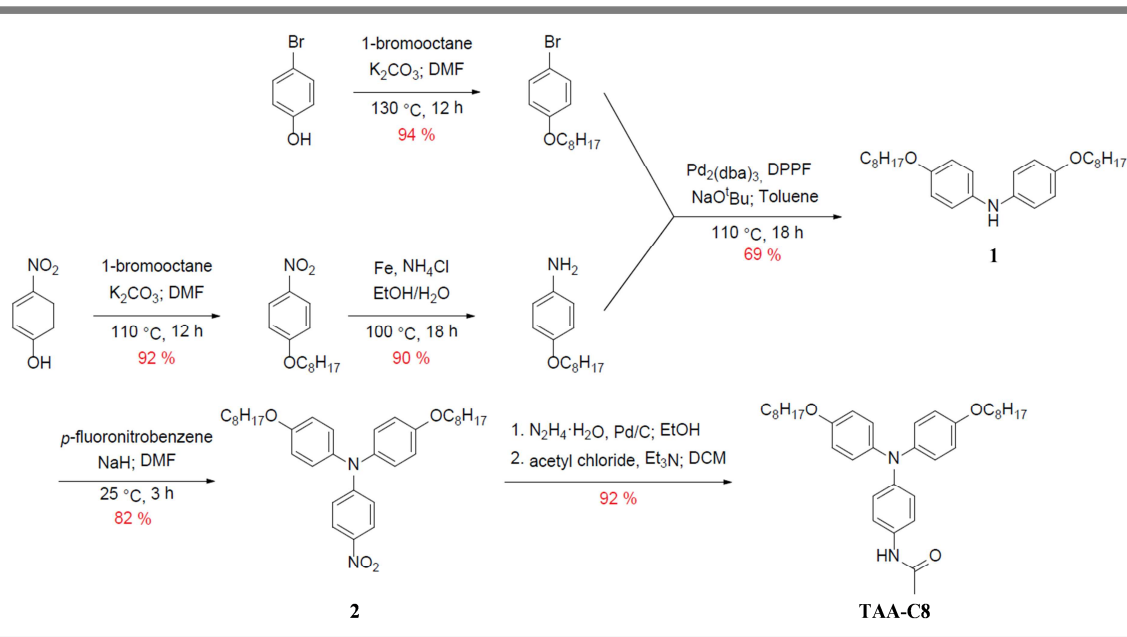
Figure 113. A-B) Schematic representation of the photo-oxidation triggered self-assembly and electric-field induced alignment process, of triarylamine nanowires in a nanotrench geometry; C) AFM image of triarylamine nanowires formed in nano trench. A $1 \text{ mg} \cdot \text{ml}^{-1}$ solution in $\text{C}_2\text{H}_2\text{Cl}_4$ is drop casted, in the dark, on nano patterned gold/nickel electrodes, while an electric-field is applied. The device is then submitted to white light irradiation. Fibers grow aligned in the direction of the electric-field, thereby strongly connecting the two electrodes (surface scale, $250 \times 250 \text{ nm}^2$). This Figure is adapted from reference 26.

In conclusion, only few examples reporting on electric-field induced alignment of supramolecular structures can be found in literature. Even less articles have been published on the *in situ* self-assembly of supramolecular structures, under the application of an electric-field. Moreover, in the reports found, the *in situ* constructions are mainly sol-gel processes. No examples could be found in which the electric-field is used to both initiate nucleation and growth, and align the resulting fibers. Having already studied the alignment of TAA nanowires over 100 nm, we wanted to extend its scope. Hence, we wanted to develop a spatially addressed supramolecular electropolymerization process in which a single stimulus is used to ensure electro-oxidation at the anode (nucleation), and directional supramolecular polymerization in a direct current electric-field (growth).

II.3 Results and Discussion

A. Synthesis

The study of spatially addressed supramolecular electropolymerization of triarylamine monoamides presented here was carried out using the triarylamine monoamide TAA-C8. TAA-C8 is synthesized via the previously published protocol depicted in **Scheme 8** (synthesis protocols can be found in *Materials and Methods. Synthesis*).¹⁴ The intermediary product **2**, is obtained by aromatic nucleophilic substitution of the fluoride atom in *p*-fluoronitrobenzene by the nitrogen atom of intermediary product **1**. Intermediary product **2** is then transformed into its corresponding aniline after a reduction reaction using palladium on charcoal as catalyst and hydrazine as hydrogen source. It is then subsequently acetylated to yield the final product N-(4-(bis(4-(octyloxy)phenyl)amino)phenyl)acetamide (TAA-C8) (¹H NMR spectrum in **Figure A1**).



Scheme 8. Synthetic pathway towards triarylamine monoamide TAA-C8

B. Supramolecular electropolymerization in presence of electrolytes

As stated before, in order to have a single stimulus for both spatially addressed nucleation and directional growth, we envisioned to substitute photo-oxidation by electrochemical oxidation to trigger the supramolecular polymerization process. Previously, chloride anions, generated upon light irradiation of the chlorinated solvent, functioned as counter-ions to the TAA^{•+} radical cations present. Using an electrochemical trigger, electrolytes would need to be introduced to act as counter-ions.

Therefore, we first investigated whether the presence of electrolytes would affect the supramolecular polymerization process.

In the presence of relatively high concentrations of commonly used electrolytes ($[TAA-C8] = 1$ mM; $[electrolyte] = 100$ mM in tetrachloroethane), the absorption spectra obtained after photo-oxidation were nearly identical (Figure 114). Both in absence and in presence of electrolytes a stable absorption band around 750 nm, indicating the presence of radical cations delocalized on the phenyl rings around one nitrogen center, arises. This is one of the typical optical signatures associated with supramolecular polymerization of TAA. Another aspect of supramolecular polymerization is the high association between the chloride counter-ions and the radical cations inside the supramolecular polymers (chloride counter ions cannot be detected by ^{35}Cl NMR). In the absorption spectra, a hypsochromic shift can be observed, which depends on the nature of the electrolyte present. This indicates that the electrolytes are, just as the chloride anions, closely associated with the TAA-C8 radicals and supramolecular polymers. These observations prove that the presence of high concentrations of electrolytes do not affect the supramolecular polymerization process.

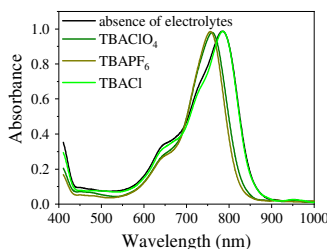


Figure 114. Normalized absorption spectra of 0.1 mM TAA-C8 in solutions in TCE after photo-induced self-assembly in the absence and presence of different commonly used electrolytes (100 mM).

Next, we explored the electrochemical behavior of TAA-C8 and if an electrochemical trigger could lead to supramolecular polymerization. Cyclic voltammetry (CV) of a 1 mM TAA-C8 solution in TCE plus 100 mM TBAPF₆, revealed a first oxidation peak at $E_{1/2} = -71$ mV, which is associated with the formation of its radical cation TAA-C8^{•+} (Figure 115A). A second peak is found at $E_{1/2} = 704$ mV and corresponds to a second oxidation towards the di-cation TAA-C8²⁺.

Spectroelectrochemistry performed on such a solution shows the development of the characteristic absorption band at 750 nm as it passes over the first oxidation potential (Figure 115B, solid line). The resulting spectrum perfectly matches with the one observed after photo-irradiation (Figure 115B, dashed line), indicating successful self-assembly. Furthermore, the formation of supramolecular polymers, in the presence of electrolytes and in the absence of light, was also verified by ^1H NMR spectroscopy. The behavior of a 5 mM TAA-C8 solution in deuterated chloroform containing 0.1 mM TBAPF₆ was studied while holding a potential of 0.2 V vs Fc/Fc⁺ for 30 min. In

this period of time approximately 1% of TAA-C8⁺ is formed by electro-oxidation, as determined by coulometry (Figure A2). The resulting ¹H NMR spectrum shows the full disappearance of the aromatic proton resonance signals. A similar result is obtained after electro-oxidation of TAA-C8 in the absence of electrolyte but submitted to a high potential of 25 V for 30 minutes (Figure 115C). The disappearance of the NMR signals after the oxidation of a small percentage of TAA molecules is a typical sign of the formation of large anisotropic stacks of TAAs as elucidated in our previous works.

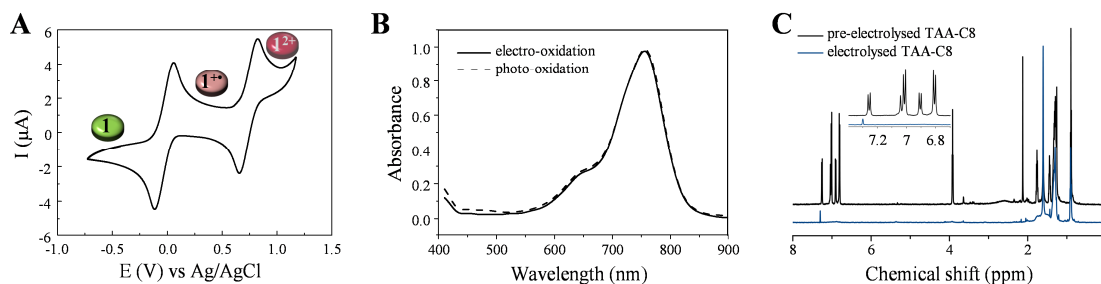


Figure 115. A) Cyclic voltammogram of 0.1 mM TAA-C8 in TCE in presence of 100 mM TBAPF₆ recorded at a scan rate of 100 mVs⁻¹; B) normalized absorption spectra of electro- and photo-oxidized 0.1 mM TAA-C8 solutions in TCE in the presence of 100 mM TBAHPF; C) ¹H NMR spectra taken before and after electrolysis for a TAA-C8 solution in TCE-*d*₂ held at 25 V for 30 minutes, in absence of electrolytes.

Finally, drop cast samples of electro-oxidized solutions, imaged by TEM and AFM, confirm the formation of supramolecular triarylamine nanowires (Figure 116A). By analogy with our previous investigations and accordingly to a series of control experiments³⁹⁴ we postulate that the electrochemically triggered self-assembly mechanism involves the following sequence (Figure 116B):

- i*) Diffusion of neutral TAA-C8 into the double layer
- ii*) Oxidation of the neutral species at the electrode surface producing TAA-C8⁺
- iii*) Migration of the radical cation into the diffusion layer
- iv*) Nucleation of the radical species
- v*) Growth of the supramolecular fibers by addition of neutral monomers onto the nuclei

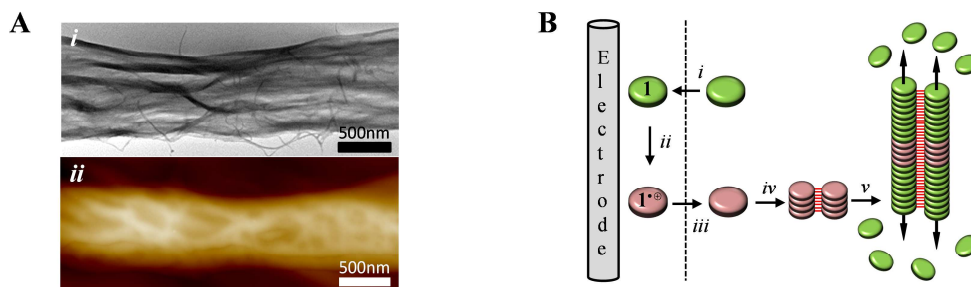


Figure 116. A) TEM (*i*) and AFM (*ii*) images of supramolecular polymers formed by an electrochemically triggered supramolecular polymerization process; B) simplified electrochemical

mechanism of the nucleation / growth supramolecular polymerization process activated by electro-oxidation.

C. Supramolecular electropolymerization in absence of electrolytes

In the previous section is shown, for the first time, that triarylamine monoamides can undergo supramolecular polymerization after an electrochemical trigger. However, as described in the bibliographic section, this system still has some interconnected limitations for their integration in electronic devices:

- At low voltages nanowires cannot be aligned over distances longer than ~ 100 nm because of the shielding effect of the solvent, the presence of TAA-C8^{•+} radicals and the presence of counter ions in the solvent.
- At low voltages and in absence of counter ions no nanowires could be grown. This is probably due to the difficulty to generate TAA-C8^{•+} in absence of counter ions.
- The large electric-field required to trigger self-assembly and needed to align fibers over longer distances would lead to parasitic heating and electrochemical degradation (short-circuits occurred probably because of the redox activity of the chlorinated solvent).

In order to circumvent these problems we probed the possibility to electropolymerize TAA-C8 at higher voltages, but in absence of counter ions and in a solvent of low dielectric constant. TAA-C8 was found to be soluble in alkanes at elevated temperatures, and heptane was used as solvent for the experiments to follow. Upon cooling of the solution to at least 8.4 °C and at a critical gelation concentration of 2.5 mg/mL, thermoresponsive fibrillar organogels formed (Figure 117AB). Particularly interesting is the large hysteresis showing a good stability of the gel when heating up to $T \approx 30$ °C (Figure 117C).

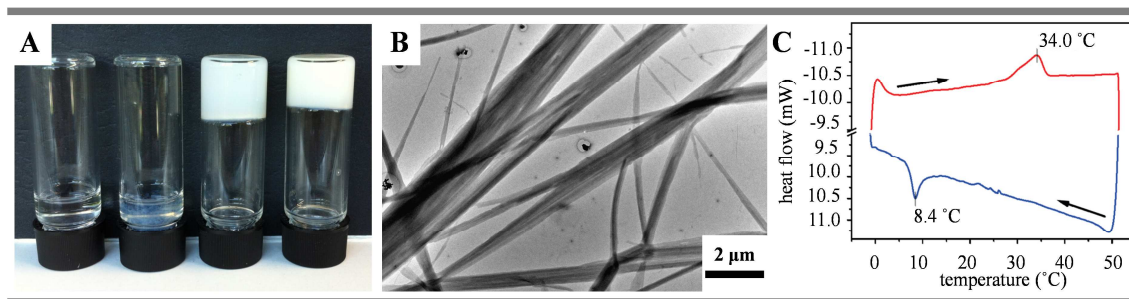


Figure 117. A) solutions and gels obtained after cooling down 1, 2, 5 and 10 mg/mL TAA-C8 solutions (from left to right) in heptane to 0°C; B) TEM image of the self-assembled polymers upon gelation of a 5 mg/mL solution; C) differential scanning calorimetry (μ DSC) results of a 26 mg/mL heptane organogel of TAA-C8, recorded at a scan rate of 0.5 °C/min. The heating and cooling cycles are colored red and blue respectively. At 34 °C an endothermic peak corresponding to gel melting is present. The exothermic peak that corresponds to the gelation process is located at 8.4 °C.

We then tested if electropolymerization of such a solution could be triggered inside an ITO electrochemical cell in which the electrodes are spaced 4 μm away (Figure M1). First, a 5 mg/mL solution, obtained at 60 $^{\circ}\text{C}$ and cooled down to room temperature, which is above its gelation temperature, was inserted into a sealed ITO cell (to prevent evaporation). After application of a $1 \times 10^7 \text{ V}\cdot\text{m}^{-1}$ electric-field, a dense array of fibers formed, which was visualized by cross-polarized optical microscopy (POM), Figure 118A. As no counter ions are present, we questioned whether fiber formation within the electrical field requires a direct electrical contact with the electrode to start nucleation. Therefore, we inserted the same solution into an ITO cell of which the electrodes are coated with a photoresist. This time no fiber formation occurred, except at the edges that contained flaws in the photoresist (Figure 118B). We can thus conclude that *i*) fiber formation is not triggered by a sol-gel transition and *ii*) a direct electrical contact is necessary for complete supramolecular polymerization. This indicates that, even without electrolyte, the direct contact between TAA-C8 and the electrode, in high electric-fields, creates an oxidized seeding surface from which neutral TAA fibers can grow.

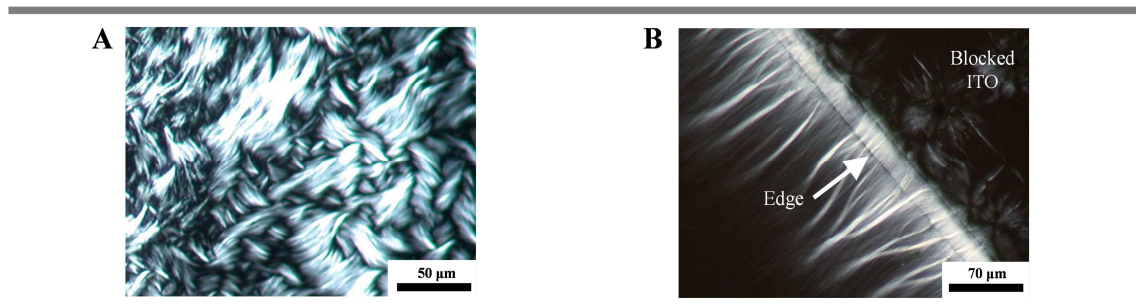


Figure 118. A) Cross-polarized optical microscopy image of TAA-C8 supramolecular polymers formed in an ITO cell: a 5 mg/mL solution was cooled down to room temperature and then inserted into a ITO cell with a gap of 4 μm . Inside the cell the solution was subjected to a DC electric-field to trigger the supramolecular polymerization; B) cross-polarized optical microscopy image of an ITO cell produced in the same manner as in (A). Here the ITO electrodes are blocked, thereby preventing electropolymerization of the TAA-C8 monomers.

D. Spatially addressed supramolecular electropolymerization and alignment in an electric-field

After having elucidated the process towards electro-chemically induced supramolecular polymerization in heptane and in absence of counter ions, we then turned to the orientation and alignment of said fibers between commercially available interdigitated microelectrodes (IDEs) with 10 μm electrode gaps (Figure M2). The protocol described below was followed for the remainder of experiments:

- i*) Dissolving TAA-C8 in heptane at 60 $^{\circ}\text{C}$.

- ii) Cooling of the solution down to 30 °C, which is well above the gelation temperature, regardless of its concentration.
- iii) Drop casting 5 μL of the solution onto the IDE while applying a direct current electric-field.
- iv) The electric-field was switched off after 5 minutes, the time needed for all solvent to evaporate.

Upon solvent evaporation the possibility exists that sol-gel processes take place. We thus first had to ascertain ourselves that polymerization is the result of electro-oxidation and does not originate from thermal or concentration effects. In a first control experiment, which was conducted in absence of an electric-field, only amorphous and unlocalized material was present on the IDE (Figure 119A-C). In a second control experiment, a solution previously cooled down below its gelation temperature and partly re-solubilized by heating at 30 °C, was drop casted in absence of an electrical field. Although macroscopically in a dissolved state, some fibers do remain in suspension and after solvent evaporation a disordered network of fibers was observed (Figure 119D). This control experiment was repeated in presence of a $1.25 \times 10^7 \text{ V}\cdot\text{m}^{-1}$ DC electric-field. However, the fibers did not show any further alignment (Figure 119E). From these three control experiments we can conclude that 1) in the time span needed for solvent evaporation gelation does not take place, which also excludes the involvement of dielectrophoretic alignment processes; 2) solutions should not be allowed to cool down below the gelation temperature, because even after re-heating fibers remain in suspension; 3) reorientation of fibers by an electric-field, after entanglement, is not possible.

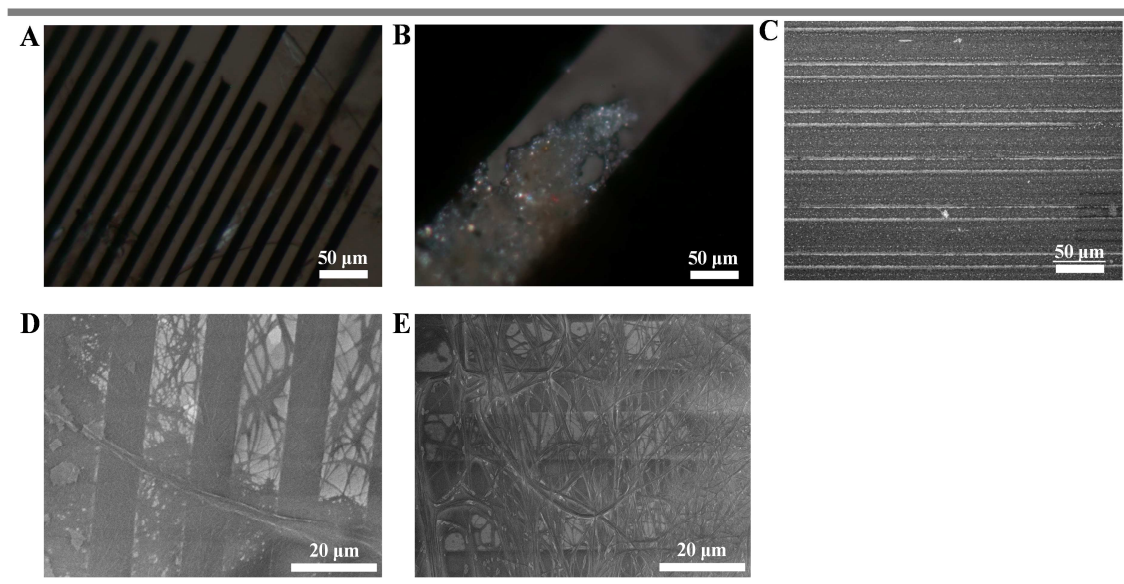


Figure 119. A-B) POM images and C) SEM images of the *in situ* self-assembly of TAA-C8 from a 5 mg/mL heptane solution drop-casted onto the IDEs in absence of a DC electric-field. A) No fibers are present; B) deposition of amorphous material; C) deposition of amorphous material; D-E) SEM images of (D) a 5 mg/mL heptane TAA-C8 gel, re-solubilized at 30 °C and drop-casted onto an IDE in absence of a DC electric-field; E) a 5 mg/mL heptane TAA-C8 gel, re-solubilized at 30 °C and drop-

casted onto a IDE, while a DC electric-field was applied for the entire time needed for solvent evaporation (5 minutes).

Having excluded supramolecular polymerization by other effects than electropolymerization, we continued the study of electric-field induced alignment. A concentration of 5 mg/mL was used to determine the electric-field strength required for alignment, as this concentration resulted systematically in fully filled IDEs. First, we observed that a minimal E_f of $1 \times 10^6 \text{ V}\cdot\text{m}^{-1}$ is required for electropolymerization. Although, electropolymerization occurs under these conditions, the resulting fibers are highly disordered (Figure 120A-B). The minimal E_f required for alignment was $5 \times 10^6 \text{ V}\cdot\text{m}^{-1}$ and alignment proved optimal at an electric-field of $1.25 \times 10^7 \text{ V}\cdot\text{m}^{-1}$ (Figure 120C-D). At this potential, homogeneous alignment of mono-disperse fibers filling all gaps with an orientation parallel to the applied electric-field was observed. The aligned fibers were visualized by POM, SEM and AFM. Using POM, dense bundles of fibers located in the electrode gaps were observed (Figure 121A). However, using SEM, only some isolated fibers passing over the cathode could be visualized, as no good contrast was possible in the gap region due to the large number of fibers present (Figure 121B). This indicates that fiber density is highest in the gap region and that fibers can span distances much longer than the $10 \mu\text{m}$ gap length. This observation was confirmed by AFM imaging (Figure 121C). Moreover, the 3D AFM image (Figure 121D) illustrates well the precise topology of the bridging fibers, showing that the supramolecular polymers are following the curvature of the electric-field during their growth.

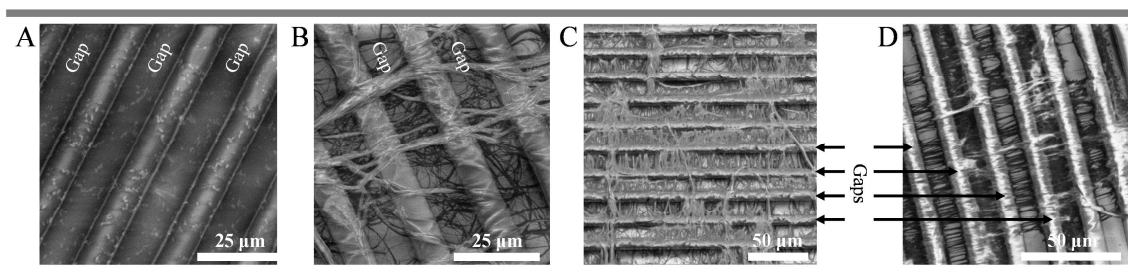


Figure 120. SEM images of *in situ* self-assembly of TAA-C8 from a 5 mg/mL heptane solution between IDEs in the presence of a DC electric-field. Fibers are oriented perpendicular to the electrodes, *i.e.* parallel to the electric-field applied. A) $E_f = 5 \times 10^5 \text{ V}\cdot\text{m}^{-1}$: deposition of amorphous material, no electro-oxidation has taken place; B) $E_f = 1 \times 10^6 \text{ V}\cdot\text{m}^{-1}$: lowest electric-field for which fibers are observed, it is thus the minimal electric-field required for electro-oxidation; C) $E_f = 5 \times 10^6 \text{ V}\cdot\text{m}^{-1}$; D) $E_f = 1.25 \times 10^7 \text{ V}\cdot\text{m}^{-1}$, optimal electric-field for alignment of *in situ* self-assembled fibers.

Working at the optimal electric-field strength, we then varied the concentration and noticed that at a 2 mg/mL concentration isolated fibers that span the entire gap are present in majority (Figure 121E-F). This allowed us to study in detail the fibers present in electrode gaps. We clearly observed that the nucleation always starts from the anode (+ electrode) with the fibers growing towards the cathode (– electrode), following the electric-field’ lines. Additionally, deposition of amorphous material is

visible on the cathode, evidencing that no oxidation takes place here (Figure A3). The supramolecular electropolymerization is depicted schematically in Figure 122A.

This spatially addressed nucleation/growth process was definitely proved by its *in situ* visualization (Annexes Chapter II). The experiments are performed with a 2 mg / mL solution for two reasons. First, we wanted to observe single fibers crossing the gap region. Secondly, as nucleation does not start everywhere at the same time, both shorter and longer fibers can be present. Because of this, at a 5 mg/mL concentration, the fibers are too dense and too disperse in length to observe the polymerization process well. Furthermore, it proved difficult to capture the nucleation/growth process since the limit of the optical microscope was reached. Bigger objectives could not be used because of the working distances: 2 mm glass slides had to be traversed. Furthermore, the gold electrodes caused optical artefacts in many of the videos. Satisfyingly, however, in the resulting video it can clearly be observed that nucleation starts at the anode, directly after drop-casting of the material. In a time span of 11 seconds fibers have grown in direction of the electric-field towards the cathode. It can be seen that no fibers grow from the cathode; no nucleation takes place in the gap region either.

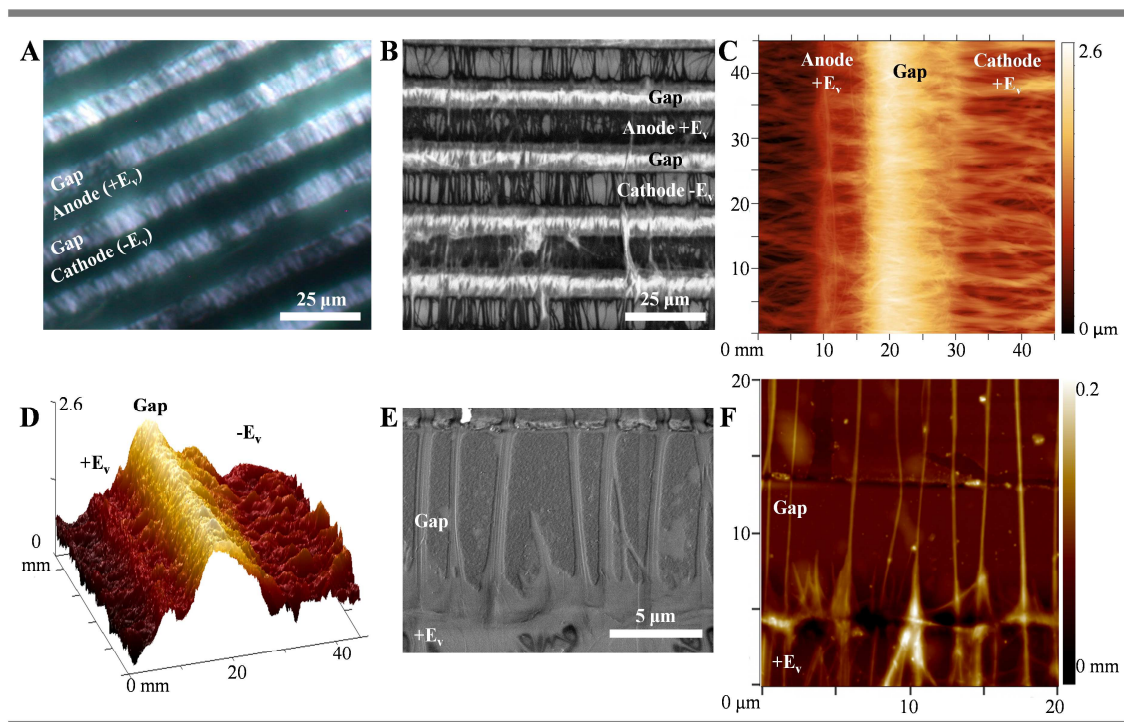


Figure 121. A) POM, B) SEM C) and AFM images of IDEs after drop-casting of a 5 mg/mL TAA-C8 solution in the presence of a $1.25 \times 10^7 \text{ V}\cdot\text{m}^{-1}$ electric-field; D) generated 3D representation of the topography of the AFM image shown in (C); E) SEM and F) AFM image of IDEs after drop-casting a 2 mg/mL TAA-C8 solution in the presence of a $1.25 \times 10^7 \text{ V}\cdot\text{m}^{-1}$ electric-field. Noteworthy is the observation that nucleation solely takes place from the anode.

The quality of alignment was evaluated by calculating the order parameter S ($0 \leq S \leq 1$), which is plotted in **Figure 122B** as a function of the electric-field strength. At the optimal field strength of $1.25 \times 10^7 \text{ V}\cdot\text{m}^{-1}$, average order parameters of 0.94 ± 0.08 and 0.87 ± 0.09 were found, for single fibers that span the electrode gap (2 mg/mL) and single fibers that span the cathode respectively. This indicates that increasing the TAA concentration increases the number of fibers spanning the gaps without modifying the very high quality of the alignment.

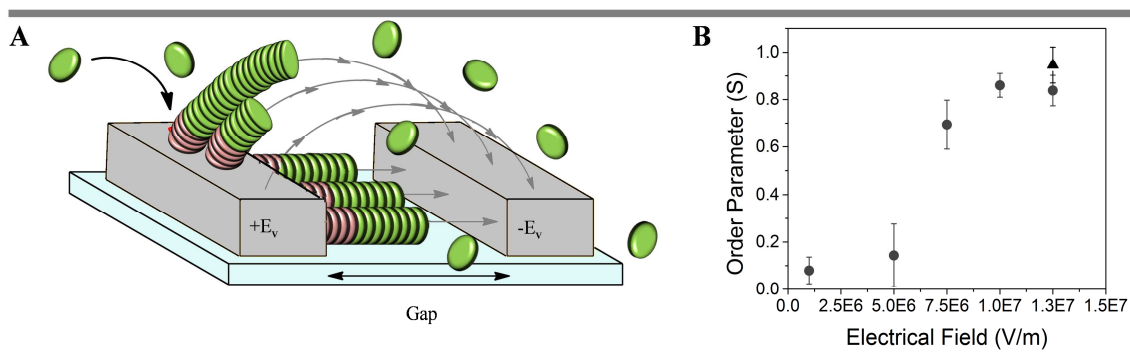


Figure 122. A) 3D schematic representation of the supramolecular electropolymerization process occurring between IDEs as observed in Figure 121D. The green and red ovals represent TAA-C8 and TAA-C8•+, respectively; B) plot of the order parameter S as a function of the electric-field strength applied (dots: [TAA-C8] = 5 mg/mL; triangle: [TAA-C8] = 2 mg/mL). The error bars are calculated from four different regions of the same IDEs.

The alignment of the supramolecular polymers was equally investigated by grazing-incidence wide-angle X-ray scattering (GIWAXS). The obtained data are currently still being treated. Nonetheless, some preliminary conclusions can be drawn from the raw data presented in **Figure 123**. When the X-ray beam is aligned perpendicular to the supramolecular polymers **Figure 123AB**, and thus parallel to the electrodes, the diffraction peaks characteristic for the supramolecular self-assembly are found. We can thus confirm the highly ordered supramolecular architecture of the fibers. Stronger diffractions can be seen along q_z (indicated by the dashed white box in **A**). The sharpness of these peaks provides information on the alignment of the polymers between the electrodes (their average deviation from the normal). If the polymers would be randomly positioned a circular signal would have been obtained. The fact that the peaks are narrow and rapidly decrease in intensity along q_x indicates that the polymers are aligned along the electric fields lines with high order. This could further be confirmed by the spectrum obtained when the laser is turned over a 90° angle (**Figure 123C**). However, no diffraction planes are found, because the beam was not able to penetrate in between the electrodes. In **Figure 123D** the GIWAXS map of a clean IDE is presented for comparison.

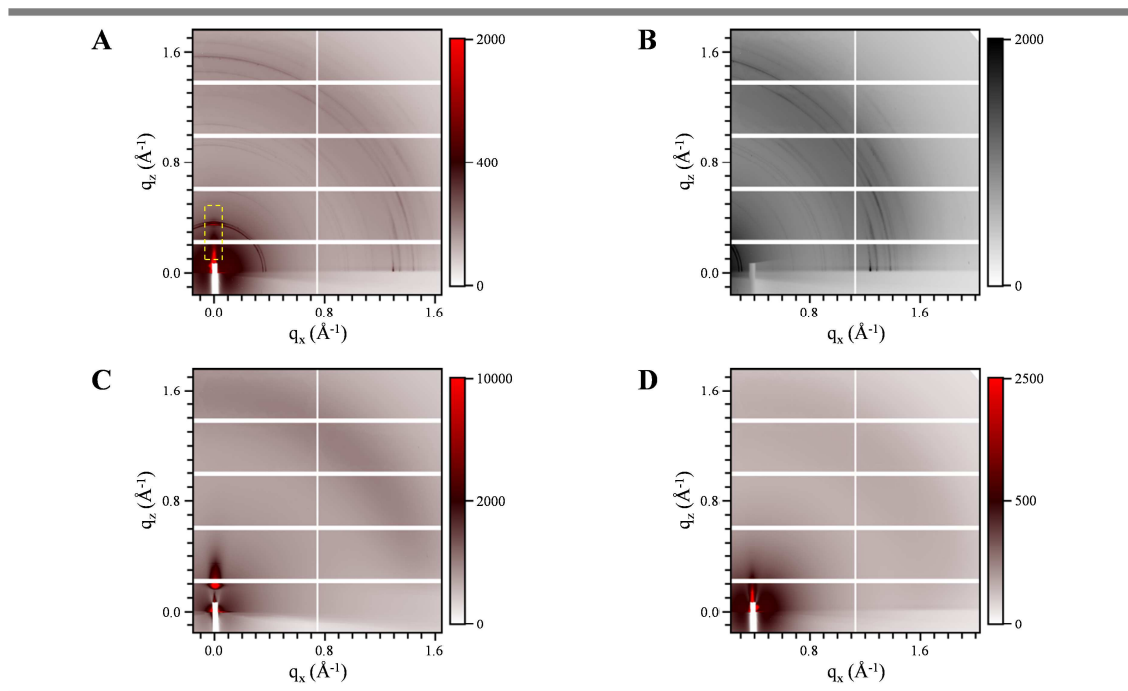


Figure 123. GIWAXS maps of a 5 mg/mL TAA-C8 film drop casted onto a 10 μm IDE under an applied $1.25 \times 10^7 \text{ V}\cdot\text{m}^{-1}$ DC electric-field. A-B) X-ray beam is focused perpendicular to the supramolecular polymers at 9.913° (A) and 14.913° (B); C) X-ray beam is focused parallel to the supramolecular polymers, at 9.913° ; D) X-ray beam is parallel to the gold electrodes of a bare IDE, at 9.913° (blanc sample)

Finally, we turned to IDEs with more complex geometries, namely circular concentric interdigitated electrodes. As can be seen in **Figure 124**, the supramolecular polymers bridged circular IDEs with as much accuracy as the linear IDEs presented before. These experiments show that the supramolecular electro-polymerization process and the electric-field induced alignment are able to take place over large areas (**Figure 124A**). Furthermore, we proved that the wires precisely follow any point in the electric-field's lines (**Figure 124BC**).

Using microarray point electrodes, we were able to grow single supramolecular wires between two pores of 5 μm in diameter and over a distance of 50 μm in length (**Figure 124D**). As fiber growth is only observed when pores are aligned in the DC field direction, the POM images confirms once again that nucleation occurs at the anode and the fibers grow towards the cathode. Moreover, such accurate bridging of two points over 50 μm is, to the best of our knowledge, unprecedented in literature.

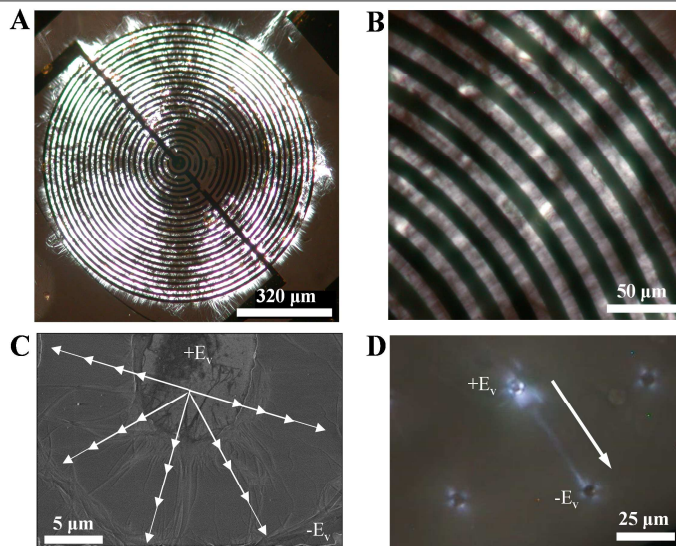


Figure 124. A-B) POM images with two different magnifications of a concentric circular IDE obtained from a 5 mg/mL TAA-C8 solution in the presence of an applied field of $1.25 \times 10^7 \text{ V}\cdot\text{m}^{-1}$; C) SEM image of a U-turn in the concentric circular IDE leading to a radial orientation of fibers in the device (2 mg/mL); D) POM image of a micro array electrode showing a single fiber grown from the anode to the cathode, parallel to the electric-field (white arrow) and over a distance of 50 μm.

E. Charge transport in *in situ* electropolymerized and aligned TAA-C8 supramolecular polymers

The supramolecular system developed in the previous sections is, as explained before, of particular interest in the field of organic supramolecular electronics. However, for the implementation of triarylamine monoamide nanowires into electronic devices, the electronic transport in the fibers should be investigated.

First, we studied the stability of the system formed, or in other words, the reproducibility of the *IV* characteristics over time. Several phenomena could contribute to irreproducible *IV* characteristics. First of all, because of the high electric-field used to induce supramolecular electro-oxidation and alignment, radicals are present in the system. Depending on the decay rate of the radicals and the time of measurement, different results could be obtained. Furthermore, as no counter ions are present to stabilize the radical cations formed upon electro-oxidation, it is likely that they will decay rapidly after the *Ef* has been switched off. We determined that after applying a constant 50 V bias for a duration of 5 minutes, the current measured reaches a plateau (Figure 125A). After removing the constant electric-field, and measuring periodically the current at 100V, we found that it decreases exponentially in intensity. A neutral and stable system is reached after about 75 minutes (Figure 125B).

Secondly, if solvent would remain present in the system, the application of an electric-field could lead to re- alignment processes. A stable system (stable IV curve) was formed after drying the sample for 20 to 50 minutes at 50 °C.

Now that we know how to reach a stable system, we continued by measuring IV^2 curves (Figure 125C), in order to extract the charge carrier mobility within the supramolecular polymers bridging IDEs of lateral geometry. Samples were prepared by drop casting 35 mg/mL solutions onto 10 μm IDEs. Such a high concentration was chosen to ensure that all electrode gaps are fully filled with fibers. The charge carrier mobility was calculated using the space charge limited current (SCLC) approximation, which is justified by the low concentration of charge carriers introduced in the system.⁴²⁰ The change in slope of the IV^2 curve signifies the transition to a trap-free SCLC regime, which is used for the charge carrier mobility calculation. The calculation is based on the assumptions that 1) all monomers participate in fiber formation; 2) the whole electrode surface is covered in fibers; 3) all fibers formed are connected to the electrodes. Thus, the presented mobility will be the lowest possible charge carrier mobility.

It should also be noted that the trap-free SCLC regime could not always be reached, and often low currents were measured, in accordance with the conductive behavior of neutral TAA self-assembled supramolecular polymers.

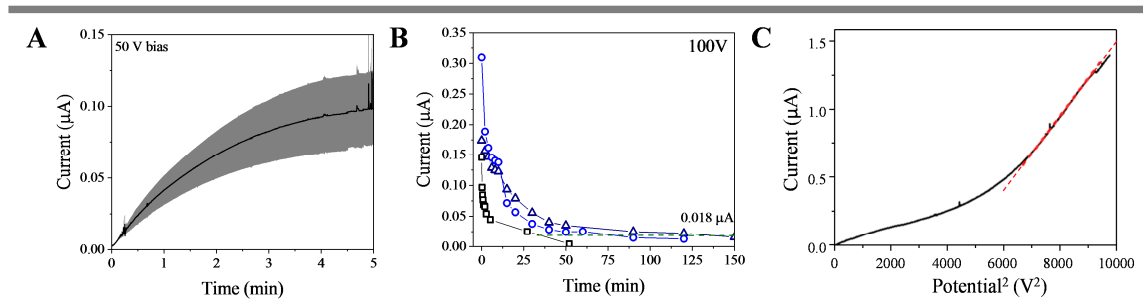


Figure 125. A) Current in function of time, recorded at a continuously applied bias of 50 V. The black line is the average, the grey area represents the standard deviation; B) current in function of time, recorded at an applied bias of 100 V, after the continuously applied field of 50 V was switched off; C) IV^2 curve recorded for a 35 mg/mL TAA-C8 drop cast solution onto a 10 μm IDE.

The charge carrier mobility is derived from the current – voltage curves ~ 35 mg/mL TAA-C8 solutions, using equation II.1

$$\mu = \frac{8L^3}{9A\epsilon} \frac{dI}{dV^2} \quad (9)$$

Where μ is the charge carrier mobility, L is the length of the fibers (here we used the width of the electrode gap), A is the sum of the cross sectional areas of all the fibers, ϵ is the dielectric constant

(assumed to be close to heptane) and dI/dV^2 is the slope of the current potential curve in the trap-free regime. The calculations can be found in the *Annexes Chapter II*; the results are presented in **Table 4**. The calculated mobilities lie close to the theoretical prediction published in the literature.⁴¹²

Table 4. Charge carries mobilities calculated from solutions of ~ 35 mg/mL on IDEs with 5 or 10 μm electrode gaps.

Concentration (mg/mL)	Electrode gap (μm)	Charge carrier mobility (cm^2/Vs)
35	5	0.112
35-36.2	10	0.025-0.56

II.4 Conclusions and Perspectives

We used a triarylamine mono-amide, TAA-C8, to develop the first supramolecular electropolymerization process that simultaneously triggers nucleation specifically at the anode, and allows for directional growth towards the cathode, following the electric-field lines. We have shown that with this process, control over the placement and orientation of supramolecular polymers in between electrodes can be attained. The distances bridged were increased from 100 nm to 10 μm using lateral IDEs with respect to our previous method. Moreover, a precision unprecedented in literature is demonstrated by the bridging of two point electrodes of 5 μm in diameter placed 50 μm apart, by a single nanowire.

This system could still be improved. For example, the conductance of the supramolecular polymers was low. This could be enhanced by (chemical) doping of the fibers afterwards. Changing TAA-C8 by a tris-amide (TATA) could further improve the conductance, as will be explained in Chapter IV. Another perspective concerns the reversibility of the system. The supramolecular polymers formed between the electrodes proved stable for over a year. However, it might be interesting to develop a system in which the fibers are assembled and disassembled by redox-cycling to obtain devices with on/off switch capability. Although this might be difficult to achieve with triarylamine, using the results of this study, it could be conceivable using other molecules with redox functionalities that self-assemble by forming charge transfer nuclei.

In general, the results obtained in this work could be used to spatially control self-assembly processes for the construction of optoelectronic devices, ranging from sensors to solar cells;^{14,392} It could also be pursued for the development of waste-free electrochemistry tools to control (living) supramolecular polymerizations. Or even the development of 3D electrical wiring in organogels. Finally, one can imagine that it could be used to design out-of-equilibrium redox environments for self-organized systems.⁴²¹

CHAPTER III. TOWARDS SUPRAMOLECULAR TRIARYLAMINE- BASED PLASMONIC STRUCTURES

III.1 Introduction

This third chapter is the continuation of the study on plasmonic properties of triarylamine supramolecular polymers, previously commenced in our research group. As detailed in *Chapter 1.4 D. Physical properties of triarylamine self-assemblies*, plasmonic coupling and transport between gold nanoparticles and triarylamine fibers,^{22,24} as well as plasmonic propagation of light in oxidized triarylamine crystals,¹⁷ have been demonstrated.

Organic waveguides usually exhibit a photoluminescence mechanism in which energy is transferred along closely packed chromophores in the form of exciton polaritons generated by the light induced excitation of the molecules.⁴²² However, energy transfer is commonly limited to the nanometer range. Making use of a plasmonic wave-guiding mechanism, which uses the coupling of light with free metallic electrons, propagation lengths up to the centimeter range³⁵² can be achieved. Normally plasmonic wave-guiding is exclusively observed in metallic structures. However, oxidized TAA supramolecular polymers equally possess metallic electrons in their through space charge transfer band.¹⁶ Making use of this property, the plasmonic propagation of light was evidenced in triarylamine trisacetamide (TATA-Ac) single crystals.¹⁷ Our first goal is to explore up to which length scale surface plasmons could propagate along TATA-Ac crystals. Therefore we envisioned the formation of millimeter to centimeter long single TATA-Ac crystals.

As mentioned before, plasmonic effects are usually observed in metals. Nevertheless, some organic materials equally possess delocalized electrons in band-like electronic structures (e.g. tetrathiofulvalene-tetracyanoquinodimethane). These materials, which are called organic metals, could potentially have plasmonic properties. However, to the best of our knowledge and despite advances in organic metals as photonic and plasmonic materials, no examples exist of plasmonic organic nanoparticles. Here we conceived the generation and characterization of triarylamine nanoparticles in order to examine whether localized surface plasmons could be generated.

III.2 Bibliography

A. Plasmonics and the plasmonic effect

A plasmon is a quasi-particle that can be defined as the collective oscillations of free electrons (i.e. quantified plasma oscillations) in the same manner as photons can be defined as the collective oscillations of light (i.e. quantified optical oscillations) and phonons as the collective oscillations of a lattice (i.e. quantified mechanical oscillations). The behavior of plasmons is largely dominated by electromagnetic fields. Bulk plasmons (present in e.g. metals) are generated when an electromagnetic wave (light) with a frequency above the frequency of the free electrons (plasma frequency) passes over the material. Electromagnetic waves below the plasma frequency will be screened by the free electrons of the material and the light is reflected. Above the plasma frequency the free electrons cannot respond rapidly enough to screen the electromagnetic wave. In this case, electromagnetic modes are transmitted into the material and the free electrons experience an oscillation force in the direction of the electromagnetic field lines. At the appropriate wavelength (resonant wavelength) the free electrons will collectively and coherently oscillate in resonance with the incident electromagnetic field. This is known as the plasmonic response.^{423,424} A more commonly studied type of plasmons are surface plasmons. They are generated when an electromagnetic wave interacts with free electrons on a surface, or at any interface of materials, of opposite dielectric sign. Because of the momentary uniform electromagnetic force, imposed by the electromagnetic wave, the free electrons on the surface, now called surface plasmons, will oscillate in resonance with the free electrons present in the bulk material. They are electromagnetically coupled. Furthermore, their momentum is larger than that of light of the same frequency. This means that the electromagnetic fields associated with them cannot propagate away from the surface and the surface plasmons are thus effectively trapped.

There exist two types of surface plasmons: localized and propagating surface plasmons.³⁵⁹⁻³⁶¹ Localized surface plasmons are supported by structures in which the free electrons oscillate at the resonance frequency in three directions; there is a uniform electromagnetic field. Only structures considerably smaller than the wavelength of the incident light are able to experience such a uniform electromagnetic field. This is the case, for example, for spherical plasmonic nanoparticles. Propagating surface plasmons are supported by structures that experience a non-uniform electromagnetic field. This is the case for nano rods and wires in which only one dimension (or two) is much smaller than the wavelength of the incident light. Here, the free electrons oscillate in (at least) one dimension at the resonant wavelength, causing them to propagate along the surface. As mentioned earlier, surface plasmons can be generated at any interface of materials of opposite dielectric sign. They are thus not limited to quantum systems and can be supported by structures of all length scales.³⁶⁰

A particle experiencing plasmonic resonance exhibits far-field and near-field effects. For example, it creates an evanescent near field wave around its structure. The far-field effect is the extinction of incident light due to absorption and scattering (Figure 126A) and is strongly dependent on composition, size and morphology of the nanoparticle. The contribution of the scattering component increases with increasing particle size (Figure 126B).⁴²⁴ At the same time, the absorption spectra will show a blue-shift with particles of decreasing size (Figure 126C).⁴²⁵ More precisely, with decreasing size the gap between valence bands is reduced, which causes a shift towards higher resonance frequencies. The absorption by particles of increasing electron densities is equally blue-shifted. On the other hand, with increasing dielectric constant of the surrounding media, red-shifts are observed. The precise shape and orientation of nanoparticles results in additional resonances and more complex absorption spectra (Figure 126D). Furthermore, particles exhibiting higher levels of anisotropy have a larger scattering component.⁴²⁴

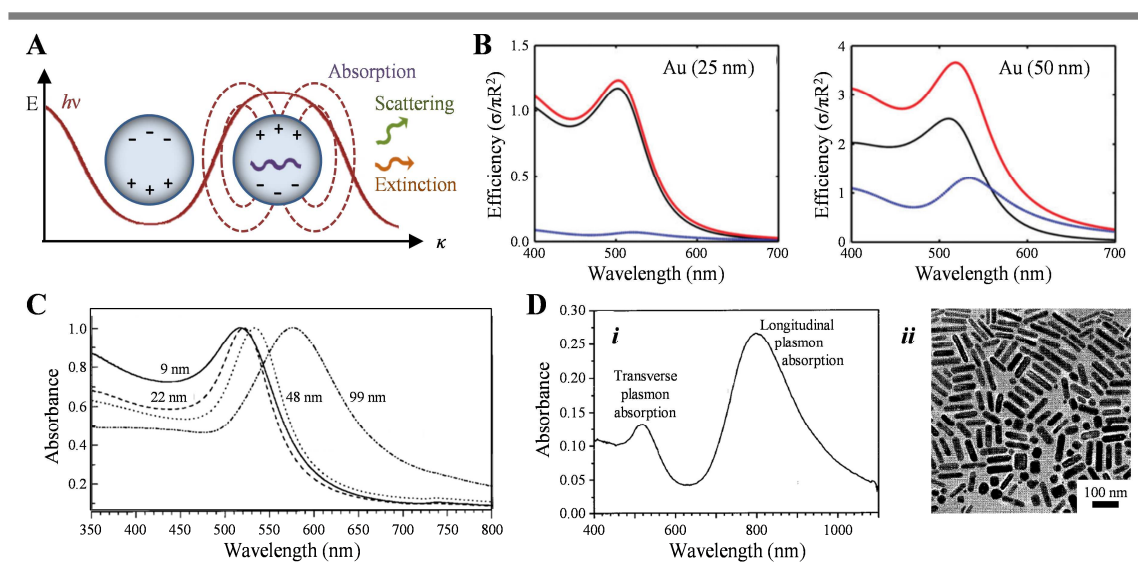


Figure 126. A) Schematic representation of the excitation of a nanoparticle generating a plasmonic response: charge oscillation (purple wave), creation of an evanescent near-field (red dashed circles), light extinction by absorption and scattering far-field effects; B) the contribution of absorption (black line) and scattering (blue line) to light extinction (red line) for spherical nanoparticles of radii 25 nm (left) and 50 nm (right).⁴²⁴ The data are obtained by Mie theory calculations; C) absorption spectra of spherical gold nanoparticles with diameters of 9, 22, 48 and 99 nm, demonstrating the typical blue-shift with decreasing particle size;⁴²⁵ D) absorption spectrum (i) of cylindrical gold nanoparticles (ii, TEM image) demonstrating two absorption bands corresponding to the transverse and longitudinal absorption of the particles.⁴²⁵ This Figure is adapted from references^{424,425}

B. Plasmonic coupling

Besides morphology, composition and size, the plasmonic response of a structure can also be tuned by placing it in close proximity (distance < diameter) of other plasmonic structures. Due to near-field coupling between two nanoparticles, they will act as if one structure, exhibiting new optical

responses. A red-shift will be observed with decreasing distance between two nanoparticles, as shown in Figure 127A.⁴²³ However, the plasmon resonance modes cannot longer be described by classical electromagnetic theory. Instead, based on both theoretical calculations and experimental results, the hybridization theory was developed.^{423,426,427} This theory is analogous to the hybridization theory of atomic orbitals, which describes the linear combination of atomic orbitals into molecular bonding and anti-bonding orbitals. In the same manner plasmonic modes of coupled (nano) structures will hybridize to form new bright (“bonding”) and dark (“anti-bonding”) hybridized plasmonic modes (Figure 127B).^{427,428} This theory has proved to be able to successfully predict plasmonic properties of particles of different morphologies, such as spheres³⁶⁰, cavities³⁶⁰, rods⁴²⁶, discs⁴²⁶ and chains of particles⁴²⁹ (Figure 127C).

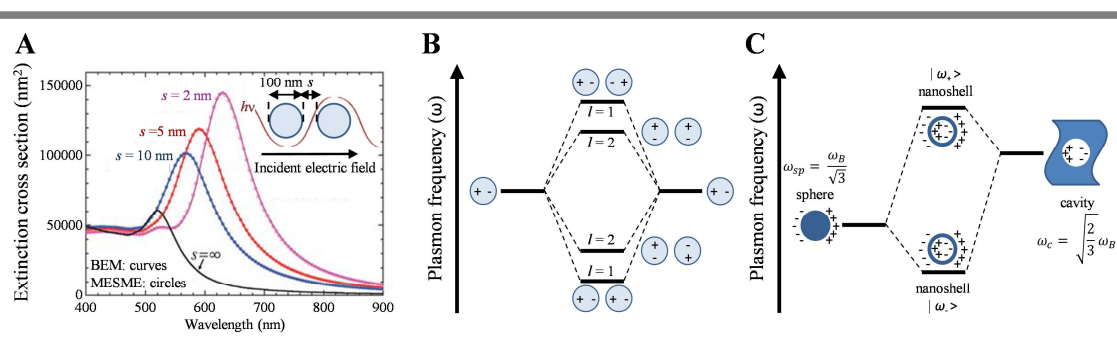


Figure 127. A) Extinction of incident light by two spherical gold nanoparticles of 100 nm in diameter and placed at a distance s from each other. The data is calculated by the boundary element method (BEM) and multiple elastic scattering of multipole expansions method (MESME);⁴²³ B) schematic representation of the energy diagram / plasmon frequency of two spherical nanoparticle upon hybridization. This generates two bright plasmon modes ($l = 1$) and two dark plasmon modes ($l = 2$). C) schematic representation of the energy diagram / plasmon frequency of the hybridization of plasmons of a spherical nanoparticle and a cavity. This Figure is adapted from references^{423,427,428}

C. Plasmonic wave-guiding

As discussed in *Chapter I.4 D. Physical properties of triarylamine self-assemblies*, metallic-plasmonic wave-guides allow the propagation of light in the form of surface plasmons along their structure by the coupling of their free conducting electrons to the incident light.^{352,353} The conversion of light into surface plasmons is spin-forbidden. However, this process can take place due to symmetry breaking, at the distal end of the wave-guide, at defects or by coupling to neighbouring nanoparticles.³⁵⁴ The in-coupling of light can be achieved either by irradiation with a laser source, or by a nearby evanescent field originating from excited state molecules, nanoparticles, or quantum dots.³⁵⁴ Out-coupling of light occurs at defects, kinks and at the other distal end of the nanowire.

Plasmonic wave-guides are able to guide light down to the nanometer range. However, the length over which the light can propagate depends on the propagation length of the plasmons. This propagation length depends directly on the energy losses that occur due to absorption by the material.

The extent of this absorption depends on the dielectric function of the wave-guide and the oscillation frequency of the plasmons.³⁵² Plasmons that can relatively easily couple to or transform into their photonic modes give rise to absorption. The oscillation frequency could also lead to additional energy losses caused by radiative (scattering) and non-radiative (Joule heating) processes. On the other hand, there are several ways in which the propagation wavelength can be increased. First of all, by ensuring evenly-distributed electric fields around the wave-guides. In this manner high intensity electric fields at edges of the interface are diminished, leading to smaller electric fields inside the wave-guide itself and resulting in decreased absorptive losses.⁴³⁰ Moreover, it is generally known that single crystals are able to guide plasmons more easily than polycrystalline nanostructures. To date propagation lengths have been reported spanning from tens of micrometers⁴³⁰ to several millimeters³⁵², even up to the centimeter range.³⁵³ These exceptionally long distances have been obtained using coupled surface plasmon-polariton modes supported by symmetrically clad thin metal films. However, in these cases, the electromagnetic fields extend far into the dielectric, thereby losing its sub-wavelength character.³⁵³ Another parameter defining the quality of the wave-guide is its ability to transform photons into plasmons, which is called the in-coupling efficiency. The in-coupling efficiency depends strongly on the geometry of the distal end of the nanostructure, its diameter and the thickness of the layer between the wave-guide and the substrate underneath.⁴³⁰ Usually, sharp-edged, rough ends or the presence of defects and neighbouring nanoparticles will increase the probability that the momentum of the incident light and free electrons match, which is a criterion for the formation of surface plasmons.

D. Characterization techniques

Both the far field and near field effects of plasmonic structures can be characterized. Far field effects are detected by microscopy techniques, such as optical and fluorescence microscopy. Here, the resolution is limited by the diffraction limit and thus lower spatial resolutions are obtained than for near-field techniques. Nevertheless, they are widely applied because they are easier to perform, more readily available at most research institutes and less expensive. Far-field experiments can be divided in measurements of light scattering, extinction, and absorption, all processes that are governed by plasmonic modes.

Dark-field scattering⁴²⁴ is widely used to characterize the plasmonic properties of nanoparticles. For this method to function several conditions have to be fulfilled: *i*) sample of isolated nanoparticles; *ii*) excitation at large incident angles and collection at small angles to ensure that light reflected by the substrate is not detected. Depending on the NPs plasmon resonance, which is directly related to its nature, size and shape, the scattered light shifts in wavelength (Figure 128A). Polarized scattering experiments allow investigations into a particles orientation and (an)isotropy. For wave-guides, optical microscopy can give strong indications whether a plasmonic mechanisms takes place. A light source is focused through the objective of the microscope to illuminate the nanowire. Plasmonic

wave-guides will not display any wave-guiding if the light source is positioned away from the ends, defects and kinks, which are needed for the in-coupling of light by symmetry breaking. When the light is positioned on these positions, the out-coupling of light will be observed at defects, kinks and at the other distal end of the nanowire (Figure 128B).⁴³¹

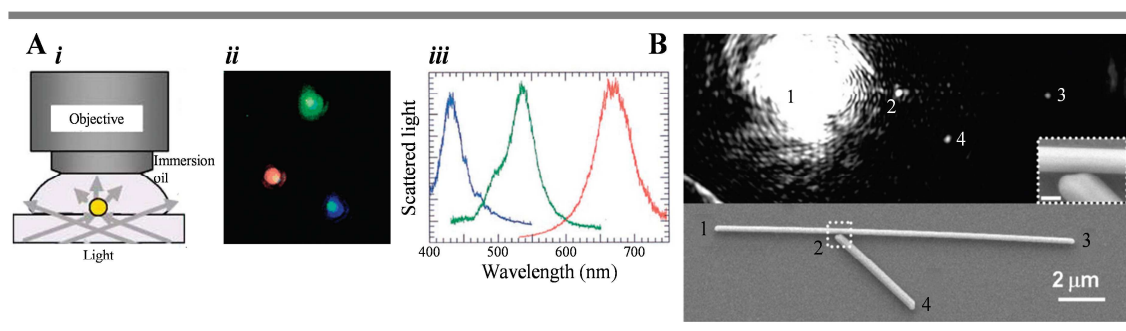


Figure 128. A) Dark-field illumination geometry (i) used to obtain a dark-field scattering image (ii) of silver nanoparticles of various sizes and the corresponding scattering spectra (iii);⁴²⁴ B) Optical microscopy image (top) and corresponding SEM image (bottom) of a silver nanowire. At position 1 the nanowire is irradiated, plasmon propagation along the wire occurs and the out-coupling of light is observed at the nanobranch (position 2), and at the distal ends (positions 3 and 4).⁴³¹ This Figure is adapted from references 424 and 431.

In extinction experiments, the decrease in light intensity due to both absorption and scattering is measured (Figure 129A). A change in sign in collected light intensity demonstrates the transition from scattering dominated extinction to absorption dominated extinction (for larger and smaller NPs respectively). To investigate the isotropy of NPs, differential interference microscopy is used.⁴²⁴ Here the incident light, that is composed of two orthogonally polarized components, creates images constructed from constructive and destructive interference patterns. Isotropic NPs demonstrate evenly distributed constructive and destructive patterns because its refractive index is identical in both polarization directions. On the other hand, anisotropic NPs will display varying constructive and destructive intensities depending on the orientation of the NP with respect to the polarization direction (Figure 129B). Another variation is spatial modulation spectroscopy.

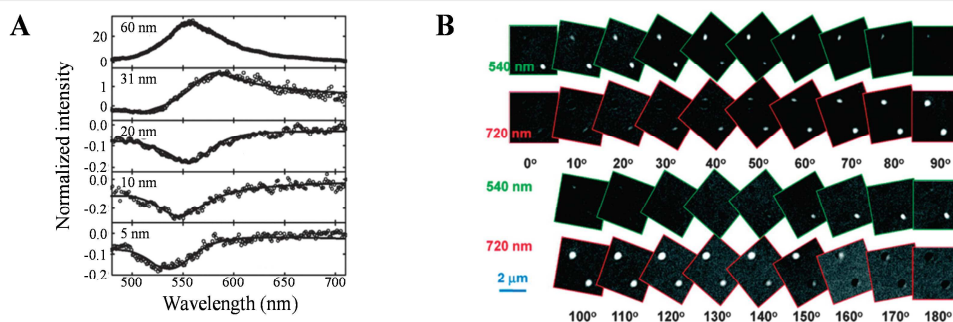


Figure 129. A) Normalized extinction spectra of gold NPs of varying diameter, recorded by a super-continuum white light confocal microscope; B) Differential interference microscopy images taken in

function of 10 different polarization directions for two gold nanorods at two different excitation wavelengths. This Figure is adapted from reference⁴²⁴

Although for small NPs extinction experiments are essentially absorption measurements, for larger NPs other methods have been developed. After absorption, the excited NP first builds up heat by electron-phonon coupling and subsequently releases it by coupling to the vibrational modes of the surrounding media. The change in temperature causes a change of medium refractive index, which is registered by photothermal detectors.⁴²⁴ The photothermal signal is thus directly related to the NPs absorption cross-section. As in scattering and extinction experiments, also polarized absorption measurements exist to study the anisotropy of a NP.

Often, far-field techniques use fluorescent molecules or quantum dots in the near-field of the NP or wave-guide to convert plasmon modes into signals more easily detected in the far-field.³⁵⁴ It was the group of Xu that demonstrated that the near-field, generated by propagating surface plasmons on silver nanowires, could efficiently be visualized, with minimal perturbations, using quantum dot (QD) luminescence (Figure 130).⁴³² CdSe@ZnS QDs were deposited onto the nanowires separated by a 30 – 50 nm thick Al₂O₃ layer as not to interfere with the near-field. Their excitation is directly proportional to the local electric field and thus the near-field distribution brought about by plasmonic modes can be visualized along the whole structure.

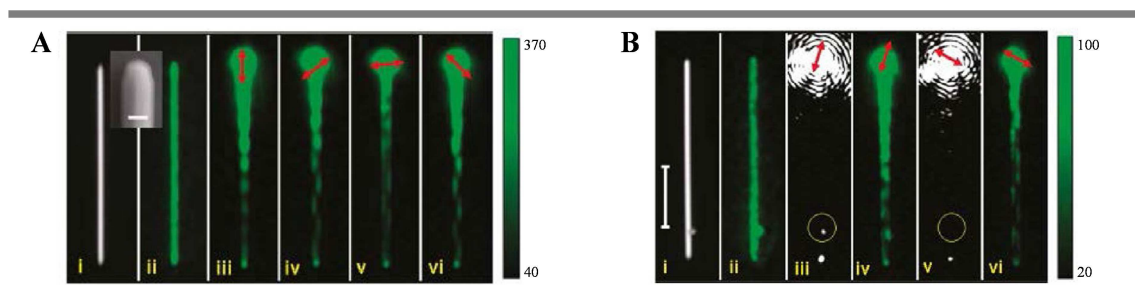


Figure 130. A) Optical microscopy image (i) and SEM image (inset) of an Ag nanowire. Using wide-field excitation, QD emission reveals the uniform coating of the Ag wire with QDs (ii). QD emission images (iii-vi) using different polarizations angles of incident light, demonstrating different near-field distributions around the nanowire; B) optical microscopy image (i) of an Ag nanowire with adjacent NP. Using wide-field excitation, QD emission reveals the uniform coating of the Ag wire and NP with QDs (ii). Scattering (iii, v) and QD emission images (iv-vi) using different polarizations angles of incident light, demonstrating that the emission from the adjacent NP can be controlled by the plasmonic mode generated. This Figure is adapted from reference⁴³²

Another widely-used technique for the visualization of propagating surface plasmons is bleach-imaged plasmon propagation (BIIPP). This technique was first proposed by Solis and co-workers.⁴³³ The plasmonic waveguide is coated with a thin film of a fluorescent polymer. When a plasmon-exciton is created, by excitation of the distal end of the wave-guide, its local near field causes photo bleaching of the thin polymer film. The degree of photo bleaching, measured by confocal fluorescence microscopy, decreases in function of distance along the wave-guide and is directly

related to propagation length of the plasmons. Subtraction of the fluorescence spectra obtained after and before excitation allows the visualization of plasmonic propagation (Figure 131).

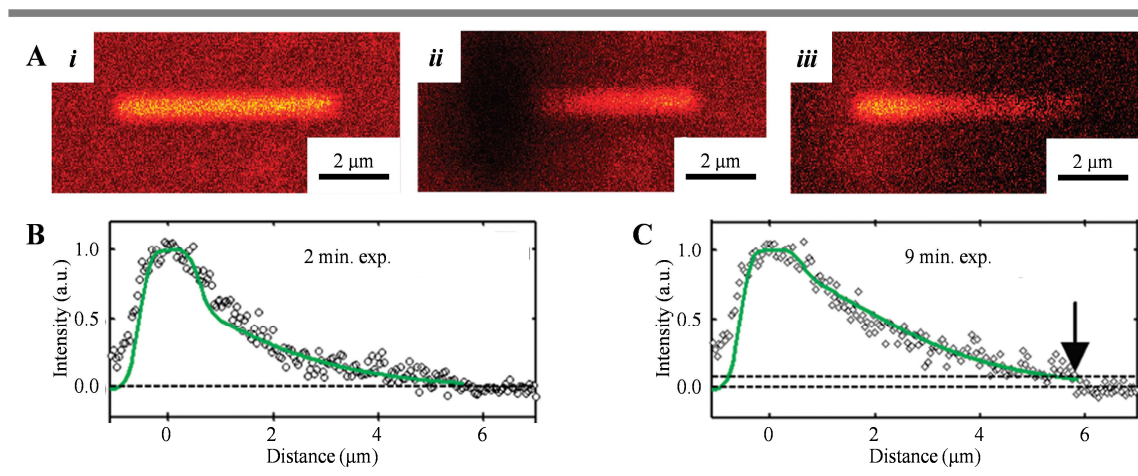


Figure 131. Visualization of plasmon propagation by BLIPP. A) Confocal fluorescence images of an Au nanowire coated in MEH-PPV dye *i)* prior to laser excitation, *ii)* after 9 minutes of excitation and *iii)* the difference image obtained by subtracting *(i)* by *(ii)*; Average fluorescence intensity (image *iii)* in function of distance along the nanowire after 2 (B) and 9 (C) minutes of laser excitation. This Figure is adapted from reference ⁴³³

Although the characterization of a plasmonic structure's optical properties are predominantly performed using far-field techniques, near-field techniques are usually more powerful tools and resolutions from the nanometer down to the atomic scale can be obtained. Many techniques exist that allow for the visualization of the near-field surrounding a material, such as scanning near-field optical microscopy, scanning photoionization microscopy, photoemission electron microscopy, nonlinear luminescence or fluorescence microscopy, nonlinear photopolymerization, near-field ablation, cathodoluminescence and electron energy loss spectroscopy. Out of these techniques, scanning near-field optical microscopy (SNOM) is the only technique in which the electromagnetic near-field of a sample is directly visualized. Both the amplitude and phase of the near-field can be mapped, which allows for the detection of different plasmonic modes and their propagation and coupling to other structures. Doing so, electro and magnetic vector field maps can be constructed, either simultaneously or separately. Different variations on this technique, such as 3D-SNOM,⁴³⁴ plasmon SPNOM⁴³⁵ and dual-SNOM⁴³⁶, as well as the design of specialized tips, demonstrate the great potential of this technique for the design and characterization of optoelectronic devices.

In scanning photoionization microscopy (SPIM), it is not the optical near field that is mapped, but instead the materials photoionization properties.^{437,438} This technique is based on the fact that plasmonic modes not only affect the materials optical properties, but also their photoionization dynamics. Photoemission electron microscopy (PEEM) is based on the same principle. Here, the nanostructure is excited by a light source and the distribution of emitted excited electrons (local

fluctuations in excited electron emission) is used to create a two dimensional image.⁴³⁹ It has the advantage that, in contrast to scanning microscopy techniques, images can be created in real time. Furthermore, higher resolutions can be obtained.

Non-linear luminescence or fluorescence microscopy⁴⁴⁰ uses modest energy levels to excite the sample. Per consequence, the sample mainly displays luminescence or fluorescence in regions where the near-field is enhanced by plasmonic effects. A drawback of this technique is that the sample needs to be coated by a dye or photopolymers.⁴³⁹ This means that it is a destructive method. Additionally, it could also alter the plasmonic modes of the sample itself. The same is true for non-linear photopolymerization⁴⁴⁰, in which the extend of two-photon photopolymerization of SU-8, coated onto the sample, is a quantitative measure for the near-field enhancement around nanoparticles.

Near-field ablation also creates an image of the optical near field in an indirect manner.⁴⁴¹ The nanoparticles are deposited on a smooth substrate (e.g. Si), which is hit by a short laser pulse in perpendicularly direction. When nanoparticles are present, the field is locally enhanced by the interaction between the light source and the free electrons of the nanostructure. And, as the laser has a relatively low intensity, only at these positions will the substrate be ablated. Afterwards, using AFM or SEM techniques the substrate surface is imaged. Using this technique, not only a resolution down to a few nanometers can be achieved, but most importantly no image artifacts are generated due to distortions of the near-field by the presence of a probe or tip.

Cathodoluminescence (CL) microscopy and electron energy loss spectroscopy (EELS) are two electron microscopy techniques used in plasmon detection.^{442,443} In both techniques, an electron beam hits the sample. The electrons in the electron beam, which carry electromagnetic fields, polarize the sample (NPs) upon encounter. As a result, the NP creates an induced electromagnetic field. This induced electromagnetic field is then mapped. In cathodoluminescence, this is done by detecting the energy, in the form of light, emitted by the sample (NPs) into the far-field, as a result of the bombardment. In EELS this is achieved by collecting the energy of the electrons transmitted through a sample. Upon transmission, the electrons from the electron beam interact with the free, valence and core electrons of the sample. Depending on the interaction, the electrons transmitted lose more or less energy. As the electron beam is equally able to interact with both localized atomic orbitals and delocalized bands, also energy transfer and plasmonic coupling effects can be detected. Furthermore, the characteristic collective excitations of the free electrons (plasmons) are detected below the low energy-loss region (< 50 eV) in an EELS spectra.⁴⁴⁴ From an EELS spectra the plasmonic modes can be extracted. Moreover, shifts in these spectra contain information on plasmonic coupling and nanoparticle shape. In contrast to the previous techniques, both CL and EELS are non-invasive and causes minimal sample damage.

E. Organic nanoparticles

Fabrication of organic nanoparticles can be achieved by two methods: bottom-up and top-down.⁴⁴⁵ In the bottom-up approach, coarsening of single atoms or molecules is controlled towards the formation of nanoparticles. In opposition, fragmentation of larger particles into smaller nanoparticles is the basis of the top-down approach.

The bottom-up approach is mainly based on chemical fabrication methods, such as reprecipitation, chemical reduction, ion association, water-oil emulsions, photochemistry, supercritical fluids and cryochemical synthesis. Reprecipitation, or solvent replacement, is a widely used method in which particle size can be controlled by solvent volume and temperature variations. The advantage is that it is carried out under mild conditions. However, only diluted solutions can be obtained. Chemical reduction is one of the most commonly used methods for metal nanoparticle generation, but is only applied for a limited number of organic materials, such as perylene nanoparticles. Ion association is a more commonly used technique. Especially because it has the advantage that no organic solvents need to be employed, and the size of the nanoparticles can be controlled by fine-tuning of the cation to anion ratio.

Nanoparticles can equally be obtained using water in oils emulsions. In this method, nanoparticles crystallize inside droplets by a decrease in temperature. The particle size is thus directly dependent on the droplet size of the emulsion. The photochemical method, which utilizes light irradiation to react a polymer surface with a vapor phase, is used for the formation of acridine dye nanoparticles. Another method is called supercritical fluid technology. The solvent, usually carbon dioxide, is saturated with the material of interest. Then it is brought to its super critical state and diffused through a nozzle into air or a liquid solvent. This is accompanied by a drop in pressure and, as a consequence, the material precipitates. The obvious disadvantage is that only a limited number of compounds are soluble in carbon dioxide. Usually, secondary solvents that (partly) dissolve in super critical carbon dioxide are needed. However, they will contaminate the nanostructure composition and additional procedures (e.g. gaseous anti-solvents, supercritical extraction, and solution enhanced dispersion) need to be applied to reduce this effect. The last method is cryochemical synthesis. A solution containing the dissolved material is deep frozen, forming cryogranules consisting of solidified solvent and material. Then, the solvent is eliminated by freeze-drying and the material sublimates. Nanoparticle size and properties are controlled by the rate of these two processes.

The top-down approach, on the other hand, utilizes primarily physical methods for nanoparticle generation, such as mechanical grinding and laser ablation. Although grinding is one of the most frequently used techniques (either in dry or wet state, using ball and mills of different sizes), many drawbacks have been identified. The main disadvantage is the lack in control over the nanoparticle

shape, uniformity and size-distribution. Furthermore, the surface of grinded particles is often amorphous and contains many defects. This effect is reduced in wet-grinding, but here partial dissolution of the material and subsequent uncontrolled aggregation or crystallization could take place. Moreover, the particles regularly show aggregation problems. This could be avoided in wet-grinding using anti-solvents or by the addition of stabilizing agents. Another general problem is that a relatively large percentage of particles exceeding $> 5 \mu\text{m}$ will be present. Finally, one must keep in mind that impurities, from the ball and mill, could contaminate the sample. In laser ablation, large particles suspended in a poor solvent are fragmentized into nanoparticles by the impact of an intense laser pulse. This allows the formation of stable colloidal solutions, without the need of stabilizing agents. Furthermore, the nanoparticle size can be controlled by tuning of the laser source. However, where grinding is a suitable method for industrial scale production of particles, only small volumes of nanoparticle solutions can be obtained by laser ablation. Also, due to the intensity of the laser source, the organic material could deteriorate.

The fabrication and characterization of organic nanoparticles has received much attention because they, just as their metallic counter parts, can be used in a wide variety of applications. For instance, they are being incorporated in OLED (AIE based luminescent particles) and OFET devices. They are also applied in analyte detection and in green chemistry as nanocatalysts. A large field of application, however, lies in biochemistry and medicine. They are generally less toxic than metal nanoparticles and are more easily dispersed in aqueous solutions.

handedness alternates between two consecutive monomers and the dihedral angle rotates 60° , thus forming a helical snow-flake structure (Figure 132Bi). In this configuration, all amide groups are involved in intercolumnar hydrogen bonding. As a result, all columns are spaced at equidistance. In the column the distance between two nitrogen centers (d1) is 4.173 \AA , the distance between two orthogonal carbons (with respect to the nitrogen center) (d2) is 3.608 \AA , and the distance between an ortho carbon and an ortho hydrogen (d3) is 2.708 \AA (Figure 132Bii-iii). Between columns, methanol molecules are trapped in cavities of a diameter (d4) of 7.9 \AA (Figure 132C).

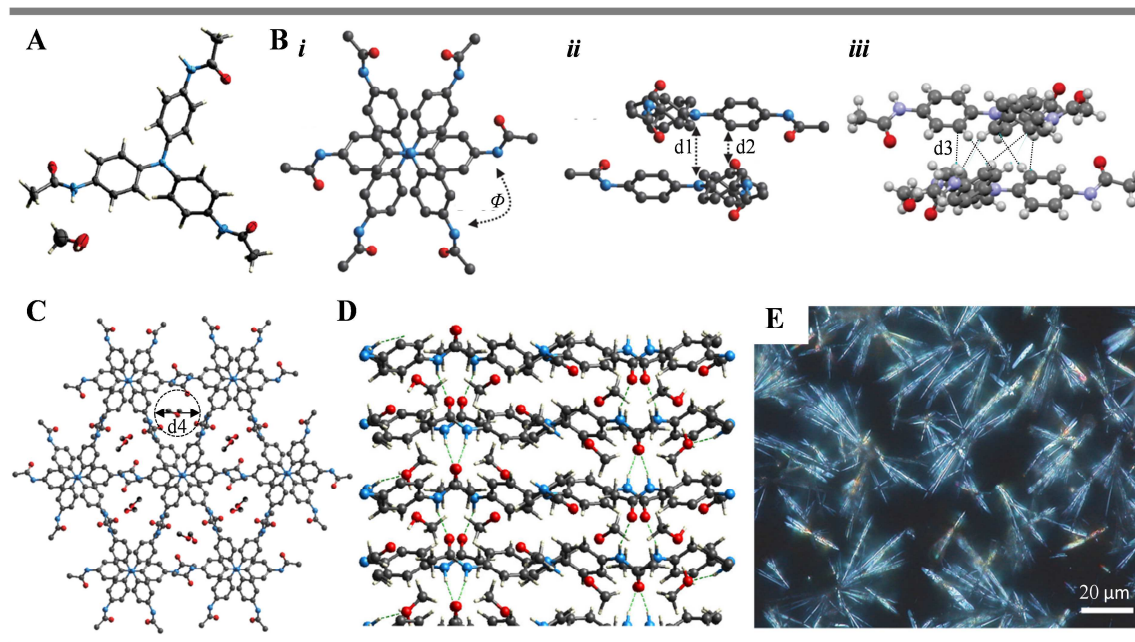


Figure 132. A) Thermal ellipsoid output (50%) of TATA-Ac monomer; B) top (i) and side (ii-iii) views of two stacked TATA-Ac monomers demonstrating the snowflake arrangement (i) and important inter column distances d1-d3 (ii-iii); C) top view of crystal structure (2 molecules thick) showing the intercolumnar cavities and the methanol molecules trapped within; D) side view of crystal structure (2 columns) demonstrating the inter molecular hydrogen bonding network; E) Photograph of the single crystals by optical microscopy under crossed polarizers.

We hypothesized that, by increasing the rate of nucleation, short crystals with a more narrow size distribution could be formed. By rapid nucleation, a large number of nuclei are formed and the size of the crystals will be limited by the amount of remaining monomers. Three methods were tested: i) increased rate of evaporation; ii) decreased solubility due to a decrease in temperature; iii) seeding. Using the methanol toluene solvent mixture, these three methods lead to the direct precipitation of amorphous material. In contrast, crystallization does take place in a methanol ethyl acetate (5:95) solvent mixture. When placed in an ice-bath, both short ($10\text{-}30 \mu\text{m}$) and longer ($100\text{-}500 \mu\text{m}$) crystals were formed (Figure 133A). When the solution is seeded mainly longer crystals were present (Figure 133B). Thus, no successful method could be established to obtain short crystals with monodisperse length distributions.

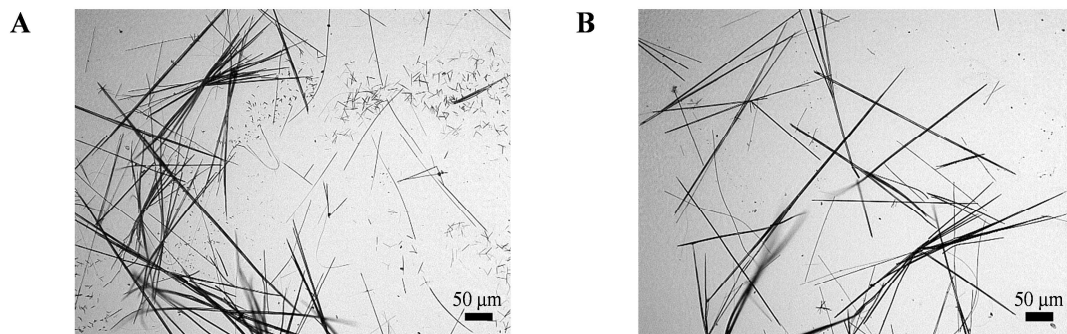


Figure 133. Optical microscopy photographs of TATA-Ac crystals formed in a methanol ethyl acetate solvent mixture (5:95) by slow evaporation. A) vial was placed in an ice-bath; B) solution was seeded.

ii. Large TATA-Ac crystals

The first objective of this project is to determine over which distances plasmonic wave guiding by a TATA-Ac crystal could take place. Therefore the crystallization process describe above was optimized to grow longer single crystals. Several methods were tested, including slow evaporation, liquid phase super saturation, layering and vapor diffusion. The results are summarized in **Table 5**. Only the slow evaporation of a 1.5 mM TATA-Ac methanol ethyl acetate (5:95) mixture resulted in crystals. Here, the good solvent (methanol) has a lower boiling point (64.7 °C) than the poor solvent (ethyl acetate; 77.1 °C). As a consequence, upon evaporation of methanol (increase in concentration toluene), TATA-Ac molecules favor aggregation. Because of the slow rate of evaporation, a self-assembly process towards the formation of single crystals occurs under thermodynamic control.

Table 5. Overview of the different crystallization methods tested and their results.

Method	Conc. (mM)	Solvents	Ratio	Result
Slow evaporation	6.0	MeOH Toluene	75:25	Amorphous precipitate
	8.0	MeOH Toluene	75:25	Amorphous precipitate
	12.0	MeOH Toluene	75:25	Amorphous precipitate
	16.0	MeOH Toluene	75:25	Amorphous precipitate
	24.0	MeOH Toluene	75:25	Amorphous precipitate
	6.0	MeOH Ethyl acetate	5:95	Amorphous precipitate
Super saturation	1.5	MeOH Ethyl acetate	5:95	Crystals
	16.0	MeOH	100	Amorphous precipitate
	16.0	EtOH	100	Amorphous precipitate
Layering	16.0	MeOH Cyclohexane	50:50 in NMR tube	Amorphous precipitate
Vapor diffusion	16.0	MeOH Hexane		Amorphous precipitate
	16.0	MeOH Toluene		Amorphous precipitate

To further improve the crystallization process, solvent ratio, TATA-Ac concentration and temperature were varied in crystallization tests. Samples are prepared by dissolving TATA-Ac in methanol (stirred at 60 °C for ~ 20 minutes) before adding ethyl acetate. This order of preparation is important because, when TATA-Ac is added directly to the solvent mixture, the material would not dissolve, even after prolonged stirring and heating. First the ratio between the solvents was varied (5, 25, 50, 75 and 95% of methanol). Only at 5% methanol crystallization would occur. In all other samples TATA-Ac remains in solution. Then the concentration of TATA-Ac was varied. At 1 mg/mL (2.4 mM) TATA-Ac would directly precipitate as amorphous material when cooling down to room temperature by the addition of ethyl acetate. At 1 mg / 1.5 mL (1.6 mM) millimeter sized crystals are formed after two days (Figure 134A). Interestingly, the same results were obtained with and without slow evaporation. At a concentration of 1 mg / 2 mL (1.2 mM) the molecules stay in solution. Finally, the effect of temperature was studied. Millimeter sized crystals form when room temperature ethyl acetate is added to the methanol solution. Thin centimeter sized crystals are obtained when ethyl acetate is heated prior to addition to a hot methanol solution (Figure 134B). Even larger crystals (two to three centimeters in length and ~ 40 μm in width) are obtained when the hot solution is allowed to slowly cool down to room temperature over the course of 54 hours (Figure 134C). Optical microscopy shows that the crystals are virtually defect free. Moreover, under crossed polarizers, birefringence (non-zero difference in the two refractive index planes) is observed.

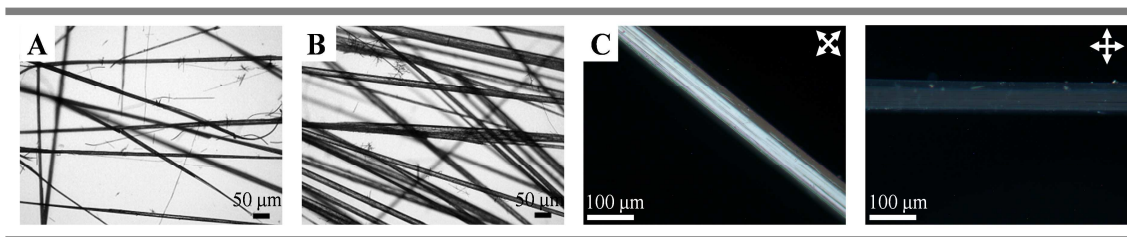


Figure 134. Crystals obtained from 1.6 mM TATA-Ac methanol and ethyl acetate (5:95) solutions. A) optical microscopy image of crystals obtained from a room temperature solution; B) optical microscopy image of crystals obtained from solution of 70 °C that is cooled down to room temperature on the bench; C) cross polarized optical microscopy image (left: 45°, right: 0°) of a single crystal obtained from a solution slowly cooled to room temperature over the course of 54 hours, demonstrating birefringence.

The structure and quality of the crystals were then verified by atomic force microscopy (AFM). Its crystalline structure was confirmed by the characteristic presence of terraces. Sometimes, amorphous material was deposited on the surface (Figure 135A). In order to clear the surface of amorphous deposits the crystals were rinsed. However, as can be seen in Figure 135B, this would generally lead to defects. Fortunately, the surfaces of most crystals were found to be free of amorphous material and defects (Figure 135C). Thus the crystals were not rinsed before any experiments (all chapters included). From the topography images we observe that columns of stacked TATA-Ac molecules are predominantly positioned parallel to the long axis of the crystal. Terraces, on the contrary, are found in all directions, although they always follow the same direction for large crystalline areas. The minimal terrace depths, measured from the height profiles, are approximately $\sim 15 \pm 4 \text{ \AA}$ (Figure 135E). This corresponds to the diameter of a single TATA-Ac column (distance measured from the central nitrogen atom to the methyl end group is 7.896 Å).

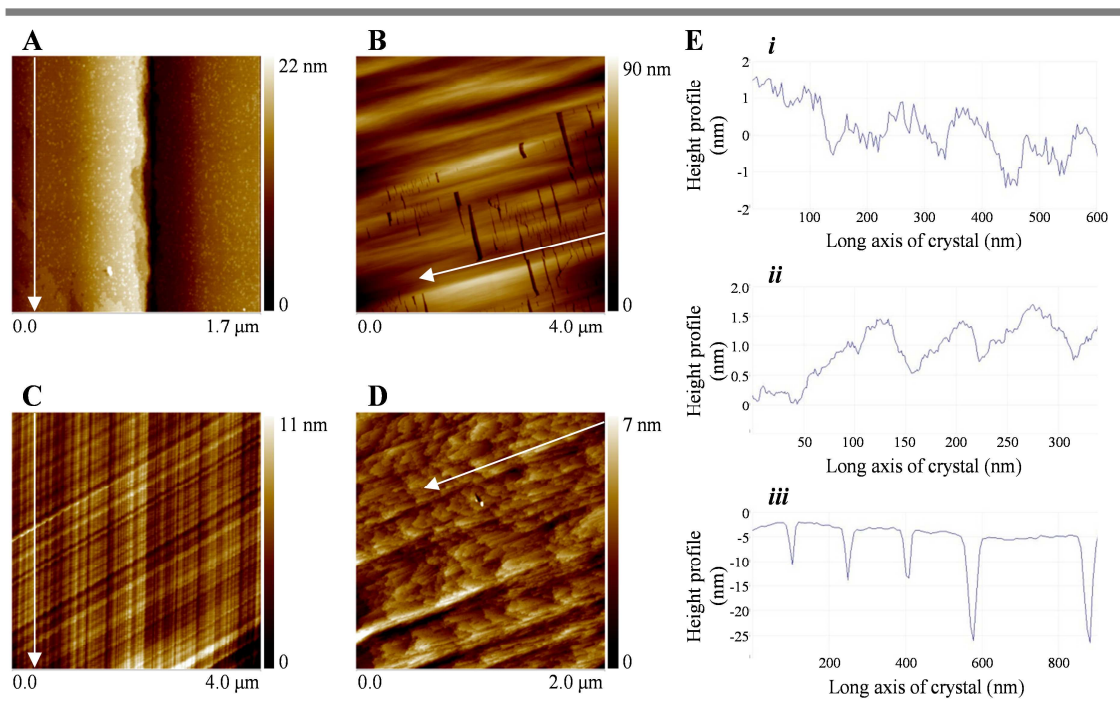


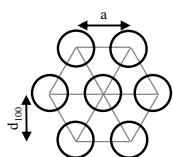
Figure 135. AFM images of TATA-Ac crystals obtained by a slow cooling process in a 1.6 mM solution of methanol ethyl acetate (5:95). The white arrows point in the direction of the long axis of the crystal. A) crystal surface displaying a large terrace parallel to the length of the crystal. A deposit of some amorphous material is visible on its surface; B) crystal displaying defects perpendicular to the crystals length; C) crystal surface free of amorphous material and defects. Terraces are found diagonal to the crystal length. Columns of stacked TATA-Ac in the direction of the crystal length are clearly distinguished; D) the end of a crystal displaying discontinued columns; E) height profiles of the surface of AFM images C (i), D (ii) and B (iii).

The structure was further investigated by X-ray scattering of a powder obtained by grinding down large TATA-Ac crystals (Figure 136A). The positions of diffraction peaks correspond to the distances between diffractive planes and are calculated using the relationship:

$$d = 2\pi/q \quad (10)$$

For crystals, the ratios between diffraction peak positions are characteristic for the crystal system they are formed in. For example, a crystal of hexagonal symmetry will exhibit diffraction peak ratios of 1, $3^{1/2}$, $4^{1/2}$, $7^{1/2}$, $9^{1/2}$, etc.. By comparing the distances obtained from the spectrum and the distances calculated using the diffraction peak ratios, we found that large TATA-Ac crystals self-assemble in a hexagonal symmetry system (Figure 136B). In this comparison the peak corresponding to 11.48 Å is taken as the first diffraction peak, because the peak at smaller angles corresponds to a distance of 47.82 Å, which is much larger than expected for distances between diffractive planes.

In hexagonal systems, the distances between adjacent centers can be calculated as follows:



$$q = 2\pi/d_{100}$$

$$a = d_{100}/\left(\frac{\sqrt{3}}{2}\right)$$

(11)

The thus calculated distance between nitrogen centers of adjacent columns matches, almost perfectly, with the value given by the crystallographic structure (13.256 and 13.254 Å respectively). Other diffraction peaks are present, demonstrating the complexity of the crystal structure and number of diffraction planes. Finally, the slope in the SAXS region of the spectrum gives information on the scattering behavior of the material. Smooth materials exhibit slopes of -4, materials with rough surfaces show slopes between -3 and -4, and mass fractals have slopes between -1 and -3. For TATA-Ac the slope measured is roughly -3.7, which indicates that the primary particles in the powder have relatively smooth surfaces. Below q is 0.01 the slope decreases, probably due to aggregations between particles.

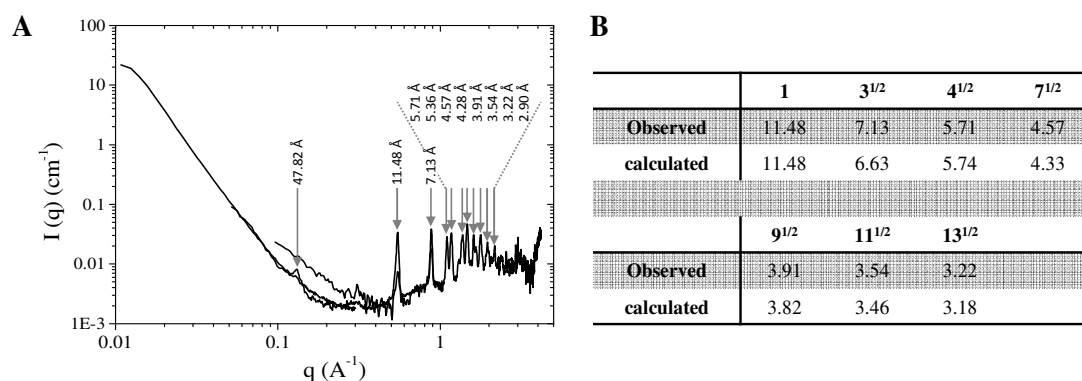


Figure 136. A) X-ray diffraction pattern of TATA-Ac powder in the SAXS, MAXS and WAXS regions; B) Table summarizing the observed and calculated distances between diffraction planes for hexagonal packing.

Finally, crystallographic measurements on single large crystals were performed to determine the crystal system (Figure 137). The monomers are stacked in mono-columnar arrangements with their nitrogen centers positioned along the main axis, just as in small crystals. Also, the same 60° dihedral angle rotation between two consecutive molecules, as well as trapped methanol molecules in between stacks, is observed (Figure 137AB). However, in contrast to small crystals that self-assemble in a monoclinic system, the crystallographic structure of large crystals show hexagonal symmetry, confirming the result found in X-ray scattering (Figure 137C). Although all amide groups are still involved in intercolumnar hydrogen bonding (Figure 137Cii-iii), the intermolecular distances inside a stack are slightly longer (Figure 137E). The distance between two stacked nitrogen centers has increased from 4.173 Å to 4.513 Å, an augmentation of 8.1%. The minimal distances found between

two orthogonal carbons (with respect to the nitrogen center) increases from 3.608 Å to 3.684 Å (+ 2.1%) and between an ortho carbon and an ortho hydrogen from 2.708 Å to 2.828 Å (+ 0.14%). The distance between nitrogen centers of adjacent stacks however, has decreased from 13.254 Å to 13.129 Å (- 0.94%). Furthermore, for the two stacks in the center of the unit cell, the *L* and *D* handedness, between two consecutive monomers, alternates. However, the handedness could not be resolved for the stacks positioned on the four axis of the unit cell (Figure 137D). This could mean that there is an equal probability for the molecules to be in *D* or *L* configuration.

The fact that large crystals (obtained by slow cooling of an ethyl acetate methanol 95:5 solvent mixture) assemble in a slightly different crystal lattice than small crystals (obtained from by slow evaporation of a methanol toluene 75:25 solvent mixture) could impact its physical properties. Especially, considering the increased distance between consecutive nitrogen centers inside a column, which could lead to reduced electronic coupling. Furthermore, the fact that the same molecule is able to self-assemble into different crystalline structures depending on the crystallization method used remains intriguing. This would allow us to study the properties of different supramolecular structures using the same molecule. Moreover, crystallography suggested that large crystals display twinning. This means that different stacking orientations can be found in one crystal. This could equally impact the physical properties, because nitrogen centers are not necessarily stacked in the direction of the long axis of the crystal.

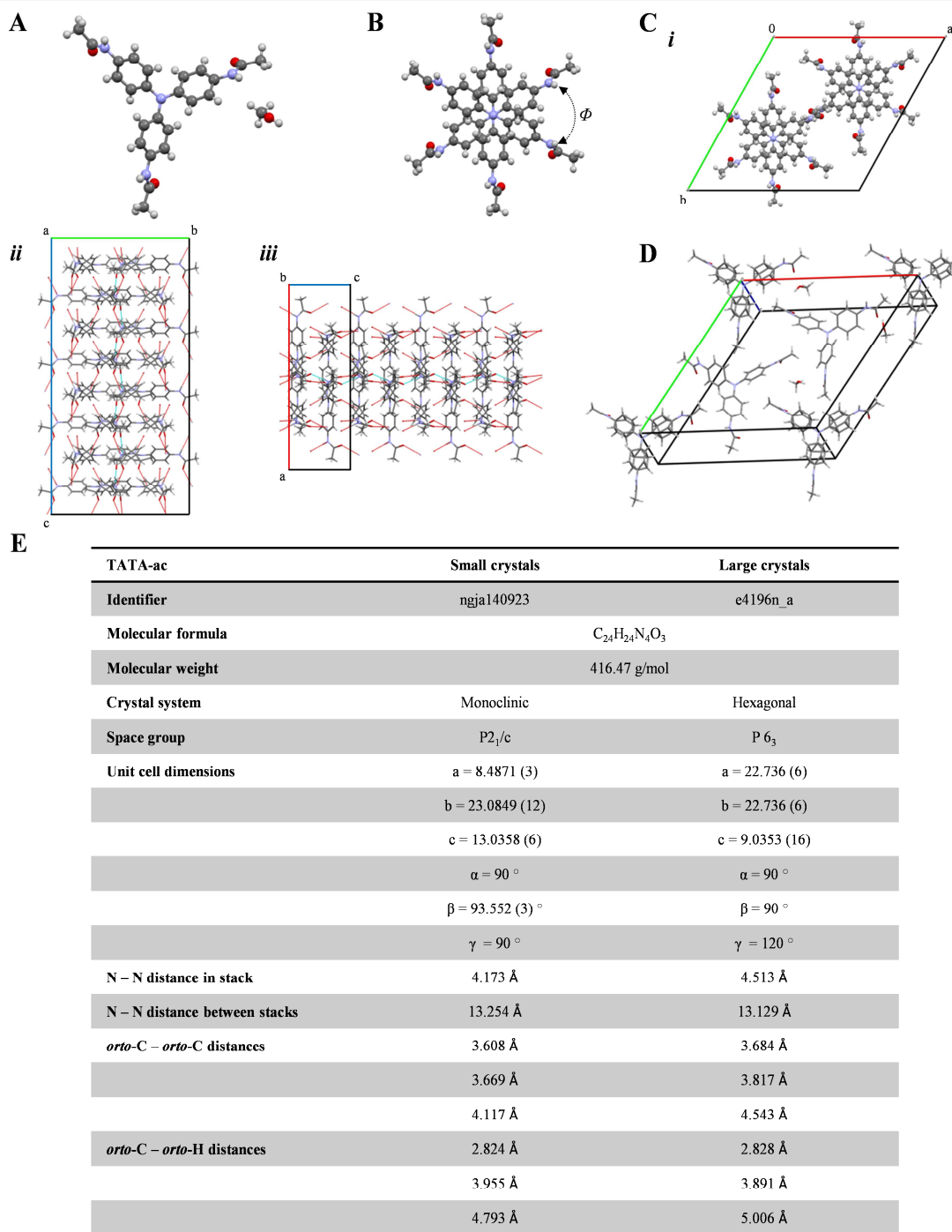


Figure 137. A) Ball and stick output of a single TATA-Ac and MeOH molecule; B) top (i) and side (ii) views of two stacked TATA-Ac molecules; C) view along the c-axis (i), a-axis (ii) and b-axis (iii) of the crystal structure (2 columns) demonstrating the intermolecular hydrogen bonding network; D) table summarizing crystal packing characteristics for small and large TATA-Ac crystals.

iii. TATA-Ac nanoparticles

The second objective of this project is to investigate whether localized plasmonic modes can be supported on triarylamine-based nanoparticles. To observe such a plasmonic effect, the particles should *i)* have dimensions approximately ten times smaller than the incident wavelength; *ii)* should possess free metallic electrons. In this section we tried to fulfill the first requirement, by controlling the self-assembly process towards the formation of nanoparticles. The second requirement can be accomplished by oxidizing TATA self-assemblies, which creates of a through space half-filled polaronic band. This will be discussed in the next section.

There are two manners in which nanostructures can be obtained: top-down and bottom-up. First a top-down strategy was envisioned. TATA-Ac is, even without crystallization process, composed of micrometer sized crystal structures. In addition, it is difficult to dissolve even at low concentrations. Therefore, we reasoned that it would be easier to control the breakdown of crystals into nanoparticles (top-down approach), than it is to control and stop the initial self-assembly process (bottom-up approach).

In the top-down approach, large TATA-Ac crystals were grown as reported in the previous section (methanol ethyl acetate 5:95). Afterwards, the crystallization solvent is removed, in order to eliminate all non-assembled material, and crystals are re-suspended in pure ethyl acetate. In our first methodology, the crystals are broken down by tip sonication and subsequently centrifuged and filtered (0.45 μm and 0.2 μm PTFE syringe filter) to remove large particles. After direct drop casting on cleaned glass slides, spherical TATA-Ac nanoparticles could be observed by AFM imaging (**Figure 138A**). However, aggregation takes place. This is undesirable because for plasmonic analysis (e.g. dark field scattering) individual particles are required. To investigate whether aggregation takes place in solution or due to solvent evaporation effects upon drop casting, samples were prepared by drop casting on a TEM grid, and by spin casting. In both cases, AFM imaging showed aggregations of particles. Thus, aggregation takes place in solution. Aggregation could occur because of the methyl groups that are exposed on the surface of the columns. Consequently we argued that the particles could be stabilized by using more apolar solvents, such as toluene or cyclohexane.

Although tip sonication is a very promising approach, we did not continue in this line. The initial results could not be reproduced, and particle size could not be optimized (e.g. by varying the settings during sonication), because of failure of the apparatus.

In our second methodology we used a glass mortar and pestle to grind down crystals in a small volume of cyclohexane. Then, just as for the first methodology, samples were centrifuged and filtered to remove large aggregates. As can be seen in **Figure 138B**, the particles obtained are approximately 10

times larger than the ones obtained by tip sonication. Nonetheless, the particles are rather regular in size and do not aggregate. Currently we are optimizing this approach by varying the time of grinding (or turns made by the pestle).

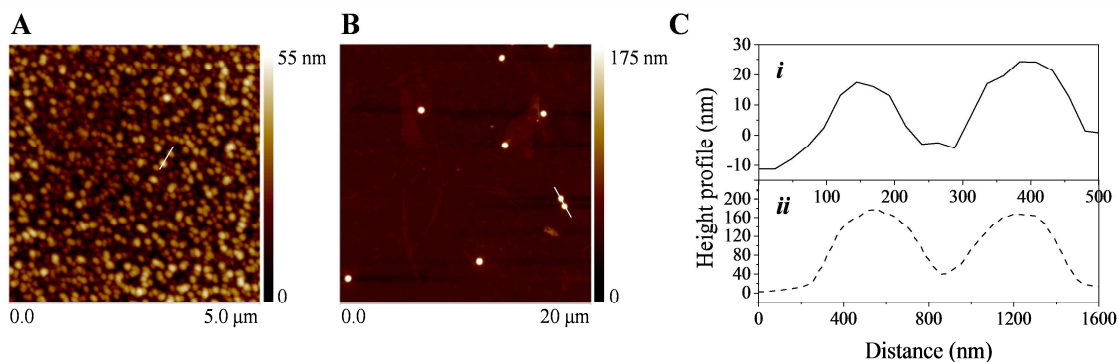


Figure 138. AFM images of TATA-Ac nanoparticles obtained by A) tip sonication of large crystals in ethyl acetate; B) grinding of large crystals in cyclohexane with a glass mortar. Both procedures were followed by centrifugation and filtering to remove large aggregates. The white lines indicate the sections where the height profiles, presented in C, have been taken.

Recently, we have obtained promising preliminary results using reprecipitation. TATA-Ac is dissolved in a methanol chloroform mixture (25:75) to a final concentration of 0.5 mM and irradiated for one hour. While stirring, 10 or 100 μL of the TATA-Ac solution is added to 10 mL of ethyl acetate or toluene, resulting in final concentrations of 0.5 and 5 μM . TEM and AFM imaging of drop casts on TEM grids show large populations of small isolated nanoparticles (Figure 139; Figure A6 and Figure A7).

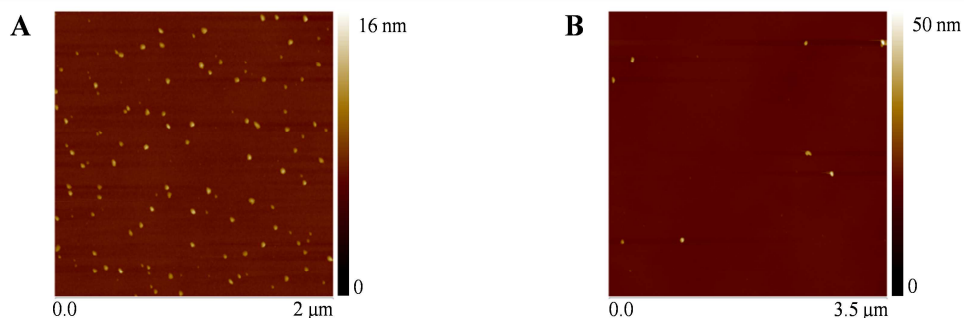


Figure 139. AFM images 0.5 μM (A) and 5 μM (B) drop cast samples (ethylacetate) on TEM grids.

In Figure 140, the height profiles of nanoparticles of average size are shown, as well as the height distribution in the populations. They suggest that particle size can be controlled by sample concentration: ~ 6.5 nm and 21.5 nm sized nanoparticles are obtained for 0.5 μM and 5 μM samples in ethyl acetate respectively. Reprecipitation in toluene generally generated larger particles. Moreover, in toluene, when increasing the TATA-Ac volume, also less defined structures were present.

To determine whether the nanoparticles are amorphous aggregates or structured self-assemblies, photospectroscopy and fluorescence spectra were recorded. Absorption spectra did not show the characteristic absorption bands for oxidized self-assembled TATAs. A band at 300 nm is present, which corresponds to neutral non-assembled TAA and TATA, while bands at 800 nm and 1100 nm, characteristic for oxidized supramolecular structure, were absent. On the other hand, fluorescence spectra, of samples excited with 300 nm light, show a large fluorescence band with a shoulder (Figure 140B). This shoulder can be attributed to a vibrational state. Normally, such bands are only visible at low temperatures or for highly structured materials. It is thus a strong indication that TATA-Ac nanoparticles obtained by reprecipitation do have a crystalline structure.

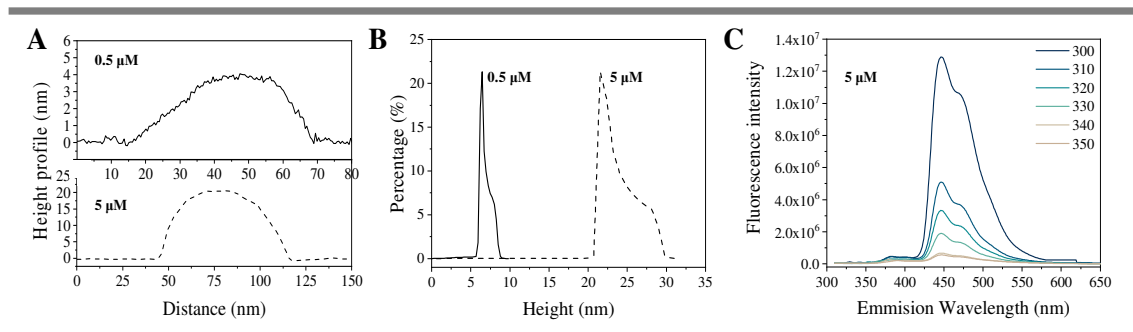


Figure 140. A) Height profiles of average sized nanoparticles in ethyl acetate; B) height distribution of nanoparticles in ethyl acetate (0.5 μM population of ~ 100 nanoparticles; 5 μM population of ~ 20 nanoparticles); C) fluorescence spectra of 5 μM sample in ethyl acetate.

iv. TATA-C4 nanoparticles

Although it is difficult to control the bottom-up self-assembly of TATA-Ac monomers into nanoparticles, we reasoned that it should be more feasible with a more soluble molecule, such as TATA-C4. The short alkyl chains enhance the molecules solubility, thereby giving an opportunity to control the self-assembly initiation and rate. The fact that the alkyl chains are short gives the possibility to self-assemble, not just in long soft fibers as is the case for e.g. TATA-C12, but also into more organized structures. This was demonstrated by optical microscopy images of drop cast samples of a 15 mM TATA-C4 solution in methanol tetrachloroethane (TCE) (5:95) after one hour of light irradiation. Due to solvent evaporation, the monomers are forced to self-assemble into small crystalline structures (Figure 141A). However, when a spin cast is performed, not rods, but cubic particles are present (Figure 141B). We decided to study this system further in order to obtain small TATA-C4 nanoparticles, of crystalline structure, for the development of potential plasmonic organic nanoparticles.

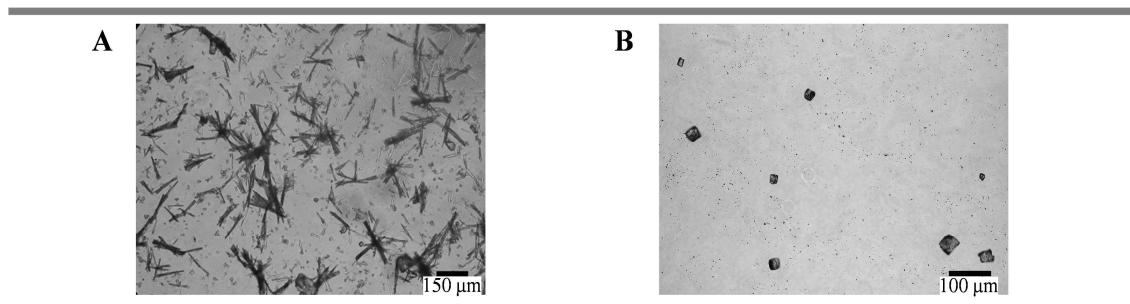


Figure 141. Optical microscopy images of a 15 mM TATA-C4 solution in methanol TCE (5:95), irradiated for an hour. A) drop cast sample; B) spin cast sample.

We adopted the following basic protocol: *i*) 15 mM TATA-C4 in a methanol TCE solvent mixture; *ii*) sonication of the material in solution for a duration of 5 minutes to break down large aggregates; *iii*) heating of the material at 100 °C to fully dissolve it; *iv*) cooling down to room temperature on the bench while *v*) being irradiated for a duration of 60 minutes. In order to observe the structures present in such a solution, we drop casted the sample on a TEM grid and performed SEM and AFM imaging (Figure 142). By SEM mainly cubes are well visualized. The majority of the images showed cubes of an average size of +/- 150 nm, although much larger ones are also present. AFM imaging revealed the coexistence of nanocubes and fibers.

In the next series of experiments we focused on obtaining solely nanocubes. This can be achieved either by favoring the formation of cubes over fibers, or by separating the two species afterwards.

First, we investigated the effect of several parameters on the formation of cubes and fibers. We started by varying the percentage of methanol in the TCE methanol solvent mixture (2.5, 5, 10, 20 vol%). However, a clear difference between samples could not be observed (Figure A8). Only at higher percentages, more amorphous material seemed to be present (seen from optical microscopy images). Therefore, we maintained the original concentration of 5 vol% methanol in TCE. Then, because TATA molecules are able to self-assemble without an oxidation trigger, we investigated the variation of irradiation time on the self-assembly process (0, 5, 15, 30 and 60 minutes). Once more, the various samples did not show apparent differences (Figure A9). However, we started to observe that two types of fibrous structures are often present, soft entangled fibers and more rigid fibers (Figure 143).

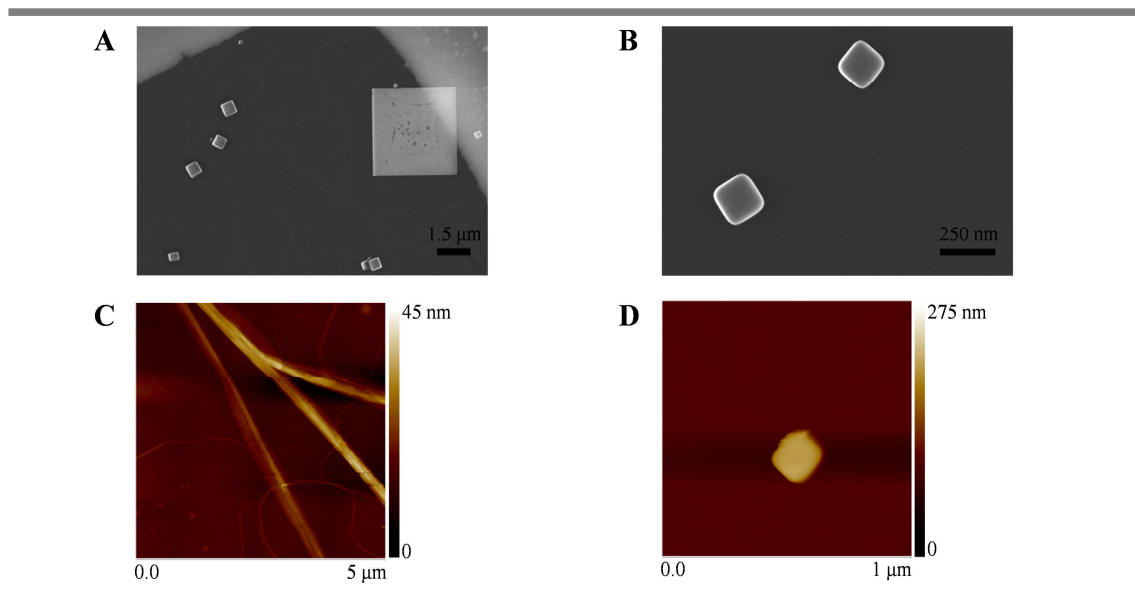


Figure 142. SEM (A,B) and AFM (C,D) images of a 15 mM TATA-C4 solution in methanol TCE (5:95), irradiated for an hour and drop casted on a TEM grid.

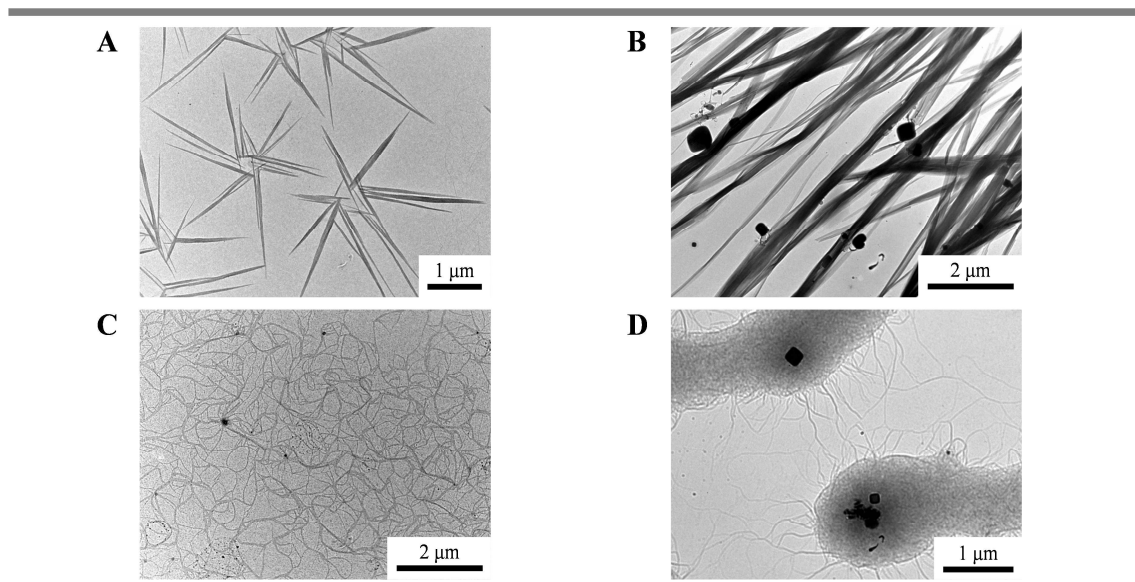


Figure 143. TEM images of fibrous structures usually found in TATA-C4 samples. A) rigid fibers; B) large directional soft fibers; C) loosely entangles fibers; D) dense clusters of entangled fibers.

The next parameter investigated was the cooling rate. The formation of different structures is governed by both thermodynamic and kinetic equilibria and association constants. By varying the temperature during self-assembly, one structure might be favored over another. Usually, one would expect the thermodynamically more stable structure to be formed by a slow cooling process, whereas the kinetically favored product would form upon a rapid decrease in temperature. However, both fibers and cubes are present in *i*) samples cooled slowly over the course of 3 hours, *ii*) samples cooled on the bench and *iii*) samples cooled rapidly by immersion in an ice-bath (Figure A10 and Figure A11).

Finally, we varied the TATA-C4 concentration (0.1, 1, 2.5, 5, 10, 15 mM, **Figure A12**). Although with increasing concentration there is a tendency for larger bundles of fibers to form, no clear effect could be observed on the formation of nanocubes. Thus, in conclusion we can state that by varying the solvent ratio, irradiation time, cooling rate or TATA-C4 concentration, the formation of nanocubes, although they are commonly present, cannot be favored over the formation of fibers. The effects of other parameters, such as different solvents or solvent mixtures, can still be investigated.

We equally investigated the possibility to separate the fibers from the nanocubes after self-assembly. Three main techniques were attempted: *i*) dilution; *ii*) centrifugation; *iii*) filtration. If nanocubes are the thermodynamically more stable species, dilution of the solution would dissolve the fibers while the nanocubes remain intact. Then, by centrifugation, the nanocubes can be collected. As can be seen in **Figure 144A**, centrifugation is an effective method to concentrate nanocube populations. However, in these samples fibers are still present. Moreover, after resuspension of the concentrated nanocubes in the methanol TCE solvent mixture, the nanocubes appear to have more rounded edges and fibers spawn out from there (**Figure 144B-D**). The hypothesis is that after resuspension, nanocubes partially dissolve and from this dissolved material fibrous structures then grow. The dilution prior to centrifugation could equally contribute to this. Resuspensions in various solvents were investigated in order to reduce this effect. Cyclohexane and toluene, two solvents that seem suitable for the stabilization of TATA-Ac nanoparticles, give rise to a dense network of fibers (**Figure A13AD**). Addition of 10 % of ethanol, to increase the solvent mixture polarity, creates a less dense, but still omnipresent fibrous network (**Figure A13EF**). Interestingly, a new observation was made: cubes are found inside circles of fibers (**Figure A14**). Other solvents are still under investigation.

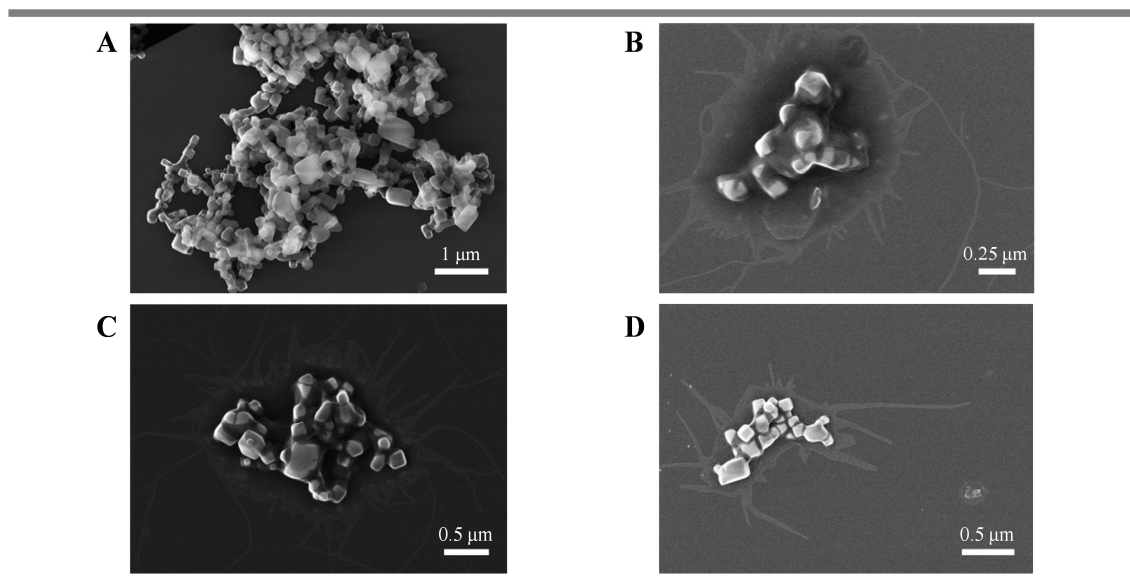


Figure 144. SEM images of 15 mM TATA-C4 solutions in methanol TCE (5:95), irradiated for an hour, diluted B) 2x; A, C) 5x; D) 10x, centrifuged and drop casted on a TEM grid.

Finally we tested whether nanocubes could be separated from fibers by filtration (0.2 μm PTFE syringe filter). In these samples, no nanocubes are detected (Figure A15). They presumably remain behind in the syringe filter. However, they could not be recovered.

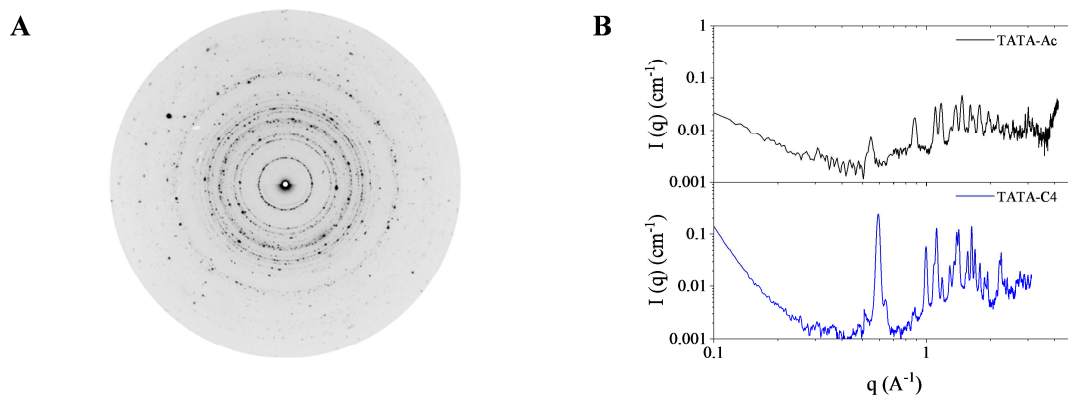


Figure 145. A) X-ray diffraction pattern of TATA-C4 powder; B) X-ray diffraction spectrum of TATA-Ac and TATA-C4.

X-ray scattering, on a TATA-C4 powder, obtained after purification by recrystallization, was performed in order to establish whether or not TATA-C4 self-assemblies have a crystalline nature. As can be seen from Figure 145A, TATA-C4 indeed forms crystal structures and not amorphous aggregates. When we compare its X-ray diffraction pattern with that of TATA-Ac (Figure 145B), and by determining the diffraction peak distance ratios, it is evident that they do not self-assemble in the same hexagonal crystal lattice. Moreover, it seems that multiple structures are present in the powder (just as in the nanoparticle samples). The largest distance between reflective planes (peak at smallest q) corresponds to the nitrogen – nitrogen distance between columns. This distance was found to be smaller for TATA-C4 self-assembled structures than for TATA-Ac crystals. We have already demonstrated that in TATA-Ac crystals the columns are brought together by hydrogen bonding. In order to explain the smaller distance found, we postulate that columns of TATA-C4 do not participate in hydrogen bonding; instead the columns are brought together by van der Waals interactions.

C. Redox properties

To obtain plasmonic structures, the presence of free un-paired electrons is imperative. Therefore, the redox properties of TATA-Ac and TATA-C4 were investigated using photospectroscopy and electron paramagnetic resonance (EPR).

TATA-Ac was dissolved in a chloroform methanol (95:5) solvent mixture by heating at 60 $^{\circ}\text{C}$ to obtain a 0.5 mM solution. This solution was then irradiated and the photo-oxidation process was followed by photospectroscopy (Figure 146A). At time zero only bands < 350 nm are observed, confirming that TATA-Ac is in a molecularly dissolved state without the presence of any radical

cations. With increasing irradiation times the solution turns from colorless to green, which is an indication of the formation of radicals. Furthermore, this green color persists for multiple weeks, demonstrating the high stability of the radicals under these conditions. Upon irradiation, absorption bands around 400 nm, 450-500 nm, 600 nm and 800 nm appear. This absorption spectrum corresponds to the spectrum obtained for small TATA-Ac crystals in a chloroform suspension (Figure A17A).¹⁷ The absorption band at 400 nm stems from π - π stacking of the TATA backbone after oxidation and confirms self-assembly. The band at 800 nm (and at 600 nm: Jahn-Teller effect) is characteristic for the formation of radical cations delocalized between a nitrogen center and its phenyl rings. The band around 450-500 nm is particularly interesting because it is generally not observed for TATA molecules. Neutral and oxidized monomers do not show this band and neither do any oxidized soft supramolecular polymers of the TATA family.¹⁶ It was only observed for small oxidized TATA-Ac crystals in chloroform suspensions and was attributed to Davydov splitting in the crystals.¹⁷ Davydov splitting is the red-shifted absorption transition which results from the splitting of excited state energy levels in *J*-aggregates.⁴⁴⁶ However, upon drop casting a 0.5 mM TATA-Ac chloroform methanol (95:5) solution, mostly amorphous material was observed (Figure A16). The absence of crystals can be explained by the 5 vol% of methanol, which was necessary to dissolve the molecules. Although no crystals are present, small assemblies might be, which would explain the identical absorption bands that are obtained. To gain further insight into the nature of the radical cations generated, EPR experiments were performed. A 1 mM TATA-Ac solution was prepared as previously described and EPR spectra were recorded during photo-oxidation (Figure 146B). A three-line patterned signal, characteristic for unpaired electrons localized on nitrogen atoms, appears and increases in intensity with irradiation time. After 30 minutes, the maximum intensity has been reached, which is slightly faster than observed by UV-vis spectroscopy. Upon comparison with a TEMPO standard (Figure A 19) the radical cation content in the TATA-Ac self-assembled structures was estimated to be between 1 and 3 percent, which is slightly lower than was previously measured for small TATA-Ac crystals.¹⁷

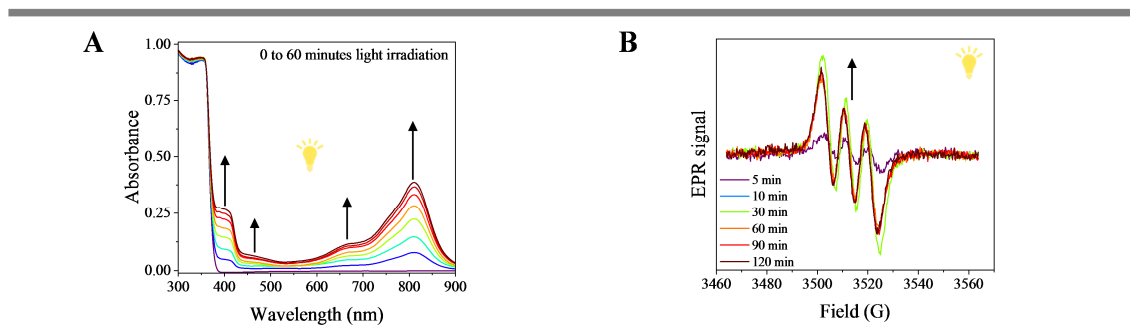


Figure 146. A) Absorption and B) EPR spectra of 0.5 mM and 1 mM TATA-Ac solutions in methanol chloroform (5:95) during various stages in the photo-oxidation process.

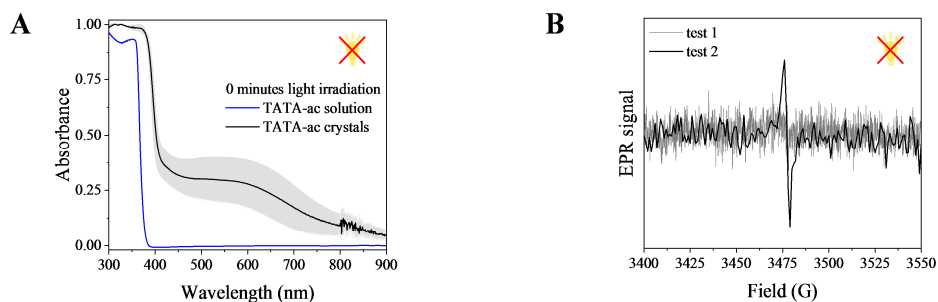


Figure 147. A) Absorption and B) EPR spectra of neutral TATA-Ac crystals recorded in solid state. In (A) the spectra of neutral TATA-Ac monomers in solution (blue line) and of neutral TATA-Ac crystals (black line) are presented. The grey area represents the standard deviation.

The absorption spectrum of large neutral crystals (**Figure 147A**), recorded in the solid state using an integrating sphere (IS), displays a large band between 450 and 700 nm that arises from the self-assembled structure in absence of radical cations. The EPR spectrum of neutral crystals confirms that no unpaired electrons are present in the structure as no EPR signal could be recorded (**Figure 147B**).

Next, the absorption and EPR measurements were repeated after photo-oxidation by resuspension in chloroform and light irradiation. Absorption spectra display the characteristic bands at 600, 800 (delocalized radicals on the phenyl rings) and 1100 nm (through space delocalized radicals) (**Figure 148A**). However, in contrast to the self-assembled structures measured from chloroform methanol solutions, the band at 450-500 nm is not clearly present. Furthermore, EPR measurements demonstrate that, even after one hour of photo-oxidation, only a small amount of radicals are present (< 1 %) (**Figure 148B**). Thus, the absence of the 450-500 nm absorption band can be related to the low number of radicals present in the crystals, which reduces the likelihood of forming *J*-aggregates between radical species. Moreover, samples show large differences in absorption intensity, signifying that photo-oxidations performed in this manner do not always occur with the same efficiency.

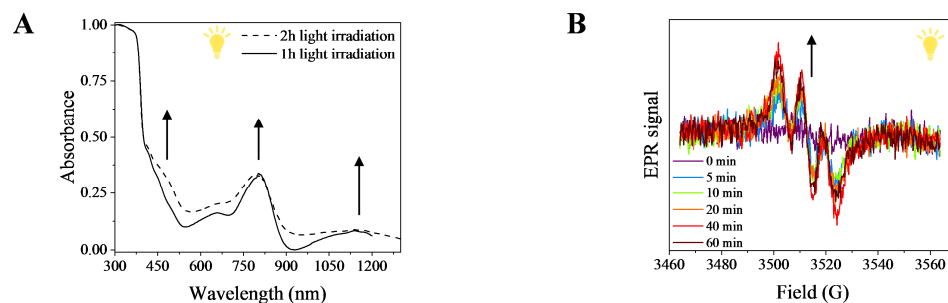


Figure 148. A) Absorption and B) EPR spectra of TATA-Ac crystals, photo-oxidized in a chloroform suspension, and recorded in solid state, after removal of the solvent.

Photo-oxidation was equally attempted during the crystallization process by adding 5 vol% of chloroform to the crystallization solution. Although large crystals do form, photo-oxidation efficiency was poor, as demonstrated by its absorption spectrum (Figure A17BC). Another commonly used oxidation method is chemical oxidation by iodine. Large crystals were oxidized by placing them in a sealed environment containing I_2 vapors. In general, the absorption intensities were too high to distinguish absorption bands and no conclusions can be drawn from the spectra (Figure A18). However, EPR experiments demonstrate a linear increase in signal in function of oxidation time (Figure 149). Interestingly, now an asymmetric one-line pattern is observed. This could be the result of several phenomena. First of all, the one-line pattern could be attributed to an orbital delocalized over the stacked nitrogen atoms. This hypothesis is supported by the extent of charge transfer possible inside the crystals. Indeed, on the contrary to other TATA self-assemblies, even neutral TATA-Ac crystals demonstrate high conductivities (Chapter IV 3C. Triarylamine trisacetamide crystals). This equally explains the small one-line patterned signal observed for neutral crystals in Figure 147B. Upon I_2 oxidation, the crystals are doped and the intensity of this signal increases. In this case, the asymmetry is not a measurement artifact because the areas are approximately equal. However, signal saturation might possibly be at its origin. The one-line pattern and asymmetry could also be caused by structural defects, such as dangling bonds and gaps, induced by the iodine.⁴⁴⁷ This idea is reinforced by the observation that crystals oxidized by iodine often show significantly more defects (Figure A18C). Low concentrations of iodine efficiently oxidize organic materials, as is shown for pentacene crystals by Brinkmann and Turek.⁴⁴⁷ Only at higher concentrations does iodine diffuse into the crystal structure and form intercalates. Therefore we postulate that the one-line pattern first arises due to oxidation of the crystal and introduction of radical cations in a delocalized orbital, however, for longer oxidation times, the generation of defects also partially attributes to the signal increase.

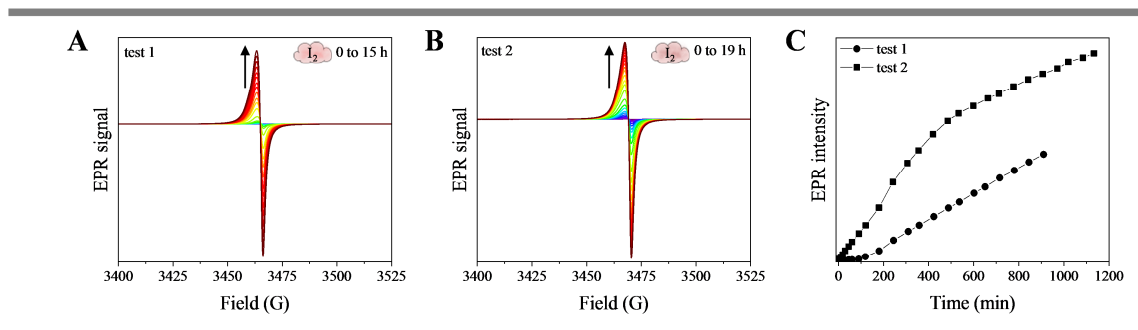


Figure 149. A-B) EPR spectra, recorded in solid state, of TATA-Ac crystals oxidized by I_2 vapors. In B) the I_2 grains were placed in closer proximity to the sample; C) intensity of the EPR signal, obtained after double integration, in function of oxidation time.

From both the photospectroscopy and EPR measurements it is clear that the oxidation of large TATA-Ac crystals is more difficult to achieve and measure, than it is for small crystals oxidized in their chloroform suspension. The following hypotheses could explain this observation:

- Radical cation instability after solvent removal and/or exposure to air
- With increasing size, less oxidation sites are readily accessible
- Oxidation is less efficient due to the crystal structure

The first hypothesis states that the radical cations formed during photo-oxidation in chloroform decay rapidly after removal of solvent and exposure to air. The kinetics of radical decay is uncontrolled in our experiments and reproducibility could be compromised by small time differences between irradiation and measurement. This would explain the variances found in absorption band intensities. However, conductivity experiments performed on dried thin films of TATA fibers (*Chapter IV*), as well as absorption measurements on crystalline TATA-Ac thin films,¹⁷ demonstrate that radicals generally remain present in the self-assemblies after solvent evaporation.

The second hypothesis states that with increasing crystal size, the number of accessible redox centers decreases. With increasing crystal size the volume to area ratio becomes less favorable, which means that a greater percentage of redox centers is buried inside the crystal. Furthermore, radicals generated on the crystal surface, or at its distal ends, probably cannot transfer over the whole length of the crystalline structure, as with increasing size also the number of defects augments.

In the third hypothesis we postulate that there might be a relation between the oxidation efficiency and crystal structure. Small crystals that crystallize in a monoclinic system can be readily photo-oxidized, while large crystals that crystallize in a hexagonal system cannot. Although there should be no difference in the amount of radicals present during nucleation, when photo-oxidation occurs at a later stage the amount of radicals generated also depends on their diffusion within the crystal. In large crystals the distance between nitrogen centers in a stack is larger, which might result in reduced charge transfer. Consequently, the charges stay closer to the crystal surface and fewer charges will be generated due to repulsion effects.

Next, we investigated the redox properties of TATA-C4 by photospectroscopy. In **Figure 150** absorption spectra, recorded during photo-oxidation of a 15 mM TATA-C4 solution in methanol TCE (5:95), are presented. At short irradiation times all characteristic bands, expect the one at 450-500 nm, are present. This corresponds to absorption spectra generally obtained for the TATA family.¹⁶ First, mainly the band at 1100 nm, characteristic for delocalized radical cations, increases in intensity. After a couple of minutes, the band characteristic for delocalized radical cations on the phenyl rings of nitrogen centers rises. Its intensity continues to increase with increasing irradiation times. After 10 to 15 minutes of photo-oxidation the bands at 600 and 800 nm start to broaden until they overlap. This

can be due to precipitation of the material, or due to the presence of different species (nanocubes and fibers).

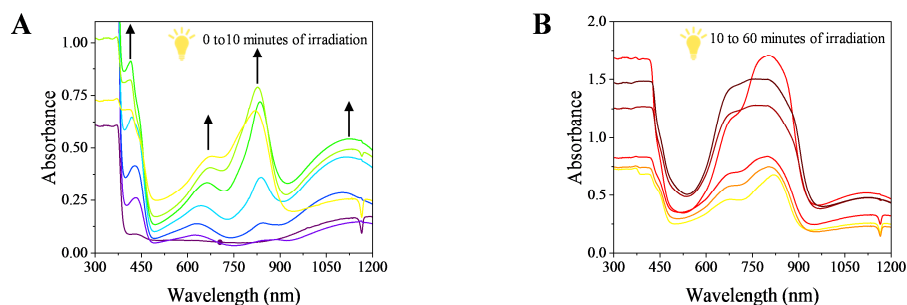


Figure 150. Absorption spectra of a 15 mM TATA-C4 solution in methanol TCE (5:95) A) during the first 8 minutes of irradiation; B) between 10 and 60 minutes of irradiation.

D. Plasmonic properties

i. Waveguiding

As detailed in *Chapter 1.4 D. Physical properties of triarylamine self-assemblies*, the plasmonic propagation of light was evidenced in small oxidized TATA-Ac crystals.¹⁷ Both neutral and oxidized crystals demonstrated waveguiding when pointing a laser, focused through a microscope objective, on one end of the crystal and observing the output at the other end (**Figure 151A**). A photo luminescent mechanism was ruled out because *i*) the crystals do not absorb the wavelength of the lasers used; *ii*) no fluorescence was observed (**Figure 151C**) and *iii*) no wave-guiding is observed when the laser is pointed anywhere but at the distal end (**Figure 151Aiii**). Fluorescence bleaching experiments (**Figure 151D**) showed that neutral crystals exhibit a passive wave-guiding mechanism, whereas oxidized crystals display a plasmonic wave-guiding mechanism. Light scattering along the surface of dye covered crystals is the cause for photo bleaching on neutral crystals. On the other hand, in oxidized crystals, the photo bleaching distance significantly increases due to the evanescent near-field of the energy propagating inside the crystal. Thus, the metallic electrons present in the half-filled polaronic band, generated by photo-oxidation, are able to couple to the incident light and transfer the energy through the crystal by plasmon resonance.

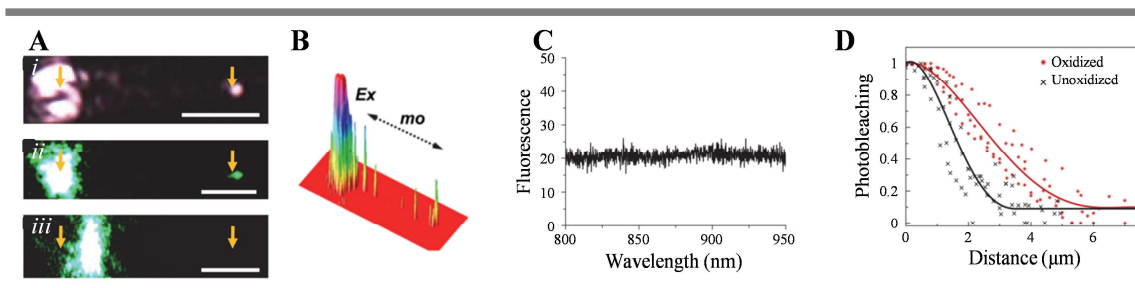


Figure 151. A) Optical waveguiding in TATA-Ac crystals upon irradiation with a 785 nm (*i*) or 532 nm (*ii-iii*) laser. In (*i*) and (*ii*) the laser is focused on left distal end and a wave-guided out-put is observed at the other distal end. In (*iii*) the laser is focused away from the end, here no wave-guiding is observed. The scale bars represent 4 μm; B) 3D representation, obtained from the microscopy images, of the light intensity during wave-guiding along the crystal. In (*i*) multiple outputs are visible because of defects in the crystal. In (*ii*) and (*iii*) the propagation of light along neutral (*ii*) and oxidized (*iii*) crystals coated with indocyanine dye is presented; C) fluorescence spectrum of an oxidized crystal excited by a 785 nm laser; D) photo-bleaching results in function of the distance from the irradiated distal end of oxidized and unoxidized crystals coated with indocyanine dye after performing the wave-guiding experiment. This Figure is adapted from reference ¹⁷

Next, wave guiding experiments were performed using the newly obtained larger TATA-Ac crystals. To start, the crystals were examined using the same experimental set-up as previously described. For this purpose the crystals needed to be broken down into smaller pieces in order to fit in the field of the objective. Through the objective, a 785 or 532 nm laser was focused on one distal end of the crystals, and a clear out-put could be observed at the other distal end (Figure 152). On average, the crystals displaying wave-guiding measured 285 μm in length and 62 μm in width, although waveguiding has been observed in crystals up to 485 μm long. Moreover, approximately 95% of all neutral crystals displayed wave-guiding, 40% of the photo-oxidized crystals and 50% of crystals oxidized by I₂ vapors. The reduced percentage of oxidized crystals that showed waveguiding could directly be related to the quality of the crystals, as more structural defects were present (Figure A20). The higher amount of defects observed in crystals used for wave guiding experiments are probably caused by the fracturing of crystals into smaller pieces. Moreover, oxidation by I₂ vapors could further affect the structure integrity of the crystal. When structural defects are present, multiple light outputs along the crystal structure were observed (Figure A20). When the laser is focused away from the ends and defects, no wave-guiding was observed (Figure 152*iii*).

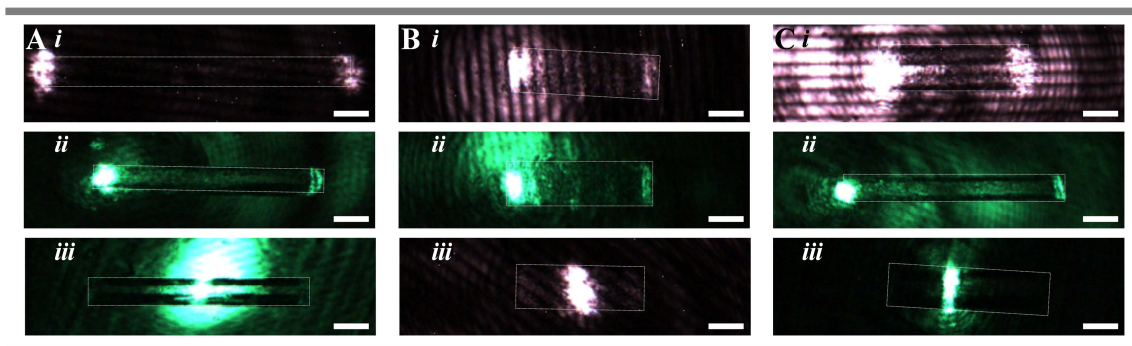
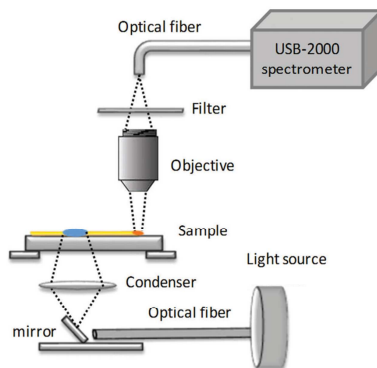


Figure 152. Optical microscopy images of neutral (A), photo-oxidized (B) and I₂ vapor oxidized (C) TATA-Ac crystals demonstrating optical wave-guiding after illumination of the left distal end of the crystals with a 785 nm (i) and a 532 nm (ii) laser. No waveguiding is observed when the laser is focused in the middle of the crystal. The white dotted rectangles trace the outlines of the crystals. The scale bar represents 50 μm .

The goal of these experiments was to determine over which distances light could propagate in TATA-Ac crystals. Here, using the large TATA-Ac crystals it was demonstrated waveguiding is possible over at least 485 μm . However, the original crystals are much longer. Furthermore, the fracturing of crystals lead to structural defects and reduced wave guiding efficiency. Therefore, before determining the waveguiding mechanism, it was decided to envision another experimental set-up in which the distal end of a crystal can be illuminated outside the objective field. In collaboration with Dr Pfohl and Prof Reiter from Freiburg University, waveguiding experiments were performed using the set-up presented in **Scheme 10**. A blue LED was focused on one distal end that lay outside the objective field, while the light out-put could be observed at the other distal end, which was positioned inside the objective field. However, no wave-guiding was observed for any crystals. We hypothesize that the in-coupling of light is inefficient because the light source is *i*) composed of a band of wavelengths; *ii*) incoherent; *iii*) less focused (50 μm spot instead of 2 μm spot) and thus less intense. Yet, changing the blue LED light source for a laser light source is not applicable. The light source is aligned onto the crystal by eye, and this would not be possible with a laser. Therefore, the waveguiding experiments were discontinued.



Scheme 10. Schematic representation of the UV-Vis photospectrometer coupled to optical microscope used for waveguiding measurements. This Figure is adapted from reference ⁴⁴⁸

ii. Plasmonic nanoparticles

We have shown that by reprecipitation stable suspensions of isolated TATA-Ac nanoparticles can be obtained. The absorption spectrum of a 5 μM TATA-Ac NP suspension shows an absorption band at 500 nm (Figure 153AB). This band cannot be attributed to electronic transitions normally occurring in TATA self-assemblies, which gives rise to the strong supposition that it is a plasmonic band. Such bands are generally observed in solutions of gold or silver nanoparticles (~ 520 nm absorption band for 10 nm sized AuNPs). Here, the wavelength at which the absorption intensity is maximal, is red-shifted for larger particles. Thus, in order to ensure that we have a plasmonic absorption band, the absorption spectra of solutions containing TATA-Ac NPs of different sizes should be recorded. In Figure 153C, the fluorescence spectra of the same solution are presented. The solution is excited by a range of at wavelengths which TATA-Ac crystals normally do not absorb (450 – 600 nm). Yet, an emissive signal is recorded. The shift of this peak indicates that the putative emission is caused by scattering of the incident light. However, when excited with a wavelength between 510 and 540 nm, where the NPs absorb, the emission wavelength does not shift. This indicates that the response originates from the nanoparticles and might be caused by the plasmon effect.

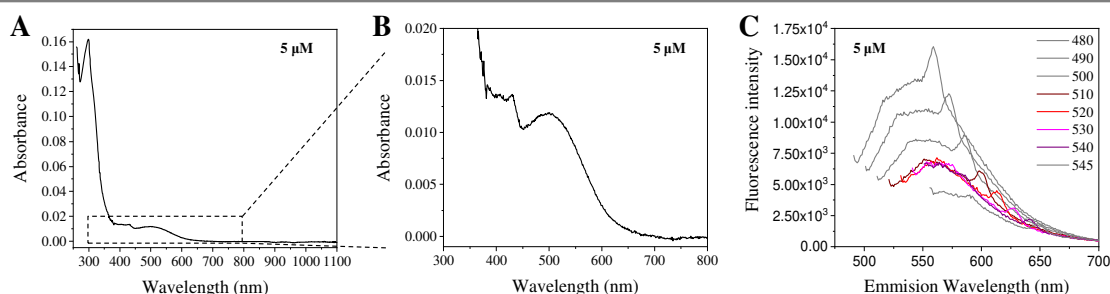


Figure 153. A) Absorption spectrum recorded for a 5 μM TATA-Ac nanoparticle solution in ethyl acetate; B) zoom of the spectrum presented in (A); C) fluorescence spectra of the same solution when excited with 480 – 545 nm light.

III.4 Perspectives

Towards TATA-Ac plasmonic nanoparticles

In order to develop a reliable method to obtain TATA-Ac nanoparticles, we will continue our investigation on the formation of NPs using the reprecipitation method. Of particular interest is the formation of NPs of tunable size, which could be achieved by varying temperature and the volumes used. Although we have a strong indication of the NPs crystalline nature, TEM and X-ray analysis might shed more light on the precise crystal structure formed. Furthermore, it would be desirable to obtain both doped and neutral NPs from irradiated and non-irradiated solutions respectively. The comparison of neutral and doped NPs will help elucidate if the doped NPs generated have a plasmonic character, as only doped TATA-Ac crystals have demonstrated plasmonic properties so far. The characterizations envisioned for the NPs are:

- UV-Vis-NIR photospectroscopy of NP solutions of different size. If the absorption band at 500 nm is a plasmonic band, a red-shift will be observed with increasing NP size.
- EELS in collaboration with the Laboratorio de Microscopias Avanzadas (LMA) at the Instituto de Nanociencia de Aragon (INA) - Universidad de Zaragoza (Spain).
- Dark-field scattering and/or other far field or near-field techniques discussed in the bibliography section.

Towards TATA-C4 plasmonic particles

We would equally like to continue our study on TATA-C4 NP formation. Although several parameters could still be investigated to favor the formation of cubes over fibers (e.g. different solvents and/or solvent mixtures), it would be interesting to test the reprecipitation method developed for TATA-Ac NP formation. When stable and isolated NPs are obtained, we anticipate to perform the same characterizations as described for TATA-ac NPs.

III.5 Conclusions

The first objective of this project was to investigate over which length scales surface plasmons could propagate along TATA-Ac crystals. Therefore, the crystallization process was optimized for the acquisition of larger crystals. We demonstrated that the self-assembly process of TATA-Ac can be efficiently controlled by either a slow solvent evaporation process in methanol – toluene, for the formation of small ~40 μm crystals, or by a slow cooling process in methanol – ethyl acetate, for the formation of crystals up to 3 cm in length. The small crystals are formed in a cubic lattice, whereas the large crystals are formed in a hexagonal crystal lattice. In order to act as plasmonic wave-guides, the crystals need to be oxidized. This was easier achieved for the small crystals than for the larger ones. We postulated that this could be the result of *i*) radical cation instability after solvent removal and/or exposure to air; *ii*) the increased size, which leads to less readily accessible oxidation sites; *iii*) less efficient oxidation due to the crystal structure. Yet, we demonstrated that the large crystals retain their wave-guiding abilities over at least 500 μm . Unfortunately, measurements over longer distances could not be performed due to limitations in the experimental set-up.

The second objective was to investigate whether localized surface plasmon modes could be supported by TATA self-assembled nanostructures. As only structures approximately ten times smaller than the wavelength of the incident light exhibit plasmonic responses, we developed several top-down and bottom-up approaches to obtain TATA nanoparticles. Using TATA-C4, we hypothesized that, because of the longer alkyl chains that increase the molecule's solubility, a bottom-up methodology could be more easily established. However, TATA-C4 samples show the presence of different self-assemblies, such as cubic nanoparticles and fibers. The formation of one structure over the other proved difficult to achieve, and also their separation is challenging. Because of the presence of multiple self-assembled structures, the samples have not yet been characterized for plasmonic effects.

Also for TATA-Ac NP formation multiple approaches have been investigated. Top down approaches included sonication or wet grinding of large particles into small particles, and particles of ~ 30 and ~ 150 nm were obtained respectively. Reprecipitation, a bottom-up approach, led to particles of 5 – 20 nm, depending on the volumes used. This later method has the advantage that no aggregation takes place. Preliminary results indicate that the nanoparticles have a crystalline structure. Furthermore, both absorption and fluorescence experiments suggest that the oxidized nanoparticles exhibit a plasmonic effect.

CHAPTER IV. ELECTRONIC TRANSPORT IN VARIOUS TRIARYLAMINE SUPRAMOLECULAR POLYMERS

IV.1 Introduction

Typically triarylamines are characterized by their electronic and optical properties. These properties are enhanced in triarylamine supramolecular polymers due to the close stacking between the central nitrogen centers, which results in strong electronic coupling. This was already demonstrated by the alignment of supramolecular triarylamine polymers in between electrodes with 80 nm electrode gap channels, under the influence of an electric field.²⁶ The fibers, formed upon photo-oxidation, exhibit exceptional conductivities ($> 5 \times 10^3 \text{ S}\cdot\text{m}^{-1}$) and low contact resistance ($< 2 \times 10^4 \text{ }\Omega\cdot\text{m}$) due to the presence of metal-like electrons in their structure.

However, depending on the chains and functionalities on the periphery, triarylamines self-assemble in different ways. For example, although mono- and trisamides are both able to self-assemble into soft supramolecular polymers, they grow from double and mono columnar nuclei respectively, which represent a fundamental difference between similar final supramolecular states. Furthermore, the lengths of alkyl chains determine whether crystals or polymers in solution or physical gels are formed. These chains alter the distance between molecules in a single stack, as well as the distance between single fibers and thus affects the extend of charge transfer between them. In crystalline state, charge transport should be enhanced due to the close and near perfect stacking of nitrogen centers and low amounts of defects present. Moreover, different crystalline states can be obtained with the same molecule depending on the crystallization process.

Returning to the topic of gels, also chemical gels can be realized by covalent capture of a physical gel structure. This results in robust materials, but it equally leads to loss of dynamic character, which might affect the charge transport.

Another interesting difference in self-assembled states can be found by the addition of chiral chains. Enantiomeric pure molecules are able to form supramolecular polymers of different helicity by formation under either thermodynamic or kinetic control. The self-assembly process can even be governed by peptide-enzyme catalysis instead of the traditional nucleation and growth mechanism.

In this chapter a comparative study has been performed in order to establish if, and to what extent, these differences in molecular structure, nucleation processes and supramolecular architecture affect the electronic conductivity properties of the resulting self-assemblies.

IV.2 Bibliography

A. Conductivity and charge transport

Electric conductivity (σ) is the ability of a material to transport an electric charge and is expressed in Siemens per centimeter ($\text{S}\cdot\text{cm}^{-1}$). It corresponds to the inverse of the resistivity (ρ) (equation 12):

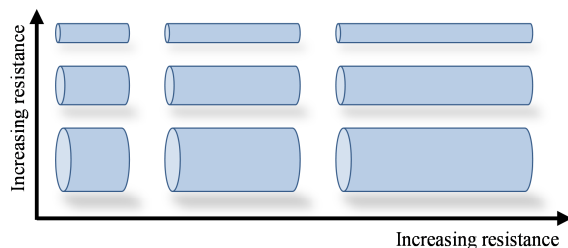
$$\sigma = 1/\rho \quad (12)$$

Both the conductivity and resistivity of a material are intensive properties. This signifies that they are bulk properties and only depend on the nature of the material, and not its size or macroscopic morphology. In contrast, a materials electric resistance (Ω), which is its opposition to the flow of electric current, is an extensive property. Thus, it also depends on the materials size. It is defined as the potential (V) across a material divided by the current (I) that passes through it (equation 13). Just as the resistivity is the inverse of the conductivity, the resistance is the inverse of the conductance (G) (equation 14).

$$R = V/I \quad (13)$$

$$G = 1/R = I/V \quad (14)$$

The relation between the resistance of a material and its morphology is depicted in **Scheme 11**, where it can be seen that the resistance of a material increases (conductance decreases) with increasing length and decreasing diameter of the material in question.

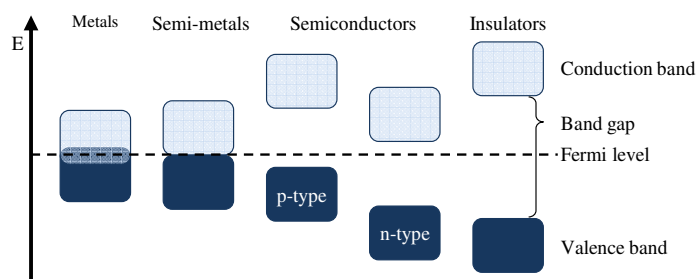


Scheme 11. The electric resistance is an object property that increases with increasing object length and decreasing object diameter.

The relationship between resistance and resistivity is expressed in equation 15 and the relationship between conductance and conductivity in equation 16. Here A is the materials cross sectional area and l its length.

$$\rho = R \times A/l \quad (15)$$

$$\sigma = G \times l/A \quad (16)$$



Scheme 12. Schematic representation of the relative energy levels of the valence and conduction bands in metals, semi-metals, semi-conductors and insulators.

How the charges are transported through a material depends on the distribution of their energy levels. In atoms, charges are confined to the energy level of their atomic orbital. In materials, however, the energy levels of atomic and molecular orbitals lie closely together and hence form energy bands (**Scheme 12**). At absolute zero temperature, the valence band comprises the highest energy levels that are occupied by electrons. The conduction band comprises the lowest energy levels in which normally no electrons reside. In metals, as well as some other highly conducting materials, the valence and conduction bands overlap and form delocalized energy levels over the whole volume of the material. This means that there is no activation energy required for an electron (or hole) to

move from one point to another and charges can move freely throughout the material. As a result, such materials, display high mobilities and conductivities.

In semi-metals the bands touch but do not overlap. In contrast to metals, this means that there is no density of states (DOS) at the Fermi level. In semi-conductors the valence and conductance bands are spaced further away, giving rise to a small band-gap (0.1 – 3 eV). In order for the electrons to move through the material, they need to overcome this energy barrier. Their conductivity is thus temperature dependent, acting as an insulator at low temperatures and as a conductor at higher temperatures. Whether a semi-conductor is *n*- or *p*- type depends on the facility with which electrons or holes are injected by the electrodes. Usually it is considered *n*- or *p*- type when its electron affinity or ionization energy approaches the Fermi-level of the electrodes. Charge transport in these materials is generally described by hopping and/or tunneling mechanisms.

For hopping to occur, the atomic orbitals of a molecule or material need to overlap. If this is the case, the charge carrier can *hop* from one localized energy state to another. The probability of hopping between two orbitals is exponential and depends on the energy barrier between the two localized states. During the hopping process, the charge carrier loses the information concerning its amplitude and phase. It is thus an incoherent charge transport mechanism. In contrast, tunneling is a coherent charge transport process, in which the charge carrier retains its amplitude and phase.

Insulators have a much larger band-gap (>3 eV) and electrons cannot move freely under normal circumstances.

B. Charge carrier mobility

Charge transport is commonly characterized by the charge carrier mobility (μ) inside the (semi-) conductor. It is expressed as the volts that passes through a centimeter squared of material per second ($\text{cm}^2 \cdot \text{V}^{-1} \cdot \text{s}^{-1}$). In absence of an external electric field, charges migrate around an average point in space and their transport is purely diffusive. Therefore, it can be expressed as a diffusion equation (equation 17). The mobility can then be calculated using the Einstein-Smoluchowski relation (equation 18):

$$\langle x^2 \rangle = nDt \quad (17)$$

$$\mu = eD/k_B T \quad (18)$$

In the first equation, x^2 is the mean square displacement, n is 2, 4, or 6 depending on the dimensionality of diffusion (one, two or three dimensional), D is the diffusion coefficient and t the time. In equation 18, e is the electron charge, D the diffusion coefficient, k_B the Boltzmann constant and T the temperature in Kelvin.

In the presence of an external electric field, a drift causes a displacement of the average point in space around which charge carriers diffuse. The charge carrier mobility in a material, free of any traps, is expressed as (equation 19):

$$\mu = v/E_f \quad (19)$$

In which v is the velocity of the charge carriers and E_f the amplitude of the external electric field applied. However, normally, traps are present. Either evenly distributed over the whole material or positioned at grain boundaries. In the first case, charge carrier mobility is presented by the multiple trapping and release model. In this model, charges are continuously trapped in localized energy states, and released into delocalized energy states by thermal activation, during their migration through the material. The overall mobility is then given by equation 20:

$$\mu = \mu_0 \alpha \exp(-E_t/kT) \quad (20)$$

Here μ_0 is the mobility in absence of traps, α the ratio between delocalized energy states (used in band-like transport) and localized energy states (traps), and E_t the trapping energy.

When traps are positioned at grain boundaries, the second case, no thermal activation is needed for charge carriers to be released. Instead they use a tunneling mechanism to escape the traps.

Multiple parameters influence charge carrier mobility, such as molecular packing, disorder, presence of impurities, temperature, electric field, charge-carrier density, size/molecular weight, and pressure.⁴⁴⁹ The main factor influencing charge carrier mobility is the molecular packing. When the packing allows for optimal intermolecular interactions, higher mobilities are measured. This explains the anisotropy in charge transfer often found in crystals. For example, molecules that are packed in a herringbone structure, such as pentacene, show two dimensional charge transport in the crystal plane, but limited conductivity between crystal layers. Even in the crystal plane, as was shown for pentacene single crystals, charge carrier mobility varies along the crystal axis from 0.7 to 2.3 cm²·V⁻¹·s⁻¹.⁴⁵⁰ The work of Rovira and co-workers illustrates how much the mobility can vary depending of the crystal

structure, using multiple tetrathiafulvalene (TTF) derivatives that crystallize in three different crystal structures (Figure 154).⁴⁵¹

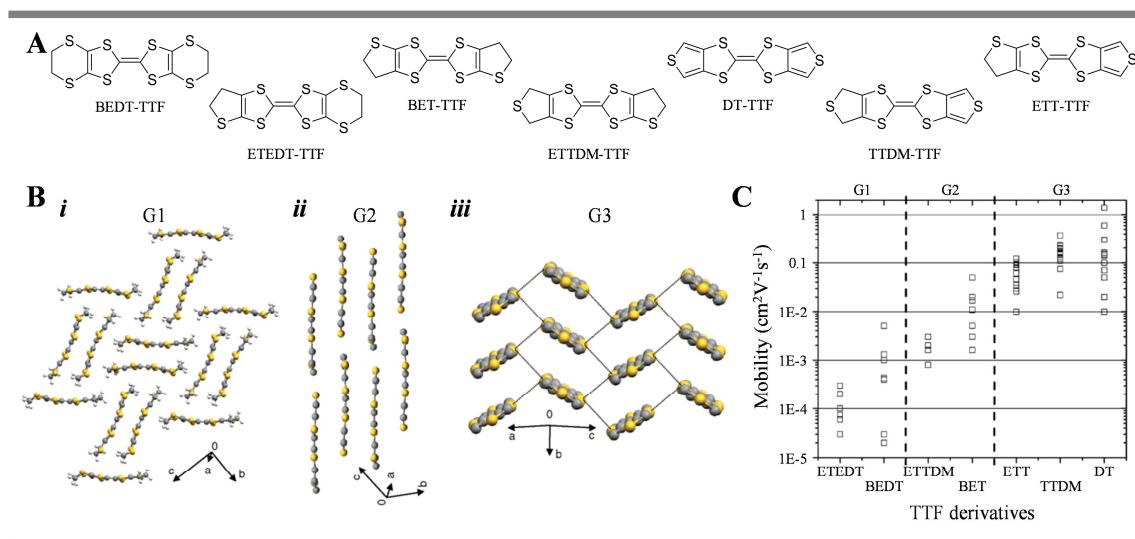


Figure 154. A) Molecular structures of TTF derivatives studied by Rovira and co-workers; B) crystal structure of ETEDT that represents the first group (G1) (*i*), ETTDM that crystallizes in a linear fashion (G2) (*ii*) and TTDM that crystallizes in a herringbone structure (G3) (*iii*); C) charge carrier mobilities of TTF derivatives. The TTF derivatives have been organized by their crystal structure (G1, G2 and G3) with a dashed line separating them. This Figure is adapted from reference ⁴⁵¹

Another factor affecting charge carrier mobility is the amount of disorder (traps) present. Diagonal disorder are variations in molecular frontier energy levels that create localized energy states and disrupts band-like transport.⁴⁴⁹ It arises from freedom in conformational molecular structure, the presence of impurities, or electrostatic and polarization effects of the surrounding molecules. With decreasing order, the mobility decreases, as was demonstrated by Debije using π -conjugated discotic hexathiohexyl triphenylene (HHTT) that transitions from a crystalline solid to an isotropic phase, via a columnar meso phase and a helical plastic phase (Figure 155).⁴⁵²

A second type of disorder is called off-diagonal disorder and arises from variations in inter molecular interactions due to molecule positions and orientations. This type of disorder can either reduce charge transport or, in contrast, create a conduction pathway.⁴⁴⁹

The disorder present in a material is highly dependent on the deposition method used. For example, pentacene charge carrier mobility can vary six orders of magnitude depending on the deposition conditions. As conditions often vary between research groups, it is difficult to directly compare data.¹⁷³

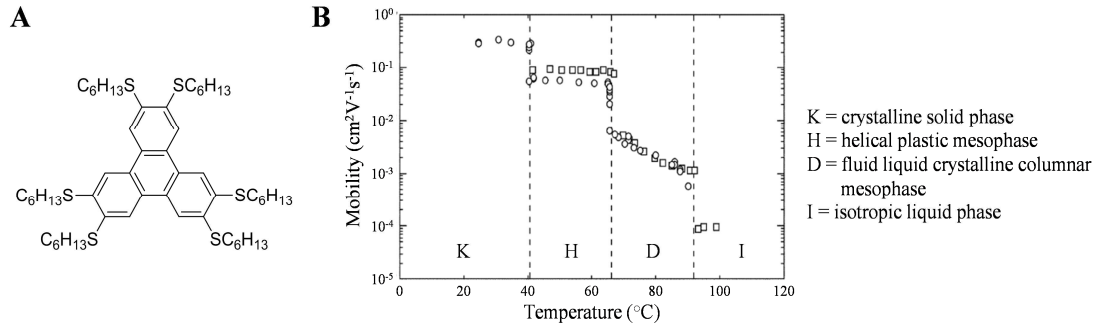


Figure 155. A) Molecular structure of HHTT; B) plot of charge carrier mobilities measured for HHTT, using TOF (squares) or PR-TRMC (circles) methods, in function of the temperature and liquid crystal phase. This Figure is adapted from reference ⁴⁵²

Also the temperature has a large influence on charge transport.⁴⁴⁹ In materials where band-like charge transport takes place, such as crystals and highly ordered materials, the mobility decreases with increasing temperature following $\mu \sim T^{-n}$ ¹ due to increased scattering of phonons. In disordered materials, where charge transport primarily takes place by hopping, the mobility increases with increasing temperature, as energetic barriers can more easily be overcome. In such materials, the temperature dependence of charge transport follows Arrhenius-like law (equation 21):

$$\mu_0 = \mu_\infty \exp(-E_{act}/k_B T) \quad (21)$$

In which E_{act} is the activation energy, which increases with increasing disorder. The electric field only affects charge transport in ultra-pure crystals, and then only in the dimension where charge transport is optimal.⁴⁴⁹ In these materials, the mobility decreases with increasing electric field. In disordered materials the inverse effect is observed. Here, the mobility increases with increasing electric fields and charge carriers follow Poole-Frenkel behavior (equation 22):

$$\mu(E_f) = \mu_0 \exp(\gamma \sqrt{E_f}) \quad (22)$$

$$\gamma = B \left[\frac{1}{k_B T} - \frac{1}{k_B T_0} \right] \quad (23)$$

In which γ is temperature dependent, as can be seen from equation 23. Here, B is a constant characteristic of the material and T_0 is much higher than room temperature. Impurities only affect

¹ n is an empirical value that differs from material to material. It typically lies between 0.5 and 3

charge carrier mobility if their frontier orbitals fall into the HOMO-LUMO gap of the (semi-) conductor materials. The pressure influences charge carrier mobility because it alters the intermolecular distances, and thus the intermolecular interactions.⁴⁵³ This effect was demonstrated in pentacene and tetracene crystals by the group of Firsbie (Figure 156).⁴⁵⁴

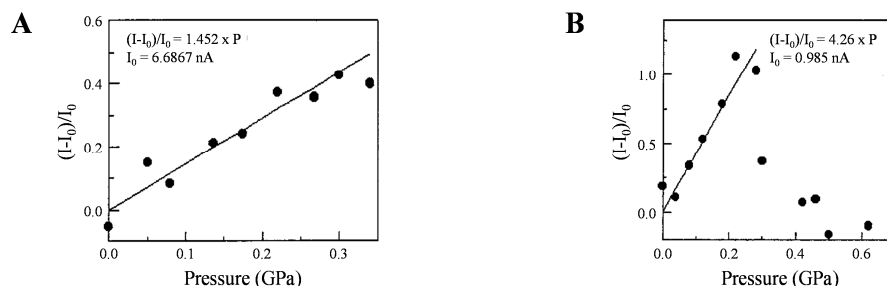
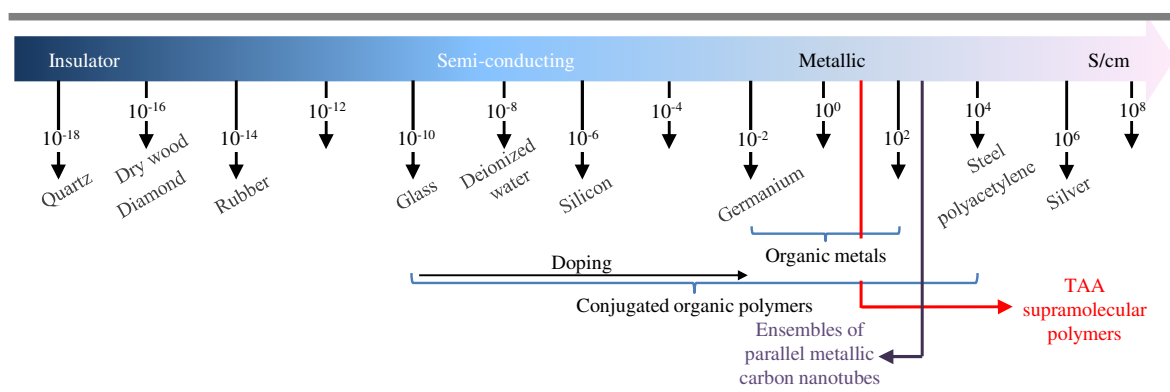


Figure 156. Normalized photocurrent measured versus the hydrostatic pressure applied under a 20 V bias for pentacene (A) and tetracene (B). This Figure is adapted from reference⁴⁵⁴

Finally, charge carrier mobility is also dependent on the charge carrier density. This is one of the reasons why there is often a difference in mobilities measured in similar OFET or diode devices.

C. Charge transport in various organic supramolecular materials

In Scheme 13, the proximate conductivities of some common insulators, semi-conductors and metals are presented. As can be seen, photo-oxidized triarylamine supramolecular polymers, that were aligned in between gold electrodes separated 80 nm apart, have very good charge transport properties ($5 \times 10^3 \text{ S} \cdot \text{m}^{-1}$).²⁶ Regarding organic semi-conductors, only single-walled metallic carbon nanotubes with ballistic charge transport exhibit higher conductivities ($10^4 - 10^5 \text{ S} \cdot \text{m}^{-1}$).⁴⁵⁵



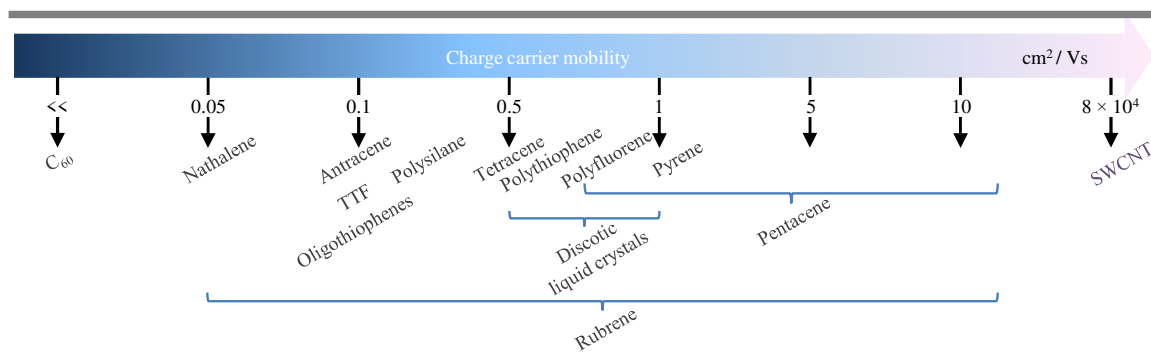
Scheme 13. Schematic representation of the electric conductivity, expressed in $\text{S} \cdot \text{cm}^{-1}$, of some common insulators, semi-conductors and metallic conductors.

Here, we will mainly discuss some of the advances made in the development of conductive organic supramolecular semi-conductors for their application into supramolecular organic electronics. However, first, it is important to position the conductivities of a few well known organic semi-conductors on our scale. In **Scheme 14** the approximate charge carrier mobilities of organic semi-conductors can be found. The charge carrier mobilities given are purely indicative: as explained in the previous section, it depends strongly on the experimental conditions used, doping, film morphology, etc..

Examples of organic semi-conductors are oligoacenes (e.g pentacene, tetracene and derivatives such as rubrene), oligothiophenes, discotic liquid crystals (e.g. triphenylenes, hexabenzocoronene, perylenediimide, metal phthalocyanine cores), triphenylamines, perylenes, tetrathiafulvalenes, fullerenes derivatives and graphene. Conjugated organic polymers are also widely used as semi-conductors in organic electronics. The best known are polyparaphenylene, polyparaphenylenevinylene, polyfluorene, polythiophene, polysilane, polyacetylene, and polyaniline. Generally, it can be stated that amorphous materials display lower charge carrier mobilities ($< 0.1 \text{ cm}^2 \cdot \text{V}^{-1} \cdot \text{s}^{-1}$). The mobilities increase with increasing crystallinity towards $0.1\text{-}20 \text{ cm}^2 \cdot \text{V}^{-1} \cdot \text{s}^{-1}$. Typical conjugated organic polymers show mobilities around $0.1 \text{ cm}^2 \cdot \text{V}^{-1} \cdot \text{s}^{-1}$.

Out of these materials, graphene, a semi-metal, is the best conductor, and charge carrier mobilities up to $10^4 - 10^5 \text{ cm}^2 \cdot \text{V}^{-1} \cdot \text{s}^{-1}$ have been reported.⁴⁵⁶ Closely related to graphene is fullerene. In contrast, it is an insulator. Only when functionalized to other groups or metals does it display any conductivity.⁴⁵⁷ The other organic semi-conductors position themselves in the range in between. Oligoacenes are recognized among the best organic semi-conductors used in organic electronics. Their charge carrier mobilities increases with increasing number of acene units, as more crystalline materials are formed. However, at high acene numbers their processability becomes more difficult. The most commonly used is pentacene, whose charge carrier mobility can reach up to $15 \text{ to } 40 \text{ cm}^2 \cdot \text{V}^{-1} \cdot \text{s}^{-1}$.

Some conjugated organic polymers, with excellent conductivities, have reached similar conductivities as metals at room temperature.⁴⁵⁸ The best conducting polymers are polyacetylene ($\sim 1.1 \times 10^4 \text{ S} \cdot \text{cm}^{-1}$) and carbon nanotubes ($\sim 1 \times 10^4 \text{ S} \cdot \text{cm}^{-1}$). Polypyrrole and polyaniline are fairly comparable and polyaniline performs the poorest ($\sim 1 - 10 \text{ S} \cdot \text{cm}^{-1}$).



Scheme 14. Schematic representation of the charge carrier mobilities, expressed in $\text{cm}^2 \cdot \text{V}^{-1} \cdot \text{s}^{-1}$, of some common organic semi-conductors.

Self-assembled supramolecular organic structures can be advantageous as semi-conductors in electro organic devices because of improved electronic communication between molecules, its dynamic character and self-healing properties (*Chapter I.3 C. Supramolecular electronics*). The two main classes of supramolecular organic semi-conductors, aromatic molecules and sulfur based heterocycles, will be discussed in the sections below.

i. Aromatic molecules

Aromatic molecules, such as aromatic fluorinated dendrons, perylenetetracarboxylic diimides, fluorine- and anthracene-conjugated peptide β -sheets and hexabenzocoronenes, have been reported to form conducting supramolecular polymers (**Figure 157**).

Examples from the first group were reported by Percec *et al.*, who prepared liquid crystal phases by the columnar supramolecular self-assembly of semi-fluorinated tapered dendrons functionalized with various electroactive aromatic donors or acceptors (**Figure 157i**).⁴⁵⁹ In the columns, the fluorinate part is placed on the edge, thus shielding the electroactive aromatic core from moisture. Due to the close packing, one dimensional stacking and perpendicular orientation to the surface, charge carrier mobilities ($10^{-4} - 10^{-3} \text{ cm}^2 \cdot \text{V}^{-1} \cdot \text{s}^{-1}$) 2 to 5 orders of magnitude greater than analogues amorphous material were obtained.

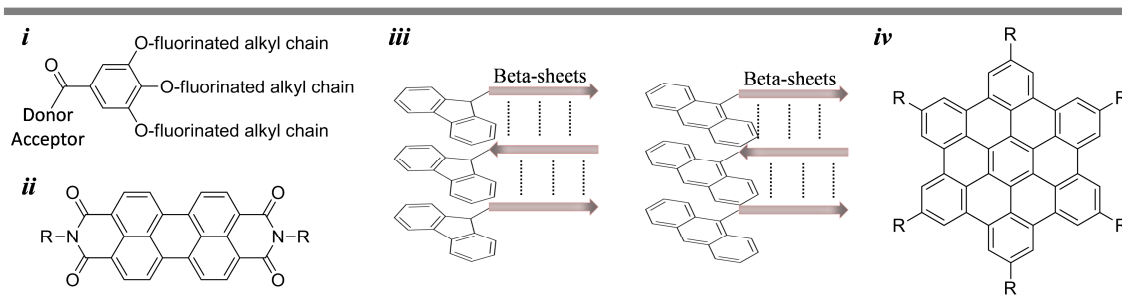


Figure 157. Molecular structure of *i*) aromatic fluorinated dendrons; *ii*) perylenetetracarboxylic diimides; *iii*) fluorine- and anthracene-conjugated peptide β -sheets and *iv*) hexabenzocoronenes, used to form conducting supramolecular polymers.

Perylenetetracarboxylic diimides (PTCDIs) (Figure 157ii) are one of the most important supramolecular conducting polymers. PTCDIs are able to stack via π - π interactions due to their planar π -conjugated structure. The architecture of the self-assembled structure, as well as its stability, can be tuned by the introduction of (functional) sidechains on the PTCDI moiety. For instance, spherical assemblies are obtained when functionalized with nonyldecyl chains and one-dimensional stacks when functionalized with linear alkyl chains.⁴⁶⁰ Furthermore, they exhibit high thermal and photo stabilities. Upon reduction (e.g. by hydrazine), stable anionic species are formed. The charges can be transferred inside the supramolecular polymer via co-facial π -electronic delocalization. This was demonstrated by the group of S. Moore.⁴⁶⁰ They measured conductivities of $10^{-3} \text{ S}\cdot\text{m}^{-1}$ and $0.5\text{-}0.1 \text{ S}\cdot\text{m}^{-1}$ (in air and air saturated by hydrazine vapors respectively) for fibers deposited between gold electrodes spaced 50-100 nm apart (Figure 158), the latter value being two orders of magnitude greater than the conductivity of undoped silicon. The *IV* curve becomes non-linear at higher biases, which indicates that injection-limited charge transport takes place.

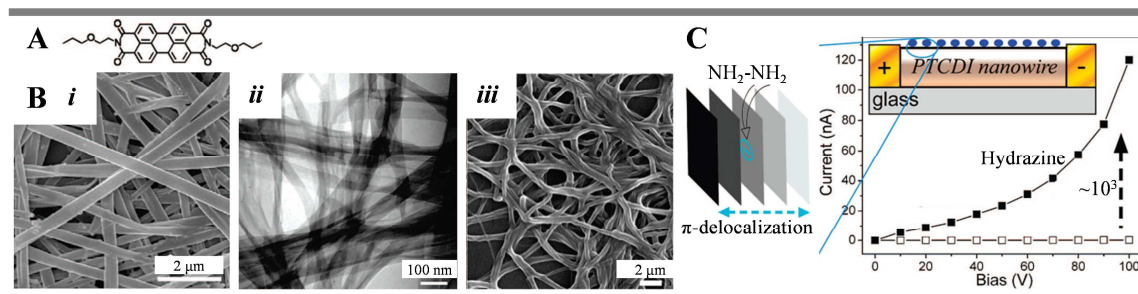


Figure 158. A) Molecular structure of PTCDI functionalized with ethoxypropane: B) SEM images of supramolecular fibers formed by rapid dispersion (*i*), bisolvent phase transfer (*ii*) and vapor diffusion self-assembly (*iii*); C) on the left is schematically represented the enhanced 1D electrical conductivity through co-facial π -electronic delocalization. On the right the *IV* curve measured on a single fiber in air (white squares) and in air saturated by hydrazine vapor (black squares). In the inset the two-electrode device is illustrated. This Figure is adapted from reference 460.

Fluorine- and anthracene-conjugated peptide β -sheets (Figure 157iii) are studied mostly because of their biocompatibility and applicability in biological (inspired) applications. An example is the self-assembly of a LLKK oligopeptide linked to an anthracene moiety that self-assembles into β -sheets (peptide part) with additional π - π stacking (anthracene part) in a head-to-tail arrangement.⁴⁶¹ Under optimal conditions conductivities of $10 \text{ S}\cdot\text{m}^{-1}$ were measured. On the other hand, amorphous anthracene only displayed a conductivity of $10^{-8} \text{ S}\cdot\text{m}^{-1}$. This large increase in conductivity is explained by the improved electronic communication between anthracene units, as well as by the presence of benzene (solvent) in the fibers that act as doping agent.

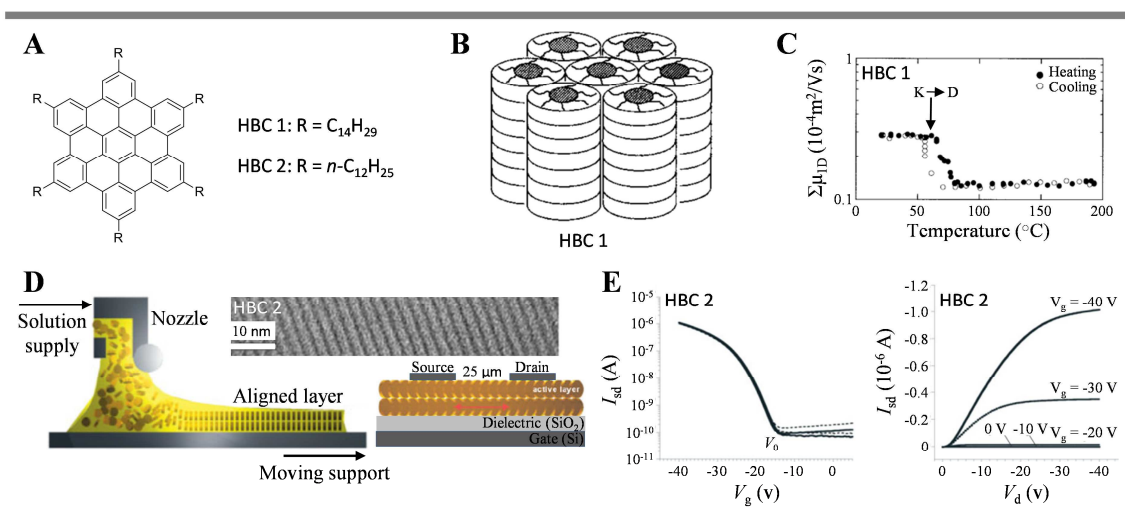


Figure 159. A) Molecular structure of HBC 1 and 2 studied in the group of Müllen; B) hexagonal columnar mesophase of HBC 1; C) one dimensional intracolumnar charge carrier mobility of HBC 1 in function of temperature. The transition from a crystalline solid (K) to the hexagonal columnar mesophase (D) is indicated by an arrow; D) schematic depiction of the zone-casting technique used to obtain homogeneous films with single columnar arrangements in the zone-casting direction, as can be seen in the TEM image. On the right the OFET device fabricated by this method is depicted; E) on the left: transfer curves of the top-contact OFET device with HBC 2 as active layer ($V_g = -40\text{V}$); on the right: current-voltage output characteristics measured along the columnar alignment. This figure is adapted from references^{462,463}

The last example of aromatic molecules, forming conductive supramolecular polymers, given here, are hexabenzocoronenes (HBCs) (Figure 157iv). It was the group of Müllen that performed pioneering work in this field. The HBCs, substituted with alkyl chains, form discotic monomers that self-assemble into liquid-crystalline materials that exhibit high charge carrier mobilities ($0.5 \times 10^{-4} \text{ m}^2\text{V}^{-1}\text{s}^{-1}$), comparable to highly oriented pyrolytic graphite ($3 \times 10^{-4} \text{ m}^2\cdot\text{V}^{-1}\cdot\text{s}^{-1}$ perpendicular to the sheets) (Figure 159B-C).⁴⁶³ Such HBCs have been incorporated into OFET devices by a zone-casting technique that produces columnar uni-axially aligned self-assembled structures (Figure 159D-E).⁴⁶² The OFET displayed on/off ratios of 10^4 , a turn-on voltage of -15V and charge mobilities of $1 \times 10^{-6} \text{ m}^2\cdot\text{V}^{-1}\cdot\text{s}^{-1}$. The group of Aida reported conductive self-assembled graphitic nanotubes from amphiphilic HBC in THF and THF/water (Figure 160A-B). The tubes are helical structures of π -stacked coronenes

surrounded by hydrophilic glycol chains.⁴⁶⁴ Upon oxidation (1 eq. of NOBF_4) the nanotube transitions from an insulator to semi-conductor state, with conductivities equivalent to gallium nitride nanotubes.^{465,466}

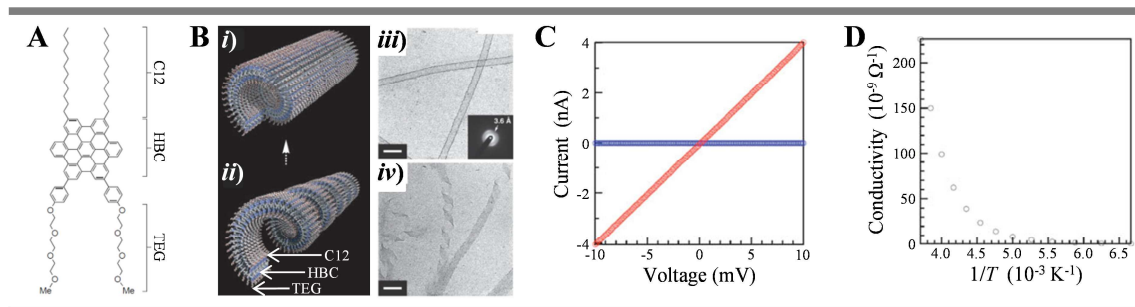


Figure 160. A) Molecular structure of the amphiphilic HBC molecule studied by Aida; B) illustration of self-assembled supramolecular graphitic nanotubes from amphiphilic HBC formed in THF (i) and in THF/water (ii). TEM images of the nanotubes formed in THF (iii) and in THF/water (iv). The scale bar represents 50 nm. The inset in (iii) is the electron diffraction pattern of the nanotubes; C) *IV* curves of neutral (bleu) and oxidized (red) nanotubes at 285 K; D) conductivity of a single oxidized nanotube at 270-150 K. This Figure is reproduced from⁴⁶⁴

ii. Sulfur-based heterocycles

The second type of conductive supramolecular polymers are (oligo)thiophene derivatives. They have been incorporated into (opto-) electronic devices because of their small band gap, high charge carrier mobilities and high fluorescence quantum yields.²⁹⁹ Several approaches exist to generate sulfur-based heterocyclic self-assembled polymers.

For example, the structures can be built via the cooperative effect of hydrogen-bonding between thiophene spacers and π - π stacking of the central sulfur-based heterocycles. This was first demonstrated by Feringa.⁴⁶⁷ They obtained lamellar supramolecular polymers (20 – 100 μm by 2 – 10 μm) self-assembled by co-facial stacking of the molecules (Figure 161A-B). This co-facial stacking enhances the charge carrier mobility to the same level of covalently conjugated polythiophene ($5 \times 10^3 \text{ cm}^2 \cdot \text{V}^{-1} \cdot \text{s}^{-1}$ and $7 \times 10^3 \text{ cm}^2 \cdot \text{V}^{-1} \cdot \text{s}^{-1}$ respectively). Furthermore, the bisurea molecule that does not contain a central thiophene moiety, displays a conductivity signal as low as the detection limit.

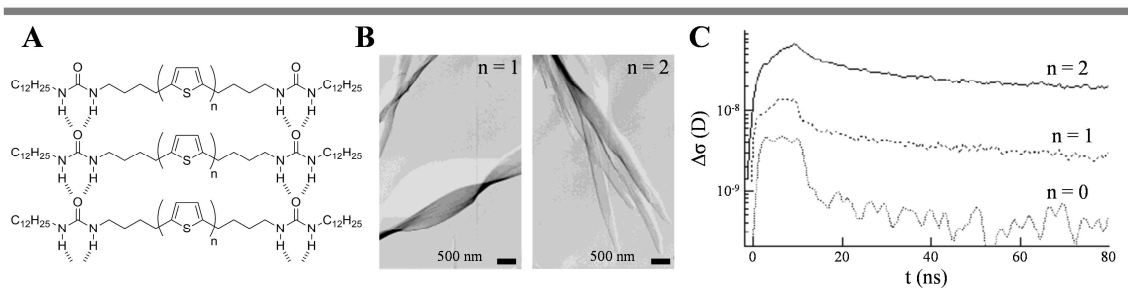


Figure 161. A) Illustration of the supramolecular self-assembly of bisurea molecules, with no, one or two thiophene moieties, into ribbons; B) TEM images of lamellar fibers of bisurea mono- and bis-thiophene molecules; C) Dose-normalized transient conductivity (Sm^2J^{-1}), measured by pulse-radiolysis time-resolved microwave conductivity technique after radiation induction, of three bisurea molecules. This Figure is adapted from ⁴⁶⁷

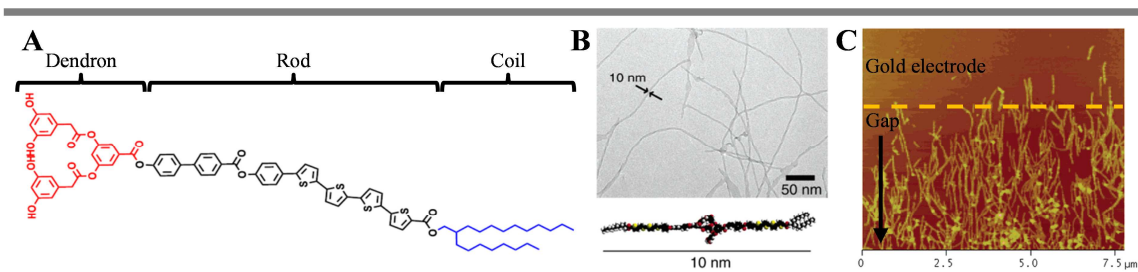


Figure 162. A) Molecular structure of thiophene-based dendron rodcoil molecule; B) TEM image of supramolecular thiophene-based dendron rodcoil polymers dropcasted on amorphous carbon; C) AFM image of supramolecular thiophene-based dendron rodcoil polymers aligned in an AC electrical field on an Au/Cr patterned mica substrate. This Figure is adapted from ⁴⁰⁶

A second manner in which conductive thiophene-based supramolecular polymers can be obtained was demonstrated by the group of Stupp (Figure 162).⁴⁰⁶ Here the authors used dendrons, capable of hydrogen bonding, functionalized with oligothiophenes to obtain rodcoils upon gelation. The self-assembled structures show conductivities ($7.9 \times 10^{-3} \text{ S}\cdot\text{m}^{-1}$) three orders of magnitude greater than in amorphous state. Moreover, to ensure optimal conductivity conditions, the supramolecular polymers were aligned perpendicular to the electrodes using an alternating current electric field.

The final group comprises tetrathiafulvalene (TTF) molecules. Upon oxidation, TTF becomes aromatic and forms TTF/TTF⁺ charge transfer complexes that are capable of electric conductivity. The degree of conductivity directly depends on the extent of the CT interactions in the complexes. Generally, these mixed-valence charge transfer complexes are in crystalline state. However, soft supramolecular fibers can be obtained by functionalization of TTF. One example comes from the group of Shirai, who functionalized TTF with (*R*)- and (*S*)-methylbenzylamide end groups.⁴⁶⁸ It self-assembles into long supramolecular polymers of $\sim 30 - 60$ nm in diameter, by the formation of TTF CT complexes in the presence of F₄TCNQ and by intermolecular hydrogen bonding between the chiral amide end-groups (Figure 163A-B). The resulting fibers demonstrate either right or left handed

helicity (pitch = 60 nm) depending on the chirality of the end-groups (Figure 163B*i*). Films exhibited a semi-conducting character with conductivities of $5.0 \times 10^{-6} \text{ S} \cdot \text{m}^{-1}$ (Figure 163C-D).

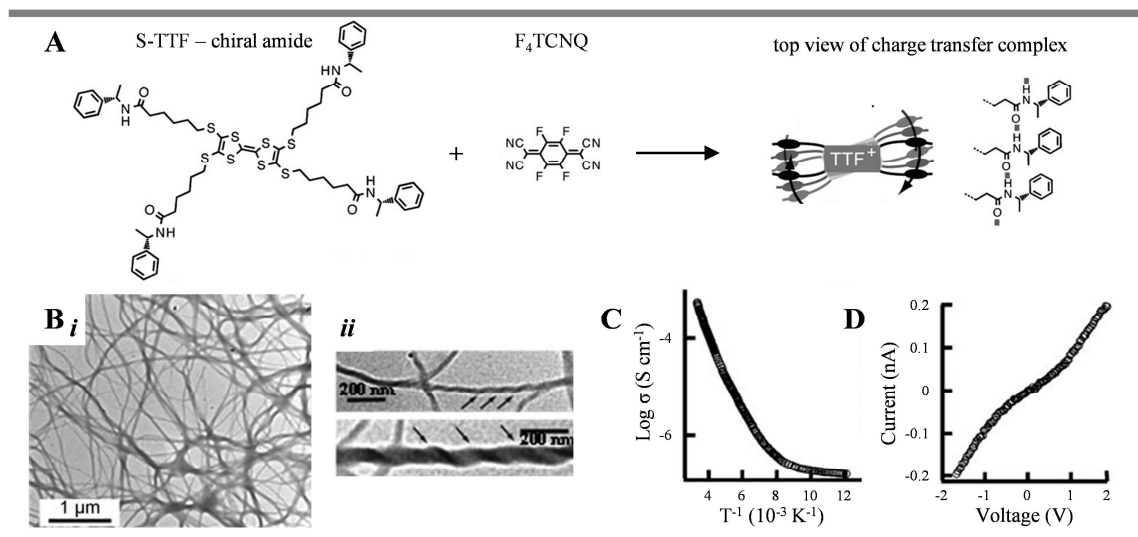


Figure 163. A) Schematic representation of self-assembly process of TTF appended with chiral amide in the presence of F₄TCNQ; B) TEM images of the resulting fibers (*i-ii*). Top image of (*i*) is R-TTF fiber and bottom image (*ii*) is S-TTF fiber; C) Electric conductivity in function of temperature for a S-TTF film (gold electrodes, 500 μm electrode gap); D) *IV* curve recorded for a S-TTF fiber by PCI-AFM. This figure is adapted from reference ⁴⁶⁸

IV.3 Results and Discussion

A. Synthesis

The synthesis of the different triarylamine molecules studied in this chapter can be found in *Materials and methods. Synthesis*.

B. Triarylamine mono- and trisamide supramolecular polymers

In the first part of this study we compare the conductance of several triarylamine mono- and trisamide supramolecular polymers (TAA-C1, TAA-C8, TATA-C4, TATA-C9, and TATA-C12, **Figure 164**). As explained in the bibliography section, their conductivity is an intrinsic property that remains unchanged following changes in global morphology, such as polymer length and width. Regarding these aspects, TAA and TATA have nearly identical morphologies. Therefore, by comparing their conductances, one might deduce if they exhibit similar conductivities. Any measured differences in conductivity could then be ascribed to differences in their supramolecular arrangement.

Based on previous knowledge (*Chapter 1.4C. Supramolecular triarylamine polymers*), two main differences in supramolecular arrangement exist in the series of molecules investigated. First, TAA self-assembles from double columnar nuclei while TATA grows in single columns. This could affect the electronic communication between adjacent columns and, consequently, play a role in the stability and delocalization of radical cations formed during oxidation. Secondly, the molecules bear alkyl chains of varying lengths. These alkyl chains form an isolating layer around the conducting nitrogen centers. With increasing alkyl chain lengths, this isolation layer thickens. This could *i*) impair conductivity because nitrogen centers are less available for oxidation; *ii*) have no direct effect; *iii*) improve conductivity because the radical cations generated are protected and less prone to decay.

The sections below are structured by the physical state of the supramolecular polymers. First, the conductance of TAA and TATA supramolecular polymers in solution is investigated. Then, by increasing the concentration above the gelation concentration, the conductance of TATA-C12 physical gels is studied. Finally, the conductance of TAA and TATA in thin film state is examined by drop-casting solutions of preformed supramolecular polymers onto IDEs.

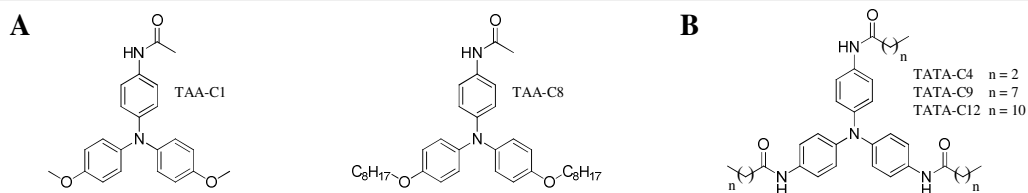


Figure 164. Molecular structures of the triarylamine mono- (A) and trisamides (B), bearing unbranched alkyl chains of varying length that are studied in this chapter.

i. TAA and TATA supramolecular polymers in solution

The first series of experiments are performed on TAA and TATA solutions, inside ITO electrochemical cells with a 4 μm cell gap (Figure M1). In Figure 165, *IV* curves recorded for solutions of TAA and TATA in TCE (15 mM) are presented. Prior to light irradiation, little to no conduction is measured (Figure 165A). Upon light irradiation, photo-oxidation and supramolecular polymerization take place. As a result, the samples transition to a conductive state showing Ohmic behavior (Figure 165B). This is accompanied by an increase in conductivity of three orders of magnitude. The resistance is approximately $\sim 485 \Omega$.

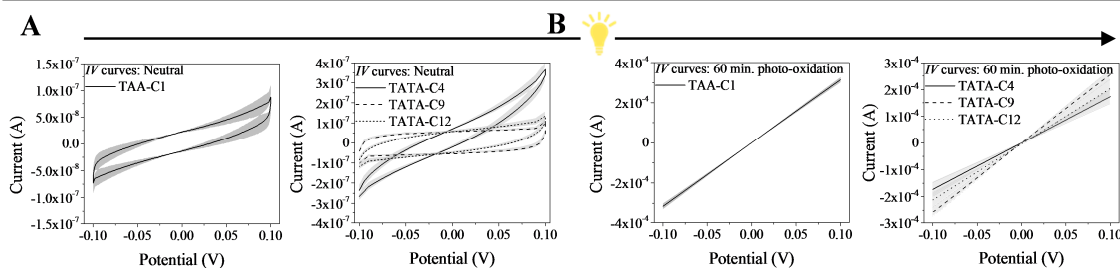


Figure 165. *IV* curves of 15 mM TAA-C1, TATA-C4, TATA-C9 and TATA-C12 solutions prepared in TCE, inserted in ITO cells and recorded before (A) and after 60 minutes of photo-oxidation inside the ITO cells (B). The grey areas correspond to the standard deviation taken over two to three experiments.

During the early stages of photo-oxidation, a catalytic amount of radicals is present leading to the complete supramolecular polymerization of all monomers. During the first 60 seconds of photo-oxidation, TAA shows a larger increase in conductance compared to TATAs (Figure 166). This could mean that in this time frame *i*) more radical cations are generated in TAA solutions than in TATA solutions and/or *ii*) supramolecular polymerization rate is higher for TAA than for TATA. Multiple factors could contribute to this. First of all, TAA have two octyloxy groups on the periphery, which are electron donating. They stabilize the radical and lower the oxidation potential. Oxidation is thus more easily achieved. Secondly, as TAA have only two alkyl chains instead of three, the nitrogen centers might be more accessible for oxidation. Also the rates of nucleation and growth are important aspects to consider. A higher conductance could easily be explained by a larger number of supramolecular polymers that span the electrode gap. Finally, other factors, such as absorption cross-

section, could also contribute to the larger increase in conductance observed during the first minutes of photo-oxidation of TAA.

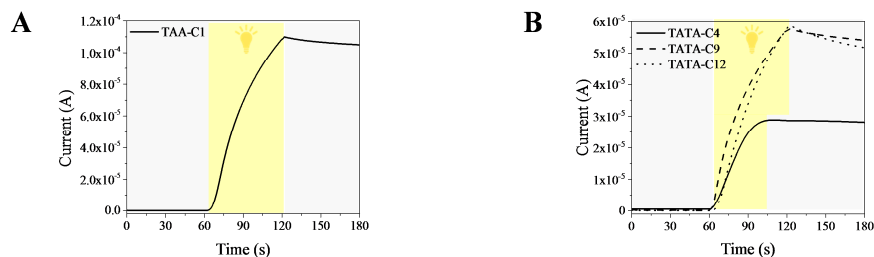


Figure 166. Plots of the current recorded at 0.1 V versus the time for A) TAA-C1 and B) TATA-C4, TATA-C9 and TATA-C12. The samples are photo-oxidized between $t = 60$ and 120 seconds, as indicated by the light yellow area.

At longer irradiation times, when the supramolecular polymers are already formed, not isolated molecules but molecules within supramolecular structures are oxidized. Just as before, the nitrogen centers of TATAs are less accessible for oxidation because they are screened by three alkyl chains. This could lead to a reduced oxidation efficiency.

However, radical species might be more stable in TATA supramolecular polymers. TATAs self-assemble in a mono-columnar arrangement instead of a double columnar arrangement. This means that radical decay, which is a bimolecular process, is less likely to occur.

Furthermore, from photospectroscopic studies performed in earlier works, it is known that after 60 minutes of photo-oxidation the amount of radical cations inside fibers does not significantly increase anymore.^{14,16} This signifies that no more charges can be generated inside the structures because of electrostatic repulsion effects. By all atomic calculations, the radical delocalization length in defect free TAA fibers was determined to be 80 nm (1 TAA^{•+} for 160 neutral TAA).¹⁵ However, the delocalization length in TATA fibers might not be the same. Radical cations in TAA fibers experience electrostatic repulsion in two dimensions, because it is assembled in a double columnar arrangement. In contrast, radical cations in TATA fibers are assembled in mono columnar arrangements. Thus, they might have a reduced sensitivity for radical species in adjacent columns. As a consequence, more radicals could be present, which could in turn lead to higher conductivities.

Considering the previous discussions, it is surprising that despite the differences in supramolecular assembly, oxidation efficiencies, radical stabilities and possible charge carrier density, no significant differences are observed between the currents measured for TAA and TATA supramolecular fibers after 60 minutes of photo-oxidation (Figure 165). We can conclude that conductivities of TAA and TATA supramolecular polymers are similar. This strongly indicates that the self-assembly of the stacked nitrogen cores, which are responsible for charge transport, is similar

enough to ensure good conductivity, regardless of the substituents placed on the periphery. Such behavior is opposed to many other organic semi-conductors that typically show large differences in charge transport depending on the morphology of their amorphous, crystalline or self-assembled state, making of triarylamine supramolecular polymers in solution/gels a robust material with constant and reliable conductivity properties.

A marked difference between TAA and TATA supramolecular polymers is the stability of the conductance over time. When the conduction is plotted in function of irradiation time and the time it subsequently spends in the dark (Figure 167), TAA-C1 exhibits a linear decrease in current in the dark, while it remains stable for TATA supramolecular polymers. This observation can be explained by the stability of the radical cations generated by photo-oxidation. Radical decay is a bimolecular process¹⁵ and, per consequence, it is more likely to occur in TAA supramolecular polymers that are assembled in a double columnar arrangement.

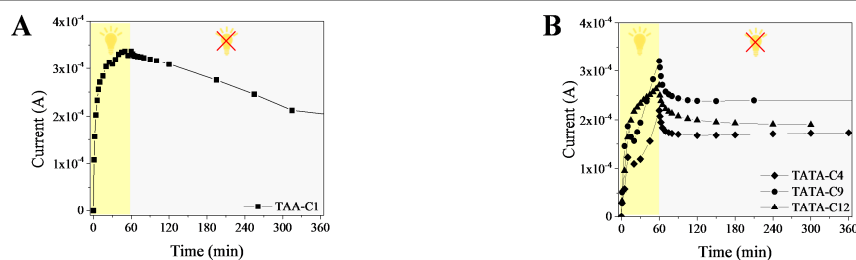


Figure 167. Comparison of the conductance over time between TAA and TATA molecules. Plots of the currents measured at an applied bias of 0.1 V versus the time, recorded for 15 mM TAA-C1 (A), TATA-C4, TATA-C9 and TATA-C12 (B) solutions prepared in TCE and inserted in ITO cells. The light yellow areas correspond to the light irradiation time, the light grey areas to the time the ITO cells were subsequently kept in the dark.

TATA supramolecular polymers bearing alkyl chains of varying lengths did not show significant differences in currents measured (Figure 165B). The alkyl chain length dictates the thickness of the isolating layer surrounding the nitrogen core, and it could be expected that, as the length increases, the electronic communication between nitrogen centers inside a stack and between fibers decreases. However, here we demonstrate that, in solution, this does not have a direct effect on the conductance.

ii. TAA and TATA supramolecular polymers as physical gels

We were equally interested in the differences in conduction through supramolecular polymers in solutions and physical gels (Figure 168).¹⁶ In both cases some conduction is possible through preformed fibers prior to light irradiation (applied bias of 0.1 V; Figure 168A). In gels, significantly more fibers are present and, in accordance, the resistance measured is at least one order of magnitude lower (10^6 and $10^5 \Omega$ for fibers in solution and gel respectively). However, their resistance remains high, as expected for non-doped species. During the first 60 seconds of light irradiation, the resistance

drops 3 to 4 orders of magnitude and the conductance in solution and gel is initially comparable. The resistance stabilizes in the dark as expected for TATA supramolecular polymers. When irradiation is performed for longer times (60 minutes), conductance in gels is ~ 2 orders of magnitude higher than in solution, which is expected because, due to the higher concentration, more supramolecular polymers are present and more radical cations can be generated (Figure 168B). After photo-oxidation, both the fibers in solution and gel are in conductive states and display Ohmic behavior ($\sim 485 \Omega$ and $\sim 315 \Omega$ respectively), as can be deduced from their *IV* curves.

An interesting difference is observed for short irradiation times of 15 seconds (Figure 168C). In TATA solutions, the current initially decreases, but very rapidly stabilizes after such a short light pulse. On the other hand, for gels, the current measured after the light pulse increases over time with 30 – 50% before stabilizing.¹⁶ This is related to the optimization of the supramolecular structure by the diffusion of polarons in the electric field. Both an increase in coherence length and a decrease in structural defects was observed by AFM imaging and SAXS.¹⁶ On the contrary, polymers formed by photo-oxidation are directly assembled in an optimized morphology. Because virtually no polymers were present before photo-oxidation, no enhancement of supramolecular structure takes place by polaron diffusion.

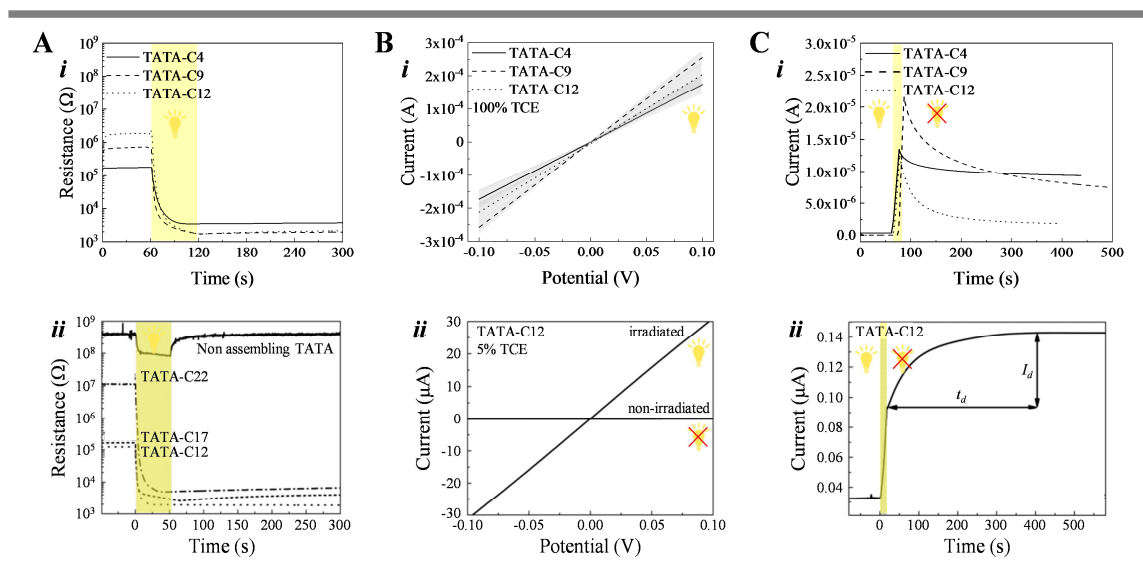


Figure 168. Comparison of conductance between TATA supramolecular polymers in solution and in gel state. A) plot of the resistance versus the time recorded under the applied bias of 0.1 V, for 15 mM TATA solutions (i) and physical 17 mM gels (ii) both formed in TCE. The light yellow area corresponds to the irradiation time; B) *IV* curves recorded for 15 mM TATA solutions in pure TCE (i) and 17 mM TATA physical gels in a methanol toluene (5:3) solvent mixture to which 5 vol% TCE was added (ii). The light grey areas corresponds to the standard deviation taken over three experiments; C) plot of the current versus the time recorded under the applied bias of 0.1 V for 15 mM TATA solutions (i) and physical 17 mM gels (ii) both formed in TCE. The light yellow area corresponds to the irradiation time. All curves of physical gels are adapted from reference¹⁶

An important factor to consider when reviewing these experiments is the contribution of ionic current to the total current measured. In previous work this issue has been investigated by including a non self-assembling TATA (tri(bromophenyl)amine) in the series of molecules investigated.¹⁶ In contrast to assembling TATA, it only displays a small response to photo-oxidation and returns to its non-conductive state as soon as the light source is removed (Figure 168Aii). Furthermore, upon addition of 10% of tetrabutylammonium chloride to a TATA-C12 gel, the conductance remains unaffected. We can thus conclude that ionic conduction is negligible in our systems.

iii. Thin films

Also the conductivity of photo-oxidized TAA and TATA supramolecular polymer thin films were probed (see Annexes Chapter IV for sample preparation) by recording the *IV* characteristics of oxidized supramolecular polymers drop casted onto IDEs of 10 μm channels. Thin films of TAA-C1 and TAA-C8 both exhibit conductance, although lower currents are measured in comparison with its solution (Figure 169A). This could be attributed to *i*) the increase of electrode gap from 4 to 5 μm ; *ii*) decrease in active area (decrease in electrode surface). Notably, TAA-C8 displays reduced conductance and therefore we hypothesize that also the alkyl chains contributed to the reduced conductance, as they could hinder fiber to electrode contact. This effect is even more pronounced in TATA thin films: TATA-C4 thin films exhibit conductance with a resistance of 240 Ω , while very little current was measured for TATA-C9 and TATA-C12 thin films (Figure 169B).

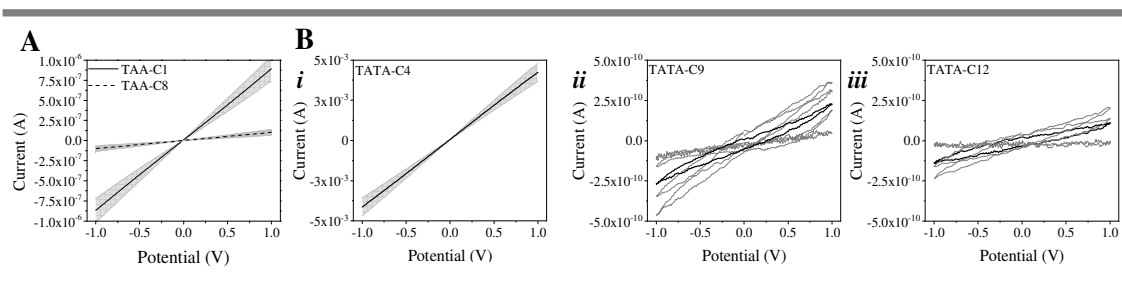


Figure 169. *IV* curves recorded for TAA (A) and TATA (B) thin films obtained by drop casting a 15 mM irradiated solution onto IDEs, under an applied bias of 0.5 V. The films were dried under vacuum before measurements to remove all solvent.

The difference between TATA-C4, TATA-C9 and TATA-C12 thin films can also be explained by the morphology of the supramolecular polymers. As can be seen in Figure 170, TATA-C4 forms more crystalline-like structures, which normally improves charge transport, whereas TATA-C12 forms large bundles of flexible supramolecular polymers.

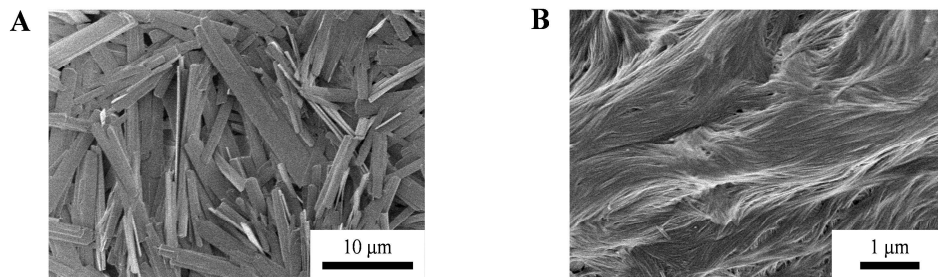


Figure 170. SEM images of TATA-C4 (A) and TATA-C12 (B) thin films formed on IDEs.

C. Triarylamine trisacetamide crystals

Triarylamine trisacetamides (TATA-Ac) are able to form crystals (Figure 171) due to reduced steric hindrance from alkyl chains and triple hydrogen bonding (Chapter III 3B. *Self-assembly and crystallization*). Compared to the supramolecular polymers studied in the previous section, nitrogen centers are stacked more closely together in TATA-Ac self-assemblies due to its crystalline form. This could improve electronic communication. Furthermore, less structural defects are present in crystalline materials, which could equally benefit charge transport. Therefore, enhanced conductivity properties for TATA-Ac crystals are expected.

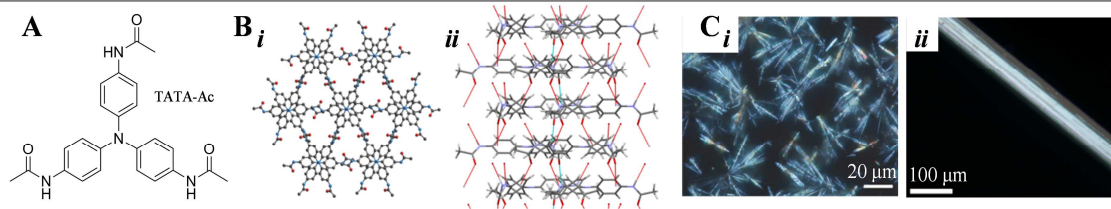


Figure 171. A) Molecular structure of TATA-Ac; B) top (i) and side (ii) view of the crystal structure. In (i) 7 columns are presented, in (ii) two; C) depending on the crystallization conditions small (i) or large (ii) crystals are obtained. The nitrogen centers are stacked in the direction of the long axis of the crystal.

i. Conductivity of small neutral crystals deposited on OFET substrates

The conductivity of crystals was examined in collaboration with Prof Thomas Heiser and Dr Patrick L  v  que from ICube, employing OFET structures (Figure M4). First, short neutral crystals were tested. Initial experiments show low conductivities (Figure 172A), which is expected for neutral crystals that do not contain radical cations. Surprisingly, with increasing surface coverage of the OFET channels, high currents were measured, even exceeding the compliance (10^{-2} A) of the measurement unit at 10 V (Figure 172B). Thus, these experiments demonstrate that, even without photo-oxidation, TATA-Ac exhibits conductivity properties. This is a remarkable feature considering all previous experiments demonstrate poor conductivities for neutral TATA self-assemblies. In

general, conductance is possible only upon oxidation, which creates an inter-molecular charge transfer band.

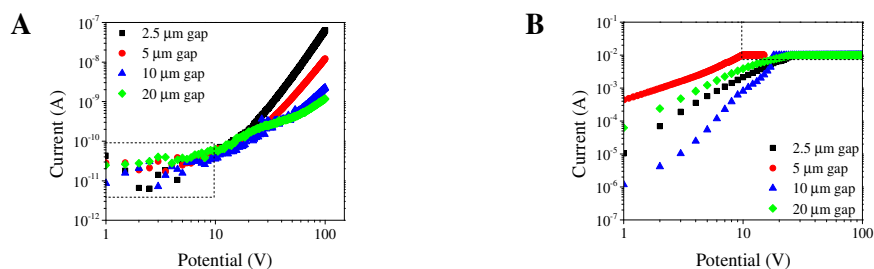


Figure 172. Log-log IV curves recorded for small neutral TATA-Ac crystals. A) low surface coverage. The points inside the dashed rectangle are situated below the minimum detection threshold of the current-measuring unit; B) high surface coverage. The points inside the dashed rectangle are situated above the current-compliance of the measuring unit.

More insight on the conduction can be gained from the IV characteristics. A linear relationship ($I \sim V$) is found at low surface coverage and low potential ($V \leq 11$ V), as well as at high surface coverage for the measurement on a 5 μm OFET channel-length. This linear relationship indicates an Ohmic behavior (10^{11} and 10^3 Ω for low and high surface coverage respectively). In contrast, the IV slope approaches a quadratic relation ($I \sim V^2$) at high surface coverage for the measurement on a 2.5 and 20 μm OFET channel-length, and low surface coverage for the 2.5 and 5 μm gap OFET above 11 V (10^9 and 10^3 Ω respectively). Such a quadratic relationship could signify a space charge limited current (SCLC) regime, but it can also be a signature of an injection-limited current. The high currents measured, especially for the high-surface coverage devices, can be explained by two hypotheses. The first hypothesis states that unintentional doping of the crystals occurs when exposed to air. Indeed, while all the electrical characterizations are performed inside a N_2 containing glove-box, crystal deposition on top of the substrates was performed in ambient air. Unintentional doping can lead to very high charge-carrier mobilities with no gate-voltage influence on the IV characteristics and thus very high currents. However, it is difficult to imagine that the crystals are doped to such extends just by a short contact with air. Moreover, EPR measurements on neutral crystals, equally performed under atmospheric conditions, did not display a signal. The second hypothesis states that crystals are only moderately doped by their short contact with air, below the detection limit of EPR. In this case, the mobility inside the crystals would be even higher than in the former case. Such high charge carrier mobility could be the result of the close packing of nitrogen centers and the presence of an orbital delocalized over nitrogen atoms inside a stack as suggested by the one-line EPR pattern.

Unfortunately, the charge carrier mobilities could not easily be calculated. The measurements at low surface coverage could not be used because the OFET channels are not entirely covered by the crystals. At high surface coverage the OFET channels are completely covered. Nevertheless, there is

no effect of the gate voltage on the drain-source current, preventing the use of conventional OFET equations to extract the charge-carrier mobility. Furthermore, the observed quadratic IV dependence could not be unambiguously ascribed to a SCLC regime rendering the mobility calculation very hazardous. Moreover, it was difficult to obtain reproducible results as the current measured depended heavily on the amount of crystals present on the OFET structures. Likewise, crystal orientation could also adversely affect the reproducibility.

Interestingly, in a second set of experiments, the crystals did demonstrate an OFET effect (influence of the gate-voltage on the drain-source current), which was not previously observed (Figure 173A and Figure A25). In OFET structures, the mobilities measured represent the charge-carrier mobility at the semiconductor/dielectric interface in the substrate-plane. It is possible that the OFET effect was not previously observed because the rigidity of the crystals prevented any charge accumulation in the channel. Using the linear and saturated regimes (Figure 173BC), we determined the hole mobilities inside the ensemble of small neutral crystals. Generally, the calculations show hole mobilities of 10 to $30 \times 10^{-9} \text{ cm}^2 \cdot \text{V}^{-1} \cdot \text{s}^{-1}$. In these calculations (Materials and Methods Chapter IV) the assumption is made that the whole OFET structure is covered in crystals. However, from optical microscopy photographs, it can be seen that only a small number of crystals are present (Figure A24). Correcting for the low surface coverage, the actual hole mobilities are one order of magnitude higher. Taking into account poor electrode contact (as observed from the IV curves) and poor contact with the gate dielectric, the hole mobilities might even be higher. For now, the results suggest moderate to normal hole mobilities compared to other organic semi-conductors.

Using thermal annealing, we expected to favor the contact between the crystals and the electrodes as well as the contact between the crystals and the dielectric, and therefore more accurate results. The melting temperature of TATA-Ac crystals is $255 \text{ }^\circ\text{C}$, and thermal-annealing was performed at $150 \text{ }^\circ\text{C}$. However, it led to a degradation of the samples (Figure A24B).

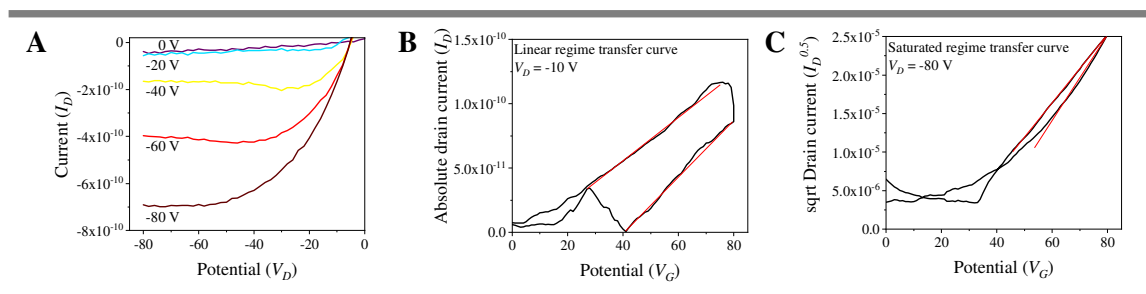


Figure 173. A) Output characteristics of OFETs treated with HMDS with a $20 \text{ }\mu\text{m}$ large-channel covered by small neutral TATA-Ac crystals. The gate voltage applied (V_G) ranges from 0 to -80 V ; Transfer characteristics measured on the same device in the linear (B) and saturation (C) regime.

The samples displaying OFET effects were subsequently photo-oxidized by light irradiation in a chloroform saturated atmosphere. The samples became green, a well-known optical indication for the

formation of radical cations in the system (Figure A24D). Although most transistors displayed similar results as obtained before oxidation upon the first sweep (Figure 174), the majority failed during the second sweep. The samples seem to be unstable after oxidation, just as was observed after thermal annealing. However, in this case, the presence of chloride counter ions could contribute to it.

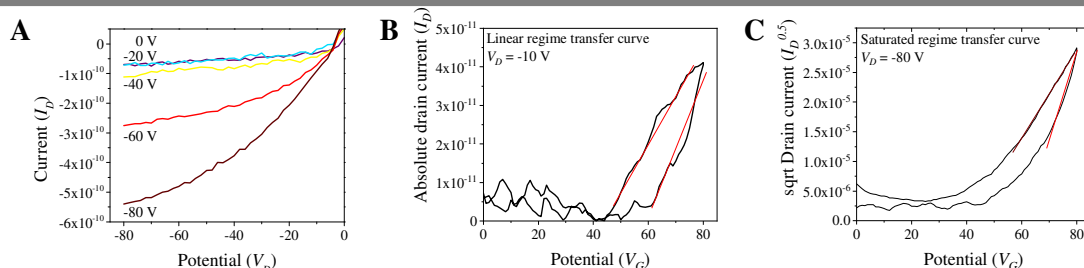


Figure 174. A) Output characteristics of OFETs with a 5 μm large-channel covered by small photo-oxidized TATA-Ac crystals (CHCl_3 vapors for 30 minutes). The gate voltage applied (V_G) ranges from 0 to -80 V; Transfer characteristics measured on the same device in the linear (B) and saturation (C) regime.

An attempt was made to perform the same measurements on photo-oxidized small TATA-Ac crystals, and neutral and photo-oxidized large crystals (Figure A21 and Figure A22). However, measurement results varied significantly. Not only due to the lack in control on surface coverage and crystal orientation, but also due to the varying effectiveness of photo-oxidation and the time elapsed between photo-oxidation and the measurement.

ii. Conductivity of small and large neutral crystal using conductive-AFM

In order to circumvent reproducibility problems encountered due to surface coverage and crystal orientation, the conductivity of single crystals were measured by conductive-AFM (C-AFM). For C-AFM measurements crystals were deposited on a SiO_2 substrate with 50 nm thick gold electrodes (Figure 175). By positioning the AFM tip at a distance zero from the electrode, mainly charge transfer in the direction perpendicular to the stacking direction is measured (yellow arrow in Figure 175B). Moving the tip further away, both charge transport perpendicular to the stacking direction and charge transfer along the stacked nitrogen centers takes place (orange arrow in Figure 175B). At distances much longer than the height of the crystal, mainly charge transfer along the stacked nitrogen centers contributes to the measured conductivity (red arrow in Figure 175B). In the two sub-sections below, the charge transport of small and large TATA-Ac crystals will be discussed.

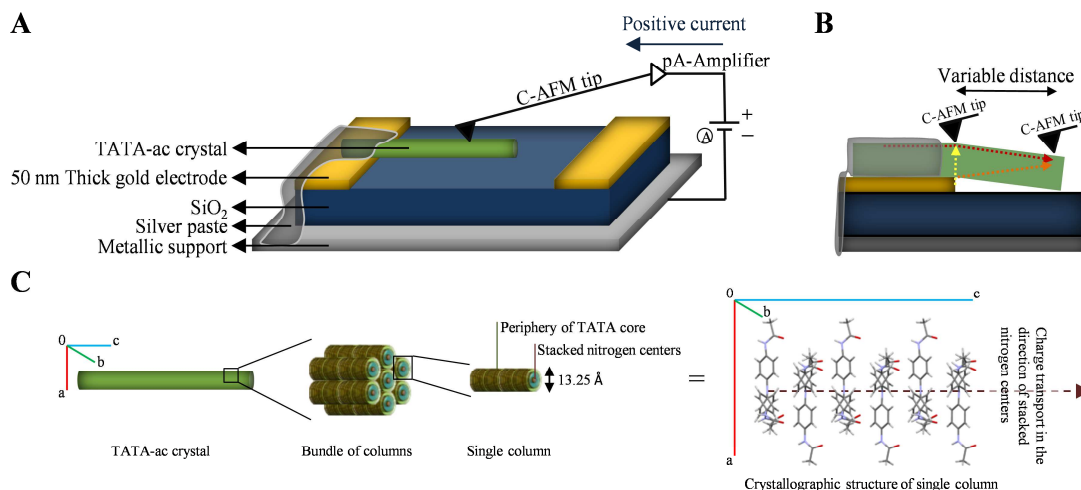


Figure 175. A) Schematic representation of the conductive-AFM set-up for single TATA-Ac crystal measurements; B) schematic representation demonstrating the possible paths for charge transport inside the single crystal. The red arrow represents charge transport in the nitrogen center stacking direction, the yellow arrow charge transport perpendicular to the nitrogen center stacking direction, and the orange arrow charge transport through the whole crystal; C) internal structure of the crystal demonstrating the orientation of the columns in the direction of the long axis of the crystal.

C-AFM on small neutral TATA-Ac crystals

First, small neutral crystals were studied. In these experiments the crystals were not coated by silver paste. As a result most crystals did not display any conductivity due to poor electrode contact. In **Figure 176B** the topographic and contact current images of a crystal that does display conductivity are presented. The crystal quality is not optimal, as can be seen from the topographic images. Nonetheless, at a distance between 0 to 1 μm from the electrode, the crystal surface is relatively defect free. In this region, at an applied bias of 5 V, a stable current of ~ 18 pA was measured (**Figure 176C**). This corresponds to a resistance of $28 \times 10^{10} \Omega$. Assuming the current travels through the whole crystal (length = 1×10^{-4} cm; width $\approx 2 \times 10^{-4}$ cm; height $\approx 350 \times 10^{-7}$ cm), the resistivity is $\sim 2 \times 10^7 \Omega\cdot\text{cm}$, and the conductivity is $5 \times 10^{-8} \text{ S}\cdot\text{cm}^{-1}$. The hole mobility can be approximated using equation 24:

$$\rho = \frac{1}{q \times p \times \mu_p} \quad (24)$$

Here, ρ is the resistivity, q the elementary charge (1.6×10^{-19}) and p the concentration of charge carriers, which is estimated to be $\sim 10^{-13} - 10^{-15}$ per cm^3 (range of charge carrier concentrations in normal organic semi-conductors). The hole mobility lies in the range between 3×10^{-4} and $3 \times 10^{-2} \text{ cm}^2 \cdot \text{V}^{-1} \cdot \text{s}^{-1}$. In **Figure 176D** the conductivities and hole mobilities obtained at other applied voltages

are listed. Worth mentioning is that the mobilities obtained by C-AFM measurements are 4 to 6 orders of magnitude higher than the ones measured for crystals on an OFET structure.

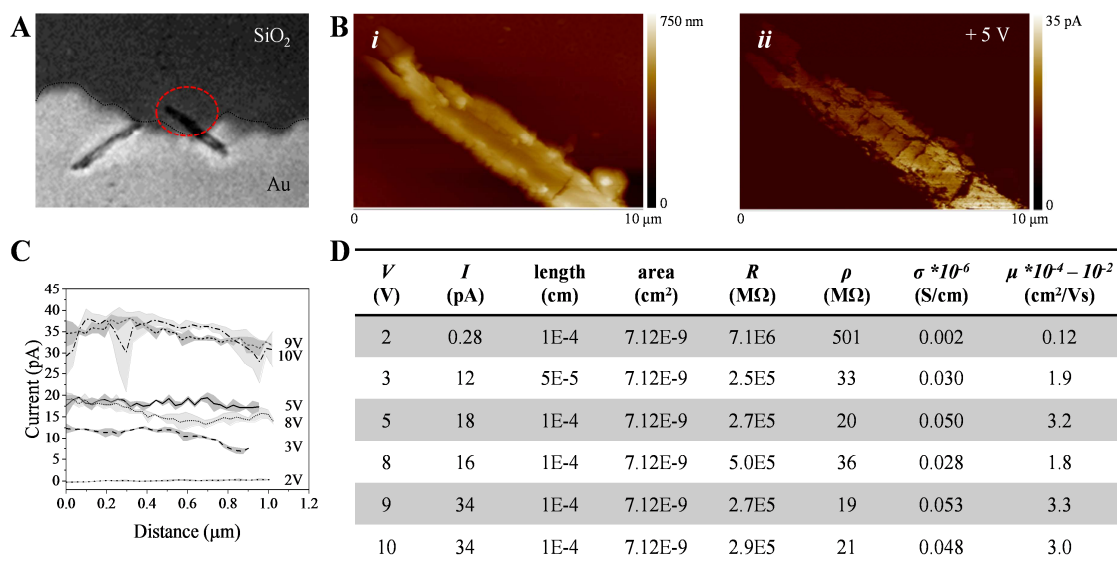


Figure 176. A) optical microscopy photograph of two small TATA-Ac crystals positioned both on the gold electrode and on the SiO₂ insulator; B) height (*i*) and contact current (*ii*) image (at a 5 V bias) of the small TATA-Ac crystal indicated by the red circle in (A); C) current recorded over the first 1000 nm of the crystal; D) table summarizing the conductive properties.

Currents as a function of the distance from the electrode are recorded for different potentials (Figure 177A). Although the curves appear to be linear, not enough points are present to construct a reliable *IV* curve. Therefore, no hypothesis can be drawn on the type of charge transport. The current increases above a threshold potential (V_{th}) that lies between two and three volt. Then a resistance of approximately 270 G Ω is measured, which increases to 380 G Ω at a distance of 5 μ m from the electrode. In Figure 177B, the *I-d* characteristics at 5 V are presented. The current shows a linear decrease, as indicated by the red dotted line. The sudden drops in current are directly related to defects in the crystal surface. No evident difference can be observed in slope in proximity of the electrodes and further away. This could suggest that there is only one charge transport mechanism. As the conductivity persists over longer distances, where the distance from the electrode (10 μ m) is much longer than the height of the crystal (~356 nm), we postulate that primarily conductivity along the crystal (TATA-Ac stacking direction) takes place.

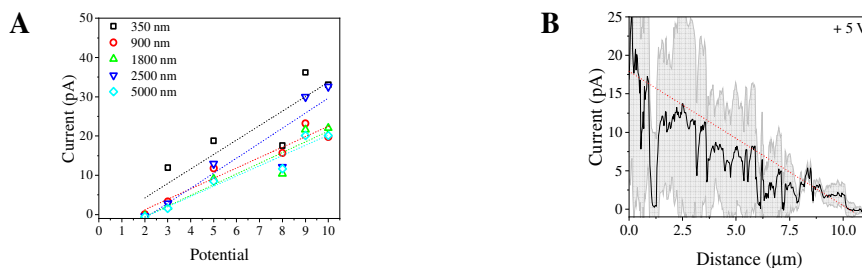


Figure 177. A) *IV* curves recorded for the crystal presented in **Figure 176** as a function of the potential for different distances from the electrode; B) *Id* curves recorded for the same crystal at an applied bias of 5V. The black solid line is the averaged current, the grey area corresponds to the standard deviation.

C-AFM on large neutral TATA-Ac crystals

Then, we continued with measurements on large neutral TATA-Ac crystals. The ends of the crystals positioned on the gold electrodes were coated in silver paste. As a result, electrode contact is enhanced and almost all crystals displayed conductivity. In **Figure 178A**, the *IV* curves of two crystals are presented. One shows the minimal currents measured, the other the highest currents measured out of all crystals tested. The currents recorded seemed to depend directly on the quality of the crystal. As can be seen from topographic images in **Figure 178B**, the crystal demonstrating low conductivity had more surface defects than the crystal exhibiting higher conductivities. Thus, conductivity properties extracted from the blue curve are the closest to the true intrinsic properties. Just as for small crystals, the current increases linearly after surpassing a threshold potential of $\sim 2\text{V}$. The slope of the blue *IV* curve in proximity of the electrodes corresponds to a resistance of $37\text{ G}\Omega$.

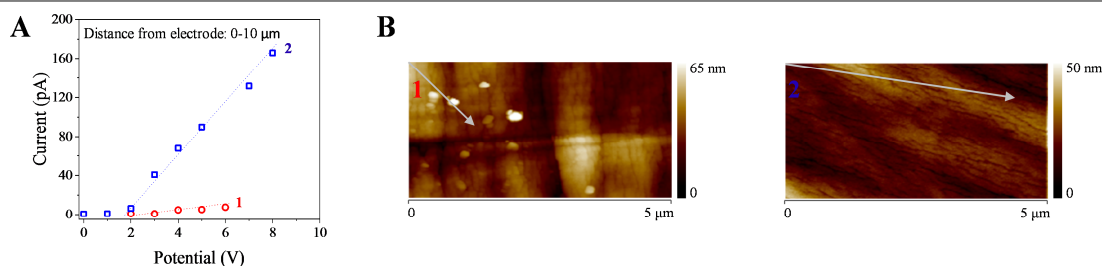


Figure 178. A) *IV* curves recorded for two large neutral TATA-Ac crystals. The currents presented are an average over $10\ \mu\text{m}^2$ at the electrodes edge; B) topographic AFM images of the two crystals. The grey arrows present the direction of the long axis of the crystals.

For all crystals tested, the *Id* curves demonstrate a stable current over a distance of $10\ \mu\text{m}$ (**Figure 179A**). For the lower quality crystal the current remains constant over at least $40\ \mu\text{m}$. The higher quality crystal shows a linear decrease in current after $10\ \mu\text{m}$ and a change in slope at $20\ \mu\text{m}$ (**Figure 179B**). From other crystals we observe that the off-set in linear decrease can vary significantly between 10 and $50\ \mu\text{m}$. We calculated the resistivity, conductivity and hole mobility for the high

quality crystal in the same manner as done for the small crystals (Figure 179C). At a distance of 10 μm , where relatively few defects are present and the current is stable, a current of 90 pA was recorded at an applied bias of 5 V, which corresponds to a resistance of $5.6 \times 10^{10} \Omega$. At a distance of 40 μm a current of 30 pA was recorded, corresponding to a resistance of $17 \times 10^{10} \Omega$. The crystal has a width of $\sim 33 \mu\text{m}$. The height could not be measured because the height difference between the crystal and the substrate is too large for the AFM. Therefore, we estimated that the crystal is round and has an area of $8.6 \times 10^{-6} \text{cm}^2$. Because the distance from the electrode is approximately equal to the height of the crystal, we assume that the current travels through the whole crystal. This leads to a resistivity of $\sim 4.8 \times 10^8 \Omega\cdot\text{cm}$, a conductivity of $2 \times 10^{-9} \text{S}\cdot\text{cm}^{-1}$, and a hole mobility of $\sim 1.3 \times 10^{-5} - 10^{-3} \text{cm}^2 \cdot \text{V}^{-1} \cdot \text{s}^{-1}$ at 5 V in proximity of the electrode. At 40 μm the resistivity is $\sim 3.6 \times 10^8 \Omega\cdot\text{cm}$, a conductivity of $2.8 \times 10^{-9} \text{S}\cdot\text{cm}^{-1}$, and a hole mobility of $\sim 1.8 \times 10^{-5} - 10^{-3} \text{cm}^2 \cdot \text{V}^{-1} \cdot \text{s}^{-1}$. In Figure 179C all conductivities and hole mobilities are summarized. Probably, the true values are still higher, because some defects were always present. In order to obtain more information on anisotropic charge transport, measurement point much further away from the electrode should be taken.

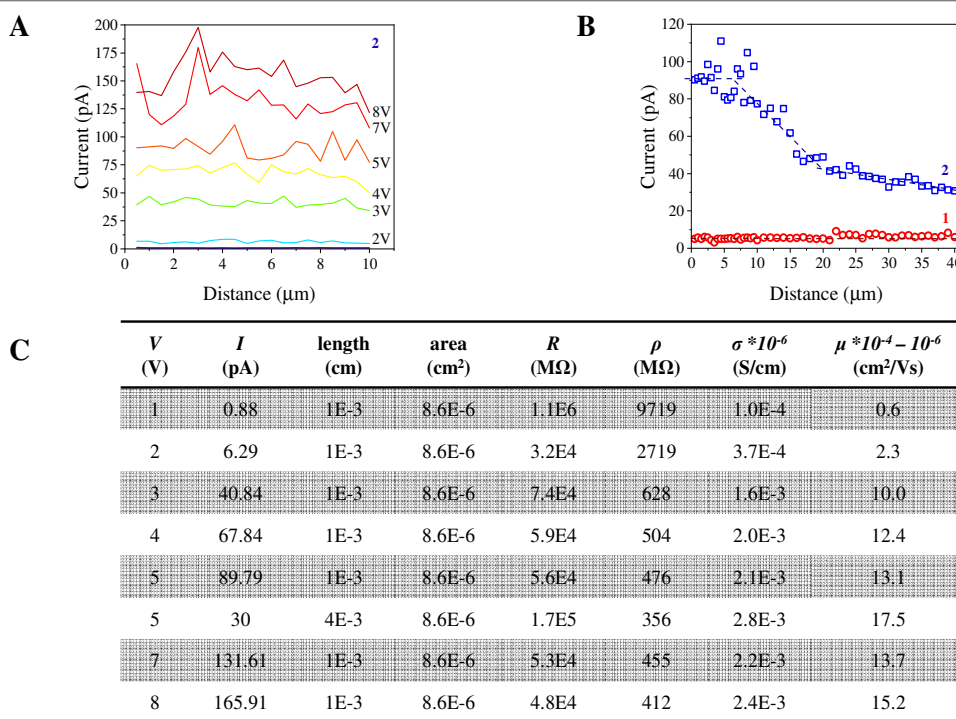


Figure 179. A) I_d curves of crystal 2, measured along 10 μm at various potentials; B) I_d curves of crystal 1 and 2, measured along 40 μm at an applied potential of 5 V; C) table summarizing the conductive properties of crystal 2.

C. Triarylamine norbornene supramolecular physical and chemical gels

Triarylamine trisamides functionalized with norbornene end groups (TANBE) form physical gels after supramolecular polymerization and chemical gels after subsequent ring opening metathesis polymerization (ROMP) (Figure 180A). Dr Ting Liang, former PhD student in our research group, synthesized these molecules in order to enhance the mechanical and thermal robustness of triarylamine gels for their further implementation in practical applications.⁴⁶⁹ The results of this study have been published in Chemistry A European Journal.⁴⁷⁰ Overall, the experiments show that the structures of the supramolecular polymers and their physical gels are preserved during covalent cross-linking by ROMP (Figure 180B). Moreover, the storage modulus increases by two orders of magnitude (Figure 180C). As electronic devices are one of the main applications of triarylamine supramolecular polymers, here, we investigated the effect that covalent capture of physical gels has on their conductance.

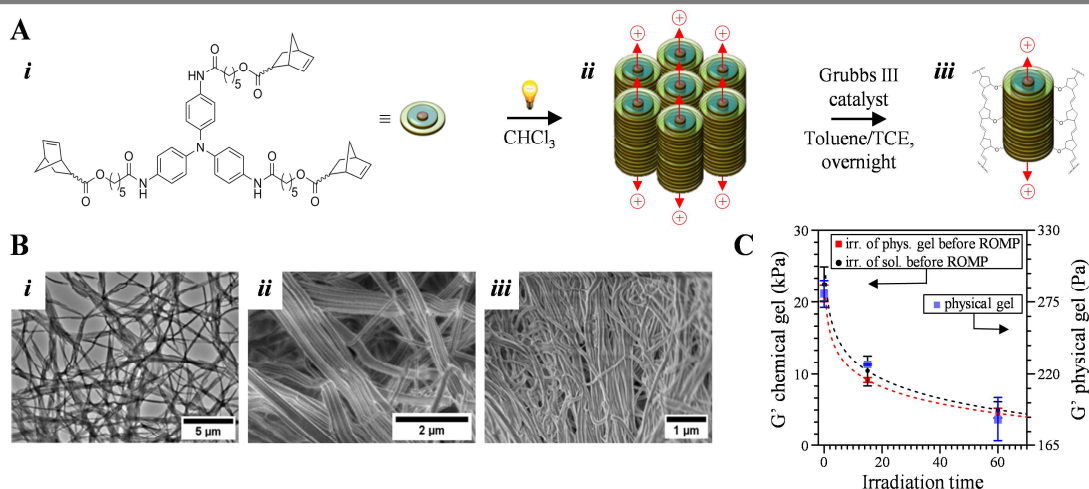


Figure 180. A) Molecular structure and schematic representation of triarylamine norbornene (TANBE) (i) and its supramolecular polymerization upon photo-oxidation in chlorinated solvents (ii), as well as the covalent capture of the supramolecular polymers using ROMP with Grubbs III catalyst; B) SEM images of a 1 mM TANBE solution in toluene (i) and a 15 mM TANBE gel (toluene : TCE, 90:5) obtained after 60 minutes of light irradiation before (ii) and after (iii) chemical cross-linking by ROMP; C) plot of the storage modulus (G') in function of light irradiation time. The blue squares correspond to physical gels, the red squares to chemical gels formed from physical gels irradiated prior to chemical cross-linking, and the black dots to chemical gels irradiated formed from solutions irradiated prior to supramolecular polymerization and covalent cross-linking.

i. Conductance of gels

First, we compared the conductance of TANBE and TATA-C12 supramolecular polymers in solution (Figure 181). 17 mM monomeric solutions were prepared in TCE and inserted into ITO electrochemical cells with a gap of 4 μm , while protected from light. At time zero, some conduction is possible through preformed polymers. Upon photo-oxidation the resistance drops and the conductivity

increases by two to three orders of magnitude. After switching off the light source, the resistance stabilizes and remains stable over long times. *IV* curves were recorded right after photo-oxidation and show equivalent conductance for TANBE and TATA-C12 supramolecular polymers. We can thus conclude that TANBE and simple TATA supramolecular polymers have identical conductivity properties. This result further highlights the observation made in section Chapter IV 3B. *Triarylamine mono- and trisamide supramolecular polymers* that the conductivity through stacked nitrogen core motifs remains unperturbed by the substituents on the periphery. It equally implies that the results obtained for physically and chemically cross-linked TANBE gels, could be generalized to the TATA family as a whole.

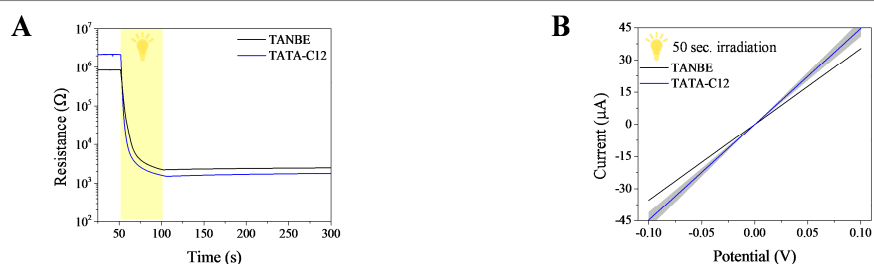


Figure 181. A) Plot of the resistance versus time for 17 mM TANBE (black line) and TATA-C12 (blue line) supramolecular polymer solutions in pure TCE. The light yellow area in the plot corresponds to the light irradiation time; B) *IV* curves recorded directly after the experiment performed in (A). The grey areas correspond to the standard deviation taken over three experiments.

A solvent mixture of toluene TCE (90:10) was chosen for the formation of physical gels because toluene reinforces supramolecular polymerization, while the addition of TCE ensures the possibility of photo-oxidation. The main function of TCE, however, was to lower the gelation temperature (from 82 °C to 63 °C) to guarantee that no aggregates will be present prior to temperature dependent rheological measurements. In a first set of experiments, solutions irradiated for 0, 15, 30 and 60 minutes were inserted in ITO cells, protected from light and let to gelate. The neutral gels thus obtained show little conductivity (Figure 182A). However, a steep increase in conductivity is observed at short irradiation times, which stabilizes after 60 minutes. Gels formed from irradiated solutions show Ohmic behavior and a conductive state (Figure 182B).

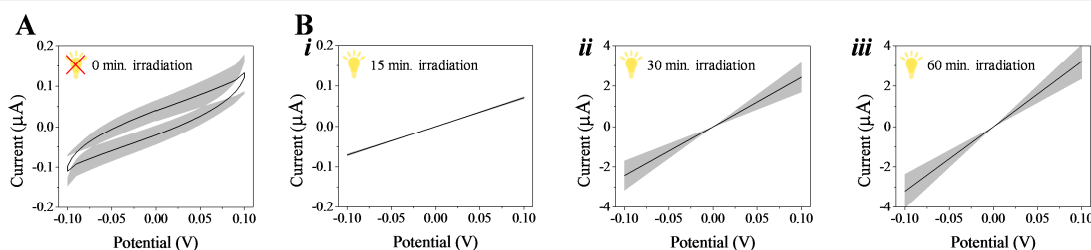


Figure 182. Conductivity experiments performed on physical gels formed from 15 mM TANBE toluene tetrachloroethane (90:10) solvent mixtures. A) *IV* curves recorded for physical gels from

non-irradiated solutions; B) *IV* curves recorded for physical gels from solutions irradiated for 15 (i), 30 (ii) and 60 (iii) minutes. The grey areas surrounding the curves represent the standard deviation taken over three to four experiments.

In a second series of experiments, non-irradiated solutions were inserted into ITO cells and light irradiation was performed after gelation inside the cells. Upon light irradiation the physical gels reach conductivities approximately 20 times greater than previously recorded ($\sim 2 \mu\text{A}$ for physical gels formed from irradiated solutions and $\sim 40 \mu\text{A}$ for physical gels irradiated after gelation inside the ITO cell, measured at an applied bias of 0.1 V) (Figure 183). Interestingly, where previously the conductivity stabilizes after switching of the light source, now it increases steadily over the course of a hundred hours until reaching a resistance of $\sim 2500 \Omega$ (Figure A26). We postulate that the large differences in currents measured stems from the amount of radical cations formed during the time of light irradiation. Using the same light source, more charges can be generated inside ITO cells, which are just $4 \mu\text{m}$ thick, than in a solution contained in a 1 mL glass vial. The considerable increase in conductivity observed for physical gels kept in the dark after light irradiation can be attributed to the fibers undergoing supramolecular optimization.¹⁶

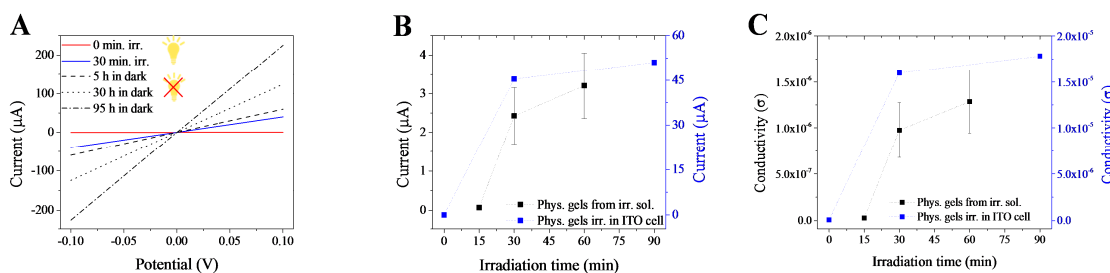


Figure 183. Conductivity experiments performed on physical gels formed from 15 mM TANBE toluene tetrachloroethane (90:10) solvent mixtures. A) *IV* curves recorded for neutral physical gels (red line), physical gels irradiated for 30 minutes (blue line) and physical gels irradiated for 30 minutes and left in the dark for 5 (dashed line), 30 (dotted line) and 95 hours (dash dot line); B) plots of currents measured at an applied bias of 0.1V in function of light irradiation time ; C) plot of the calculated minimal conductivity at an applied bias of 0.1V in function of light irradiation time.

Reticulation of physical gels into chemical ones, while conserving the supramolecular structure, was achieved via ROMP using Grubbs III catalyst. Chemical gels are obtained from neutral physical gels and from physical gels irradiated before or after gelation. As they could no longer be inserted into commercial ITO cells by the capillary effect, their conductivity was probed using a home-made ITO cell (Figure M3). Unfortunately, all measured currents were 4 orders of magnitude lower than the conductivities measured for their physical gel counterparts (Figure 184). We speculate that two factors are at the origin of this observation. First, the dynamic character of the physical gel is lost upon chemical cross-linking. As a consequence, the supramolecular polymers can no longer recombine and rearrange their structure to enhance their contact with the electrodes. This results in impeded charge injection and extraction. Secondly, by chemical cross-linking, the insulating layer surrounding the

conductive nitrogen centers increases. This reduces the probability of charge transfer both between fibers and at the fiber electrode interface, thereby reducing the overall conductivity.

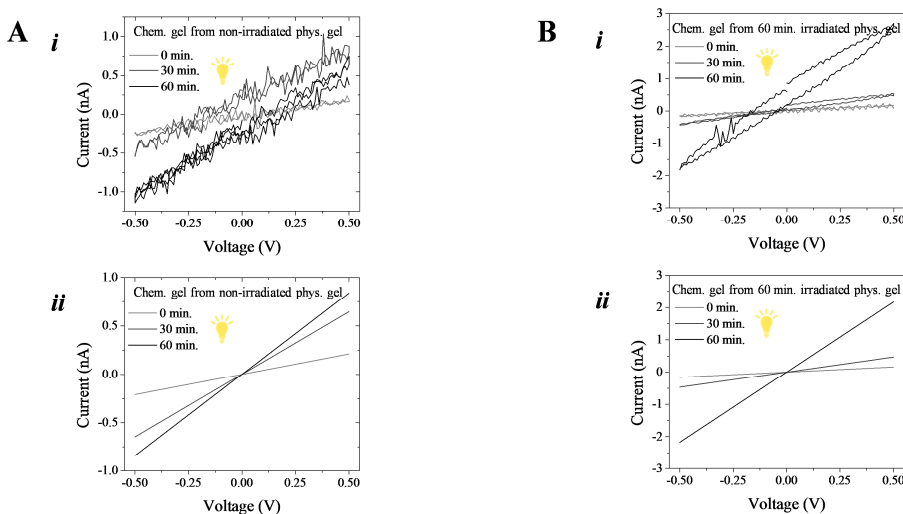


Figure 184. *iV* curves recorded for TANBE chemical gels obtained from 15 mM physical gels, formed in toluene tetrachloroethane (90:10) solvent mixtures, non-irradiated (A) and irradiated for 60 minutes (B) prior to ROMP. In (i) raw data are presented, in (ii) the corresponding linear fits through the origin.

ii. Local conductivity and charge transport properties

Although long-range conductivity in chemical gels was demonstrated to be low, this does not necessarily reflect the local optical and charge transfer properties. Therefore, the local charge transfer character of TANBE supramolecular polymers in solution, physical gels, and chemical gels were investigated by photospectroscopy.⁴⁶⁹ UV-Vis-NIR spectra of a 0.1 mM TANBE solution in chloroform, recorded during light-induced supramolecular polymerization, show the rise of an absorption band around 1150 nm, which signifies that intermolecular through-space radical cation charge transfer takes place between stacked nitrogen centers. At longer irradiation times mainly the absorption band at 800 nm, characteristic for radical cations localized on a nitrogen center, increases in intensity (Figure 185A). The same trend is observed in Vis-NIR spectra of a physical gel (Figure 185B). However, the band at 800 nm does not reach high intensities compared to the band at 1150 nm. This indicates that, in physical gels, primarily delocalized radical cations are generated.

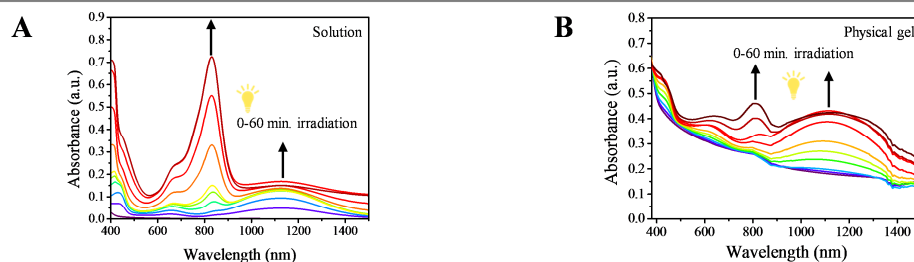


Figure 185. Vis-NIR spectra of A) a 0.1 mM TANBE solution in CHCl₃ upon photo-oxidation; B) a physical gel formed from a 15 mM TANBE toluene tetrachloroethane (90:10) solvent mixture upon photo-oxidized after gelation. The arrows indicate the evolution of the absorption bands at 800 and 1100 nm.

Interestingly, whether localized or delocalized radical cations are present in chemical gels depends on the preparation method. A chemical gel obtained after ROMP of a neutral physical gel displays a large absorption band at 800 nm (Figure 186A). Hence mainly localized radicals are present. This is expected because the supramolecular structure it inherited did not undergo optimization upon photo-oxidation. Therefore, radicals formed after ROMP are relatively confined to the nitrogen center. Chemical gels prepared from irradiated physical gels show much larger augmentations in the absorption intensities at 1100 nm (Figure 186B-C). Introduction of radical cations leads to intermolecular through-space charge transfer processes, which is made possible because the chemical gels inherited the optimized arrangement of the supramolecular stacks. In chemical gel obtained from physical gels irradiated for 60 minutes, more delocalized radical cations are present than localized ones.

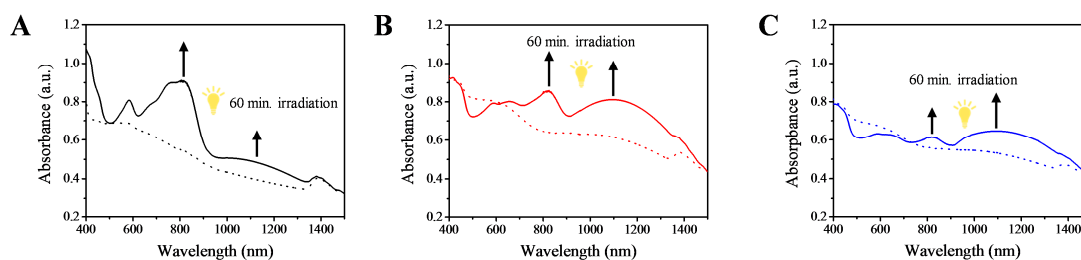


Figure 186. Vis-NIR spectra of chemical gels obtained by ROMP of neutral physical gels (A) and physical gels irradiated for 15 (B) and 60 minutes (C) in gel state. The dotted lines correspond to chemical gels thus obtained, the solid lines to chemical gels re-irradiated for an additional 60 minutes.

IV.4 Perspectives

A. Application in photovoltaic devices

In collaboration with Prof Graetzel, head of the Laboratory of Photonics and Interfaces EPFL, at the école polytechnique fédérale de Lausanne, we are currently investigating the use of TATA supramolecular polymers in perovskite solar cells as hole transporting materials.

The incorporation of TATA-C12 supramolecular polymers has augmented the photo-conversion efficiency significantly. As we have observed that higher conductivities can be reached for thin films of TATA with short alkyl chains, they are currently also studying the incorporation of TATA-C4. Unfortunately, the research is still in its early stages and the work cannot be presented here.

B. Further comparisons between different TAA and TATA supramolecular polymers

First, we would like to further deepen our understanding in the charge transport in TATA-Ac crystals. In this regard we envision performing the following experiments:

- Additional measurements using OFET architectures in which the channels are entirely filled by crystals.
- Perform C-AFM measurements on small neutral crystals that have been coated by silver paste in order to enhance the electrode contact. To obtain more accurate information on the charge transport mechanism, we would need to record *IV* curves containing more data points, at short and long distances from the electrode, on crystals displaying relatively few defects.
- Perform C-AFM measurements on large neutral crystals that are relatively defect free. Just as for the small crystals, reliable *IV* curves should be constructed at distances close and further away from the electrode with regards to the crystal size.

Secondly, we would like to continue to deepen our understanding in charge transport in triarylamine based supramolecular polymers by investigating fibers made of enantiomeric pure chiral monomers that are able to self-assemble into polymers of opposite helicity depending on whether they are formed under thermodynamic or kinetic control. Here, one would expect a better conductivity for the thermodynamically more stable structure, because the supramolecular polymers are longer, stiffer and should contain less structural defects.

Finally, it could be interesting to compare the conductance of ‘normal’ TATA fibers with fibers whose self-assembly process is governed by peptide-enzyme catalysis instead of the traditional nucleation and growth mechanism, in order to further test the robustness of the conductivity properties of triarylamine self-assemblies.

IV.5 Conclusions

First, we have compared the conductances of triaryl mono- and trisamide supramolecular polymers, in solution and gel state. Overall, these series of experiments demonstrate that, although the derivatives have different molecular structures, nucleation and growth mechanisms, supramolecular architectures and physical states, they transition into a conductive state following photo-oxidation and display Ohmic behavior. The resistances measured are within the same orders of magnitude oxidation ($\sim 300 - 500 \Omega$). This means that conductivity through the core motif is seemingly independent of the substituents on the periphery. Thus, triarylamine supramolecular architectures are robust and reliable with regards to their charge transport properties. The minor differences found among the studied structures are related to kinetics associated.

At short irradiation times mono-amides show a larger increase in conductance, which could be attributed to *i*) the presence of octyloxy groups on the periphery which lower the oxidation potential; *ii*) the easier accessibility of the nitrogen centers. When, after 60 minutes of photo-oxidation, the samples are placed in the dark, the conductivity of TAA supramolecular polymers decreases, while it stabilizes for TATA supramolecular polymers. This is explained by the fact that radical cation reduction is a bimolecular process, which means radical decay is more probable in the double columnar arrangement of monoamides. The only difference between solutions and gels is that, for gels, optimization of the supramolecular structure occurs upon photo-oxidation.

When using the same derivatives to form thin films, only molecules appended with short alkyl chains (carbon atoms ≤ 4) showed significant conductance (TATA-C4 $\sim 240 \Omega$). This can be explained by *i*) the less efficient electronic contact between a triarylamine thin film and the electrodes when larger insulating chains are present around the triarylamine core; *ii*) the crystallinity of the polymers formed.

Triarylamine trisacetamides, able to form crystals, exhibit conductivity even in absence of any oxidation process. At high surface coverage of the OFET channels, the currents measured at low potential are in the same order of magnitude of polymers that had been photo-oxidized for 60 minutes. We postulate that the crystals might be unintentionally doped to a certain extent. Overall, these results suggest the presence of a delocalized orbital over the nitrogen atoms inside a stack, due to the close packing of nitrogen centers. Conductive AFM analyses on single neutral crystals demonstrate that the conductivity depends on the quality of the crystal (amount of defects) and precise stacking orientation. The resistances of small and large crystals respectively, are 30 and 400 G Ω . Mobilities lie in the range of $10^{-4} - 10^{-2} \text{ cm}^2 \cdot \text{V}^{-1} \cdot \text{s}^{-1}$ and $10^{-5} - 10^{-3} \text{ cm}^2 \cdot \text{V}^{-1} \cdot \text{s}^{-1}$. Furthermore, large currents could be measured over distances as long as 70 μm .

Triarylamine trisamides decorated with norbornene end-groups, and thus able of chemical cross-linking by ring-opening metathesis polymerization (ROMP), have been used to make physical and chemical gels to enhance their mechanical strength for their incorporation into applications. The conductivities of the physical gels are very similar to TATA gels. However, upon chemical cross-linking, no significant conductance could be measured. We hypothesize that this is due to either the loss of its dynamic character, and thereby decrease in electrical contact, or to the increase of the insulating layer around the conductive nitrogen core. Nevertheless, by choosing the right preparation conditions, the local optical and conducting properties can be retained and tuned.

GENERAL CONCLUSIONS AND PERSPECTIVES

During the three years of my PhD, I have worked with the aim to deepen our understanding of the structure-function relationship of triarylamine supramolecular polymers. More precisely, their electric transport and plasmonic properties in relation with their chemical and supramolecular structures towards their possible integration into electronic devices.

In the first chapter, we have developed the first example of a supramolecular electropolymerization process. This supramolecular electropolymerization process is particularly interesting for the bottom-up fabrication of organic responsive nano- and micro-circuitries. The developed methodology permits spatially addressed nucleation at the anode, and directional growth of the supramolecular polymers following the lines of the electrical field applied. We have demonstrated the *in situ* directional growth of the supramolecular polymers using solely an electrical field to trigger both the self-assembly process and their alignment between micrometer sized interdigitated electrodes and point electrodes spaced 50 μm apart. The general approach presented here could, in principle, be extended to the fabrication of organic devices incorporating other supramolecular polymers or self-assemblies made of molecules with red-ox functionalities.

In the second chapter, we aimed to investigate the plasmonic properties of TATA self-assembled structures. We were especially interested in the formation of organic plasmonic nanoparticles, because of the fundamental ground breaking milestone it would represent for organic electronics. Towards this goal, we developed different methods to obtain TATA-Ac NPs. Among various successful strategies, reprecipitation led to the formation of stable NP suspensions in which the NP size could be controlled by the relative volumes used. Moreover, the aggregates formed were shown to be of crystalline nature. Excitingly, preliminary results indicate that the NPs do, in fact, give a plasmonic response.

TATA-C4 was also studied for the preparation of NPs. Interestingly, TATA-C4 shows the ability to form different self-assembled structures, such as fibers, rods and nanocubes. The developed systems of both TATA-Ac and TATA-C4 nanoparticles will be followed, in the near future, by studies to better understand their plasmonic response in function of nature, size, crystal arrangement and morphology.

In the final chapter, we have compared the charge transport in various triarylamine-based supramolecular polymers. We believe that these studies will be of interest in the search of the

appropriate molecule to construct organic electronic devices. We have shown that, although triarylamine mono- and trisamides both reach similar conductivities after oxidation, the stability of the radicals cations, and thus the stability of the currents that can be obtained, differ. Monoamides, that grow into double columnar arrangements, display a faster increase in conductivity upon doping, but equally a more rapid decrease in conductivity when they are subsequently placed in the dark. In contrast, the conductivity of trisamides, that self-assemble in single columns, demonstrate a stable conductivity in the dark. We have also shown that the increasing length of the chains surrounding the nitrogen core negatively affects the electrode contact and/or electronic communication between fibers. For the shortest alkyl chain, the triarylamine is appended by acetamide groups, we made the intriguing observation that the enhanced electronic communication, due to the optimized molecular structure, leads to conductive properties even in a formally 'neutral' state.

For the integration of TAA and TATA supramolecular gels into devices, it could be preferable to equally enhance their mechanical strength. This can be achieved by functionalizing the triarylamine trisamides with norbornene end-groups and subsequent ROMP, by which chemical gels can be obtained. Although we did not succeed in measuring long range conductivity properties, it was shown that the local optical and conducting properties can be retained and tuned by choosing the right preparation conditions.

The combined work presented in this thesis contributes to our understanding of the relationship between the molecular structure of triarylaminines and the supramolecular self-assembled architectures that they form. Moreover, it further reinforces our insight of the diversity of structures that can be obtained by any single molecular framework, even by subtle changes of experimental conditions. I believe this paves the way towards future investigations on triarylamine self-assembly processes that will lead to their integration in devices. We have equally demonstrated the unique and enhanced properties of the self-assembled structures, the factors that contribute to them, as well as how to integrate the self-assemblies in organic supramolecular electronic devices. Therefore, the work presented here, because of its findings, the described approaches to control self-assembled structures and its functional properties, is a solid contribution to the field of supramolecular electronics and should help to push forward the work on supramolecular systems in general.

OUTLOOK AND PERSPECTIVES

The scientific advances made during the three years of my PhD, have contributed to our understanding of the structure – function relationship between the molecular structure of triarylamine and their supramolecular self-assembled architectures. The ultimate objective has always been to work towards the incorporation of triarylamine supramolecular structures into electronic devices to push forward the field of organic supramolecular electronics, in academia and towards industry. Thus, we have tried to elucidate the electric transport and plasmonic properties in relation with their chemical and supramolecular structures. This has helped us to come one step closer to integrating triarylamine supramolecular polymers in actual electronic devices. Now, several ideas emerged and have taken form. Here, I would like to present these projects, in the hopes that they will be investigated in the years to come.

Triarylamine as potential thermoelectric materials

With the advances made in the elucidation of the charge transport properties of triarylamine supramolecular polymers, we have posed ourselves the question whether they could be used as thermoelectric materials. In thermoelectric materials, heat, originating from the earth or sun, is directly converted into an electric current. Moreover, as many devices generate heat while operating, heat-waste recovery can be realized.

We believe that triarylamine supramolecular polymers could possibly demonstrate a large thermoelectric effect because they have shown to be good electric conductors in doped state, and, as it is an organic material, probably has poor thermal conductive properties, which are two fundamental requirements for efficient thermoelectric materials. Their efficiency should be investigated by determining *i*) their Seebeck coefficient (built-in potential resisting diffusion), which is a proportionality constant and thermodynamical state function that expresses the ratio between the potential difference generated by the temperature gradient applied; *ii*) its thermal conductivity, which should be poor; *iii*) their figure of Merit (ZT), which is the product of the temperature and the maximum electro-thermal energy conversion efficiency; *iv*) their power factor, which is the Seebeck coefficient divided by the electrical resistivity.

In order to study these characteristics, thin films of triarylamine supramolecular polymers need to be prepared. We have already shown, by ellipsometry, that thin films of ~ 30 – 40 nm can be constructed by spin casting 15 to 20 mM solutions of TATA fibers. As these films need to be highly

conductive, we propose the use of triarylamine trisamide (TATAs) supramolecular polymers, because they have shown better stabilities in electrical conductivity after oxidation. More specifically, TATA-C4 might be an excellent candidate, because it displays high conductances in thin film state due to its short alkyl chains, which ensures improved polymer – electrode contacts.

I believe that this project is of general interest as it responds to the increasing urge for the development of new, alternative energy sources. Indeed, the world-wide electricity-consumption is ever growing, while traditional fuels (e.g. coal and natural gas) are becoming less abundant and have a massive negative impact on our environment.

100% quantum efficiency OLEDs: chiral triarylamines as spin filter

Triarylamine derivatives have been intensely investigated as hole transporting and emissive materials in organic light emitting diodes. Here, we would like to propose to incorporate it as an additional spin filter layer, to break the 25% EL quantum efficiency limit of single state emitting OLEDs.

Semi-conducting chiral supramolecular polymers exhibit spin selectivity. Thus, by employing chiral supramolecular polymers, we can control whether electrons with spin states ‘*up*’ or ‘*down*’ are conducted in majority and transferred into the emitting layer. This will lead to a reduced formation of triplet excited states, and an increase in singlet state emission.

To realize a TAA spin filter, we envision growing chiral triarylamine polymers, using triarylamine derivatives functionalized with chiral and enantiomerically pure side chains, from a surface. The magnetic and conductive substrate (Ni/Au) will first be covered in a monolayer of triarylamine tris-thiols. The thiol groups ensure that it adheres strongly to the gold. The triarylamine motif ensures that, in a second step, the chiral triarylamine molecules can stack onto it and grow from the surface.

Using magnetic conducting AFM the current can be measured in function of the applied potential and magnetic polarity. The magnetic polarity (sign of the magnetic field) changes the spin states ($m_s = +\frac{1}{2}$, $m_s = -\frac{1}{2}$), and ensures the injection of electrons of primarily one spin state. If the triarylamine supramolecular polymers are indeed spin selective, the currents recorded will depend on the magnetic polarity. Control experiments, with achiral supramolecular polymers, or equal amounts of right and left handed chiral supramolecular polymers, should not show this dependence.

ANNEXES

The annexes are organized by chapter. The figures are presented in order of apparition in the main text.

Chapter II

Purity of TAA-C8 after passing through a SiO₂ column

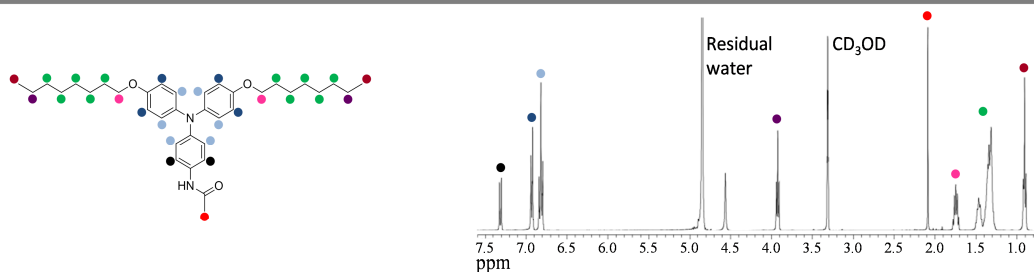


Figure A1. ¹H NMR spectrum (400 MHz) of TAA-C8 recorded in CD₃OD at 298 K.

Calculation of percentage of TAA-C8^{•+} radical cations formed during electro-oxidation

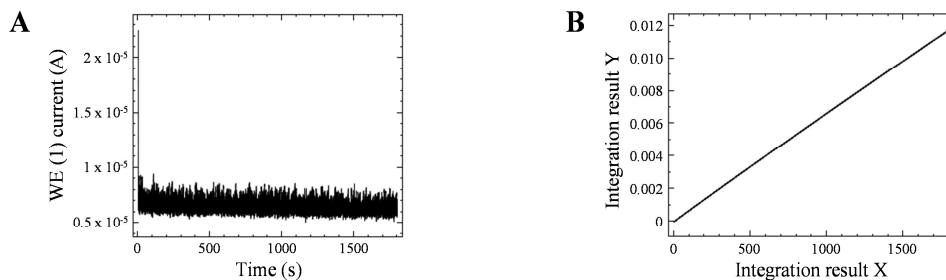


Figure A2. A) Plot of the current in function of the time during electrolysis of a 5.2 mM TAA-C8 solution in CDCl₃ containing 0.1 M TBAPF₃; B) plot of the current integrated over time.

A 5.2 mM TAA-C8 solution (2 mL) in deuterated chloroform containing 0.1M TBAPF₃ was electro-oxidized with a three-probe system (platinum WE (1), silver wire RE, platinum CE). The solution was submitted to an amperometric method (0.6 V vs Ag wire, 0.2 vs Fc/Fc⁺) for a duration of half an hour.

By integrating the current over the time (Figure A2) one finds a current injection of 0.01178 C into the solution. The amount of moles of radical cations is obtained by applying the Faraday constant:

$$\text{Mol of TAA-C8}^{*+} = 0.01178 \text{ C} / 96485 \text{ Cmol}^{-1} = 1.22 \times 10^{-7}$$

The concentration of TAA-C8⁺⁺ in the solution is:

$$[\text{TAA-C8}^{*+}] = \text{Mol of TAA-C8}^{*+} / \text{volume} = 1.22 \times 10^{-7} \text{ mol} / 0.002 \text{ L} = 6.10 \times 10^{-5} \text{ M}$$

The percentage of radicals per neutral TAA-C8 in the solution is:

$$\text{Percentage TAA-C8}^{*+} = 100\% \times 6.10 \times 10^{-5} \text{ M} / 5.2 \times 10^{-3} \text{ M} = 1.2\%$$

Additional images of the field induced alignment of *in situ* electropolymerized supramolecular polymers

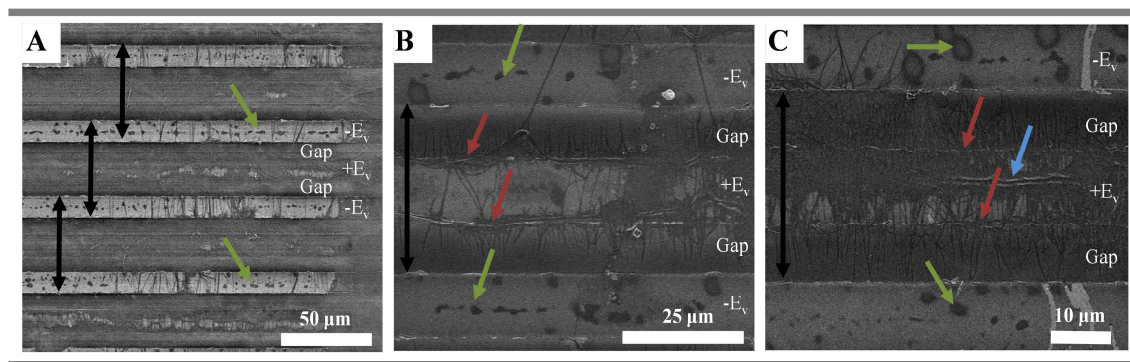


Figure A3. Scanning electron microscopy images of *in situ* electropolymerized supramolecular TAA-C8 polymers from a heptane solution drop casted onto IDEs under an applied DC electric field. A) a 2 mg / mL TAA-C8 solution was drop casted while an $1.25 \times 10^7 \text{ Vm}^{-1}$ Ef was applied; B-C) a 3 mg / mL TAA-C8 solution was drop casted while an $1.25 \times 10^7 \text{ Vm}^{-1}$ Ef was applied. The direction of polymer growth is indicated by the double headed black arrows. Green arrows indicate the presence of amorphous material on the cathodes. Red arrows indicate the nucleation point of polymers at the edges of the anodes. Blue arrows indicate polymers in the middle of the electrode gap growing perpendicular to the electric field.

A video of the *in situ* electropolymerization and field induced alignment can be found at:

<https://onlinelibrary.wiley.com/doi/full/10.1002/anie.201809756>

Calculation of charge carrier mobility

Solutions of 35 mg/mL were prepared. This high concentration was chosen to ensure that the electrode gaps are entirely filled with the supramolecular polymers.

Electrode length	m	1.75×10^{-3}
Electrode gap width	m	1.0×10^{-5}
Electrode thickness	m	1.5×10^{-7}
Number of electrode gaps		29
Avogadro's constant	mol^{-1}	6.02214×10^{23}
Concentration TAA-C8	mg / mL	35
	Mol / m ³	65
Dielectric constant (ϵ)	F / m	1.69×10^{-11}
Slope of IV^2 curve	A / V ²	2.74×10^{-10}

First, the total volume of the gaps in between the electrodes (V_{IDE}) is calculated:

$$V_{IDE} = \text{electrode length} \times \text{electrode thickness} \times \text{electrode gap width} \times \text{number of electrode gaps}$$

$$V_{IDE} = 1.75 \times 10^{-3} \text{ m} \times 1.5 \times 10^{-7} \text{ m} \times 1.0 \times 10^{-5} \text{ m} \times 29 = 7.61 \times 10^{-14} \text{ m}^3$$

Then, the number of moles of TAA-C8 (n_1), and the number of TAA-C8 molecules (N_1), that are present in the gaps, are calculated:

$$n_1 = [\text{TAA-C8}] \times V_{IDE}$$

$$n_1 = 65 \text{ mol/m}^3 \times 7.61 \times 10^{-14} \text{ m}^3 = 4.95 \times 10^{-12} \text{ mol}$$

$$N_1 = n_1 \times \text{Avogadro's constant}$$

$$N_1 = 4.95 \times 10^{-12} \text{ mole} \times 6.02214 \times 10^{23} \text{ mol}^{-1} = 2.98 \times 10^{12}$$

We estimated the area of one TAA-C8 molecule (S_1), and the distance between two TAA-C8 cores (d_{1-1}):

$$S_1 = 1.5 \text{ nm} \times 1.15 \text{ nm} = 1.7525 \times 10^{-18} \text{ m}^2$$

$$d_{1-1} = 5 \times 10^{-10} \text{ m}$$

With this information the number of molecules present in a single supramolecular polymer bridging the gap between electrodes ($N_{1 \text{ in polymer}}$) is calculated:

$$N_{1 \text{ in polymer}} = \text{electrode gap width} / \text{the distance between the TAA-C8 cores}$$

$$N_{1 \text{ in polymer}} = 1.0 \times 10^{-5} \text{ m} / 5 \times 10^{-10} \text{ m} = 2 \times 10^4$$

The total number of polymers ($N_{polymers}$) present in the gaps is then:

$$N_{polymers} = \# \text{ TAA-C8 molecules } (N_1) / \# \text{ TAA-C8 molecules present in polymer } (N_1 \text{ in polymer})$$

$$N_{polymers} = 2.98 \times 10^{12} / 2 \times 10^4 = 1.49 \times 10^8$$

The total cross-sectional area ($S_{polymers}$) of all these polymers is:

$$S_{polymers} = \# \text{ of polymers } (N_{polymers}) \times \text{area of one TAA-C8 molecule } (S_1)$$

$$S_{polymers} = 1.49 \times 10^8 \times 1.7525 \times 10^{-18} \text{ m}^2 = 2.57 \times 10^{-10} \text{ m}^2$$

Now we can use equation 9:

$$\mu = \frac{8L^3}{9A\epsilon} \frac{dI}{dV^2} \quad (9)$$

In which:

$$\mu = \frac{8 \times \text{electrode gap width}^3}{9 \times S_{polymers} \times \epsilon} \times \text{slope} = 0.56 \text{ cm}^2/\text{Vs}$$

Chapter III

Analysis performed after TAA-Ac and TATA-C4 synthesis

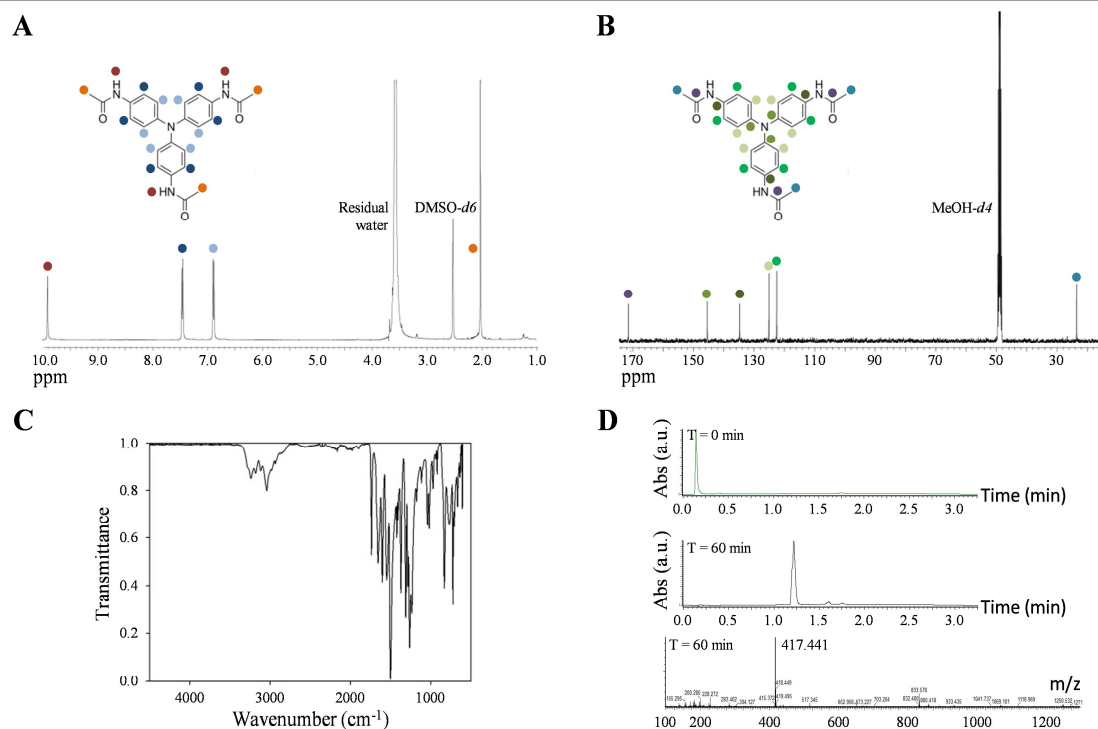


Figure A4. TATA-Ac analyses. A) ^1H NMR spectrum obtained in $\text{DMSO-}d_6$; B) ^{13}C NMR spectrum obtained in $\text{MeOH-}d_4$; C) infra-red spectrum; D) (top) absorption chromatograms recorded by UPLC after 0 and 60 minutes reaction time; (bottom) experimental ESI spectrum recorded by UPLC after 60 minutes reaction time.

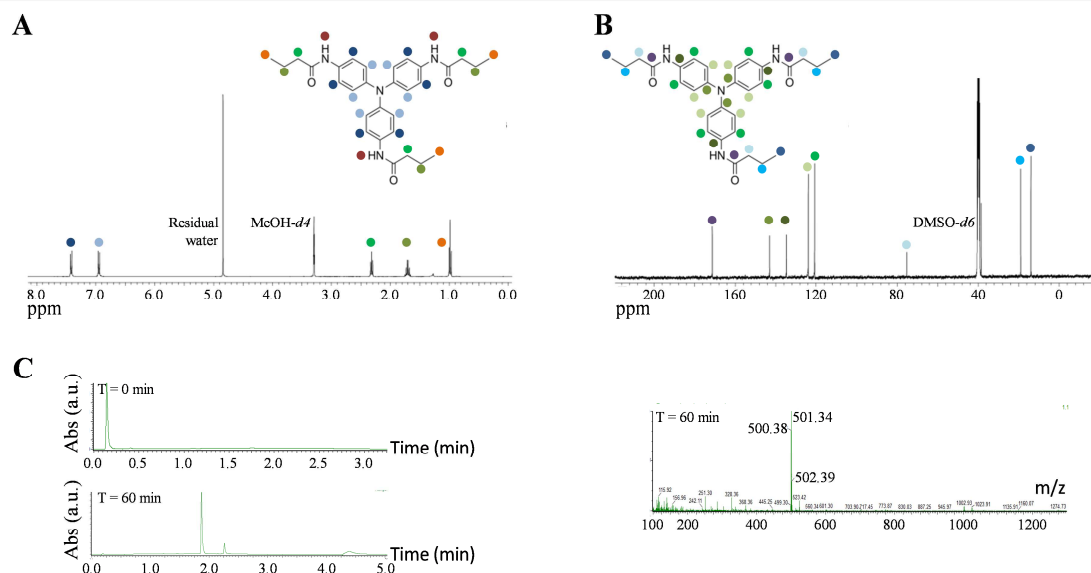


Figure A5. TATA-C4 analyses. A) ^1H NMR spectrum obtained in $\text{MeOH-}d_4$; B) ^{13}C NMR spectrum obtained in $\text{DMSO-}d_6$; C) (left) absorption chromatograms recorded by UPLC after 0 and 60 minutes reaction time; (bottom) experimental ESI spectrum recorded by UPLC after 60 minutes reaction time.

TATA-Ac nanoparticle formation

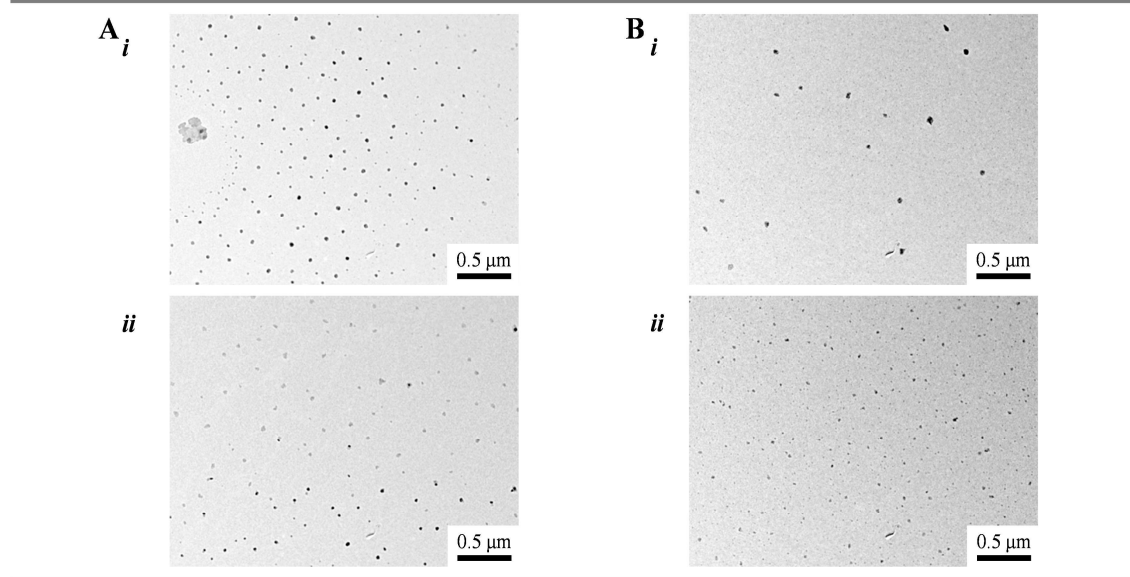


Figure A6. TEM images of drop casted solutions obtained by adding A) 10 μL ; B) 100 μL of a 1 mM TATA-Ac solution (chloroform methanol 95:5) to 10 mL of ethyl acetate.

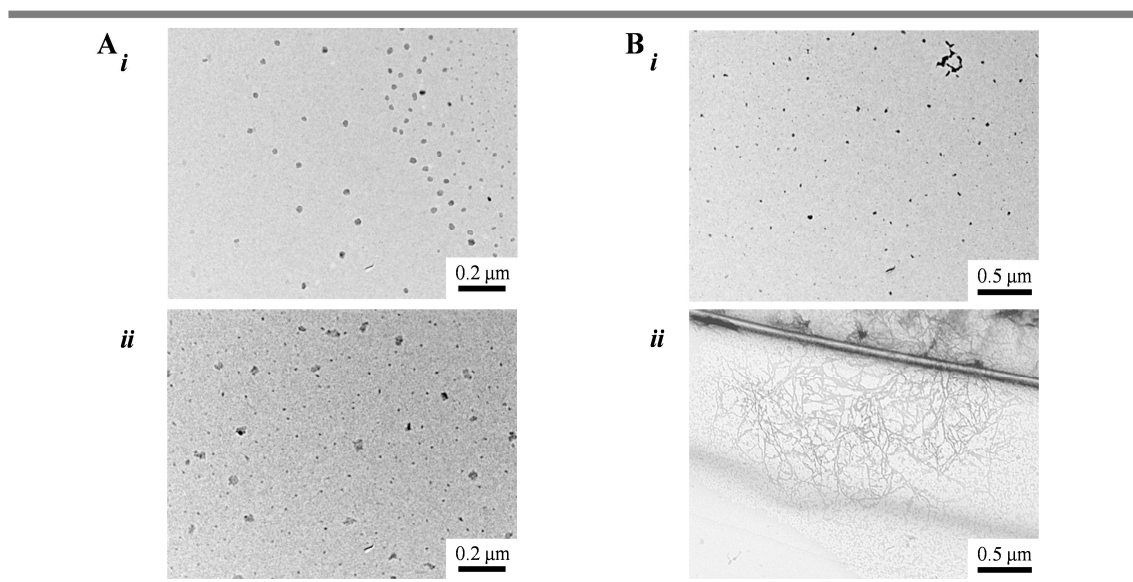


Figure A7. TEM images of drop casted solutions obtained by adding A) 10 μL ; B) 100 μL of a 1 mM TATA-Ac solution (chloroform methanol 95:5) to 10 mL of toluene.

TATA-C4 nanoparticle formation

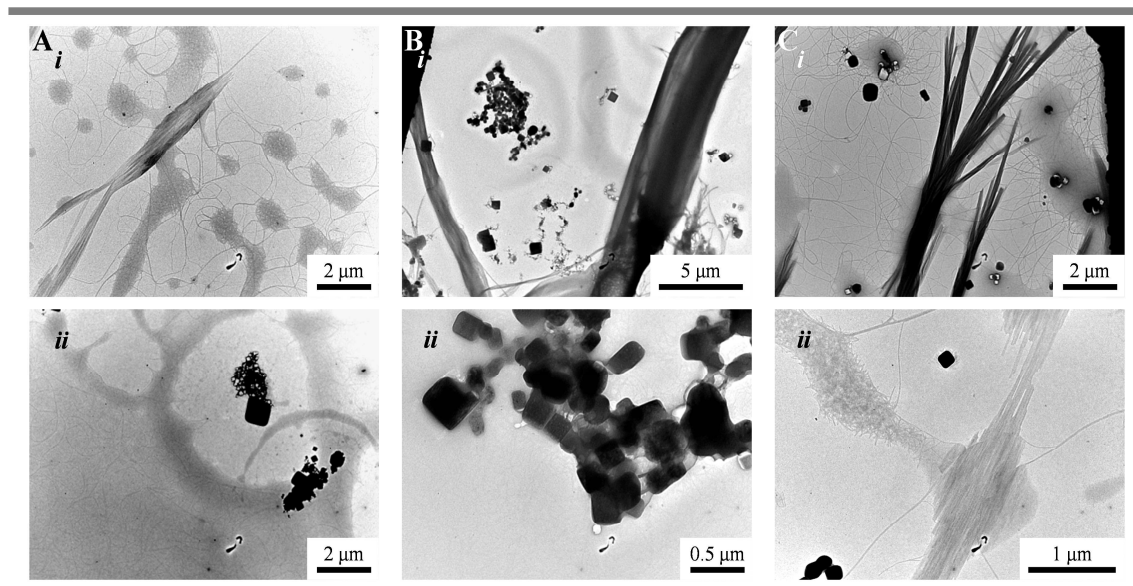


Figure A8. TEM images of 15 mM TATA-C4 solutions in a tetrachloroethane containing A) 2.5%; B) 5%; C) 20% vol% methanol. The solutions were irradiated for 60 minutes prior to drop casting on a TEM grid.

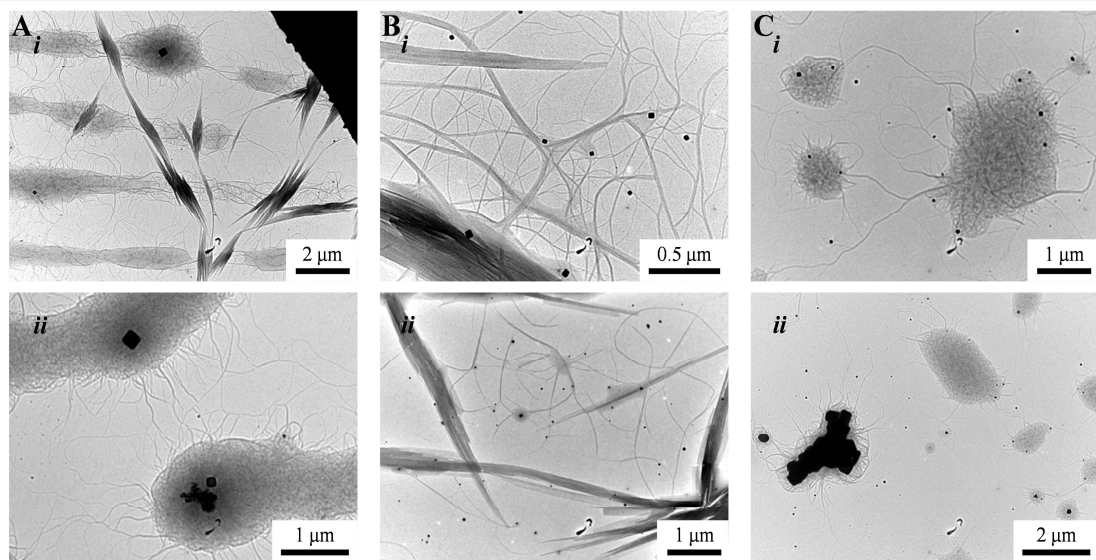


Figure A9. TEM images of 15 mM TATA-C4 solutions in tetrachloroethane containing 5 vol% of methanol drop casted after A) 0; B) 15; C) 60 minutes of irradiation.

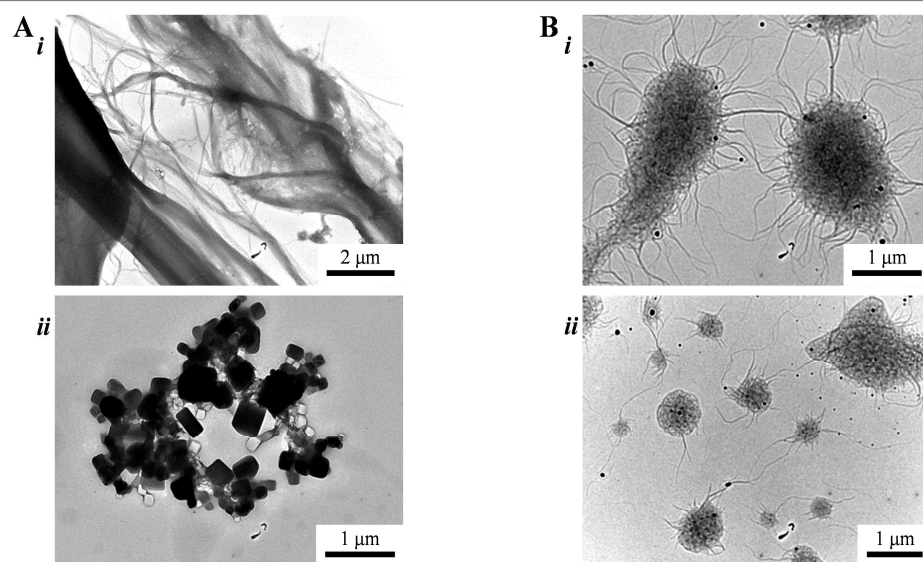


Figure A10. TEM images of 15 mM TATA-C4 solutions in tetrachloroethane containing 5 vol% of methanol. Both samples were irradiated for 60 minutes. A) sample was allowed to cool down on the bench; B) sample was cooled down to room temperature over the course of three hours by placing the sample in a cryostat.

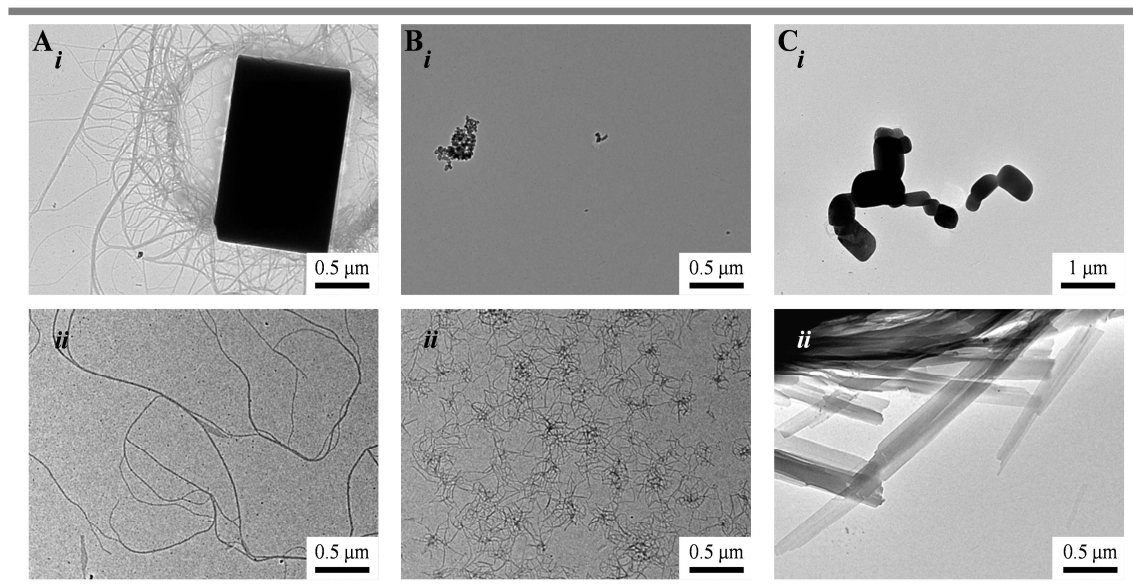


Figure A11. TEM images of 15 mM TATA-C4 solutions in tetrachloroethane containing 5 vol% of methanol. All samples were irradiated for 60 minutes, diluted five times and centrifuged before drop casting. A) sample is cooled down rapidly by immersion in an ice-bath; B) sample was allowed to cool down on the bench; C) sample was cooled down to room temperature over the course of three hours by placing the sample in a cryostat.

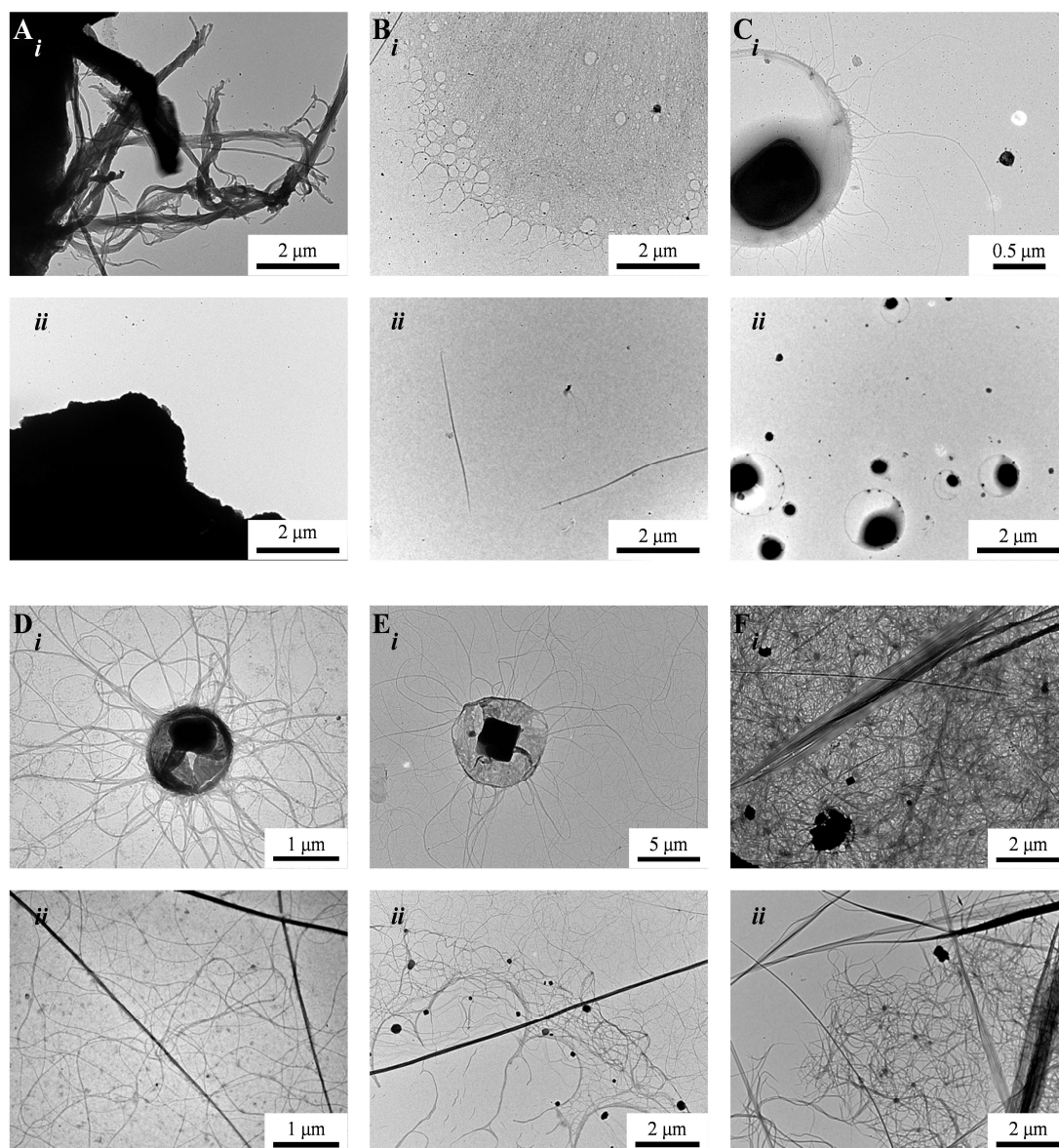


Figure A12. TEM images of A) 0.1 mM; B) 1.0 mM; C) 2.5 mM; D) 10 mM; E-F) 15 mM TATA-C4 solutions in tetrachloroethane containing 5 vol% of methanol. The samples were not irradiated and were cooled down on the bench. After centrifugation the precipitate was re-suspended in A-C, F) toluene or D-E) toluene containing 10 vol% of ethanol.

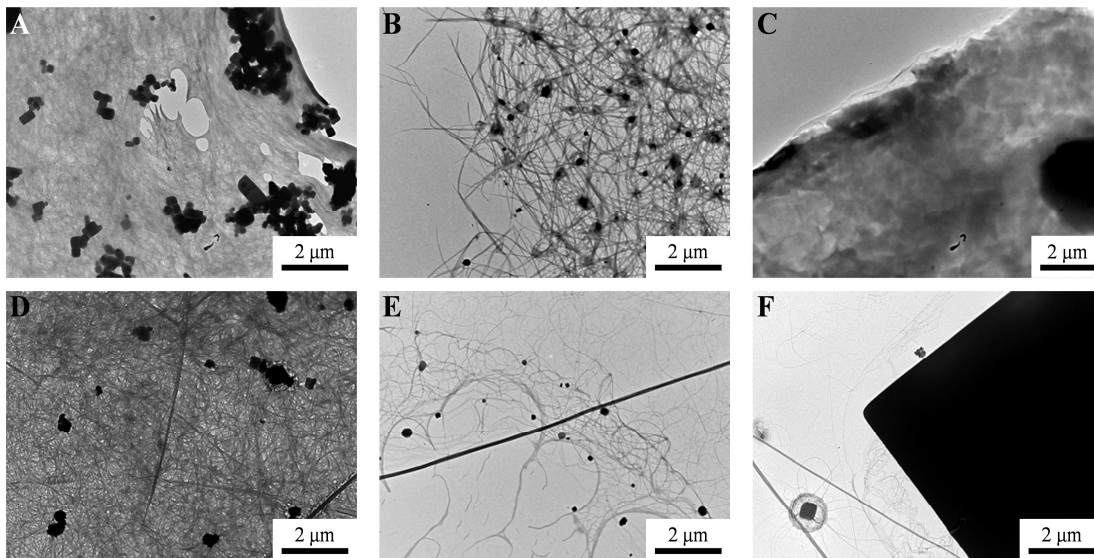


Figure A13. TEM images of 15 mM TATA-C4 solutions in tetrachloroethane containing 5 vol% methanol. The samples were prepared as follows: A) 60 minutes irradiation, 5 times dilution, centrifugation and resuspension in cyclohexane; B) no irradiation or dilution, centrifugation and resuspension in cyclohexane; C) 60 minutes irradiation, no dilution, and sequential addition of cyclohexane over two consecutive centrifugations; D) no irradiation or dilution, centrifugation and resuspension in toluene; E-F) no irradiation or dilution, centrifugation and resuspension in toluene containing 5 vol% of ethanol.

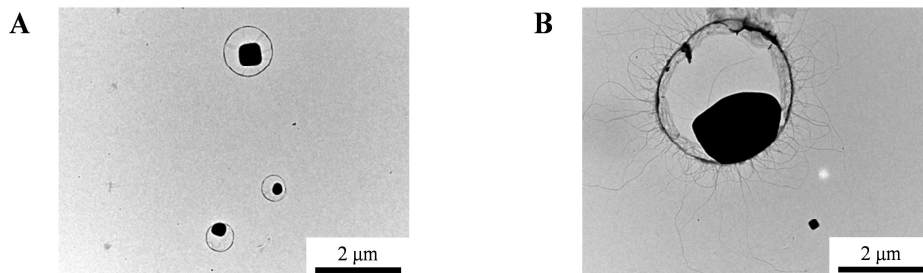


Figure A14. TEM images of 2.5 mM TATA-C4 solutions containing 5 vol% methanol, irradiated for 60 minutes, centrifuged and re-suspended in toluene.

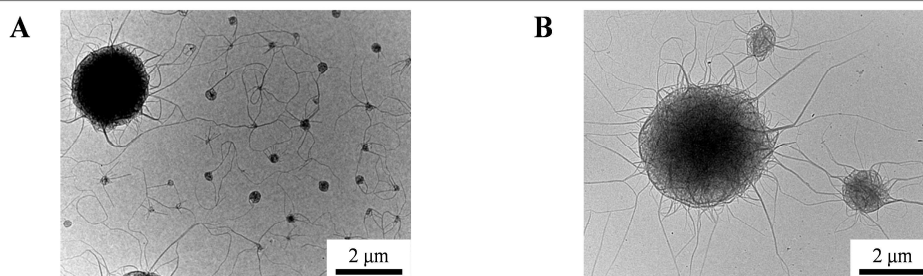


Figure A15. TEM images of 15 mM TATA-C4 solution in tetrachloroethane containing 5 vol% methanol, non-irradiated and filtrated through a 0.2 μm PTFE syringe filter.

Photospectroscopy of TATA-Ac self-assembled structures

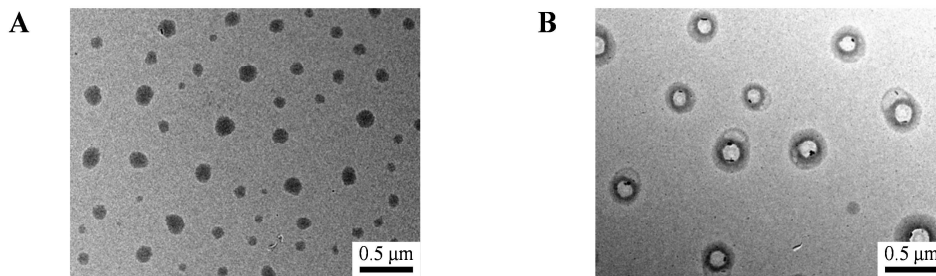


Figure A16. TEM images of 0.5 mM TATA-Ac chloroform methanol (95:5) drop casts after 60 minutes of irradiation.

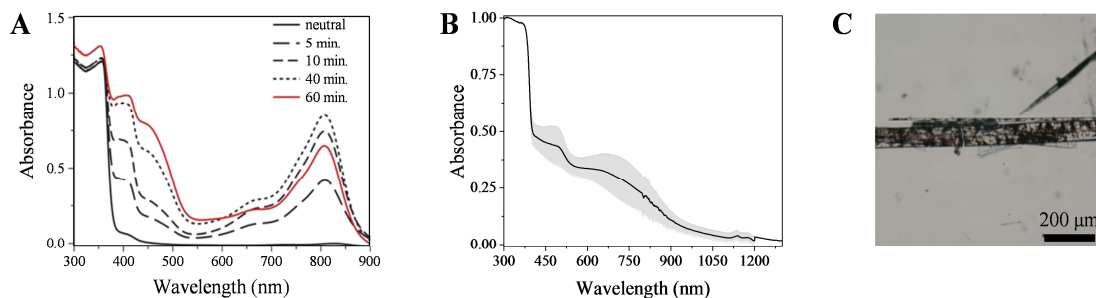


Figure A17. A) Absorption spectra of small TATA-Ac crystals in a CHCl_3 suspension recorded in transmission mode upon photo-oxidation¹⁷; B) absorption spectra of large TATA-Ac crystals obtained from a photo-oxidized crystallization solution containing 5 vol% CHCl_3 , recorded in solid state using an integrating sphere. The grey area corresponds to the standard deviation measured over 2 experiments; C) optical microscopy image of a TATA-Ac crystal obtained as described in (B).

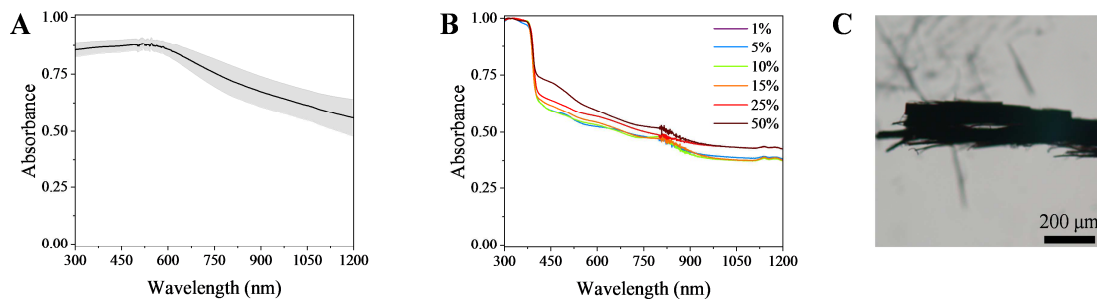


Figure A18. A) Absorption spectra of large TATA-Ac crystals oxidized by I_2 vapors, recorded in solid state using an integrating sphere. The grey area corresponds to the standard deviation measured over 3 experiments; B) absorption spectra of large TATA-Ac crystals obtained from crystallization solutions containing in between 1 and 50 vol% of 5 mM I_2 . The final concentrations of I_2 in the crystallization solutions were 0.05, 0.24, 0.46, 0.66, 0.94 and 1.69 mM; C) optical microscopy image of a TATA-Ac crystal obtained as described in (B).

Additional EPR measurements

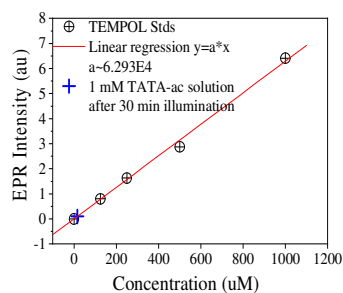


Figure A 19. EPR intensity plotted versus the concentration of a known concentration of radicals in TEMPOL solutions. The EPR intensity of a 1 mM TATA-Ac solution after 30 minutes of light irradiation is presented by the blue cross.

Additional wave guiding experiments

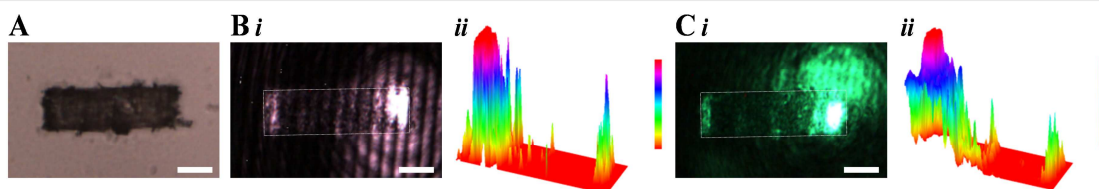


Figure A20. A) Optical microscopy image of a photo-oxidized TATA-Ac crystal displaying structure defects; B-C) optical wave-guiding of the crystal shown in (A) upon illuminating the right distal end with a 785 nm (B) and 532 nm (C) laser. The crystal shows multiple light out-puts due to the structural defects. The scale bar represents 50 μm

Chapter IV

Triarylamine trisacetamide crystals

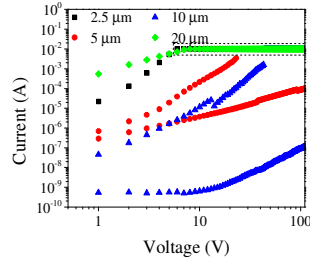


Figure A21. Log-log IV curves recorded for small oxidized TATA-Ac crystals. The points inside the dashed rectangle are situated above the maximum compliance of the measuring unit.

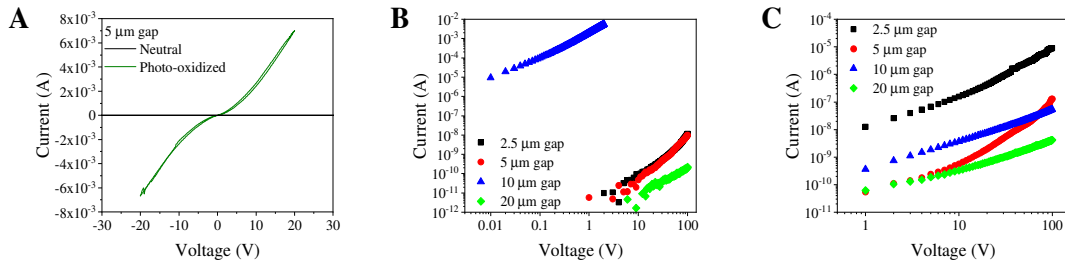


Figure A22. A) linear IV curves recorded for neutral and photo-oxidized large TATA-Ac crystals on a 5 μm OFET device; B) Log-log IV curves recorded for large neutral TATA-Ac crystals. The blue curve is not an artifact. Probably this OFET had a higher surface coverage; C)) Log-log IV curves recorded for large photo-oxidized TATA-Ac crystals. All measurements are performed on OFET structures with low surface coverage.

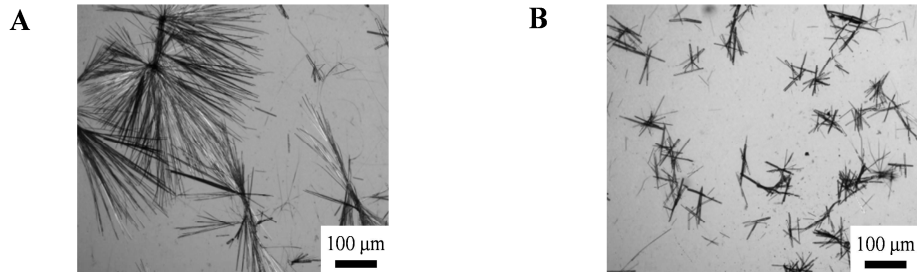


Figure A23. Optical microscopy photographs of small TATA-Ac crystals spin casted at 500 rpm (A) and 1000 rpm (B) on a glass substrate.

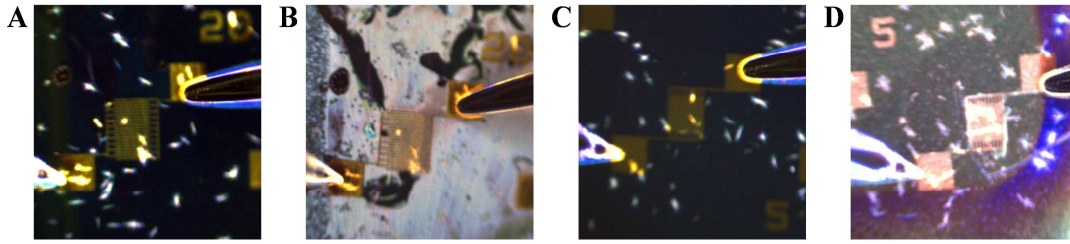


Figure A24. Optical photographs of small TATA-Ac crystals spin-casted at 1000 rpm on OFET substrates with (A-B) and without (C-D) HDMS treatment. In (B) the substrate was further subjected to thermal annealing (10 min. 150 °C). The photograph of the substrate presented in (D) was taken after photo-oxidation under chloroform vapors and light irradiation.

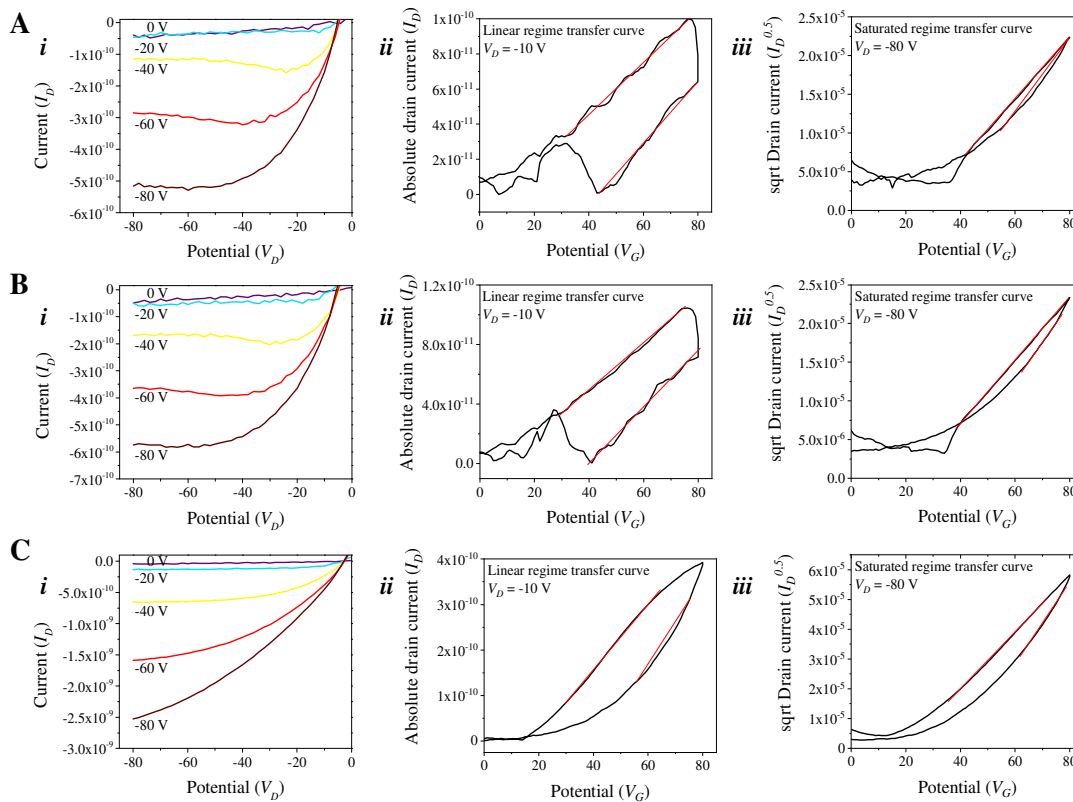


Figure A25. Three-point measurements performed on small neutral TATA-Ac crystals deposited on an OFET structures with A-B) 20 μm and C) 5 μm electrode gaps. The gate voltage applied (V_G) ranges from 0 to -80 V. Transfer curves are obtained from the linear (ii) and saturated (iii) regime.

Triarylamine norbornene supramolecular physical and chemical gels

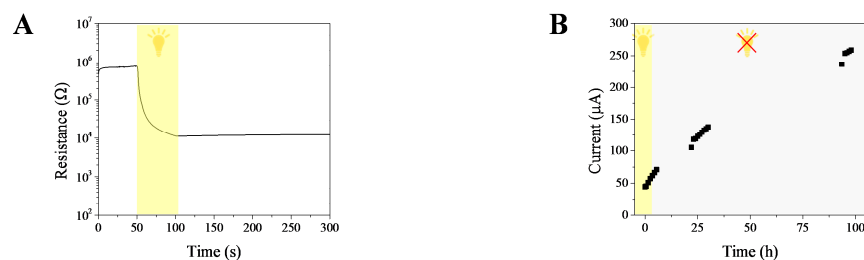


Figure A26. Conductivity experiments performed on physical gels formed inside ITO cells from non-irradiated 15 mM TANBE toluene tetrachloroethane (90:10) solvent mixtures. A) Plot of the resistance versus time. The light yellow area in the plot corresponds to the light irradiation time; B) Plot of the current measured at an applied bias of 0.1V versus time. The light yellow area in the plot signifies the irradiation time of the sample (30 minutes), the grey are the time that the sample is kept in the dark.

MATERIALS AND METHODS

Copyright disclosure: parts of this work have been used, or will be employed, for the dissemination of the results in scientific journals. Therefore, unintentional similarities might be possible.

General procedures

A. Solvents and chemicals

All solvents and chemicals were purchased at the highest commercial quality and used without further purification. Dry solvents were obtained using a double column SolvTech purification system. Water was deionized using a milli-gradient system (Millipore, Molsheim, France). Chloroform and tetrachloroethane were passed through a basic alumina column prior to their use in photo-oxidation processes. All reactions were carried out in argon atmosphere unless otherwise noted.

B. Analytical instruments

1. Spectroscopy

UV-Vis-NIR Photo Spectroscopy

All photo spectrometric measurements were carried out at ICS, with the equipment of the polymer characterization platform. UV-vis-NIR spectra of solutions, in the 190-1100 nm range and at room temperature, were recorded on a PERKIN ELMER – Lambda 25, with a fixed bandwidth of 1 nm. All other samples were measured using a VARIAN Scan Cary 5000 spectrophotometer. For solution samples, spectra were recorded in quartz cuvettes with a path length of 1 cm. UV-vis-NIR spectra of solid samples were recorded using an internal integration sphere with a sample diameter of 110 mm. Films were measured in absorption mode using a temperature controlled Linkam Platine. The temperature could be controlled by a Peltier system.

Nuclear Magnetic Resonance Spectroscopy

^1H NMR spectra were recorded on a 400 MHz Bruker Advance spectrometer. The obtained spectra were internally referenced to the residual solvent signals (CDCl_3 : 7.06 ppm, CD_3OD : 3.31 ppm, toluene- d_8 : 7.09, 7.01, 6.97 ppm, $\text{DMSO}-d_6$: 2.5 ppm). Chemical shifts are given in ppm and coupling patterns are described as singlet (s), doublet (d), triplet (t), quartet (q), multiplet (m) and broad (b).

Electron Paramagnetic Resonance Spectroscopy

EPR spectra were recorded on a X-band spectrometer (EMXplus, Bruker Biospin GmbH, Germany), equipped with a high sensitivity resonator (HSW, Bruker Biospin GmbH, Germany). All experiments were performed at room temperature ($295\text{K} \pm 1\text{K}$). The g factor was calibrated using a Bruker standard (strong pitch, giso = 2.0028). As principal experimental parameters were used a microwave frequency of ca. 9.5 GHz, a microwave power of 0.1 - 2 mW for solid and solution experiments respectively, a magnetic field sweep of ca. 200 G, a modulation amplitude of 1-2 G for solid and solution experiments respectively, a sweep time of 1-2 minutes per spectrum, a conversion time of ca 60 - 300 for solid and solution experiment respectively, and a time constant of ca. 20 - 80 ms for solid and solution experiment respectively. If needed, scans were accumulated in order to improve the signal to noise ratio (S/N). For quantitative EPR measurements, EPR intensities were calculated by doubly integrating the EPR signal after careful subtraction of polynomial baseline (degree ≤ 3) and compared to EPR standards with known amount of spins, e.g. TEMPOL (4-hydroxy-2,2,6,6-tetramethylpiperidin-1-oxyl) solution or crystal depending on the nature of the sample. The experiments were performed with Dr Bertrand Vileno, IR 3443 RENARD (Infrastructure de recherche – Réseau National de RPE interDisciplinaire).

2. Microscopy

All microscopic measurements were carried out at ICS, using the equipment of the SAMS research group (Prof N. Giuseppone, Prof M.-P. Krafft), the M³ research group (Dr A. Schröder), and the electron microscopy platform under the responsibility of Dr M. Schmutz.

Optical microscopy

Optical microscopy was carried out on a Nikon Eclipse 90i microscope (transmission mode), equipped with a Lumenera Infinity 2 CCD camera. Polarized optical microscopy (POM) was performed on a Leica DMR polarization microscope equipped with a digital camera (COOLPIX995). The videos in Chapter II were obtained with a TE200 inverted microscope (Nikon, Japan) equipped with a 40X, ELWD, Phase Contrast objective, while connected to a Keithley 2400 source meter. Phase Contrast images (6-7 frames per second) were acquired with a Diagnostic Instruments IN1800 digital camera (B&W, 8 bits). The maximum possible illumination from the halogen light of the microscope was used so as to minimize the exposure time (t_{exposure} is 65 ms).

Scanning electron microscopy

Scanning electron microscopy was carried out on a FEG-SEM Hitachi SU8010 microscope at room temperature. Images were treated using ImageJ software. For sample preparation, see Chapter II. The IDEs to analyze were simply fixed on an aluminum stud with scotch tape.

Transmission Electron Microscopy

Transmission electron microscopy was performed on a *CM12 Philips* microscope equipped with a *MVIII* (softImaging System) CCD camera. Samples were analyzed in Bright Field Mode with a LaB6 cathode and 120 kV tension. Images were treated using ImageJ software.

Atomic Force Microscopy

Atomic force microscopy topographic images were obtained using a Nanoscope 8 (Bruker) operated in Peak-Force tapping mode, which allows for the scanning of delicate and soft samples without damaging them. In Peak-Force tapping mode the probe and sample are intermittently brought into contact while the tip is scanned across the sample, eliminating lateral forces. The feedback loop keeps the maximum force (peak force) exerted on the tip at a constant value by adjusting the extension of the Z piezo. This protects the tip and sample from damage while allowing the tip sample contact area to be minimized. Because the force measurement bandwidth of a cantilever is \sim equal to its fundamental resonant frequency, by choosing a modulation frequency significantly lower than the cantilever's resonant frequency, the Peak-Force Tapping control algorithm is able to directly respond to the tip-sample force interaction. In the current implementation, the modulation frequency is 1 to 2 kHz.

Conductive atomic force microscopy images were obtained in Peak-Force TUNA (PF-TUNA) mode. The oscillation frequency (1 kHz–2 kHz) falls nicely between Tapping Mode (>50kHz), and Contact Mode (DC) interaction cycles. This mid-band operation is the single most important element for TUNA to work in an intermittent contact mode. In each tapping cycle, the tip is in contact with the sample only for a fraction of the cycle (10 – 100 μ s). The PF-TUNA module used has a bandwidth around 15 kHz across a range of gains from 10^7 V/A to 10^{10} V/A, with the noise below 100 fA on cycle-averaged current.

PF-TUNA can be operated in either imaging or spectroscopy mode. In the imaging mode, maps of the electrical current are obtained with topography and mechanical properties. In the spectroscopy mode, one can collect current-voltage (*IV*) curves. In the imaging mode, an electrically conductive probe is scanned over the sample surface in Peak-Force. During scanning, the user can apply a DC bias between the tip and the sample. The TUNA module, a low-noise, high-bandwidth linear current amplifier, senses the resulting current passing through the sample. This data is presented simultaneously with the topography image and mechanical properties maps. The observed current can be used as a measure of the local conductivity, or electrical integrity, of the sample under study. Since the system can acquire up to eight channels simultaneously, it is possible to map the major mechanical properties such as deformation, adhesion, DMT modulus, dissipation, and electrical properties such as cycle-averaged current and peak current together with topography in a single pass. Offline analysis

functions can calculate statistics of the electrical properties of different regions, sections through the data showing the spatial distribution of the properties, and/or correlation between mechanical, topographic and electrical properties.

From the current-time plot, the PF-TUNA algorithm extracts three measurements: 1) peak current; 2) cycle- averaged current; 3) contact-averaged current. Peak current is the instantaneous current at point, coinciding with peak force. This corresponds to the current measured at a defined force. Peak current may be, but is not necessarily, the maximum current, since the limited rise time (imposed by the bandwidth of the TUNA module or the resistance-capacitance of the sample) may cause a lag in the current response. Cycle-averaged current is the average current over one full tapping cycle. This includes both the current measured while tip is in contact with the surface, and while it is off the surface. Contact-averaged current is the average current only when the tip is in contact with the surface. The images and current values presented in this thesis are contact-averaged current images.

Here, Bruker's SCM-PIT-V2 probes have been used for PF-TUNA in the imaging mode. These probes have a platinum-iridium coated, electrically conductive tip. These cantilevers have a resonance frequency of about 75 kHz, a spring constant 3 N/m and a radius of the tip 25 nm.

All images, both topographic and contact-averaged current, were analyzed by Nanoscope Analysis version 1.40.

3. Grazing-Incidence Wide-Angle X-ray Scattering

GIWAXS experiments have been carried out at SOLEIL, on the line SIRIUS, by Dr P. Kekicheff (ICS – SOLEIL), Dr B. Heinrich (IPCMS), Dr A. Hemmerlé (SOLEIL) and Dr P. Fontaine (SOLEIL). The X-ray beam had the following characteristics: 10 keV and $\lambda = 1.24 \text{ \AA}$. The distance between the sample and the detector was 472 mm.

4. Conductivity experiments

Conductivity experiments on solutions, physical and chemical gels and thin films, carried out at ICS, are performed on a Keithley 2400 source meter semi-conductor characterization system as 2 point measurements. All experiments are performed under standard conditions (room temperature, air atmosphere). ITO electrochemical cells are used as received. Interdigitated electrodes are cleaned prior to use following the by Micrux recommended procedure: > 13 sweep cycles between - 1.0 and + 1.3 V in sulphuric acid.

Conductivity experiments on crystals, carried out at ICUBE, are performed on a Keithley 4200-SCS semi-conductor characterization system, using a 2 point measurement set-up when recording simple *IV* curves and a 3 point measurement set-up when a transistor effect could be detected. The transistors are cleaned prior to crystal deposition by *i*) immersion into a soap solution for 15 minutes while in a ultrasound bath at 45°C *ii*) immersion into acetone for 15 minutes while in a ultrasound bath at 45°C *iii*) immersion into isopropanol for 15 minutes while in a ultrasound bath at 45°C *iv*) drying using nitrogen gas. The substrates are subsequently treated with hexamethyldisilazane (HMDS) in order to fill the dangling bonds of the SiO₂.

Chapter II

Electrochemical experiments

Electrochemical experiments were conducted using a *PG-Stat Autolab* instrument in a three-probe configuration (2 mm platinum WE or 10 μm platinum microWE, platinum wire CE, silver wire RE). The counter electrode (CE) and TAA-C8 solution were separated by a Vicor glass bridge filled with electrolyte solution.

Spectro-electrochemical experiments were conducted using a platinum wire mesh transmission with a silver wire RE and a platinum foil CE. The absorption spectra recorded were obtained using either an Avaspec-2048 equipped with an Avalight-DH-S-Bal light source and a Thorlabs GG-420 nm Glass longpass filter, or a Cary 5000 instrument from Agilent Technologies. The potential applied to the solution was imposed by a Keithley 2400 source-meter. Using a Horiba Jobin Yvon Fluoromax-4 the photo-oxidation wavelength was determined. Absorption spectra were recorded with a Shimadzu UV-2101PC.

^1H NMR spectroscopy of an electro-oxidized TAA-C8 solution

To obtain a ^1H NMR spectrum free from signals originating from the electrolyte, TAA-C8 was electro-oxidized using platinum foils separated at a distance of 0.5 cm from each other. The potential applied was steadily increased until an increase in current was observed on the TCE- d_2 solution (25 V). In absence of electrolytes, it was impossible to correct the drop in potential in the solution.

Generalities on the electrode devices

ITO cells: commercial ITO electrochemical cells, purchased from *Instec*, with an active ITO area of 10 x 10 mm, a 4 μm cell gap and no alignment layer (ref. S100A040uNOPI) were used (Figure M1). ITO cells with blocked ITO layers by a photoresist were obtained from the same provider, with the same geometry.

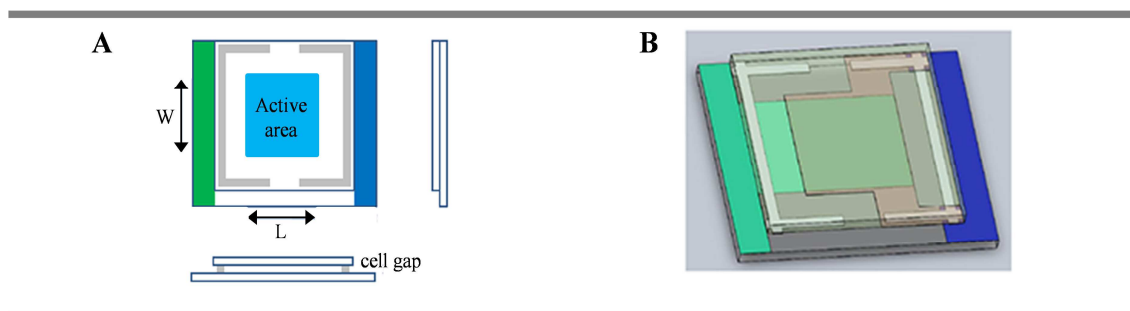


Figure M1. Schematic depiction of ITO electrochemical cells purchased from *Instec*.

Interdigitated electrodes: commercial gold interdigitated micro-electrodes (IDEs) were purchased from *MicruX Technologies*. The IDEs consist of 15 electrode pairs spaced 10 μm apart (ED-IDA1-AU) (Figure M2). The electrodes are fabricated by thin-film technologies on a glass substrate and are 50 – 150 nm thick and 10 μm wide.

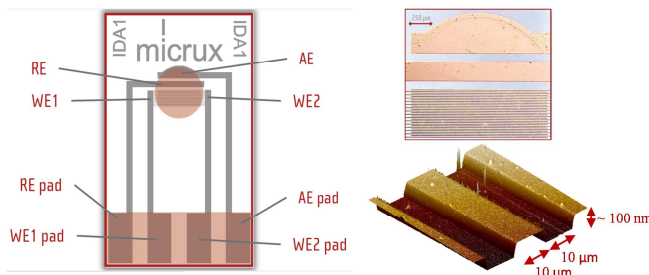


Figure M2. Schematic depiction of IDE purchased from *MicruX Technologies*. In the bottom right is an AFM topographic image of the interdigitated electrodes.

Sample preparation

Samples are prepared as described in the main text.

Visualization of TAA-C8 in situ electropolymerization and field induced alignment

The *in situ* electropolymerization and subsequent field induced alignment of TAA-C8, drop casted from a heptane solution onto IDEs, was visualized using an optical microscope with a 40x objective in transmission mode using phase contrast. A video was recorded by taking images of the substrate every six to seven seconds, using binning 1, exposure time 65 and gain 1.

In order to be positioned under the microscope, the IDE needed to be placed on a glass slide. To ensure no diffraction takes place at this interface, an immersion oil was applied in between. The protocol for substrate preparation was identical to the normal procedure. We used a 2 mg / mL TAA-C8 concentration so single fibers could be observed. Furthermore, nucleation does not take place everywhere at the same time. As a consequence both shorter and longer fibers are present at any given time. Using a concentration higher than 2 mg / mL would result in dense fiber formation of disperse lengths and it would be difficult to observe the nucleation and growth process properly.

Chapter III

Sample preparation

Crystallization: small neutral crystals are obtained by slow evaporation (~ 9 days) of a 12.8 mM TATA-Ac solution in methanol chloroform (75:25). Small photo-oxidized crystals can be obtained from chloroform suspensions in two ways. In the first method, a TATA-Ac chloroform solution is photo-oxidized for a period of one hour, followed by a slow evaporation process. In the second method, neutral crystals are resuspended in chloroform and photo-oxidized for an hour. Large neutral crystals are obtained by a slow cooling process (~54 hours) of a 1.6 mM TATA-Ac solution in methanol ethylacetate (5:95). Large oxidized crystals were obtained after crystallization by photo-oxidation of their resuspension in chloroform, or by I₂ vapors.

EPR samples: 1 mM TATA-Ac solutions (methanol chloroform 5:95) were prepared and photo-oxidized for two hours. Samples were taken during this process using glass capillaries (Hirschmann, 50 µL), which were subsequently sealed at both ends and transferred into the EPR cavity for measurement. Solid samples were prepared by crushing large neutral, photo- or I₂- oxidized crystals to a powder and transferring them into 4/3.2 mm O.D./I.D. EPR quartz tubes (Wilmad). Crystals were photo-oxidized in a chloroform suspension, then the solvent was removed by filtration and crystals were measured directly. *In situ* oxidation of the crystals by I₂ vapors was realized by suspending an I₂ grain in the EPR tube using a cotton veil. The I₂ was placed above the sample and out-side the EPR cavity. The EPR tube was sealed during the kinetics experiment.

TATA-ac nanoparticles: The glass mortar and pestle used are made of borosilicate glass and can contain a volume of 5 mL.

Wave-guiding experiments

Set-up 1: Wave guiding experiments were performed at ICPEES using a Raman confocal microscope (contact Christoph Mélat). A 532 or 785 nm laser was focussed through a 10 x objective (NA 0.25, WD 10.6 mm), and light output was observed at the other distal end. The 532 and 785 laser spots were 2.6 and 3.83 µm large, resulting in lateral and axial resolutions of 1.30 – 41.45 µm and 1.92 – 61.29 µm. Before each measurement the diaphragm was adjusted to *i*) the dimensions of the field; *ii*) obtain good optical quality; *iii*) ensure uniform lightning. Usually, diaphragm 4 or 3 were employed, which let pass a forth or a third of the laser.

Set-up 2: Wave guiding experiments were performed at the Physikalisches Institut of Albert-Ludwigs-Universität in Freiburg, Germany, in the collaboration with Dr Pfohl and Prof Reiter. A

Zeiss A1 microscope was used to image the crystals, a blue LED that emits in the 450 – 490 nm range was used as light source.

Chapter IV

Conductivity experiments

Solutions and physical gels: Conductivity experiments on solutions and physical gels are performed using commercial ITO electrochemical cells, obtained from *Instec*, with an active ITO area of 10 x 10 mm, a 4 μm cell gap and no alignment layer (ref. S100A040uNOPI) (Figure M1).

Chemical gels: Conductivity experiments on chemical TATA-Norbornene (TANBE) gels are carried out in a home-made ITO cell (Figure M3).

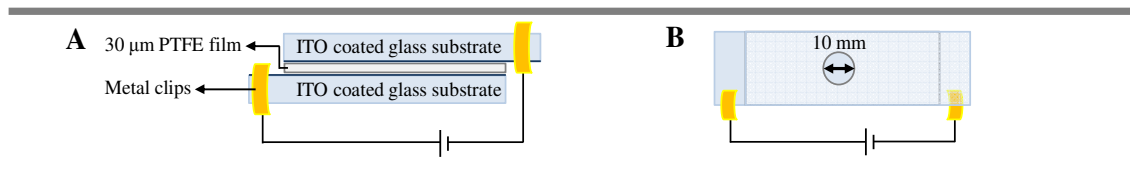


Figure M3. Schematic representation of the side (A) and top (B) view of the home-made ITO cell used to perform conductivity experiments on chemical gels.

Thin films: Conductivity experiments on thin films are performed using commercial gold interdigitated micro-electrodes, obtained from *MicruX Technologies*, made of 15 electrode pairs spaced 5 μm apart (Figure M2).

Crystals: Conductivity experiments on TATA-Ac crystals were performed on standard OFET structures with bottom-gate and bottom-contacts (Figure M4). The gate, a *p*-doped silicon substrate, is coated by a 230 μm thick dielectric silicon oxide layer. On top of this layer interdigitated drain and source electrodes, gold on top of ITO, are positioned. Each substrate consists of 16 transistors: 4 with 2.5 μm electrode gaps (*l*), 4 of 5 μm , 4 of 10 μm and 4 of 20 μm . The channel width is 10 mm. The experiments are performed in collaboration with Prof Thomas Heiser and Dr Patrick L  v  que from ICube, Cronenbourg.

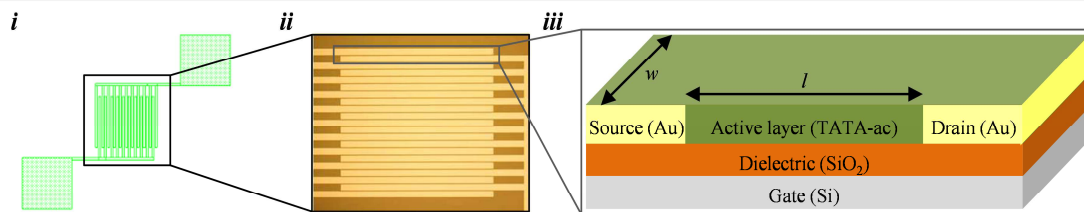


Figure M4. Schematic representation of the OFET structure. To the left (i) the lay-out of a single transistor; in the middle (ii) a magnification of a single transistor showing the interdigitated structure electrode structure; to the right (iii) the cross-section of the OFET structure.

Single crystal conductivity experiments were performed by C-AFM. The crystals were deposited on SiO_2 substrates onto which 50 nm thick gold electrodes were evaporated (Figure M5). The substrates were prepared by Nicolas Zimmermann (ICube). The experiments were carried out at ICS (Prof Mounir Maaloum).

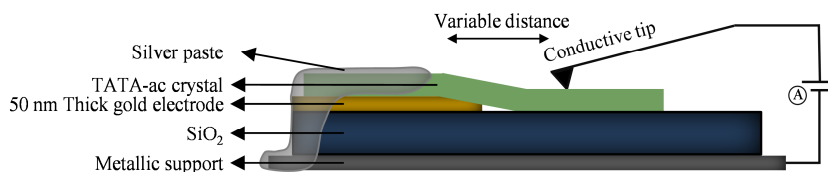


Figure M5. Schematic representation of C-AFM set-up.

Photo-oxidation

Solution and gels: Samples were photo-oxidized either by placing a vial containing the solution, or by placing an ITO cell, in proximity of a light source. As light source, a halogen lamp (10 Wcm^{-2}), positioned 5 cm from the sample, is used.

Thin films: Thin films are made of solutions that have been photo-oxidized prior to drop casting, as described in the last paragraph

Crystals: Crystals were either photo-oxidized prior to deposition, by re-suspension in chloroform, or after by placing the substrate in a chloroform saturated atmosphere, and subsequent light irradiation for 60 minutes.

Sample preparation

Solutions and physical gels: Samples are prepared as described in the main text. Chlorinated solvents are passed over an aluminum oxide column to ensure no radical species are present. Fresh samples were prepared for all experiments and protected from light. To generate reproducible results, a complete and uniform insertion of samples in ITO cells is important. Samples that gelate rapidly,

such as TANBE, were inserted in ITO cells at elevated temperatures, using a heated syringe. The ITO cells were placed in a cryostat programmed at 50 °C prior to sample insertion. Measurements on physical gels are performed 30 minutes after insertion of the solution to ensure complete cooling and supramolecular polymerization.

Thin films: 10 µL TAA and TATA 15 mM solutions, irradiated for 60 minutes, were drop casted onto IDEs with 5 µm electrode gaps, under an applied bias of 0.5V. The electric field was maintained for 5 to 10 minutes, until solvent evaporation. The samples were consequently placed under vacuum for 10 minutes to remove all remaining solvent.

Crystals: Crystallization methods for large and small TATA-ac crystals are discussed in *Chapter IV*. Large TATA-ac crystals were placed on the substrates, using tweezers, in a purely random manner. Small crystals were deposited in several ways. The deposition of small amounts of crystals was realized using a syringe. Large numbers of crystals were deposited by pouring some of the crystallization solution directly on the substrate. In the transistor experiments (investigation of OFET effect), 1 mL of crystallization solution was spin casted (1000 rpm) onto the substrate. This resulted in the deposition of small crystals of more or less uniform size. Substrates prepared by spin casting at lower rpm (500) often showed the presence of larger crystals and aggregates. In all three cases, the orientation of crystals was random. For C-AFM measurements the part of the crystals positioned on the gold electrodes was coated with a silver paste to ensure good electrical contact.

Hole mobility calculations

Charge carrier mobilities were calculated from the linear and saturated regimes using the following equations derived by Horowitz¹⁷³:

$$\text{Linear regime} \quad I_{SD} = \frac{W}{L} \mu C (V_G - V_T) V_{SD} \quad (23)$$

$$\text{Saturated regime} \quad I_{SD} = \frac{W}{2L} \mu C (V_G - V_T)^2 \quad (24)$$

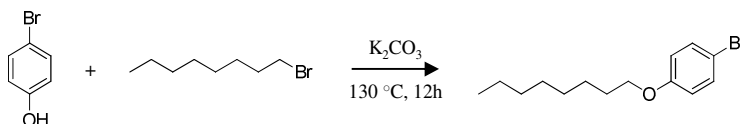
Symbol	Parameter	Value
I_{SD}	Current applied between the source and drain	Obtained from curve
V_{SD}	Voltage applied between the source and drain	10 V
V_G	Gate voltage	Obtained from curve
V_T	Threshold voltage at which the current starts to increase	Obtained from curve
C	Capacitance of the gate dielectric	15.0065 nF/cm ²
W	Width of the electrode gap	2.5, 5, 10 or 20 x 10 ⁻⁶ m
L	Length of the electrode gap	10 x 10 ⁻³ m

The mobilities measured depend on several factors, such as the contact between the crystal and dielectric, the number of traps and defects, but also the polarity of the dielectric. The reduction in mobility caused by contact resistance is corrected performing four-probe measurements. In the calculations it assumption is made that the whole OFET surface in covered in crystals.

Synthesis

TAA-C8: N-(4-{bis[4-octyloxy]phenyl}amino)phenyl)acetamide³⁹⁴

Step 1: 1-Bromo-4-(octyloxy)benzene



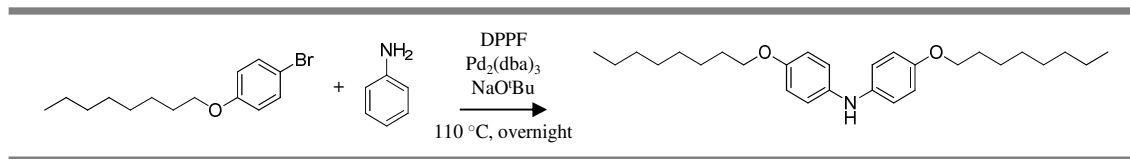
This precursor molecule was synthesized by Dr A. Osypenko before my PhD started. As large amounts were present, there was no need to resynthesize it.

4-Bromophenol (10.0 g, 57.8 mmol) was dissolved in DMF (40 mL) in a Schlenk flask. To this colorless solution, potassium carbonate (14.5 g, 105 mmol) was added and the solution was stirred for 10 minutes. Then 1-bromooctane (9.14 mL, 52.5 mmol) was added and the reaction was allowed to proceed for 12 hours, at 130 °C under stirring. The reaction was cooled down to room temperature and was subsequently diluted with water (200 mL) and 3 M NaOH (200 mL). The aqueous phase was extracted with diethylether (2 x 200 mL), the organic phases were washed with 1 M NaOH (100 mL) and brine (100 mL). After drying over Na_2SO_4 the solvent was evaporated under reduced pressure. 1-Bromo-4-(octyloxy)benzene was obtained as a colorless oil (94%).

$^1\text{H NMR}$ (400 MHz, $CDCl_3$, 25 °C): δ = 7.36 (d, J = 8.9 Hz, 2H), 6.77 (d, J = 8.9 Hz, 2H), 3.91 (t, J = 6.7 Hz, 2H), 1.77 (tt, J = 6.7, 6.7 Hz, 2H), 1.47-1.41 (m, 2H), 1.39-1.24 (m, 8H), 0.89 (t, J = 6.7 Hz, 3H).

$^{13}\text{C NMR}$ (100 MHz, $CDCl_3$, 25 °C): δ = 158.4, 132.3, 116.5, 112.7, 68.4, 32.0, 29.5, 29.4, 29.3, 26.2, 22.8, 14.2.

Step 2: 4-(octyloxy)-N-[4-(octyloxy)phenyl]aniline



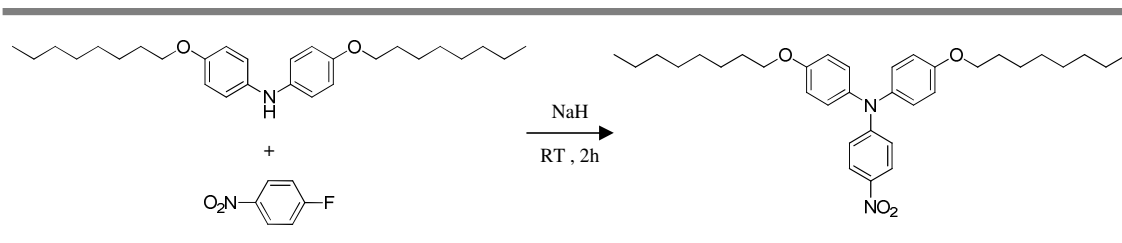
This precursor molecule was synthesized by Dr A. Osypenko before my PhD started. As large amounts were present, there was no need to resynthesize it.

In a Schlenk flask, diphenylphosphinoferrocene (DPPF, 657 mg, 1.15 mmol) and tris(dibenzylideneacetone)dipalladium (Pd₂(dba)₃, 160 mg, 0.169 mmol) were dissolved in dry toluene (50 mL). Distilled 1-bromo-4-(octyloxy)benzene (8.2 g, 28.8 mmol) was added to the solution after 15 minutes of stirring together with sodium tert-butoxide (NaO^tBu, 5.42 g, 56.4 mmol). Then, after an additional 5 minutes of stirring, freshly distilled aniline (7.0 g, 31.6 mmol) was added. The reaction mixture was allowed to proceed overnight at 110 °C. Afterwards, the reaction was cooled down to room temperature and subsequently diluted with dichloromethane (250 mL). This organic phase was washed with saturated NH₄Cl (2 x 100 mL), water (100 mL) and brine (2 x 100 mL). After drying over Na₂SO₄ the solvent was evaporated under reduced pressure. 4-(octyloxy)-N-[4-(octyloxy)phenyl]aniline was obtained as a grey-pearl powder (69%) after purification over a SiO₂ chromatography column (eluent = dichloromethane : TEA, 100 : 1) and recrystallization from boiling *i*-propyl alcohol.

¹H NMR (400 MHz, acetone-*d*₆, 25 °C): δ = 6.95 (d, *J* = 8.9 Hz, 4H), 6.81 (d, *J* = 8.9 Hz, 4H), 6.69 (brs, 1H), 3.92 (t, *J* = 6.5 Hz, 4H), 1.74 (tt, *J* = 6.8, 6.8 Hz, 4H), 1.47 (tt, *J* = 6.8, 6.8 Hz, 4H), 1.41-1.25 (m, 16H), 0.89 (t, *J* = 7.0 Hz, 6H).

¹³C NMR (100 MHz, acetone-*d*₆, 25 °C): δ = 154.3, 139.4, 119.7, 116.2, 69.0, 32.6, 30.3, 30.2, 30.1, 26.9, 23.4, 14.4.

MS (ESI): *m/z* calculated for C₂₈H₄₃NO₂ [M]⁺, 425.33; found 425.51. calculated for C₂₈H₄₄NO₂ [M+H]⁺, 426.34; found 426.52.

Step 3: *N*-(4-nitrophenyl)-4-(octyloxy)-*N*-[4-(octyloxy)phenyl]aniline

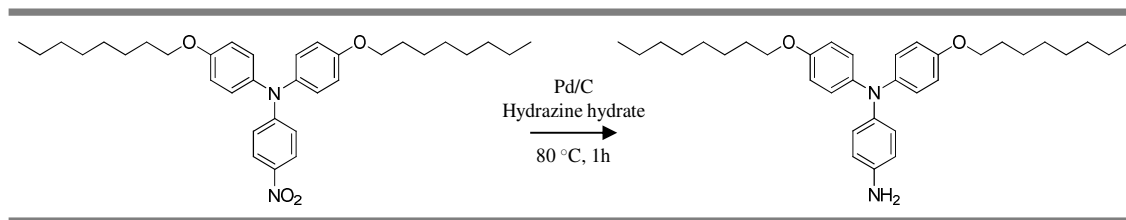
This precursor molecule was synthesized by Dr A. Osypenko before my PhD started. As large amounts were present, there was no need to resynthesize it. The synthesis protocol followed was previously published in *Angew. Chem. Int. Ed.*, **2010**, *49*, 6974-6978.¹⁴

4-(octyloxy)-*N*-[4-(octyloxy)phenyl]aniline (3.78 g, 8.88 mmol) was dissolved with sodium hydride (240 mg, 9.77 mmol) in DMF (20 mL) and stirred for 15 minutes at room temperature. Then, over an course of 30 minutes, *p*-fluoronitrobenzene (1.57 g, 11.1 mmol) was added dropwise to the solution that would turn to a deep-orange to red color. After an additional 2 hours of stirring, the reaction mixture was diluted with diethyl ether (250 mL). The organic phase was washed with saturated NH₄Cl (2 x 100 mL), water (5 x 50 mL) and brine (100 mL). After drying over Na₂SO₄ the solvent was evaporated under reduced pressure. *N*-(4-nitrophenyl)-4-(octyloxy)-*N*-[4-(octyloxy)phenyl]aniline was obtained as an orange-red oil (82%) after purification over an SiO₂ chromatography column (eluent = pentane : dichloromethane, 1 : 1).

¹H NMR (400 MHz, CDCl₃, 25 °C): δ = 7.99 (d, *J* = 9.4 Hz, 2H), 7.11 (d, *J* = 9.0 Hz, 4H), 6.89 (d, *J* = 9.0 Hz, 4H), 6.75 (d, *J* = 9.4 Hz, 2H), 3.95 (t, *J* = 6.6 Hz, 4H), 1.79 (tt, *J* = 6.6, 6.6 Hz, 4H), 1.51-1.41 (m, 4H), 1.41-1.21 (m, 16H), 0.89 (t, *J* = 7.2 Hz, 6H).

MS (ESI): *m/z* calculated for C₃₄H₄₆N₂O₄ [M]⁺, 546.35; found 456.48. calculated for C₃₄H₄₇N₂O₄ [M + H]⁺, 547.35; found 547.51.

Step 4: 1-N, 1-N-bis(4-(octyloxy)phenyl)benzene-1,4-diamine



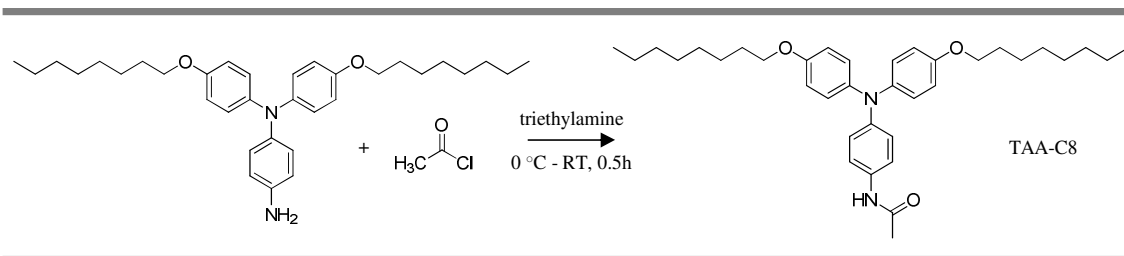
This precursor molecule was synthesized by Dr A. Osypenko before my PhD started. As large amounts of product were present, there was no need to resynthesize it. The synthesis protocol followed was previously published in *Angew. Chem. Int. Ed.*, **2010**, *49*, 6974-6978.¹⁴

In a 100 mL round-bottom flask equipped with a reflux condenser, N-(4-nitrophenyl)-4-(octyloxy)-N-[4-(octyloxy)phenyl]aniline (1.2 g, 2.19 mmol) was dissolved in ethanol (25 mL). After the careful addition of palladium on charcoal (50 mg), the solution was heated up to 80 °C and hydrazine hydrate (2 mL, 41.1 mmol) was added dropwise, over the course of 30 minutes, under vigorous stirring. Under reflux, the reaction mixture was stirred for an additional 30 minutes. Finally, the reaction mixture was cooled down to room temperature and the Pd/C catalyst was removed by filtration through a pad of Celite ®. The crude product was obtained as a yellowish solid after solvent evaporation under reduced pressure.

¹H NMR (400 MHz, CDCl₃, 25 °C): δ = 6.96 (d, *J* = 8.9 Hz, 4H), 6.89 (d, *J* = 8.5 Hz, 2H), 6.77 (d, *J* = 8.9 Hz, 4H), 6.58 (d, *J* = 8.6 Hz, 2H), 3.92 (t, *J* = 6.5 Hz, 4H), 3.56 (brs, 2H), 1.82 – 1.75 (m, 4H), 1.51 – 1.44 (m, 4H), 1.40 – 1.28 (m, 16H), 0.93 (t, *J* = 6.5 Hz, 6H).

¹³C NMR (100 MHz, CDCl₃, 25 °C): δ = 154.0, 142.0, 141.6, 140.1, 125.5, 124.1, 115.9, 114.9, 68.1, 31.7, 29.3 (2C), 29.1, 26.0, 22.5, 14.0

MS (ESI): *m/z* calculated for C₃₄H₄₈N₂O₂ [M]⁺ 516.38; found 516.59.

Step 5: *N*-(4-{bis[4-octyloxy]phenyl}amino)phenyl)acetamide

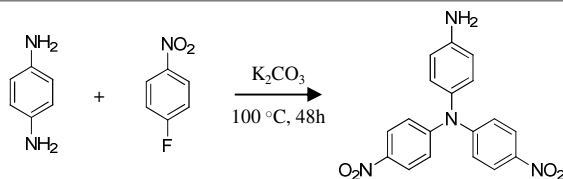
This precursor molecule was synthesized by Dr A. Osypenko before my PhD started. As large amounts of crude product were present, there was no need to resynthesize it. Only the purification was performed. The synthesis protocol followed was previously published in *Angew. Chem. Int. Ed.*, **2010**, *49*, 6974-6978.¹⁴

Freshly prepared 1-N,1-N-bis(4-(octyloxy)phenyl)benzene-1,4-diamine (1.0 g, 1.94 mmol) was dissolved in dichloromethane (20 mL) together with triethylamine (538 μ L, 3.87 mmol). The solution was brought down to 0 °C by placing it in an ice-bath and acetyl chloride (276 μ L, 3.87 mmol) was added drop-wise. Afterwards, the ice-bath was removed and the reaction solution was allowed to warm up to room temperature. The reaction would proceed for an additional 30 minutes, before dilution with dichloromethane (200 mL). The organic phase was washed with 1M HCl (2 x 50 mL), 1M NaOH (2 x 50 mL), water (2 x 100 mL) and brine (100 mL). After drying over Na₂SO₄ the solvent was evaporated under reduced pressure. *N*-(4-{bis[4-octyloxy]phenyl}amino)phenyl)acetamide (TAA-C8) was obtained as an off-white solid (92%) after purification over an SiO₂ chromatography column (eluent = cyclohexane : ethyl acetate, 85 : 15).

¹H NMR (400 MHz, CD₃OD, 25 °C): δ = 7.3 (d, *J* = 9.0 Hz, 2H), 6.89 (d, *J* = 9.0 Hz, 4H), 6.81 (d, *J* = 9.0 Hz, 2H), 6.76 (d, *J* = 9.0 Hz, 4H), 3.88 (t, *J* = 6.5 Hz, 4H), 2.08 (s, 3H), 1.77-1.67 (m, 4H), 1.50-1.39 (m, 4H), 1.40-1.23 (m, 16H), 0.89 (t, *J* = 7.0 Hz, 6H).

¹³C NMR (100 MHz, CD₃OD, 25 °C): δ = 171.3, 156.5, 146.7, 142.5, 133.1, 127.0, 122.8, 122.4, 116.4, 69.3, 33.0, 30.51, 30.48, 30.43, 27.2, 23.7, 23.6, 14.5.

MS (ESI): *m/z* calculated for C₃₆H₅₀N₂O₃ [M]⁺, 558.38; found 558.64.

TATA-ac: Triarylamine triacetamide^{16,17}Step 1: 1-N,1-N-bis(4-nitrophenyl)benzene-1,4-diamine³⁴

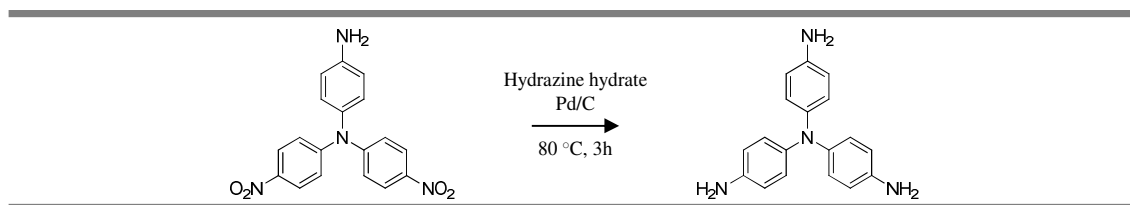
The synthesis protocol followed was adapted from *New J. Chem.*, **2004**, 28, 1235

In a 250 mL schlenk, 1,4-benzenediamine (2 g, 18.5 mmol) and potassium carbonate (9.83 g, 71.1 mmol) were dissolved in dry DMSO (28 mL) under argon atmosphere. Some K_2CO_3 normally remains undissolved. To this light beige colored solution, 4-fluoronitrobenzene (5.16 g, 3.88 mL, 36.6 mmol) was added using a syringe. Within a couple of minutes the reaction mixture would turn into a dark red-brown color. It was then heated to 100 °C and left to react for 48 hours. Afterwards, the reaction mixture was allowed to cool down to room temperature. 1-N,1-N-bis(4-nitrophenyl)benzene-1,4-diamine was obtained as a dark red solid (91%) by precipitation in 300 mL of water and subsequent washing with water (5 x 50 mL). Analysis were in accordance to the literature.³⁴

$^1\text{H NMR}$ (400 MHz, $CDCl_3$, 25 °C): δ = 8.12 (d, J = 9.3 Hz, 4H), 7.13 (d, J = 9.3 Hz, 4H), 6.96 (d, J = 8.6 Hz, 2H), 6.73 (d, J = 806 Hz, 2H), 3.84 (brs, 2H)

$^{13}\text{C NMR}$ (100 MHz, $CDCl_3$, 25 °C): δ = 152.2, 146.1, 142.3, 135.2, 129.1, 125.6, 121.6, 116.6

MS (ESI): m/z calculated for $C_{18}H_{14}N_4O_4$ $[M]^+$, 350.10; found 350.29; calculated for $C_{18}H_{15}N_4O_4$ $[M+H]^+$, 351.11; found 351.29

Step 2: 1-N,1-N-bis(4-aminophenyl)benzene-1,4-diamine⁴⁷¹

The synthesis protocol followed was adapted from *CrystEngComm*, **2013**, *15*, 5337

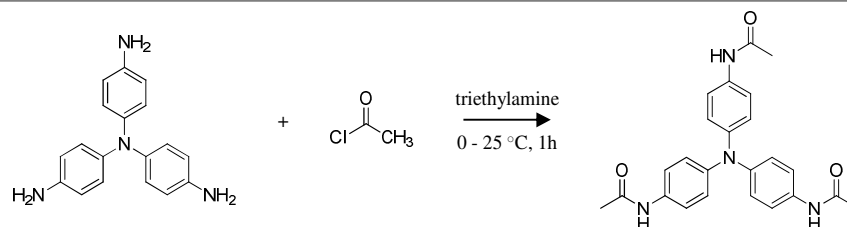
In a 250 mL round-bottom two-neck flask, equipped with a reflux condenser, 1-N,1-N-bis(4-nitrophenyl)benzene-1,4-diamine (5.01 g, 14.3 mmol) was dissolved, without further purification or recrystallization, in a mixture of ethanol (100 mL) and dioxane (50 mL). To this solution and under argon atmosphere, palladium on carbon (0.8 g, 0.752 mmol) was added carefully. After heating up to 80 °C, hydrazine hydrate (20 g, 19.4 mL, 399 mmol) was added dropwise using a syringe pump over a period of 60 min, while stirring vigorously. Under continued stirring at 80 °C, the reaction was allowed to proceed for three hours. After cooling down to room temperature, the Pd/C catalyst was removed by filtration through a pad of Celite® and washed several times with methanol. The crude product was obtained after solvent evaporation under reduced pressure. Recrystallization from boiling ethanol provided pure 1-N,1-N-bis(4-aminophenyl)benzene-1,4-diamine. When necessary, the product was further purified. The crude was dissolved in 1M HCl (4 - 6 mole HCl to 1 mole of product). Activated carbon (1-2 g, depending on the amount of TAA) is added and the solution is heated to 50-75 °C for half an hour. The activated carbon is removed by filtration through a pad Celite® or through a filter paper, and washed several times with small amounts of water. The filtrate is then basified with 3-6 M NaOH to pH 12-14 under stirring. The pure product precipitates as a grey solid (82%), which is collected by filtration and washed with NaHCO₃ and water. Analysis were in accordance to the literature.⁴⁷¹

¹H NMR (400 MHz, Acetone-*d*₆, 25 °C): δ = 6.71 (d, *J* = 8.7 Hz, 6H), 6.55 (d, *J* = 8.8 Hz, 6H), 4.28 (brs, 6H).

¹³C NMR (100 MHz, Acetone-*d*, 25 °C): δ = 143.9, 140.7, 125.3, 116.0

MS (ESI): *m/z* calculated for C₁₈H₁₈N₄ [M]⁺, 290.15; found 290.38; calculated for C₁₈H₁₉N₄ [M+H]⁺, 291.16; found 291.38

Step 3: triarylamine trisacetamide

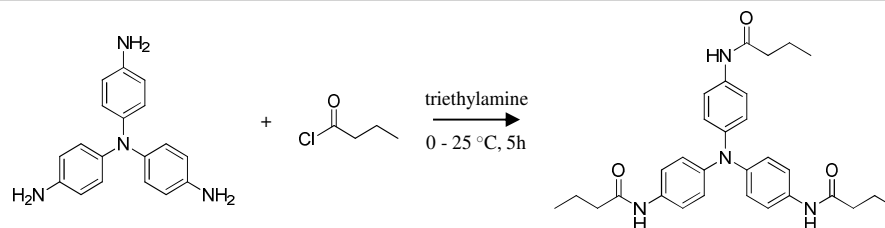


In a 250 mL round-bottom flask, 1-N,1-N-bis(4-aminophenyl)benzene-1,4-diamine (2.54 g, 8.74 mmol) and triethylamine (3.54 g, 4.86 mL, 35 mmol) were dissolved in THF (250 mL). The solution was brought down to 0 °C by placing it in an ice-bath. To this stirred and cold solution, acetyl chloride (2.74g, 2.5 mL, 35 mmol), mixed in 15 mL THF, was added in a drop-wise manner. Directly upon addition a white precipitate forms. The ice-bath was removed and the reaction would proceed for an additional 60 minutes. Afterwards the crude product was retrieved by filtration through a patch of Celite ®. After recrystallization from boiling ethanol and further purification by passing through a SiO₂ column (eluent = ethyl acetate methanol 95:5), triarylamine trisacetamide was obtained as small white crystals (46%).

¹H NMR (400 MHz, DMSO-*d*₆, 25 °C): δ = 9.95 (s, 3H), 7.46 (d, *J* = 8.9 Hz, 6H), 6.87 (d, *J* = 8.9 Hz, 6H), 2.01 (s, 9H)

¹³C NMR (100 MHz, MeOD, 25 °C): δ = 171.5, 145.5, 134.8, 125.16, 122.57, 23.65

MS (ESI): *m/z* calculated for C₂₄H₂₅N₄O₃ [M+H]⁺, 417.18; found 417.44

TATA-C4: Triarylamine trisbutyramide^{16,17}

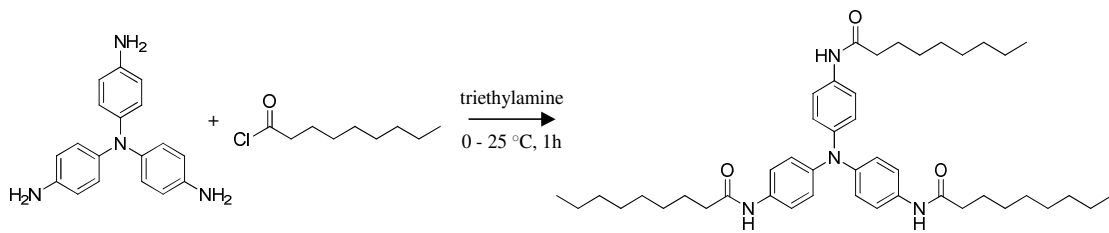
The synthesis protocol followed was adapted from *J. Am. Chem. Soc.*, **2014**, *136*, 11382-11388.¹⁶

In a 250 mL round-bottom flask, 1-N,1-N-bis(4-aminophenyl)benzene-1,4-diamine (2.02 g, 6.96 mmol) and triethylamine (2.82 g, 3.87 mL, 27.8 mmol) were dissolved in a THF (100 mL) and dichloromethane (50 mL) solvent mixture. The solution was brought down to 0 °C by placing it in an ice-bath. To this stirred and cold solution, butyryl chloride (2.97 g, 2.91 mL, 27.8 mmol), mixed in 15 mL THF, was added in a drop-wise manner. Directly upon addition a white precipitate forms. The ice-bath was removed and the reaction would proceed for an additional 5 hours. Afterwards the crude product was retrieved solvent evaporation under reduced pressure. After recrystallization from boiling ethanol and washing of the precipitate with cold ethanol and diethyl ether, triarylamine trisbutyramide was obtained as a white crystalline solid (88%).

¹H NMR (400 MHz, MeOD, 25 °C): δ = 7.33 (d, 6H), 6.86 (d, 6H), 2.23 (t, 6H), 1.62 (m, 6H), 0.899 (t, 9H)

¹³C NMR (100 MHz, MeOD, 25 °C): δ = 171.3, 143.1, 134.8, 123.9, 120.8, 75.41, 19.2, 14.1

MS (ESI): m/z calculated for C₃₀H₃₇N₄O₃ [M+H]⁺, 501.6; found 501.34

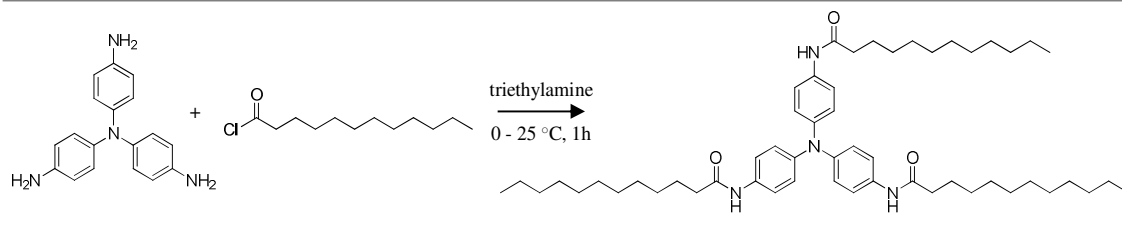
TATA-C9: N-{4-[bis(nonanamidophenyl)amino]phenyl}nonanamide¹⁶

This compound was synthesized by Dr A. Osypenko before my PhD started. As large amounts of product were present, there was no need to resynthesize it. Only the purification was performed. The synthesis protocol followed was adapted from *J. Am. Chem. S. Chem.*, **2014**, *136*, 11382-11388.¹⁶

In a 250 mL round-bottom flask 1-N,1-N-bis(4-aminophenyl)benzene-1,4-diamine (1.0 g, 3.44 mmol) and triethylamine (1.9 mL, 13.8 mmol) were dissolved in a THF (25 mL) and dichloromethane (50 mL) solvent mixture. The solution was brought down to 0 °C by placing it in an ice-bath. To this stirred and cold solution, nonanoyl chloride (2.43 g, 13.8 mmol), mixed in 15 mL THF, was added in a drop-wise manner over a period of 15 minutes. Directly upon addition a white precipitate forms. The ice-bath was removed and the reaction would proceed for an additional hour, after which the solvent was evaporated under reduced pressure. The crude product was diluted in 300 mL of THF and washed with 1 M HCl / brine (1:2, 100 mL), 1 M NaOH / brine (1:2, 2 × 50 mL), saturated NH₄Cl (50 mL) and brine (100 mL). After drying over Na₂SO₄, the solvent was evaporated under reduced pressure. N-{4-[bis(nonanamidophenyl)amino]phenyl}nonanamide (TATA-C8) was obtained as an off-white solid after recrystallization from boiling ethanol and washing of the precipitate with cold ethanol and diethyl ether (2.3 g, 94%).

¹H NMR (400 MHz, DMSO-*d*₆, 25 °C): δ = 9.76 (s, 3H), 7.47 (d, *J* = 8.8 Hz, 6H), 6.87 (d, *J* = 8.9 Hz, 6H), 2.26 (t, *J* = 7.3 Hz, 6H), 1.57 (tt, *J* = 7.2, 7.2 Hz, 6H), 1.35 – 1.15 (m, 31H), 0.86 (t, *J* = 7.2 Hz, 9H)

MS (ESI): *m/z* calculated for C₄₅H₆₆N₄O₃ [M]⁺ 710.51; found 710.64: calculated for C₄₅H₆₇N₄O₃ [M+H]⁺ 711.52; found 711.63

TATA-C12: N-{4-[bis(dodecanamidophenyl)amino]phenyl}dodecanamide¹⁶

This compound was synthesized by Dr A. Osypenko before my PhD started. As large amounts of product were present, there was no need to resynthesize it. Only the purification was performed. The synthesis protocol followed was adapted from *J. Am. Chem. S. Chem.*, **2014**, *136*, 11382-11388.¹⁶

In a 250 mL round-bottom flask 1-N,1-N-bis(4-aminophenyl)benzene-1,4-diamine (0.75 g, 2.58 mmol) and triethylamine (1.44 mL, 10.3 mmol) were dissolved in a THF (100 mL) and dichloromethane (100 mL) solvent mixture. The solution was brought down to 0 °C by placing it in an ice-bath. To this stirred and cold solution, lauroyl chloride (2.26 g, 10.3 mmol), mixed in 15 mL THF, was added in a drop-wise manner over a period of 15 minutes. Directly upon addition a white precipitate forms. The ice-bath was removed and the reaction would proceed for an additional hour, after which the solvent was evaporated under reduced pressure. The crude product was diluted in 350 mL of THF and washed with 1 M HCl / brine (1:2, 100 mL), 1 M NaOH / brine (1:2, 2 × 50 mL), saturated NH₄Cl (50 mL) and brine (100 mL). After drying over Na₂SO₄, the solvent was evaporated under reduced pressure. N-{4-[bis(dodecanamidophenyl)amino]phenyl}dodecanamide (TATA-C11) was obtained as an off-white solid after recrystallization from boiling ethanol and washing of the precipitate with cold ethanol and diethyl ether (1.8 g, 83%).

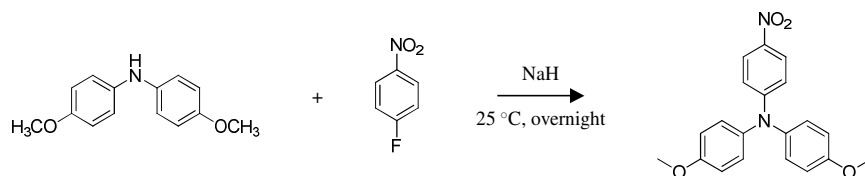
¹H NMR (400 MHz, CD₃OD/Toluene-*d*₈, 25 °C): δ = 7.54 (d, *J* = 9.0 Hz, 6H), 6.97 (d, *J* = 9.0 Hz, 6H), 2.33 (t, *J* = 7.5 Hz, 6H), 1.70 (tt, *J* = 7.5, 7.5 Hz, 6H), 1.43 – 1.18 (m, 31H), 0.86 (m, 48H), 0.89 (t, *J* = 7.0 Hz, 9H)

¹³C NMR (100 MHz, CD₃OD/Toluene-*d*₈, 25 °C): δ = 174.0, 145.1, 134.8, 125.0, 122.2, 37.9, 32.9, 30.7, 30.6 (2C), 30.5, 30.4, 30.3, 26.9, 23.6, 14.6

MS (ESI): *m/z* calculated for C₅₄H₈₄N₄O₃ [M]⁺ 836.65; found 836.89

TAA-C1: N-{4[bis(4-methoxyphenyl)amino]phenyl}acetamide

Step 1: 4-methoxy-N-(4-methoxyphenyl)-N-(4-nitrophenyl)aniline



This precursor molecule was synthesized by Dr A. Osypenko before my PhD started. As large amounts of product were present, there was no need to resynthesize it. The synthesis protocol followed originates from *Angew. Chem. Int. Ed.*, **2010**, *49*, 6974 – 6978.¹⁴

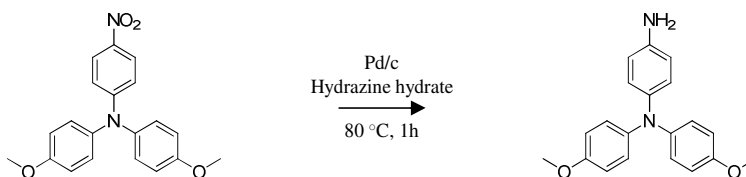
In a 50 mL round-bottom flask, 4,4'-dimethoxydiphenylamine (1.0 g, 4.36 mmol) was dissolved in dry DMF. To this solution, sodium hydride (210 mg, 5.23 mmol) was added and, as a result, the solution turned from white to slightly green. Then, *p*-fluoronitrobenzene (510 μ L, 4.8 mmol) was added in a dropwise manner over the course of 30 minutes. Upon addition, the green colour turned to brown. Afterwards, the reaction was left to proceed overnight. The next day, the solution was diluted with 150 mL water, extracted with 300 mL of diethyl ether, and dried over anhydrous N_2SO_4 . 4-methoxy-N-(4-methoxyphenyl)-N-(4-nitrophenyl)aniline was obtained as a pure compound (1.43 g, 94%) after passing through a SiO_2 column (eluent = pentane : diethyl ether, 95:5).

¹H NMR (400 MHz, $CDCl_3-d_1$, 25 °C): δ = 7.99 (d, J = 9.4 Hz, 2H), 7.13 (d, J = 9.0 Hz, 4H), 6.91 (d, J = 9.0 Hz, 4H), 6.75 (d, J = 9.4 Hz, 2H), 3.82 (s, 6H)

¹³C NMR (100 MHz, $CD_3OD/Toluene-d_8$, 25 °C): δ = 157.8, 154.3, 139.2, 138.4, 128.3, 125.7, 115.9, 115.4, 55.7

MS (ESI): m/z calculated for $C_{20}H_{18}N_2O_4$ $[M]^+$ 350.13; found 350.31; calculated for $C_{20}H_{19}N_2O_4$ $[M+H]^+$ 351.13; found 351.31

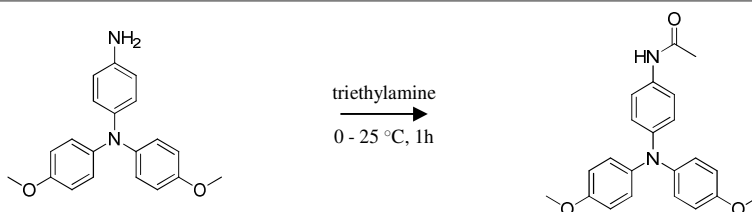
Step 2: N-N-bis(4-methoxyphenyl)benzene-1,4-diamine



This precursor molecule was synthesized by Dr A. Osypenko before my PhD started. As large amounts of product were present, there was no need to resynthesize it.

In a 100 mL round-bottom flask equipped with a reflux condenser, 4-methoxy-N-(4-methoxyphenyl)-N-(4-nitrophenyl)aniline was dissolved in ethanol. After the careful addition of palladium on charcoal, the solution was heated up to 80 °C and hydrazine hydrate was added dropwise in a dropwise manner, over the course of 30 minutes, under vigorous stirring. Under reflux, the reaction mixture was stirred for an additional 30 minutes. Finally, the reaction mixture was cooled down to room temperature and the Pd/C catalyst was removed by filtration through a pad of Celite ®. The crude product was obtained as a yellowish solid after solvent evaporation under reduced pressure.

Step 3: *N*-{4[bis(4-methoxyphenyl)amino]phenyl}acetamide



This compound was synthesized by Dr A. Osypenko before my PhD started. As large amounts of product were present, there was no need to resynthesize it.

Freshly prepared *N*-*N*-bis(4-methoxyphenyl)benzene-1,4-diamine was dissolved in dichloromethane (20 mL) together with triethylamine (538 μ L, 3.87 mmol). The solution was brought down to 0 °C by placing it in an ice-bath and acetyl chloride was added in a dropwise manner. Afterwards, the ice-bath was removed and the reaction solution was allowed to warm up to room temperature. The reaction would proceed for an additional 30 minutes, before dilution with dichloromethane (200 mL). The organic phase was washed with 1M HCl (2 x 50 mL), 1M NaOH (2 x 50 mL), water (2 x 100 mL) and brine (100 mL). After drying over Na₂SO₄ the solvent was evaporated under reduced pressure. *N*-(4-{bis[4-octyloxy]phenyl}amino)phenyl)acetamide (TAA-C8) was obtained as an off-white solid after purification over an SiO₂ chromatography column (eluent = cyclohexane : ethyl acetate, 85 : 15).

REFERENCES

- (1) Merz, V.; Weith, W. Vermischte Mittheilungen. *Berichte der Dtsch. Chem. Gesellschaft* **1873**, *6*, 1511–1520.
- (2) Naumov, V. A.; Samdal, S.; Naumov, A. V.; Gundersen, S.; Volden, H. V. Molecular Structure of Triphenylamine in the Gas Phase. *Russ. J. Gen. Chem.* **2005**, *75*, 1956–1961.
- (3) Lambert, C.; Nöll, G. The Class II/III Transition in Triarylamine Redox Systems. *J. Am. Chem. Soc.* **1999**, *121*, 8434–8442.
- (4) Amthor, S.; Noller, B.; Lambert, C. UV / Vis / NIR Spectral Properties of Triarylamines and Their Corresponding Radical Cations. **2005**, *316*, 141–152.
- (5) Quinton, C.; Alain-Rizzo, V.; Dumas-Verdes, C.; Miomandre, F.; Clavier, G.; Audebert, P. Redox-Controlled Fluorescence Modulation (Electrofluorochromism) in Triphenylamine Derivatives. *RSC Adv.* **2014**, *4*, 34332–34342.
- (6) Cias, P.; Slugovc, C.; Gescheidt, G. Hole Transport in Triphenylamine Based OLED Devices: From Theoretical Modeling to Properties Prediction. *J. Phys. Chem. A* **2011**, *115*, 14519–14525.
- (7) Fitzgerald, E. A.; Wuelfing, P.; Richtol, H. H. The Photochemical Oxidation of Some Substituted Aromatic Amines in Chloroform. *J. Phys. Chem.* **1971**, *75*, 2737–2741.
- (8) Heckmann, A.; Lambert, C. Organic Mixed-Valence Compounds: A Playground for Electrons and Holes. *Angew. Chem. Int. Ed.* **2012**, *51*, 326–392.
- (9) Sreenath, K.; Suneesh, C. V.; Gopidas, K. R.; Flowers, R. A. Generation of Triarylamine Radical Cations through Reaction of Triarylamines with Cu(II) in Acetonitrile. A Kinetic Investigation of the Electron-Transfer Reaction. *J. Phys. Chem. A* **2009**, *113*, 6477–6483.
- (10) Quinton, C.; Alain-Rizzo, V.; Dumas-Verdes, C.; Clavier, G.; Miomandre, F.; Audebert, P. Design of New Tetrazine-Triphenylamine Bichromophores - Fluorescent Switching by Chemical Oxidation. *European J. Org. Chem.* **2012**, *7*, 1394–1403.
- (11) Field, J. E.; Combariza, M. Y.; Vachet, W.; Venkataraman, D. Spontaneous Assembly of a Hydrogen-Bonded Tetrahedron Aggregates from an Ethanol / Water Solution. *Chem. Commun.* **2002**, *19*, 2260–2261.
- (12) Shi, D.; Ren, Y.; Jiang, H.; Cai, B.; Lu, J. Synthesis, Structures, and Properties of Two Three-Dimensional Metal-Organic Frameworks, Based on Concurrent Ligand Extension. *Inorg. Chem.* **2012**, *51*, 6498–6506.
- (13) Cui, J.; Huang, Q.; Veinot, J. C. G.; Yan, H.; Wang, Q.; Hutchison, G. R.; Richter, A. G.; Evmenenko, G.; Dutta, P.; Marks, T. J. Anode Interfacial Engineering Approaches to Enhancing Anode/Hole Transport Layer Interfacial Stability and Charge Injection Efficiency in Organic Light-Emitting Diodes. *Langmuir* **2002**, *18*, 9958–9970.
- (14) Moulin, E.; Niess, F.; Maaloum, M.; Buhler, E.; Nyrkova, I.; Giuseppone, N. The Hierarchical Self-Assembly of Charge Nanocarriers: A Highly Cooperative Process Promoted by Visible Light. *Angew. Chem. Int. Ed.* **2010**, *49*, 6974–6978.
- (15) Nyrkova, I.; Moulin, E.; Armao, J. J.; Maaloum, M.; Heinrich, B.; Rawiso, M.; Niess, F.; Cid, J. J.; Jouault, N.; Buhler, E.; Semenov, A. N.; Giuseppone, N. Supramolecular Self-Assembly and Radical Kinetics in Conducting Self-Replicating Nanowires. *ACS Nano* **2014**, *8*, 10111–10124.
- (16) Armao, J. J.; Maaloum, M.; Ellis, T.; Fuks, G.; Rawiso, M.; Moulin, E.; Giuseppone, N. Healable Supramolecular Polymers as Organic Metals. *J. Am. Chem. Soc.* **2014**, *136*, 11382–11388.
- (17) Armao, J. J.; Rabu, P.; Moulin, E.; Giuseppone, N. Long-Range Energy Transport via Plasmonic Propagation in a Supramolecular Organic Waveguide. *Nano Lett.* **2016**, *16*, 2800–2805.
- (18) Moulin, E.; Niess, F.; Fuks, G.; Jouault, N.; Buhler, E.; Giuseppone, N. Light-Triggered Self-Assembly of Triarylamine-Based Nanospheres. *Nanoscale* **2012**, *4*, 6748–6751.
- (19) Busseron, E.; Cid, J.-J.; Wolf, A.; Du, G.; Moulin, E.; Fuks, G.; Maaloum, M.; Polavarapu, P.; Ruff, A.; Saur, A.-K.; Ludwigs, S.; Giuseppone, N. Light-Controlled Morphologies of Self-Assembled Triarylamine–Fullerene Conjugates. *ACS Nano* **2015**, *9*, 2760–2772.
- (20) Domoto, Y.; Busseron, E.; Maaloum, M.; Moulin, E.; Giuseppone, N. Control over Nanostructures and Associated Mesomorphic Properties of Doped Self-Assembled Triarylamine Liquid Crystals. *Chem. - A Eur. J.* **2015**, *21*, 1938–1948.
- (21) Faramarzi, V.; Niess, F.; Moulin, E.; Maaloum, M.; Dayen, J. F.; Beaufrand, J. B.; Zanettini, S.; Doudin, B.; Giuseppone, N. Light-Triggered Self-Construction of Supramolecular Organic Nanowires as Metallic Interconnects. *Nat. Chem.* **2012**, *4*, 485–490.

References

- (22) Armao, J. J.; Domoto, Y.; Umehara, T.; Maaloum, M.; Contal, C.; Fuks, G.; Moulin, E.; Decher, G.; Javahiry, N.; Giuseppone, N. Supramolecular Organic Nanowires as Plasmonic Interconnects. *ACS Nano* **2016**, *10*, 2082–2090.
- (23) Schneider, S.; Licsandru, E.-D. E.-D.; Kocsis, I.; Gilles, A.; Dumitru, F.; Moulin, E.; Tan, J.; Lehn, J.-M. J.-M.; Giuseppone, N.; Barboiu, M. Columnar Self-Assemblies of Triarylamine Scaffolds for Artificial Biomimetic Channels for Ion and for Water Transport. *J. Am. Chem. Soc.* **2017**, *139*, 3721–3727.
- (24) Armao IV, J. J.; Nyrkova, I.; Fuks, G.; Osypenko, A.; Maaloum, M.; Moulin, E.; Arenal, R.; Gavat, O.; Semenov, A.; Giuseppone, N. Anisotropic Self-Assembly of Supramolecular Polymers and Plasmonic Nanoparticles at the Liquid-Liquid Interface. *J. Am. Chem. Soc.* **2017**, *139*, 2345–2350.
- (25) Moulin, E.; Armao, J. J.; Giuseppone, N. Triarylamine-Based Supramolecular Polymers: Structures, Dynamics, and Functions. *Acc. Chem. Res.* **2019**, *52*, 975–983.
- (26) Faramarzi, V.; Niess, F.; Moulin, E.; Maaloum, M.; Dayen, J. F.; Beaufrand, J. B.; Zanettini, S.; Doudin, B.; Giuseppone, N. Light-Triggered Self-Construction of Supramolecular Organic Nanowires as Metallic Interconnects. *Nat. Chem.* **2012**, *4*, 485–490.
- (27) Goldberg, I.; Nimerovsky, M. Uber Triphenylamin Und Triphenylamin-Carbonsaure. *Berichte der Dtsch. Chem. Gesellschaft* **1907**, *40*, 2448–2452.
- (28) Goldberg, I. Ueber Phenyliringen Bei Gegenwart von Kupfer Als Katalysator. *Berichte der Dtsch. Chem. Gesellschaft* **1906**, *39*, 1691–1692.
- (29) Gorvin, J. H. The Synthesis of Di- and Triarylamine through Halogen Displacement by Base-Activated Arylamines: Comparison with the Ullmann Condensation. *J. Chem. Soc. Perkin Trans. 1* **1988**, *6*, 1331–1335.
- (30) Ma, D.; Cai, Q.; Zhang, H. Mild Method for Ullmann Coupling Reaction of Amines and Aryl Halides. *Org. Lett.* **2003**, *5*, 2453–2455.
- (31) Cho, S. H.; Kim, J. Y.; Kwak, J.; Chang, S. Recent Advances in the Transition Metal-Catalyzed Two Fold Oxidative C-H Bond Activation Strategy for C-C and C-N Bond Formation. *Chem. Soc. Rev.* **2011**, *40*, 5068–5083.
- (32) Paul, F.; Patt, J.; Hartwig, J. F. Palladium-Catalyzed Formation of Carbon-Nitrogen Bonds. *J. Am. Chem. Soc.* **1994**, *116*, 5969–5970.
- (33) Guram, A. S.; Buchwald, S. L. Palladium-Catalyzed Aromatic Aminations with in Situ Generated Aminostannanes. *J. Am. Chem. Soc.* **1994**, *116*, 7901–7902.
- (34) Rozalska, I.; Kulyk, P.; Kulszewicz-Bajer, I. Linear 1,4-Coupled Oligoanilines of Defined Length: Preparation and Spectroscopic Properties. *New J. Chem.* **2004**, *28*, 1235.
- (35) Sobolev, A. N.; Belsky, V. K.; Romm, I. P.; Chernikova, N. Y.; Guryanova, E. N. Structural Investigation of the Triaryl Derivatives of the Group V Elements. IX. Structure of Triphenylamine, C₁₈H₁₅N. *Acta Crystallogr. Sect. C* **1985**, *41*, 967–971.
- (36) Wang, B. C.; Liao, H. R.; Chang, J. C.; Chen, L.; Yeh, J. T. Electronic Structure and Molecular Orbital Study of Hole-Transport Material Triphenylamine Derivatives. *J. Lumin.* **2007**, *124*, 333–342.
- (37) Sasaki, Y.; Kimura, K.; Kubo, M. Electron Diffraction Investigation of Triphenylamine. *J. Chem. Phys.* **1959**, *31*, 477.
- (38) Reva, I.; Lapinski, L.; Chattopadhyay, N.; Fausto, R. Vibrational Spectrum and Molecular Structure of Triphenylamine Monomer: A Combined Matrix-Isolation FTIR and Theoretical Study. *Phys. Chem. Chem. Phys.* **2003**, *5*, 3844–3850.
- (39) Cauquis, G.; Serve, D. Anodic Voltammetry of Some Aromatic Amines in Chloroform Absorption Spectra and Association Phenomena of the Corresponding Cation Radicals. *Anal. Chem.* **1972**, *44*, 2222–2224.
- (40) Cauquis, G.; Delhomme, H.; Serve, D. Les Proprietes Electrochimiques Des Diphenylamines et de Leurs Produits d'oxydation En Milieu Organique - III. Les Diphenylamines p,p'-Disubstituees et l'evolution de Leur Radical Cation Primaire. *Electrochim Acta* **1976**, *21*, 557.
- (41) Schmidt, W.; Steckhan, E. Uber Organische Elektronenubersystemen, I Elektrochemische Und Spektroskopische Untersuchung Bromsubstituierter Triarylamin-Redoxsysteme. *Chem. Ber.* **1980**, *113*, 557.
- (42) Seo, E. T.; Nelson, R. F.; Fritsch, J. M.; Marcoux, L. S.; Leedy, D. W.; Adams, R. N. Anodic Oxidation Pathways of Aromatic Amines. Electrochemical and Electron Paramagnetic Resonance Studies. *J. Am. Chem. Soc.* **1966**, *88*, 3498–3503.
- (43) Dapperheld, S.; Steckhan, E.; Brinkhaus, K. G.; Esch, T. Organic Electron Transfer Systems, II Substituted Triarylamine Cation-Radical Redox Systems – Synthesis, Electrochemical and Spectroscopic Properties, Hammet Behavior, and Suitability as Redox Catalysts. *Chem. Ber.* **1991**, *124*, 2557–2567.
- (44) Sreenath, K.; Thomas, T. G.; Gopidas, K. R. Cu(II) Mediated Generation and Spectroscopic Study of the Tris(4-Anisyl)Amine Radical Cation and Dication. Unusually Shielded Chemical Shifts in the Dication. *Org. Lett.* **2011**, *13*, 1134–1137.

References

- (45) Shirota, Y.; Kageyama, H. Charge Carrier Transporting Molecular Materials and Their Applications in Devices. *Chem. Rev.* **2007**, *107*, 953–1010.
- (46) Iwan, A.; Sek, D. Polymers with Triphenylamine Units: Photonic and Electroactive Materials. *Prog. Polym. Sci.* **2011**, *36*, 1277–1325.
- (47) Costa, J. C. S.; Taveira, R. J. S.; Lima, C. F. R. A. C.; Mendes, A.; Santos, L. M. N. B. F. Optical Band Gaps of Organic Semiconductor Materials. *Opt. Mater.* **2016**, *58*, 51–60.
- (48) Rybakiewicz, R.; Zagorska, M.; Pron, A. Triphenylamine-Based Electroactive Compounds: Synthesis, Properties and Application to Organic Electronics. *Chem. Pap.* **2017**, *71*, 243–268.
- (49) Amthor, S.; Lambert, C. [2.2]Paracyclophane-Bridged Mixed-Valence Compounds: Application of a Generalized Mulliken–Hush Three-Level Model. *J. Phys. Chem. A* **2006**, *110*, 1177–1189.
- (50) Lambert, C.; Moos, M.; Schmiedel, A.; Holzapfel, M.; Schäfer, J.; Kess, M.; Engel, V. How Fast Is Optically Induced Electron Transfer in Organic Mixed Valence Systems? *Phys. Chem. Chem. Phys.* **2016**, *18*, 19405–19411.
- (51) Renz, M.; Theilacker, K.; Lambert, C.; Kaupp, M. A Reliable Quantum-Chemical Protocol for the Characterization of Organic Mixed-Valence Compounds. *J. Am. Chem. Soc.* **2009**, *131*, 16292–16302.
- (52) Barlow, S.; Risko, C.; Chung, S.; Tucker, N. M.; Coropceanu, V.; Jones, S. C.; Levi, Z.; Bredas, J.; Marder, S. R. Intervalence Transitions in the Mixed-Valence Monocations of Bis (Triarylamines) Linked with Vinylene and Phenylene-Vinylene Bridges. *J. Am. Chem. Soc.* **2005**, *127*, 16900–16911.
- (53) Lancaster, K.; Odom, S. A.; Jones, S. C.; Thayumanavan, S.; Marder, S. R.; Brédas, J.-L.; Coropceanu, V.; Barlow, S. Intramolecular Electron-Transfer Rates in Mixed-Valence Triarylamines: Measurement by Variable-Temperature ESR Spectroscopy and Comparison with Optical Data. *J. Am. Chem. Soc.* **2009**, *131*, 1717–1723.
- (54) Kattnig, D. R.; Mladenova, B.; Grampp, G.; Kaiser, C.; Heckmann, A.; Lambert, C. Electron Paramagnetic Resonance Spectroscopy of Bis(Triarylamine) Paracyclophanes as Model Compounds for the Intermolecular Charge-Transfer in Solid State Materials for Optoelectronic Applications. *J. Phys. Chem. C* **2009**, *113*, 2983–2995.
- (55) Lambert, C.; Amthor, S.; Schelter, J. From Valence Trapped to Valence Delocalized by Bridge State Modification in Bis(Triarylamine) Radical Cations: Evaluation of Coupling Matrix Elements in a Three-Level System. *J. Phys. Chem. A* **2004**, *108*, 6474–6486.
- (56) Lambert, C.; Risko, C.; Coropceanu, V.; Schelter, J.; Amthor, S.; Gruhn, N. E.; Durivage, J. C.; Brédas, J. L. Electronic Coupling in Tetraanisylarylenediamine Mixed-Valence Systems: The Interplay between Bridge Energy and Geometric Factors. *J. Am. Chem. Soc.* **2005**, *127*, 8508–8516.
- (57) Low, P. J.; Paterson, M. A. J.; Yufit, D. S.; Howard, J. A. K.; Cherryman, J. C.; Tackley, D. R.; Brook, R.; Brown, B. Towards an Understanding of Structure-Property Relationships in Holetransport Materials: The Influence of Molecular Conformation on Oxidation Potential in Poly(Ar_v)Amines. *J. Mater. Chem.* **2005**, *15*, 2304–2315.
- (58) Lambert, C.; Nöll, G. Tuning of Intervalence Charge Transfer Energies by Substituents in One-Dimensional Bis(Triarylamine) Systems. *J. Chem. Soc. Perkin Trans. 2* **2002**, *2*, 2039–2043.
- (59) Shirota, Y.; Kobata, T.; Noma, N. Starburst Molecules for Amorphous Molecular Materials. 4,4',4''-Tris(N,N -Diphenylamino)Triphenylamine and 4,4',4''-Tris[N-(3-Methylphenyl)-N-Phenylamino]Triphenylamine. *Chem. Lett.* **1989**, *18*, 1145–1148.
- (60) Heun, S.; Borsenberger, P. M. A Comparative Study of Hole Transport in Vapor-Deposited Molecular Glasses of N,N',N'',N'''-Tetrakis(4-Methylphenyl)-(1,1'-Biphenyl)-4,4'-Diamine and N,N'-Diphenyl-N,N'-Bis(3-Methylphenyl)-(1,1'-Biphenyl)-4,4'-Diamine. *Chem. Phys.* **1995**, *200*, 245–255.
- (61) Heun, S.; Borsenberger, P. M. Hole Transport in Triarylamine Doped Polymers. *Phys. B* **1995**, *216*, 43–52.
- (62) Burschka, J.; Dualeh, A.; Kessler, F.; Baranoff, E.; Cevy-Ha, N. L.; Yi, C.; Nazeeruddin, M. K.; Grätzel, M. Tris(2-(1 H -Pyrazol-1-Yl)Pyridine)Cobalt(III) as p-Type Dopant for Organic Semiconductors and Its Application in Highly Efficient Solid-State Dye-Sensitized Solar Cells. *J. Am. Chem. Soc.* **2011**, *133*, 18042–18045.
- (63) Abate, A.; Leijtens, T.; Pathak, S.; Teuscher, J.; Avolio, R.; Errico, M. E.; Kirkpatrick, J.; Ball, J. M.; Docampo, P.; McPherson, I.; Snaith, H. J. Lithium Salts as “Redox Active” p-Type Dopants for Organic Semiconductors and Their Impact in Solid-State Dye-Sensitized Solar Cells. *Phys. Chem. Chem. Phys.* **2013**, *15*, 2572–2579.
- (64) Goppert-Mayer, M. Elementary Processes with Two Quantum Jumps. *Ann. Phys.* **1931**, *9*, 273–294.
- (65) Goppert-Mayer, M. On The Probability of Two Light Quantum Working Together in an Elementary Act. *Naturwissenschaften* **1929**, *17*, 932.

References

- (66) Kaiser, W.; Garrett, C. G. B. Two-Photon Excitation in CaF Eu²⁺. *Phys. Rev. Lett.* **1961**, *7*, 229–231.
- (67) He, G. S.; Tan, L.; Zheng, Q.; Prasad, P. N. Multiphoton Absorbing Materials: Molecular Designs, Characterizations, and Applications. *Chem. Rev.* **2008**, *108*, 1245–1330.
- (68) Guo, L.; Wong, M. S. Multiphoton Excited Fluorescent Materials for Frequency Upconversion Emission and Fluorescent Probes. *Adv. Mater.* **2014**, *26*, 5400–5428.
- (69) Pawlicki, M.; Collins, H. A.; Denning, R. G.; Anderson, H. L. Two-Photon Absorption and the Design of Two-Photon Dyes. *Angew. Chem. Int. Ed.* **2009**, *48*, 3244–3266.
- (70) Myung Kim, H.; Rae Cho, B. Two-Photon Materials with Large Two-Photon Cross Sections. Structure-Property Relationship. *Chem. Commun.* **2009**, *2*, 153–164.
- (71) Jagatap, B. N.; Meath, W. J. Contributions of Permanent Dipole Moments to Molecular Multiphoton Excitation Cross Sections. *J. Opt. Soc. Am. B* **2008**, *19*, 2673.
- (72) Hua, J. L.; Li, B.; Meng, F. S.; Ding, F.; Qian, S. X.; Tian, H. Two-Photon Absorption Properties of Hyperbranched Conjugated Polymers with Triphenylamine as the Core. *Polymer* **2004**, *45*, 7143–7149.
- (73) Drobizhev, M.; Suo, Z.; Kruk, M.; Rebane, A.; Karotki, A.; Dzenis, Y.; Spangler, C. W. Uncovering Coherent Domain Structure in a Series of π -Conjugated Dendrimers by Simultaneous Three-Photon Absorption. *J. Phys. Chem. B* **2004**, *108*, 4221–4226.
- (74) Drobizhev, M.; Karotki, A.; Spangler, C. W.; Rebane, A.; Suo, Z.; Dzenis, Y. Strong Cooperative Enhancement of Two-Photon Absorption in Dendrimers. *J. Phys. Chem. B* **2003**, *107*, 7540–7543.
- (75) Drobizhev, M.; Karotki, A.; Rebane, A.; Spangler, C. W. Dendrimer Molecules with Record Large Two-Photon Absorption Cross Section. *Opt. Lett.* **2001**, *26*, 1081.
- (76) Drobizhev, M.; Rebane, A.; Suo, Z.; Spangler, C. W. One-, Two- and Three-Photon Spectroscopy of π -Conjugated Dendrimers: Cooperative Enhancement and Coherent Domains. *J. Lumin.* **2005**, *111*, 291–305.
- (77) Drobizhev, M.; Christensson, N.; Rebane, A.; Suo, Z.; Spangler, C. W.; Mongin, O.; Blanchard-Desce, M. Coherent Domain Structure in Linear and Dendrimer Chromophores Studied by One-And Three-Photon Absorption Spectroscopy. *Proc. SPIE - Int. Soc. Opt. Eng.* **2005**, *5934*, 1–9.
- (78) Lu, C.; Cui, Y.; Huang, W.; Yun, B.; Wang, Z.; Hu, G.; Cui, J.; Lu, Z.; Qian, Y. Vibrational Resonance Enhanced Broadband Multiphoton Absorption in a Triphenylamine Derivative. *Appl. Phys. Lett.* **2007**, *91*, 2005–2008.
- (79) Wei, P.; Bi, X.; Wu, Z.; Xu, Z. Synthesis of Triphenylamine-Cored Dendritic Two-Photon Absorbing Chromophores. *Org. Lett.* **2005**, *7*, 3199–3202.
- (80) Makarov, N. S.; Mukhopadhyay, S.; Yesudas, K.; Brédas, J. L.; Perry, J. W.; Pron, A.; Kivala, M.; Müllen, K. Impact of Electronic Coupling, Symmetry, and Planarization on One- and Two-Photon Properties of Triarylamines with One, Two, or Three Diarylboryl Acceptors. *J. Phys. Chem. A* **2012**, *116*, 3781–3793.
- (81) Malval, J. P.; Achelle, S.; Bodiou, L.; Spangenberg, A.; Gomez, L. C.; Soppera, O.; Guen, F. R. Le. Two-Photon Absorption in a Conformationally Twisted D- π -A Oligomer: A Synergic Photosensitizing Approach for Multiphoton Lithography. *J. Mater. Chem. C* **2014**, *2*, 7869–7880.
- (82) Chen, P.; Marshall, A. S.; Chi, S.-H.; Yin, X.; Perry, J. W.; Jäkle, F. Luminescent Quadrupolar Borazine Oligomers: Synthesis, Photophysics, and Two-Photon Absorption Properties. *Chem. - A Eur. J.* **2015**, *21*, 18237–18247.
- (83) Jiang, Y.; Wang, Y.; Hua, J.; Tang, J.; Li, B.; Qian, S.; Tian, H. Multibranching Triarylamine End-Capped Triazines with Aggregation-Induced Emission and Large Two-Photon Absorption Cross-Sections. *Chem. Commun.* **2010**, *46*, 4689–4691.
- (84) Li, K.; Jiang, Y.; Ding, D.; Zhang, X.; Liu, Y.; Hua, J.; Feng, S.-S.; Liu, B. Folic Acid-Functionalized Two-Photon Absorbing Nanoparticles for Targeted MCF-7 Cancer Cell Imaging. *Chem. Commun.* **2011**, *47*, 7323–7325.
- (85) Ishow, E.; Brosseau, A.; Clavier, G.; Nakatani, K.; Tauc, P.; Fiorini-Debuisschert, C.; Neveu, S.; Sandre, O.; Leautic, A. Multicolor Emission of Small Molecule-Based Amorphous Thin Films and Nanoparticles with a Single Excitation Wavelength. *Chem. Mater.* **2008**, *20*, 6597–6599.
- (86) Tian, Y.; Chen, C. Y.; Cheng, Y. J.; Young, A. C.; Tucker, N. M.; Jen, A. K. Y. Hydrophobic Chromophores in Aqueous Micellar Solution Showing Large Two-Photon Absorption Cross Sections. *Adv. Funct. Mater.* **2007**, *17*, 1691–1697.
- (87) Allain, C.; Schmidt, F.; Lartia, R.; Bordeau, G.; Fiorini-Debuisschert, C.; Charra, F.; Tauc, P.; Teulade-Fichou, M.-P. Vinyl-Pyridinium Triphenylamines: Novel Far-Red Emitters with High Photostability and Two-Photon Absorption Properties for Staining DNA. *ChemBioChem* **2007**, *8*, 424–433.
- (88) Lartia, R.; Allain, C.; Bordeau, G.; Schmidt, F.;

- Fiorini-Debuisschert, C.; Charra, F.; Teulade-Fichou, M. P. Synthetic Strategies to Derivatizable Triphenylamines Displaying High Two-Photon Absorption. *J. Org. Chem.* **2008**, *73*, 1732–1744.
- (89) Dumat, B.; Bordeau, G.; Faurel-Paul, E.; Mahuteau-Betzer, F.; Saettel, N.; Metge, G.; Fiorini-Debuisschert, C.; Charra, F.; Teulade-Fichou, M. P. DNA Switches on the Two-Photon Efficiency of an Ultrabright Triphenylamine Fluorescent Probe Specific of at Regions. *J. Am. Chem. Soc.* **2013**, *135*, 12697–12706.
- (90) Stokes, G. G. On the Change of Refrangibility of Light. *Philos. Trans. R. Soc. London* **1853**, *143*, 385.
- (91) Luo, J.; Xie, Z.; Xie, Z.; Lam, J. W. Y.; Cheng, L.; Chen, H.; Qiu, C.; Kwok, H. S.; Zhan, X.; Liu, Y.; Zhu, D.; Tang, B. Z.; Tang, B. Z.; Tang, B. Z. Aggregation-Induced Emission of 1-Methyl-1,2,3,4,5-Pentaphenylsilole. *Chem. Commun.* **2001**, *18*, 1740–1741.
- (92) Chen, Y.; Lam, J. W. Y.; Kwok, R. T. K.; Liu, B.; Tang, B. Z. Aggregation-Induced Emission: Fundamental Understanding and Future Developments. *Mater. Horizons* **2019**, *6*, 428–433.
- (93) Mei, J.; Leung, N. L. C.; Kwok, R. T. K.; Lam, J. W. Y.; Tang, B. Z. Aggregation-Induced Emission: Together We Shine, United We Soar! *Chem. Rev.* **2015**, *115*, 11718–11940.
- (94) Mei, J.; Hong, Y.; Lam, J. W. Y.; Qin, A.; Tang, Y.; Tang, B. Z. Aggregation-Induced Emission: The Whole Is More Brilliant than the Parts. *Adv. Mater.* **2014**, *26*, 5429–5479.
- (95) Ning, Z.; Chen, Z.; Zhang, Q.; Yan, Y.; Qian, S.; Cao, Y.; Tian, H. Aggregation-Induced Emission (AIE)-Active Starburst Triarylamine Fluorophores as Potential Non-Doped Red Emitters for Organic Light-Emitting Diodes and Cl₂ Gas Chemodosimeter. *Adv. Funct. Mater.* **2007**, *17*, 3799–3807.
- (96) Qian, G.; Dai, B.; Luo, M.; Yu, D.; Zhan, J.; Zhang, Z.; Dongge, M.; Wang, Z. Y. Band Gap Tunable, Donor-Acceptor-Donor Charge-Transfer Heteroquinoid-Based Chromophores: Near Infrared Photoluminescence and Electroluminescence. *Chem. Mater.* **2008**, *20*, 6208–6216.
- (97) Hu, R.; Lager, E.; Aguilar-Aguilar, A.; Liu, J.; Lam, J. W. Y.; Sung, H. H. Y.; Williams, I. D.; Zhong, Y.; Wong, K. S.; Peña-Cabrera, E.; Tang, B. Z. Twisted Intramolecular Charge Transfer and Aggregation-Induced Emission of BODIPY Derivatives. *J. Phys. Chem. C* **2009**, *113*, 15845–15853.
- (98) Cho, Y. J.; Kim, S. Y.; Cho, M.; Han, W. S.; Son, H. J.; Cho, D. W.; Kang, S. O. Aggregation-Induced Emission of Diarylamino- π -Carborane Triads: Effects of Charge Transfer and π -Conjugation. *Phys. Chem. Chem. Phys.* **2016**, *18*, 9702–9708.
- (99) Ishi-I, T.; Ikeda, K.; Ogawa, M.; Kusakaki, Y. Light-Emitting Properties of Donor-Acceptor and Donor-Acceptor-Donor Dyes in Solution, Solid, and Aggregated States: Structure-Property Relationship of Emission Behavior. *RSC Adv.* **2015**, *5*, 89171–89187.
- (100) Skardžiute, L.; Kazlauskas, K.; Dodonova, J.; Bucevičius, J.; Tumkevičius, S.; Juršenas, S. Optical Study of the Formation of Pyrrolo[2,3-d]Pyrimidine-Based Fluorescent Nanoaggregates. *Tetrahedron* **2013**, *69*, 9566–9572.
- (101) Wu, J. H.; Chen, W. C.; Liou, G. S. Triphenylamine-Based Luminogens and Fluorescent Polyimides: Effects of Functional Groups and Substituents on Photophysical Behaviors. *Polym. Chem.* **2016**, *7*, 1569–1576.
- (102) Hua, J.; Tian, H.; Zhang, H. Properties of Triarylamine Derivatives with AIE and Large Two-Photon Absorbing Cross-Sections. In *Aggregation-Induced Emission: Fundamentals*; John Wiley and Sons Ltd: Chichester, United Kingdom, 2013; Vol. 1–2, pp 169–184.
- (103) Huang, W.; Wang, H.; Sun, L.; Li, B.; Su, J.; Tian, H. Propeller-like D- π -A Architectures: Bright Solid Emitters with AIEE Activity and Large Two-Photon Absorption. *J. Mater. Chem. C* **2014**, *2*, 6843–6849.
- (104) Wang, B.; He, N.; Li, B.; Jiang, S.; Qu, Y.; Qu, S.; Hua, J. Aggregation-Induced Emission and Large Two-Photon Absorption Cross-Sections of Diketopyrrolopyrrole (DPP) Derivatives. *Aust. J. Chem.* **2012**, *65*, 387.
- (105) Huang, W.; Tang, F.; Li, B.; Su, J.; Tian, H. Large Cyano- and Triazine-Substituted D- π -A- π -D Structures as Efficient AIEE Solid Emitters with Large Two-Photon Absorption Cross Sections. *J. Mater. Chem. C* **2014**, *2*, 1141–1148.
- (106) Wang, B.; Wang, Y.; Hua, J.; Jiang, Y.; Huang, J.; Qian, S.; Tian, H. Starburst Triarylamine Donor-Acceptor-Donor Quadrupolar Derivatives Based on Cyano-Substituted Diphenylaminestylbenzene: Tunable Aggregation-Induced Emission Colors and Large Two-Photon Absorption Cross Sections. *Chem. - A Eur. J.* **2011**, *17*, 2647–2655.
- (107) Alternative energy tutorials <http://www.alternative-energy-tutorials.com/energy-articles/solar-cell-i-v-characteristic.html>.
- (108) Mahmood, A. Triphenylamine Based Dyes for Dye Sensitized Solar Cells: A Review. *Sol. Energy* **2016**, *123*, 127–144.
- (109) Wang, J.; Liu, K.; Ma, L.; Zhan, X. Triarylamine: Versatile Platform for Organic, Dye-Sensitized,

- and Perovskite Solar Cells. *Chem. Rev.* **2016**, *116*, 14675–14725.
- (110) Ning, Z.; Tian, H. Triarylamine: A Promising Core Unit for Efficient Photovoltaic Materials. *Chem. Commun.* **2009**, *37*, 5483–5495.
- (111) Agarwala, P.; Kabra, D. A Review on Triphenylamine (TPA) Based Organic Hole Transport Materials (HTM) for Dye Sensitized Solar Cells (DSSCs) and Perovskite Solar Cells (PSCs): Evolution and Molecular Engineering. *J. Mater. Chem. A* **2017**, *5*, 1348–1373.
- (112) Min, J.; Luponosov, Y. N.; Baran, D.; Chvalun, S. N.; Shcherbina, M. A.; Bakirov, A. V.; Dmitryakov, P. V.; Peregodova, S. M.; Kausch-Busies, N.; Ponomarenko, S. A.; Ameri, T.; Brabec, C. J. Effects of Oligothiophene π -Bridge Length on Physical and Photovoltaic Properties of Star-Shaped Molecules for Bulk Heterojunction Solar Cells. *J. Mater. Chem. A* **2014**, *2*, 16135–16147.
- (113) Lin, H. W.; Lin, L. Y.; Chen, Y. H.; Chen, C. W.; Lin, Y. T.; Chiu, S. W.; Wong, K. T. A New Donor-Acceptor Molecule with Uniaxial Anisotropy for Efficient Vacuum-Deposited Organic Solar Cells. *Chem. Commun.* **2011**, *47*, 7872–7874.
- (114) Roquet, S.; Cravino, A.; Leriche, P.; Aleveque, O.; Pierre Frere, J.; Roncali, J. Triphenylamine-Thienylenevinylene Hybrid Systems With. *J. Am. Chem. Soc.* **2006**, *128*, 3459–3466.
- (115) Cravino, A.; Roquet, S.; Alévêque, O.; Leriche, P.; Frère, P.; Roncali, J. Triphenylamine - Oligothiophene Conjugated Systems as Organic Semiconductors for Opto-Electronics. *Chem. Mater.* **2006**, *18*, 2584–2590.
- (116) Cravino, A.; Roquet, S.; Leriche, P.; Alévêque, O.; Frère, P.; Roncali, J. A Star-Shaped Triphenylamine π -Conjugated System with Internal Charge-Transfer as Donor Material for Hetero-Junction Solar Cells. *Chem. Commun.* **2006**, *13*, 1416–1418.
- (117) Lim, K.; Lee, S. Y.; Song, K.; Sharma, G. D.; Ko, J. Synthesis and Properties of Low Bandgap Star Molecules TPA-[DTS-PyBTTh3]₃ and DMM-TPA[DTS-PyBTTh3]₃ for Solution-Processed Bulk Heterojunction Organic Solar Cells. *J. Mater. Chem. C* **2014**, *2*, 8412–8422.
- (118) Chen, Y.-H.; Lin, L.-Y.; Lu, C.-W.; Lin, F.; Huang, Z.-Y.; Lin, H.-W.; Wang, P.-H.; Liu, Y.-H.; Wong, K.-T.; Wen, J.; Miller, D. J.; Darling, S. B. Vacuum-Deposited Small-Molecule Organic Solar Cells with High Power Conversion Efficiencies by Judicious Molecular Design and Device Optimization. *J. Am. Chem. Soc.* **2012**, *134*, 13616–13623.
- (119) Chiu, S. W.; Lin, L. Y.; Lin, H. W.; Chen, Y. H.; Huang, Z. Y.; Lin, Y. T.; Lin, F.; Liu, Y. H.; Wong, K. T. A Donor-Acceptor-Acceptor Molecule for Vacuum-Processed Organic Solar Cells with a Power Conversion Efficiency of 6.4%. *Chem. Commun.* **2012**, *48*, 1857–1859.
- (120) Huang, F.; Chen, K. S.; Yip, H. L.; Hau, S. K.; Acton, O.; Zhang, Y.; Luo, J.; Jen, A. K. Y. Development of New Conjugated Polymers with Donor- π -Bridge-Acceptor Side Chains for High Performance Solar Cells. *J. Am. Chem. Soc.* **2009**, *131*, 13886–13887.
- (121) Li, H.; Luo, H.; Cao, Z.; Gu, Z.; Shen, P.; Zhao, B.; Chen, H.; Yu, G.; Tan, S. Synthesis and Photovoltaic Performances of Conjugated Copolymers with 4,7-Dithien-5-Yl-2,1,3-Benzothiadiazole and Di(p-Tolyl)Phenylamine Side Groups. *J. Mater. Chem.* **2012**, *22*, 22913–22921.
- (122) Kitamura, T.; Ikeda, M.; Shigaki, K.; Inoue, T.; Anderson, N. A.; Ai, X.; Lian, T.; Yanagida, S. Phenyl-Conjugated Oligoene Sensitizers for TiO₂ Solar Cells. *Chem. Mater.* **2004**, *16*, 1806–1812.
- (123) Joly, D.; Pellejà, L.; Narbey, S.; Oswald, F.; Meyer, T.; Kervella, Y.; Maldivi, P.; Clifford, J. N.; Palomares, E.; Demadrille, R. Metal-Free Organic Sensitizers with Narrow Absorption in the Visible for Solar Cells Exceeding 10% Efficiency. *Energy Environ. Sci.* **2015**, *8*, 2010–2018.
- (124) Zhou, N.; Prabakaran, K.; Lee, B.; Chang, S. H.; Harutyunyan, B.; Guo, P.; Butler, M. R.; Timalisina, A.; Bedzyk, M. J.; Ratner, M. A.; Vegiraju, S.; Yau, S.; Wu, C. G.; Chang, R. P. H.; Facchetti, A.; Chen, M. C.; Marks, T. J. Metal-Free Tetrathienoacene Sensitizers for High-Performance Dye-Sensitized Solar Cells. *J. Am. Chem. Soc.* **2015**, *137*, 4414–4423.
- (125) Tan, L. L.; Huang, J. F.; Shen, Y.; Xiao, L. M.; Liu, J. M.; Kuang, D. Bin; Su, C. Y. Highly Efficient and Stable Organic Sensitizers with Duplex Starburst Triphenylamine and Carbazole Donors for Liquid and Quasi-Solid-State Dye-Sensitized Solar Cells. *J. Mater. Chem. A* **2014**, *2*, 8988–8994.
- (126) Yum, J.-H.; Baranoff, E.; Kessler, F.; Moehl, T.; Ahmad, S.; Bessho, T.; Marchioro, A.; Ghadiri, E.; Moser, J.-E.; Yi, C.; Nazeeruddin, M. K.; Grätzel, M. A Cobalt Complex Redox Shuttle for Dye-Sensitized Solar Cells with High Open-Circuit Potentials. *Nat. Commun.* **2012**, *3*, 631.
- (127) Zeng, W.; Cao, Y.; Bai, Y.; Wang, Y.; Shi, Y.; Zhang, M.; Wang, F.; Pan, C.; Wang, P. Efficient Dye-Sensitized Solar Cells with an Organic Photosensitizer Featuring Orderly Conjugated Ethylenedioxythiophene and Dithienosilole Blocks. *Chem. Mater.* **2010**, *22*, 1915–1925.
- (128) Yella, A.; Lee, H.-W.; Tsao, H. N.; Yi, C.; Chandiran, A. K.; Nazeeruddin, M. K.; Diau, E.; Yeh, C.-Y.; Zakeeruddin, S. M.; Grätzel, M. Porphyrin-Sensitized Solar Cells with Cobalt

- (II/III)-Based Redox Electrolyte Exceed 12 Percent Efficiency. *Science* **2011**, *334*, 629–633.
- (129) Yella, A.; Mai, C. L.; Zakeeruddin, S. M.; Chang, S. N.; Hsieh, C. H.; Yeh, C. Y.; Grätzel, M. Molecular Engineering of Push-Pull Porphyrin Dyes for Highly Efficient Dye-Sensitized Solar Cells: The Role of Benzene Spacers. *Angew. Chem. Int. Ed.* **2014**, *53*, 2973–2977.
- (130) Mathew, S.; Yella, A.; Gao, P.; Humphry-Baker, R.; Curchod, B. F. E.; Ashari-Astani, N.; Tavernelli, I.; Rothlisberger, U.; Nazeeruddin, M. K.; Grätzel, M. Dye-Sensitized Solar Cells with 13% Efficiency Achieved through the Molecular Engineering of Porphyrin Sensitizers. *Nat. Chem.* **2014**, *6*, 242–247.
- (131) Jeon, N. J.; Lee, H. G.; Kim, Y. C.; Seo, J.; Noh, J. H.; Lee, J.; Seok, S. I. O-Methoxy Substituents in Spiro-OMeTAD for Efficient Inorganic-Organic Hybrid Perovskite Solar Cells. *J. Am. Chem. Soc.* **2014**, *136*, 7837–7840.
- (132) Polander, L. E.; Pahner, P.; Schwarze, M.; Saalfrank, M.; Koerner, C.; Leo, K. Hole-Transport Material Variation in Fully Vacuum Deposited Perovskite Solar Cells. *APL Mater.* **2014**, *2*, 081503.
- (133) Li, H.; Fu, K.; Boix, P. P.; Wong, L. H.; Hagfeldt, A.; Grätzel, M.; Mhaisalkar, S. G.; Grimsdale, A. C. Hole-Transporting Small Molecules Based on Thiophene Cores for High Efficiency Perovskite Solar Cells. *ChemSusChem* **2014**, *7*, 3420–3425.
- (134) Shirota, Y.; Kobata, T.; Noma, N. Starburst Molecules for Amorphous Molecular Materials. 4,4',4''-Tris(N,N-Diphenylamino)Triphenylamine and 4,4',4''-Tris[N-(3-Methylphenyl)-N-Phenylamino]Triphenylamine. *Chem. Lett.* **1989**, *18*, 1145–1148.
- (135) Shirota, Y.; Kobata, T.; Noma, N. Starburst Molecules for Amorphous Molecular Materials. 4,4',4''-Tris(N,N-Diphenylamino)Triphenylamine and 4,4',4''-Tris[N-(3-Methylphenyl)-N-Phenylamino]Triphenylamine. *Chem. Lett.* **1989**, *18*, 1145–1148.
- (136) Akiji Higuchi, Hiroshi Znada, T. K.; and Yasuhiko Shirota. Amorphous Molecular Materials: Synthesis and Properties of a Novel Starburst Molecule, 4,4',4''-Tri(N-Phenothiazinyl)Triphenylamine. *Adv. Mater.* **1991**, *3*, 549–550.
- (137) Choi, H.; Paek, S.; Lim, N.; Lee, Y. H.; Nazeeruddin, M. K.; Ko, J. Efficient Perovskite Solar Cells with 13.63 % Efficiency Based on Planar Triphenylamine Hole Conductors. *Chem. - A Eur. J.* **2014**, *20*, 10894–10899.
- (138) Choi, H.; Park, S.; Paek, S.; Ekanayake, P.; Nazeeruddin, M. K.; Ko, J. Efficient Star-Shaped Hole Transporting Materials with Diphenylethenyl Side Arms for an Efficient Perovskite Solar Cell. *J. Mater. Chem. A* **2014**, *2*, 19136–19140.
- (139) Huang, C.; Fu, W.; Li, C. Z.; Zhang, Z.; Qiu, W.; Shi, M.; Heremans, P.; Jen, A. K. Y.; Chen, H. Dopant-Free Hole-Transporting Material with a C3h Symmetrical Truxene Core for Highly Efficient Perovskite Solar Cells. *J. Am. Chem. Soc.* **2016**, *138*, 2528–2531.
- (140) Tanaka, H.; Tokito, S.; Taga, Y.; Okada, A. Novel Hole-Transporting Materials Based on Triphenylamine for Organic Electroluminescent Devices. *Chem. Commun.* **1996**, *18*, 2175–2176.
- (141) Kroeze, J. E.; Hirata, N.; Schmidt-Mende, L.; Orizu, C.; Ogier, S. D.; Carr, K.; Grätzel, M.; Darrant, J. R. Parameters Influencing Charge Separation in Solid-State Dye-Sensitized Solar Cells Using Novel Hole Conductors. *Adv. Funct. Mater.* **2006**, *16*, 1832–1838.
- (142) Reddy, S. S.; Gunasekar, K.; Heo, J. H.; Im, S. H.; Kim, C. S.; Kim, D. H.; Moon, J. H.; Lee, J. Y.; Song, M.; Jin, S. H. Highly Efficient Organic Hole Transporting Materials for Perovskite and Organic Solar Cells with Long-Term Stability. *Adv. Mater.* **2016**, *28*, 686–693.
- (143) Jeon, N. J.; Noh, J. H.; Kim, Y. C.; Yang, W. S.; Ryu, S.; Seok, S. I. Solvent Engineering for High-Performance Inorganic-Organic Hybrid Perovskite Solar Cells. *Nat. Mater.* **2014**, *13*, 897–903.
- (144) Heo, J. H.; Im, S. H.; Noh, J. H.; Mandal, T. N.; Lim, C. S.; Chang, J. A.; Lee, Y. H.; Kim, H. J.; Sarkar, A.; Nazeeruddin, M. K.; Grätzel, M.; Seok, S. I. Efficient Inorganic-Organic Hybrid Heterojunction Solar Cells Containing Perovskite Compound and Polymeric Hole Conductors. *Nat. Photonics* **2013**, *7*, 486–491.
- (145) Zhang, W.; Smith, J.; Hamilton, R.; Heeney, M.; Kirkpatrick, J.; Song, K.; Watkins, S. E.; Anthopoulos, T.; McCulloch, I. Systematic Improvement in Charge Carrier Mobility of Air Stable Triarylamine Copolymers. *J. Am. Chem. Soc.* **2009**, *131*, 10814–10815.
- (146) Kuwabara, Y.; Ogawa, H.; Inada, H.; Noma, N.; Shirota, Y. Thermally Stable Multilayered Organic Electroluminescent Devices Using Novel Starburst Molecules, 4,4',4''-Tri(N-Carbazolyl)Triphenylamine (TCTA) and 4,4',4''-Tris(3-Methylphenylphenylamino)Triphenylamine (m-MTDATA), as Hole-Transport Materials. *Adv. Mater.* **1994**, *6*, 677–679.
- (147) Li, J.; Ma, C.; Tang, J.; Lee, C. S.; Lee, S. Novel Starburst Molecule as a Hole Injecting and Transporting Material for Organic Light-Emitting Devices. *Chem. Mater.* **2005**, *17*, 615–619.
- (148) Jiang, Z.; Ye, T.; Yang, C.; Yang, D.; Zhu, M.; Zhong, C.; Qin, J.; Ma, D. Star-Shaped Oligotriarylamines with Planarized Triphenylamine Core: Solution-Processable, High-Tg Hole-Injecting and Hole-Transporting

- Materials for Organic Light-Emitting Devices. *Chem. Mater.* **2011**, *23*, 771–777.
- (149) Moonsin, P.; Prachumrak, N.; Rattanawan, R.; Keawin, T.; Jungsuttiwong, S.; Sudyoasuk, T.; Promarak, V. Carbazole Dendronised Triphenylamines as Solution Processed High T g Amorphous Hole-Transporting Materials for Organic Electroluminescent Devices. *Chem. Commun.* **2012**, *48*, 3382–3384.
- (150) Thelakkat, M. Star-Shaped, Dendrimeric and Polymeric Triarylamine as Photoconductors and Hole Transport Materials for Electro-Optical Applications. *Macromol. Mater. Eng.* **2002**, *287*, 442–461.
- (151) Thelakkat, M.; Schmitz, C.; Hohle, C.; Strohriegel, P.; Schmidt, H. W.; Hofmann, U.; Schloter, S.; Haarer, D. Novel Functional Materials Based on Triarylamine-Synthesis and Application in Electroluminescent Devices and Photorefractive Systems. *Phys. Chem. Chem. Phys.* **1999**, *1*, 1693–1698.
- (152) Yin, Z.; Liu, R.; Li, C.; Masayuki, T.; Liu, C.; Jin, X.; Zhu, H. N¹,N¹,N³,N³-Tetra([1,1'-Biphenyl]-4-Yl)-N⁵,N⁵-Diphenylbenzene-1,3,5-Triamine: Synthesis, Optical Properties and Application in OLED Devices as Efficient Hole Transporting Material. *Dyes and Pigments* **2015**, *122*, 59–65.
- (153) Shirota, Y.; Okumoto, K.; Inada, H. Thermally Stable Organic Light-Emitting Diodes Using New Families of Hole-Transporting Amorphous Molecular Materials. *Synth. Met.* **2000**, *111*, 387–391.
- (154) Naito, K.; Miura, A. Molecular Design for Nonpolymeric Organic Dye Glasses with Thermal Stability: Relations between Thermodynamic Parameters and Amorphous Properties. *J. Phys. Chem.* **1993**, *97*, 6240–6248.
- (155) Hreha, R. D.; George, C. P.; Haldi, A.; Domercq, B.; Malagoli, M.; Barlow, S.; Brédas, J. L.; Kippelen, B.; Marder, S. R. 2,7-Bis(Diarylamino)-9,9-Dimethylfluorenes as Hole-Transport Materials for Organic Light-Emitting Diodes. *Adv. Funct. Mater.* **2003**, *13*, 967–973.
- (156) Noda, T.; Ogawa, H.; Noma, N.; Shirota, Y. Organic Light-Emitting Diodes Using a Novel Family of Amorphous Molecular Materials Containing an Oligothiophene Moiety as Colour-Tunable Emitting Materials. *J. Mater. Chem.* **1999**, *9*, 2177–2181.
- (157) Okumoto, K.; Ohara, T.; Noda, T.; Shirota, Y. A Thermally Stable Greenish Blue Organic Electroluminescent Device Using Anovel Emitting Amorphous Molecular Material. *Synth. Met.* **2001**, *121*, 1655–1656.
- (158) Cho, J. S.; Kojima, Y.; Yamamoto, K. A Novel Oligothiophene Derivative as a Hole-Transport with Emitting Material for OLED. *Polym. Adv. Technol.* **2003**, *14*, 52–57.
- (159) Adachi, C.; Tsutsui, T.; Saito, S. Organic Electroluminescent Device Having a Hole Conductor as an Emitting Layer. *Appl. Phys. Lett.* **1989**, *55*, 1489–1491.
- (160) Doi, H.; Kinoshita, M.; Okumoto, K.; Shirota, Y. A Novel Class of Emitting Amorphous Molecular Materials with Bipolar Character for Electroluminescence. *Chem. Mater.* **2003**, *15*, 1080–1089.
- (161) Lee, T. H.; Tong, K. L.; So, S. K.; Leung, L. M. Synthesis and Electroluminescence of Thiophene-Based Bipolar Small Molecules with Different Arylamine Moieties. *Synth. Met.* **2005**, *155*, 116–124.
- (162) Fang, Q.; Xu, B.; Jiang, B.; Fu, H.; Zhu, W.; Jiang, X.; Zhang, Z. A Novel Fluorene Derivative Containing Four Triphenylamine Groups: Highly Thermostable Blue Emitter with Hole-Transporting Ability for Organic Light-Emitting Diode (OLED). *Synth. Met.* **2005**, *155*, 206–210.
- (163) Kimura, M.; Kuwano, S.; Sawaki, Y.; Fujikawa, H.; Noda, K.; Taga, Y.; Takagi, K. New 9-Fluorene-Type Trispirocyclic Compounds for Thermally Stable Hole Transport Materials in OLEDs. *J. Mater. Chem.* **2005**, *15*, 2393–2398.
- (164) Huang, J.; Su, J. H.; Li, X.; Lam, M. K.; Fung, K. M.; Fan, H. H.; Cheah, K. W.; Chen, C. H.; Tian, H. Bipolar Anthracene Derivatives Containing Hole- and Electron-Transporting Moieties for Highly Efficient Blue Electroluminescence Devices. *J. Mater. Chem.* **2011**, *21*, 2957–2964.
- (165) Kim, S. K.; Yang, B.; Park, Y. Il; Ma, Y.; Lee, J. Y.; Kim, H. J.; Park, J. Synthesis and Electroluminescent Properties of Highly Efficient Anthracene Derivatives with Bulky Side Groups. *Org. Electron. physics, Mater. Appl.* **2009**, *10*, 822–833.
- (166) Jia, W. L.; Feng, X. D.; Bai, D. R.; Lu, Z. H.; Wang, S.; Vamvounis, G. Mes2B(p-4,4'-Biphenyl-NPh(1-Naphthyl)): A Multifunctional Molecule for Electroluminescent Devices. *Chem. Mater.* **2005**, *17*, 164–170.
- (167) Hancock, J. M.; Gifford, A. P.; Zhu, Y.; Lou, Y.; Jenekhe, S. A. N-Type Conjugated Oligoquinoline and Oligoquinoxaline with Triphenylamine End Groups: Efficient Ambipolar Light Emitters for Device Applications. *Chem. Mater.* **2006**, *18*, 4924–4932.
- (168) Li, W.; Pan, Y.; Xiao, R.; Peng, Q.; Zhang, S.; Ma, D.; Li, F.; Shen, F.; Wang, Y.; Yang, B.; Ma, Y. Employing ~100% Excitons in OLEDs by Utilizing a Fluorescent Molecule with Hybridized Local and Charge-Transfer Excited State. *Adv. Funct. Mater.* **2014**, *24*, 1609–1614.
- (169) Tao, Y.; Wang, Q.; Yang, C.; Zhong, C.; Qin, J.;

- Ma, D. Multifunctional Triphenylamine/Oxadiazole Hybrid as Host and Exciton-Blocking Material: High Efficiency Green Phosphorescent OLEDs Using Easily Available and Common Materials. *Adv. Funct. Mater.* **2010**, *20*, 2923–2929.
- (170) Ding, L.; Dong, S. C.; Jiang, Z. Q.; Chen, H.; Liao, L. S. Orthogonal Molecular Structure for Better Host Material in Blue Phosphorescence and Larger OLED White Lighting Panel. *Adv. Funct. Mater.* **2015**, *25*, 645–650.
- (171) Gong, S.; Zhao, Y.; Wang, M.; Yang, C.; Zhong, C.; Qin, J.; Ma, D. Versatile Benzimidazole/Triphenylamine Hybrids: Efficient Nondoped Deep-Blue Electroluminescence and Good Host Materials for Phosphorescent Emitters. *Chem. - An Asian J.* **2010**, *5*, 2093–2099.
- (172) Braga, D.; Horowitz, G. High-Performance Organic Field-Effect Transistors. *Adv. Mater.* **2009**, *21*, 1473–1486.
- (173) Horowitz, G. Organic Field-Effect Transistors. *Adv. Mater.* **1998**, *10*, 365–377.
- (174) Veres, J.; Ogier, S. D.; Leeming, S. W.; Cupertino, D. C.; Khaffaf, S. M. Low-k Insulators as the Choice of Dielectrics in Organic Field-Effect Transistors. *Adv. Funct. Mater.* **2003**, *13*, 199–204.
- (175) Majewski, L. A.; Schroeder, R.; Grell, M. Low-Voltage, High-Performance Organic Field-Effect Transistors with an Ultra-Thin TiO₂ Layer as Gate Insulator. *Adv. Funct. Mater.* **2005**, *15*, 1017–1022.
- (176) Schroeder, R.; Majewski, L. A.; Grell, M.; Maunoury, J.; Gautrot, J.; Hodge, P.; Turner, M. Electrode Specific Electropolymerization of Ethylenedioxythiophene: Injection Enhancement in Organic Transistors. *Appl. Phys. Lett.* **2005**, *87*, 2003–2006.
- (177) Sonntag, M.; Kreger, K.; Hanft, D.; Strohriegl, P.; Setayesh, S.; De Leeuw, D. Novel Star-Shaped Triphenylamine-Based Molecular Glasses and Their Use in OFETs. *Chem. Mater.* **2005**, *17*, 3031–3039.
- (178) Yasuda, T.; Suzuki, T.; Takahashi, M.; Tsutsui, T. Synthesis and Carrier Transport Properties of Triarylamine-Based Amorphous Polymers for Organic Field-Effect Transistors. *Chem. Lett.* **2009**, *38*, 1040–1041.
- (179) Hüttner, S.; Sommer, M.; Steiner, U.; Thelakkat, M. Organic Field Effect Transistors from Triarylamine Side-Chain Polymers. *Appl. Phys. Lett.* **2010**, *96*, 2008–2011.
- (180) Anglin, T. C.; Sohrabpour, Z.; Massari, A. M. Nonlinear Spectroscopic Markers of Structural Change during Charge Accumulation in Organic Field-Effect Transistors. *J. Phys. Chem. C* **2011**, *115*, 20258–20266.
- (181) Reitzenstein, D.; Quast, T.; Kanal, F.; Kullmann, M.; Ruetzel, S.; Hammer, M. S.; Deibel, C.; Dyakonov, V.; Brixner, T.; Lambert, C. Synthesis and Electron Transfer Characteristics of a Neutral, Low-Band-Gap, Mixed-Valence Polyradical. *Chem. Mater.* **2010**, *22*, 6641–6655.
- (182) Chaing, C. J.; Chen, J. C.; Kuo, Y. J.; Tsao, H. Y.; Wu, K. Y.; Wang, C. L. 2,2'-Bis(Trifluoromethyl)Biphenyl as a Building Block for Highly Ambient-Stable, Amorphous Organic Field-Effect Transistors with Balanced Ambipolarity. *RSC Adv.* **2016**, *6*, 8628–8638.
- (183) Sprick, R. S.; Hoyos, M.; Morrison, J. J.; Grace, I. M.; Lambert, C.; Navarro, O.; Turner, M. L. Triarylamine Polymers of Bridged Phenyls by (N-Heterocyclic Carbene)-Palladium Catalysed C-N Coupling. *J. Mater. Chem. C* **2013**, *1*, 3327–3336.
- (184) Ingram, I. D. V.; Tate, D. J.; Parry, A. V. S.; Sprick, R. S.; Turner, M. L. A Simple Method for Controllable Solution Doping of Complete Polymer Field-Effect Transistors. *Appl. Phys. Lett.* **2014**, *104*.
- (185) Sprick, R. S.; Hoyos, M.; Wrackmeyer, M. S.; Sheridan Parry, A. V.; Grace, I. M.; Lambert, C.; Navarro, O.; Turner, M. L. Extended Conjugation in Poly(Triarylamine)s: Synthesis, Structure and Impact on Field-Effect Mobility. *J. Mater. Chem. C* **2014**, *2*, 6520–6528.
- (186) Cheng, S.; Chien, Y. C.; Huang, T.; Liu, C.; Liou, G. Linkage Effects of Triphenylamine-Based Aromatic Polymer Electrets on Electrical Memory Performance. *Polymer* **2018**, *148*, 382–389.
- (187) Madec, M. B.; Morrison, J. J.; Sanchez-Romaguera, V.; Turner, M. L.; Yeates, S. G. Organic Field Effect Transistors from Ambient Solution Processed Poly(Triarylamine)-Insulator Blends. *J. Mater. Chem.* **2009**, *19*, 6750–6755.
- (188) Smith, J.; Hamilton, R.; Qi, Y.; Kahn, A.; Bradley, D. D. C.; Heeney, M.; McCulloch, I.; Anthopoulos, T. D. The Influence of Film Morphology in High-Mobility Small-Molecule Polymer Blend Organic Transistors. *Adv. Funct. Mater.* **2010**, *20*, 2330–2337.
- (189) Pitsalidis, C.; Pappa, A. M.; Hunter, S.; Laskarakis, A.; Kaimakamis, T.; Payne, M. M.; Anthony, J. E.; Anthopoulos, T. D.; Logothetidis, S. High Mobility Transistors Based on Electro-spray-Printed Small-Molecule/Polymer Semiconducting Blends. *J. Mater. Chem. C* **2016**, *4*, 3499–3507.
- (190) Smith, J.; Heeney, M.; McCulloch, I.; Malik, J. N.; Stingelin, N.; Bradley, D. D. C.; Anthopoulos, T. D. Percolation Behaviour in High Mobility P-Channel Polymer/Small-Molecule Blend Organic Field-Effect Transistors. *Org. Electron. physics, Mater. Appl.* **2011**, *12*, 143–147.

References

- (191) Hwang, D. K.; Fuentes-Hernandez, C.; Berrigan, J. D.; Fang, Y.; Kim, J.; Potscavage, W. J.; Cheun, H.; Sandhage, K. H.; Kippelen, B. Solvent and Polymer Matrix Effects on TIPS-Pentacene/Polymer Blend Organic Field-Effect Transistors. *J. Mater. Chem.* **2012**, *22*, 5531–5537.
- (192) Park, W.-T.; Noh, Y.-Y. High Performance Organic Field-Effect Transistor with Low-Temperature Processed DiF-TESADT Large Crystal for Flexible Electronics. *J. Nanosci. Nanotechnol.* **2016**, *16*, 8470–8472.
- (193) Dheepika, R.; Sonalin, S.; Imran, P. M.; Nagarajan, S. Unsymmetrical Starburst Triarylamines: Synthesis, Properties, and Characteristics of OFETs. *J. Mater. Chem. C* **2018**, *6*, 6916–6919.
- (194) Wren, E. J.; Mutkins, K.; Aljada, M.; Burn, P. L.; Meredith, P.; Vamvounis, G. The Effect of Dendronisation of Arylamine Centred Chromophores on Field Effect Transistor Performance. *Polym. Chem.* **2010**, *1*, 1117–1126.
- (195) Paek, S.; Cho, N.; Cho, S.; Lee, J. K.; Ko, J. Planar Star-Shaped Organic Semiconductor with Fused Triphenylamine Core for Solution-Processed Small-Molecule Organic Solar Cells and Field-Effect Transistors. *Org. Lett.* **2012**, *14*, 6326–6329.
- (196) Swensen, J. S.; Wang, L.; Rainbolt, J. E.; Koech, P. K.; Polikarpov, E.; Gaspar, D. J.; Padmaperuma, A. B. Characterization of Solution Processed, p-Doped Films Using Hole-Only Devices and Organic Field-Effect Transistors. *Org. Electron. physics, Mater. Appl.* **2012**, *13*, 3085–3090.
- (197) Yu, X.; Yu, J.; Zhou, J.; Huang, J.; Jiang, Y. Hole Mobility Enhancement of Pentacene Organic Field-Effect Transistors Using 4,4',4''-Tris[3-Methylphenyl(Phenyl)Amino] Triphenylamine as a Hole Injection Interlayer. *Appl. Phys. Lett.* **2011**, *99*, 3–6.
- (198) Li, J.; Shi, W.; Shu, L.; Yu, J. Performance Enhancement of P-Type Organic Field-Effect Transistor through Introducing Organic Buffer Layers. *J. Mater. Sci. Mater. Electron.* **2015**, *26*, 8301–8306.
- (199) Dharmapurikar, S. S.; Arulkashmir, A.; Das, C.; Muddellu, P.; Krishnamoorthy, K. Enhanced Hole Carrier Transport Due to Increased Intermolecular Contacts in Small Molecule Based Field Effect Transistors. *ACS Appl. Mater. Interfaces* **2013**, *5*, 7086–7093.
- (200) Rybakiewicz, R.; Gawrys, P.; Tsikritzis, D.; Emmanouil, K.; Kennou, S.; Zagorska, M.; Pron, A. Electronic Properties of Semiconducting Naphthalene Bisimide Derivatives - Ultraviolet Photoelectron Spectroscopy versus Electrochemistry. *Electrochim. Acta* **2013**, *96*, 13–17.
- (201) Keyworth, C. W.; Chan, K. L.; Labram, J. G.; Anthopoulos, T. D.; Watkins, S. E.; McKiernan, M.; White, A. J. P.; Holmes, A. B.; Williams, C. K. The Tuning of the Energy Levels of Dibenzosilole Copolymers and Applications in Organic Electronics. *J. Mater. Chem.* **2011**, *21*, 11800–11814.
- (202) Hwang, D. K.; Fuentes-Hernandez, C.; Kim, J. B.; Potscavage, W. J.; Kippelen, B. Flexible and Stable Solution-Processed Organic Field-Effect Transistors. *Org. Electron. physics, Mater. Appl.* **2011**, *12*, 1108–1113.
- (203) Jung, M.-H.; Song, K. H.; Ko, K. C.; Lee, J. Y.; Lee, H. Nonvolatile Memory Organic Field Effect Transistor Induced by the Steric Hindrance Effects of Organic Molecules. *J. Mater. Chem.* **2010**, *20*, 8016.
- (204) Bharath, D.; Chithiravel, S.; Sasikumar, M.; Cherreddy, N. R.; Shanigaram, B.; Bhanuprakash, K.; Krishnamoorthy, K.; Rao, V. J. A Detailed Study on the Thermal, Photo-Physical and Electrochemical Properties and OFET Applications of D- π -A- π -D Structured Unsymmetrical Diketopyrrolopyrrole Materials. *RSC Adv.* **2015**, *5*, 94859–94865.
- (205) Song, Y.; Di, C. A.; Xu, W.; Liu, Y.; Zhang, D.; Zhu, D. New Semiconductors Based on Triphenylamine with Macrocyclic Architecture: Synthesis, Properties and Applications in OFETs. *J. Mater. Chem.* **2007**, *17*, 4483–4491.
- (206) Kudo, A.; Miseki, Y. Heterogeneous Photocatalyst Materials for Water Splitting. *Chem. Soc. Rev.* **2009**, *38*, 253–278.
- (207) Eberhart, M. S.; Wang, D.; Sampaio, R. N.; Marquard, S. L.; Shan, B.; Brennaman, M. K.; Meyer, G. J.; Dares, C.; Meyer, T. J. Water Photo-Oxidation Initiated by Surface-Bound Organic Chromophores. *J. Am. Chem. Soc.* **2017**, *139*, 16248–16255.
- (208) Okura, I.; Kim-thuan, N. Hydrogen Evolution Promoted by Hydrogenase from Reduced Methyl Viologen under Irradiation by Near-Ultraviolet Light. *J. Mol. Catal.* **1979**, 449–451.
- (209) Okura, I.; Kim-thuan, N. Photoreduction of Methyl Viologen by Triphenylamine and Hydrogen Generation with Hydrogenase. *J. Mol. Catal.* **1980**, *8*, 385–390.
- (210) Katakis, D.; Mitsopoulou, C.; Vrachnou, E. Photocatalytic Splitting of Water: Increase in Conversion and Energy Storage Efficiency. *J. Photochem. Photobiol. A Chem.* **1994**, *81*, 103–106.
- (211) Hoogeveen, D. A.; Fournier, M.; Bonke, S. A.; Fang, X. Y.; Mozer, A. J.; Mishra, A.; Bäuerle, P.; Simonov, A. N.; Spiccia, L. Photo-Electrocatalytic Hydrogen Generation at Dye-Sensitised Electrodes Functionalised with a Heterogeneous Metal Catalyst. *Electrochim. Acta* **2016**, *219*, 773–780.

References

- (212) Zhu, M.; Dong, Y.; Du, Y.; Mou, Z.; Liu, J.; Yang, P.; Wang, X. Photocatalytic Hydrogen Evolution Based on Efficient Energy and Electron Transfers in Donor-Bridge-Acceptor Multibranching-Porphyrin-Functionalized Platinum Nanocomposites. *Chem. Eur. J.* **2012**, *18*, 4367–4374.
- (213) Huo, J.; Zeng, H. A Novel Triphenylamine Functionalized Bithiazole-Metal Complex with C60 for Photocatalytic Hydrogen Production under Visible Light Irradiation. *J. Mater. Chem. A* **2015**, *3*, 6258–6264.
- (214) Huo, J.; Zeng, H. Silver Nanoparticles-Sensitized Cobalt Complex for Highly-Efficient Photocatalytic Activity. *Appl. Catal. B Environ.* **2016**, *199*, 342–349.
- (215) Jing, X.; He, C.; Yang, Y.; Duan, C. A Metal-Organic Tetrahedron as a Redox Vehicle to Encapsulate Organic Dyes for Photocatalytic Proton Reduction. *J. Am. Chem. Soc.* **2015**, *137*, 3967–3974.
- (216) Choi, S. K.; Yang, H. S.; Kim, J. H.; Park, H. Organic Dye-Sensitized TiO₂ as a Versatile Photocatalyst for Solar Hydrogen and Environmental Remediation. *Appl. Catal. B Environ.* **2012**, *121–122*, 206–213.
- (217) Ho, P. Y.; Wang, Y.; Yiu, S. C.; Yu, W. H.; Ho, C. L.; Huang, S. Starburst Triarylamine Donor-Based Metal-Free Photosensitizers for Photocatalytic Hydrogen Production from Water. *Org. Lett.* **2017**, *19*, 1048–1051.
- (218) Karlsson, S.; Boixel, J.; Pellegrin, Y.; Blart, E.; Becker, H. C.; Odobel, F.; Hammarström, L. Accumulative Electron Transfer: Multiple Charge Separation in Artificial Photosynthesis. *Faraday Discuss.* **2012**, *155*, 233–252.
- (219) Li, F.; Fan, K.; Xu, B.; Gabrielsson, E.; Daniel, Q.; Li, L.; Sun, L. Organic Dye-Sensitized Tandem Photoelectrochemical Cell for Light Driven Total Water Splitting. *J. Am. Chem. Soc.* **2015**, *137*, 9153–9159.
- (220) Shit, S. C.; Khilari, S.; Mondal, I.; Pradhan, D.; Mondal, J. The Design of a New Cobalt Sulfide Nanoparticle Implanted Porous Organic Polymer Nanohybrid as a Smart and Durable Water-Splitting Photoelectrocatalyst. *Chem. - A Eur. J.* **2017**, *23*, 14827–14838.
- (221) Suryani, O.; Higashino, Y.; Mulyana, J. Y.; Kaneko, M.; Hoshi, T.; Shigaki, K.; Kubo, Y. A Near-Infrared Organic Photosensitizer for Use in Dye-Sensitized Photoelectrochemical Water Splitting. *Chem. Commun.* **2017**, *53*, 6784–6787.
- (222) Duke, C. B.; Noolandi, J.; Thieret, T. The Surface Science of Xerography. *Surf. Sci.* **2002**, *500*, 678–698.
- (223) Pai, D. M.; Springett, B. E. Physics of Electrophotography. *Rev. Mod. Phys.* **1993**, *65*, 163–211.
- (224) Klupfel, K.-W.; Sus, O.; Behmenburg, H.; Neugebauer, W. Material for Electrophotographic Purposes. US Patent 3180730, 1965.
- (225) Brantly, T. B.; Contois, L. E.; Fox, C. J. Photoconductive Elements Containing as Photoconductors Triarylamines Substituted by Active Hydrogen-Containing Groups. US Patent 3658520, 1972.
- (226) Tamura, H.; Kami, H.; Ohta, K.; Suzuki, T.; Niimi, T.; Kojima, N. Electrophotographic Photoreceptor, and Process Cartridge and Image Forming Apparatus Using the Photoreceptor. US Patent 6326112B1, 2001.
- (227) Suzuki, T.; Tamura, H.; Ikuno, H.; Nagai, K.; Li, H. Electrophotographic Photoconductor, and Image Forming Apparatus and Process Cartridge for an Image Forming Apparatus Using the Same. US Patent 20080020305 A1, 2008.
- (228) Ghosh, K.; Masanta, G. Triphenylamine-Based Novel PET Sensors in Selective Recognition of Dicarboxylic Acids. *Tetrahedron Lett.* **2006**, *47*, 2365–2369.
- (229) Ghosh, K.; Masanta, G.; Fröhlich, R.; Petsalakis, I. D.; Theodorakopoulos, G. Triphenylamine-Based Receptors in Selective Recognition of Dicarboxylic Acids. *J. Phys. Chem. B* **2009**, *113*, 7800–7809.
- (230) Ghosh, K.; Saha, I. Triphenylamine-Based Simple Chemosensor for Selective Fluorometric Detection of Fluoride, Acetate and Dihydrogenphosphate Ions in Different Solvents. *J. Incl. Phenom. Macrocycl. Chem.* **2011**, *70*, 97–107.
- (231) Yang, Y.; Li, B.; Zhang, L.; Guan, Y. Triphenylamine Based Benzimidazole and Benzothiazole: Synthesis and Applications in Fluorescent Chemosensors and Laser Dyes. *J. Lumin.* **2014**, *145*, 895–898.
- (232) Ponnuel, K.; Padmini, V. Turn-on Fluorescence Chemosensor for Fluoride Ions and Its Applicability in Imaging of Living Cells. *J. Lumin.* **2016**, *169*, 289–294.
- (233) Yang, P.-C.; Wen, H.-W.; He, H.-J. Synthesis and Chemosensory Properties of Triphenylamine-Substituted Conjugated Polyfluorene Containing a Terminal Di(2-Picolyl)Amine Moiety. *RSC Adv.* **2015**, *5*, 101826–101833.
- (234) Juang, R.; Wen, H.; Chen, M.; Yang, P. Enhanced Sensing Ability of Fluorescent Chemosensors with Triphenylamine-Functionalized Conjugated Polyfluorene. *Sensors Actuators B. Chem.* **2016**.
- (235) Pan, C.; Wang, K.; Ji, S.; Wang, H.; Li, Z.; He, H.; Huo, Y. Schiff Base Derived Fe³⁺-Selective Fluorescence Turn-off Chemosensors Based on

References

- Triphenylamine and Indole: Synthesis, Properties and Application in Living Cells. *RSC Adv.* **2017**, *7*, 36007–36014.
- (236) Geng, T.; Zhu, Z.; Wang, X.; Xia, H.; Wang, Y.; Li, D. Poly{tris[4-(2-Thienyl)Phenyl]Amine} Fluorescent Conjugated Microporous Polymer for Selectively Sensing Picric Acid. *Sensors Actuators B. Chem.* **2017**, *244*, 334–343.
- (237) Xia, Y.; Zhang, H.; Zhu, X.; Zhang, G.; Yang, X.; Li, F.; Zhang, X.; Fang, M.; Yu, J.; Zhou, H. A Highly Selective Two-Photon Fluorescent Chemosensor for Tracking Homocysteine via Situ Reaction. *Dyes and Pigments* **2018**.
- (238) Feng, I.; Li, Y.; Yang, M. Hyperbranched Copolymer Containing Triphenylamine and Divinyl Bipyridyl Units for Fluorescent Chemosensors. *J. Polym. Sci. Part A Polym. Chem.* **2009**, *47*, 222–230.
- (239) Wang, K. L.; Liou, W. T.; Liaw, D. J.; Chen, W. T. A Novel Fluorescent Poly(Pyridine-Imide) Acid Chemosensor. *Dyes and Pigments* **2008**, *78*, 93–100.
- (240) Gu, D.; Yang, G.; He, Y.; Qi, B.; Wang, G.; Su, Z. Triphenylamine-Based PH Chemosensor: Synthesis, Crystal Structure, Photophysical Properties and Computational Studies. *Synth. Met.* **2009**, *159*, 2497–2501.
- (241) Mahapatra, A. K.; Hazra, G.; Das, N. K.; Goswami, S. A Highly Selective Triphenylamine-Based Indolylmethane Derivatives as Colorimetric and Turn-off Fluorimetric Sensor toward Cu²⁺ Detection by Deprotonation of Secondary Amines. *Sensors Actuators B Chem.* **2011**, *156*, 456–462.
- (242) Cheng, X.; Li, S.; Jia, H.; Zhong, A.; Zhong, C.; Feng, J.; Qin, J.; Li, Z. Fluorescent and Colorimetric Probes for Mercury(II): Tunable Structures of Electron Donor and π -Conjugated Bridge. *Chem. - A Eur. J.* **2012**, *18*, 1691–1699.
- (243) Li, Y.; Zheng, M.; Wang, J.; Gao, Y.; Zhang, B.; Yang, W. Two-Photon Absorption and Fluorescence Fluoride-Sensing Properties of N-Octyl-3,6-Bis[4-(4-(Diphenylamino)Phenyl)Phenyl]-1,4-Diketo-Pyrrolo[3,4-c] Pyrrole. *Dyes and Pigments* **2014**, *104*, 97–101.
- (244) Li, Q.; Wang, Z.; Song, W.; Ma, H.; Dong, J.; Quan, Y.; Ye, X.; Huang, Z. A Novel D- π -A Triphenylamine-Based Turn-on Colorimetric and Ratiometric Fluorescence Probe for Cyanide Detection. *Dyes and Pigments* **2018**.
- (245) Tang, X.; Liu, W.; Wu, J.; Zhao, W.; Zhang, H.; Wang, P. A Colorimetric Chemosensor for Fast Detection of Thiols Based on Intramolecular Charge Transfer. *Tetrahedron Lett.* **2011**, *52*, 5136–5139.
- (246) Chen, C. H.; Leung, M. K. The Nature of 6,6'-Bis(Triphenylamine) Substituted BINOL as Chromophoric and Fluorogenic Hybrid Chemosensor for Selective Fluoride Detection. *Tetrahedron* **2011**, *67*, 3924–3935.
- (247) Qu, Y.; Qu, S.; Yang, L.; Hua, J.; Qu, D. A Red-Emission Diketopyrrolopyrrole-Based Fluoride Ion Chemosensor with High Contrast Ratio Working in a Dual Mode: Solvent-Dependent Ratiometric and “Turn on” Pathways. *Sensors Actuators, B Chem.* **2012**, *173*, 225–233.
- (248) Vacareanu, L.; Teofilia, I.; Grigoras, M. Metal Complexation of Aromatic Oligoazomethines Bearing Cyano Groups: An Optical and Electrochemical Study. *Macromol. Res.* **2013**, *21*, 1059–1068.
- (249) Acharyya, K.; Chowdhury, A.; Mondal, B.; Chakraborty, S.; Mukherjee, Sarathi, P. Building Block Dependent Morphology Modulation of Cage Nanoparticles and Recognition of Nitroaromatics. *Chem. - A Eur. J.* **2017**.
- (250) Zhang, M.; Yin, S.; Zhang, J.; Zhou, Z.; Lal, M.; Lu, C.; Stang, P. J. Metallacycle-Cored Supramolecular Assemblies with Tunable Fluorescence Including White-Light Emission. *Proc. Natl. Acad. Sci.* **2017**, 1–6.
- (251) Zhang, B.; Yan, J.; Shang, Y.; Wang, Z. Synthesis of Fluorescent Micro- and Mesoporous Polyaminals for Detection of Toxic Pesticides. *Macromolecules* **2018**, *51*, 1769–1776.
- (252) Noworyta, K.; Kutner, W.; Wijesinghe, C. A.; Srou, S. G.; D'Souza, F. Nicotine, Cotinine, and Myosmine Determination Using Polymer Films of Tailor-Designed Zinc Porphyrins as Recognition Units for Piezoelectric Microgravimetry Chemosensors. *Anal. Chem.* **2012**, *84*, 2154–2163.
- (253) Zhan, Y.; Yang, P.; Li, G.; Zhang, Y.; Bao, Y. Reversible Piezofluorochromism of Triphenylamine-Based Benzothiazole Derivative with Strong Fluorescence Response to Volatile Acid Vapors. *New J. Chem.* **2016**.
- (254) Wan, M.; Zou, Y.; Tan, S.; Li, Y. Two Thieno[3,4b]Pyrazine-Containing Copolymers: Synthesis, Characterization, and Application in Mercury Ions Detection. *Polym. Adv. Technol.* **2010**, *21*, 256–262.
- (255) Lehn, J. Supramolecular Chemistry-Scope and Perspectives Molecules, Supermolecules, and Molecular Devices. *Angew. Chem. Int. Ed.* **1988**, *27*, 89–112.
- (256) Lehn, J. From Supramolecular Chemistry towards Constitutional Dynamic Chemistry and Adaptive Chemistry. *Chem. Soc. Rev.* **2007**, *36*, 151–160.
- (257) Fischer, E. Einfluss Des Configuration Auf Die Wirkung Der Enzyme I. *Berichte der Dtsch. Chem. Gesellschaft* **1894**, *24*, 2985.

References

- (258) Hardie, M. J. Hydrogen Bonded Network Structures Constructed from Molecular Hosts. *Struct. Bond.* **2004**, *111*, 139–174.
- (259) Whitesides, G. M. Self-Assembly at All Scales. *Science* **2002**, *295*, 2418–2421.
- (260) Gulik-Krzywicki, T.; Fouquey, C.; Lehn, J.-M. Electron Microscopic Study of Supramolecular Liquid Crystalline Polymers Formed by Molecular-Recognition-Directed Self-Assembly from Complementary Chiral Components. *Proc. Natl. Acad. Sci.* **1993**, *90*, 163–167.
- (261) Fouquey, C.; Lehn, J.-M.; Levelut, A.-M. Molecular Recognition Directed Self-Assembly of Supramolecular Liquid Crystalline Polymers from Complementary Chiral Components. *Adv. Mater.* **1990**, *2*, 254–257.
- (262) Lehn, J. Dynamers: Dynamic Molecular and Supramolecular Polymers. *Prog. Polym. Sci.* **2005**, *30*, 814–831.
- (263) Huang, F.; Scherman, O. A. Supramolecular Polymers. *Chem. Soc. Rev.* **2012**, *41*, 5879–5880.
- (264) Brunsveld, L.; Folmer, B. J. B.; Meijer, E. W.; Sijbesma, R. P. Supramolecular Polymers. *Am. Chem. Soc.* **2001**, *101*, 4071–4097.
- (265) Aida, T.; Meijer, E. W.; Stupp, S. I. Functional Supramolecular Polymers. *Science* **2012**, *335*, 813–817.
- (266) Greef, T. F. A. De; Smulders, M. M. J.; Wolfs, M.; Schenning, A. P. H. J.; Sijbesma, R. P.; Meijer, E. W.; Counterpart, C. Supramolecular Polymerization. **2009**, 5687–5754.
- (267) Ciferri, A. Supramolecular Polymerizations. *Macromol. Rapid Commun.* **2002**, *23*, 511–529.
- (268) Dudowicz, J.; Freed, K. F.; Douglas, J. F. Lattice Model of Equilibrium Polymerization. IV. Influence of Activation, Chemical Initiation, Chain Scission and Fusion, and Chain Stiffness on Polymerization and Phase Separation. *J. Chem. Phys.* **2003**, *119*, 12645–12666.
- (269) Flory, P. J. Principles of Polymer Chemistry. *Cornell University Press*. Ithaca, NY 1953.
- (270) Martin, R. B. Comparisons of Indefinite Self-Association Models. *Chem. Rev.* **1996**, *96*, 3043–3064.
- (271) van der Schoot, P. Theory of Supramolecular Polymerization. In *Supramolecular Polymers*; Taylor & Francis: London, U.K., 2005; pp 1–13.
- (272) Henderson, J. R. Physics of Isodesmic Chemical Equilibria in Solution. *Phys. Rev.* **1997**, *55*, 5731.
- (273) Douglas, J. F.; Dudowicz, J.; Freed, K. F. Lattice Model of Equilibrium Polymerization. VII. Understanding the Role of “Cooperativity” in Self-Assembly. *J. Chem. Phys.* **2008**, *128*, 1–18.
- (274) Ghosh, A. K.; Mukerjee, P.; Ghosh, A. K.; Mukerjee, P.; Ghosh, A. K.; Mukerjee, P. Multiple Association Equilibria in the Self-Association of Methylene Blue and Other Dyes. *J. Am. Chem. Soc.* **1970**, *92*, 6408–6412.
- (275) Connors, K. A. *Binding Constants: The Measurement of Molecular Complex Stability*; Wiley: New York, 1987.
- (276) Zhao, D.; Moore, J. S. Nucleation-Elongation: A Mechanism for Cooperative Supramolecular Polymerization. *Org. Biomol. Chem.* **2003**, *1*, 3471–3491.
- (277) Dainton, F. S.; Ivin, K. J. Some Thermodynamic and Kinetic Aspects of Addition Polymerization. *Quart. Revs.* **1958**, *12*, 61–92.
- (278) Dainton, F. S.; Ivin, K. J. Reversibility of the Propagation Reaction in Polymerization Processes and Its Manifestation in the Phenomenon of a “Ceiling Temperature.” *Nature* **1948**, *162*, 705–707.
- (279) Ferrone, F. Analysis of Protein Aggregation Kinetics. *Methods Enzymol.* **1999**, *309*, 256–274.
- (280) Firestone, M. P.; De Levie, R.; Rangarajan, S. K. On One-Dimensional Nucleation and Growth of “Living” Polymers I. Homogeneous Nucleation. *J. Theor. Biol.* **1983**, *104*, 535–552.
- (281) Powers, E. T.; Powers, D. L. The Kinetics of Nucleated Polymerizations at High Concentrations: Amyloid Fibril Formation near and above the “Supercritical Concentration.” *Biophys. J.* **2006**, *91*, 122–132.
- (282) Frieden, C. Protein Aggregation Processes: In Search of the Mechanism. *Protein Sci.* **2007**, *16*, 2334–2344.
- (283) Kuhn, W. Über Die Gestalt Fadenförmiger Moleküle in Lösungen. *Kolloid-Zeitschrift* **1934**, *68*, 2–15.
- (284) Yang, L.; Tan, X.; Wang, Z.; Zhang, X. Supramolecular Polymers: Historical Development, Preparation, Characterization, and Functions. *Chem. Rev.* **2015**, *115*, 7196–7239.
- (285) Pauling, L.; Corey, R. B. Configurations of Polypeptide Chains With Favored Orientations Around Single Bonds: Two New Pleated Sheets. *Proc. Natl. Acad. Sci.* **1951**, *37*, 729–740.
- (286) Velten, U.; Rehahn, M. First Synthesis of Soluble, Well Defined Coordination Polymers from Kinetically Unstable Copper(I) Complexes. *Chem. Commun.* **1996**, *1*, 2639–2640.
- (287) Hunter, C. A.; Sanders, J. K. M. The Nature of π - π Interactions. *J. Am. Chem. Soc.* **1990**, *112*, 5525–5534.

References

- (288) Vyborna, Y.; Vybornyi, M.; Rudnev, A. V.; Häner, R. DNA-Grafted Supramolecular Polymers: Helical Ribbon Structures Formed by Self-Assembly of Pyrene-DNA Chimeric Oligomers. *Angew. Chem. Int. Ed.* **2015**, *54*, 7934–7938.
- (289) Tian, Y. K.; Shi, Y. G.; Yang, Z. S.; Wang, F. Responsive Supramolecular Polymers Based on the Bis[Alkynylplatinum(II)] Terpyridine Molecular Tweezer/Arene Recognition Motif. *Angew. Chem. Int. Ed.* **2014**, *53*, 6090–6094.
- (290) Zhang, X.; Chen, Z.; Würthner, F. Morphology Control of Fluorescent Nanoaggregates by Co-Self-Assembly of Wedge- and Dumbbell-Shaped Amphiphilic Perylene Bisimides. *J. Am. Chem. Soc.* **2007**, *129*, 4886–4887.
- (291) Das, A.; Ghosh, S. Stimuli-Responsive Self-Assembly of a Naphthalene Diimide by Orthogonal Hydrogen Bonding and Its Coassembly with a Pyrene Derivative by a Pseudo-Intramolecular Charge-Transfer Interaction. *Angew. Chem. Int. Ed.* **2014**, *53*, 1092–1097.
- (292) Meyer, E. E.; Rosenberg, K. J.; Israelachvili, J. Recent Progress in Understanding Hydrophobic Interactions. *Proc. Natl. Acad. Sci.* **2006**, *103*, 15739–15746.
- (293) Liu, Y.; Yu, C.; Jin, H.; Jiang, B.; Zhu, X.; Zhou, Y.; Lu, Z.; Yan, D. A Supramolecular Janus Hyperbranched Polymer and Its Photoresponsive Self-Assembly of Vesicles with Narrow Size Distribution. *J. Am. Chem. Soc.* **2013**, *135*, 4765–4770.
- (294) Van Der Zwaag, D.; Pieters, P. A.; Korevaar, P. A.; Markvoort, A. J.; Spiering, A. J. H.; De Greef, T. F. A.; Meijer, E. W. Kinetic Analysis as a Tool to Distinguish Pathway Complexity in Molecular Assembly: An Unexpected Outcome of Structures in Competition. *J. Am. Chem. Soc.* **2015**, *137*, 12677–12688.
- (295) Boekhoven, J.; Van Rijn, P.; Brizard, A. M.; Stuart, M. C. A.; Van Esch, J. H. Size Control and Compartmentalization in Self-Assembled Nanostructures of a Multisegment Amphiphile. *Chem. Commun.* **2010**, *46*, 3490–3492.
- (296) Guo, D. S.; Liu, Y. Calixarene-Based Supramolecular Polymerization in Solution. *Chem. Soc. Rev.* **2012**, *41*, 5907–5921.
- (297) Ashton, P. R.; Baxter, I.; Cantrill, S. J.; Fyfe, M. C. T.; Glink, P. T.; Stoddart, F. J.; White, A. J. P.; Williams, D. J. Supramolecular Daisy Chains. *Angew. Chem. Int. Ed.* **1998**, *37*, 1294–1297.
- (298) Schenning, A. P. H. J.; Meijer, E. W. Supramolecular Electronics; Nanowires from Self-Assembled π -Conjugated Systems. *Chem. Commun.* **2005**, *26*, 3245–3258.
- (299) Moulin, E.; Cid, J. J.; Giuseppone, N. Advances in Supramolecular Electronics - From Randomly Self-Assembled Nanostructures to Addressable Self-Organized Interconnects. *Adv. Mater.* **2013**, *25*, 477–487.
- (300) Forrest, S. R. Electronic Appliances on Plastic. *Nature* **2004**, *428*, 911–918.
- (301) Meyer zu Heringdorf, F.-J.; Reuter, M. C.; Tromp, R. M. Growth Dynamics of Pentacene Thin Films. *Nature* **2001**, *412*, 517–520.
- (302) Meijer, E. W.; Schenning, A. P. H. J. Material Marriage in Electronics. *Nature* **2002**, *419*, 353–354.
- (303) Moulin, E.; Cid, J. J.; Giuseppone, N. Advances in Supramolecular Electronics - From Randomly Self-Assembled Nanostructures to Addressable Self-Organized Interconnects. *Adv. Mater.* **2012**, *25*, 477–487.
- (304) Wang, J.; He, C.; Wu, P.; Wang, J.; Duan, C. An Amide-Containing Metal–Organic Tetrahedron Responding to a Spin-Trapping Reaction in a Fluorescent Enhancement Manner for Biological Imaging of NO in Living Cells. *J. Am. Chem. Soc.* **2011**, *133*, 12402–12405.
- (305) Roberts, D. a; Castilla, A. M.; Ronson, T. K.; Nitschke, J. R. Post-Assembly Modi Fi Cation of Kinetically Metastable Fe. *J. Am. Chem. Soc.* **2014**, *136*, 8201–8204.
- (306) Yao, Q.; Su, J.; Pascanu, V.; Yun, Y.; Zheng, H.; Chen, H.; Liu, L.; Abdelhamid, H. N.; Zou, X. Series of Highly Stable Isostructural Lanthanide Metal – Organic Frameworks with Expanding Pore Size and Tunable Luminescent Properties. *Chem. Mater.* **2015**, *27*, 5332–5339.
- (307) Hua, C.; Abrahams, B. F.; D’Alessandro, D. M. Controlling Interpenetration in Electroactive Co(II) Frameworks Based on the Tris(4-(Pyridin-4-Yl)Phenyl)Amine Ligand. *Cryst. Growth Des.* **2016**, *16*, 1149–1155.
- (308) Wu, P.; He, C.; Wang, J.; Peng, X.; Li, X.; An, Y.; Duan, C. Photoactive Chiral Metal–Organic Frameworks for Light-Driven Asymmetric α -Alkylation of Aldehydes. *J. Am. Chem. Soc.* **2012**, *134*, 14991–14999.
- (309) Shi, D.; Guo, X.; Lai, T.; Zheng, K.; Wu, Q.; Sun, C.; He, C.; Zhao, J. A Tetrazole-Containing Triphenylamine-Based Metal–Organic Framework: Synthesis and Photocatalytic Oxidative C[Sbnd]C Coupling Reaction. *Inorg. Chem. Commun.* **2019**, *105*, 9–12.
- (310) Tan, Y. X.; He, Y. P.; Yuan, D.; Zhang, J. Use of Aligned Triphenylamine-Based Radicals in a Porous Framework for Promoting Photocatalysis. *Appl. Catal. B Environ.* **2018**, *221*, 664–669.
- (311) Yang, X.-F.; Liu, M.; Zhu, H.-B. Two Unique Isomorphic Zn²⁺ and Co²⁺-Based Metal–Organic Frameworks Comprising Octahedral Cage. *Inorg.*

- Chem. Commun.* **2017**, *83*, 40–43.
- (312) Wu, X.-X.; Fu, H.-R.; Han, M.-L.; Zhou, Z.; Ma, L.-F. Tetraphenylethylene Immobilized Metal–Organic Frameworks: Highly Sensitive Fluorescent Sensor for the Detection of Cr2O7²⁻ and Nitroaromatic Explosives. *Cryst. Growth Des.* **2017**, *17*, 6041–6048.
- (313) Wang, D.; Hu, Z.; Xu, S.; Li, D.; Zhang, Q.; Ma, W.; Zhou, H.; Wu, J.; Tian, Y. Fluorescent Metal–Organic Frameworks Based on Mixed Organic Ligands: New Candidates for Highly Sensitive Detection of TNP. *Dalt. Trans.* **2019**, *48*, 1900–1905.
- (314) Hua, C.; Baldansuren, A.; Tuna, F.; Collison, D.; D’Alessandro, D. M. In Situ Spectroelectrochemical Investigations of the Redox-Active Tris[4-(Pyridin-4-Yl)Phenyl]Amine Ligand and a Zn²⁺ Coordination Framework. *Inorg. Chem.* **2016**, *55*, 7270–7280.
- (315) Hua, C.; Ge, J. Y.; Tuna, F.; Collison, D.; Zuo, J. L.; D’Alessandro, D. M. Redox State Manipulation of a Tris(p-Tetrazolylphenyl)Amine Ligand and Its Mn²⁺ Coordination Frameworks. *Dalt. Trans.* **2017**, *46*, 2998–3007.
- (316) Peng, Z.; Yi, X.; Liu, Z.; Shang, J.; Wang, D. Triphenylamine-Based Metal–Organic Frameworks as Cathode Materials in Lithium-Ion Batteries with Coexistence of Redox Active Sites, High Working Voltage, and High Rate Stability. *ACS Appl. Mater. Interfaces* **2016**, *8*, 14578–14585.
- (317) Pham, T.; Forrest, K. A.; McDonald, K.; Space, B. Modeling PCN-61 and PCN-66: Isostructural Rht - Metal–Organic Frameworks with Distinct CO₂ Sorption Mechanisms. *Cryst. Growth Des.* **2014**, *14*, 5599–5607.
- (318) Akintola, O.; Ziegenbalg, S.; Buchholz, A.; Görls, H.; Plass, W. A Robust Anionic Pillared-Layer Framework with Triphenylamine-Based Linkers: Ion Exchange and Counterion-Dependent Sorption Properties. *CrystEngComm* **2017**, *19*, 2723–2732.
- (319) Wang, Y.; He, M.; Gao, X.; Li, S.; He, Y. A Metal–Organic Framework Based on a Custom-Designed Diisophthalate Ligand Exhibiting Excellent Hydrostability and Highly Selective Adsorption of C₂H₂ and CO₂ over CH₄. *Dalt. Trans.* **2018**, *47*, 7213–7221.
- (320) Zhao, F.-J.; Tan, Y.-X.; Wang, W.; Ju, Z.; Yuan, D. Optimizing H₂, D₂, and C₂H₂ Sorption Properties by Tuning the Pore Apertures in Metal–Organic Frameworks. *Inorg. Chem.* **2018**, *57*, 13312–13317.
- (321) Steiner, C.; Gliemann, B. D.; Meinhardt, U.; Gurrath, M.; Meyer, B.; Kivala, M.; Maier, S. Self-Assembly and Stability of Hydrogen-Bonded Networks of Bridged Triphenylamines on Au(111) and Cu(111). *J. Phys. Chem. C* **2015**, *119*, 25945–25955.
- (322) Müller, K.; Moreno-López, J. C.; Gottardi, S.; Meinhardt, U.; Yildirim, H.; Kara, A.; Kivala, M.; Stöhr, M. Cyano-Functionalized Triarylamine on Coinage Metal Surfaces: Interplay of Intermolecular and Molecule-Substrate Interactions. *Chem. - A Eur. J.* **2016**, *22*, 581–589.
- (323) Lambert, C.; Kriegisch, V.; Terfort, A.; Zeysing, B. Heterogeneous Electron Transfer Processes in Triarylamine- and Ferrocene-Based Self-Assembled Monolayers. *J. Electroanal. Chem.* **2006**, *590*, 32–36.
- (324) Lambert, C.; Kriegisch, V. Heterogeneous Electron Transfer Processes in Self-Assembled Monolayers of Amine Terminated Conjugated Molecular Wires. *Langmuir* **2006**, *22*, 8807–8812.
- (325) Yu, Y.; Chien, S.-C.; Sun, J.; Hettiaratchy, E. C.; Myers, R. C.; Lin, L.-C.; Wu, Y. Excimer-Mediated Intermolecular Charge Transfer in Self-Assembled Donor–Acceptor Dyes on Metal Oxides. *J. Am. Chem. Soc.* **2019**, *141*, 8727–8731.
- (326) Wang, Q.; Zakeeruddin, S. M.; Cremer, J.; Bäuerle, P.; Humphry-baker, R. Supporting Information Cross Surface Ambipolar Charge Percolation in Molecular Triads on Mesoscopic Oxide Films Synthesis and Characterization of PMI-T2-TPA. *J. Am. Chem. Soc.* **2005**, *3*, 181–182.
- (327) Bardecker, J. A.; Ma, H.; Kim, T.; Huang, F.; Liu, M. S.; Cheng, Y. J.; Ting, G.; Jen, A. K. Y. Self-Assembled Electroactive Phosphonic Acids on ITO: Maximizing Hole-Injection in Polymer Light-Emitting Diodes. *Adv. Funct. Mater.* **2008**, *18*, 3964–3971.
- (328) Huang, Q.; Evmenenko, G.; Dutta, P.; Marks, T. J. Molecularly “Engineered” Anode Adsorbates for Probing OLED Interfacial Structure-Charge Injection/Luminance Relationships: Large, Structure-Dependent Effects. *J. Am. Chem. Soc.* **2003**, *125*, 14704–14705.
- (329) Huang, Q.; Li, J.; Evrnenenko, G. A.; Dutta, P.; Marks, T. J. Systematic Investigation of Nanoscale Adsorbate Effects at Organic Light-Emitting Diode Interfaces. Interfacial Structure - Charge Injection - Luminance Relationships. *Chem. Mater.* **2006**, *18*, 2431–2442.
- (330) Lee, J.; Jung, B. J.; Lee, J. I.; Chu, H. Y.; Do, L. M.; Shim, H. K. Modification of an ITO Anode with a Hole-Transporting SAM for Improved OLED Device Characteristics. *J. Mater. Chem.* **2002**, *12*, 3494–3498.
- (331) Li, J.; Marks, T. J. For Improved Charge Injection in Organic Light-Emitting Diodes. **2008**, *19*, 4873–4882.
- (332) Shang, Z.; Liu, D.; Wang, T.; Yu, X.; Li, B.; Li, W.; Hu, W.; Zhou, X. Enhanced Hole-Injection

References

- Property in an OLED with a Self-Assembled Monolayer of Hole-Transporting TPD on Thin Au as the Anode. *Trans. Tianjin Univ.* **2018**, *24*, 580–586.
- (333) Hosseini, M.; Rivera-Nazario, D. M.; Echegoyen, L. A. Self-Assembled Monolayers of C60-Triphenylamine Dyads as Photo-Switched Interfacial Layers for Potential Application in Photovoltaic Cells. *ACS Appl. Mater. Interfaces* **2014**, *6*, 3712–3720.
- (334) Mutlu, A.; Can, M.; Tozlu, C. Performance Improvement of Organic Solar Cell via Incorporation of Donor Type Self-Assembled Interfacial Monolayer. *Thin Solid Films* **2019**, *685*, 88–96.
- (335) Chang, J. C.; Lai, C. C.; Chiu, S. H. A Redox-Controllable Molecular Switch Based on Weak Recognition of BPX26C6 at a Diphenylurea Station. *Molecules* **2015**, *20*, 1775–1787.
- (336) Wolf, A.; Moulin, E.; Cid, J. J.; Goujon, A.; Du, G.; Busseron, E.; Fuks, G.; Giuseppone, N. PH and Light-Controlled Self-Assembly of Bistable [C2] Daisy Chain Rotaxanes. *Chem. Commun.* **2015**, *51*, 4212–4215.
- (337) Mandal, A. K.; Gangopadhyay, M.; Das, A. Photo-Responsive Pseudorotaxanes and Assemblies. *Chem. Soc. Rev.* **2015**, *44*, 663–676.
- (338) Kim, J.; Lee, J.; Kim, W. Y.; Kim, H.; Lee, S.; Lee, H. C.; Lee, Y. S.; Seo, M.; Kim, S. Y. Induction and Control of Supramolecular Chirality by Light in Self-Assembled Helical Nanostructures. *Nat. Commun.* **2015**, *6*, 6959.
- (339) Kim, T.; Mori, T.; Aida, T.; Miyajima, D. Dynamic Propeller Conformation for the Unprecedentedly High Degree of Chiral Amplification of Supramolecular Helices. *Chem. Sci.* **2016**, *7*, 6689–6694.
- (340) Adelizzi, B.; Filot, I. A. W.; Palmans, A. R. A.; Meijer, E. W. Unravelling the Pathway Complexity in Conformationally Flexible N - Centered Triarylamine Trisamides. *Chem. - A Eur. J.* **2017**, *23*, 6103–6110.
- (341) Haedler, A. T.; Meskers, S. C. J.; Zha, R. H.; Kivala, M.; Schmidt, H.-W.; Meijer, E. W. Pathway Complexity in the Enantioselective Self-Assembly of Functional Carbonyl-Bridged Triarylamine Trisamides. *J. Am. Chem. Soc.* **2016**, *138*, 10539–10545.
- (342) Osypenko, A.; Moulin, E.; Gavot, O.; Fuks, G.; Maaloum, M.; Giuseppone, N. Temperature Controlled Hierarchical Supramolecular Polymerization of Chiral Triarylaminines. **2019**, Manuscript in preparation.
- (343) Adelizzi, B.; Aloï, A.; Markvoort, A. J.; Ten Eikelder, H. M. M.; Voets, I. K.; Palmans, A. R. A.; Meijer, E. W. Supramolecular Block Copolymers under Thermodynamic Control. *J. Am. Chem. Soc.* **2018**, *140*, 7168–7175.
- (344) Adelizzi, B.; Aloï, A.; Van Zee, N. J.; Palmans, A. R. A.; Meijer, E. W.; Voets, I. K. Painting Supramolecular Polymers in Organic Solvents by Super-Resolution Microscopy. *ACS Nano* **2018**, *12*, 4431–4439.
- (345) Haedler, A. T.; Kreger, K.; Issac, A.; Wittmann, B.; Kivala, M.; Hammer, N.; Köhler, J.; Schmidt, H.-W.; Hildner, R. Long-Range Energy Transport in Single Supramolecular Nanofibres at Room Temperature. *Nature* **2015**, *523*, 196–199.
- (346) Akande, A.; Bhattacharya, S.; Cathcart, T.; Sanvito, S. First Principles Study of the Structural, Electronic, and Transport Properties of Triarylamine-Based Nanowires. *J. Chem. Phys.* **2014**, *140*.
- (347) Licsandru, E. D.; Schneider, S.; Tingry, S.; Ellis, T.; Moulin, E.; Maaloum, M.; Lehn, J. M.; Barboiu, M.; Giuseppone, N. Self-Assembly of Supramolecular Triarylamine Nanowires in Mesoporous Silica and Biocompatible Electrodes Thereof. *Nanoscale* **2016**, *8*, 5605–5611.
- (348) Joannopoulos, J. D.; Villeneuve, P. R.; Fan, S. Photonic Crystals: Putting a New Twist on Light. *Nature* **1997**, *356*, 143–149.
- (349) Kao, C. K. No Title. *Ericssson Rev* **1979**, *56*, 92–94.
- (350) Yablonovitch, E. Inhibited Spontaneous Emission in Solid-State Physics and Electronics. *Phys. Rev. Lett.* **1987**, *58*, 2059–2062.
- (351) John, S. Strong Localization of Photons in Certain Disordered Dielectric Superlattices. *Phys. Rev. Lett.* **1987**, *58*, 2486–2489.
- (352) Barnes, W. L.; Dereux, A.; Ebbesen, T. W. Surface Plasmon Subwavelength Optics. *Nature* **2003**, *424*, 824–830.
- (353) Barnes, W. L. Surface Plasmon–Polariton Length Scales: A Route to Sub-Wavelength Optics. *J. Opt. A Pure Appl. Opt.* **2006**, *8*, S87–S93.
- (354) Lal, S.; Hafner, J. H.; Halas, N. J.; Link, S.; Nordlander, P. Noble Metal Nanowires: From Plasmon Waveguides to Passive and Active Devices. *Acc. Chem. Res.* **2012**, *45*, 1887–1895.
- (355) Hoerhold, H.-H.; Tillmann, H.; Raabe, D.; Helbig, M.; Elflein, W.; Braeuer, A. H.; Holzer, W.; Penzkofer, A. Synthesis of TPD-Containing Polymers for Use as Light-Emitting Materials in Electroluminescent and Laser Devices. In *proc. SPIE*; Kafafi, Z. H., Ed.; 2001; Vol. 4105, p 431.
- (356) Philip, R.; Holzer, W.; Penzkofer, A.; Tillmann, H.; Hörhold, H. H. Photo-Physical and Lasing Characterization of Neat Films of 4-Methyl-TPD and of an Alternating Copolymer of 4-Methyl-TPD

References

- with MEH-PPV. *Synth. Met.* **2003**, *132*, 297–308.
- (357) Chen, Q.-D.; Fang, H.-H.; Xu, B.; Yang, J.; Xia, H.; Chen, F.-P.; Tian, W.-J.; Sun, H.-B. Two-Photon Induced Amplified Spontaneous Emission from Needlelike Triphenylamine-Containing Derivative Crystals with Low Threshold. *Appl. Phys. Lett.* **2009**, *94*, 201113.
- (358) So, H.; Watanabe, H.; Yahiro, M.; Yang, Y.; Oki, Y.; Adachi, C. Highly Photostable Distributed-Feedback Polymer Waveguide Blue Laser Using Spirobifluorene Derivatives. *Opt. Mater.* **2011**, *33*, 755–758.
- (359) Rycenga, M.; Cobley, C. M.; Zeng, J.; Li, W.; Moran, C. H.; Zhang, Q.; Qin, D.; Xia, Y. Controlling the Synthesis and Assembly of Silver Nanostructures for Plasmonic Applications. *Chem. Rev.* **2011**, *111*, 3669–3712.
- (360) Lal, S.; Link, S.; Halas, N. J. Nano-Optics from Sensing to Waveguiding. **2007**, 641–648.
- (361) Shalaev, V. M. Optical Negative-Index Metamaterials. *Nat. Photonics* **2007**, *6*, 41–48.
- (362) Neal, T. D.; Okamoto, K.; Scherer, A.; Liu, M. S.; Jen, A. K. Y. Time Resolved Photoluminescence Spectroscopy of Surface-Plasmon-Enhanced Light Emission from Conjugate Polymers. *Appl. Phys. Lett.* **2006**, *89*, 1–4.
- (363) Zhou, Z.; Yu, Y.; Sun, N.; Möhwald, H.; Gu, P.; Wang, L.; Zhang, W.; König, T. A. F.; Fery, A.; Zhang, G. Broad-Range Electrically Tunable Plasmonic Resonances of a Multilayer Coaxial Nanohole Array with an Electroactive Polymer Wrapper. *ACS Appl. Mater. Interfaces* **2017**, *9*, 35244–35252.
- (364) Takahara, J.; Yamagishi, S.; Taki, H.; Morimoto, A.; Kobayashi, T. Guiding of a One-Dimensional Optical Beam with Nanometer Diameter. *Opt. Lett.* **1997**, *22*, 475.
- (365) Alu, A.; Engheta, N. Optical ‘Shorting Wires.’ *Opt. Express* **2007**, *15*, 13773.
- (366) Osypenko, A. Supramolecular Self-Assemblies of Triarylamines: Fundamental Studies and Applications, 2016.
- (367) Liu, Y.; Chen, S.; Lam, J. W. Y.; Lu, P.; Kwok, R. T. K.; Mahtab, F.; Kwok, H. S.; Tang, B. Z. Tuning the Electronic Nature of Aggregation-Induced Emission Luminogens with Enhanced Hole-Transporting Property. *Chem. Mater.* **2011**, *23*, 2536–2544.
- (368) Yuan, W. Z. W. Z. W. Z. W. Z.; Gong, Y.; Chen, S.; Shen, X. Y.; Lam, J. W. Y. Y.; Lu, P.; Lu, Y.; Wang, Z.; Hu, R.; Xie, N.; Kwok, H. S.; Zhang, Y.; Sun, J. Z.; Tang, B. Z. Efficient Solid Emitters with Aggregation-Induced Emission and Intramolecular Charge Transfer Characteristics: Molecular Design, Synthesis, Photophysical Behaviors, and OLED Application. *Chem. Mater.* **2012**, *24*, 1518–1528.
- (369) Lin, G.; Peng, H.; Chen, L.; Nie, H.; Luo, W.; Li, Y.; Chen, S.; Hu, R.; Qin, A.; Zhao, Z.; Tang, B. Z. Improving Electron Mobility of Tetraphenylethene-Based AIEgens to Fabricate Nondoped Organic Light-Emitting Diodes with Remarkably High Luminance and Efficiency. *ACS Appl. Mater. Interfaces* **2016**, *8*, 16799–16808.
- (370) Chua, L.-L.; Ho, P. K. H.; Sirringhaus, H.; Friend, R. H. Observation of Field-Effect Transistor Behavior at Self-Organized Interfaces. *Adv. Mater.* **2004**, *16*, 1609–1615.
- (371) Mtangi, W.; Tassinari, F.; Vankayala, K.; Vargas Jentsch, A.; Adelizzi, B.; Palmans, A. R. A.; Fontanesi, C.; Meijer, E. W.; Naaman, R. Control of Electrons’ Spin Eliminates Hydrogen Peroxide Formation During Water Splitting. *J. Am. Chem. Soc.* **2017**, *139*, 2794–2798.
- (372) Zhao, Z.; Liu, J.; Yip Lam, J. W.; Chan, C. Y. K.; Qiu, H.; Tang, B. Z. Luminescent Aggregates of a Starburst Silole-Triphenylamine Adduct for Sensitive Explosive Detection. *Dyes and Pigments* **2011**, *91*, 258–263.
- (373) Wenfeng, L.; Hengchang, M.; Ziqiang, L. Self-Assembled Triphenylamine Derivative for Trace Detection of Picric Acid. *RSC Adv.* **2014**, *4*, 39351–39358.
- (374) Duraimurugan, K.; Balasaravanan, R.; Siva, A. Electron Rich Triphenylamine Derivatives (D- π -D) for Selective Sensing of Picric Acid in Aqueous Media. *Sensors Actuators B. Chem.* **2016**.
- (375) Wang, L.; Li, L.; Cao, D. Synthesis, Photoluminescence, Chromogenic and Fluorogenic Discrimination of Fluoride and Cyanide Based on a Triphenylamine-Tri(2-Formyl BODIPY) Conjugate. *Sensors Actuators B. Chem.* **2016**.
- (376) Shi, W.; Zhao, S.; Su, Y.; Hui, Y.; Xie, Z. Barbituric Acid-Triphenylamine Adduct as an AIEE-Type Molecule and Optical Probe for Mercury(II). *New J. Chem.* **2016**, *40*, 7814–7820.
- (377) Wang, H.; Liu, Q.; Hu, Y.; Liu, M.; Huang, X.; Gao, W.; Wu, H. A Multiple Stimuli-Sensitive Low-Molecular-Weight Gel with an Aggregate-Induced Emission Effect for Sol-Gel Transition Detection. *ChemistryOpen* **2018**, *7*, 457–462.
- (378) Xu, D.; Liu, X.; Lu, R.; Xue, P.; Zhang, X.; Zhou, H.; Jia, J. New Dendritic Gelator Bearing Carbazole in Each Branching Unit: Selected Response to Fluoride Ion in Gel Phase. *Org. Biomol. Chem.* **2011**, *9*, 1523–1528.
- (379) Zhang, H.; Qu, Y.; Gao, Y.; Hua, J.; Li, J.; Li, B. A Red Fluorescent ‘Turn-on’ Chemosensor for Hg²⁺ Based on Triphenylamine-Triazines Derivatives with Aggregation-Induced Emission Characteristics. *Tetrahedron Lett.* **2013**, *54*, 909–

- 912.
- (380) Lu, N.; Jiang, T.; Tan, H.; Hang, Y.; Yang, J.; Wang, J.; Qu, X.; Hua, J. A Red Fluorescent Turn-on Chemosensor for Al³⁺ Based on a Dimethoxy Triphenylamine Benzothiadiazole Derivative with Aggregation-Induced Emission. *Anal. Methods* **2017**, *9*, 2689–2695.
- (381) Yang, X.; Chen, X.; Lu, X.; Yan, C.; Xu, Y.; Hang, X.; Qu, J.; Liu, R. A Highly Selective and Sensitive Fluorescent Chemosensor for Detection of CN⁻, SO₃²⁻ and Fe³⁺ Based on Aggregation-Induced Emission. *J. Mater. Chem. C* **2015**.
- (382) Wei, Y.; Wang, L.; Huang, J.; Zhao, J.; Yan, Y. Multifunctional Metallo-Organic Vesicles Displaying Aggregation-Induced Emission: Two-Photon Cell-Imaging, Drug Delivery, and Specific Detection of Zinc Ion. *ACS Appl. Nano Mater.* **2018**, *1*, 1819–1827.
- (383) Liu, X.; Zhang, X.; Lu, R.; Xue, P.; Xu, D.; Zhou, H. Low-Dimensional Nanostructures Fabricated from Bis(Dioxaborine)Carbazole Derivatives as Fluorescent Chemosensors for Detecting Organic Amine Vapors. *J. Mater. Chem.* **2011**, *21*, 8756–8765.
- (384) Ma, H.; Li, F.; Zhang, Y.; Li, X.; Li, T.; Shen, F.; Zhang, M. Supramolecular Self-Assembly Carbazolyl Radicals Nanospheres Triggered by Ultraviolet Light for Explosives Sensing. *Talanta* **2016**, *160*, 133–137.
- (385) Cui, Y.; Chen, Z. M.; Jiang, X. F.; Tong, J.; Yu, S. Y. Self-Assembly and Anion Sensing of Metal-Organic [M₆L₂] Cages from Fluorescent Triphenylamine Tri-Pyrazoles with Dipalladium(II,II) Corners. *Dalt. Trans.* **2017**, *46*, 5801–5805.
- (386) Kong, L.; Tian, Y. P.; Chen, Q. Y.; Zhang, Q.; Wang, H.; Tan, D. Q.; Xue, Z. M.; Wu, J. Y.; Zhou, H. P.; Yang, J. X. Self-Assembly of Metal Ion Induced Highly Emissive Fluorophore-Triphenylamine Nanostructures: Enhanced Two-Photon Action Cross-Section for Bioimaging Applications. *J. Mater. Chem. C* **2015**, *3*, 570–581.
- (387) Cui, Y.; Chen, Q.; Zhang, D.-D.; Cao, J.; Han, B.-H. Triphenylamine-Based Fluorescent Conjugated Copolymers with Pendant Terpyridyl Ligands as Chemosensors for Metal Ions. *J. Polym. Sci. A* **2010**, *48*, 1310–1316.
- (388) Stuart, M. A. C.; Huck, W. T. S.; Genzer, J.; Müller, M.; Ober, C.; Stamm, M.; Sukhorukov, G. B.; Szleifer, I.; Tsukruk, V. V.; Urban, M.; Winnik, F.; Zauscher, S.; Luzzinov, I.; Minko, S. Emerging Applications of Stimuli-Responsive Polymer Materials. *Nat. Mater.* **2010**, *9*, 101–113.
- (389) Russev, M. M.; Hecht, S. Photoswitches: From Molecules to Materials. *Adv. Mater.* **2010**, *22*, 3348–3360.
- (390) Nakahata, M.; Takashima, Y.; Yamaguchi, H.; Harada, A. Redox-Responsive Self-Healing Materials Formed from Host–Guest Polymers. *Nat. Commun.* **2011**, *2*, 511.
- (391) Goujon, A.; Du, G.; Moulin, E.; Fuks, G.; Maaloum, M.; Buhler, E.; Giuseppone, N. Hierarchical Self-Assembly of Supramolecular Muscle-Like Fibers. *Angew. Chem. Int. Ed.* **2016**, *55*, 703–707.
- (392) Jain, A.; George, S. J. New Directions in Supramolecular Electronics. *Mater. Today* **2015**, *18*, 206–214.
- (393) Babu, S. S.; Praveen, V. K.; Ajayaghosh, A. Functional π -Gelators and Their Applications. *Chem. Rev.* **2014**, *114*, 1973–2129.
- (394) Ellis, T. K.; Galerne, M.; Armao, J. J.; Osypenko, A.; Martel, D.; Maaloum, M.; Fuks, G.; Gavot, O.; Moulin, E.; Giuseppone, N. Supramolecular Electropolymerization. *Angew. Chem. Int. Ed.* **2018**, *57*, 15749–15753.
- (395) Wang, B.; Tang, J.; Wang, F. Electrochemical Polymerization of Aniline. *Synth. Met.* **1987**, *18*, 323–328.
- (396) Wei, Y.; Chan, C. C.; Tian, J.; Jang, G. W.; Hsueh, K. F. Electrochemical Polymerization of Thiophenes in the Presence of Bithiophene or Terthiophene: Kinetics and Mechanism of the Polymerization. *Chem. Mater.* **1991**, *3*, 888–897.
- (397) Bachman, J. C.; Shao-Horn, Y.; Kavian, R.; Lee Seung, W.; Graham, D. J.; Nocera, D. G.; Kim, D. Y.; Noda, S.; Shao-Horn, Y. Electrochemical Polymerization of Pyrene Derivatives on Functionalized Carbon Nanotubes for Pseudocapacitive Electrodes. *Nat. Commun.* **2015**, *6*, 7040.
- (398) Diaz, A. F.; Kanazawa, K. K.; Gardini, G. P. Electrochemical Polymerization of Pyrrole. *J. Chem. Soc. Chem. Commun.* **1979**, 635–636.
- (399) Waltman, R.; Bargon, J. Electrically Conducting Polymers: A Review of the Electropolymerization Reaction, of the Effects of Chemical Structure on Polymer Film Properties, and of Applications towards Technology. *Can. J. Chem.* **1986**, *64*, 76–95.
- (400) Beouch, L.; Boileau, S.; Chevrot, C.; Tran-Van, F. Electropolymerization of Hydrogen Bond Supramolecular Associations between Terthiophene-3-Acetic Acid and 4,4'-Bipyridine. *Polym. Int.* **2017**, *66*, 1389–1394.
- (401) Xu, X. D.; Yao, C. J.; Chen, L. J.; Yin, G. Q.; Zhong, Y. W.; Yang, H. B. Facile Construction of Structurally Defined Porous Membranes from Supramolecular Hexakistriphenylamine Metallacycles through Electropolymerization. *Chem. - A Eur. J.* **2016**, *22*, 5211–5218.

References

- (402) Yin, G.; Chen, L.; Wang, C.; Yang, H. Fabrication of Neutral Supramolecular Polymeric Films via Post-Electropolymerization of Discrete Metallacycles. *Chinese J. Chem.* **2018**, *36*, 134–138.
- (403) Su, B.; Wu, Y.; Jiang, L. The Art of Aligning One-Dimensional (1D) Nanostructures. *Chem. Soc. Rev.* **2012**, *41*, 7832–7856.
- (404) Li, L.; Beniash, E.; Zubarev, E. R.; Xiang, W.; Rabatic, B. M.; Zhang, G.; Stupp, S. I. Assembling a Lasing Hybrid Material with Supramolecular Polymers and Nanocrystals. *Nat. Mater.* **2003**, *2*, 689–694.
- (405) Zubarev, E. R.; Pralle, M. U.; Sone, E. D.; Stupp, S. I. Self-Assembly of Dendron Rodcoil Molecules into Nanoribbons. *J. Am. Chem. Soc.* **2001**, *123*, 4105–4106.
- (406) Messmore, B. W.; Hulvat, J. F.; Sone, E. D.; Stupp, S. I. Synthesis, Self-Assembly, and Characterization of Supramolecular Polymers from Electroactive Dendron Rodcoil Molecules. *J. Am. Chem. Soc.* **2004**, *126*, 14452–14458.
- (407) Duzhko, V.; Singer, K. D. Self-Assembled Fibers of a Discotic Phthalocyanine Derivative: Internal Structure, Tailoring of Geometry, and Alignment by a Direct Current Electric Field. *J. Phys. Chem. C* **2007**, *111*, 27–31.
- (408) Duzhko, V.; Du, J.; Zorman, C. A.; Singer, K. D. Electric Field Patterning of Organic Nanoarchitectures with Self-Assembled Molecular Fibers. *J. Phys. Chem. C* **2008**, *112*, 12081–12084.
- (409) Castillo, J.; Tanzi, S.; Dimaki, M.; Svendsen, W. Manipulation of Self-Assembly Amyloid Peptide Nanotubes by Dielectrophoresis. *Electrophoresis* **2008**, *29*, 5026–5032.
- (410) Cristadoro, A.; Ai, M.; Räder, H. J.; Rabe, J. P.; Müllen, K. Electrical Field-Induced Alignment of Nonpolar Hexabenzocoronene Molecules into Columnar Structures on Highly Oriented Pyrolytic Graphite Investigated by STM and SFM. *J. Phys. Chem. C* **2008**, *112*, 5563–5566.
- (411) Kuwahara, R.; Fujikawa, S.; Kuroiwa, K.; Kimizuka, N. Controlled Polymerization and Self-Assembly of Halogen-Bridged Diruthenium Complexes in Organic Media and Their Dielectrophoretic Alignment. *J. Am. Chem. Soc.* **2012**, *134*, 1192–1199.
- (412) Akande, A.; Bhattacharya, S.; Cathcart, T.; Sanvito, S. First Principles Study of the Structural, Electronic, and Transport Properties of Triarylamine-Based Nanowires. *J. Chem. Phys.* **2014**, *140*, 074301.
- (413) van der Asdonk, P.; Kragt, S.; Kouwer, P. H. J. Directing Soft Matter in Water Using Electric Fields. *ACS Appl. Mater. Interfaces* **2016**, *8*, 16303–16309.
- (414) Henning-Knechtel, A.; Wiens, M.; Lakatos, M.; Heerwig, A.; Ostermaier, F.; Haufe, N.; Mertig, M. Dielectrophoresis of Gold Nanoparticles Conjugated to DNA Origami Structures. *Beilstein J. Nanotechnol.* **2016**, *7*, 948–956.
- (415) Sardone, L.; Palermo, V.; Devaux, E.; Credgington, D.; De Laos, M.; Marletta, G.; Cacialli, F.; Van Esch, J.; Samorì, P. Electric-Field-Assisted Alignment of Supramolecular Fibers. *Adv. Mater.* **2006**, *18*, 1276–1280.
- (416) Heeres, A.; Van Der Pol, C.; Stuart, M.; Friggeri, A.; Feringa, B. L.; Van Esch, J. Orthogonal Self-Assembly of Low Molecular Weight Hydrogelators and Surfactants. *J. Am. Chem. Soc.* **2003**, *125*, 14252–14253.
- (417) Yoshio, M.; Shoji, Y.; Tochigi, Y.; Nishikawa, Y.; Kato, T. Electric Field-Assisted Alignment of Self-Assembled Fibers Composed of Hydrogen-Bonded Molecules Having Laterally Fluorinated Mesogens. *J. Am. Chem. Soc.* **2009**, *131*, 6763–6767.
- (418) Shoji, Y.; Yoshio, M.; Yasuda, T.; Funahashi, M.; Kato, T. Alignment of Photoconductive Self-Assembled Fibers Composed of π -Conjugated Molecules under Electric Fields. *J. Mater. Chem.* **2010**, *20*, 173–179.
- (419) Musumeci, C.; Hutchison, J. A.; Samorì, P. Controlling the Morphology of Conductive PEDOT by in Situ Electropolymerization: From Thin Films to Nanowires with Variable Electrical Properties. *Nanoscale* **2013**, *5*, 7756–7761.
- (420) Rose, A. Space-Charge-Limited Currents in Solids. *Phys. Rev.* **1955**, *97*, 1538–1544.
- (421) Merindol, R.; Walther, A. Materials Learning from Life: Concepts for Active, Adaptive and Autonomous Molecular Systems. *Chem. Soc. Rev.* **2017**, *46*, 5588–5619.
- (422) Yan, Y.; Zhao, Y. S. Organic Nanophotonics: From Controllable Assembly of Functional Molecules to Low-Dimensional Materials with Desired Photonic Properties. *Chem. Soc. Rev.* **2014**, *43*, 4325–4340.
- (423) Myroshnychenko, V.; Rodríguez-Fernández, J.; Pastoriza-Santos, I.; Funston, A. M.; Novo, C.; Mulvaney, P.; Liz-Marzán, L. M.; García De Abajo, F. J. Modelling the Optical Response of Gold Nanoparticles. *Chem. Soc. Rev.* **2008**, *37*, 1792–1805.
- (424) Olson, J.; Dominguez-Medina, S.; Hoggard, A.; Wang, L. Y.; Chang, W. S.; Link, S. Optical Characterization of Single Plasmonic Nanoparticles. *Chem. Soc. Rev.* **2015**, *44*, 40–57.
- (425) Link, S.; El-Sayed, M. A. Spectral Properties and Relaxation Dynamics of Surface Plasmon Electronic Oscillations in Gold and Silver Nanodots and Nanorods. *J. Phys. Chem. B* **1999**,

References

- 103, 8410–8426.
- (426) Jain, P. K.; El-Sayed, M. A. Plasmonic Coupling in Noble Metal Nanostructures. *Chem. Phys. Lett.* **2010**, *487*, 153–164.
- (427) Prodan, E.; Radloff, C.; Halas, N. J.; Nordlander, P. A Hybridization Model for the Plasmon Response of Complex Nanostructures. *Science* **2003**, *302*, 419–422.
- (428) Wang, H.; Brandl, D. W.; Nordlander, P.; Halas, N. J. Plasmonic Nanostructures: Artificial Molecules. *Acc. Chem. Res.* **2007**, *40*, 53–62.
- (429) Slaughter, L. S.; Willingham, B. A.; Chang, W. S.; Chester, M. H.; Ogden, N.; Link, S. Toward Plasmonic Polymers. *Nano Lett.* **2012**, *12*, 3967–3972.
- (430) Nauert, S.; Paul, A.; Zhen, Y. R.; Solis, D.; Vigdeman, L.; Chang, W. S.; Zubarev, E. R.; Nordlander, P.; Link, S. Influence of Cross Sectional Geometry on Surface Plasmon Polariton Propagation in Gold Nanowires. *ACS Nano* **2014**, *8*, 572–580.
- (431) Fang, Y.; Li, Z.; Huang, Y.; Zhang, S.; Nordlander, P.; Halas, N. J.; Xu, H. Branched Silver Nanowires as Controllable Plasmon Routers. *Nano Lett.* **2010**, *10*, 1950–1954.
- (432) Wei, H.; Li, Z.; Tian, X.; Wang, Z.; Cong, F.; Liu, N.; Zhang, S.; Nordlander, P.; Halas, N. J.; Xu, H. Quantum Dot-Based Local Field Imaging Reveals Plasmon-Based Interferometric Logic in Silver Nanowire Networks. *Nano Lett.* **2011**, *11*, 471–475.
- (433) Solis, D.; Chang, W. S.; Khanal, B. P.; Bao, K.; Nordlander, P.; Zubarev, E. R.; Link, S. Bleach-Imaged Plasmon Propagation (BIIPP) in Single Gold Nanowires. *Nano Lett.* **2010**, *10*, 3482–3485.
- (434) Bazylewski, P.; Ezugwu, S.; Fanchini, G. A Review of Three-Dimensional Scanning Near-Field Optical Microscopy (3D-SNOM) and Its Applications in Nanoscale Light Management. *Appl. Sci.* **2017**, *7*, 973.
- (435) Specht, M.; Pedarnig, J. D.; Heckl, W. M.; Hänsch, T. W. Scanning Plasmon Near-Field Microscope. *Phys. Rev. Lett.* **1992**, *68*, 476–479.
- (436) Klein, A. E.; Janunts, N.; Schmidt, S.; Bin Hasan, S.; Etrich, C.; Fasold, S.; Kaiser, T.; Rockstuhl, C.; Pertsch, T. Dual-SNOM Investigations of Multimode Interference in Plasmonic Strip Waveguides. *Nanoscale* **2017**, *9*, 6695–6702.
- (437) Monti, O. L. A.; Baker, T. A.; Nesbitt, D. J. Imaging Nanostructures with Scanning Photoionization Microscopy. *J. Chem. Phys.* **2006**, *125*.
- (438) Schweikhard, V.; Grubisic, A.; Baker, T. A.; Thomann, I.; Nesbitt, D. J. Polarization-Dependent Scanning Photoionization Microscopy: Ultrafast Plasmon-Mediated Electron Ejection Dynamics in Single Au Nanorods. *ACS Nano* **2011**, *5*, 3724–3735.
- (439) Sun, Q.; Ueno, K.; Yu, H.; Kubo, A.; Matsuo, Y.; Misawa, H. Direct Imaging of the near Field and Dynamics of Surface Plasmon Resonance on Gold Nanostructures Using Photoemission Electron Microscopy. *Light Sci. Appl.* **2013**, *2*, 1–8.
- (440) Ueno, K.; Juodkazis, S.; Mizeikis, V.; Sasaki, K.; Misawa, H. Clusters of Closely Spaced Gold Nanoparticles as a Source of Two-Photon Photoluminescence at Visible Wavelengths. *Adv. Mater.* **2008**, *20*, 26–30.
- (441) Leiderer, P.; Bartels, C.; König-Birk, J.; Mosbacher, M.; Boneberg, J. Imaging Optical Near-Fields of Nanostructures. *Appl. Phys. Lett.* **2004**, *85*, 5370–5372.
- (442) Kociak, M.; Stéphan, O. Mapping Plasmons at the Nanometer Scale in an Electron Microscope. *Chem. Soc. Rev.* **2014**, *43*, 3865–3883.
- (443) García De Abajo, F. J. Optical Excitations in Electron Microscopy. *Rev. Mod. Phys.* **2010**, *82*, 209–275.
- (444) Colliex, C.; Kociak, M.; Stéphan, O. Electron Energy Loss Spectroscopy Imaging of Surface Plasmons at the Nanometer Scale. *Ultramicroscopy* **2016**, *162*, A1–A24.
- (445) Utekhina, A. Y.; Sergeev, G. B. Organic Nanoparticles. *Russ. Chem. Rev.* **2011**, *80*, 219–233.
- (446) Würthner, F.; Kaiser, T. E.; Saha-Möller, C. R. J. Aggregates: From Serendipitous Discovery to Supramolecular Engineering of Functional Dye Materials. *Angew. Chem. Int. Ed.* **2011**, *50*, 3376–3410.
- (447) Brinkmann, M.; Videva, V. S.; Bieber, A.; Andf, J. J.; Turek, P.; Zuppiroli, L.; Bugnon, P.; Schaer, M.; Nuesch, F.; Humphry-Baker, R. Electronic and Structural Evidences for Charge Transfer and Localization in Iodine-Doped Pentacene. *J. Phys. Chem. A* **2004**, *108*, 8170–8179.
- (448) Motamen, S.; Schörner, C.; Raithe, D.; Malval, J. P.; Jarroson, T.; Serein-Spirau, F.; Simon, L.; Hildner, R.; Reiter, G. Low Loss Optical Waveguiding in Large Single Crystals of a Thiophene-Based Oligomer. *Phys. Chem. Chem. Phys.* **2017**, *19*, 15980–15987.
- (449) Coropceanu, V.; Cornil, J.; da Silva Filho, D. A.; Olivier, Y.; Silbey, R.; Bredas, J. Charge Transport in Organic Semiconductors. *Chem Rev.* **2007**, *107*, 926–952.
- (450) Lee, J. Y.; Roth, S.; Park, Y. W. Anisotropic Field Effect Mobility in Single Crystal Pentacene. *Appl. Phys. Lett.* **2006**, *88*, 2004–2007.

References

- (451) Mas-Torrent, M.; Hadley, P.; Bromley, S. T.; Ribas, X.; Tarrés, J.; Mas, M.; Molins, E.; Veciana, J.; Rovira, C. Correlation between Crystal Structure and Mobility in Organic Field-Effect Transistors Based on Single Crystals of Tetrathiafulvalene Derivatives. *J. Am. Chem. Soc.* **2004**, *126*, 8546–8553.
- (452) Warman, J. M.; De Haas, M. P.; Dicker, G.; Grozema, F. C.; Piris, J.; Debije, M. G. Charge Mobilities in Organic Semiconducting Materials Determined by Pulse-Radiolysis Time-Resolved Microwave Conductivity: π -Bond-Conjugated Polymers versus π - π -Stacked Discotics. *Chem. Mater.* **2004**, *16*, 4600–4609.
- (453) Chandrasekhar, M.; Guha, S.; Graupner, W. Squeezing Organic Conjugated Molecules - What Does One Learn? *Adv. Mater.* **2001**, *13*, 613–618.
- (454) Rang, Z.; Haraldsson, A.; Kim, D. M.; Ruden, P. P.; Nathan, M. I.; Chesterfield, R. J.; Frisbie, C. D. Hydrostatic-Pressure Dependence of the Photoconductivity of Single-Crystal Pentacene and Tetracene. *Appl. Phys. Lett.* **2001**, *79*, 2731–2733.
- (455) Tawfick, S.; O'Brien, K.; Hart, A. J. Flexible High-Conductivity Carbon-Nanotube Interconnects Made by Rolling and Printing. *Small* **2009**, *5*, 2467–2473.
- (456) Chen, F.; Xia, J.; Ferry, D. K.; Tao, N. Dielectric Screening Enhanced Performance in Graphene FET. *Nano Lett.* **2009**, *9*, 2571–2574.
- (457) Ivetić, M.; Mojović, Z.; Matija, L. Electrical Conductivity of Fullerene Derivatives. *Mater. Sci. Forum* **2002**, *413*, 49–52.
- (458) Kaiser, A. B. Electronic Transport Properties of Conducting Polymers and Carbon Nanotubes. *Repts Prog. Phys.* **2001**, *64*, 1–49.
- (459) Percec, V.; Glodde, M.; Bera, T. K.; Miura, Y.; Shiyankovskaya, I.; Singer, K. D.; Balagurusamy, V. S. K.; Heiney, P. A.; Schnell, I.; Rapp, A.; Spiess, H. W.; Hudson, S. D.; Duan, H. Self-Organization of Supramolecular Helical Dendrimers into Complex Electronic Materials. *Nature* **2002**, *417*, 384–387.
- (460) Zang, L.; Che, Y.; Moore, J. S. One-Dimensional Self-Assembly of Planar π -Conjugated Molecules: Adaptable Building Blocks for Organic Nanodevices. *Acc. Chem. Res.* **2008**, *41*, 1596–1608.
- (461) Sun, Y.; Jiang, L.; Schuermann, K. C.; Adriaens, W.; Zhang, L.; Boey, F. Y. C.; Decola, L.; Brunsveld, L.; Chen, X. Semiconductive, One-Dimensional, Self-Assembled Nanostructures Based on Oligopeptides with π -Conjugated Segments. *Chem. - A Eur. J.* **2011**, *17*, 4746–4749.
- (462) Pisula, W.; Menon, A.; Stepputat, M.; Lieberwirth, I.; Kolb, U.; Tracz, A.; Siringhaus, H.; Pakula, T.; Müllen, K. A Zone-Casting Technique for Device Fabrication of Field-Effect Transistors Based on Discotic Hexa-Perihexabenzocoronene. *Adv. Mater.* **2005**, *17*, 684–688.
- (463) Craats, A. M. van de; Warman, J. M.; Müllen, K.; Geerts, Y.; Brand, J. D. Rapid Charge Transport Along Self-Assembling Graphitic Nanowires. *Adv. Mater.* **1998**, *10*, 36–38.
- (464) Hill, J. P.; Jin, W.; Kosaka, A.; Fukushima, T.; Ichihara, H.; Shimomura, T.; Ito, K.; Hashizume, T.; Ishii, N.; Aida, T. Self-Assembled Hexa-Perihexabenzocoronene Graphitic Nanotube. *Science* **2004**, *304*, 1481–1483.
- (465) Goldberger, J.; He, R.; Zhang, Y.; Lee, S.; Yan, H.; Choi, H.-J.; Yang, P. Single-Crystal Gallium Nitride Nanotubes. *Nature* **2003**, *422*, 599–602.
- (466) Yamamoto, Y. Electroactive Nanotubes from π -Conjugated Discotic Molecules. *Bull. Chem. Soc. Jpn.* **2011**, *84*, 17–25.
- (467) Schoonbeek, F. S.; Esch, J. H. Van; Wegewijs, B.; Rep, D. B. A.; Haas, M. P. De; Klapwijk, T. M.; Kellogg, R. M.; Feringa, B. L. Efficient Intermolecular Charge Transport in Mono- and Bithiophene Bisurea Compounds. *Angew. Chem. Int. Ed.* **1999**, *10*, 1393–1397.
- (468) Tatewaki, Y.; Hatanaka, T.; Tsunashima, R.; Nakamura, T.; Kimura, M.; Shirai, H. Conductive Nanoscopic Fibrous Assemblies Containing Helical Tetrathiafulvalene Stacks. *Chem. - An Asian J.* **2009**, *4*, 1474–1479.
- (469) Lian, T. Supramolecular Polymers of Triarylamines: Studies in Aqueous Medium and Covalent Capture of Their Self-Assemblies, Universite de Strasbourg, 2017.
- (470) Liang, T.; Collin, D.; Galerne, M.; Fuks, G.; Vargas Jentzsch, A.; Maaloum, M.; Carvalho, A.; Giuseppone, N.; Moulin, E. Covalently Trapped Triarylamine-Based Supramolecular Polymers. *Chem. - A Eur. J.* **2019**, *25*, 14341–14348.
- (471) Tzeng, B.-C.; Cao, A.; Selvan, T.; Chang, T.-Y. Polyrotaxane Frameworks Containing N,N',N''-(4,4',4''-Nitrilotris(4,1-Phenylene))Triisonicotinamide: Structural and Luminescent Properties. *CrystEngComm* **2013**, *15*, 5337.

Study of the Structure – Function Relationship of Triarylamine-Based Supramolecular Polymers

Résumé

Nous avons étudié la relation entre la structure moléculaire, l'auto-assemblage et les propriétés physiques émergentes des polymères supramoléculaires de triarylamine (TAA), en vue de leur intégration dans des dispositifs électroniques. Tout d'abord, nous avons développé le premier exemple d'électropolymérisation supramoléculaire. Ici, un champ électrique est appliqué à la fois pour déclencher la polymérisation et pour aligner simultanément les fibres en croissance entre les électrodes avec une précision remarquable. Ensuite, nous avons étudié les structures plasmoniques à base de TAA et démontré que la lumière peut se propager le long des cristaux de TAA, jusqu'à $\sim 500 \mu\text{m}$, par un mécanisme actif de guidage des ondes plasmoniques. Les mêmes dérivés du TAA peuvent également former des nanoparticules, et les résultats préliminaires montrent qu'ils présentent des propriétés plasmoniques. Enfin, nous avons comparé le transport des charges dans divers polymères supramoléculaires à base de TAA. Nous avons mené ces études sur plusieurs structures moléculaires et supramoléculaires différents. Nous avons constaté que les conductivités mesurées sont étonnamment comparables indépendamment de la longueur des chaînes alkyles et du nombre de groupes amide, ce qui est vrai pour les solutions et les gels. Dans les films minces, la présence de longues chaînes latérales réduit le contact électronique des fibres entre elles et avec les électrodes. De même, nous avons démontré que les gels TAA améliorés mécaniquement, par ROMP, conservent leurs propriétés optiques et de transport des charges locales. Enfin, nous avons découvert que les cristaux de TAA non dopés conduisent des charges, alors que le dopage est normalement nécessaire pour obtenir des auto-assemblages conducteurs de TAA.

MOTS CLÉS: chimie supramoléculaire, polymérisation supramoléculaire, triarylamine, électropolymérisation, alignement anisotrope, plasmonique, guides d'ondes, nanoparticules, électronique organique supramoléculaire

Résumé en anglais

We studied the relationship between the molecular structure, self-assembly, and the emerging physical properties of triarylamine (TAA) supramolecular polymers, aiming at their integration into electronic devices. First, we have developed the first example of supramolecular electropolymerization. Here, an electric field is applied to both trigger polymerization and simultaneously align the growing fibers between the electrodes with remarkable precision. Then, we investigated TAA-based plasmonic structures and demonstrated that light is able to propagate along TAA crystals, up to $\sim 500 \mu\text{m}$, by an active plasmonic wave-guiding mechanism. The same TAA derivatives can also form nanoparticles, and preliminary results show that they exhibit plasmonic properties. Finally, we compared charge transport in various TAA-based supramolecular polymers. We conducted these studies across several different molecular structures and supramolecular arrangements. We found that the measured conductivities are surprisingly comparable independently of the length of the alkyl chains and the number of amide groups, which is true for solutions and gels. In thin films, the presence of long side chains reduces the electronic contact of the fibers with each other and with the electrodes. Similarly, we demonstrated that mechanically enhanced TAA gels, by ROMP, retain their local optical and charge transport properties. Lastly, we discovered that un-doped TAA crystals conduct charges, whereas doping is normally necessary to obtain conductive TAA self-assemblies.

KEY-WORDS: supramolecular chemistry, supramolecular polymerization, triarylamine, electropolymerization, anisotropic alignment, plasmonics, wave-guides, nanoparticles, supramolecular organic electronics